CHALMERS UNIVERSITY OF TECHNOLOGY
Gothenburg, Sweden
www.chalmers.se

CHALMERS
UNIVERSITY OF TECHNOLOGY

PHD THESIS

We are now living in a fascinating era in which we know that the stars in the sky are orbited by planets. In this thesis, I take the reader on a cosmic quest for new worlds by introducing the process of detection and characterisation of five exoplanet systems. I describe the challenges we encounter along the way and elaborate on ways to solve them, with a special focus on the multi-dimensional Gaussian process approach for modelling stellar activity in radial velocity timeseries.

ISKRA GEORGIEVA

A Cosmic Quest for New Worlds

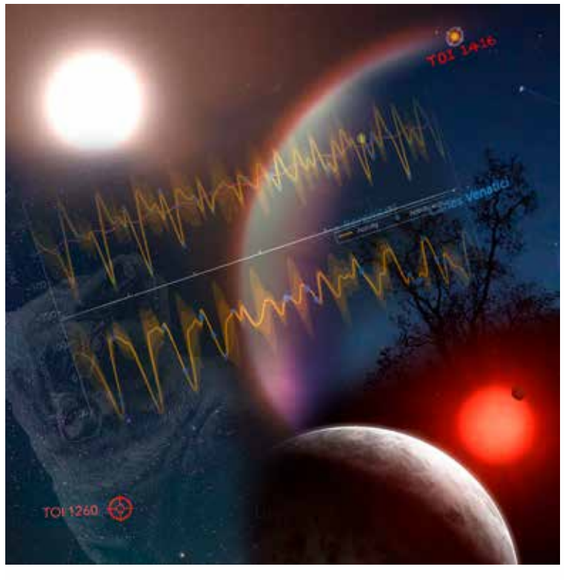

A Cosmic Quest for New Worlds

Characterising Exoplanet Signals via Radial Velocity and Transit Photometry

ISKRA GEORGIEVA

DEPARTMENT OF SPACE, EARTH AND ENVIRONMENT
CHALMERS UNIVERSITY OF TECHNOLOGY
Gothenburg, Sweden 2023
www.chalmers.se

2023

THESIS FOR THE DEGREE OF DOCTOR OF PHILOSOPHY

A Cosmic Quest for New Worlds

Iskra Georgieva

CHALMERS
UNIVERSITY OF TECHNOLOGY

Division of Astronomy and Plasmaphysics
Department of Space, Earth and Environment
Chalmers University of Technology
Gothenburg, Sweden, 2023

A Cosmic Quest for New Worlds

Iskra Georgieva

Technical Report No. 2023-5340
ISSN 0346-718X
This thesis has been prepared using LaTeX.

Division of Astronomy and Plasma physics
Department of Space, Earth and Environment
Chalmers University of Technology
SE-412 96 Gothenburg, Sweden
Phone: +46 (0)31 772 1000
www.chalmers.se

Printed by Chalmers Reproservice
Gothenburg, Sweden, June 2023

"We go about our daily lives understanding almost nothing of the world. We give little thought to the machinery that generates the sunlight that makes life possible, to the gravity that glues us to an Earth that would otherwise send us spinning off into space, or to the atoms of which we are made and on whose stability we fundamentally depend. Few of us spend much time wondering why nature is the way it is, where the cosmos came from, or whether it was always there, if time will one day flow backwards or whether there are ultimate limits to what humans can know. What is the smallest piece of matter, why we remember the past and not the future, and why there is a universe?"

- Carl Sagan

Abstract

Since the first unambiguous detection of a planet around a Sun-like star, the interest in the new and exciting field of exoplanets has grown immensely. New and exciting developments are seen at a pace unparalleled for most subfields of astronomy. In this thesis, I describe the two most successful techniques for exoplanet detection and characterisation – transits and radial velocities – and the challenges commonly encountered in extracting the planets from the data.

Transit photometry allows us to measure the planet radius, while radial velocity measurements give us the planet's minimum mass. These methods' true strength, however, manifests in their combination as it allows us to estimate the true mass, which, together with the radius, gives us the planet's bulk density. This is a powerful quantity, which allows us to construct models and make predictions about the structure and composition of a planet's interior, as well as its atmosphere. Zeroing in on the latter two is currently one of the biggest challenges for exoplanet characterisation.

I describe the process of detecting a planet in a stellar light curve, and how transits and radial velocities are modelled together in order to determine the planet parameters. This is then followed by the ideal theoretical approach, which can be used to study a system in practice. However, the current challenges in exoplanet characterisation surpass the ideal case, leading us to explore more complex models. I then discuss the biggest nemesis to planet discovery, particularly in radial velocity timeseries – stellar activity, and the problem of its often stochastic manifestation. A special focus is given to one method for its mitigation – modelling the radial velocities alongside activity indicators. This is the core concept of multi-dimensional Gaussian process regression, particularly with the quasi-periodic covariance function, which is used in a large part of this work.

Finally, the last part if the thesis shows that while the ideal planet case can sometimes be applicable for quiet stars, as is the case of the TOI-2196 system, extending to non-parametric models, such as Gaussian processes, can help us to detect planets in complicated datasets, as demonstrated by the cases of the TOI-1260, TOI-733, TOI-776 and TOI-1416 systems.

Keywords: Exoplanet, planetary systems, transits, radial velocities.

List of Publications

This thesis is based on the following publications:

[A] **I. Y. Georgieva**, C. M. Persson, O. Barragán, G. Nowak, M. Fridlund, D. Locci, E. Palle, R. Luque, I. Carleo, D. Gandolfi, S. R. Kane, J. Korth, K. G. Stassun, J. Livingston, E. C. Matthews, K. A. Collins, S. B. Howell, L. M. Serrano, S. Albrecht, A. Bieryla, C. E. Brasseur, D. Ciardi, W. D. Cochran, K. D. Colon, I. J. M. Crossfield, Sz. Csizmadia, H. J. Deeg, M. Esposito, E. Furlan, T. Gan, E. Goffo, E. Gonzales, S. Grziwa, E. .W. Guenther, P. Guerra, T. Hirano, J. M. Jenkins, E. L. N. Jensen, P. Kabáth, E. Knudstrup, K. W. F. Lam, D. W. Latham, A. M. Levine, R. A. Matson, S. McDermott, H. L. M. Osborne, M. Paegert, S. N .Quinn, S. Redfield, G. R. Ricker, J. E. Schlieder, N. J. Scott, S. Seager, A. M. S. Smith, P. Tenenbaum, J. D. Twicken, R. Vanderspek, V. Van Eylen, J. N. Winn, "Hot planets around cool stars – two short-period mini-Neptunes transiting the late K-dwarf TOI-1260". Monthly Notices of the Royal Astronomical Society, Volume 505, Issue 4, pp.4684-4701, 2021.

[B] **Iskra Y. Georgieva**, C.M. Persson, E. Goffo, L. Acuña, A. Aguichine, L.M. Serrano, K.W.F. Lam, D. Gandolfi, K.A. Collins, S.B. Howell, F. Dai, M. Fridlund, J. Korth, M. Deleuil, O. Barragán, W.D. Cochran, S. Csizmadia, H.J. Deeg, E. Guenther, A.P. Hatzes, J.M. Jenkins, J. Livingston, R. Luque, O. Mousis, H.L.M. Osborne, E. Palle, S. Redfield, V. Van Eylen, J.D. Twicken, J.N. Winn, A. Al Qasim, K.I. Collins, C.L. Gnilka, D.W. Latham, H.M. Lewis, H.M. Relles, G.R. Ricker, P. Rowden, S. Seager, A. Shporer, T. Tan, A. Vanderburg, R. Vanderspek, "TOI-733 b: a planet in the small-planet radius valley orbiting a Sun-like star". Astronomy & Astrophysics, 2023, in press.

[C] **Iskra Y. Georgieva**, Oscar Barragán, Carina M. Persson, "On the RV detection of low-mass transiting planets with multi-dimensional Gaussian processes". To be submitted.

[D] Carina M. Persson, **Iskra Y. Georgieva**, D Gandolfi, L. Acuña, A. Aguichine, A. Muresan, E. Guenther, J. Livingston, K. A. Collins, F. Dai, M. Fridlund, E. Goffo, J. S. Jenkins, P. Kabáth, J. Korth, A. M. Levine, L. M. Serrano, J. Vines, O. Barragán, I. Carleo, K. D. Colon, W. D. Cochran, J. L. Christiansen, H. J. Deeg, M. Deleuil, D. Dragomir, M. Esposito, T. Gan, S. Grziwa,

A. P. Hatzes, K. Hesse, K. Horne, J M. Jenkins, J. F. Kielkopf, P. Klagyivik, K. W. F. Lam, D. W. Latham, R. Luque, J. Orell-Miquel, A. Mortier, O. Mousis, N. Narita, H. L. M. Osborne, E. Palle1, R. Papini, G. R. Ricker, H. Schmerling, S. Seager, K. G. Stassun, V. Van Eylen, R. Vanderspek, G. Wang, J. N. Winn, B. Wohler, R. Zambelli, and C. Ziegler, "TOI-2196 b: A rare planet in the hot Neptune desert transiting a G-type star". Astronomy & Astrophysics, vol. 666, no. 10, id.A184, 15 pp, 2022.

[E] M. Fridlund, **I.Y. Georgieva**, A. Bonfanti, Y. Alibert, C.M. Persson, D. Gandolfi, M. Beck, A. Deline, S. Hoyer, G. Olofsson, T.G. Wilson, O. Barragán, L. Fossati, A.J. Mustill, A. Brandeker, A. Hatzes, H.-G. Florén, U. Simola, M.J. Hooton, R. Luque, S.G. Sousa, J.A. Egger, A. Antoniadis Karnavas, S. Salmon, V. Adibekyan, R. Alonso, G. Anglada, T. Bárczy, D. Barrado Navascues, S.C.C. Barros, W. Baumjohann, T. Beck, W. Benz, X. Bonfils, C. Broeg, J. Cabrera, S. Charnoz, A. Collier Cameron, Sz. Csizmadia, M.B. Davies, H. Deeg, M. Deleuil, L. Delrez, O.D.S. Demangeon, B.-O. Demory, D. Ehrenreich, A. Erikson, M. Esposito, A. Fortier, M. Gillon, M. Güdel, K. Heng, K.G. Isaak, L.L. Kiss, J. Korth, J. Laskar, A. Lecavelier des Etangs, M. Lendl, J. Livingstone, C. Lovis, D. Magrin, P.F.L. Maxted, A.J. Muresan, V. Nascimbeni, R. Ottensamer, I. Pagano, E. Pallé, G. Peter, G. Piotto, D. Pollacco, D. Queloz, R. Ragazzoni, N. Rando, H. Rauer, S. Redfield, I. Ribas, N.C. Santos, G. Scandariato, D. Ségransan, L.M. Serrano, A.E. Simon, A.M.S. Smith, M. Steller, Gy.M. Szabó, N. Thomas, S. Udry, V. Van Eylen, V. Van Grootel, and N.A. Walton, "Planets observed with CHEOPS – Two super Earths orbiting the red dwarf star TOI-776". Submitted to Astronomy & Astrophysics.

[F] H. J. Deeg, **I.Y. Georgieva**, G. Nowak, C.M. Persson, B.L. Cale, F. Murgas, E. Pallé, D. Godoy Rivera, F. Dai, D. R. Ciardi, J.M. Akana Murphy, P.G. Beck, C.J. Burke, I. Carleo, W.D. Cochran, K.A. Collins, Sz. Csizmadia, M. El Mufti, M. Fridlund, A. Fukui, D. Gandolfi, R.A. García, E. W. Guenther, P. Guerra, S. Grziwa, H. Isaacson, K. Isogai, P. Kábath, J. Korth, K.W.F. Lam, D.W. Latham, R. Luque, M.B. Lund, J.H. Livingston, S. Mathis, S. Mathur, N. Narita, J. Orell-Miquel, H.L.M. Osborne, H. Parviainen, P.P. Plavchan, S. Redfield, D.R. Rodriguez, R.P. Schwarz, S. Seager, A.M.S. Smith, V. Van Eylen, J. Van Zandt, J.N. Winn, and C. Ziegler, "TOI-1416: A system with a super-Earth planet with a 1.07d period". Astronomy & Astrophysics, 11 May

2023, in press.

Other publications by the author, not included in this thesis, are:

[G] K.W.F. Lam, ..., **I.Y. Georgieva**, et al, "Discovery of TOI-1260d and the characterization of the multiplanet system". *MNRAS*, 2023, 519, 1.

[H] O. Barragán, ..., **I.Y. Georgieva**, et al, "The young HD 73583 (TOI-560) planetary system: two 10-$M_\oplus$ mini-Neptunes transiting a 500-Myr-old, bright, and active K dwarf". *MNRAS*, 2022, 514, 2.

[I] J. Šubjak, ..., **I.Y. Georgieva**, et al, "TOI-1268b: The youngest hot Saturn-mass transiting exoplanet". *A&A*, 2022, 661, A107.

[J] L.M. Serrano, ..., **I.Y. Georgieva**, et al, "A low-eccentricity migration pathway for a 13-h-period Earth analogue in a four-planet system". *Nature Astronomy*, 2022, 6.

[K] A.M.S. Smith, ..., **I.Y. Georgieva**, et al, "K2-99 revisited: a non-inflated warm Jupiter, and a temperate giant planet on a 522-d orbit around a sub-giant". *MNRAS*, 2022, 510, 4.

[L] K.W.F. Lam, ..., **I. Georgieva**, et al, "GJ 367b: A dense, ultrashort-period sub-Earth planet transiting a nearby red dwarf star". *Science*, 2021, 375, 6572.

[M] V. Van Eylen, ..., **I. Georgieva**, et al, "Masses and compositions of three small planets orbiting the nearby M dwarf L231-32 (TOI-270) and the M dwarf radius valley". *MNRAS*, 2021, 507, 2.

[N] R. Luque, ..., **I. Georgieva**, et al, "A planetary system with two transiting mini-Neptunes near the radius valley transition around the bright M dwarf TOI-776". *A&A*, 2021, 645, 41.

[O] M. Fridlund, ..., **I. Georgieva**, et al, "The TOI-763 system: sub-Neptunes orbiting a Sun-like star". *MNRAS*, 2020, 498, 4503.

[P] I. Carleo, ..., **I. Georgieva**, et al, "The Multiplanet System TOI-421 – a warm Neptune and a super puffy mini-Neptune transiting a G8 V star in a visual binary". *AJ*, 2020, 160, 114 .

[Q] G. Nowak, ..., **I. Georgieva**, et al, "K2-280 b - a low density warm sub-Saturn around a mildly evolved star". *MNRAS*, 2020, 497, 4423.

[R] P. Bluhm, ..., **I. Georgieva**, et al, "Precise mass and radius of a transiting super-Earth planet orbiting the M dwarf TOI-1235: a planet in the radius gap?". *A&A*, 2020, 639, 132.

[S] J. Šubjak, ..., **I. Georgieva**, et al, "TOI-503: The First Known Brown-dwarf Am-star Binary from the TESS Mission". *AJ*, 2020, 159, 151.

[T] D. Hidalgo, ..., **I. Georgieva**, et al, "Three planets transiting the evolved star EPIC 249893012: a hot 8.8-$M_\oplus$ super-Earth and two warm 14.7 and 10.2-$M_\oplus$ sub-Neptunes". *A&A*, 2020, 636, 89.

[U] M.R. Díaz, ..., **I. Georgieva**, et al, "TOI-132 b: A short-period planet in the Neptune desert transiting a V = 11.3 G-type star". *MNRAS*, 2020, 493, 973.

[V] L.D. Nielsen, ..., **I. Georgieva**, et al, "Mass determinations of the three mini-Neptunes transiting TOI-125". *MNRAS*, 2020, 492, 5399.

[W] C.X. Huang, ..., **I. Georgieva**, et al, "TESS Spots a Hot Jupiter with an Inner Transiting Neptune". *ApJL*, 2020, 892, 7.

[X] K.W.F. Lam, ..., **I. Georgieva**, et al, "It Takes Two Planets in Resonance to Tango around K2-146". *ApJ*, 2020, 159, 120.

[Y] C.M. Persson, ..., **I. Georgieva**, et al, "Greening of the brown-dwarf desert. EPIC 212036875b: a 51 M_J object in a 5-day orbit around an F7 V star". *A&A*, 2019, 628, 64.

Acknowledgments

First and foremost, I am immensely grateful to my supervisor, Carina Persson, and my co-supervisor, Malcolm Fridlund, for giving me the chance to catch a glimpse at what a career in academia is like. But even more importantly, for letting me get closer to the stars and the wonderful alien worlds that lie beyond – indeed a childhood dream of mine that I never thought could come true. I thank Carina and Malcolm for their unwavering support and guidance throughout the entire duration of my research. Their constructive feedback and encouragement, often expressed in ensuring me that I do, in fact, have what it takes to do this, have been invaluable in shaping both my work and personality. I will always fondly remember our adventures together – from our first conference together to Los Angeles, to our last epic one in Las Vegas and the Grand Canyon.

I would also like to thank my collaborators in KESPRINT for helping me feel a part of a big, supportive, and friendly team, and the opportunities and experiences that come with that. I am also a proud member of the "KESPRINT poetry writing subcommittee", and one of my most fun memories of the PhD is writing Malcolm's hilarious 70th birthday poem and performing it together with my co-conspirators.

I thank the COVID boredom for facilitating my friendship with Oscar Barragán. Oscar and I had a lot of fun times, and I even learnt some important and useful stuff! This PhD would without a doubt have been a very different experience if it hadn't been for his existence.

A heartfelt thanks goes to my family for their support, even when they don't understand or care much about my research topic. Your love and encouragement when I rambled on about my science problems were instrumental in keeping me sane and motivated.

Last but certainly not least, I want to express my appreciation to all my friends near and far, even if your name is not specifically listed here, who have been there to celebrate the highs and commiserate the lows. I thank you for your hilarious memes, ridiculous gifs, and making me feel smart, rare, and special. You help me remember to look at things from the outside, and how amazing what I do really is.

Thank you all for being a part of this wild ride and making it a memorable journey.

Acronyms

ARIEL	Atmospheric remote-sensing infrared exoplanet large survey
AU	Astronomical unit
CHEOPS	Characterising exoplanet satellite
CoRoT	Convection, rotation and planetary transits
CCF	Cross-correlation function
EB	Eclipsing binary
ESPRESSO	Echelle spectrograph for rocky exoplanets and stable spectroscopic observations
EXPRES	Extreme precision spectrograph
FOV	Field of view
GP	Gaussian process
QP	Quasi-periodic
HabEx	Habitable exoplanet observatory
HARPS	High accuracy radial velocity planet searcher
HST	Hubble space telescope
JWST	James Webb space telescope
LUVOIR	Large UV/Optical/Infrared surveyor
MCMC	Markov chain Monte Carlo
PLATO	Planetary transits and oscillations
RV	Radial velocity
TESS	Transiting exoplanet survey satellite

Definitions

This section contains a non-exhaustive list of notation and constants in SI units commonly used throughout this work. The values are as per Prša et al. (2016).

- $M_\star$ – stellar mass
- $R_\star$ – stellar radius
- M_p – planet mass
- R_p – planet radius
- $M_\odot$ – Solar mass, 1.988×10^{30} kg
- $R_\odot$ – Solar radius, 6.957×10^{8} m
- $M_\oplus$ – Earth mass – 5.971×10^{24} kg
- $R_\oplus$ – Earth radius – 6.3781×10^{6} m
- M_J – Jupiter mass – 1.898×10^{27} kg
- R_J – Jupiter radius – 7.1492×10^{7} m
- AU – Astronomical unit – 1.496×10^{11} m
- pc – parsec – 3.086×10^{16} km

	Spectral class	Mass, $M_\odot$	Radius, $R_\odot$	Effective temperature, K	Fraction from all main-sequence stars, %
Early → Late	O	≥ 18	≥ 7.2	≥ 31,500	~0.00003
	B	2.3 - 18	2.2 – 7.2	10,000 - 31,500	0.13
	A	1.7 - 2.3	1.75 – 2.2	7,300 - 10,000	0.6
	F	1.07 - 1.7	1.13 - 1.75	6,000 - 7,300	3
	G	0.9 - 1.07	0.83 - 1.13	5,300 - 6,000	7.5
	K	0.58 - 0.9	0.6 - 0.83	3,900 - 5,300	12
	M	0.08 - 0.58	≤ 0.6	2,300 - 3,900	75

Table 1: Basic stellar spectral classification. The values and ranges are as per Pecaut & Mamajek (2013) and are approximate.

Contents

CHAPTER 1

Introduction

For thousands of years the Solar system planets were the only planets whose existence humanity was aware of. Iconic images of the planets and their moons obtained by famous Solar system missions, like the Pioneer, Mariner, Viking, Voyager and Cassini probes, have inspired generations of young minds. But our knowledge of planetary physics was completely based on the bodies gravitationally bound to our Sun.

This began to change only a few decades ago when the family of known planets extended beyond the Solar system, when the first planets around a pulsar[1] were unambiguously confirmed in 1992 (Wolszczan & Frail 1992), followed by the discovery of the first planet around a Sun-like star in 1995 (Mayor & Queloz 1995). The latter was awarded the Nobel prize in physics in 2019. Since these first discoveries, the field of exoplanetology has exploded.

But why did it take so long?

While a complete answer to this question is multi-faceted, possibly the simplest one is that exoplanets are billions of times fainter than their host stars. Adding the fact that they are small and far away, to this day, they are ex-

[1] A compact stellar remnant, which emits electromagnetic pulses of radiation, mostly in radio.

tremely difficult to find by direct imaging, which is the first technique for astronomical observations that became available[2]. We had to wait for the invention of other sophisticated indirect methods and even longer, for the technological leaps needed to realise them. What is more, we can now not only detect the planets, but can also begin to characterise them by finding out information about them, the systems they inhabit, their environment and history, by observation and modelling. These advances will eventually enable us to answer questions regarding the place of the Solar system, and specifically the Earth, in the tapestry of the current exoplanet census.

This thesis focuses on the two currently most common and successful exoplanet discovery techniques, what information they provide that allows us to characterise the planets, and the modelling strategies we adopt to accomplish this.

But first things first...

1.1 What is an exoplanet?

It may come as a surprise, but coming up with a general but strict definition for a planet is not straight-forward.

Definitions

Starting from the official definition of a planet in the Solar system adopted by the International Astronomical Union (IAU) in 2006 [3], in order for a body to be classified as a planet, it must fulfil three requirements:

1. The body orbits the Sun.
2. It has sufficient mass for its self-gravity to overcome rigid body forces so that it assumes hydrostatic equilibrium (nearly round) shape.
3. It has cleared the neighbourhood around its orbit.

[2] Galileo Galilei was the first observational astronomer who used a telescope to observe the heavens in the early 17th century.

[3] The specific resolutions can be consulted at: `https://www.iau.org/static/resolutions/Resolution_GA26-5-6.pdf`

In the context of exoplanets, however, this definition needs to be extended and generalised since it addresses only the lower limit of a planet's mass. This is not practically useful since current observations cannot yet detect dwarf planets[4] around distant stars, and thus a distinction between exoplanets and smaller bodies is not yet as pertinent as the upper planetary mass bound. The IAU recommendation from 2003 is that the limit between sub-stellar bodies (brown dwarfs) and regular planets should be taken to be the calculated mass limit required for the onset of deuterium burning, i.e. $\sim 13\ M_{\rm J}$. This has, however, been challenged by a number of authors. Chabrier et al. (2014), for example, state that this mass limit should be fluid owing to the differing formation mechanisms between brown dwarfs (BDs) and gas giant planets. Hatzes & Rauer (2015) and Persson et al. (2019), on the other hand, point out that an upper planetary mass limit should be significantly higher than $13\ M_{\rm J}$ since the evolutionary path of BDs and giant planets is similar, with the only significant difference being the very brief period of deuterium burning in the early stages. In this work, I will use $\sim 75\ M_{\rm J}$ as an upper limit for bodies of planetary nature, which roughly corresponds to the onset of hydrogen burning.

Planet categories

The over 5300[5] exoplanets discovered to date (including confirmed planets with both mass and radius, and statistically validated ones) show us that planets can be categorised by radius[6] (Borucki et al. 2011), and mass (Charbonneau et al. 2009; Stevens & Gaudi 2013) in the following way:

- Terrestrial, Earth-like – $R < 1.25\ R_\oplus$, $M < 2\ M_\oplus$
- Super-Earths – $R \sim\ 1.25 - 2\ R_\oplus$, $M \sim\ 2 - 10\ M_\oplus$
- Neptunes – $R \sim\ 2 - 6\ R_\oplus$, $M \sim\ 10 - 100\ M_\oplus$
- Giant planets – $R \sim\ 6 - 15\ R_\oplus$, $M \sim\ 0.3 - 75\ M_J$

[4] IAU definition: a celestial body that orbits the Sun, has enough mass to assume a nearly round shape, has not cleared the neighborhood around its orbit, and is not a moon.
[5] Data from `https://exoplanetarchive.ipac.caltech.edu/` as of 9 March 2023.
[6] The measured planet radius is the (solid) core plus atmosphere (if opaque at observing wavelength).

These categories are broad and are by no means strict definitions. Different authors may use different bounds, and other physically motivated ones exist. Moreover, the transition from one planet type to another is smooth and it is thus often difficult to distinguish between them. One such important blurred region is the one between the upper end of the super-Earths and the lower end of the Neptunes, as described below. But first, let us have a look at some basic characteristics of the different planet classes.

Earth-like planets are considered to have an Earth-like composition, i.e. silicate rock and metals, similar to the terrestrial planets in the Solar system (Mercury, Venus, Earth and Mars). Apart from a metallic core and a silicate mantle, terrestrial planets may also feature secondary, possibly outgassed, atmospheres.

Super-Earths share common characteristics with the lower end of the Neptune-size planets, the so-called **mini-Neptunes** ($2 - 3\ R_\oplus$). Apart from not having an analog in our Solar system, these two groups share the inconvenience that their composition cannot be uniquely constrained solely by knowing their bulk densities (i.e. mass and radius). They are inferred to range from abundant in H-He on the low density end, through H_2O-rich, to being terrestrial (solid surface) without or with an atmosphere, at the high density end.

Neptunian planets, as the name suggests, are considered to be similar to Uranus and Neptune, containing significant mass fractions of ices, rock, as well as H and He. It should be noted, however, that this is a very broad category and the **mini-Neptunes** have more in common with the Super-Earths than with their larger counterparts. Some of the smaller mini-Neptunes are also sometimes thought to be the predecessors of Super-Earths, transitioning into the latter after losing some or all of their atmosphere.

Finally, **giant planets** – Jupiters, super-Jupiters and brown dwarfs – are loosely constrained to have $> 50\%$ H-He by mass with atmospheres accreted from the original nebula (i.e. primary atmospheres).

Planet nomenclature

The names of exoplanets have two parts – 1) a word or abbreviation, usually followed by numbers, and 2) a lower-case letter. The first part is the name of the star – either its catalogue name or the name of the instrument or facility that discovered it. Stars can have multiple designations as they may exist

in different catalogues, but famous catalogue names (e.g. GJ or HD) take precedence over instrument names, wherever possible.

The second part of the name, the letter, tells of the order in which the planet was discovered. The first planet that is discovered in a system is given the letter b, followed by letters c, d, and so on, for every subsequent planet found in the system. Often the inner-most planet is found first, and it is given the letter b. If multiple planets are discovered at the same time, they are given letters b, c, d, and so on, in order of their distance from the star. This, however, is not always the case.

The names of planets orbiting binary (or multiple) stars can be somewhat confusing. For example, a planet orbiting the binary Kepler-16AB is named Kepler-16(AB)b.

1.2 Exoplanet detection

The nearest exoplanet to Earth orbiting the closest star to the Sun is Proxima Centauri b. One would think that it being located at roughly 1.3 pc away from us would allow us to use a direct technique, like imaging, to study it. Unfortunately, since it is so close to its star that it takes 11.2 days to complete an orbit around it, it is drowning in the star's glare. And this is true for planets several AU[7] away from their stars. In fact, if we base our expectations of exoplanets on the Solar system planets, we would find many surprises. One of them is that a large fraction of the exoplanets found to date have similar, and even shorter orbital periods to Proxima Centauri b. Thus, at least for now, we mainly rely on indirect methods to detect and study exoplanets.

Below I outline the two most well-known such methods, which have yielded about 95% [8] of the confirmed exoplanets known to date, and represent the foundation of this work. These are the **transit** and the **radial velocity** (RV) methods. Other successful detection methods exist, the most note-worthy of which, in decreasing order of exoplanet yield, are microlensing (Bond et al. 2004), direct imaging (Boccaletti 2011), transit timing variations (TTVs, Ballard et al. 2011) and astrometry (Sahlmann et al. 2013; Curiel et al. 2022). These will not be described in detail in this work and the interested reader is

[7] The Astronomical Unit is the average distance from the Earth to the Sun.

[8] This value, together with abundant information about exoplanets can be found at: `https://exoplanetarchive.ipac.caltech.edu/`

referred to the references in the text for more thorough descriptions.

Neither transit nor RV is a novel method – both were discussed by (Struve 1952) – but it was not until the end of the last century when they were successfully utilised for exoplanet detection. The field of exoplanets has exploded since then, thanks to concentrated effort in improving the instrumentation and growing interest since the early discoveries.

The transit method

The fundamental idea of a transit is simple and most of us have likely seen a transit at least once. In fact, a transit is a special case of an eclipse, such that a smaller body obscures the light from a larger one when it passes in front of it. If the inclination of a planet's orbit around its host star is close to 90° in the plane of the sky (i.e. edge-on orbit has $i = 90°$), then the presence of this planet can be inferred by detecting the periodic dips of stellar flux caused by the partial occultation of the stellar disc (see Fig. 1.1). Intuitively, the missing flux, i.e. the transit depth, can thus be related to the size of the planet blocking the star. If we do not know the size of the star, we will at least know the size ratio of the planet and the star, $R_\mathrm{p}/R_\star$. Thankfully, nowadays we usually have relatively precise estimates of stellar radii through spectroscopy, combined with parallax from astrometry, and photometry. This, combined with the periodicity of the dips, gives us the first fundamental parameters: the planet's radius, orbital period and distance from the star.

Unfortunately, a transit can only be seen by an observer if the orbital geometry of the system is favourable. Given interstellar distances, a transit would be visible if the portion of the celestial sphere swept out by the planet's shadow is in the line of sight of an observer on Earth. Assuming the orbital inclination of planets is random and that the planet radius is small compared to the stellar radius such that $R_\mathrm{p} \ll R_*$, the probability of a transit is $\approx 0.0046\,(R_\star/R_\odot)\,(1\mathrm{AU}/a)$, where $R_\odot$ is the radius of the Sun, and a – the semi-major axis of the planet's orbit (Chapter 2.1). So if a planet orbits a Sun-like star at a distance of 1 AU, the probability of a transit is just 0.46%, while at the distance of Jupiter (5.2 AU), this probability drops to 0.09%. More generally, this expression shows that the planets we are most likely to detect using the transit method, as shown in Fig. 1.2, are hot planets in close orbits to their stars. Furthermore, a transiting Jupiter around a star the size of the Sun (a G-type star) would cause a dip of about 1%, while an Earth-size

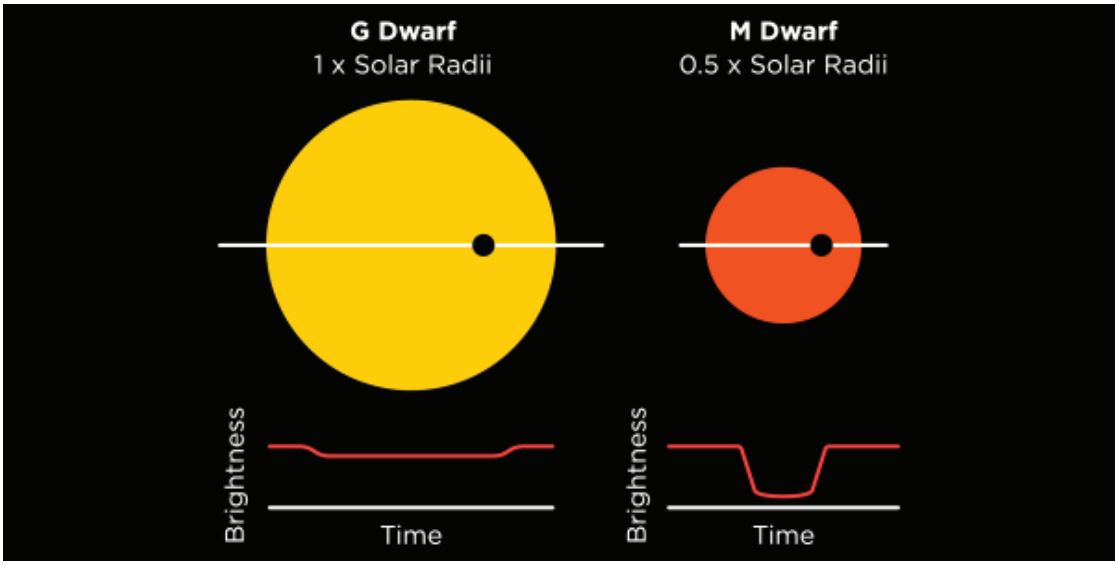

Figure 1.1: Illustration of a planetary transit. Comparison between a planet of the same size transiting a Sun-like star (left) and a smaller, less bright star (right). This difference in transit depth demonstrates why it is easier to detect smaller planets around less massive stars. Image credit: The Center for Astrophysics | Harvard & Smithsonian.

planet would only result in about 0.01% loss of total flux. The square of the stellar radius is inversely proportional to the transit depth (see Chapter 2), so smaller, less luminous stars, such as M and K stars (Table 1), would cause a much larger reduction in flux (Collier Cameron 2016), as illustrated in Fig. 1.1.

Transit surveys

Consequently, to overcome this low geometric probability, photometric transit surveys are designed to observe a large number of target stars simultaneously. The first successful projects for transit detection started at the beginning of the century, namely the Transatlantic Exoplanet Survey (TrES, Alonso et al. 2004), the Hungarian Automated Telescope (HATNet, HATSouth Bakos et al. 2004, 2013), Wide-Angle Search for Planets (WASP, Pollacco et al. 2006), and the Kilodegree Extremely Little Telescope (KELT, Pepper et al. 2007). These are ground-based surveys, which led to the discovery of hundreds of short-period ($P_{\rm orb} < 10$ days) exoplanets transiting bright stars.

The discoveries yielded by these missions, however, are mostly of hot gi-

ant planets, the so-called hot Jupiters (Fig. 1.2). This is because the Earth's atmosphere makes it hard to detect planets smaller than Neptune from the ground – changes in temperature and air density can cause fluctuations in the brightness of the star. Since the blocked flux (transit depth) is related to $(R_P/R_*)^2$, smaller planets can be detected from the ground if they orbit smaller, less bright stars (Fig. 1.1). Indeed, this was shown to be the case with two more ground-based searches focusing on M-dwarfs – MEarth (Nutzman & Charbonneau 2008; Irwin et al. 2015) and TRAPPIST (Gillon et al. 2011).

Atmospheric noise, however, is not the only reason why small planets around hotter, including Sun-like, stars, continued to evade detection. Ground-based observations are limited by daylight and weather conditions, and thus preclude uninterrupted observations from being conducted. Furthermore, space is not contaminated by light pollution from cities and other light sources, which results in clearer and more precise observations. Finally, a wider range of wavelengths is accessible from space, including ultraviolet and infrared, which are not observable from the ground due to atmospheric absorption. Observations at wavelengths different from optical can yield precious information of the exoplanet's atmosphere, composition, and temperature.

Despite the fact that space missions are significantly more costly to develop, launch and maintain compared to ground-based telescopes, the above reasons gave strong enough grounds for the onset of space-based transit photometry. Thus, the first exoplanet-dedicated space telescope – Convection, Rotation and planetary Transits [9](CoRoT, Baglin et al. 2006) – came to the rescue, and led to the discovery of 40 extrasolar planets. CoRoT was operational from 2006 to 2012 and perhaps its most notable discovery is CoRoT-7b – the first rocky super-Earth with a measured radius.

The most productive mission to date, however, is the Kepler Space Telescope[10]. The nominal mission (Borucki et al. 2010), hereafter Kepler, was launched in 2009, prior to which only ∼50 exoplanets were known. It observed 150,000 stars in the direction of the constellations Cygnus and Lyra continuously for four years. The discoveries made during this time made it possible to obtain information about the distribution and frequency of exoplanets and some key orbital and planetary parameters, thus allowing for the

[9]`https://sci.esa.int/corot`
[10]`https://www.nasa.gov/mission_pages/kepler/main/index.html`

first statistical studies in exoplanet science to be conducted. The data showed that there are more planets than stars in our galaxy, that multi-planet systems are common, and often feature super-Earths and mini-Neptunes (Borucki 2017).

Unfortunately, by 2013 Kepler had lost two of its reaction wheels. The loss of the second one nearly put an end to the mission. Thankfully, a proposal adapting the "crippled" spacecraft to the new situation was accepted in 2014. This gave the beginning to the K2 mission (Howell et al. 2014), which utilised the same field of view (FOV) with high precision photometry as Kepler, but now with a different pointing strategy: the telescope began to monitor independent fields in the ecliptic plane. Unfortunately, this rebirth came at the cost of a substantial noise increase resulting from complex spacecraft pointing adjustment manoeuvres necessitated by the loss of the reaction wheels.

The K2 fields were called campaigns and each lasted about 80 days. This meant that K2 would not be able to find long-period planets but it offered another advantage: the stars K2 observed were brighter than the ones in Kepler's field. This made conducting radial velocity follow-up observations on K2 transiting candidates much more likely, and is the reason why, to this day, about 2100 of the planets from Kepler do not have mass estimates.

Kepler was retired when it ran out of fuel in 2018, yielding 3251 confirmed or validated exoplanets from Kepler and K2 combined[11].

Currently, there are two ongoing dedicated exoplanet missions in space. The Transiting Exoplanet Survey Satellite[12] (TESS, Ricker et al. 2015) and the CHaracterising ExOPlanet Satellite[13] (CHEOPS, Benz et al. 2021). The primary mission of TESS ended in July, 2020 and is currently in its second extended mission phase. Unlike the space-based surveys mentioned above, TESS has observed most of the sky since its launch in April 2018. This means that TESS observes many bright stars, which are easy to follow-up. Each field is monitored for only about 28 days and thus contains mostly short-period planets. Many of the TESS fields are observed multiple times, however, and over a dozen of longer period planets (> 50 days) have also been found (e.g. Orell-Miquel et al. 2023), some only via single transit events (e.g. Orell-Miquel et al. 2023) and possibly in the habitable zones of their stars (i.e. where water

[11] 2708 from Kepler and 543 from K2. ∼3000 more await confirmation. Data as of 10 March 2023, from `https://exoplanetarchive.ipac.caltech.edu/`

[12] `https://tess.mit.edu/`

[13] `https://www.esa.int/Science_Exploration/Space_Science/Cheops`

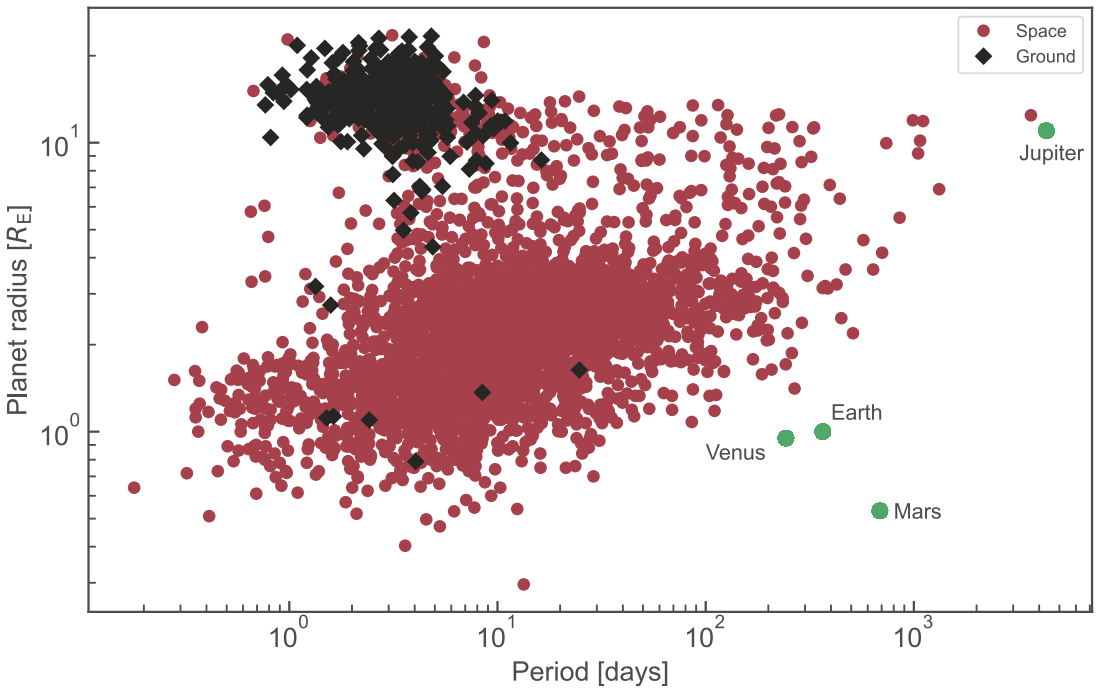

Figure 1.2: A period-radius plot of transiting planets detected from space (red) and from ground surveys (black). The sensitivity of ground-based surveys to short-period giant planets, i.e. hot Jupiters, is clear. The few small planets found using such surveys orbit small, faint stars. The black diamonds in the vicinity of $\sim$1 $R_\oplus$ correspond to the famous and heavily studied TRAPPIST-1 planets (Gillon et al. 2017).

can exist in liquid form). Some of the shorter period planets may still be found in the habitable zones of their stars, but those stars would then be low-mass ones. TESS has so far led to the confirmation of over 300 new exoplanets, with thousands more in the works.

While CHEOPS (launched December, 2019) also employs the transit method, it differs from all of the above in the sense that its primary mission is to follow-up already known exoplanets around nearby bright stars, and to improve the precision of their parameters. The highest priority planets are super-Earths up to Neptunes. Nevertheless, CHEOPS is responsible for a number of new planet discoveries (e.g. Leleu et al. 2021).

An upcoming mission with high hopes from the scientific community is PLAnetary Transits and Oscillations[14] (PLATO, Rauer et al. 2014) on track for a 2026 launch. As a transit survey mission, it will detect new planets around bright stars, with a focus on small planets in the habitable zones of Sun-like stars. It will have asteroseismology capabilities thanks to which we will obtain much lower uncertainties on the stellar parameters. Thus, PLATO will provide planet parameters of unprecedented precision (3% uncertainty on radius), as well as the age of the planetary systems (10% precision). The latter has been one of the major degenerating factors in accurately characterising exoplanets and determining the processes that sculpted the systems into the way we find them today.

The transit method is utilised by another important mission that should be mentioned here – the James Webb Space Telescope (JWST, Beichman et al. 2014). With about six times the light-collecting area of the Hubble space telescope (HST), this space observatory is the HST successor and it observes primarily in the near- to mid-infrared as opposed to visible-ultraviolet. But while JWST is intended to answer many questions about both the local and the distant (most red-shifted/oldest) universe, its role in the context of exoplanets is not to detect new and re-observe known ones like the above-described missions, but rather to study the atmospheres of known and promising planets. The method used to accomplish this is transmission spectroscopy, which uses in- and out-of-transit observations of a host star to obtain a planet's atmospheric spectrum. One of the key JWST findings so far is the first ever detection of carbon dioxide in the atmosphere of an exoplanet, namely WASP-39 b (JWST Transiting Exoplanet Community Early Release Science Team et al.

[14] `https://sci.esa.int/web/plato`

2023). JWST is also equipped with coronographs, which are able to block out the intense light from a host star and thus, in some special cases, reveal direct images of planets – a very rare accomplishment (Carter et al. 2022).

The radial velocity method

To describe the radial velocity (RV) method, it would help to recall Newton's third law: "for every action, there is an equal and opposite reaction". As is well known, planets orbit stars[15] due to gravitational attraction, the strength of which is dictated by the masses of the bodies involved. In other words, just like planets are pulled on by their stars, so the stars are pulled on by the planets they are orbited by. This results in a scenario where a planet and a star orbit a point of equilibrium, their mutual center of mass, or barycenter, causing the star to wobble around this center of mass. Since we cannot directly see the planet, we can try and measure the line-of-sight (radial) component of the star's velocity. This is done by using a technique called Doppler spectroscopy which involves comparing the measured wavelengths of well-known spectral lines to the rest wavelengths of the same spectral lines measured in a laboratory. If the wavelengths are shifted towards the red end of the spectrum, corresponding to a positive RV, this indicates that the star is moving away from us; conversely, when the wavelengths are blue-shifted, the RV is negative, meaning that the star is moving toward us (Fig. 1.3). The periodicity and magnitude of the RV can tell us if a planet orbits the star.

To detect the RV of a star induced by the presence of a planet, we need spectrographs with precision of about 0.01-100 $\mathrm{m\,s^{-1}}$ depending on the mass and period of the planet we are trying to detect. To illustrate, Jupiter induces a RV variation on the Sun of 11.2 $\mathrm{m\,s^{-1}}$ at its distance of 5.2 AU ($P_{\mathrm{orb}} = 11.9$ years). If Jupiter was instead in a 3-day orbit, similar to the early exoplanet discoveries, the corresponding RV amplitude would be $\sim 150\ \mathrm{m\,s^{-1}}$. Looking at the Earth, the RV in its current orbit is about 0.01 $\mathrm{m\,s^{-1}}$ which goes up to 0.6 $\mathrm{m\,s^{-1}}$ if we moved the Earth to an orbit of 1 day. The take-away from this example is that the RV method, like the transit method, is biased towards giant planets in short orbits, as evident from Fig. 1.4 because the induced RV variation is larger if the planet orbits closer to the star. A more in-depth ex-

[15] In some cases planets may be ejected form their orbits due to collisions, or gravitational instabilities of their orbits, and are thus not associated with any particular star system. These are referred to as "rogue" planets.

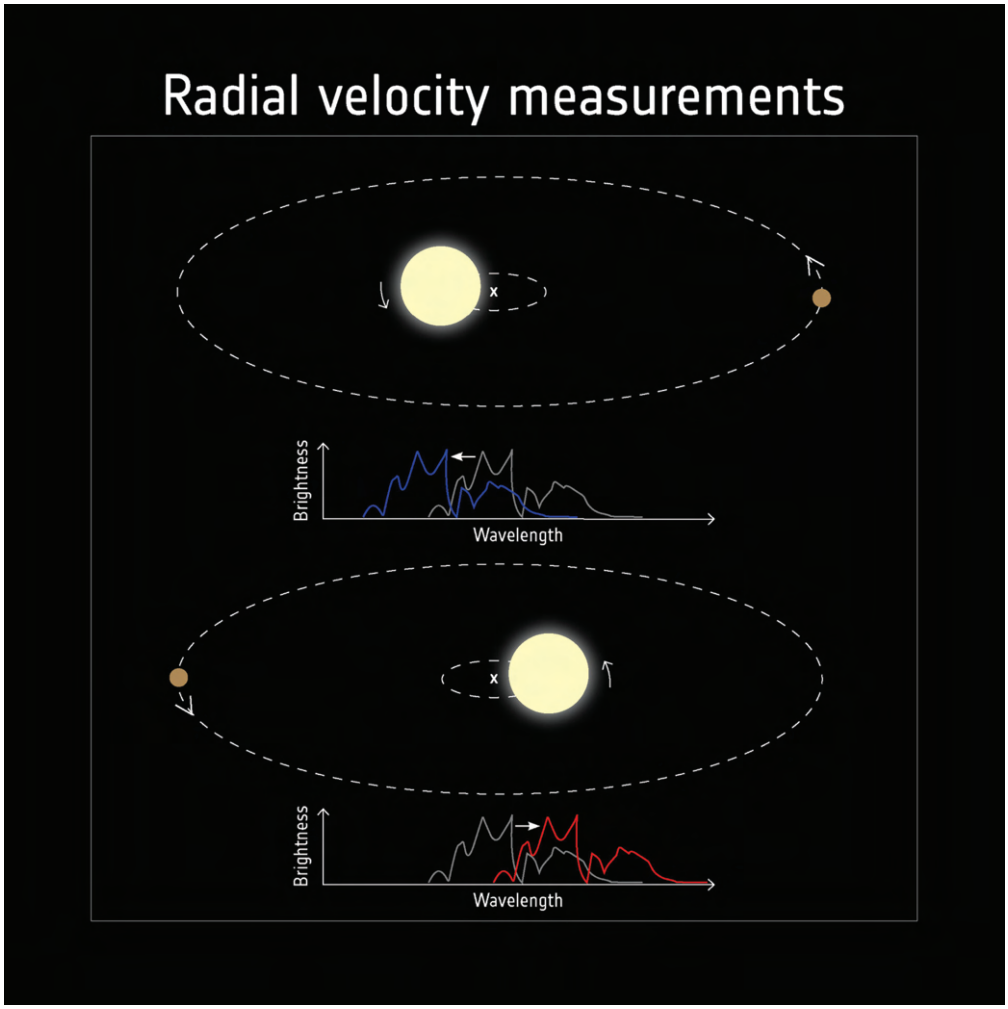

Figure 1.3: The Doppler shift of spectral lines. When the radial component of a star's motion is toward the observer, the spectral lines are blueshifted. Conversely, when the star moves away from the observer, the lines are redshifted. Image credit: ESA.

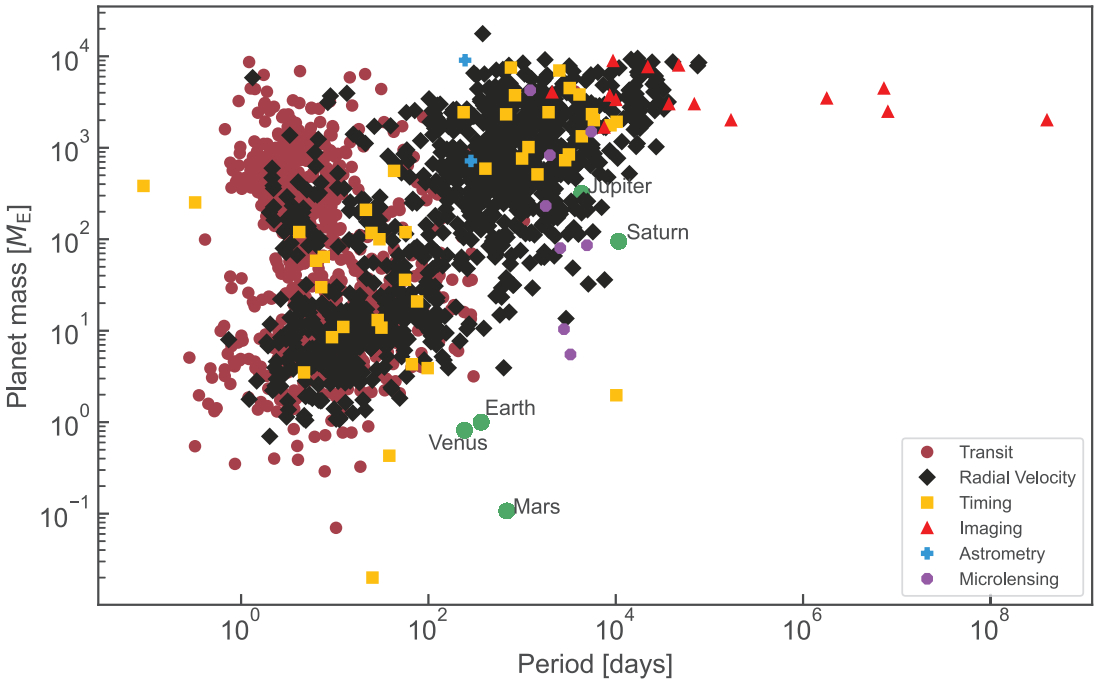

Figure 1.4: Period-mass plot of all planets detected with various methods, which also have a mass estimate (whether as part of the detection, or as a follow-up effort). A large number of the planets in Fig. 1.2 are not found here due to the fact that many of the transiting planets were discovered by the Kepler mission, which observed stars too faint to follow-up with Doppler spectroscopy. The second thing clear from this plot is that cold Jupiters are in fact more common than the hot Jupiters (see text). This feature cannot be observed in Fig. 1.2 due to observational biases inherent to the transit method. It can also be seen that the planets detected via direct imaging are several AU away from their stars. Astrometry has so far contributed only two to the known planets but many more are expected in the coming years. Finally, as evident also in Fig. 1.2, the bottom right regions are nearly empty. This demonstrates the fact that our detection methods are not yet sensitive to small, long-period planets, such are planets in the habitable zones of Sun-like stars.

planation of the mechanics of this approach, as well as limitations and caveats, will be discussed in the next chapter.

To date (9 March 2023), the RV method is responsible for 1029 exoplanet discoveries[16], including the first planet in orbit around a Sun-like star (Mayor & Queloz 1995). This planet was 51 Pegasi b (or 51 Peg b) – a Jupiter-mass planet in a 4.2-day orbit around the 1.1 $M_\odot$ star, 51 Pegasi, in the constellation of Pegasus. Before this, there were a number of potential discoveries using the same technique which could not be verified at the time due to insufficient and suboptimal quality of the data. Some of those were later confirmed once additional data became available (e.g. Campbell et al. 1988; Latham et al. 1989; Hatzes & Cochran 1993).

As Fig. 1.4 shows, the majority of RV-detected planets are in the high-mass Jupiter range due to detection limitations inherent to the method. Since the early RV discoveries the precision of RV instrumentation, as well as data reduction and modelling techniques have been continuously improving, allowing for the mass determination of ever smaller planets at wider orbital separations. The lower end of the mass range in Fig. 1.4 exists thanks to second generation spectrographs with precision of $\sim$1 $\mathrm{m\,s^{-1}}$ like HARPS and HARPS-N (Mayor et al. 2003; Cosentino et al. 2012), and more recently ESPRESSO (Pepe et al. 2010, 2020) and EXPRES (Jurgenson et al. 2016), among others, which both approach the cm-level precision needed to detect Earth-like planets in Earth-like orbits.

As we have seen, the RV method has fallen behind the transit method in terms of exoplanet yield. But what is, in fact, crucial here, is that the two methods go hand-in-hand. When the information derived from them is combined (planet radius from transits, and planet mass from RV), we are able to obtain an estimate of a planet's bulk density, and to finally formulate theoretical models about the structure and composition of exoplanets. However, the major difficulty in this effort is the fact that only about 20% of the planets with radii discovered to date have any kind of indication about their mass, with two-thirds of these being giant planets. Much fewer still, have uncertainties on their parameters low enough to allow characterisation.

[16]Data from the NASA Exoplanet Archive, `https://exoplanetarchive.ipac.caltech.edu/docs/counts_detail.html`

1.3 A myriad of worlds and architectures

Exoplanet diversity

The discovery of 51 Peg b came as a shock to the astronomical community because it was believed that gas giant planets form far away from their stars. While understandably met with skepticism initially, the planetary nature of 51 Peg b was soon confirmed. The floodgates were opened and over the next decades the surprising discoveries kept on pouring in.

Once hard to fathom, we now know that closely packed multi-planet systems are not uncommon: e.g. Kepler-11 (Lissauer et al. 2011) with up to six planets inside Mercury's orbit, and TRAPPIST-1 (Gillon et al. 2011) – an ultra-cool dwarf orbited by seven transiting planets with comparable to Earth's sizes and masses, where two or three of them could potentially be habitable. Extreme environments like the ultra short period (USP) planets, characterised by orbital periods of $\lesssim$ 1 day and often featuring very high densities ($\gtrsim$ 9 g cm^{-3}, Essack et al. 2023; Espinoza et al. 2020) are now a well-established subclass of planets. Another stark example are planets orbiting short-period eclipsing binaries, i.e. circumbinary planets, with PH1b (or Kepler-64 b, Schwamb et al. 2013) known to orbit an eclipsing binary bound to another binary system, making it the first (and so far only) confirmed transiting planet orbiting in a quadruple star system. Adding to these the growing number of discovered planets with extreme spin-orbit misalignment (e.g. 55 Cnc e, Bourrier & Hébrard 2014), and the systems involving multiple planets in resonance (e.g. TOI-178 with six transiting planets, five of which in resonance, Leleu et al. 2021), the worlds beyond our own are as numerous as they are different.

All of these individual milestones taken together reveal a never before suspected exoplanet diversity: the single biggest discovery in the field of exoplanets.

Demographics

To put these findings into perspective and to enable us to jump from analyses of individual planets to studying similarities and differences between systems, we turn to population studies. Exoplanet demographics is thus an integral part of exoplanet science. It is intimately related to exoplanet characterisation and

aims at understanding the distribution and frequency of exoplanets over a wide range of parameters, helping us to answer questions about planet formation and evolution.

A non-exhaustive list of important findings, as summarised by Gaudi et al. (2021), includes:

- The occurrence rate of giant planets around solar-type stars increases with distance from the host stars up until the snow line, after which point it starts to drop (Cumming et al. 2008);
- The frequency of giant planets which orbit at a distance smaller than ∼2.5 AU, increases with stellar mass and metallicity (Fischer & Valenti 2005);
- The discovery of the hot Neptune desert – the apparent lack of exoplanets with masses $\sim 0.1\ M_{\rm J}$ and periods less than 2–4 days (Mazeh et al. 2016);
- "Peas in a pod" - clustering of planets of similar sizes in planetary systems (Weiss et al. 2018);
- Decreasing host star metallicity with the occurrence of small planets (Petigura et al. 2018).

The small-planet radius valley and its possible origins

The element of exoplanet demographics that pertains most closely to the topic of this work, however, is to do with the types of exoplanets that are not found in our Solar system. As indicated for the first time by microlensing studies (Sumi et al. 2010), and soon after confirmed by results from both HARPS statistical surveys (Howard et al. 2010), and first results from the Kepler mission (Borucki et al. 2011), small planets ($< 4R_\oplus$), and in particular super-Earths and mini-Neptunes ($1 \lesssim R_\oplus \lesssim 4$, Petigura et al. 2013) are much more common than giant planets, especially with periods of < 50 days.

Looking more closely at this population, one of the most prominent results from Kepler requires a special mention. Specifically, the so-called radius gap (or radius valley) – the apparent scarcity of planets in the 1.5 and 2 $R_\oplus$ range (Fulton et al. 2017; Van Eylen et al. 2018, 2021), resulting in a bi-modal distribution of the $1 \lesssim R_\oplus \lesssim 4$ planets with $P_{\rm orb} < 100$ days. Thus, two clear

populations arise: the super-Earths of $1 \lesssim R_\oplus \lesssim 1.5$, and the mini-Neptunes of $2 \lesssim R_\oplus \lesssim 3$. Models suggest that for close-in planets with $a \lesssim 0.1$ AU this is likely due to XUV/X-ray photoevaporation – intense radiation from the host star causes mini-Neptunes to lose their envelopes on timescales of $\sim$ hundreds of Myr, eventually leaving bare cores (Owen & Wu 2013; Lopez & Fortney 2014).

Another plausible mechanism which provides an explanation for the radius gap is core-powered mass loss (Ginzburg et al. 2016, 2018; Gupta & Schlichting 2019, 2020). In this case, the atmospheric mass loss is due to a combination of stellar bolometric luminosity and a planet's gravitational binding energy. The latter is converted into thermal energy during the planet's accretion phase and is released outwards from the core and radiated away through the atmosphere, resulting in hydrodynamic escape. This theory produces similar observable demographic effects on the exoplanet population as photoevaporation, but it operates on very different timescales – on the order of Gyr. It is an active field of research (e.g., Rogers et al. 2021) and work on estimating the more dominant of the two effects and the scenarios in which each is more likely to prevail is ongoing. One key obstacle to achieving this is the relatively low number of known planets orbiting young stars. There are ongoing efforts towards enriching the current census with young planets (e.g. Newton et al. 2019; Wood et al. 2023), which will hopefully break the degeneracy between photoevaporation and core-powered mass loss in the coming years.

Recently, another idea intended to explain the radius valley, which does not require any physical mechanisms beyond standard planet formation models, has gained traction. Planets containing a significant fraction of water in one phase or another, i.e. water worlds, may be the missing link between the planets below the gap and the ones above it. According to Zeng et al. (2021) planets with equilibrium temperatures higher than 900 K and masses lower than 20 $M_\oplus$ can have their sizes explained by compositions dominated by water ice, without the need for substantial gas envelopes. This suggests that the distribution of sub-Neptune planets can be described by the following three types: rocky planets, water worlds with small amount of gas, and water worlds with a large amount of gas. The first two types are responsible for the two peaks in the radius distribution, and the latter being on the larger side of the sub-Neptunes.

In line with this result, Luque & Pallé (2022) then demonstrated that for M

dwarfs the radius gap is not observed. Instead a density gap separates rocky from water-rich exoplanets, with the latter being found in their current relatively highly irradiated orbits via type I migration from beyond the snow line. Luque & Pallé (2022) further indicate that their conclusions can be extended to hotter stars but were unable to conclusively do so due to a lack of data. A number of studies claiming discoveries of planets consistent with water worlds have recently been made by e.g. Diamond-Lowe et al. (2022); Cherubim et al. (2023); Piaulet et al. (2023), with the latter also emphasising the not so firm separation between rocky and volatile-rich planets. While the above results further affirm Luque & Pallé (2022)'s findings, Rogers et al. (2023) raise caution by pointing out that mass and radius are insufficient to determine the compositions of many sub-Neptunes. They add that currently super-Earths do appear to be more common around mature, more-luminous stars, in turn indicating that thermally-driven atmospheric escape cannot be neglected just yet.

In other words, as the above examples and discussion show, there is a wealth of trends, some well-established, others so far only suspected, in places we did not expect to find any. Thus, the answers to many fundamental questions are, unfortunately, not yet within our grasp. We are still unable to give answers to questions like "How (un)common is our Solar system?" and "How common are planets in general?". The reasons for this are beyond enumeration but range between the biases due to the sensitivities of our detection methods, the reliability and representativeness of the current exoplanet census, insufficient information about the hosts, as well as the difficulty associated with combining the results from different surveys.

Nevertheless, TESS and CHEOPS continue to add new members to the ocean of planets, as well as to improve their radii and ephemerides. The Gaia space observatory (Gaia Collaboration et al. 2016, 2018, 2021) holds great significance to the study of exoplanets in the greatly improved precision it has brought to the parameters of the planet hosting stars, particularly the stellar radii. Gaia has truly been a game changer since the flaws in our understanding of the planets are inextricable from the flawed knowledge of the stellar hosts, as the next chapters will show. Together with the much anticipated yield of some tens of thousands of previously unknown cold Jupiters (Perryman et al. 2014), Gaia continues to be a most valuable player in the study of exoplanets.

JWST's impressive performance thus far and the long-awaited secrets regarding exoplanet atmospheres it will continue to unveil will hopefully be followed by upcoming facilities, like the Atmospheric Remote-sensing Infrared Exoplanet Large-survey (ARIEL, Tinetti et al. 2021). The latter will allow us to further improve our current understanding of exoplanet atmospheres. PLATO and the microlensing-utilising Roman Space Telescope (Roman, Spergel et al. 2015), as well as exciting new direct imaging surveys, e.g. HabEx (Gaudi et al. 2020), LUVOIR (The LUVOIR Team 2019), LIFE (Quanz 2019), on the other hand, will finally put planets in the most under-explored regions of parameter space and allow us to study them in unprecedented ways.

CHAPTER 2

A closer look at the theory behind transits and radial velocities

2.1 Orbital elements

In orbiting systems, all bodies are bound in orbits around a mutual center of mass called a barycenter. There are six fundamental orbital elements[1], which describe a Keplerian orbit. These are eccentricity, e; the semi-major axis, a; longitude of the ascending node, Ω; argument of pericenter, ω; inclination, i; and true anomaly, ν. A schematic of such an orbit and its elements is shown in Fig. 2.1.

Ω, ω, ν and i are angles which describe the orientation of the orbit with respect to the reference frame, while a and e describe the size and shape of the orbit.

- e – the orbital eccentricity ranges between 0 and 1 for closed elliptical orbits, where a circular orbit corresponds to $e = 0$.
- a – the semi-major axis is half the major (long) axis of an ellipse. For a

[1] Different texts differ slightly in which and/or the number of elements they present.

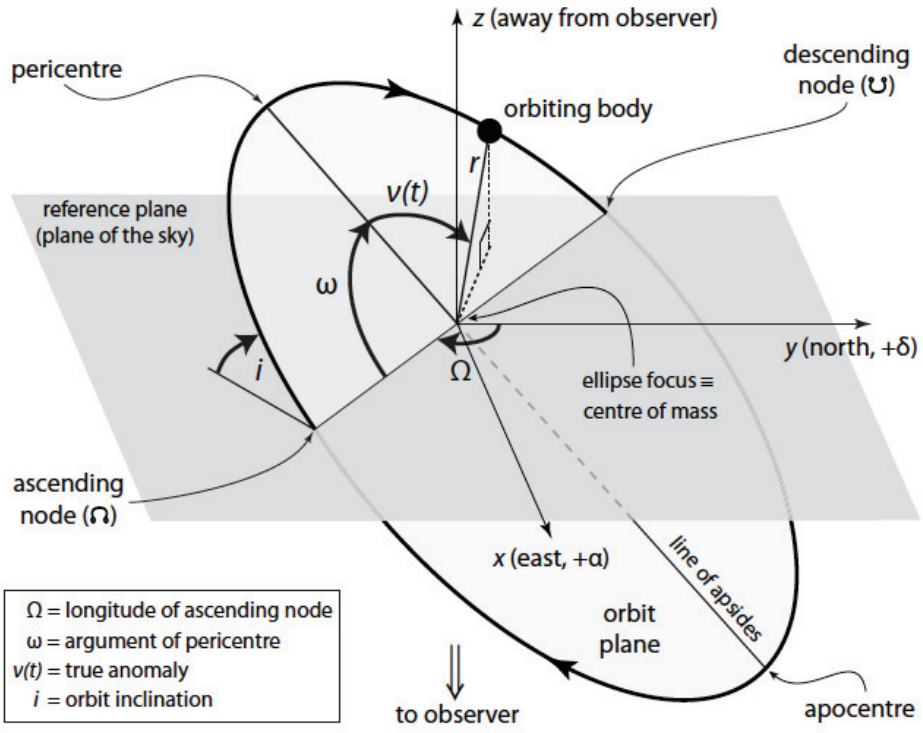

Figure 2.1: The mechanics of an elliptical orbit, including the six fundamental orbital elements: the semi-major axis, a; eccentricity, e; true anomaly, ν; argument of pericenter, ω; longitude of the ascending node, Ω; and inclination, i. The reference plane represents the plane of the sky. Image credit: Perryman (2018).

circular orbit, i.e. at $e = 0$, a is simply given by the radius of the circle.

- Ω – the longitude of the ascending node is measured in the reference plane and marks the angle between a reference line to the node at which the orbital plane crosses the reference plane and the orbiting body moves away from the observer.

- ω – the argument of pericenter is the angle between pericenter (where the orbiting body is closest to the barycenter) and the ascending node. ω is undefined for circular orbits and is assigned a value of $\pi/2$ in such cases.

- i – the inclination of the orbit with respect to the reference plane. $i = 0°$ corresponds to a face-on orbital orientation, i.e. perpendicular to the plane of the sky.

- ν – the true anomaly is the angle between the position of the orbiting body and the pericenter and thus defines the body's location in the orbit at any given time.

2.2 Transit method

This section presents some theoretical background for the transit method. The information is not meant to be exhaustive and is to serve as a basic guide to the most crucial elements of this technique. More thorough descriptions can be found in texts from e.g. Seager & Mallén-Ornelas (2003) and Winn (2010).

Transit observables

There are four quantities that can be derived from photometric stellar time series (light curve) containing transits. As shown in Fig. 2.2, these are the period, P – the time between two consecutive transits, the transit depth, given by the amount of missing stellar flux during a transit; ΔF, the total transit duration between first and fourth contact points; t_{T}, and the transit duration between contact points 2 and 3; t_{F}, i.e. when the planet is fully contained in the stellar disc.

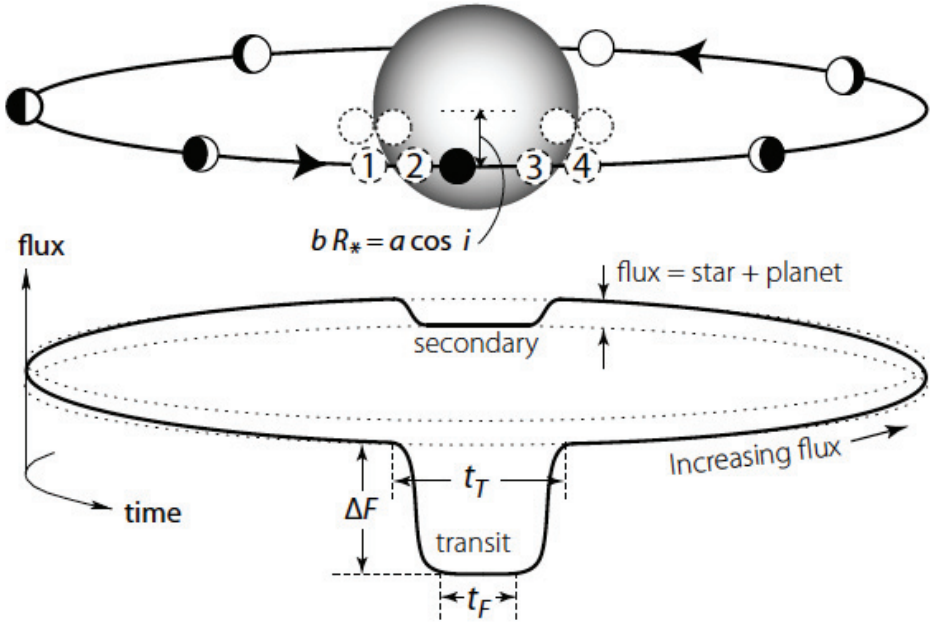

Figure 2.2: Diagram illustrating the mechanics of transits and occultations. Contact points 1-2 correspond to the planet ingress, while points 3-4 – to the egress. The total transit duration, t_{T}, is between points 1 and 4, while t_{F} is between 2 and 3. The impact parameter, b, is 0 if the planet transits straight through the middle of the star, corresponding to the longest transit duration and steepest transit flanks. b grows up to a maximum value of 1 the farther from the middle of the stellar disc a planet transits. The least amount of flux is received during a transit, and the genuine stellar flux is recorded during the secondary eclipse, i.e. when the planet goes behind the star. During the rest of the orbit, the planet shows different amounts of its face as it is illuminated by the star, reaching a maximum total flux just before it goes behind the star, when its face is fully illuminated. Image credit: Perryman (2018).

If we assume that $M_{\rm p} \ll M_\star$, the period, P, together with the mass of the star ($M_\star$), obtained via e.g. spectroscopic observations and stellar modelling, can give us the semi-major axis of the orbiting body using Kepler's third law:

$$a \simeq \left(GM_* \left(\frac{P}{2\pi} \right)^2 \right)^{1/3} \tag{2.1}$$

The amount of light periodically blocked when an opaque object passes in front of a star, or the ratio of flux observed during a transit, ΔF, to the flux with no transit, F, gives the squared planet to star radius ratio:

$$\frac{\Delta F}{F} \simeq \left(\frac{R_{\rm p}}{R_\star} \right)^2 \tag{2.2}$$

For brevity, the ratio $\Delta F/F$ will hereafter be referred to as ΔF. This equation also illustrates the fact that solely from the missing flux, we only know the planet radius relative to the stellar radius, once again highlighting the importance of knowing the host star well.

The transit duration represents the fraction of the period during which the sum of the radii of star and planet is greater than the projected distance between the center of the two bodies. Adapted from Seager & Mallén-Ornelas (2003), this can be expressed in the following way:

$$t_{\rm T} = \frac{P}{\pi} \arcsin \left(\frac{R_*}{a} \left\{ \frac{\left[1 + (R_p/R_*)\right]^2 - b^2}{1 - \cos^2 i} \right\}^{1/2} \right) \tag{2.3}$$

The form of this equation can be further simplified by defining the impact parameter, b, as $b = a \cos i / R_*$, which for the case of a planet in a circular orbit passing through the middle of the stellar disc is set to zero, since $\cos i = 0$, when $i = 90°$. In addition, if $R_\star$ and thus $R_{\rm p}$ are known, as per Perryman (2018), eq. 2.3 then becomes:

$$t_{\rm T} \simeq 13 \left(\frac{M_\star}{M_\odot} \right)^{-1/2} \left(\frac{a}{1 \text{ AU}} \right)^{1/2} \left(\frac{R_\star}{R_\odot} \right) \text{ hours} \tag{2.4}$$

This translates to ~ 25 hours for a planet at the distance of Jupiter, and ~ 13 hours at the distance of Earth.

The geometry of a transit, together with the aforementioned parameters, is

illustrated in Fig. 2.2.

Other physical quantities

The stellar density, $\rho_\star$, is an important parameter that can be used diagnostically to test if the value obtained from the transit light curve is consistent with the spectroscopically derived one. Alternatively, in the absence of a reliable spectroscopic estimate, a high signal-to-noise transit light curve can be used to derive a value for $\rho_\star$. If the value suggests a giant host star, depending on the fraction of missing flux, the transiting companion can be discarded as a less interesting (from a planet hunting perspective) massive body.

Assuming the planet is much smaller and less massive than the host star, the stellar density, $\rho_\star$, can be calculated as:

$$\rho_\star \approx \frac{3\pi}{\mathrm{G}} \frac{1}{P^2} \left(\frac{a}{R_\star} \right)^3 \tag{2.5}$$

If, on the other hand, the stellar parameters are well constrained and known to be reliable, an alternative equation taking into account t_F and t_T can be used to estimate the period in the cases of suspected single transit events (see Perryman 2018).

Another useful quantity that can be calculated solely from transit photometry is the planet's equilibrium temperature, T_eq. If the stellar effective temperature[2], T_eff, is known either through spectral classification tables or stellar models, A is the planet's Bond albedo[3], and assuming efficient heat redistribution and isotropic planetary emission, then:

$$T_\mathrm{eq} = T_\mathrm{eff}(1 - A)^{1/4} \sqrt{\frac{R_\star}{2a}} \tag{2.6}$$

Finally, the insolation received at the planet, F_P, can be calculated via the following expression:

$$F_\mathrm{p} = \left(\frac{R_\star}{R_\odot} \right)^2 \left(\frac{T_\mathrm{eff}}{T_\odot} \right)^4 \left(\frac{\mathrm{AU}}{a} \right)^2 F_\oplus, \tag{2.7}$$

[2]The temperature of a blackbody that would emit the same total amount of electromagnetic radiation.

[3]The portion of the incident stellar radiation on a body that is reflected back out into space.

where $R_\odot$ and $T_\odot$ are the radius and effective temperature of the Sun, and $F_\oplus = 1360$ W m^2 is the insolation received at Earth.

Challenges and caveats

Limb darkening

Limb darkening is the phenomenon which causes stars to appear brighter towards the middle of the disc and darker (redder) towards the edge (limb). When an observer looks straight on towards the centre of a stellar disc, the angle of the line of sight to the center of the disc is zero. However, looking towards the limb of a star, this angle increases, and the observer is only able to see into shallower layers of the stellar atmosphere, as compared to looking at the center. Because deeper layers are generally hotter than shallow layers, photons from the limb appear redder and photons originating from areas closer to the centre appear bluer.

The effect limb darkening has on transits is such that it causes real transits to have rounded bottoms, as opposed to flat bottoms if considering a uniform stellar disc. This blurs the distinction between the different contact points (Fig. 2.2), most prominently affecting the impact parameter, b, and thus misinterpreting the transit depth and other parameters. Planets in close orbits are most strongly impacted by this phenomenon because their transit durations are very short resulting in very round-bottomed transit shapes. Planets more widely separated from their stars take a much longer time to transit through the center of the star and thus have longer, flatter bottoms.

There are a number of limb darkening laws[4] that have been developed by different authors in an attempt to account for this effect. Perhaps the most popular one, which balances computational time and complexity, is the quadratic law.

For a more detailed discussion regarding limb darkening in the context of transits, see e.g. Mandel & Agol (2002).

Stellar activity in light curves

Stellar activity, and most notably starspots, can also affect the transit depth, and thus the estimate of the planet radius.

[4]It is worth noting that the limb darkening laws are not really "laws" in the full sense of the word, but rather fitting formulas.

Two cases are worth mentioning in this context, as discussed in Pont et al. (2008). The first is when the star is spotted and the transit chord passes through the spots. In the cases of very clear transits, for e.g. large planets around bright stars, a bump in flux can be seen when a transiting planet crosses a spot. However, in most cases, the signal-to-noise ratio and/or the observing cadence of the light curve are insufficient to allow for this to be recognised. Thus, the observer is unaware that the radius of the planet may be underestimated due to the planet blocking a smaller portion of the overall flux.

The second case is when the star is heavily spotted but the planet does not cross any of the spotted regions. This scenario has the opposite effect: the planet radius is overestimated because the planet blocks a bright, unspotted region of the stellar disc, which in turn contributes a larger fraction of the total flux as compared to spotted regions.

Nevertheless, starspots have an important role in understanding the rotation and differential rotation of stars, and in the cases when a transiting planet crosses a spot, it may be possible to derive information about the stellar obliquity with respect to the planet's orbit (Sanchis-Ojeda et al. 2013).

Sources of false positive transit detections

The secondary eclipse, or occultation, as illustrated in Fig. 2.2, can be used as an important diagnostic tool to help avoid misidentifying a transiting companion as a planet. As described by Collier Cameron (2016), only the largest and most irradiated planets can produce occultations visible in a light curve, and the larger the eclipsing body, the larger the occultation. Similar to the depth of a transit, a light curve with a very prominent secondary dip often means that the eclipsing body is likely self-luminous, thus pointing to an eclipsing binary[5] (EB) scenario. On the other hand, based on Kepler data Bryson et al. (2013) showed that about 40% of transits are caused by background eclipsing binaries when looking in the direction of the galactic plane, dropping to 10% when moving to larger latitudes. This demonstrates that identifying the true source of a transit is a crucial part of vetting planet candidates in photometric data.

Usually it is easy to distinguish between a planetary transit and a transit

[5] An eclipsing binary is a system of two stars orbiting each other in such a way that one star passes in front of the other from the viewer's perspective.

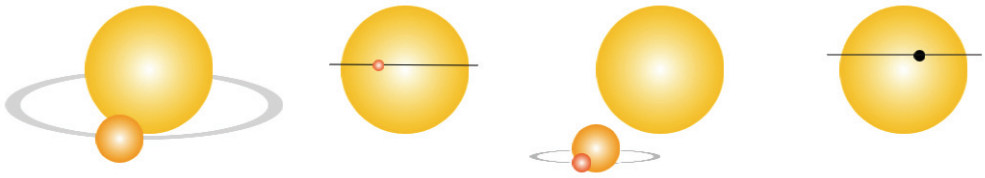

Figure 2.3: Four possible scenarios which could cause a transit-like feature. From left to right: a grazing stellar binary, a red dwarf transiting a star that is much larger, a blended eclipsing binary, a genuine transiting planet. For more details, see text.

of a smaller, less bright star because the depth of the latter would be much higher than the former. Sometimes, however, a bright background star, not necessarily physically bound to the EB, can add to the total flux received from the target, diluting the transit event and causing it to appear shallower, concealing the non-planetary nature of the transit source. Alternatively, a grazing EB with stars of similar mass will produce a small dip in brightness, which can be mistaken for a planetary transit. In such a scenario the occulted area would be much smaller than the area of the occulting object. Another possible scenario is when a small dim star transits in front of a larger, brighter star. Since Jupiter is the size of a late-type M-dwarf, $\sim 0.1\ M_{\odot}$, the transit depth caused by such a star transiting a Sun-like star may easily be mistaken for a Jupiter-sized planet. These typical examples of false-positive detections are illustrated in Fig. 2.3.

Luckily, there are tests that are employed by pipelines to reveal these scenarios. Some common examples are the even-odd transit depth, where a significant difference between even and odd transit depths and durations could point to an EB; the photocenter in and out of transit shift test checks if the target star is the true transit source. Alternatively, follow-up photometric adaptive optics observations (e.g. Ciardi et al. 2015), as well as observations at different wavelengths (e.g. Parviainen et al. 2019), can be performed to rule out false positive scenarios.

2.3 Radial velocity method

As briefly described in Sect. 1.2, all the bodies in an orbital system orbit the barycenter, including the central body. In the RV case, the body of interest is the star, which executes a Keplerian orbit around the barycenter, and can be described by Fig. 2.1. The line-of-sight (radial) component of the orbital velocity, i.e. the **radial velocity**, v_r of the star is given by

$$v_{\mathrm{r}} = v_{\mathrm{z}} + K[\cos(\omega + v) + e\cos\omega], \tag{2.8}$$

where v_z is the systemic velocity, i.e. the radial component of the proper motion of the barycenter with respect to the observer, and K is the **radial velocity semi-amplitude**,

$$K = \left(\frac{2\pi G}{M_\star^2 P}\right)^{1/3} \frac{M_{\mathrm{p}} \sin i}{\sqrt{1-e^2}} \tag{2.9}$$

This is the case for a two-body system. It is common, however, that planets are found in multi-planet systems. In such a case, the star is still the gravitationally dominating body and the interaction between the relatively low-mass planets can be neglected. To solve for the Keplerian orbit of each planet, we would then have

$$v_{\mathrm{r}} = v_z + \sum_{i=1}^{N} K_i \left[\cos\left(\omega_i + \nu_i\right) + e_i \cos\omega_i\right], \tag{2.10}$$

where N is the number of planets, and each planet i has its own set of parameters.

The uncertainties in M_{p} are generally dominated by the noise of the dataset, which also dictates the precision of P and K. If the star is not well understood so that the stellar parameters are not well-constrained, the uncertainty in $M_\star$ can further deteriorate the precision of M_{p}.

Furthermore, from eq. 2.9 we can see that K scales linearly with M_{p} but is inversely proportional to both $P^{1/3}$ and $M_\star^{2/3}$. This explains why longer-period planets induce a smaller K to more massive stars, which also demonstrates why the first planets to be found were indeed close-in giant planets.

Combining the two methods

A RV timeseries can give information about $P_{\rm orb}$, K and e. Estimating the planetary mass, $M_{\rm p}$, however, depends on the inclination, i (eq. 2.9), which cannot be found from RV data. This, and the fact that most planets are not transiting, is why the majority of RV-discovered planets only have an $M_{\rm p} \sin i$ estimate, i.e. the planet's minimum mass. The i can, however, be found from transit observations via the impact parameter, b, as mentioned in the previous section.

Here, it is worth reiterating that combining the planet radius and inclination from transits with the minimum mass from RV observations gives us the planet's bulk density, which allows us to perform a first-step planet characterisation. By comparing the position of the planet on a mass-radius diagram with composition models, we can make predictions about the planet's composition and internal structure.

Finally, with the two methods together, we are able to extract the following important parameters: T_0 (the mid-transit time), P, e, ω, $R_{\rm p}/R_\star$, $a/R_\star$, i, and K. These can help us derive one more physical parameter, the planet's surface gravity, $g_{\rm p}$. Originally from Southworth et al. (2007):

$$g_{\rm p} \equiv \frac{GM_{\rm p}}{R_{\rm p}^2} = \frac{2\pi}{P} \frac{\sqrt{1-e^2}K}{R_{\rm p}^2/a^2 \sin i}. \tag{2.11}$$

In the not-so-rare cases when we do not know the host star as well as needed, the right side of this equation allows us to eliminate the dependence on the stellar parameters and thus avoid any uncertainty associated with them. It is also worth noting that, since $R_\star$, unlike $M_\star$, can be determined with good accuracy, the planet's bulk density can be found by combining $g_{\rm p}$ and $R_\star$ (Rodríguez Martínez et al. 2021).

Alternatively, we can use the standard equation for Newton's law of universal gravitation, i.e. the middle part of eq. 2.11, in the cases when we do have information about the star, and compare the two estimates for $g_{\rm p}$ as a coherence check.

Challenges

RVs are measured by comparing the wavelengths of Doppler-shifted spectral features of a stellar photosphere to the rest wavelengths of said features, λ_0,

such that

$$\frac{\Delta\lambda}{\lambda_0} = \frac{v_r}{c}, \tag{2.12}$$

where $\Delta\lambda$ is the difference between the shifted and rest wavelengths of a spectral line, and c is the speed of light. In practice this is done by comparing an observed spectrum with a template spectrum, where the latter is shifted in velocity space so that it matches the former. The better the correlation between the spectra, i.e. the more features that can be precisely matched between the two spectra, the better the achieved RV precision.

This leads us to the first challenge.

Spectral lines strength

For the above process to be successful, the star must have prominent spectral features. Hotter, and thus more massive stars, have fewer, broader and shallower spectral lines since the number and depth of spectral lines decrease with increasing $T_{\rm eff}$. Stars with a high rotational period, i.e. fast rotators, are also difficult to study due to rotational broadening of the lines. This is caused by the redshifting of the light from the star's receding hemisphere, while the light from the approaching hemisphere is blueshifted. Finding the position of the centroid makes the detection of Doppler shifts in such lines challenging. In contrast, cooler, metal-rich[6] stars produce many deep and narrow lines, which are much easier to study (Hatzes 2016).

Activity in spectroscopic data

As in the case with photometric surveys, stellar spectroscopy is also significantly affected by different sorts of stellar activity, also referred to as stellar jitter. There are variable sources for this activity, which are driven by processes taking place in different regions of stars. Stellar activity is the biggest nuisance in the search particularly for sub-Neptune-sized planets since it can conceal or even emulate the weaker planet-induced signals. I outline some common groups of activity sources following Dumusque et al. (2011).

Granulation of the stellar surface (for stars with convective shells) is caused

[6]In astronomy, elements different from hydrogen and helium are referred to as metals.

by convection in the star's outer layers. These can have lifetimes of minutes to a few days, depending on the size of the granules. This is a pattern familiar from the surface of the Sun and is caused by hot, bright parcels (the granules) rising to the top, surrounded by darker regions where the gas has cooled, sinking back into the interior. The effect is that the stellar surface is dominated by the granules, which move toward the observer, resulting in a net convective blueshift. The RV jitter caused by this effect depends on the size of the granules.

Stellar oscillations represent vibrations or pulses in brightness caused by pressure waves in the stellar interior rebounding at the surface. This phenomenon lasts for a few tens of minutes (Bedding et al. 2001).

Both granulation and oscillations cause an RV jitter of a few $\mathrm{m\,s^{-1}}$ and can be mitigated by employing a suitable observing strategy (Dumusque et al. 2011).

Stellar jitter is, however, dominated by active surface regions such as starspots, plages and faculae[7]. These are magnetically driven, with field lines inhibiting the convection process, thus preventing these regions from manifesting the aforementioned net blueshift. This results in the overall stellar RV varying with stellar rotation as these features rotate in and out of view. As expected, the amplitude of the RV variation resulting from active surface regions changes during a stellar activity cycle. As shown by Meunier et al. (2010), in the case of the Sun this is 40 $\mathrm{cm\,s^{-1}}$ during solar minimum, and 140 $\mathrm{cm\,s^{-1}}$ during solar maximum. This is expected to be similar for Sun-like stars, but late type stars, like cool K and M dwarfs, tend to be more magnetically active (e.g., Reiners et al. 2010; Andersen & Korhonen 2015) and the aforementioned values are expected to be higher.

[7]Spots are cooler, while plages and faculae are hotter than their surroundings.

CHAPTER 3

From photons to worlds

3.1 Finding transits in light curve data

A major setback in exoplanet detection is the presence of systematics (red noise) in the timeseries photometry. This noise has an instrumental and spacecraft environment-related origin and is very much a factor in the exoplanet detection effort. Well-established data preprocessing pipelines developed by the Kepler and TESS teams, as well as alternatives provided by the community, generate stellar light curves with common instrumental systematics as well as dilution from nearby sources removed (e.g. Smith et al. 2012; Stumpe et al. 2012; Jenkins et al. 2016). These light curves go through rigorous and multi-stage testing before they are made available to the public and are in most cases of optimal quality. One can, however, also extract their own light curves from the raw pixel data using simple aperture photometry[1] with a custom aperture. This may be required in cases when the default option is not the optimal one, e.g. in crowded fields, or a bright companion contributing flux to the aperture. The so extracted custom light curves can then be

[1] Aperture photometry is the summing up all the pixel values as a function of time in a specific aperture.

detrended using a variety of techniques.

While red noise is generally taken care of at the preprocessing stage, the light curves still contain stellar activity of the periodic and aperiodic kind, in the form of brightness variations and stellar surface structures. This is useful in the cases when the nature of the stellar activity is of interest, e.g. when the stellar rotation period is identifiable and thus easy to determine. However, this is only considered a nuisance signal when trying to extract the signals corresponding to any transiting planets. Adverse effects resulting from stellar rotation, eruption events, star spots, pulsations, among others, together with the actual light curve precision achieved, are the main reasons for missing small planets. The "temper" of the star, thus, presents a significant challenge, and a substantial effort in accounting for it has been put in through the years since the first transit detection by Henry et al. (2000) and Charbonneau et al. (2000). Techniques involve detrending using the Savitzky-Golay high-pass filter (Savitzky & Golay 1964), polynomial (Gautier et al. 2012) or median filter (Tal-Or et al. 2013), wavelets (e.g., Jenkins et al. 2010), or Gaussian process (GP) regression (e.g., Aigrain et al. 2015), among others.

Once all the signals which are not of interest to the transit hunter are removed, the time comes to move on to the core goal of light curve analysis. In terms of exoplanets, this is to detect new planets and analyse the size and shape of an exoplanet transit in order to obtain the candidate's radius and orbital period. Due to different scenarios that can cause a false positive detection (Sect. 2.2), combined with the low probability of a transit actually occurring, hundreds of thousands of light curves need to be studied for every genuine planet. Based on these constraints, to find the needle in the haystack, we utilise transit detection algorithms (TDAs), the most well-known and commonly used of which being the box-fitting least squares (BLS) algorithm (Kovács et al. 2002). The main premise is that a transit event is a steep and shallow dip with a short duration, making it appear boxlike. BLS phase-folds the light curve at a wide range of periods and extracts the boxlike event by fitting a square box to the phase range. The period which delivers the lowest χ^2 is selected as the correct one. There is an abundance of literature on the topic, however, and a wide selection of TDAs exists, some based on or related to BLS (e.g., Renner et al. 2008; Grziwa et al. 2012). Others are not: e.g. Cabrera et al. (2012) use a second order polynomial to approximate the transit shape, while Hippke & Heller (2019) use a transit-like search function,

taking into account limb darkening and ingress and egress. Many TDAs are complete packages and include light curve detrending and frequency filtering or transit masking to facilitate the search for additional companions.

TDAs do not or cannot reliably test for the different astrophysical false-positive scenarios. Therefore, the final step is the visual examination of the transit events that passed all tests. These include checking for the difference between even and odd transits, the presence of secondary eclipses, the depth and shape of the transits and the overall consistency between the parameters.

Alternatively, algorithms capable of distinguishing between false positives and genuine planetary transits (Fig. 2.3) can also be used. A number of these have been developed through the years, e.g. `VESPA` (Morton 2012), `PASTIS` (Díaz et al. 2014), `TRICERATOPS` (Giacalone et al. 2021), originally motivated by the need to validate the many Kepler planets too faint for RV follow-up. Many of the planets known to date have been validated using these techniques. While widely used and largely considered reliable, it should be noted that some previously validated planets have later been found to be false positives (e.g. Csizmadia et al. 2023). The results from these pipelines should thus be taken with caution.

To illustrate, I show in Fig. 3.1 the light curve of K2-99, which reveals a Jupiter-size planet in an 18.25-day orbit around a relatively bright (V_{mag} = 11.1) subgiant[2] star, as reported by Smith et al. (2017). The light curve presented here (grey dots in Fig. 3.1) is from K2's sixth observing field, or campaign[3], and was systematics-removed by the pipeline developed by Vanderburg & Johnson (2014), which became the most widely-used one for the two-wheeled K2 mission. The four transits of K2-99 b are easily identifiable by eye. The star is relatively quiet, manifesting clear long-term variability, which is easy to remove by any of the traditional methods mentioned above. In this case, and analogous to Paper A (Sect. 5, Georgieva et al. 2021), I used GP regression[4] to identify the best-fitting model to the data (red curve) and subtracted it from the original light curve (grey dots) to obtain the detrended one (blue dots).

[2] A subgiant is a star that is larger and brighter than a star of the same spectral class and has begun the final stages of its life.

[3] This target was observed again in Campaign 17, which is not included in this example.

[4] The light curve was detrended using the Python package `citlalicue`, available at `https://github.com/oscaribv/citlalicue`.

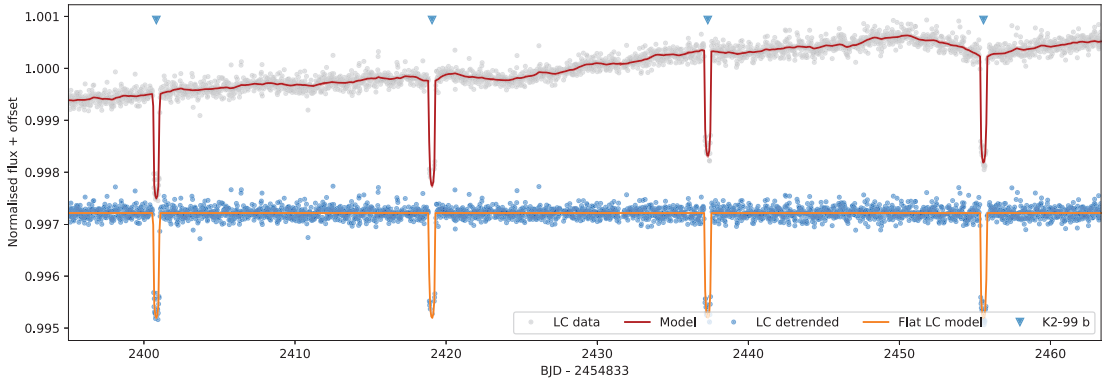

Figure 3.1: K2-99 Campaign 6 light curve by Vanderburg & Johnson (2014) in grey with GP and transits overplotted in red, and resulting detrended light curve in blue. Individual transits of the Jupiter-size planet K2-99 b are marked with blue triangles.

3.2 Joint modelling of transits and RVs

As mentioned in Chapter 1, by combining transit photometry with RV measurements, we can measure a planet's radius and true mass and determine its mean density. As further shown in Chapter 2, RV and light curves are described by time-dependent parametric equations. These can be compared to models to infer a planetary system's parameters. This is typically done by using Bayesian model-fitting techniques. The value of Bayesian statistics is in its power to formulate a framework for providing quantitative answers to inverted questions such as the probability of a set of events explaining an observed outcome. This approach is well suited for the problems of exoplanet characterisation since it allows us to infer parameters which we cannot observe directly due to the nature of transit and RV observations.

Still, posing such a problem in a Bayesian way is by itself only half of the story. Solving it involves computing the probability distribution that a set of parameters explains a given set of data. Since this cannot be solved analytically in all but the simplest cases, one convenient and popular solution to such a numerically demanding problem is provided by the Markov chain Monte Carlo (MCMC) method (Metropolis et al. 1953; Hastings 1970). MCMC has become an essential tool for data analysis and has been steadily growing in popularity in the astronomical community. To determine the physical parameters of an exoplanet system we turn to this well-tested approach for the

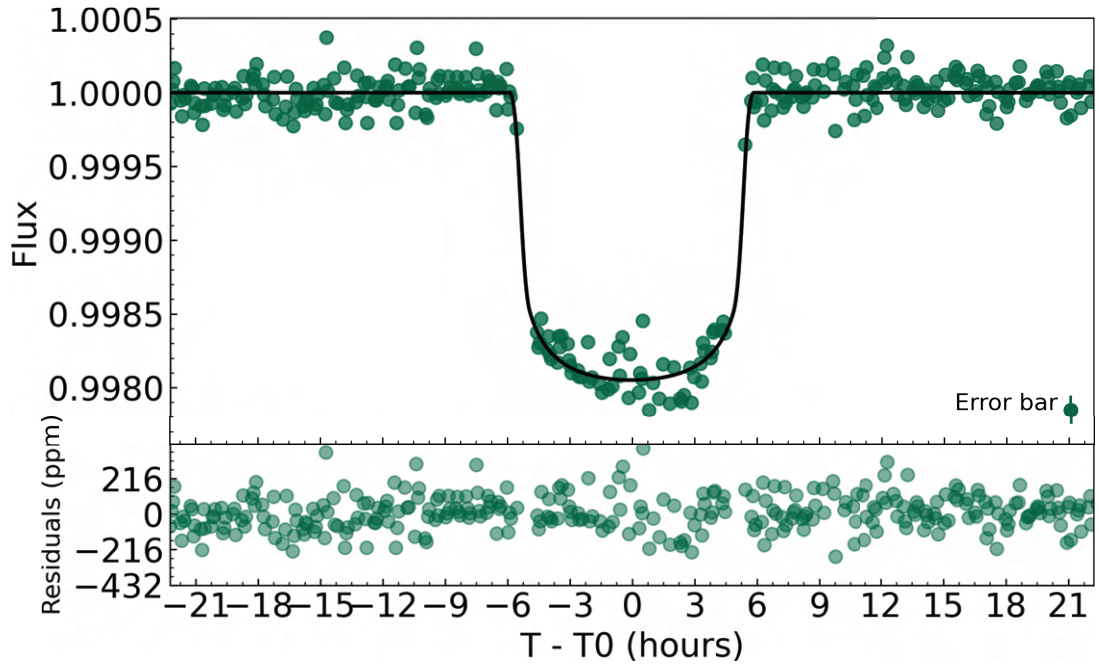

Figure 3.2: K2-99 light curve with residuals phasefolded to the orbital period of K2-99 b. The black curve is the best-fitting transit model. Representative errorbar is in the bottom right.

simultaneous modelling of transit photometry and RV data, using the code `pyaneti` (Barragán et al. 2019a).

The continued story of the K2-99 system can be followed in the below figures. The deep phasefolded transit with the best-fitting model shown in Fig. 3.2 yields a radius of $1.26 \pm 0.05\ R_{\rm J}$. The RVs give a semi-amplitude of $K = 55 \pm 4\ \mathrm{m\,s^{-1}}$, which combined with an inclination of $i = 88.5^{+1.0}_{-1.5}$ degrees, translates $M = 0.95 \pm 0.08\ M_{\rm J}$. What is interesting to notice from Fig. 3.3 that is not evident from the light curve in Fig. 3.1, is that the planet has an eccentric orbit, corresponding to $e = 0.2^{+0.06}_{-0.04}$. But perhaps the most intriguing part is the negative linear trend in the RV timeseries (Fig. 3.3, top panel): what this trend indicates is the presence of an outer companion with unconstrained parameters.

More recently obtained additional observations have revealed the nature of K2-99 b's distant neighbour to be that of another gas giant planet on an eccentric orbit and a minimum mass of $M_{\rm c} \sin i = 8.4 \pm 0.2\ M_{\rm J}$. A more detailed description of the system can be found in Smith et al. (2017, 2022).

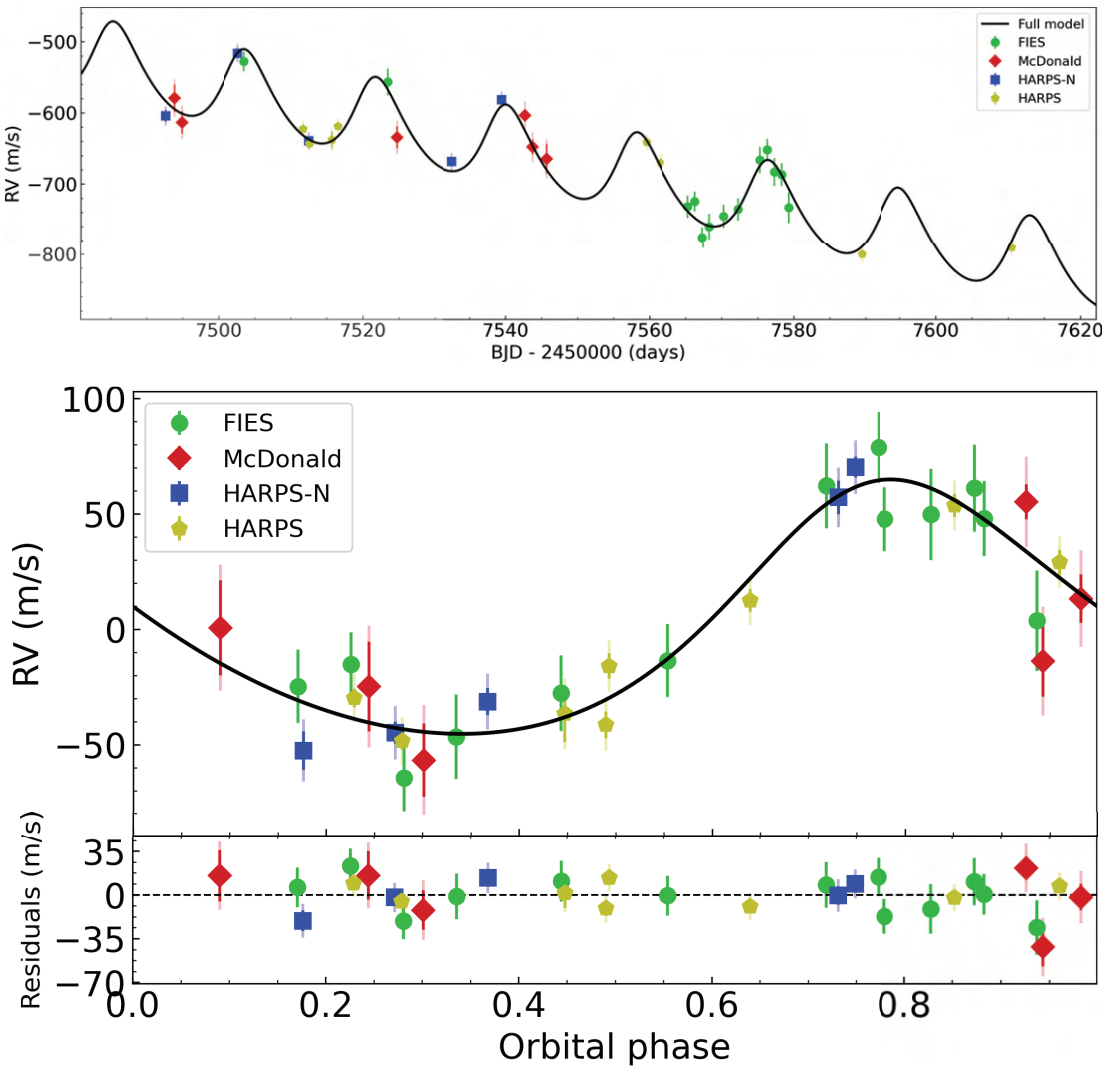

Figure 3.3: Top: K2-99 RV timeseries. The different colour markers represent data from the different instruments. The black curve is the RV planet model. A clear downward linear trend is visible, indicative of the presence of another planet in a wider orbit. Bottom: RV data folded on the orbital period of K2-99 b, again with solid black curve representing the best-fitting model. Both plots show the eccentric nature of this planet's orbit. The deviation from a sinusoid (i.e. circular orbit) evident in both panels is the signature of an eccentric orbit, in this case corresponding to $e = 0.2$.

3.3 The harsh reality

The K2-99 system presented above shares certain traits with one of the systems forming a part of this thesis – TOI-2196 (Chapter 4.4, Persson et al. 2022). They both feature a linear trend in the RV data pointing to the presence of an outer companion, and an overall clean and elegant solution. But unfortunately, they may give a false impression as they are only rare examples of a straight-forward solution, for which Kepler's laws of planetary motion and Newton's laws of universal gravitation work beautifully.

The mass and radius of K2-99 b reported in the previous section correspond to a precision of ∼4% and 8.4%, respectively, while for TOI-2196b we have 5% on the mass, and ∼4.3% on the radius. Of the 5300 discovered planets, 87 boast the latter precision, of which only 12 are small planets ($< 4R_\oplus$)[5]. This is symptomatic of the challenges described in the previous chapter. Even with the most precise spectrographs currently available, such as EXPRES and ESPRESSO, with their recently reached ∼40 $\mathrm{cm\,s^{-1}}$ (Zhao et al. 2023) and ∼30 $\mathrm{cm\,s^{-1}}$ (Barros et al. 2022), respectively, the ability of RV surveys to detect and characterise small planets is still limited by stellar activity. In the more complex cases when the stochastic nature of stellar photospheric variability is evident in the signal, such as the case of the TOI-1260 (Chapter 4.1, Georgieva et al. 2021), TOI-733 (Chapter 4.2, Georgieva et al. 2023b), TOI-776 (Chapter 4.5, Fridlund et al. 2023), TOI-1416 (Chapter 4.6, Deeg et al. 2023) systems, to obtain a planetary solution we must employ more sophisticated strategies.

Magnetically-driven stellar variability produces time-varying distortions in the spectral line profiles of stars. These lead to systematic errors, which reduce the spectroscopic measurements' precision, limiting the ability to measure the masses of both newly-discovered and known low-mass exoplanets. This is particularly true for planets with orbital periods of a few tens of days and higher (Collier Cameron et al. 2021). But depending on the variability of the star and the time-sampling of the data, shorter period planets can also be affected by either being missed or reaching too low mass precision to afford characterisation.

Stellar activity has traditionally often been accounted for by being modelled as one or multiple sinusoids at the star's rotation period and its harmonics

[5] As of 9 March 2023. Data from `https://exoplanetarchive.ipac.caltech.edu/`.

(Queloz et al. 2009; Boisse et al. 2011). This is the so-called pre-whitening (Hatzes et al. 2010), which in many cases is a sufficient approach. In others it can be too simplistic and lead to spurious detections (see e.g., Rajpaul et al. 2016), since it does not take into account the temporal evolution of active regions and assumes the removed signals are periodic and long-lasting.

Recently, several strategies aiming at dealing with stellar activity mitigation for the more complex cases have been put forward. Photospheric temperature and pressure affect atomic transitions differently, so individual spectral lines are affected by activity to a different extent (Davis et al. 2017). Taking advantage of this, Dumusque (2018) demonstrated that deriving line by line RVs in this way, as opposed to the traditional approach using the cross-correlation function (CCF) between the observed and the template spectrum (see Sect. 2.3), can mitigate photospheric-induced RVs and thus account for the nuisance activity signal. The possibility to remove activity signals solely by identifying changes in the spectral line shapes using machine learning techniques was demonstrated by de Beurs et al. (2022), while Collier Cameron et al. (2021), on the other hand, proposed a complex algorithm which makes use of the RVs derived from the CCF between an observed spectrum and a digital mask.

The pipelines for spectroscopic data reduction, i.e. the Data Reduction Software (DRS, Lovis & Pepe 2007), `serval` (Zechmeister et al. 2018) and TERRA (Anglada-Escudé & Butler 2012), use the well-established approach of using a Gaussian distribution fit to the CCF. Any present planets affect the shift of the CCF but stellar activity affects its shape, so Simola et al. (2019) proposed the use of a skew normal (SN) fit instead, to account for asymmetry. Simola et al. (2022) use the SN approach to reduce the data, and, if favoured by statistical evidence (i.e. the Bayesian information criterion[6]), they propose adding a further step prior to modelling the planets, namely the use of a change point detection method to split the timeseries into chunks where the stellar behaviour can be approximately described as stationary.

The de Beurs et al. (2022) and Collier Cameron et al. (2021) approaches have been tested on simulated data as well as data of the solar spectrum, while Simola et al. (2022) yielded improved mass precision on previously known planets orbiting active stars, including TOI-776, which forms part of this

[6]The BIC is a popular criterion employed for model selection and is based on the likelihood function.

thesis. All of above the are novel methods and active fields of research, showing great promise for future applications to exoplanets.

Modelling stellar activity with Gaussian processes

Until approaches such as the ones just described gain enough traction, however, we rely on stochastic modelling techniques like GP regression (e.g. Haywood et al. 2014; Angus et al. 2018), hereafter GPR, whose application to modelling of both transit and RV data in the presence of stellar activity has gained popularity in the last decade.

GPs are a powerful machine-learning technique (Rasmussen 2004) and represent an infinite-dimensional generalisation of the familiar Gaussian distribution. In conjunction with a Bayesian formulation, they can be utilised for building flexible non-parametric models. Their most common use, and the end to which they are addressed in this work, is in fitting a function to data, i.e. regression. GPs offer a solution to the problem of finding a function that fits a given set of points by assigning a probability to each potential solution. The mean of this probability distribution is considered the most likely fit to the data. This probabilistic approach allows for the inclusion of confidence levels in the solution (Rasmussen 2004).

A brief overview

To begin learning about Gaussian processes, it is necessary to understand the basic mathematical principles that underlie them. The following brief description is based on the works of Haywood et al. (2014); Rajpaul et al. (2015); Angus et al. (2018); Barragán et al. (2022), and the recent review article by Aigrain & Foreman-Mackey (2022).

The foundation of the GP is the Gaussian (normal) distribution, particularly the multivariate aspect, where each variable is normally distributed, and the joint distribution is also Gaussian. The multivariate Gaussian distribution is characterised by a mean vector μ and a covariance matrix Σ. In some applications the mean function is constant or zero, but in the case of planet detection in activity-contaminated RV data, the mean function is the function of interest. Meanwhile, the variance along each dimension is modeled by Σ, which also determines the correlation between the different random variables. A valid covariance matrix is positive semi-definite and symmetric.

The diagonal of Σ describes the variance σ_i^2 of the i-th random variable, while the off-diagonal elements σ_{ij} reflect the correlation between the i-th and j-th random variables.

Thus, the definition of a GP is:

$$X \sim \mathcal{N}(\mu, \mathbf{\Sigma}),$$

meaning that X follows a multivariate Gaussian distribution. For N time-series, following the above description, the covariance matrix Σ is then given by:

$$\mathbf{\Sigma} = \begin{pmatrix} \boldsymbol{\sigma}^{1,1} & \boldsymbol{\sigma}^{1,2} & \cdots & \boldsymbol{\sigma}^{1,N} \\ \boldsymbol{\sigma}^{2,1} & \boldsymbol{\sigma}^{2,2} & \cdots & \boldsymbol{\sigma}^{2,N} \\ \vdots & \vdots & \ddots & \vdots \\ \boldsymbol{\sigma}^{N,1} & \boldsymbol{\sigma}^{N,2} & \cdots & \boldsymbol{\sigma}^{N,N} \end{pmatrix}$$

One reason why GPs are so popular is because of their connection to the central limit theorem, which suggests that the assumption of a Gaussian distribution is approximately, if not exactly, accurate. A beneficial property of Gaussian distributions is their ability to maintain their Gaussian nature under the processes of conditioning and marginalisation. This means that the resulting distributions from these operations will also be Gaussian, making certain statistical and machine learning problems easier to solve. In brief, marginalisation can be thought of as performing integration on one of the dimensions of a Gaussian distribution[7], while conditioning can be viewed as slicing through the multivariate distribution, creating a new Gaussian distribution with fewer dimensions. This is an important point because, technically, the parameters of the Gaussian Process are all the unknown functions that possess the same predetermined mean vector and covariance matrix and could be the source of the observed data. However, these parameters are consistently marginalised over – we don't directly work with individual functions, except in situations where we are providing visual examples by drawing samples. We don't observe the unidentified function that produced the data firsthand, but we deduce a probability distribution for it through our imprecise observations.

[7]This follows from the definition of marginal distribution which refers to the probability distribution of a subset of variables in a larger multivariate distribution, obtained by integrating or summing out the other variables.

Gaussian process regression

Probably the easiest way to understand GPR is to link it to a concept familiar to most – least-squares regression. The former has the added benefit of taking into account correlated noise. If the measurement errors of a set of observations are samples from a Gaussian distribution with mean 0 and variance σ^2, and if said variances are known, relatively simple mathematical manipulation (e.g., Aigrain & Foreman-Mackey 2022) shows that maximising the likelihood of the dataset is equivalent to performing χ^2 minimisation. Put simply, the least-squares regression method gives the Maximum Likelihood Estimate (MLE) of the parameters, assuming white Gaussian noise with a predetermined variance.

The way to introduce the covariance matrix into the χ^2 picture is to think of the matrix as entirely diagonal, with the variances linked to each observation predetermined. If, however, this assumption is relaxed and the matrix was allowed to have non-zero off-diagonal elements determined by a covariance function, it would be possible to model stochastic signals and correlated noise. In fact, the core of building the covariance matrix for GPR is choosing (or designing) an adequate covariance function, or kernel function, and significant care needs be taken in making this decision. While the mean function represents the information we have about the deterministic part of the signal (a Keplerian or a transit model), the kernel function is meant to reflect our knowledge and assumptions about the stochastic part.

Inference

As briefly mentioned before, MCMC is a popular computational method that uses Markov chains (a sequence of random variables where each variable depends only on the previous one) and Monte Carlo methods (random sampling) for performing Bayesian inference on complex models where it is difficult to calculate the posterior distribution analytically. For the modelling efforts in this work, I have used the MCMC sampling, as implemented in the code `pyaneti`. We first define a likelihood function that models the data, in our case a Gaussian likelihood, where we use a vector of residuals between the data and the mean function evaluated at each timestamp, thus effectively having a zero mean. We then choose a prior distribution that encodes our prior beliefs about the model parameters and use Bayes' theorem to obtain the posterior

distribution of those parameters given the data.

At times, we want to analyse the stochastic behavior of a dataset and predict its properties. GPs are well capable of making predictions and this is one of their main applications. But in timeseries astronomical datasets, such as RV datasets, there are often unknown, apparently random signals that need to be modelled, whether they arise from astrophysical or instrumental factors. In the context of the current application, these signals are unwanted and need to be accounted for in order to detect the signals of interest, i.e. the presence of planets, and accurately measure their parameters. To do this, we need to estimate the posterior distribution over the GP hyperparameters, which is impossible to do analytically. The MCMC samples are utilised to approximate the posterior probability distributions for specific hyperparameters that are of interest. For example, when using a GP to model correlated noise in data, we may be interested in the impact of the noise on the mean function's parameters rather than the noise itself. To achieve this, we would marginalise the posterior samples over the nuisance parameters.

The quasi-periodic covariance function

As previously mentioned, the kernel function is a crucial part of modelling with GPs. The covariance matrix determined by the kernel function shapes the distribution and characteristics of the function to be predicted, by providing a similarity measure between pairs of input points. Entries in the covariance matrix indicate how much two points influence each other, and the kernel function controls the possible shapes the predicted function can take.

Ideally, the kernel of choice would incorporate some prior knowledge about the process that is to be modelled. The variation in the brightness of a star is due to stellar activity – the presence of spots, plages, and other features on the star's surface. The quasi-periodic (QP) kernel has been shown to be a good choice to model such behaviour because it can capture the periodic patterns in the activity-containing spectroscopic data, while also allowing for some variability in the overall periodicity. All modelling involving GPR that this work is based on uses the following formulation of the QP kernel:

$$\gamma(t_i, t_j) = \exp\left[-\frac{\sin^2[\pi(t_i - t_j)/P_{\mathrm{GP}}]}{2\lambda_{\mathrm{p}}^2} - \frac{(t_i - t_j)^2}{2\lambda_{\mathrm{e}}^2}\right], \tag{3.1}$$

The periodic component, P_{GP}, measures the distance between periodic rep-

etitions, and the similarity between observations at different times. The $\sin^2$ function ensures that the covariance is periodic and varies smoothly as the time difference between observations changes. However, stellar activity can also exhibit some variability in the period due to e.g., changes in the star's rotation or evolution of the size and distribution of active surface features. The QP covariance function can account for this variability by including another parameter, the so-called evolutionary timescale, λ_e, which allows for QP behaviour to be captured. Finally, the harmonic complexity parameter, λ_p, can be added to the QP kernel to capture more complex periodic patterns in the data. This can be useful for modelling stars that exhibit multiple periods or for capturing the interaction between different features on the star's surface. The addition of the harmonic complexity parameter can further control the extent to which different points in the data are correlated. This increases the flexibility of the model in capturing more complex periodic patterns, which, however, carries certain risks (Georgieva et al. 2023a).

This flexibility generally makes GPs look like they can fit any data well, which can be misleading. Therefore, it is useful to inform the GP and constrain said flexibility by adding any available information about the system. As put forward by Rajpaul et al. (2015), additional data such as ancillary RV-contemporaneous activity indicator timeseries can become useful. Activity indicators, as their name implies, are sensitive to stellar activity only, making them uniquely suited for decorrelating this activity from RV data in the effort of disentangling the genuine planetary signal(s), as done by e.g. Mayo et al. (2018); Barragán et al. (2019b). The method assumes that the signals caused by the star's activity in all observables can be described by a single underlying GP and its time derivative(s). Active regions on a star's surface affect various observed parameters differently; some are affected only by the area covered by the regions and can be described by a GP function only, while others are affected by how the regions evolve over time and require a GP *and* (at least) its first derivative (see e.g., Dumusque et al. 2014). RVs are influenced by both the position *and* evolution of the active regions, so activity-induced RV data can be modeled using both a GP and its derivative to account for both effects. On the other hand, some activity indicators (including all of the ones used in the papers that are part of this work) are only affected by the fraction of the stellar surface covered by active regions, and thus do not need the GP derivative to be described. This is what the multi-dimensional GP regression

effectively represents: modelling RVs alongside one or more activity indicators deemed suitable for disentangling the type of activity present in the RV data. A key assumption is that this activity is described in both data sets by the same underlying GP function, which can be loosely interpreted as the fraction of active regions covering the stellar surface at a given time.

This is the very approach used to obtain the best possible precision for the parameters of the planets in TOI-1260 (Georgieva et al. 2021), TOI-733 (Georgieva et al. 2023b) and TOI-1416 (Deeg et al. 2023) – the exoplanet systems that, together with TOI-2196 (Persson et al. 2022) and TOI-776 (Fridlund et al. 2023), form the basis of this work.

CHAPTER 4

Paper summaries

4.1 Paper A

In this paper we present the detection and characterisation of two short-period mini-Neptunes in the 2-3 $R_\oplus$ range orbiting the late K-type star TOI-1260. The transit detections were based on photometry from TESS observing sectors 14 and 21. TOI-1260 b is the inner planet with a radius of $\approx 2.3\ R_\oplus$ and period of 3.13 days. TOI-1260 c is its outer neighbour, with a radius of $\approx 2.8\ R_\oplus$ and period of 7.49 days. Subsequent follow-up Doppler measurements with HARPS-N allowed us to make a 6-sigma detection for the mass of planet b, yielding $M_b \approx 8.6\ M_\oplus$ and a 3.6-sigma detection on the mass of planet c, $M_c \approx 11.8\ M_\oplus$.

The star exhibits a complex variability pattern, the effects of which we removed from the TESS light curves using a GP. For the spectroscopic measurements, said pattern could not be modelled effectively using a trivial sinusoid fitting approach. Thus, to disentangle the planetary signals from the stellar variability-induced signal present in the data, we used the above-described multi-GP regression approach, where we modelled the RVs alongside the time-series of the S-index activity indicator – an indicator for chromospheric activ-

ity.

As previously stated, the radius gap unravels (at least) two distinct populations. The composition of some super-Earths and many mini-Neptunes, particularly in the region 2-3 $R_\oplus$, is still somewhat of a mystery. To find out possible compositions and structures of these planets, we decided to perform simulations of temporal atmospheric escape under photoevaporation.Assuming the presence of a primordial H/He atmosphere for both planets, we found that planet b is unlikely to have retained it. However, being in a highly irradiated orbit, planet b is possibly a water-rich planet, featuring a thick steam atmosphere. This could mean that the planet is in fact a dense, rocky core with an expansive atmosphere, inflating its radius. On the other hand, we find that planet c may have retained such a primordial atmosphere throughout its evolution.

Another interesting result is that we uncovered the likely presence of a third planet, external to the other two. The transit of this planet is not visible in sector 14, and its existence was initially only hinted at by a single transit event visible in sector 21. Further analysis of the light curve data of sector 21 showed that a second transit of this tentative planet is possibly overlapping with a transit of planet c. We performed a multi-transit analysis of this simultaneous event, and found that this scenario explains the data better. Assuming this outer planet is real, we estimated a radius of $\sim$ 2.75 $R_\oplus$ and a period of 16.6 days, making it a warm mini-Neptune. Such a period puts a transit of this planet in the spacecraft downlink time interval in sector 14, explaining the absence of this planet in the light curve for that sector. Furthermore, this orbital period corresponds to about half the rotation period of the star that our GP analysis helped us find. Given our relatively short and suboptimally sampled RV dataset, despite our best efforts, we could not claim a solid confirmation of planet d since the precision of the mass detection we reached was less than 2-sigma.

Follow-up observations by CHEOPS and TESS have since confirmed the existence of this planet (Lam et al. 2023). The radius of the 16.6-day planet was shown to have a radius of $\approx$ 3.09 $R_\oplus$. Their estimate agrees with our analysis to within 2-sigma, while the reported updated radii of the two inner planets agree perfectly with our own, but with an improved precision, as expected. Interestingly, the radii of the TOI-1260 planets make the system a perfect example of the "peas in a pod" scenario.

TOI-1260 is a good example of the challenges associated with both transit detection and mass determination via Doppler spectroscopy due to the presence of stellar activity of stochastic nature.This necessitated the use of the multi-GP approach on the spectroscopic data to ensure the highest possible precision for the planet parameters, given the limitations of the dataset. In addition, the ambiguity of the planet compositions highlights that performing additional observations and thorough analyses on mini-Neptunes can help to find out if some mini-Neptunes may in fact be super-Earths with inflated radii (Turbet et al. 2020) – an idea that has been growing in popularity in the field.

My contribution: Light curve detrending, joint transit and RV modelling, writing up the corresponding sections, describing the atmospheric modelling, general discussion and responsibility for putting the paper together.

4.2 Paper B

This paper reports the discovery of TOI-733 b – a planet orbiting a star similar to our Sun, residing in the small planet radius gap. The planet is hot, with an equilibrium temperature of about 1055 K. Our team used data from the HARPS spectrograph to determine that the planet has a radius of about 1.992 $R_\oplus$ and an orbital period of approximately 4.88 days. Using these measurements, we were able to estimate the planet's mass to be around 5.72 $M_\oplus$. We did this by first performing frequency analysis of the RV data, which enabled us to identify the stellar rotation period. We then applied the multi-GP approach described previously. The activity indicator that worked best in this case was the Full Width at Half Maximum (FWHM), which measures the width of the spectral lines. Thus, based on the above-derived values, we concluded that the planet has a moderate density, putting it somewhere between rocky and volatile-rich planets on the mass-radius diagram.

Interior and atmospheric modeling were also conducted to try and narrow down the possible structure and composition of TOI-733 b. The results of these analyses suggest that the planet may have had a H/He atmosphere that was lost, leaving behind a secondary atmosphere of heavier elements. Alternatively, the planet may have formed as a water world and did not experience atmospheric mass loss. The question of whether TOI-733 b has a secondary

atmosphere or is an ocean planet is still unclear. The answer could potentially differentiate between a Neptune-like planet that lost its ∼10% of H/He to leave behind a steam atmosphere of heavier volatiles, and one that formed and remained relatively the same throughout its evolution.

TOI-733 b shares certain traits with one well-known planet – π Men c: both planets orbit stars of similar type and age, have similar radii, and receive a similar amount of stellar irradiation. Models suggest that water plays a significant role in the interior and possibly the envelope of π Men c, as recent transmission spectroscopy observations suggest. While, TOI-733 b is not a promising target for follow-up transmission or emission spectroscopy, a careful consideration could show that some of the conclusions derived for π Men c could be true for TOI-733 b as well. Confirming that TOI-733 b and other planets with similar features are primarily composed of water could indicate that there is a group of planets that belong in the radius gap and are not just transient occupants.

The paper emphasises the importance of well-characterised planets in this parameter space (i.e. the radius valley separating super-Earths from mini-Neptunes) to facilitate understanding of the mechanisms that explain it. Both the core-powered mass loss during formation and the XUV photoevaporation mechanism during evolution are able to physically explain the presence of the radius valley. Further research and high-precision follow-up are needed to fully understand these mechanisms and determine which one is dominant.

My contribution: Light curve detrending, joint transit and RV modelling, frequency analysis, writing up the corresponding sections, general discussion and responsibility for putting the paper together.

4.3 Paper C

Soon after the initial discovery of planets outside our solar system, it became evident that stellar activity in RV data posed a problem. We now understand that stars with irregular activity patterns require special modelling consideration. As the search for smaller and less massive planets, including Earth-like planets, intensifies, finding ways to deal with this issue becomes increasingly urgent. Unfortunately, current detection methods and instruments lack the precision required to distinguish a small planetary signal from the larger and

much less coherent signal of an active star. Furthermore, insufficient RV data and random sampling of planet-hosting stars exacerbate this problem, making it difficult or impossible to detect low-mass planets.

We thus designed a study to test the detectability of planets with three different semi-amplitudes, K (3, 10, and 30 $\mathrm{m\,s^{-1}}$) and four different orbital periods around stars with various types of activity (dictated by a select variety of hyperparameters), using a multi-GP approach. We tested the effects of data availability by trying all of the above scenarios with 40, 60 and 80 data points. We find that non-detections are common, particularly for the smallest K. We also find that the model was less able to explain the data in cases of high stellar activity. The quasi-periodic covariance function used in our modelling was overall effective in identifying the correct stellar rotation period, apart from the cases when the active regions' evolution timescale was shorter than the rotation period. This does not seem to have an effect on the detectability of the planets, however. We noted also, that the harmonic complexity is the biggest setback to both planet and GP hyperparameter recovery, especially in the cases of fast rotators. This behaviour corresponds to planets around young stars, and is evident even in the highest K values tested, if only in the cases of 30 datapoints. We also relate high harmonic complexity to the tendency of the model to overfit.

We only consider the case of a single planet in a circular orbit, and leave more detailed investigations of multi-planet scenarios, with or without eccentricities, as well as more complex and realistic sampling scenarios, to future work.

My contribution: Preparing the synthetic datasets, modelling them, interpreting the results via different visualisation techniques, as well as general responsibility for writing and putting the paper together.

4.4 Paper D

In this paper, we present the discovery and characterisation of TOI-2196 b – a rare hot Neptune type planet found orbiting a G-type star. The discovery was made using data from TESS and confirmed with RV measurements collected with the HARPS spectrograph.

The orbital period of TOI-2196 b is 1.2 days, which places it in an unpopular

region of the radius-insolation diagram – the hot Neptune desert – where only a small number of short-period Neptune-like planets have been found. Normally, planets found in such orbits are highly irradiated and tend to be either small and rocky, or gas giants. Contrary to this commonly observed trend, we find TOI-2196 b to be an intermediate-sized planet with a radius of 3.51 $R_\oplus$ and a mass of 26.0 $M_\oplus$. The planet's density is thus 3.31 g cm^{-3}, twice that of Neptune, and the tight orbit implies a high equilibrium temperature of 1860 K. These results may suggest that the hot Neptune desert can be divided into two parts, a hot sub-Neptune desert devoid of planets with radii of $\approx$ 1.8-3 $R_\oplus$ and a sub-Jovian desert for radii of $\approx$ 5-12 $R_\oplus$.

Planetary interior structure models of TOI-2196 b are consistent with a H/He atmosphere mass fraction between 0.4% and 3%, with a mean value of 0.7% on top of a rocky interior. The planet may have lost some mass at a young age, but has remained a volatile-rich planet.

RV measurements show a linear trend in the data, which in turn allowed us to make another interesting discovery about this system – the presence of a distant companion. Under the assumption of zero eccentricity, we estimated a lower limit on its period and mass – 220 days and 0.65 M_J, respectively. At the current stage, it is uncertain whether this outer object is a warm or cold gas-giant, or possibly even a brown dwarf or even a very low-mass stellar companion. RV observations for this system are thus ongoing, with the intention of constraining the mass and orbital parameters of this object.

My contribution: Light curve detrending, joint transit and RV modelling, and writing up the corresponding sections.

4.5 Paper E

In this paper we present a second look at the TOI-776 system motivated by additional photometric (TESS and CHEOPS) and spectroscopic (HARPS) data. First announced by Luque et al. (2021), TOI-776 is an M-dwarf hosting two planets in the super-Earth – mini-Neptune regime.

M-dwarfs, by far the most common stellar spectral type found in our galaxy, have gained significant popularity in recent years. This is because, given the limitations of our methods and instruments, there is a higher chance of detecting potentially habitable planets through transit and RV surveys if they

are orbiting an M-dwarf. This is because M-dwarf stars have smaller radii and lower masses than Sun-like stars, which results in larger transit depths and RV amplitudes. Despite these advantages though, M-dwarfs' intrinsic faintness often makes studying exoplanets around them challenging. In the case of RV surveys, another important factor to consider is the signal induced by stellar activity, which is usually higher for cooler, more magnetically active stars. This can be made worse by interruptions to observing runs, which can cause gaps in the data. In cases where the data is sporadic, characterisation can be significantly impeded. TOI-776 is one such case where additional RV data proved to be challenging to reconcile with the first set of observations reported in the discovery paper. Thus, for our investigation, several different modelling approaches were undertaken to finally facilitate the characterisation of the planets: sinusoid fitting, GPR, as well as an SN fit onto the CCFs. The latter yielded the most robust results and enabled us to obtain RV measurements and activity indicators, which could thus be modelled by more conventional approaches. Despite these difficulties, we were able to obtain a more reliable and precise estimate of the stellar rotation period ($\sim$21 days) as compared to the reported by Luque et al. (2021), $\sim$34 days.

The overall precision improvement of the radii with the additional photometry is a factor of two. However, due to the increased activity of the host star, we only made slight or no improvements to the precision of the other planetary parameters. Using these newly obtained estimates, and in combination with the masses, we are able to classify the planets as closer to super-Earths, rather than sub-Neptunes.

TOI-776 provides a good example of how stellar-induced signals can change quickly and have a significant impact on time-domain analyses, making it difficult to separate the stellar and planetary signals. Interestingly, our second observing campaign actually made the data quality worse due to the increased activity of the host star and the presence of the data gap. This has implications for missions like JWST and PLATO, which will observe a large number of cooler stars that may show similar changes in activity on timescales of around one year.

My contribution: Light curve detrending, joint transit and RV modelling, writing up the corresponding sections, and other ad-hoc contributions.

4.6 Paper F

The star TOI-1416 is a late G or early K-type dwarf star hosting a transiting ultra-short period (USP) planet, TOI-1416 b, with a period of 1.07 days. Further observations of the star via HARPS-N RV follow-up using various instruments confirmed the existence of this planet, yielding a mass of $3.48 \pm 0.47\ M_\oplus$ and a radius of $1.62 \pm 0.08\ R_\oplus$. These give a density that is slightly lower than Earth's. Detailed joint RV and transit modelling was performed, where I tried modelling the inner planet with the Floating Chunk Offset (FCO) method (Hatzes et al. 2010; Hatzes 2014), as well as the multi-GP approach using the differential line width (dLW) activity indicator. The former is designed to determine the RV amplitudes of planets with short periods ($\lesssim 1$ day), for which nightly RV variations are expected to be greater than the uncertainties of individual RVs. This method effectively suppresses systematics that occur on time-scales longer than a single night, including instrumental and other planetary or stellar activity effects. Thus, while useful for single USP planets, it cannot model multi-planet systems. Turning once again to the multi-GP approach, and testing different planet scenarios as guided by the RV frequency analysis, the best model I found for this system uncovered a significant signal of another potential planet, TOI-1416 c, with a period of either 27.4 or 29.5 days, This latter signal may be contaminated by a signal related to the Moon's synodic period. As a result, the exact properties of planet c cannot be confirmed at this stage. If planet c is indeed real, it would have a radius between 3 and 8 times that of Earth, placing it above the period-radius valley. In contrast, planet b is situated below the valley, although its position in the period-radius plane is not well-defined in this region.

As a USP planet, TOI-1416 b has a very hot surface temperature of around 1570 K. Various models are considered to explain the composition of TOI-1416 b. Because of the high temperatures expected on the planet's surface and interior, a model proposing a melted interior containing a significant amount of water dissolved in magma is believed to be the most viable explanation for the planet's density, which is lower than what would be expected from a purely silicate composition. Although any atmosphere the planet may have is unlikely to have a significant impact on its mass, it may be suitable for observation through transmission spectroscopy using the JWST. Additionally, the planet's surface may be within the range of detection for emission spectroscopy.

The discovery of TOI-1416 b adds to our understanding of the distribution

of super-Earth type planets. USPs are not a distinct group, but rather part of a continuous distribution of planets with periods ranging from less than a day to up to around 30 days. This distribution is limited at smaller radii by the "Neptune desert" and at larger radii by the "period-radius valley" that separates super-Earths from sub-Neptune planets. The discovery of more USPs requires a revision of the lower limits of the Neptune desert to include planets with a radius of 1.6 $R_\oplus$ and a mass of 8.9 $M_\oplus$ for periods shorter than 2 days. Subgroups of super-Earths with specific properties may emerge depending on factors such as the type or age of the host star, the presence of other planets, and insolation. This information can reveal different pathways in the evolutionary history of these planets, such as high and low eccentricity migration channels that lead to short orbital periods.

My contribution: Light curve detrending, joint transit and RV modelling, frequency analysis, writing up the corresponding sections, and other ad-hoc contributions.

CHAPTER 5

Future outlook

From the first protoplanetary disk to ever be observed in 1984, through the early discoveries in the 1990s of a planet around a pulsar (Wolszczan & Frail 1992) and a planet around a Sun-like star (Mayor & Queloz 1995), in just a few decades we have moved from being skeptical about the presence of planets around other stars to the now well-established knowledge that planets are prevalent, as well as diverse. Ground-based surveys and the pioneering CoRoT mission gave us the first glimpses of a fact the Kepler mission finally solidified – that there are more planets in our galaxy than there are stars. This started a paradigm shift in the way we think about planetary systems.

TESS and the many more planets around bright stars it will undoubtedly continue to give us, coupled with RVs of unprecedented precision from the most modern spectrographs (e.g. ESPRESSO and EXPRES), will allow us to study less massive planets in wider orbits with improved accuracy. CHEOPS has already lead to the improvement of the radius estimates and ephemerides of several planets, as well as the discovery of additional ones, and now in its extended mission[1] will continue to do so in the coming years. With its on-

[1] https://www.unibe.ch/news/media_news/media_relations_e/media_releases/2023/media_releases_2023/cheops_mission_extended/index_eng.html

board coronagraph, JWST has the capability to directly image planets around bright stars , as well as to probe exoplanet atmospheres using infrared transit spectroscopy. The discoveries that JWST is leading us to will certainly propel us into the next era of exoplanet science.

Unfortunately, questions like "How common is the Solar system architecture?" will continue to remain unanswered for the next few years. However, PLATO, with its large field of view, long observing windows and asteroseismology capabilities, will allow us to know our stars, while perhaps finding the first true Earth analogs, and potentially even Earth 2.0.

Bibliography

Aigrain S., Foreman-Mackey D., 2022, arXiv e-prints, p. arXiv:2209.08940

Aigrain S., Hodgkin S. T., Irwin M. J., Lewis J. R., Roberts S. J., 2015, MNRAS, 447, 2880

Alonso R., et al., 2004, ApJL, 613, L153

Andersen J. M., Korhonen H., 2015, MNRAS, 448, 3053

Anglada-Escudé G., Butler R. P., 2012, APJS, 200, 15

Angus R., Morton T., Aigrain S., Foreman-Mackey D., Rajpaul V., 2018, MNRAS, 474, 2094

Baglin A., et al., 2006, in 36th COSPAR Scientific Assembly. p. 3749

Bakos G., Noyes R. W., Kovács G., Stanek K. Z., Sasselov D. D., Domsa I., 2004, PASP, 116, 266

Bakos G. Á., et al., 2013, PASP, 125, 154

Ballard S., et al., 2011, ApJ, 743, 200

Barragán O., Gandolfi D., Antoniciello G., 2019a, MNRAS, 482, 1017

Barragán O., et al., 2019b, MNRAS, 490, 698

Barragán O., Aigrain S., Rajpaul V. M., Zicher N., 2022, MNRAS, 509, 866

Barros S. C. C., et al., 2022, A&A, 665, A154

Bedding T. R., et al., 2001, ApJL, 549, L105

Beichman C., et al., 2014, PASP, 126, 1134

Benz W., et al., 2021, Experimental Astronomy, 51, 109

Boccaletti A., 2011, in Beaulieu J. P., Dieters S., Tinetti G., eds, Astronomical Society of the Pacific Conference Series Vol. 450, Molecules in the Atmospheres of Extrasolar Planets. p. 163

Boisse I., Bouchy F., Hébrard G., Bonfils X., Santos N., Vauclair S., 2011, A&A, 528, A4

Bond I. A., et al., 2004, ApJL, 606, L155

Borucki W. J., 2017, Proceedings of the American Philosophical Society, 161, 38

Borucki W. J., et al., 2010, Science, 327, 977

Borucki W. J., et al., 2011, ApJ, 736, 19

Bourrier V., Hébrard G., 2014, A&A, 569, A65

Bryson S. T., et al., 2013, PASP, 125, 889

Cabrera J., Csizmadia S., Erikson A., Rauer H., Kirste S., 2012, A&A, 548, A44

Campbell B., Walker G. A. H., Yang S., 1988, ApJ, 331, 902

Carter A. L., et al., 2022, arXiv e-prints, p. arXiv:2208.14990

Chabrier G., Johansen A., Janson M., Rafikov R., 2014, in Beuther H., Klessen R. S., Dullemond C. P., Henning T., eds, Protostars and Planets VI. p. 619, doi:10.2458/azu_uapress_9780816531240-ch027

Charbonneau D., Brown T. M., Latham D. W., Mayor M., 2000, ApJL, 529, L45

Charbonneau D., et al., 2009, Nature, 462, 891

Cherubim C., et al., 2023, AJ, 165, 167

Ciardi D. R., Beichman C. A., Horch E. P., Howell S. B., 2015, ApJ, 805, 16

Collier Cameron A., 2016, Extrasolar Planetary Transits. Springer International Publishing, p. 89, doi:10.1007/978-3-319-27458-4_2

Collier Cameron A., et al., 2021, MNRAS, 505, 1699

Cosentino R., et al., 2012, in Ground-based and Airborne Instrumentation for Astronomy IV. p. 84461V, doi:10.1117/12.925738

Csizmadia S., et al., 2023, Three new M-dwarf companions from K2-mission mimicking exoplanet transits (EPIC 220397060, 201299088, 228729473), Unpublished Manuscript

Cumming A., Butler R. P., Marcy G. W., Vogt S. S., Wright J. T., Fischer D. A., 2008, PASP, 120, 531

Curiel S., Ortiz-León G. N., Mioduszewski A. J., Sanchez-Bermudez J., 2022, AJ, 164, 93

Davis A. B., Cisewski J., Dumusque X., Fischer D. A., Ford E. B., 2017, ApJ, 846, 59

Deeg H. J., et al., 2023, TOI-1416: A system with a super-Earth planet with a 1.07d period, (inpress)

Diamond-Lowe H., et al., 2022, AJ, 164, 172

Díaz R. F., Almenara J. M., Santerne A., Moutou C., Lethuillier A., Deleuil M., 2014, MNRAS, 441, 983

Dumusque X., 2018, A&A, 620, A47

Dumusque X., Udry S., Lovis C., Santos N. C., Monteiro M. J. P. F. G., 2011, A&A, 525, A140

Dumusque X., Boisse I., Santos N. C., 2014, ApJ, 796, 132

Espinoza N., et al., 2020, MNRAS, 491, 2982

Essack Z., et al., 2023, AJ, 165, 47

Fischer D. A., Valenti J., 2005, ApJ, 622, 1102

Fridlund M., et al., 2023, Planets observed with CHEOPS – Two super Earths orbiting the red dwarf star TOI-776, Manuscript submitted for publication

Fulton B. J., et al., 2017, AJ, 154, 109

Gaia Collaboration et al., 2016, A&A, 595, A2

Gaia Collaboration et al., 2018, A&A, 616, A1

Gaia Collaboration et al., 2021, A&A, 649, A1

Gaudi B. S., et al., 2020, arXiv e-prints, p. arXiv:2001.06683

Gaudi B. S., Meyer M., Christiansen J., 2021, in 2514-3433, ExoFrontiers. IOP Publishing, pp 2–1 to 2–21, doi:10.1088/2514-3433/abfa8fch2, `https://dx.doi.org/10.1088/2514-3433/abfa8fch2`

Gautier Thomas N. I., et al., 2012, ApJ, 749, 15

Georgieva I. Y., et al., 2021, MNRAS, 505, 4684

Georgieva I. Y., Barragán O., Persson C., 2023a, On the RV detection of low-mass transiting planets with multidimensional Gaussian processes, Unpublished Manuscript

Georgieva I. Y., et al., 2023b, arXiv e-prints, p. arXiv:2304.06655

Giacalone S., et al., 2021, AJ, 161, 24

Gillon M., Jehin E., Magain P., Chantry V., Hutsemékers D., Manfroid J., Queloz D., Udry S., 2011, in European Physical Journal Web of Conferences. p. 06002 (`arXiv:1101.5807`), doi:10.1051/epjconf/20101106002

Gillon M., et al., 2017, Nature, 542, 456

Ginzburg S., Schlichting H. E., Sari R., 2016, ApJ, 825, 29

Ginzburg S., Schlichting H. E., Sari R., 2018, MNRAS, 476, 759

Grziwa S., Pätzold M., Carone L., 2012, MNRAS, 420, 1045

Gupta A., Schlichting H. E., 2019, MNRAS, 487, 24

Gupta A., Schlichting H. E., 2020, MNRAS, 493, 792

Hastings W. K., 1970, Biometrika, 57, 97

Hatzes A. P., 2014, A&A, 568, A84

Hatzes A. P., 2016, The Radial Velocity Method for the Detection of Exoplanets. Springer International Publishing, p. 3, doi:10.1007/978-3-319-27458-4_1

Hatzes A. P., Cochran W. D., 1993, ApJ, 413, 339

Hatzes A. P., Rauer H., 2015, ApJL, 810, L25

Hatzes A. P., et al., 2010, A&A, 520, A93

Haywood R. D., et al., 2014, MNRAS, 443, 2517

Henry G. W., Marcy G. W., Butler R. P., Vogt S. S., 2000, ApJL, 529, L41

Hippke M., Heller R., 2019, A&A, 623, A39

Howard A. W., et al., 2010, Science, 330, 653

Howell S. B., et al., 2014, PASP, 126, 398

Irwin J. M., Berta-Thompson Z. K., Charbonneau D., Dittmann J., Falco E. E., Newton E. R., Nutzman P., 2015, in 18th Cambridge Workshop on Cool Stars, Stellar Systems, and the Sun. pp 767–772 (`arXiv:1409.0891`)

JWST Transiting Exoplanet Community Early Release Science Team et al., 2023, Nature, 614, 649

Jenkins J. M., et al., 2010, ApJL, 713, L87

Jenkins J. M., et al., 2016, in Chiozzi G., Guzman J. C., eds, Society of Photo-Optical Instrumentation Engineers (SPIE) Conference Series Vol. 9913, Software and Cyberinfrastructure for Astronomy IV. p. 99133E, doi:10.1117/12.2233418

Jurgenson C., Fischer D., McCracken T., Sawyer D., Szymkowiak A., Davis A., Muller G., Santoro F., 2016, in Evans C. J., Simard L., Takami H., eds, Society of Photo-Optical Instrumentation Engineers (SPIE) Conference Series Vol. 9908, Ground-based and Airborne Instrumentation for Astronomy VI. p. 99086T (`arXiv:1606.04413`), doi:10.1117/12.2233002

Kovács G., Zucker S., Mazeh T., 2002, A&A, 391, 369

Lam K. W. F., et al., 2023, MNRAS, 519, 1437

Latham D. W., Mazeh T., Stefanik R. P., Mayor M., Burki G., 1989, Nature, 339, 38

Leleu A., et al., 2021, A&A, 649, A26

Lissauer J. J., et al., 2011, Nature, 470, 53

Lopez E. D., Fortney J. J., 2014, ApJ, 792, 1

Lovis C., Pepe F., 2007, A&A, 468, 1115

Luque R., Pallé E., 2022, Science, 377, 1211

Luque R., et al., 2021, A&A, 645, A41

Mandel K., Agol E., 2002, ApJL, 580, L171

Mayo A. W., et al., 2018, AJ, 155, 136

Mayor M., Queloz D., 1995, Nature, 378, 355

Mayor M., et al., 2003, The Messenger, 114, 20

Mazeh T., Holczer T., Faigler S., 2016, A&A, 589, A75

Metropolis N., Rosenbluth A. W., Rosenbluth M. N., Teller A. H., Teller E., 1953, Journal of Computational Physics, 21, 1087

Meunier N., Desort M., Lagrange A. M., 2010, A&A, 512, A39

Morton T. D., 2012, ApJ, 761, 6

Newton E. R., et al., 2019, ApJL, 880, L17

Nutzman P., Charbonneau D., 2008, PASP, 120, 317

Orell-Miquel J., et al., 2023, A&A, 669, A40

Owen J. E., Wu Y., 2013, ApJ, 775, 105

Parviainen H., et al., 2019, A&A, 630, A89

Pecaut M. J., Mamajek E. E., 2013, APJS, 208, 9

Pepe F. A., et al., 2010, in McLean I. S., Ramsay S. K., Takami H., eds, Society of Photo-Optical Instrumentation Engineers (SPIE) Conference Series Vol. 7735, Ground-based and Airborne Instrumentation for Astronomy III. p. 77350F, doi:10.1117/12.857122

Pepe F., et al., 2020, arXiv e-prints, p. arXiv:2010.00316

Pepper J., et al., 2007, PASP, 119, 923

Perryman M., 2018, Transits, 2 edn. Cambridge University Press, p. 153–328, doi:10.1017/9781108304160.007

Perryman M., Hartman J., Bakos G. Á., Lindegren L., 2014, ApJ, 797, 14

Persson C. M., et al., 2019, A&A, 628, A64

Persson C. M., et al., 2022, A&A, 666, A184

Petigura E. A., Marcy G. W., Howard A. W., 2013, ApJ, 770, 69

Petigura E. A., et al., 2018, AJ, 155, 89

Piaulet C., et al., 2023, Nature Astronomy, 7, 206

Pollacco D. L., et al., 2006, PASP, 118, 1407

Pont F., Knutson H., Gilliland R. L., Moutou C., Charbonneau D., 2008, MNRAS, 385, 109

Prša A., et al., 2016, AJ, 152, 41

Quanz S., 2019, in EPSC-DPS Joint Meeting 2019. pp EPSC–DPS2019–327

Queloz D., et al., 2009, A&A, 506, 303

Rajpaul V., Aigrain S., Osborne M. A., Reece S., Roberts S., 2015, MNRAS, 452, 2269

Rajpaul V., Aigrain S., Roberts S., 2016, MNRAS, 456, L6

Rasmussen C. E., 2004, Gaussian Processes in Machine Learning. Springer Berlin Heidelberg, Berlin, Heidelberg, pp 63–71, doi:10.1007/978-3-540-28650-9_4, https://doi.org/10.1007/978-3-540-28650-9_4

Rauer H., et al., 2014, Experimental Astronomy, 38, 249

Reiners A., Bean J. L., Huber K. F., Dreizler S., Seifahrt A., Czesla S., 2010, ApJ, 710, 432

Renner S., Rauer H., Erikson A., Hedelt P., Kabath P., Titz R., Voss H., 2008, A&A, 492, 617

Ricker G. R., et al., 2015, Journal of Astronomical Telescopes, Instruments, and Systems, 1, 014003

Rodríguez Martínez R., Stevens D. J., Gaudi B. S., Schulze J. G., Panero W. R., Johnson J. A., Wang J., 2021, ApJ, 911, 84

Rogers J. G., Gupta A., Owen J. E., Schlichting H. E., 2021, MNRAS, 508, 5886

Rogers J. G., Schlichting H. E., Owen J. E., 2023, ApJL, 947, L19

Sahlmann J., Lazorenko P. F., Ségransan D., Martín E. L., Queloz D., Mayor M., Udry S., 2013, A&A, 556, A133

Sanchis-Ojeda R., Winn J. N., Fabrycky D. C., 2013, Astronomische Nachrichten, 334, 180

Savitzky A., Golay M. J. E., 1964, Analytical Chemistry, 36, 1627

Schwamb M. E., et al., 2013, ApJ, 768, 127

Seager S., Mallén-Ornelas G., 2003, ApJ, 585, 1038

Simola U., Dumusque X., Cisewski-Kehe J., 2019, A&A, 622, A131

Simola U., Bonfanti A., Dumusque X., Cisewski-Kehe J., Kaski S., Corander J., 2022, A&A, 664, A127

Smith J. C., et al., 2012, PASP, 124, 1000

Smith A. M. S., et al., 2017, MNRAS, 464, 2708

Smith A. M. S., et al., 2022, MNRAS, 510, 5035

Southworth J., Wheatley P. J., Sams G., 2007, MNRAS, 379, L11

Spergel D., et al., 2015, arXiv e-prints, p. arXiv:1503.03757

Stevens D. J., Gaudi B. S., 2013, PASP, 125, 933

Struve O., 1952, The Observatory, 72, 199

Stumpe M. C., et al., 2012, PASP, 124, 985

Sumi T., et al., 2010, ApJ, 710, 1641

Tal-Or L., et al., 2013, A&A, 553, A30

The LUVOIR Team 2019, arXiv e-prints, p. arXiv:1912.06219

Tinetti G., et al., 2021, arXiv e-prints, p. arXiv:2104.04824

Turbet M., Bolmont E., Ehrenreich D., Gratier P., Leconte J., Selsis F., Hara N., Lovis C., 2020, A&A, 638, A41

Van Eylen V., Agentoft C., Lundkvist M. S., Kjeldsen H., Owen J. E., Fulton B. J., Petigura E., Snellen I., 2018, MNRAS, 479, 4786

Van Eylen V., et al., 2021, arXiv e-prints, p. arXiv:2101.01593

Vanderburg A., Johnson J. A., 2014, PASP, 126, 948

Weiss L. M., et al., 2018, AJ, 155, 48

Winn J. N., 2010, Exoplanet Transits and Occultations. University of Arizona Press, Tucson, AZ, pp 55–77

Wolszczan A., Frail D. A., 1992, Nature, 355, 145

Wood M. L., et al., 2023, AJ, 165, 85

Zechmeister M., et al., 2018, A&A, 609, A12

Zeng L., et al., 2021, ApJ, 923, 247

Zhao L. L., et al., 2023, Nature Astronomy, 7, 198

de Beurs Z. L., et al., 2022, AJ, 164, 49

PAPER A

Hot planets around cool stars – two short-period mini-Neptunes transiting the late K-dwarf TOI-1260

I. Y. Georgieva, C. M. Persson, O. Barragán, G. Nowak, M. Fridlund, D. Locci, E. Palle, R. Luque, I. Carleo, D. Gandolfi, S. R. Kane, J. Korth, K. G. Stassun, J. Livingston, E. C. Matthews, K. A. Collins, S. B. Howell, L. M. Serrano, S. Albrecht, A. Bieryla, C. E. Brasseur, D. Ciardi, W. D. Cochran, K. D. Colon, I. J. M. Crossfield, Sz. Csizmadia, H. J. Deeg, M. Esposito, E. Furlan, T. Gan, E. Goffo, E. Gonzales, S. Grziwa, E. .W. Guenther, P. Guerra, T. Hirano, J. M. Jenkins, E. L. N. Jensen, P. Kabáth, E. Knudstrup, K. W. F. Lam, D. W. Latham, A. M. Levine, R. A. Matson, S. McDermott, H. L. M. Osborne, M. Paegert, S. N .Quinn, S. Redfield, G. R. Ricker, J. E. Schlieder, N. J. Scott, S. Seager, A. M. S. Smith, P. Tenenbaum, J. D. Twicken, R. Vanderspek, V. Van Eylen, J. N. Winn

Published in Monthly Notices of the Royal Astronomical Society, Volume 505, Issue 4, pp.4684-4701,
August 2021
©DOI: 10.1093/mnras/stab1464

MNRAS 000, 1–20 (2020) Preprint 5 August 2021 Compiled using MNRAS LATEX style file v3.0

Hot planets around cool stars – two short-period mini-Neptunes transiting the late K-dwarf TOI-1260

I. Y. Georgieva,[1]★ C. M. Persson,[1], O. Barragán[2], G. Nowak[3,4], M. Fridlund[1,5], D. Locci[6], E. Palle[3,4], R. Luque[3,4], I. Carleo[7], D. Gandolfi[8], S. R. Kane[9], J. Korth[10], K. G. Stassun[11], J. Livingston[12], E. C. Matthews[13,14], K. A. Collins[15], S. B. Howell[16], L. M. Serrano[8], S. Albrecht[17,18], A. Bieryla[15], C. E. Brasseur[19], D. Ciardi[20], W. D. Cochran[21], K. D. Colon[22], I. J. M. Crossfield[23], Sz. Csizmadia[24], H. J. Deeg[3,4], M. Esposito[25], E. Furlan[26], T. Gan[27], E. Goffo[8], E. Gonzales[28], S. Grziwa[29], E. .W. Guenther[25], P. Guerra[30], T. Hirano[31,32], J. M. Jenkins[16], E. L. N. Jensen[33], P. Kabáth[34], E. Knudstrup[17,18], K. W. F. Lam[35], D. W. Latham[15], A. M. Levine[13], R. A. Matson[36], S. McDermott[37], H. L. M. Osborne[38], M. Paegert[15], S. N .Quinn[15], S. Redfield[7], G. R. Ricker[13], J. E. Schlieder[39], N. J. Scott[16], S. Seager[13,40,41], A. M. S. Smith[24], P. Tenenbaum[16,42], J. D. Twicken[16,42], R. Vanderspek[13], V. Van Eylen[38], J. N. Winn[43]

Authors' affiliations are shown at the end of the manuscript

Accepted XXX. Received YYY; in original form ZZZ

ABSTRACT

We present the discovery and characterization of two sub-Neptunes in close orbits, as well as a tentative outer planet of a similar size, orbiting TOI-1260 – a low metallicity K6 V dwarf star. Photometry from TESS yields radii of $R_b = 2.33 \pm 0.10\ R_\oplus$ and $R_c = 2.82 \pm 0.15\ R_\oplus$, and periods of 3.13 and 7.49 days for TOI-1260 b and TOI-1260 c, respectively. We combined the TESS data with a series of ground-based follow-up observations to characterize the planetary system. From HARPS-N high-precision radial velocities we obtain $M_b = 8.6^{+1.4}_{-1.5}\ M_\oplus$ and $M_c = 11.8^{+3.4}_{-3.2}\ M_\oplus$. The star is moderately active with a complex activity pattern, which necessitated the use of Gaussian process regression for both the light curve detrending and the radial velocity modelling, in the latter case guided by suitable activity indicators. We successfully disentangle the stellar-induced signal from the planetary signals, underlining the importance and usefulness of the Gaussian Process approach. We test the system's stability against atmospheric photoevaporation and find that the TOI-1260 planets are classic examples of the structure and composition ambiguity typical for the $2 - 3\ R_\oplus$ range.

Key words: Planetary systems — planets and satellites: individual: TOI-1260b, c – planets and satellites: atmospheres – planets and satellites: composition – techniques: photometric – techniques: radial velocities, stars: low-mass

1 INTRODUCTION

Thanks to space-based photometry from missions like Convection, Rotation and planetary Transits (CoRoT, Baglin et al. 2006), Kepler and K2 (Borucki et al. 2010; Howell et al. 2014) and Transiting Exoplanet Survey Satellite (TESS, Ricker et al. 2015), the detection of shallow transits caused by small planets ($\lesssim 4\ R_\oplus$) around faint stars has been made possible. The current exoplanet census shows that the most commonly detected population of planets is well represented by the so-called sub-Neptunes ($2 \lesssim R_\oplus \lesssim 4$) and

★ E-mail: iskra.georgieva@chalmers.se

rocky super-Earths ($1 \lesssim R_\oplus \lesssim 1.5$), with the radius valley (Lopez & Fortney 2013; Owen & Wu 2013; Fulton et al. 2017; Van Eylen et al. 2018, 2021), characterized by a paucity of planets between 1.5 and 2 $R_\oplus$ (Fulton et al. 2017). This range has been shown to shift to smaller radii for low-mass stars (Fulton & Petigura 2018; Wu 2019; Cloutier & Menou 2020; Van Eylen et al. 2021). An interesting observation about this population is the apparent ambiguity of the members' structures and compositions. Valencia et al. (2007) first discussed the continuous wide range of planet compositions for a given mass and radius, while discrete reference planet models by Zeng et al. (2016, 2019) show possible combinations of a rocky core with a H-He envelope, water-dominated worlds, as well as combinations of rock and ice bounded by H-He envelopes. This ambiguity is the result of the observed overlap between both the masses and radii of the two populations. Otegi et al. (2020) report the transition range between sub-Neptunes to super-Earths to be $5 - 25\ M_\oplus$ and $2 - 3\ R_\oplus$, which the TOI-1260 planets presented in this work comfortably fall in.

Moving toward solving the aforementioned composition ambiguity would require understanding the dependence of close-in ($P_{\rm orb} < 10$ days) small ($2 - 3\ R_\oplus$) planets on parameters like the stellar mass (Fulton & Petigura 2018), metallicity (Wilson et al. 2018; Dong et al. 2018), age (Berger et al. 2020), high-energy irradiation (McDonald et al. 2019a), as well as the widely studied planetary mass, radius, period/semi-major axis. That said, while relatively precise radii are available from TESS, to place planets in the context of structure and composition models, we need precise mass estimates, and lots of them, as they are an indispensable piece of this puzzle.

The acquisition of precise masses is made possible thanks to high precision radial velocity (RV) measurements, performed by second generation spectrographs, such as ESO's HARPS (Mayor et al. 2003) and HARPS-N (Cosentino et al. 2012), HIRES (Vogt et al. 1994), CARMENES (Quirrenbach et al. 2014, 2018), and more recently ESPRESSO (Pepe et al. 2010, 2021), EXPRES (Jurgenson et al. 2016) and more. Unfortunately, stellar activity can often be a complicating factor in obtaining accurate orbital solutions for the planet candidates. Great care and caution must be taken in accounting for this activity, the complexity of which may necessitate the use of more sophisticated methods than sinusoid fitting. This problem is further exacerbated the less massive and farther out from its star a planet is, as the precision required for a solid detection grows accordingly.

In this context, we present the discovery and characterization of the TOI-1260 system – a moderately active K6 V dwarf hosting two close-in ($P < 10$ days) transiting sub-Neptunes, as well as a tentative outer planet of similar size and an implied longer period.

The paper is organized as follows. Section 2 contains a summary of the space and ground-based observations of TOI-1260 as well as frequency analysis of the RVs and activity indicators, Sect. 3 describes the stellar modelling, and in Sect. 4 we present our joint RV and transit analysis. In Sect. 5 we discuss our findings and results and we summarize our conclusions in Sect. 6.

2 OBSERVATIONS

Apart from space-based photometry from TESS, we obtained ground-based follow-up photometry from the Las Cumbres Observatory Global Telescope (LCOGT, Brown et al. 2013). We searched for stellar companions using Adaptive Optics (AO) and speckle imaging. To measure the planetary masses we observed TOI-1260 with HARPS-N.

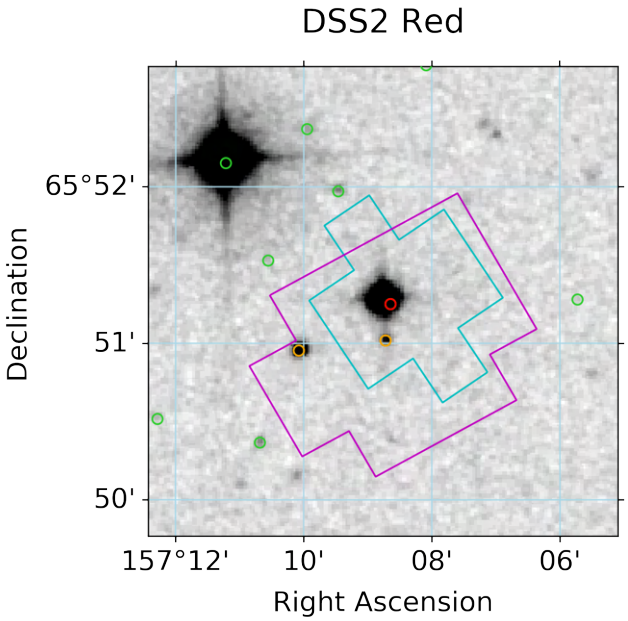

Figure 1. $3' \times 3'$ DSS2 (red filter) image with the Sectors 14 and 21 SPOC photometric apertures outlined in cyan and magenta, respectively. Colored circles denote the positions of *Gaia* DR2 sources within $2'$ of TOI-1260.

2.1 TESS photometry

TESS first observed TOI-1260 in Sector 14 between 2019 Jul 18 and 2019 Aug 15 on camera 4, CCD 3, and again in Sector 21 from 2020 Jan 21 to 2020 Feb 18 on camera 2, CCD 2. The target identifiers, coordinates, proper motion and magnitudes are listed in Table 1. Figure 1 shows a $3' \times 3'$ digitized sky survey 2 (DSS-2, red filter) image centred on TOI-1260, marked by the red circle. The orange circles inside the Science Processing Operations Center (SPOC, Jenkins et al. 2016) apertures of the two sectors are potentially contaminating sources (TIC 841176092 with $V_{\rm mag} \approx 19$ and TIC 138477027 with $V_{\rm mag} \approx 16.2$ at 13.9″ and 40″ away from TOI-1260, respectively). However, the difference image centroid analyses performed for both TOIs detected in the SPOC pipeline, together with the ground-based follow-up observations discussed in the following sections, exclude this from being the case. The SPOC pipeline (Twicken et al. 2010; Morris et al. 2017) uses Simple Aperture Photometry (SAP) to generate stellar light curves, where common instrumental systematics, including dilution, are removed via the Presearch Data Conditioning (PDCSAP) algorithm (Smith et al. 2012; Stumpe et al. 2012). The TESS data were sampled at 2-min cadence and, after removing cadences flagged as potentially affected by anomalous events, the PDCSAP flux extracted from the FITS files produced by the SPOC pipeline (grey-dotted light curves in both panels of Fig. 2) was used for both datasets to conduct the transit search.

Our transit search was realized via the MATLAB-based package EXOTRANS (Grziwa et al. 2012). EXOTRANS utilizes filtering routines based on the Stationary Wavelet Transform to remove intrinsic stellar variability as well as signals at known frequencies to allow searching for additional transits. The search itself is performed using an optimized version of the traditional well-established BLS

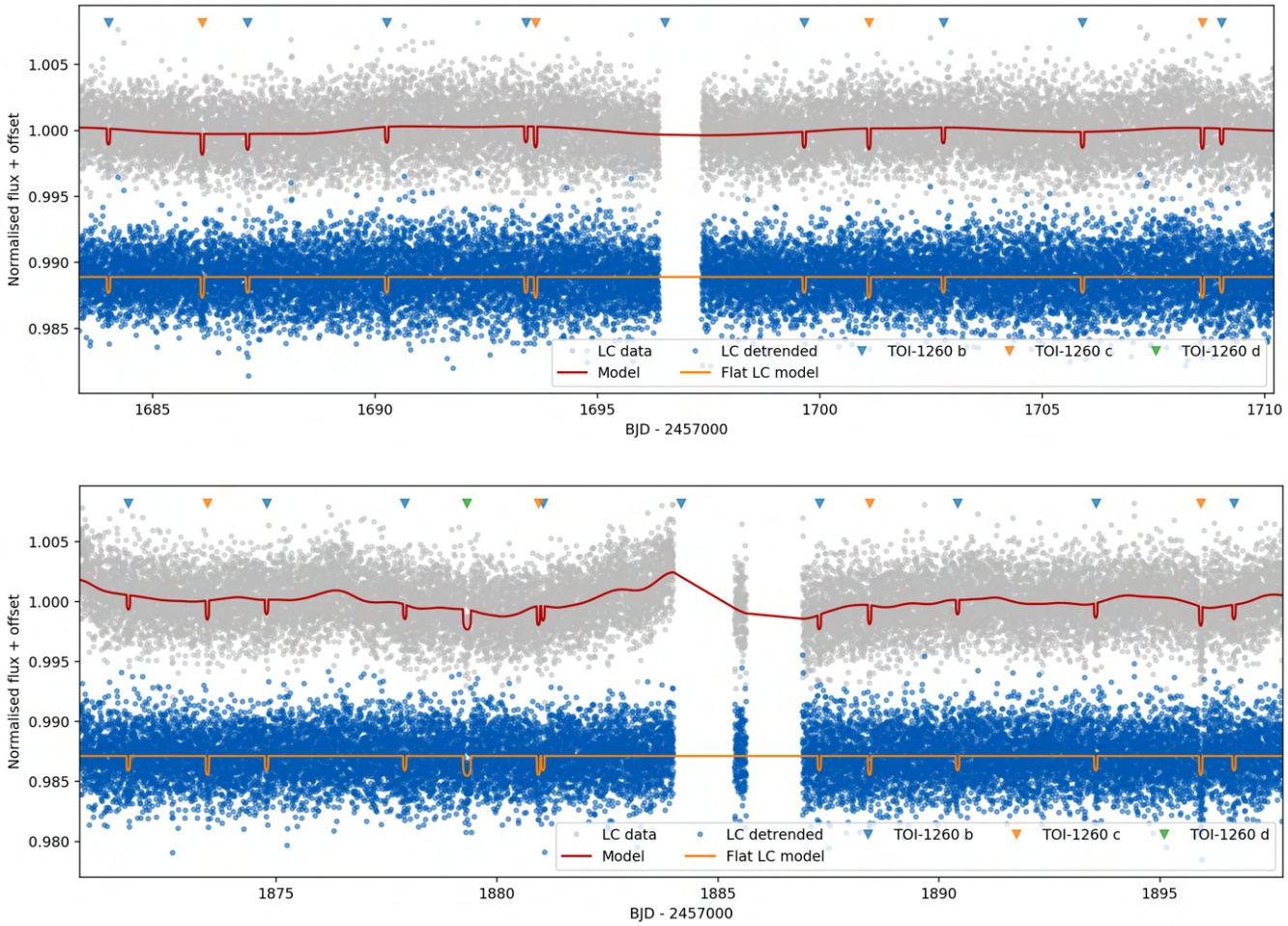

Figure 2. PDCSAP light curve in grey with GP model and transits overplotted in red, and resulting detrended light curve in blue for Sector 14 (top panel) and Sector 21 (bottom panel). The single transit event is visible in the bottom panel at 1879.3 days here plotted with a duration consistent with an arbitrary period of 40 days for visualization. Individual transits are marked with triangles.

algorithm (Kovács et al. 2002), as described in Ofir (2014). TOIs 1260.01 and 1260.02 were first discovered in the SPOC transit search (Jenkins 2002; Jenkins et al. 2010, 2017) with periods of 3.13 and 7.49 days, respectively, and announced in the TESS SPOC data validation reports (DVR, Twicken et al. 2018) and the TOI release portal[1]. We note that 1260.02 is missing from the DVR for Sector 21. Instead, in addition to 1260.01, a signal at 16.613 days was reported but was not given TOI status, likely due to the significant difference in depth between its two apparent transits, the second of which coincides with a transit of 1260.02. This is further discussed in Sect. 4.1.

EXOTRANS detected the two candidates with depths of 1222 ppm and 1685 ppm in both TESS sectors, and periods in agreement with the publicly announced 1260.01 and 1260.02, respectively. As an additional check, we further analysed the light curve data using the `lightkurve` package (Lightkurve Collaboration et al. 2018). We discovered no significant odd/even difference or a sign of a secondary eclipse. This concurs with the results in the DVRs, where the odd/even depth test and difference image centroid test also found no evidence for either signal being due to an eclipsing binary or background eclipsing binary. Encouraged by the agreement between the different pipelines, we prioritized TOI-1260 and qualified it as a promising target for follow-up observations.

Due to the complex variability TOI-1260 exhibits, we chose to remove the low frequency signals in the light curves using a Gaussian process (GP). We use the Python package `citlalicue`[2], which is a wrapper of `george` (Foreman-Mackey et al. 2014; Ambikasaran et al. 2016) and `pytransit` (Parviainen 2015). Briefly, `citlalicue` performs a GP regression (given a covariance function as provided by `george`) together with transit models (`pytransit`) to the data. The best fitting model is computed by likelihood maximization. This generates a model that contains variability and transits. `citlalicue` then removes the light curve variability model from the data to create a flattened normalized light curve with only transits.

We ran `citlalicue` with a GP created with a Matérn 3/2 covariance function together with a model of the two transiting planet candidates and an additional single transit we identified in Sector 21 at $T_0 \sim 1879.32$. Since we are not interested in the nature of the variability signal, we chose the Matérn 3/2 kernel because of

[1] https://tess.mit.edu/toi-releases/

[2] https://github.com/oscaribv/citlalicue

Table 1. Main identifiers, equatorial coordinates, proper motion, parallax, optical and infrared magnitudes, and fundamental parameters of TOI-1260.

Parameter	Value	Source
Main identifiers		
TIC	355867695	ExoFOP[a]
2MASS	J10283500+6551163	ExoFOP
UCAC4	780-023265	ExoFOP
WISE	J102834.71+655115.5	ExoFOP
APASS	59325479	ExoFOP
Equatorial coordinates, parallax, and proper motion		
R.A. (J2000.0)	$10^{h}28^{m}34.56^{s}$	*Gaia* DR3[b]
Dec. (J2000.0)	$+65°51'15.07''$	*Gaia* DR3
π (mas)	13.6226 ± 0.0147	*Gaia* DR3
μ_α (mas yr^{-1})	-177.340 ± 0.012	*Gaia* DR3
μ_δ (mas yr^{-1})	-81.693 ± 0.013	*Gaia* DR3
Optical and near-infrared photometry		
TESS	10.812 ± 0.006	TIC v8[c]
G	$11.5655 \pm 0.0.0028$ [d]	*Gaia* DR3
B_p	12.2955 ± 0.0030 [d]	*Gaia* DR3
R_p	10.7415 ± 0.0038 [d]	*Gaia* DR3
B	13.259 ± 0.088	APASS
V	11.875 ± 0.165	APASS
g	12.702 ± 0.060	APASS
J	9.698 ± 0.023	2MASS
H	9.105 ± 0.027	2MASS
Ks	8.950 ± 0.022	2MASS
$W1$	8.891 ± 0.023	All*WISE*
$W2$	8.964 ± 0.020	All*WISE*
$W3$	8.880 ± 0.023	All*WISE*
$W4$	9.215 ± 0.453	All*WISE*

[a] https://exofop.ipac.caltech.edu/
[b] Gaia Collaboration et al. (2021)
[c] Stassun et al. (2018b)
[d] Uncertainties from the VizieR Catalogue, Ochsenbein et al. (2000) .

its flexibility in dealing with stochastic correlation. We performed individual runs for each sector given that light curve variability scales may be different between the sectors.

The PDCSAP light curves of both sectors are shown in Fig. 2, along with the flattened light curves and transit models. We use these flattened light curves for our joint analysis in Sect. 4. The single transit is visible in the lower panel of Fig. 2 and its depth is approximately 1430 ppm. The feature is shown plotted assuming an arbitrary period of 40 days, which is within the range of possible periods for this possible outer planet (more on this in Sect. 4.1).

2.2 Light curve follow-up

As a further step towards confirming the planets and to try and improve the system parameters, we acquired ground-based time-series follow-up photometry of TOI-1260 as part of the TESS Follow-up Observing Program (TFOP)[3]. We used the `TESS Transit Finder`, which is a customized version of the `Tapir` software package (Jensen 2013), to schedule our transit observations. The photometric data were extracted using `AstroImageJ` (Collins et al. 2017).

[3] https://tess.mit.edu/followup

2.2.1 *LCOGT*

We observed a full transit of 1260.01 on 2020 Jan 04 and parts of the 1260.02 SPOC ephemeris 3σ window on 2019 Dec 03 and 2020 February 01 from LCOGT 1.0 m network node at McDonald Observatory. All observations were in the Pan-STARSS z-short filter. The 4096×4096 LCOGT SINISTRO cameras have an image scale of $0.''389$ per pixel, resulting in a $26' \times 26'$ field of view. The 1260.01 images were defocused and have typical stellar point-spread-functions (PSFs) with full-width-half-maximum (FWHM) $\sim 8.''3$, and circular apertures with radius $\sim 9.''7$ were used to extract the differential photometry. Regarding both epochs of TOI 1260.02, the first observations cover a partial (half) transit, and on the second occasion the observations cover a fraction of the transit ingress. Neither dataset shows a hint of the planet signal. This can be caused by data reduction systematics given the partial coverage of the transits and the relatively low light curve precision. Therefore we do not use these data for further analysis. The photometry ruled out a transit on target and ruled out possible contaminating nearby eclipsing binaries (NEBs) within $2.'5$ of the target star over the observing window.

2.2.2 *KeplerCam*

We observed overlapping transits of TOIs 1260.01 and 1260.02 (assuming the initial SPOC Sector 14 nominal ephemerides) in Sloan i'-band on 2019 November 18 from KeplerCam on the 1.2 m telescope at the Fred Lawrence Whipple Observatory. The 4096×4096 Fairchild CCD 486 detector has an image scale of $0.''336$ per pixel, resulting in a $23.'1 \times 23.'1$ field of view. The observations were focused and the resulting images have typical stellar PSFs with a FWHM of $\sim 1.''5$. Circular apertures with radius $\sim 4.''7$ were used to extract the differential photometry. The on-target light curve was inconclusive, but possible contaminating NEBs within $2.'5$ of the target star were ruled out over the 183 minute observing window.

2.3 AO with Gemini-North/NIRI

It is crucial that close visual companions are identified, since these can dilute the lightcurve and thus alter the planet properties, or even be the source of false positive signals, in the case that the visual companion is itself a binary (see e.g. Ciardi et al. 2015). We search for such companions using AO imaging using the NIRI instrument (Hodapp et al. 2003) at the Gemini-North telescope. We collected a total of 9 images of TOI-1260 on 2019 Nov 25, using the narrow-band Brγ filter which falls within the K-band. Each image had an exposure time of 3.9 s, and we dithered the telescope between each image. This allows for a sky background frame to be constructed from the science data itself, by median combining these dithered frames. Our data reduction process consisted of bad pixel removal, flat-correction and sky-background subtraction, and aligning the stellar position between frames so they could be coadded. We searched for companions in the final image visually, and did not identify companions anywhere in the field of view, which extends to at least $13''$ from the star in all directions. We used a fake star injection technique to measure the sensitivity of the data. In this process we sequentially injected fake PSFs (constructed from the measured stellar PSF, and with peak brightness 3 times the local dispersion level) into the image, every 132 mas in the radial direction and at 8 distinct position angles for each radius. We measured the significance of each fake PSF, and linearly scale this value to the flux at which a companion would be detected with 5σ significance.

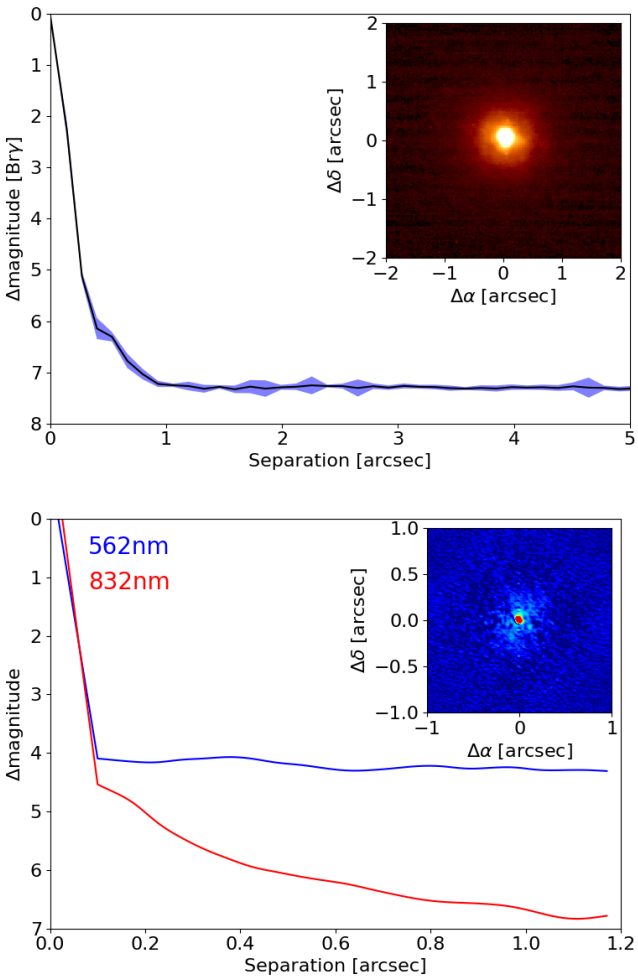

Figure 3. Upper panel: sensitivity to faint visual companions of our Gemini/NIRI observations of TOI-1260. Companions 5 magnitudes fainter than the host star can be detected beyond 270 mas and no companions are seen anywhere in the field of view, which extends at least 13″ from the target in all directions. The inset shows the central portion of the image, centered on the star, and the star appears single to the limit of our resolution. Lower panel: 5-σ sensitivity curve of speckle imaging by Gemini North/'Alopeke showing a reconstructed image of the field. No bright companions are detected within 1.2″.

The quoted sensitivity at each radius is the median sensitivity across the 8 position angles. We are sensitive to companions 5 magnitudes fainter than the star at separations beyond 270 mas, and reach a contrast limit of $\Delta K = 7.3$ mag in the wide field. The upper panel in Fig. 3 shows the sensitivity of our survey, and the inset shows an image of the target itself.

We note that the above described procedure has been used in a wide range of papers (see e.g. Günther et al. 2019; Rodriguez et al. 2019; Kostov et al. 2019).

2.4 Gemini-North/'Alopeke speckle imaging

While AO imaging is sensitive in the infrared and at wider separations from the target, speckle imaging explores the closer vicinity of the target at optical wavelengths.

TOI-1260 was observed on 2020 Feb 16 using the 'Alopeke speckle instrument on Gemini-North[4]. 'Alopeke provides simultaneously speckle imaging in two bands, 562 nm and 832 nm, with output data products including a reconstructed image, and robust limits on companion detections (Howell et al. 2011). Figure 3 (lower panel) shows our resulting contrast curves and the reconstructed 832 nm speckle image. We find that TOI-1260 is a single star with no companion brighter than about 5 - 7 magnitudes detected within 1.″2. 'Alopeke observations provide resulting spatial resolutions of 0.017 mas in the blue, and 0.026 mas in the red, yielding an inner working angle of 1.18 and 1.84 au at the distance to TOI-1260, respectively.

2.5 High-dispersion spectroscopy with TNG/HARPS-N

Currently, RV measurements are invaluable for the purpose of planetary mass determination. Such observations, however, also allow for co-added stellar spectra to be obtained, which are used to model the star and thus obtain more accurate stellar parameters.

Between 2020 Jan 14 and 2020 June 13 we collected 33 spectra with the HARPS-N spectrograph (Cosentino et al. 2012, R≈115 000) mounted at the 3.58-m Telescopio Nazionale Galileo (TNG) of Roque de los Muchachos Observatory in La Palma, Spain, under the observing programmes CAT19A_162, ITP19_1 and A40TAC_22[5]. The exposure time was set to 1350 – 3600 s, based on weather conditions and scheduling constraints, leading to a SNR per pixel of 21 – 74 at 5500 Å. The spectra were extracted using the off-line version of the HARPS-N Data Reduction Software (DRS) pipeline (Cosentino et al. 2014), version 3.7. Absolute RVs and spectral activity indicators – bisector inverse slope (BIS), full-width at half maximum (CCF_FHWM), contrast (CCF_CTR) of the cross-correlation function (CCF) and Mount-Wilson S-index – were measured using an on-line version of the DRS, the YABI tool, by cross-correlating the extracted spectra with a K5 mask (Baranne et al. 1996). We also used `serval` (Zechmeister et al. 2018) code to measure relative RVs by the template-matching, chromatic index (CRX), differential line width (dLW), and Hα index. The uncertainties of the RVs measured with `serval` are in the range 0.9 – 3.1 m s^{-1}, with a mean value of 1.6 m s^{-1}. Table A1 gives the time stamps of the spectra in BJD$_{\rm TDB}$, `serval` relative RVs along with their 1σ error bars, and spectral activity indicators measured with YABI and `serval`. In the joint RV and transit analysis presented in Section 5 we used relative RVs measured from HARPS-N spectra with `serval` by the template-matching technique.

2.5.1 *Frequency analysis of TNG/HARPS-N data*

In order to search for the Doppler reflex motion induced by the transiting planetary candidates and unveil the presence of possible additional signals we performed a frequency analysis of the RVs and spectral activity indicators measured from TNG/HARPS-N spectra. We calculated the generalised Lomb-Scargle (GLS) periodograms (Zechmeister & Kürster 2009) of the available time series and computed the theoretical 10 %, 1 %, and 0.1 % false alarm probability (FAP) levels (Fig. 4). The 151.8 day time baseline of the measurements translate into a frequency resolution of 0.006586 days^{-1}.

The strongest peak in the GLS periodogram of RVs

[4] https://www.gemini.edu/sciops/instruments/alopeke-zorro/

[5] 20 spectra were obtained from the Spanish CAT19A_162 programme (PI: Nowak), 12 spectra from ITP19_1 programme (PI: Pallé) and one spectrum from A40TAC_22 programme (PI: Gandolfi).

(FAP < 0.1%) has a frequency of ~0.031, i.e. a period of ~32.5 days (panel (a) of Fig. 4). Peaks at this frequency are also the strongest ones in the GLS periodograms of spectral activity indicators measured with the DRS pipeline, especially in the periodogram of CCF-FWHM (panel (e) of Fig. 4) and in the periodogram of dLW measured with `serval` (panel (h) of Fig. 4). The GLS periodogram of residuals after fitting two sinusoids with periods and phases corresponding to 1260.01 (f_b = 0.320 ± 0.002 days^{-1}, P_b = 3.13 ± 0.02 days) and 1260.02 (f_c = 0.133 ± 0.002 days^{-1}, P_c = 7.49 ± 0.11 days) shows two highly significant peaks (FAP < 0.1 %) at the frequency of $0.031^{+0.002}_{-0.003}$ days^{-1} and its first harmonic. This clearly shows that the strongest signal in the radial velocities has its origin in stellar activity. The RV residuals after a joint model presented in Sect. 4 (panel (c) of Fig.4) show no further significant peaks. In the GLS periodograms of the activity indicators there are no peaks at the frequencies of the candidates.

The above results show that due to the suboptimal quantity and sampling of the data, a simple periodogram inspection is not suitable for such subtle and sophisticated analysis as required by this system. For the global model we thus implement a more advanced technique as demonstrated in Sect. 4.

3 STELLAR MODELLING

3.1 Spectral analysis

We modelled the co-added high resolution (R = 115 000) HARPS-N spectra with a signal-to-noise of 125 at 5800 Å with the spectral analysis package `SME` (Spectroscopy Made Easy; Valenti & Piskunov 1996; Piskunov & Valenti 2017) version 5.22. This software package matches observations to synthetic stellar spectra calculated from grids of atmosphere models using a χ^2-minimising procedure. We used the `MARCS 2012` (Gustafsson et al. 2008) grid and also checked the final models with the `ATLAS12` model spectra (Kurucz 2013). The line data was taken from VALD (Ryabchikova et al. 2015). We derived the effective temperature ($T_{\rm eff}$), the stellar surface gravity ($\log g$), abundances, the projected stellar rotational velocity ($V \sin i_\star$), and the macroturbulent velocity ($V_{\rm mac}$), following the procedures described in Persson et al. (2018) and Fridlund et al. (2017). In summary, we used the line wings of Hα to derive $T_{\rm eff}$, and $\log g$ was modelled with the line wings of the Ca I $\lambda\lambda$6102, 6122, and 6162 triplet, and the λ6439 line. Due to the low $T_{\rm eff}$, and hence the weak line wings of Hα and the large number of metal lines contaminating the diagnostic line wings, we also used the Na doublet $\lambda\lambda$5889 and 5896 sensitive to both $T_{\rm eff}$ and $\log g$ to check our model. $V \sin i_\star$, $V_{\rm mac}$, and the iron and calcium abundances, [Fe/H] and [Ca/H], were modelled with narrow and unblended lines between λ6000 and λ6500, and the [Na/H] abundance with lines between λ5600 and λ6200. The abundances of Ca and Na were similar to Fe. The macroturbulent and radial velocities were found to be 1.5 km s^{-1} and -16.6 km s^{-1}, respectively, while the microturbulent velocity, $V_{\rm mic}$, was fixed to 1 km s^{-1}.

To check the `SME` results we also used the empirical `SpecMatch-Emp` (Yee et al. 2017) code characterising stars based on their optical spectra. The software compares the observed spectrum to a spectral library of more than 400 well-characterised stars with spectral classes M5 to F1 observed by Keck/HIRES. Since the library stars often have their radii calibrated using interferometry, the direct output is $T_{\rm eff}$, $R_\star$, and [Fe/H]. Before running the code, we transformed our co-added HARPS-N spectra into the format of Keck/HIRES spectra used by `SpecMatch-Emp` as outlined in Hirano et al. (2018).

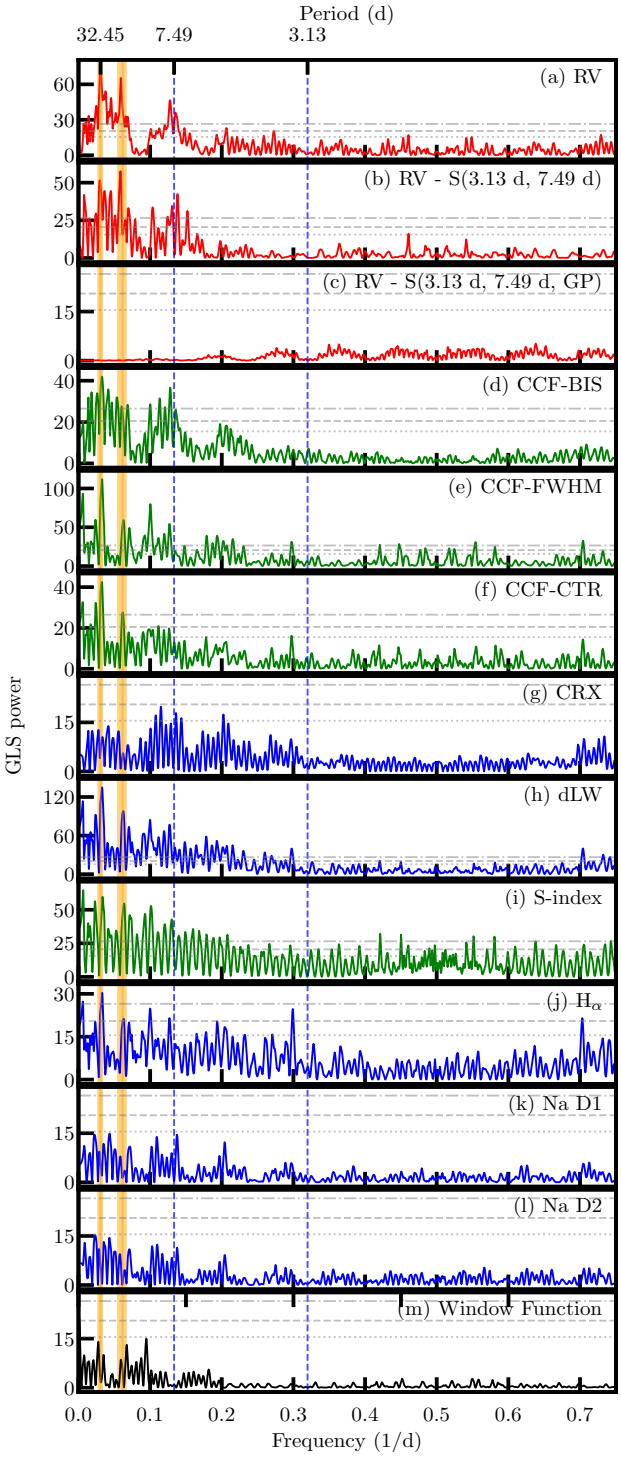

Figure 4. Generalized Lomb-Scargle periodograms of RVs of TOI-1260 (a), their residuals (b) after fitting two sinusoids with periods and phases corresponding to 1260.01 (f_b = 0.320±0.002 days^{-1}, P_b = 3.13±0.02 days) and 1260.02 (f_c = 0.133 ± 0.002 days^{-1}, P_c = 7.49 ± 0.11 days), marked as vertical blue dashed lines, and their residuals (c) after fitting final joint model presented in Sect. 4. Vertical orange areas present frequency of the GP signal ($f_{\rm GP}$ = $0.031^{+0.002}_{-0.003}$ days^{-1}, $P_{\rm GP}$ = $32.45^{+3.70}_{-2.14}$ days) and its first harmonic. Panels plotted in green show periodograms of spectral activity indicators measured with DRS pipeline and panels plotted in blue activity indicators measured with `serval`. Last panel (m) presents the window function of the data. Horizontal grey lines show the theoretical FAP levels of 10 % (dotted line), 1 % (dashed line), and 0.1 % (dash-dotted line) for each panel.

The models are in excellent agreement and we list the results in Table 2 along with the effective temperature from Gaia as a comparison. We adopt the SME results for the modelling of the stellar mass and radius in the following section.

3.2 Stellar mass and radius

We started with an independent determination of the stellar radius, and performed an analysis of the broadband spectral energy distribution (SED) of the star together with the *Gaia* DR2 parallaxes adjusted by +0.08 mas to account for the systematic offset reported by Stassun & Torres (2018). We followed the procedures described in Stassun & Torres (2016) and Stassun et al. (2017, 2018a) and pulled the JHK_S magnitudes from the *2MASS* catalogue, the $W1-W4$ magnitudes from the *WISE* catalogue, and the $GG_{\rm BP}G_{\rm RP}$ magnitudes from the *Gaia* database. Together, the available photometry spans the stellar SED over the wavelength range 0.4–22 μm. We performed a fit using NextGen stellar atmosphere models, with $T_{\rm eff}$, [Fe/H], and $\log g$ adopted from the spectroscopic analysis with SME as priors. The only additional free parameter is the extinction (A_V), which we restricted to the maximum line-of-sight value from the dust maps of Schlegel et al. (1998). The resulting fit, shown in Fig. 5, is very good with a reduced χ^2 of 1.1 and best-fit $A_V = 0.02 \pm 0.02$. Integrating the (unreddened) SED model gives the bolometric flux at Earth, $F_{\rm bol} = 7.63 \pm 0.18 \times 10^{-10}$ erg s^{-1} cm^{-2}. Taking the $F_{\rm bol}$ and $T_{\rm eff}$ together with the *Gaia* DR2 parallax, gives the stellar radius. Using this radius together with the spectroscopic $\log g$, we obtain an empirical mass estimate.

In order to obtain a uniform set of stellar parameters we used the Python code `isochrones` (Morton 2015), an MCMC fitting tool of stellar properties based on an interface interacting with the MIST (Choi et al. 2016) stellar evolution tracks. We fitted the *Gaia* DR2 parallax and the 2MASS JHK photometry, the four WISE magnitudes and the B- and V-bands from APASS, with priors on $T_{\rm eff}$, $\log g$, and [Fe/H] from SME using `MultiNest` (Buchner et al. 2014) to sample the joint posteriors. We find a bolometric luminosity of $0.139 \pm 0.005\ L_\odot$.

The above results were checked with the Bayesian `Param 1.5` (da Silva et al. 2006) on-line code using the PARSEC isochrones (Bressan et al. 2012) and the same input as for `isochrones`.

We also computed mass and radius from the empirical calibration equations by Torres (2010) from $T_{\rm eff}$, $\log g$, and [Fe/H]. Finally, we used the stellar mass-radius relations for low-mass stars from Boyajian et al. (2012) to compute the stellar mass from the radius obtained from `isochrones`.

The stellar parameters found above indicate that this star is a K6 V star supported by the empirical relations of Stassun et al. (2012) suggesting that the activity-driven radius inflation is at most ~2%, indicating a star on the main-sequence. This is also consistent with the age estimates with `Param 1.5` of $8.4^{+4.7}_{-3.7}$ Gyr.

All results of the stellar mass and radius are in very good agreement and are listed in Table 3 along with a typical mass and radius for an K6 V star for comparison. We adopt the stellar mass and radius from `isochrones` in our joint modelling of the system in Sect. 4 and list our adopted parameters for the modelling in Table 4.

3.3 Stellar activity and rotation period

We note that both Ca II H & K lines are seen in emission in the HARPS-N spectra which indicates that the star is moderately active. The activity offers a way to estimate the rotation period. We first computed the average S-index from the time series to be 1.13 ± 0.08 which was converted to $\log(R'_{HK}) = -4.86 \pm 0.03$ (Suárez Mascareño et al. 2015). This was used together with the empirical relation for late-type stars from Suárez Mascareño et al. (2015, 2016) and the star's color to predict a rotation period of 34 ± 2 days. This is within 1 σ of the 22 ± 10 days estimate obtained from $R_\star$ together with the spectroscopically determined $V \sin i_\star$, assuming that the star is equator-on oriented.

The activity predicts an age of 4.1 ± 0.2 Gyr, from the empirical relations of Mamajek & Hillenbrand (2008) which is considerably lower than derived above although still within the large uncertainties. The estimate from gyrochronology has, however, the following two caveats: this star is somewhat cooler than the nominal range of applicability of the relations, and secondly, recent work have suggested that K-dwarfs experience a stall in their spindown (Curtis et al. 2020), so that such stars can be considerably older than their observed rotation or activity may otherwise suggest.

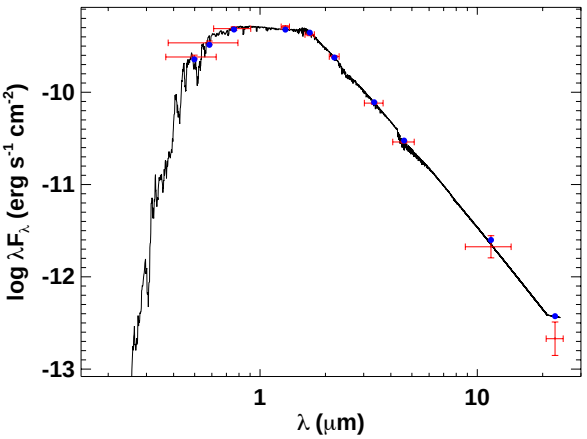

Figure 5. Spectral energy distribution of TOI-1260. Red symbols represent the observed photometric measurements, where the horizontal bars represent the effective width of the passband. Blue symbols are the model fluxes from the best-fit NextGen atmosphere model (black).

3.4 Population membership

The kinematics of this high proper motion star can be used to compute probabilities of membership in different populations in the Galaxy. Using the data in Table 1 and the methodology of Reddy et al. (2006), we find galactic velocity components of $U = -43.42$ km s^{-1}, $V = -45.96$ km s^{-1}, $W = -30.95$ km s^{-1}. We converted these velocities to the local standard of rest of the Sun to $U_{lsr} = -33.42 \pm 0.16$ km s^{-1}, $V_{lsr} = -40.66 \pm 0.12$ km s^{-1} and $W_{lsr} = -23.75 \pm 0.15$ km s^{-1}. This results in a probability of the star belonging to the thin disk population of $P(thin) = 0.95 \pm 0.02$, and to the thick disk $P(thick) = 0.0516 \pm 0.0002$, and a vanishingly low probability of the star being old enough to belong to the halo population. The thin disk of the Galaxy is expected to have formed 8.8 ± 1.7 Gyr ago (del Peloso et al. 2005) which is consistent with the derived ages.

4 JOINT RV AND TRANSIT ANALYSIS

We use the open source software `pyaneti` (Barragán et al. 2019a), which uses a Bayesian approach with MCMC sampling for planetary

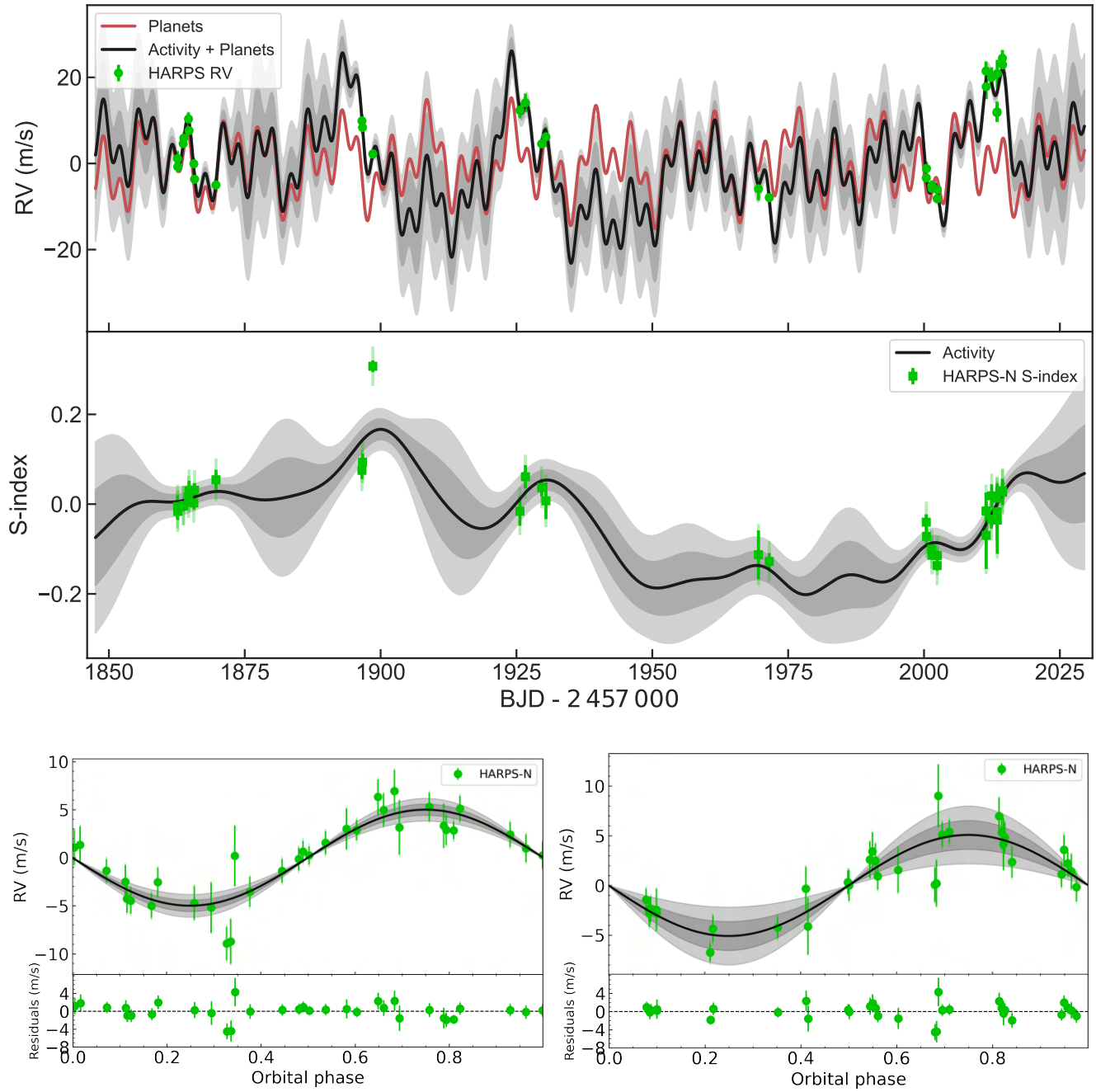

Figure 6. RV (top panel) and S-index (middle panel) time-series. The green markers in each panel represent the HARPS-N RV and S-index measurements with inferred offsets extracted. The solid dark line shows the inferred Multi-GP model, with dark and light shaded areas showing the one and two sigma credible intervals of the corresponding GP model. These regions represent ranges in which other GP curves could also explain the data, with different probability. For the RV panel we also included the RV model for the two planets (solid red line). Bottom panel: HARPS-N RV data folded on the orbital period of each candidate following the subtraction of the systemic velocities, GP signal, and the other planet. The plots also show the inferred RV model for each planet (solid black line) with 1- and 2-sigma credible intervals (shaded areas). In all the plots the nominal error bars are in green, and the error bars taking into account the jitter ($\sigma_{\mathrm{HARPS-N}}$) are semi-transparent green. The latter are < 1 m s^{-1} for the RV data and are hardly visible.

systems parameter estimation, to perform our joint transit and RV analysis, as well as the monotransit and multi-band fits.

Adopting the flattened TESS light curves derived from `citlalicue` (Sect. 2.1), together with the LCO single transit data available for 1260.01 (Sect. 2.1), we model the transits using the Mandel & Agol (2002) approach as implemented in `pyaneti`. We sample for the limb darkening parameters utilising the parametrisation q_1 and q_2 described by Kipping (2013). Instead of sampling for the scaled semi-major axis, $a/R_\star$, for each candidate, we sampled for the stellar density $\rho_\star$, as parametrized in `pyaneti`.

Section 3.3 describes that our RV measurements contain stellar-induced RV variations. For this reason we use the multi-

Table 2. Spectroscopic parameters derived with `SME` and `SpecMatch-Emp` compared to the stellar effective temperature from Gaia.

Method	$T_{\rm eff}$ (K)	[Fe/H]	$\log g$ (cgs)	$V \sin i_\star$ (km s^{-1})
`SME`[a]	4227 ± 85	-0.10 ± 0.07	4.57 ± 0.05	1.5 ± 0.7
`SpecMatch-Emp`	4207 ± 70	-0.06 ± 0.12	...	...
Gaia	4351^{+204}_{-110}	...	...	...

[a] Adopted stellar parameters.

Table 3. Stellar mass and radius and the corresponding stellar densities derived with different methods and typical mass and radius for an K6 V star.

Method	$M_\star$ ($M_\odot$)	$R_\star$ ($R_\odot$)	$\rho_\star$ (g cm^{-3})
`isochrones`[a,b]	0.66 ± 0.01	0.65 ± 0.01	3.43 ± 0.08
`Param 1.5`[b]	0.63 ± 0.02	0.63 ± 0.02	3.53 ± 0.32
`SED fitting`[b]	0.61 ± 0.08[c]	0.67 ± 0.03	...
`SpecMatch-Emp`	...	0.67 ± 0.07	...
Torres[b,d]	0.61 ± 0.04	0.65 ± 0.05	3.07 ± 0.68
Boyajian[e]	0.65 ± 0.04	...	...
Light curve model[f]	...	...	$3.46^{+0.62}_{-0.93}$
Spectral type K6 V[g]	0.66	0.65	3.39

[a] Adopted stellar mass and radius in the modelling in Sect. 4.
[b] Using $T_{\rm eff}$, $\log g$, and [Fe/H] from `SME`.
[c] Combining the SED radius with $\log g$.
[d] Torres (2010) calibration equations.
[e] Boyajian et al. (2012) calibration equation from eclipsing binaries using $R_\star$ from `isochrones`.
[f] Stellar density obtained from the light curve model (Sect. 4).
[g] Typical mass and radius for a K6 V star.

dimensional Gaussian-process approach described in Rajpaul et al. (2015) to model our RVs. This approach has been used successfully to separate planet signals from stellar activity by e.g. Barragán et al. (2019b) and Mayo et al. (2019). Briefly, it models RVs together with the activity indicators assuming the same underlying GP, $G(t)$, can describe them. This approach constrains the GP flexibility that could remove planet-induced signals. $G(t)$ can be interpreted as representing the fraction of the visible stellar disc that is covered by active regions at a given time.

For our final GP analysis we model our RVs alongside the S-index as

$$\begin{aligned} \Delta RV &= V_c G(t) + V_r \dot{G}(t), \\ \Delta S_{\rm HK} &= S_c G(t), \end{aligned} \tag{1}$$

respectively. The variables V_c, V_r, and S_c, are free parameters which relate the individual time series to the Gaussian Process $G(t)$. The RVs depend on the fraction of the stellar disc covered by active regions as well as how these regions move on the surface. For this reason RVs are modelled as a function of $G(t)$ and its time derivative. We use the S-index given that it is an activity indicator that depends on the fraction of the stellar disc covered by active regions, i.e., it can be described by $G(t)$ only. We use the quasi-periodic covariance function

$$\gamma(t_i, t_j) = \exp\left[-\frac{\sin^2[\pi(t_i - t_j)/P_{\rm GP}]}{2\lambda_{\rm P}^2} - \frac{(t_i - t_j)^2}{2\lambda_{\rm e}^2} \right], \tag{2}$$

where $P_{\rm GP}$ is the period of the activity signal, λ_p the inverse of the harmonic complexity, and λ_e is the long term evolution timescale.

Before committing to a final model setup, we tested different orbital scenarios including two circular orbits, two eccentric orbits, as well as a combination of the two – inner body with eccentric, outer body with circular orbit, and vice versa. We found that all fits including eccentric orbits provide a solution for the eccentricities consistent with zero. We also calculated the commonly used Bayesian Information Criterion (BIC) and found that the case of two circular orbits is strongly favoured with a ΔBIC = 15 better than the second best model. This is also consistent with short circularization timescales for short-period planets as well as the Van Eylen et al. (2019) finding that multi-planet systems tend to feature low eccentricities. Since both candidates are in close-in orbits, the circular case for both yields a value for the stellar density most consistent with the spectroscopically derived one, and given that the current data does not favour the solution with eccentric orbits, we use the circular orbits case scenario as our final model.

Using the above setup and the RVs from `serval`, we ran our final model with 500 chains to sample the parameter space. For the burn-in phase we used the last 5000 of the converged chains with a thin factor of 10, leading to a final number of 250,000 independent points for each sampled parameter.

As an additional test we ran a joint model without accounting for the stellar signal in any way. We find that the two planets are still detected, but the HARPS-N jitter is significantly higher (8.8 m s^{-1}) than the nominal night-to-night variation ($\approx$0.8 m s^{-1}). This points to the presence of additional signals not accounted for by this model. Nevertheless, the results of this test agree within 1σ, thus lending confidence in our choice of final model.

To ensure that our detection is not due to an artefact of the RV data reduction, as an extra check we performed our final model setup using the DRS-derived RVs. The results once again agree to within 1σ of our adopted parameters.

Lastly, to check that our results do not depend on the sampling algorithm, we used the code `juliet` (Espinoza et al. 2019) to model jointly the photometric and Doppler data. The algorithm is built on many publicly available tools for the modeling of transits (`batman`, Kreidberg 2015), RVs (`radvel`, Fulton et al. 2018), and GP (`george`, Ambikasaran et al. 2016; `celerite`, Foreman-Mackey et al. 2017), and computes efficiently the Bayesian log-evidence using the importance nested sampling included in the `dynesty` package (Speagle 2020). We use the same set of priors presented in Table 4, but for the GP we use an exponential-sine-squared kernel of the form $k_{i,j} = \sigma^2_{\rm GP,RV} \exp\left(-\alpha_{\rm GP,RV}(t_i - t_j)^2 - \Gamma_{\rm GP,RV} \sin^2\left[\frac{\pi|t_i - t_j|}{P_{\rm rot;GP,RV}}\right]\right)$ with a uniform prior in $P_{\rm rot;GP,RV}$ ranging from 22 to 43 d. The `juliet` package does not have the possibility to perform fits with multi-dimensional GP so in this case we apply it only on the RV data. Nevertheless, the fitted parameters from the joint fit with `juliet` are in perfect agreement with the results from `pyaneti`, confirming the robustness of the different analyses and the derived orbital parameters.

A summary of our results, including the fitted parameters and

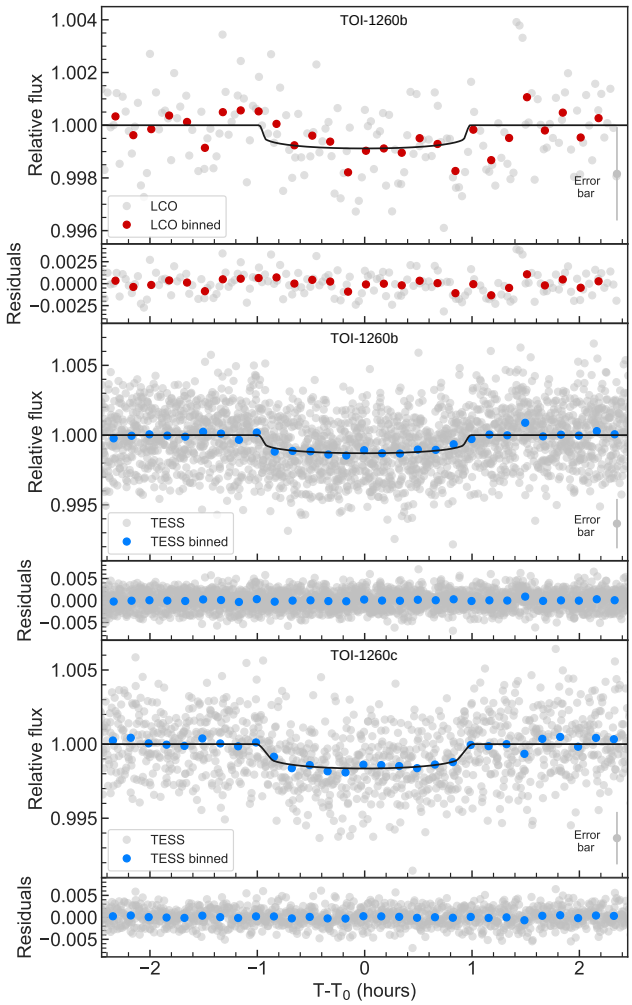

Figure 7. TOI-1260 b and TOI-1260 c transits. The panels show a flattened LCOGT and TESS light curves with residuals folded to the orbital periods of the planets. Black lines show the best-fitting transit models. The LCO and TESS radius estimates for planet b agree to nearly 1σ. Data are shown in the nominal 2-min cadence mode and binned to 10 min. Typical error bar for nominal data is shown at the bottom right for each panel.

priors are presented in Table 4. Figure 6 shows the RV and S-index timeseries together with the inferred models. It should be noted that in Fig. 6 the uncertainties of the inferred models (shadow regions) are relatively large, which is caused by the sub-optimal sampling of the data and the flexibility of the GP model. This figure illustrates the usefulness of the multi-dimensional GP used in this work as it is clear how the RV GP model is constrained by the changes in the S-index (similar to Fig. 2 of Barragán et al. 2019b).

Figure 6 also shows phase-folded RV data of planets b (1260.01) and c (1260.02) together with the corresponding inferred RV model, while Fig. 7 shows the single transit event of planet b detected by LCO as well as the phasefolded transits of both planets as obtained from TESS photometry.

4.1 Tentative outer planet

As discussed in Sect. 2.1, we report an additional transit-like event in Sector 21. A counterpart of this feature is not visible in Sector 14, although it is possible that the transit occurred during the ~1-day

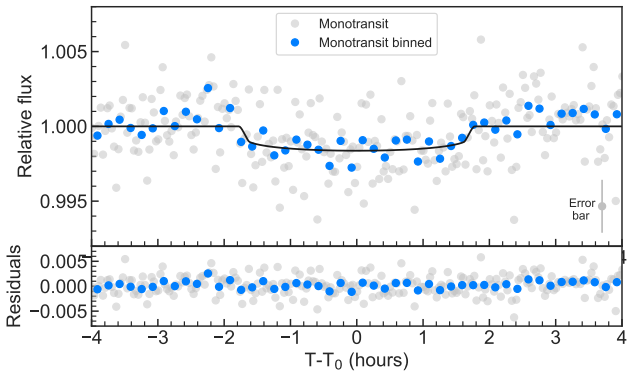

Figure 8. The single transit of the tentative outer planet d seen in Sector 21. The `pyaneti` transit model yields a T_0 of $1879.3211^{+0.0067}_{-0.0055}$ days and a depth of 1418^{+317}_{-248} ppm, which corresponds to a radius of $2.67^{+0.29}_{-0.25}$ $R_\oplus$. Data are shown in the nominal 2-min cadence mode and binned to 10 min, with typical error bar for nominal data in the bottom right.

data gap between orbits (Fig. 2). This transit-like feature does not coincide with a spacecraft momentum dump.

To model the monotransit, we again turn to `pyaneti`. We follow a similar approach as in Osborn et al. (2016). Assuming a circular orbit and based on the transit shape, our single-transit model (Fig. 8) gives a range of physically possible periods of [13.4, 56.3], a transit depth of 1418^{+317}_{-248} ppm, which in turn yields a radius of $2.67^{+0.29}_{-0.25}$ $R_\oplus$. We further narrowed down the period range based on the length of TESS observations and the apparent lack of occurrence of another such transit event during the observing windows. Our final possible periods are listed in Table B1. The binned and unbinned transit data and inferred model of the aforementioned monotransit visible in Sector 21 are displayed in Fig. 8.

In an attempt to try and explore further the physical properties of this tentative outer planet, we performed an MCMC analysis identical to our adopted one, but we added an extra planetary signal with ephemeris corresponding to the transit of the tentative planet d. We used a prior on T_0 of [8879.2, 8879.4], and a wide prior on the period of [20.0, 70.0] and created marginalized posterior distributions using `pyaneti`. We were unable to further constrain the period but we found the maximum allowed semi-amplitude to be 18.4 m s^{-1}(99% confidence interval).

We cannot constrain this further as there is also no sign of another planet in our RV dataset. However, with a maximum semi-amplitude of 18.4 m s^{-1}, this translates to a mass of 76.3 $M_\oplus$. Therefore, if the signal at 1879.32 days is caused by a transiting object, this object belongs to the planetary mass domain.

We further note that the minimum period shown in Table B1 is 20.3 days. This constraint comes from the minimum period that the tentative outer planet has to have in order to not be observed transiting again in the light curve. We however, note that there is a transit of TOI-1260 c between the range 8895.80-8896.05 BJD - 2450000 that looks significantly deeper. This can be caused by some unknown systematics in the light curve or another obscuring object. To investigate this, we performed a simple model adding an extra single transit to a model of planet c between the range 8895.80-8896.05 BJD - 2450000. We thus found that we obtain a better model to the data if we add a signal with a time of mid-transit of 8895.938 ± 0.005, depth of 1705 ± 350 ppm, and transit duration of 2.9 ± 0.3 hours. Figure 9 shows a plot with the two-transit model. These tentative transit parameters are consistent within 2-sigma

Table 4. Summary of the system parameters from the stellar modelling in Sect. 3 and the joint RV and transit modelling with `pyaneti` in Sect. 4.

Parameter	Prior[a]	Value[b]
Model Parameters for TOI-1260		
TOI-1260 b		
Orbital period $P_{\rm orb}$ (days)	$\mathcal{U}[3.1270, 3.1280]$	$3.12748^{+0.000047}_{-0.000038}$
Transit epoch T_0 (BJD - 2,450,000)	$\mathcal{U}[8684.0050, 8684.0250]$	$8684.0128^{+0.0016}_{-0.0024}$
e	$\mathcal{F}[0]$	0
$\omega_\star$	$\mathcal{F}[\pi/2]$	$\pi/2$
Scaled planetary radius $R_{\rm p}/R_\star$	$\mathcal{U}[0.01, 0.10]$	$0.0329^{+0.0014}_{-0.0012}$
Impact parameter, b	$\mathcal{U}[0, 1]$	$0.26^{+0.25}_{-0.17}$
Radial velocity semi-amplitude variation K (m s^{-1})	$\mathcal{U}[0, 25]$	$4.91^{+0.77}_{-0.83}$
TOI-1260 c		
Orbital period $P_{\rm orb}$ (days)	$\mathcal{U}[7.4925, 7.4940]$	$7.49325^{+0.00015}_{-0.00013}$
Transit epoch T_0 (BJD - 2,450,000)	$\mathcal{U}[8686.1050, 8686.1300]$	$8686.1179^{+0.0033}_{-0.0035}$
e	$\mathcal{F}[0]$	0
$\omega_\star$	$\mathcal{F}[\pi/2]$	$\pi/2$
Scaled planetary radius $R_{\rm p}/R_\star$	$\mathcal{U}[0.01, 0.10]$	0.0398 ± 0.0020
Impact parameter, b	$\mathcal{U}[0, 1]$	$0.714^{+0.067}_{-0.066}$
Radial velocity semi-amplitude variation K (m s^{-1})	$\mathcal{U}[0, 25]$	5.1 ± 1.4
GP Period $P_{\rm GP}$ (days)	$\mathcal{U}[22, 43]$	$32.5^{+3.7}_{-2.2}$
$\lambda_{\rm P}$	$\mathcal{U}[0.1, 5]$	$1.4^{+1.0}_{-0.5}$
$\lambda_{\rm e}$ (days)	$\mathcal{U}[1, 200]$	45^{+17}_{-16}
V_c (km s^{-1})	$\mathcal{U}[0, 0.1]$	$0.005^{+0.012}_{-0.004}$
V_r (km s^{-1})	$\mathcal{U}[0, 1]$	$0.22^{+0.32}_{-0.12}$
S_c	$\mathcal{U}[0, 1]$	$0.26^{+0.28}_{-0.12}$
Offset HARPS-N (km s^{-1})	$\mathcal{U}[-0.05, 0.05]$	$0.0046^{+0.0050}_{-0.0057}$
Offset S-index	$\mathcal{U}[0.5, 1.9]$	1.11 ± 0.17
Jitter term $\sigma_{\rm HARPS-N}$ (m s^{-1})	$\mathcal{J}[10^{-3}, 10^{-1}]$	$0.88^{+0.83}_{-0.61}$
Jitter term $\sigma_{\rm S-index}$	$\mathcal{J}[10^{-3}, 10^{-1}]$	$0.0431^{+0.0088}_{-0.0070}$
Limb darkening q_1, *TESS*	$\mathcal{U}[0, 1]$	$0.44^{+0.33}_{-0.24}$
Limb darkening q_2, *TESS*	$\mathcal{U}[0, 1]$	$0.36^{+0.31}_{-0.24}$
Limb darkening q_1, LCO	$\mathcal{U}[0, 1]$	$0.35^{+0.39}_{-0.24}$
Limb darkening q_2, LCO	$\mathcal{U}[0, 1]$	$0.42^{+0.32}_{-0.28}$
Jitter term σ_{TESS} ($\times 10^{-6}$)	$\mathcal{U}[0, 1 \times 10^3]$	752 ± 27
Jitter term $\sigma_{\rm LCO}$ ($\times 10^{-6}$)	$\mathcal{U}[0, 1 \times 10^3]$	141^{+15}_{-99}
Stellar density $\rho_\star$ (g cm^{-3})	$\mathcal{U}[0.1, 10]$	$3.47^{+0.89}_{-1.22}$
Derived parameters	**TOI-1260 b**	**TOI-1260 c**
Planet mass ($M_\oplus$)	$8.6^{+1.4}_{-1.5}$	$11.8^{+3.4}_{-3.2}$
Planet radius ($R_\oplus$)	$2.34^{+0.11}_{-0.09}$	2.82 ± 0.15
Planet density (g cm^{-3})	$3.69^{+0.81}_{-0.76}$	$2.87^{+0.98}_{-0.86}$
Scaled semi-major axis $a/R_\star$	$12.14^{+0.7}_{-1.2}$	$21.7^{+1.2}_{-2.2}$
Semi-major axis a (AU)	$0.0366^{+0.0022}_{-0.0036}$	$0.0656^{+0.0039}_{-0.0065}$
Orbital inclination i (deg)	$88.8^{+0.8}_{-1.4}$	$88.12^{+0.24}_{-0.39}$
Transit duration $t_{\rm tot}$ (hours)	$1.963^{+0.066}_{-0.091}$	$1.96^{+0.12}_{-0.10}$
Equilibrium temperature [c] $T_{\rm eq}$ (K)	860^{+47}_{-31}	643^{+35}_{-23}
Insolation $F_{\rm p}$ ($F_\oplus$)	91^{+22}_{-12}	$28.4^{+6.8}_{-3.9}$
Planet surface gravity[d] (cm s^{-2})	1520^{+370}_{-420}	1410^{+550}_{-500}
Planet surface gravity (cm s^{-2})	1540 ± 290	1450^{+450}_{-410}
Adopted stellar parameters		
Stellar mass ($M_\odot$)	···	0.66 ± 0.01
Stellar radius ($R_\odot$)	···	0.65 ± 0.01
Stellar density (g cm^{-3})	···	3.43 ± 0.08
Effective temperature (K)	···	4227 ± 85
Bolometric luminosity ($L_\odot$)	···	0.139 ± 0.005

Note – [a] $\mathcal{U}[a, b]$ refers to uniform priors between a and b, $\mathcal{J}[a, b]$ to modified Jeffrey's priors calculated using eq. 16 in Gregory (2005), and $\mathcal{F}[a]$ to a fixed value a. [b] Inferred parameters and errors are defined as the median and 68.3% credible interval of the posterior distribution. [c] Assuming an albedo of 0. [d] Calculated from the scaled-parameters as in Southworth et al. (2007).

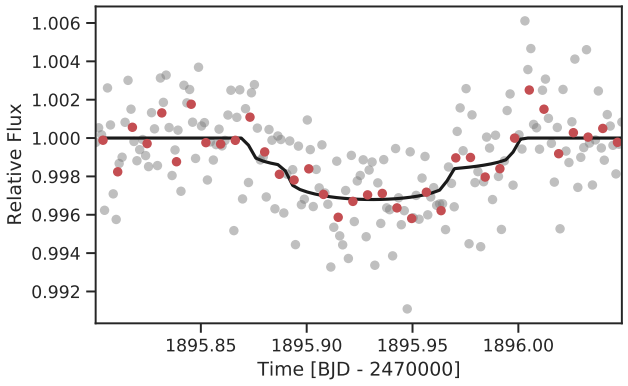

Figure 9. Two-transit model of the potentially overlapping transits of planet c and the tentative planet d, around 1895.95 BJD - 2457000. Gray circles show the flattened TESS data, with ten-minute bins as red circles, and solid line showing the inferred transit model including both planet signals.

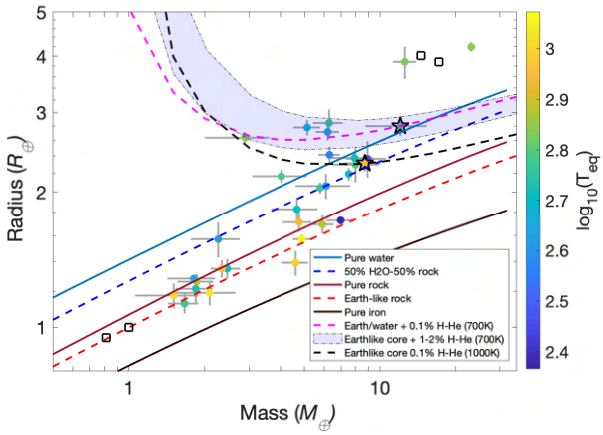

Figure 10. Mass-radius diagram of planets with measured masses better than 30% and radii better than 10% orbiting mid-M to mid-K dwarfs (3000 – 4400 K). In total there are 26 planets in 19 multi-planet systems. Models of core compositions without atmosphere (Zeng et al. 2016) and with atmosphere (Zeng et al. 2019) at different equilibrium temperatures are also plotted. TOI-1260 b and TOI-1260 c are marked with star symbols, and squares are the Solar system planets.

with our single transit event at 8879.3210683 BJD - 2450000. If this detected signal is real and it corresponds to a second transit of the tentative planet d, then its period would be ~ 16.61 days (see Sect. 2.1). Unfortunately, with this period, the only other visible transit in the available TESS light curves would have fallen in the data gap of Sector 14.

We then repeat a similar approach as the one described in Sect. 4, with an extra Keplerian signal with a tight prior on the ephemeris of the tentative 16.61-day planet but we have no clear detection of a RV signal at that period. If this planet is real, based on this three-planet model, its period, radius and transit duration would be $16.613^{+0.008}_{-0.006}$ days and $2.75^{+0.172}_{-0.177}$ $R_\oplus$ and $3.11^{+0.20}_{-0.15}$ hours, respectively. The 99% credible interval for the maximum semi-amplitude would be around 13 m s^{-1}, which in turn translates to a maximum mass of around 39 $M_\oplus$. Adding this signal has an insignificant effect on the parameters of planet b, while planet c shows a slight decrease in radius to 2.68 ± 0.14 $R_\oplus$ and an increase in mass to $13.39^{+3.49}_{-3.26}$ $M_\oplus$. Both of these agree well with our officially reported estimates in Table 4.

Based on these results, we take a conservative approach and we conclude that, based on the available information, we cannot claim a planet with a period of 16.61 days. However, if there is such a planet, it could be confirmed by photometric ground or space-based follow-up. Fortunately, TESS will observe TOI-1260 again in three more sectors – 41, 47 and 48. We note, however, that a RV follow-up would be more challenging because this tentative period is close to half the rotation period of the star.

5 DISCUSSION

5.1 Dynamical stability

The dynamical viability of multi-planet systems is an important component of assessing valid architectures. Testing dynamical integrity and subsequent orbital evolution has played a key role in understanding Kepler systems (Lissauer et al. 2011; Li et al. 2014; Kane 2015, 2019). To test the stability of the orbital solution for our two confirmed planets in the TOI-1260 system, we executed N-body integrations using the Mercury Integrator Package (Chambers 1999). We adopted the stellar, planetary masses and semi-major axes from Table 4. We further assumed initial circular orbits for both of the planets. The simulation was performed for 10^7 simulation years with a time step of 0.1 days to properly sample the relatively short orbital period of the inner planet. The results of the simulation showed no signs of instability, and the eccentricities of both planets remained below 10^{-3} for the duration of the simulation. This demonstrates that the gravitational well of the star is the overwhelmingly dominant influence on the planetary dynamics within their compact system configuration. Given the proximity of the planets to each other, we also investigated the possibility of determining upper mass limits that retain dynamical stability. We gradually increased the masses of both planets independently until the dynamical integrity of the system was compromised during a series of 10^6 year simulations. These simulations showed that the maximum masses for both planets are loosely constrained based on their dynamical interactions, with maximum masses approaching several Jupiter masses before significant instability occurs.

Tipped off by the suspected presence of an outer planet, we decided to check if the system exhibits Transit Timing Variations (TTVs). We performed a TTV analysis using `PyTTV` (Python Tool for Transit Variations, Korth 2020), which showed that a linear ephemeris can be fit between the sectors. The ephemerides from our modelling results (Table 4) and the lack of TTVs allows for future observations of the system using other facilities to be scheduled efficiently.

5.2 Characterization of the TOI-1260 planets

Two important factors that influence the radius distribution of planets are the semi-major axis and the mass of the host star (Fulton & Petigura 2018; Wu 2019; Cloutier & Menou 2020; Van Eylen et al. 2021). Both of these determine a planet's X-ray/UV irradiation evolution. Since the magnitude and evolution of the X-ray luminosity differs between sun-like and low mass stars (McDonald et al. 2019b; Luque et al. 2021), we show in Fig. 10 a mass-radius diagram with planets orbiting mid-M to mid-K stars (here defined as having $T_{\rm eff}$ between 3000 and 4400 K) measured to a precision better than 30% in mass and 10% in radius. We also plot theoretical models of planet core compositions without an atmosphere (Zeng et al. 2016)

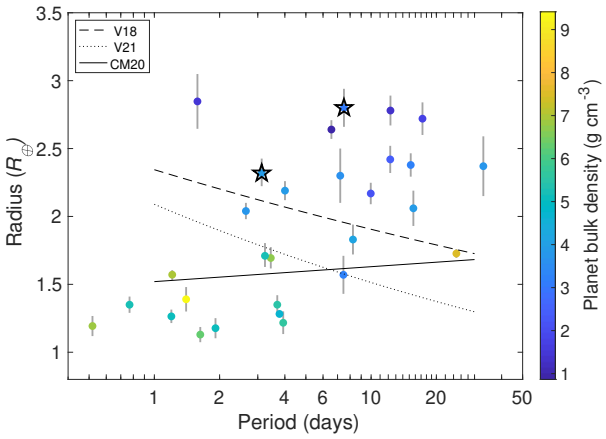

Figure 11. Radius-period diagram for the same planet population as in Fig. 10. The dashed line is the fit to the FGK radius valley from V18 (Van Eylen et al. 2018), the solid line refers to stars ≤ 4700K as per CM20, Cloutier & Menou (2020), while the dotted line – to M dwarfs with $T_{\rm eff}$ < 4000 K (Van Eylen et al. 2021). TOI-1260 b and TOI-1260 c are again marked with star symbols. Planet c is found comfortably above all three radius valleys fits, while planet b lies on the edge of the V18 fit.

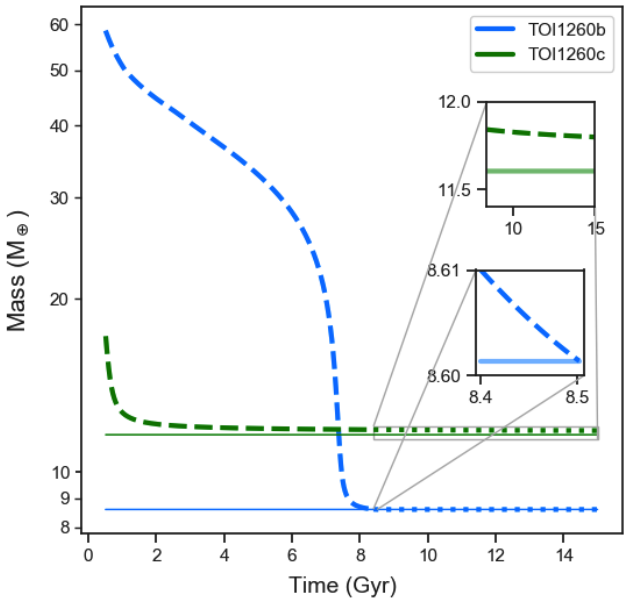

Figure 12. Mass temporal evolution of the TOI-1260 planets assuming a nominal stellar age of 8.4 Gyr, a rock/metal core and a H-He envelope of 0.1% and 2% for planets b and c, respectively. Dotted lines refer to the evolution from the current age of the system until 15 Gyr. Dashed lines refer to the inferred evolution from early to current times. The insets show a zoomed-in view of the future evolution, where the semi-transparent solid lines denote the core mass of each planet. It can be clearly seen that planet b would lose a 0.1% H-He atmosphere in about 100 Myr, while the atmosphere of planet c is stable against photoevaporation.

and with an atmosphere (Zeng et al. 2019) at different equilibrium temperatures matching TOI-1260 b and TOI-1260 c. From Fig. 10 we see that the two mini-Neptunes in the TOI-1260 system may be water worlds or rocky worlds with H-He atmospheres inflating their radii. The position of TOI-1260 b in the diagram is consistent with a planet composition of 50% Earth-like rocky core (32.5% Fe + 67.5% $MgSiO_3$) and 50% H_2O ice without an atmosphere, or an Earth-like rocky core with a H-He atmosphere of ∼ 0.1%. The position of TOI-1260 c, with $11.8^{+3.4}_{-3.2}$ $M_\oplus$, 2.82 ± 0.15 $R_\oplus$, and a bulk density of $2.87^{+0.98}_{-0.86}$ g cm^{-3}, lies above the pure water line in the diagram. The orbital period and equilibrium temperature are 7.493 days and 643 K, respectively. We find that two models fit the position in the diagram: an Earth-like rocky core with a H-He atmosphere of ∼ 2%, or alternatively, a core composed of a mix of 49.95% rock and 49.95% ices and a H-He atmosphere of ∼ 0.1%.

Since the location of the photoevaporation valley is a function of stellar mass and is thus different for low-mass vs solar-type stars, we plot in Fig. 11 the same $T_{\rm eff}$ ranges as in Fig. 10. As evident from Fig. 11, both TOI-1260 planets lie above the photoevaporation gap (Van Eylen et al. 2018; Cloutier & Menou 2020; Van Eylen et al. 2021), or close to its edge as is the case of planet b. Depending on the photoevaporation valley fit used, however, planet b could also lie exactly in the transition zone (Wu 2019). It should be noted that the Van Eylen et al. (2018) curve is based on hotter (4700 – 6500 K) and thus higher mass stars, the Cloutier & Menou (2020) and Wu (2019) curves relate to low mass stars (mid-K and cooler), while the Van Eylen et al. (2021) refers to M dwarfs with $T_{\rm eff}$ < 4000 K. We have color-coded the planet bulk densities in Fig. 11, and it is evident that the planets above the radius gap have lower densities than the planets below. The TOI-1260 planets are consistent with this trend as they have relatively low densities and their compositions are degenerated. They both are consistent with both (a) an Earth-like composition of iron and silicates, and (b) an Earth-like core with a substantial fraction of water ice. We delve into possible reasons for this ambiguity in the following sections.

5.2.1 *Mass and radius evolution induced by photoevaporation*

In order to shed light on which planet composition model TOI-1260 b and TOI-1260 c belong to, we investigate the mass and radius temporal evolution induced by atmospheric photoevaporation. To this end, we study the temporal evolution of the high-energy stellar radiation and the planetary radius. We consider a primary H-He atmosphere, a rock/iron core as per Lopez & Fortney (2014), assume circular orbits, ignore any migration effects and follow the hydrodynamic-based approximation developed by Kubyshkina et al. (2018). A major driver behind atmospheric hydrodynamic mass loss is the X-ray luminosity since X-ray heating from the star can drive a system to an intense hydrodynamic escape phase (Erkaev et al. 2007; Penz et al. 2008a; Locci et al. 2019). We estimated the current X-ray luminosity using the $\log(R'_{\rm HK})$, our SED bolometric luminosity and the relationships in Houdebine et al. (2017), obtaining $L_{\rm X} = 4.51 \times 10^{27}$ erg s^{-1}. Since the evolution of extreme ultraviolet radiation follows the evolution of X-ray radiation, we accounted for the X-ray luminosity evolution by using the prescriptions given in Penz et al. (2008b) and the relation given in Sanz-Forcada et al. (2011). Following Poppenhaeger et al. (2021), we account for the evolution of the planetary radius by means of the analytic fit given in Lopez & Fortney (2014). The analytic fit provides the radius envelope, $R_{\rm env}$, as a function, among other parameters, of the atmospheric mass fraction, $f_{\rm atm}$, and the age of the system, which in turn allows us to also account for gravitational shrinking.

Calculating the planetary mass ($M_{\rm p}$), $f_{\rm atm}$ and $R_{\rm env}$ is an iterative process. As a first step, we look at the future evolution of the system from its present age (∼ 8.4 Gyr) to 15 Gyr and assume $f_{\rm atm}$ values of 0.1% and 2% for planets b and c, respectively. These correspond to the composition scenarios of an Earth-like rocky core

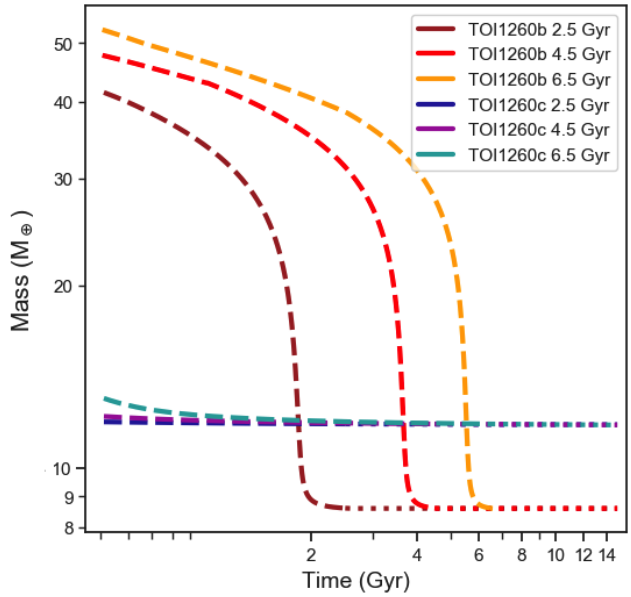

Figure 13. Mass temporal evolution of the TOI-1260 planets as per Fig. 12 but considering different stellar ages.

with a H-He envelope for both planets. We then calculate the corresponding R_{env} and estimate the core radius simply as the difference between the measured by photometry planetary radius, R_p (Table 4) and the calculated R_{env}. Next, we updated f_{atm} and M_p at each time step according to the mass loss and used them to calculate a new R_{env}, adding the latter to the core radius, to finally obtain the new R_p. We find that planet b loses its atmosphere in about 100 Myr, while planet c retains part of it until the end of the run.

5.2.2 *Effect of the stellar age*

To better understand the situation, we take this analysis one step further by tracing the system's evolution back in time. Assuming the aforementioned scenarios, since the core does not change in size or mass, we create a synthetic population of planets and assign to them the current core radii and masses of our planets. This leaves f_{atm} to dictate the total mass, while the total radius is again based on the analytic fit by Lopez & Fortney (2014). We then looked at the planets that ended up with a similar current mass, radius and f_{atm} and looked at their predicted past histories.

Figure 12 shows the result of both the future (dotted lines) and past (dashed) simulation runs. We trace the planets back to 0.5 Gyr from the assumed birth of the system and see that in the case of planet b (purple curve), we reach a mass of nearly 60 $M_\oplus$[6]. In the case of planet c (Fig. 12, green curve), we find a much more controlled mass loss process, reaching a starting point of about 17 $M_\oplus$. This, and the fact that the future evolution of the atmosphere is stable against evaporation in the long run, makes the Earth-like core with 2% atmosphere case plausible.

While it is possible to trace the planets further back in time, we stop at 0.5 Gyr since the results beyond that would be subjected to the further uncertainty associated with the stellar rotation rate during the saturation phase early in the star's life.

Due to the uncertainty in the stellar age, we decided to test the same cases as before but with lower age values. We chose ages of 2.5, 4.5 and 6.5 Gyr and reran the models for both planets (Fig. 13). In short, we find that planet b still loses its atmosphere in about the same time frame (~ 100 Myr); planet c retains a long-term stable atmosphere as before and its temporal evolution is almost completely independent of the age of the star. This result is not so surprising when we consider the fact that the X-ray luminosity is most intense in the early evolutionary stages, during which most of the atmospheric mass loss occurs. These results are generally consistent with the above findings for the nominal age, showing that the mass and radius evolution of the planets is robust for a wide range of stellar ages.

We, however, note, that 100 Myr is a short time compared to the overall life of the star, especially if the star is older. This makes it relatively unlikely that we would currently be witnessing the process of planet b losing a primary H-He atmosphere.

The fact that the nominal age is at the upper limit of the thin disc population age range (see Sect. 3.4), as well as the result that the mass evolution of both planets is well consistent with a significantly younger star, suggests the possibility that this star is, in fact, younger, which in turn emphasizes the fact that a high precision of the stellar age estimate can decrease the degeneracy in the determination of planet interiors.

5.2.3 *Planetary composition and atmospheric characterization potential*

Looking back to the two scenarios for TOI-1260 b, we consider the composition of a 50% Earth-like core and 50% water-ice case, likely mixed rather than layered as suggested by Vazan et al. (2020), to be more probable. However, the above models do not take into account planet migration or rather assume orbit migration took place quickly (a few Myr) early in the system's history, so a complex migration history could have played a role in this relatively old system. We also note that the X-ray luminosity evolution is calculated using a scaling law just for the mean value (Penz et al. 2008b) and does not account for different levels of high energy radiation to which planets could be subjected during their early evolutionary stages. The effects of stellar wind and magnetically-driven cataclysmic events originating from the stellar surface, which could affect the rate of photoevaporation, are also ignored. Furthermore, our simulations only consider the case of H-He primary atmospheres. Thus, our results do not exclude the possibility of secondary envelopes, or primary envelopes of a different composition, which may in turn be smaller and more difficult to lose under atmospheric escape processes. The latter case could mean that TOI-1260 b and TOI-1260 c are representatives of a high-metallicity population of hot Neptunes as discussed in depth by Moses et al. (2013). Hu et al. (2015) proposed the existence of He atmosphere planets, and that many sub-Neptune-sized exoplanets in short orbits could possess such atmospheres. They proposed that such an atmosphere could explain for example the emission and transmission spectra of GJ436b. While much smaller and less massive than GJ436b, TOI-1260 b has a similar orbital period and equilibrium temperature, and could be a firm candidate to posses a He atmosphere. Those atmospheres contain trace amounts of hydrogen, carbon, and oxygen, with the predominance of CO over CH_4 as the main form of carbon (Hu et al. 2015), which could fit with the overall bulk composition of the planet determined here.

Another seemingly probable scenario, considering the planets'

[6] The hydrodynamic-based approximation works in the 1 – 39 $M_\oplus$ mass range, so beyond this limit we use the energy limited approximation by Erkaev et al. (2007) to model the mass loss.

proximity to the star and the implied intense insolation, coupled with an assumed high water content of both planets, could be that the observed radii are highly inflated as the atmospheres may be well-represented by supercritical hydrospheres (Mousis et al. 2020). Unfortunately, the transmission spectroscopy metrics (TSM, Kempton et al. 2018) for TOI-1260 b and TOI-1260 c are 44 and 42, respectively. This places both planets below the recommended TSM cutoff for planets with radii above 1.5 $R_\oplus$ (TSM > 90). Still, ground-based high-resolution spectroscopy could probe for the presence of ongoing escape processes by observing the Hα lines (Yan & Henning 2018) in the near-IR, as the Lyα line will be too absorbed by the interstellar medium at the system's distance ($\sim$ 74 pc).

6 CONCLUSIONS

In this paper we present the detection and characterization of the TOI-1260 system observed by TESS in Sectors 14 and 21. This K6 V star hosts two mini-Neptunes in short-period orbits confirmed by HARPS-N radial velocities, as well as a tentative outer planet, which is seen transiting in the TESS photometry in Sector 21.

We use GP regression to disentangle the stellar from the planet signals contained in our radial velocities. GPs offer a lot of flexibility, which may lead to the removal of genuine signals of planetary origin - a risk we mitigate by using the information provided by activity indicators, i.e. the relatively novel multi-dimensional GP approach.

We note, however, that in order to improve the mass characterisation of the planets we need a strategic RV follow-up. More specifically, taking several observations within a single stellar rotation period, instead of sporadic observations, is a better strategy to disentangle stellar activity using GPs, since the latter rely on the correlation between points.

We perform simulations to evaluate the possibility of hydrodynamic atmospheric mass loss, which demonstrated the difficulty in constraining the structure and composition of planets in 2 – 3 $R_\oplus$ radius range. Our discussion thus emphasizes the fact that solely from the mass and radius we cannot distinguish between a planet being H_2O-dominated or a rocky planet with a significant envelope. Another constraint to our insight into similar systems is the large uncertainty on the systems' ages. This could be remedied from a large sample of planet systems with well-determined ages, such as is attempted to be achieved by the core sample of the PLATO mission (Rauer et al. 2014), with projected uncertainties in its age determinations to be within 10%. In this paper we further demonstrate the need to study close-in planets around low-mass stars to help constrain composition models and mass-loss mechanisms. We add that the precision to which planetary masses are measured today is often insufficient to accomplish this to a satisfactory level, complicating our overall understanding of exoplanet demographics.

ACKNOWLEDGEMENTS

This work is done under the framework of the KESPRINT collaboration (http://kesprint.science). KESPRINT is an international consortium devoted to the characterization and research of exoplanets discovered with space-based missions.

IYG, CMP, MF and JK gratefully acknowledge the support of the Swedish National Space Agency (DNR 174/18, 65/19, 2020-00104).

KWFM and ME acknowledge the support of the DFG priority program SPP 1992 "Exploring the Diversity of Extrasolar Planets" (RA714/14-1, HA3279/12-1).

HD acknowledges support from the Spanish Research Agency of the Ministry of Science and Innovation (AEI-MICINN) under grant PID2019-107061GB-C66, DOI: 10.13039/501100011033.

This work was supported by the Thüringer Ministerium für Wirtschaft, Wissenschaft und Digitale Gesellschaft.

This research has made use of the Exoplanet Follow-up Observation Program website, which is operated by the California Institute of Technology, under contract with the National Aeronautics and Space Administration under the Exoplanet Exploration Program.

This work makes use of observations from the LCOGT network.

Some of the Observations in the paper made use of the High-Resolution Imaging instrument 'Alopeke. 'Alopeke was funded by the NASA Exoplanet Exploration Program and built at the NASA Ames Research Center by Steve B. Howell, Nic Scott, Elliott P. Horch, and Emmett Quigley. 'Alopeke is mounted on the Gemini North telescope of the international Gemini Observatory, a program of NOIRLab, which is managed by the Association of Universities for Research in Astronomy (AURA) under a cooperative agreement with the National Science Foundation. on behalf of the Gemini partnership: the National Science Foundation (United States), National Research Council (Canada), Agencia Nacional de Investigación y Desarrollo (Chile), Ministerio de Ciencia, Tecnología e Innovación (Argentina), Ministério da Ciência, Tecnologia, Inovações e Comunicações (Brazil), and Korea Astronomy and Space Science Institute (Republic of Korea).

This paper includes data collected by the *TESS* mission. Funding for the *TESS* mission is provided by the NASA Explorer Program. We acknowledge the use of public TOI Release data from pipelines at the *TESS* Science Office and at the *TESS* Science Processing Operations Center. Resources supporting this work were provided by the NASA High-End Computing (HEC) Program through the NASA Advanced Supercomputing (NAS) Division at Ames Research Center for the production of the SPOC data products. This research has made use of the Exoplanet Follow-up Observation Program website, which is operated by the California Institute of Technology, under contract with the National Aeronautics and Space Administration under the Exoplanet Exploration Program.

This work has made use of data from the European Space Agency (ESA) mission *Gaia* (`https://www.cosmos.esa.int/gaia`), processed by the *Gaia* Data Processing and Analysis Consortium (DPAC, `https://www.cosmos.esa.int/web/gaia/dpac/consortium`). Funding for the DPAC has been provided by national institutions, in particular the institutions participating in the *Gaia* Multilateral Agreement.

This research has made use of the VizieR catalogue access tool, CDS, Strasbourg, France (DOI: 10.26093/cds/vizier). The original description of the VizieR service was published in A&AS 143, 23.

Based on observations made with the Italian Telescopio Nazionale Galileo (TNG) operated on the island of La Palma by the Fundación Galileo Galilei of the INAF (Istituto Nazionale di Astrofisica) at the Spanish Observatorio del Roque de los Muchachos of the Instituto de Astrofisica de Canarias under programmes CAT19A_162, ITP19_1 and A41TAC_49.

Facility: TESS, *Gaia*, TNG/HARPS-N, LCOGT.

Software: `EXOTRANS`, `lightkurve`, `citlalicue`, `george`, `pytransit`, `IRAF`, `PARAM 1.5`, `SME`, `SpecMatch-emp`, `AstroImageJ`, `pyaneti`, `juliet`, `pyTTV`.

Data availability: The data underlying this article are available in

the article and in its online supplementary material, as well as ExoFOP-TESS[7].

REFERENCES

Ambikasaran S., Foreman-Mackey D., Greengard L., Hogg D. W., O'Neil M., 2016, IEEE Transactions on Pattern Analysis and Machine Intelligence, 38, 252

Baglin A., et al., 2006, in 36th COSPAR Scientific Assembly. p. 3749

Baranne A., et al., 1996, A&AS, 119, 373

Barragán O., Gandolfi D., Antoniciello G., 2019a, MNRAS, 482, 1017

Barragán O., et al., 2019b, MNRAS, 490, 698

Berger T. A., Huber D., Gaidos E., van Saders J. L., Weiss L. M., 2020, AJ, 160, 108

Borucki W. J., et al., 2010, Science, 327, 977

Boyajian T. S., et al., 2012, ApJ, 757, 112

Bressan A., Marigo P., Girardi L., Salasnich B., Dal Cero C., Rubele S., Nanni A., 2012, MNRAS, 427, 127

Brown T. M., et al., 2013, Publications of the Astronomical Society of the Pacific, 125, 1031

Buchner J., et al., 2014, A&A, 564, A125

Chambers J. E., 1999, MNRAS, 304, 793

Choi J., Dotter A., Conroy C., Cantiello M., Paxton B., Johnson B. D., 2016, ApJ, 823, 102

Ciardi D. R., Beichman C. A., Horch E. P., Howell S. B., 2015, ApJ, 805, 16

Cloutier R., Menou K., 2020, AJ, 159, 211

Collins K. A., Kielkopf J. F., Stassun K. G., Hessman F. V., 2017, AJ, 153, 77

Cosentino R., et al., 2012, in Ground-based and Airborne Instrumentation for Astronomy IV. p. 84461V, doi:10.1117/12.925738

Cosentino R., et al., 2014, in Ground-based and Airborne Instrumentation for Astronomy V. p. 91478C, doi:10.1117/12.2055813

Curtis J. L., et al., 2020, arXiv e-prints, p. arXiv:2010.02272

Dong S., Xie J.-W., Zhou J.-L., Zheng Z., Luo A., 2018, Proceedings of the National Academy of Science, 115, 266

Erkaev N. V., Kulikov Y. N., Lammer H., Selsis F., Langmayr D., Jaritz G. F., Biernat H. K., 2007, A&A, 472, 329

Espinoza N., Kossakowski D., Brahm R., 2019, MNRAS, 490, 2262

Foreman-Mackey D., Hoyer S., Bernhard J., Angus R., 2014, george: George (v0.2.0), doi:10.5281/zenodo.11989, https://doi.org/10.5281/zenodo.11989

Foreman-Mackey D., Agol E., Ambikasaran S., Angus R., 2017, celerite: Scalable 1D Gaussian Processes in C++, Python, and Julia (ascl:1709.008)

Fridlund M., et al., 2017, A&A, 604, A16

Fulton B. J., Petigura E. A., 2018, AJ, 156, 264

Fulton B. J., et al., 2017, AJ, 154, 109

Fulton B. J., Petigura E. A., Blunt S., Sinukoff E., 2018, Publications of the Astronomical Society of the Pacific, 130, 044504

Gaia Collaboration et al., 2021, A&A, 649, A6

Gregory P. C., 2005, ApJ, 631, 1198

Grziwa S., Pätzold M., Carone L., 2012, MNRAS, 420, 1045

Günther M. N., et al., 2019, Nature Astronomy, 3, 1099

Gustafsson B., Edvardsson B., Eriksson K., Jørgensen U. G., Nordlund Å., Plez B., 2008, A&A, 486, 951

Hirano T., et al., 2018, AJ, 155, 127

Hodapp K. W., et al., 2003, PASP, 115, 1388

Houdebine E. R., Mullan D. J., Bercu B., Paletou F., Gebran M., 2017, ApJ, 837, 96

Howell S. B., Everett M. E., Sherry W., Horch E., Ciardi D. R., 2011, AJ, 142, 19

Howell S. B., et al., 2014, PASP, 126, 398

Hu R., Seager S., Yung Y. L., 2015, ApJ, 807, 8

Jenkins J. M., 2002, ApJ, 575, 493

Jenkins J. M., et al., 2010, in Radziwill N. M., Bridger A., eds, Society of Photo-Optical Instrumentation Engineers (SPIE) Conference Series Vol. 7740, Software and Cyberinfrastructure for Astronomy. p. 77400D, doi:10.1117/12.856764

Jenkins J. M., et al., 2016, in Proc. SPIE. p. 99133E, doi:10.1117/12.2233418

Jenkins J. M., Tenenbaum P., Seader S., Burke C. J., McCauliff S. D., Smith J. C., Twicken J. D., Chandrasekaran H., 2017, Kepler Data Processing Handbook: Transiting Planet Search, Kepler Science Document KSCI-19081-002

Jensen E., 2013, Tapir: A web interface for transit/eclipse observability, Astrophysics Source Code Library (ascl:1306.007)

Jurgenson C., Fischer D., McCracken T., Sawyer D., Szymkowiak A., Davis A., Muller G., Santoro F., 2016, in Evans C. J., Simard L., Takami H., eds, Society of Photo-Optical Instrumentation Engineers (SPIE) Conference Series Vol. 9908, Ground-based and Airborne Instrumentation for Astronomy VI. p. 99086T (arXiv:1606.04413), doi:10.1117/12.2233002

Kane S. R., 2015, ApJ, 814, L9

Kane S. R., 2019, AJ, 158, 72

Kempton E. M. R., et al., 2018, PASP, 130, 114401

Kipping D. M., 2013, MNRAS, 435, 2152

Korth J., 2020, PhD thesis, Universität zu Köln, https://kups.ub.uni-koeln.de/11289/

Kostov V. B., et al., 2019, AJ, 158, 32

Kovács G., Zucker S., Mazeh T., 2002, A&A, 391, 369

Kreidberg L., 2015, Publications of the Astronomical Society of the Pacific, 127, 1161

Kubyshkina D., et al., 2018, A&A, 619, A151

Kurucz R. L., 2013, ATLAS12: Opacity sampling model atmosphere program, Astrophysics Source Code Library (ascl:1303.024)

Li G., Naoz S., Valsecchi F., Johnson J. A., Rasio F. A., 2014, ApJ, 794, 131

Lightkurve Collaboration et al., 2018, Lightkurve: Kepler and TESS time series analysis in Python, Astrophysics Source Code Library (ascl:1812.013)

Lissauer J. J., et al., 2011, ApJS, 197, 8

Locci D., Cecchi-Pestellini C., Micela G., 2019, A&A, 624, A101

Lopez E. D., Fortney J. J., 2013, ApJ, 776, 2

Lopez E. D., Fortney J. J., 2014, ApJ, 792, 1

Luque R., et al., 2021, A&A, 645, A41

Mamajek E. E., Hillenbrand L. A., 2008, ApJ, 687, 1264

Mandel K., Agol E., 2002, ApJ, 580, L171

Mayo A. W., et al., 2019, AJ, 158, 165

Mayor M., et al., 2003, The Messenger, 114, 20

McDonald G. D., Kreidberg L., Lopez E., 2019a, ApJ, 876, 22

McDonald G. D., Kreidberg L., Lopez E., 2019b, ApJ, 876, 22

Morris R. L., Twicken J. D., Smith J. C., Clarke B. D., Jenkins J. M., Bryson S. T., Girouard F., Klaus T. C., 2017, Kepler Data Processing Handbook: Photometric Analysis, Kepler Science Document KSCI-19081-002

Morton T. D., 2015, isochrones: Stellar model grid package (ascl:1503.010)

Moses J. I., et al., 2013, ApJ, 777, 34

Mousis O., Deleuil M., Aguichine A., Marcq E., Naar J., Aguirre L. A., Brugger B., Gonçalves T., 2020, ApJ, 896, L22

Ochsenbein F., Bauer P., Marcout J., 2000, A&AS, 143, 23

Ofir A., 2014, A&A, 561, A138

Osborn H. P., et al., 2016, MNRAS, 457, 2273

Otegi J. F., Bouchy F., Helled R., 2020, A&A, 634, A43

Owen J. E., Wu Y., 2013, ApJ, 775, 105

Parviainen H., 2015, MNRAS, 450, 3233

Penz T., Micela G., Lammer H., 2008a, A&A, 477, 309

Penz T., Micela G., Lammer H., 2008b, A&A, 477, 309

Pepe F. A., et al., 2010, in McLean I. S., Ramsay S. K., Takami H., eds, Society of Photo-Optical Instrumentation Engineers (SPIE) Conference Series Vol. 7735, Ground-based and Airborne Instrumentation for Astronomy III. p. 77350F, doi:10.1117/12.857122

Pepe F., et al., 2021, A&A, 645, A96

Persson C. M., et al., 2018, A&A, 618, A33

Piskunov N., Valenti J. A., 2017, A&A, 597, A16

[7] https://exofop.ipac.caltech.edu/tess

Poppenhaeger K., Ketzer L., Mallonn M., 2021, MNRAS, 500, 4560
Quirrenbach A., et al., 2014, in Ramsay S. K., McLean I. S., Takami H., eds, Society of Photo-Optical Instrumentation Engineers (SPIE) Conference Series Vol. 9147, Ground-based and Airborne Instrumentation for Astronomy V. p. 91471F, doi:10.1117/12.2056453
Quirrenbach A., et al., 2018, in Evans C. J., Simard L., Takami H., eds, Society of Photo-Optical Instrumentation Engineers (SPIE) Conference Series Vol. 10702, Ground-based and Airborne Instrumentation for Astronomy VII. p. 107020W, doi:10.1117/12.2313689
Rajpaul V., Aigrain S., Osborne M. A., Reece S., Roberts S., 2015, MNRAS, 452, 2269
Rauer H., et al., 2014, Experimental Astronomy, 38, 249
Reddy B. E., Lambert D. L., Allende Prieto C., 2006, MNRAS, 367, 1329
Ricker G. R., et al., 2015, Journal of Astronomical Telescopes, Instruments, and Systems, 1, 014003
Rodriguez J. E., et al., 2019, AJ, 157, 191
Ryabchikova T., Piskunov N., Kurucz R. L., Stempels H. C., Heiter U., Pakhomov Y., Barklem P. S., 2015, Phys. Scr., 90, 054005
Sanz-Forcada J., Micela G., Ribas I., Pollock A. M. T., Eiroa C., Velasco A., Solano E., García-Álvarez D., 2011, A&A, 532, A6
Schlegel D. J., Finkbeiner D. P., Davis M., 1998, ApJ, 500, 525
Smith J. C., et al., 2012, PASP, 124, 1000
Southworth J., Wheatley P. J., Sams G., 2007, MNRAS, 379, L11
Speagle J. S., 2020, MNRAS, 493, 3132
Stassun K. G., Torres G., 2016, AJ, 152, 180
Stassun K. G., Torres G., 2018, ApJ, 862, 61
Stassun K. G., Kratter K. M., Scholz A., Dupuy T. J., 2012, ApJ, 756, 47
Stassun K. G., Collins K. A., Gaudi B. S., 2017, AJ, 153, 136
Stassun K. G., Corsaro E., Pepper J. A., Gaudi B. S., 2018a, AJ, 155, 22
Stassun K. G., et al., 2018b, AJ, 156, 102
Stumpe M. C., et al., 2012, PASP, 124, 985
Suárez Mascareño A., Rebolo R., González Hernández J. I., Esposito M., 2015, MNRAS, 452, 2745
Suárez Mascareño A., Rebolo R., González Hernández J. I., Esposito M., 2016, MNRAS, 457, 2604
Torres G., 2010, AJ, 140, 1158
Twicken J. D., Clarke B. D., Bryson S. T., Tenenbaum P., Wu H., Jenkins J. M., Girouard F., Klaus T. C., 2010, in Radziwill N. M., Bridger A., eds, Society of Photo-Optical Instrumentation Engineers (SPIE) Conference Series Vol. 7740, Software and Cyberinfrastructure for Astronomy. p. 774023, doi:10.1117/12.856790
Twicken J. D., et al., 2018, PASP, 130, 064502
Valencia D., Sasselov D. D., O'Connell R. J., 2007, ApJ, 665, 1413
Valenti J. A., Piskunov N., 1996, A&AS, 118, 595
Van Eylen V., Agentoft C., Lundkvist M. S., Kjeldsen H., Owen J. E., Fulton B. J., Petigura E., Snellen I., 2018, MNRAS, 479, 4786
Van Eylen V., et al., 2019, AJ, 157, 61
Van Eylen V., et al., 2021, arXiv e-prints, p. arXiv:2101.01593
Vazan A., Sari R., Kessel R., 2020, arXiv e-prints, p. arXiv:2011.00602
Vogt S. S., et al., 1994, in Crawford D. L., Craine E. R., eds, Society of Photo-Optical Instrumentation Engineers (SPIE) Conference Series Vol. 2198, Instrumentation in Astronomy VIII. p. 362, doi:10.1117/12.176725
Wilson R. F., et al., 2018, AJ, 155, 68
Wu Y., 2019, ApJ, 874, 91
Yan F., Henning T., 2018, Nature Astronomy, 2, 714
Yee S. W., Petigura E. A., von Braun K., 2017, ApJ, 836, 77
Zechmeister M., Kürster M., 2009, A&A, 496, 577
Zechmeister M., et al., 2018, A&A, 609, A12
Zeng L., Sasselov D. D., Jacobsen S. B., 2016, ApJ, 819, 127
Zeng L., et al., 2019, Proceedings of the National Academy of Science, 116, 9723
da Silva L., et al., 2006, A&A, 458, 609
del Peloso E. F., da Silva L., Porto de Mello G. F., Arany-Prado L. I., 2005, A&A, 440, 1153

LIST OF AFFILIATIONS

[1]Department of Space, Earth and Environment, Chalmers University of Technology, Onsala Space Observatory, 439 92 Onsala, Sweden
[2]Sub-department of Astrophysics, Department of Physics, University of Oxford, Oxford, OX1 3RH, UK
[3]Instituto de Astrofísica de Canarias, 38205 La Laguna, Tenerife, Spain
[4]Departamento de Astrofísica, Universidad de La Laguna, 38206 La Laguna, Tenerife, Spain
[5]Leiden Observatory, Leiden University, 2333CA Leiden, The Netherlands
[6]INAF - Osservatorio Astronomico di Palermo, Piazza del Parlamento 1, 90134 Palermo, Italy
[7]Astronomy Department and Van Vleck Observatory, Wesleyan University, Middletown, CT 06459, USA
[8]Dipartimento di Fisica, Università di Torino, via P. Giuria 1, 10125 Torino, Italy
[9]Department of Earth and Planetary Sciences, University of California, Riverside, CA 92521, USA
[10]Department of Space, Earth and Environment, Astronomy and Plasma Physics, Chalmers University of Technology, 412 96 Gothenburg, Sweden
[11]Vanderbilt University, Physics and Astronomy Department, Nashville, TN 37235, USA
[12]Department of Astronomy, University of Tokyo, 7-3-1 Hongo, Bunkyo-ku, Tokyo 113-0033, Japan
[13]Department of Physics and Kavli Institute for Astrophysics and Space Research, Massachusetts Institute of Technology, Cambridge, MA 02139, USA
[14]Observatoire de l'Université de Genève, Chemin des Maillettes 51, 1290 Versoix, Switzerland
[15]Center for Astrophysics | Harvard & Smithsonian, 60 Garden Street, Cambridge, MA 02138, USA
[16]NASA Ames Research Center, Moffett Field, CA 94035, USA
[17]Stellar Astrophysics Centre, Department of Physics and Astronomy, Aarhus University, Ny Munkegade 120, DK-8000 Aarhus C, Denmark
[18]Nordic Optical Telescope, Apartado 474, E-38700 Santa Cruz de La Palma, Santa Cruz de Tenerife, Spain
[19]Space Telescope Science Institute, 3700 San Martin Dr, Baltimore, MD 21218, USA
[20]NASA Exoplanet Science Institute – Caltech/IPAC Pasadena, CA 91125 USA
[21]Center for Planetary Systems Habitability and McDonald Observatory, The University of Texas, Austin TX USA [22]NASA Goddard Space Flight Center, Exoplanets and Stellar Astrophysics Laboratory (Code 667), Greenbelt, MD 20771, USA
[23]Department of Physics and Astronomy, University of Kansas, Lawrence, KS, USA
[24]Institute of Planetary Research, German Aerospace Center (DLR), Rutherfordstraße 2, 12489 Berlin, Germany
[25]Thüringer Landessternwarte Tautenburg, Sternwarte 5, D-07778Tautenberg, Germany
[26]NASA Exoplanet Science Institute, Caltech/IPAC, Mail Code 100-22, 1200 E. California Blvd., Pasadena, CA 91125, USA
[27]Department of Astronomy and Tsinghua Centre for Astrophysics, Tsinghua University, Beijing 100084, China
[28]Department of Astronomy and Astrophysics, University of California, Santa Cruz, 1156 High St. Santa Cruz , CA 95064, USA
[29]Rheinisches Institut für Umweltforschung an der Universität zu

Köln, Aachener Strasse 209, 50931 Köln [30]Observatori Astronòmic Albanyà, Camí de Bassegoda S/N, Albanyà 17733, Girona, Spain
[31]Astrobiology Center, NINS, 2-21-1 Osawa, Mitaka, Tokyo 181-8588, Japan
[32]National Astronomical Observatory of Japan, NINS, 2-21-1 Osawa, Mitaka, Tokyo 181-8588, Japan
[33]Department of Physics & Astronomy, Swarthmore College, Swarthmore PA 19081, USA
[34]Astronomical Institute ASCR, Fričova 298,251 65, Ondřejov, Czech Republic
[35]Center for Astronomy and Astrophysics, Technical University Berlin, Hardenbergstr. 36, 10623 Berlin, Germany
[36]U.S. Naval Observatory, Washington, D.C. 20392, USA
[37]Proto-Logic LLC, 1718 Euclid Street NW, Washington, DC 20009, USA
[38]Mullard Space Science Laboratory, University College London, Holmbury St Mary, Dorking, Surrey, RH5 6NT, UK
[39]NASA Goddard Space Flight Center, 8800 Greenbelt Rd., Greenbelt, MD 20771, USA
[40]Department of Earth, Atmospheric and Planetary Sciences, Massachusetts Institute of Technology, Cambridge, MA 02139, USA
[41]Department of Aeronautics and Astronautics, MIT, 77 Massachusetts Avenue, Cambridge, MA 02139, USA
[42]SETI Institute, Mountain View, CA 94043, USA
[43]Department of Astrophysical Sciences, Princeton University, 4 Ivy Lane, Princeton, NJ 08544, USA

APPENDIX A: HARPS-N DATA

APPENDIX B: MONOTRANSIT PERIODS

Table A1: Radial velocities and spectral activity indicators measured from TNG/HARPS-N spectra.

BJD_{TBD} (days) -2457000	RV ($m\,s^{-1}$)	σ_{RV} ($m\,s^{-1}$)	CRX ($m\,s^{-1}\,Np^{-1}$)	σ_{CRX} ($m\,s^{-1}\,Np^{-1}$)	dlW ($m^2\,s^{-2}$)	σ_{dlW} ($m^2\,s^{-2}$)	H_α —	σ_{H_α} —	NaD_1 —	σ_{NaD_1} —	NaD_2 —	σ_{NaD_2} —	BIS ($m\,s^{-1}$)	σ_{BIS} ($m\,s^{-1}$)	CCF_FHWM ($km\,s^{-1}$)	CCF_CTR —	S-index —	$\sigma_{S-index}$ —	SNR —	T_{exp} (s)
1862.62923	6.677	1.716	-17.725	14.096	-2.805	3.196	0.6841	0.0020	0.2004	0.0024	0.2252	0.0026	40.628	3.763	6.364	42.479	1.133	0.025	9.7	3600.0
1862.66579	4.803	1.340	-9.964	11.112	-7.302	2.351	0.6850	0.0017	0.1974	0.0020	0.2216	0.0021	50.620	3.022	6.361	42.637	1.122	0.019	45.9	3600.0
1863.67080	10.163	1.235	10.432	10.103	-17.998	1.895	0.6832	0.0013	0.1945	0.0014	0.2200	0.0015	47.085	2.120	6.360	42.878	1.134	0.012	61.2	3600.0
1863.78184	11.454	1.180	10.563	9.470	-15.791	1.870	0.6844	0.0012	0.1951	0.0014	0.2196	0.0015	52.086	2.173	6.363	42.821	1.135	0.012	59.9	3600.0
1864.64888	15.901	1.490	14.765	12.360	-3.886	2.166	0.6855	0.0018	0.1975	0.0020	0.2236	0.0022	56.202	3.091	6.371	42.728	1.154	0.021	45.1	3600.0
1864.76150	13.179	1.573	20.240	13.193	-6.655	2.239	0.6827	0.0019	0.1968	0.0021	0.2284	0.0023	46.279	3.192	6.363	42.705	1.168	0.022	44.2	3600.0
1865.63156	5.489	1.193	14.321	10.311	-8.966	2.404	0.6816	0.0017	0.1991	0.0016	0.2245	0.0018	49.886	2.354	6.380	42.741	1.141	0.014	56.3	3600.0
1865.76718	1.903	1.434	19.806	11.892	-8.575	2.433	0.6913	0.0016	0.2000	0.0016	0.2219	0.0018	47.921	2.470	6.381	42.767	1.169	0.016	54.5	3600.0
1869.71163	0.562	1.555	-9.033	12.511	-1.288	2.907	0.6875	0.0017	0.2007	0.0021	0.2282	0.0023	63.711	3.314	6.383	42.718	1.193	0.022	41.9	3600.0
1896.56585	15.450	1.436	-3.060	11.637	-1.510	2.297	0.6878	0.0016	0.2237	0.0020	0.2459	0.0021	45.665	2.994	6.384	42.720	1.214	0.019	45.9	3600.0
1896.67552	13.918	1.388	-11.290	11.143	-0.808	2.814	0.6945	0.0016	0.2284	0.0020	0.2467	0.0022	43.192	3.018	6.386	42.659	1.232	0.019	45.8	3600.0
1898.56841	7.774	1.073	-3.532	8.928	0.857	2.620	0.7382	0.0014	0.2165	0.0015	0.2407	0.0016	56.588	2.184	6.387	42.631	1.446	0.013	60.1	3600.0
1925.63670	17.927	1.749	-2.160	14.638	-1.086	3.147	0.6863	0.0023	0.2479	0.0030	0.2599	0.0032	43.613	4.335	6.393	42.655	1.123	0.032	34.8	3600.0
1926.64886	19.622	2.118	-15.619	17.407	0.278	2.686	0.7005	0.0019	0.2343	0.0025	0.2600	0.0027	61.432	3.705	6.379	42.775	1.199	0.026	39.4	3300.0
1929.63674	10.128	1.193	-1.733	10.068	-7.456	2.374	0.6858	0.0018	0.2118	0.0020	0.2432	0.0022	64.774	2.971	6.372	42.772	1.175	0.020	47.1	3006.7
1930.42198	11.743	2.290	-24.218	19.108	-6.858	3.472	0.6937	0.0028	0.2339	0.0036	0.2459	0.0039	72.455	5.391	6.359	42.761	1.026	0.054	29.6	2200.0
1969.53394	-0.344	2.607	30.922	21.458	-23.205	3.971	0.6870	0.0031	0.3179	0.0047	0.3119	0.0049	52.253	6.453	6.339	42.808	1.146	0.041	25.9	3600.0
1971.52051	-2.375	1.298	-6.884	10.783	-44.328	2.698	0.6768	0.0016	0.2088	0.0019	0.2320	0.0021	63.058	2.849	6.316	43.145	1.011	0.019	48.1	3600.0
2000.41367	2.216	1.268	-8.945	10.158	-36.375	2.377	0.6827	0.0014	0.2021	0.0017	0.2323	0.0019	70.680	2.731	6.333	43.037	1.098	0.018	48.8	3600.0
2000.45426	4.378	1.489	-35.801	10.971	-25.136	2.493	0.6822	0.0015	0.2101	0.0021	0.2300	0.0022	75.663	3.223	6.333	43.001	1.067	0.022	42.4	3600.0
2001.42014	0.440	1.116	-11.500	8.915	-47.568	1.854	0.6692	0.0011	0.1937	0.0012	0.2238	0.0014	63.516	1.940	6.312	43.220	1.038	0.010	65.8	3600.0
2001.46039	-0.236	0.949	-23.011	7.095	-48.208	1.735	0.6705	0.0010	0.1916	0.0011	0.2242	0.0012	73.278	1.702	6.312	43.235	1.024	0.009	73.8	3600.0
2002.42024	-2.632	0.905	5.811	7.749	-53.132	2.055	0.6726	0.0014	0.1975	0.0014	0.2341	0.0016	56.605	1.996	6.303	43.312	1.001	0.011	64.2	3600.0
2002.46195	-0.506	1.311	13.103	10.881	-55.646	2.419	0.6712	0.0013	0.1967	0.0014	0.2353	0.0015	63.482	1.999	6.302	43.323	1.024	0.011	64.4	3600.0
2011.40922	27.029	2.205	-0.278	18.301	-29.220	3.238	0.6777	0.0024	0.1989	0.0033	0.2373	0.0036	48.672	5.219	6.321	43.031	1.123	0.041	30.2	3300.0
2011.44218	23.398	2.840	16.880	23.534	-32.558	4.204	0.6794	0.0034	0.2268	0.0054	0.2724	0.0060	54.360	8.605	6.334	42.874	1.069	0.075	20.8	2999.1
2012.40959	25.530	1.828	20.100	14.729	-24.200	2.180	0.6723	0.0016	0.2009	0.0020	0.2305	0.0022	33.998	3.095	6.349	42.922	1.105	0.021	45.2	3300.0
2012.44888	25.937	1.907	13.461	15.545	-27.838	2.505	0.6822	0.0018	0.2038	0.0022	0.2337	0.0024	45.139	3.518	6.342	42.933	1.157	0.026	40.7	3300.0
2013.42280	17.344	1.733	30.803	13.985	-20.223	2.502	0.6878	0.0020	0.2484	0.0025	0.2671	0.0026	35.178	3.499	6.354	42.858	1.152	0.024	41.5	3300.0
2013.44892	17.566	2.332	0.142	20.049	-13.318	4.085	0.6896	0.0035	0.2526	0.0049	0.2816	0.0054	54.908	7.476	6.371	42.777	1.121	0.063	23.7	1353.0
2013.47580	26.451	3.139	39.435	26.754	-9.109	5.318	0.6887	0.0042	0.3239	0.0064	0.3563	0.0069	14.612	8.586	6.351	42.772	1.103	0.075	21.0	2273.7
2014.42732	30.021	1.846	-7.137	15.000	-13.315	2.384	0.6837	0.0017	0.2265	0.0024	0.2527	0.0025	46.902	3.644	6.370	42.766	1.168	0.027	39.5	3300.0
2014.46531	28.500	1.704	16.641	13.691	-14.391	3.104	0.6796	0.0018	0.2181	0.0024	0.2506	0.0026	39.564	3.733	6.360	42.848	1.165	0.029	39.0	3300.0

Table B1. Possible periods and period ranges for the case of a unique single transit assuming a circular orbit. The excluded values/gaps correspond to transit times when a transit event would be seen in the light curves. The calculations were performed in steps of 0.1 days and include the data gap in Sector 14 as a possible location of a missed transit. The table does not include the 16.6-day period corresponding to the scenario of overlapping transits of this tentative planet and planet c, described in the text. If this period is correct, this would imply the presence of two transits in Sector 21.

Period (days)
20.3
22.8
26.0 - 26.1
28.0 - 28.1
30.4
32.7 - 33.8
36.4 - 36.5
39.2 - 42.2
45.5 - 45.7
49.0 - 56.3

This paper has been typeset from a TEX/LATEX file prepared by the author.

PAPER B

TOI-733 b: a planet in the small-planet radius valley orbiting a Sun-like star

Iskra Y. Georgieva, C.M. Persson, E. Goffo, L. Acuña, A. Aguichine, L.M. Serrano, K.W.F. Lam, D. Gandolfi, K.A. Collins, S.B. Howell, F. Dai, M. Fridlund, J. Korth, M. Deleuil, O. Barragán, W.D. Cochran, S. Csizmadia, H.J. Deeg, E. Guenther, A.P. Hatzes, J.M. Jenkins, J. Livingston, R. Luque, O. Mousis, H.L.M. Osborne, E. Palle, S. Redfield, V. Van Eylen, J.D. Twicken, J.N. Winn, A. Al Qasim, K.I. Collins, C.L. Gnilka, D.W. Latham, H.M. Lewis, H.M. Relles, G.R. Ricker, P. Rowden, S. Seager, A. Shporer, T. Tan, A. Vanderburg, R. Vanderspek

Astronomy & Astrophysics, 2023, in press.
©DOI: 10.1051/0004-6361/202345961

Astronomy & Astrophysics manuscript no. output
May 21, 2023

TOI-733 b – a planet in the small-planet radius valley orbiting a Sun-like star ⋆⋆⋆

Iskra Y. Georgieva[1], Carina M. Persson[1], Elisa Goffo[2,3], Lorena Acuña[4,5], Artyom Aguichine[4,6], Luisa M. Serrano[2], Kristine W. F. Lam[7], Davide Gandolfi[2], Karen A. Collins[8], Steven B. Howell[9], Fei Dai[10,11,12], Malcolm Fridlund[1,13], Judith Korth[14,15], Magali Deleuil[4], Oscar Barragán[16], William D. Cochran[17], Szilárd Csizmadia[7], Hans J. Deeg[18,19], Eike Guenther[3], Artie P. Hatzes[3], Jon M. Jenkins[9], John Livingston[20,21,22], Rafael Luque[23], Olivier Mousis[4], Hannah L. M. Osborne[24], Enric Palle[18], Seth Redfield[25], Vincent Van Eylen[24], Joseph D. Twicken[9,26], Joshua N. Winn[27], Ahlam Al Qasim[24], Kevin I. Collins[28], Crystal L. Gnilka[9,30], David W. Latham[8], Hannah M. Lewis[29], Howard M. Relles[8], George R. Ricker[31], Pamela Rowden[32], Sara Seager[33,34,35], Avi Shporer[34], Thiam-Guan Tan[36], Andrew Vanderburg[37,38,12], and Roland Vanderspek[31]

(Affiliations can be found after the references)

Received Date Month YYYY; accepted Date Month YYYY

ABSTRACT

We report the discovery of a hot ($T_{\rm eq} \approx 1055$ K) planet in the small planet radius valley transiting the Sun-like star TOI-733, as part of the KESPRINT follow-up program of TESS planets carried out with the HARPS spectrograph. TESS photometry from sectors 9 and 36 yields an orbital period of $P_{\rm orb} = 4.884765^{+1.9e-5}_{-2.4e-5}$ days and a radius of $R_{\rm p} = 1.992^{+0.085}_{-0.090}$ $R_\oplus$. Multi-dimensional Gaussian process modelling of the radial velocity measurements from HARPS and activity indicators, gives a semi-amplitude of $K = 2.23 \pm 0.26$ m s^{-1}, translating into a planet mass of $M_{\rm p} = 5.72^{+0.70}_{-0.68}$ $M_\oplus$. These parameters imply that the planet is of moderate density ($\rho_{\rm p} = 3.98^{+0.77}_{-0.66}$ g cm^{-3}) and place it in the transition region between rocky and volatile-rich planets with H/He-dominated envelopes on the mass-radius diagram. Combining these with stellar parameters and abundances, we calculate planet interior and atmosphere models, which in turn suggest that TOI-733 b has a volatile-enriched, most likely secondary outer envelope, and may represent a highly irradiated ocean world – one of only a few such planets around G-type stars that are well-characterised.

Key words. Planetary systems – Planets and satellites: detection – planets and satellites: composition – planets and satellites: individual: TOI-733 – Techniques: photometric – Techniques: radial velocity

1. Introduction

The end of the last millennium astronomy saw the addition of a new field – the field of exoplanets. Since the year 2000 thousands of planets have been discovered by *CoRoT* (Baglin et al. 2006), the Kepler space telescope (*Kepler*, Borucki et al. 2010; Howell et al. 2014), and the presently operating Transiting Exoplanet Survey Satellite (TESS, Ricker et al. 2015). The latter has followed in the footsteps of the indispensable *Kepler*, having provided data that has thus far led to the confirmation of about 300[1] exoplanets, with thousands more to be confirmed in the years to come.

Space transit surveys, particularly *Kepler*, have facilitated the confirmation of the theoretically predicted (Owen & Wu 2013; Lopez & Fortney 2013) and observationally demonstrated (Fulton et al. 2017; Van Eylen et al. 2018) small planet radius gap. This region, evident in planet radius vs orbital period (equally vs planet equilibrium temperature/stellar irradiation), is characterised by a dearth of planets with radii near 1.8 $R_\oplus$ (Fulton et al. 2017; Van Eylen et al. 2018). On the lower radius side are the Super-Earths, which are rocky with or without thin secondary envelopes. On the larger radius side are the so-called mini-Neptunes with typically slightly larger cores and more significant H/He dominated envelopes. The radius valley is the manifestation of the separation between the two. The origin of the radius gap has been investigated in detail and two main theories have arisen – atmospheric photoevaporation resulting from intense stellar irradiation (Owen & Wu 2013; Lopez & Fortney 2013), and core-powered mass loss, i.e. atmospheric mass loss driven by leftover heat from formation escaping from the core (Ginzburg et al. 2018; Gupta & Schlichting 2019).

The planet mass, however, is the crucial parameter that, when combined with the radius, allows us to begin characterisation of the detected planets. The relative faintness of the stellar targets in *Kepler*'s primary mission has unfortunately made the determination of this fundamental property difficult. Currently one of the most high profile ambiguities in exoplanet science is the composition degeneracy (Valencia et al. 2007; Zeng et al. 2016, 2019) of the "in-between" planets found in the radius valley. Characterising planets with precisely determined radius and mass in this region is important as it is a key ingredient in the recipe for breaking the degeneracy. By mapping out and disentangling the structure of these interesting objects, we may be en-route to uncovering new pathways to planet formation and evolution. Thankfully, modern high-precision spectrographs

Send offprint requests to: iskra.georgieva@chalmers.se

⋆ Based on observations made with the ESO-3.6 m telescope at La Silla Observatory under programme 106.21TJ.001.

⋆⋆ Table **??** only available in electronic form at the CDS via `https://cdsarc.cds.unistra.fr/cgi-bin/qcat?J/A+A/`.

[1] `https://exoplanetarchive.ipac.caltech.edu/`. Accessed 16 January 2023.

(HARPS, HIRES, ESPRESSO, CARMENES, etc.) are hard at work, with expected planetary mass yield sufficient to allow population studies not limited only to radius (e.g., Kubyshkina & Fossati 2022).

Apart from the commonly assumed composition of silicate mantle surrounding an iron core with a H/He envelope on top, a possibility in systems which are not young (a few billion years old), is that a planet between 1.6–2.5 $R_\oplus$ can be helium enhanced (Malsky et al. 2022). But transition region planets have also been hypothesised to be water worlds, or featuring a significant H_2O content, a possible volatile atmosphere (e.g., Zeng et al. 2019, 2021; Mousis et al. 2020). Recently, Luque & Pallé (2022) showed that small planets around M dwarfs are likely to be water worlds, whose existence can be explained via type I migration from beyond the snow line, while suggesting that their conclusions can be extended to solar-type stars. The recent discussions and analyses of the systems Kepler-138 presented by Piaulet et al. (2023), K2-3 by Diamond-Lowe et al. (2022), and of TOI-1695 by Cherubim et al. (2023), also point to the possibility that water-dominated planets are more prevalent than previously thought, even at super-Earth radii.

Furthermore, we cannot currently distinguish between photoevaporation and core-powered mass loss as possible radius gap sculpting mechanisms with current population studies, as shown by Rogers et al. (2021). One of the key ingredients to achieving this, they point out, is obtaining high accuracy planet radii and stellar host masses in systems where the planets reside in or close to the radius gap. Thus, improving our understanding of the origins and histories of such planets, is a crucial part of the way to crystallise the heavily studied phenomenon of atmospheric mass loss. In this paper we present the discovery and characterisation of a planet inside the small planet radius valley, TOI-733 b (TIC 106402532), discovered by TESS in 2019. We show that its possible compositions make it a particularly interesting and important planet, which can serve as a stepping stone to showing that a population of water worlds also exists around Sun-like stars, as well as for reducing the uncertainty surrounding the aforementioned problems.

In Sect. 2, we present all space and ground-based observations performed on TOI-733, and analysis of the data. Section 3 describes our stellar modelling, while Sect. 4 summarises our transit and multi-dimensional Gaussian process (multi-GP) modelling. In Sect. 5 we present the placement of TOI-733 b among the small planet population, as well as our interior and atmospheric modelling. Our conclusions are laid out in Sect. 6.

2. TOI-733 space- and ground-based observations

To confirm the planetary nature of the candidate TOI-733.01, we rely upon space-based lightcurve photometry from TESS, follow-up ground-based photometry from Las Cumbres Observatory Global Telescope (LCOGT), speckle imaging from the Zorro instrument at the 8m Gemini South telescope, as well as spectroscopy by the HARPS spectrograph at the 3.6m telescope at La Silla observatory. Target identifiers and coordinates, together with other relevant stellar parameters are listed in Table 1.

Table 1. Basic parameters for TOI-733.

Parameter	Value
Main Identifiers	
TIC	106402532
2MASS	J10373820-4053179
WISE	J103738.22-405317.7
TYC	7714-00657-1
UCAC4	246-045192
Gaia	5392409372314518656
Equatorial coordinates (epoch 2015.5)	
R.A. (J2000.0)	$10^{\rm h}37^{\rm m}38\overset{\rm s}{.}24$
Dec. (J2000.0)	$-40\overset{\circ}{.}53\overset{\prime}{.}17\overset{\prime\prime}{.}73$
Magnitudes	
TESS	8.8411 ± 0.0060
Johnson B	10.4900 ± 0.0167
Johnson V	9.435 ± 0.019
G^a	9.2966 ± 0.0001
${G_{RP}}^a$	8.7875 ± 0.0007
${G_{BP}}^a$	9.6335 ± 0.0007
J	8.220 ± 0.026
H	7.943 ± 0.040
K	7.845 ± 0.024
WISE $W1$	7.780 ± 0.027
WISE $W2$	7.851 ± 0.020
Parallax^a (mas)	13.2847 ± 0.0127
Distance^a (pc)	75.27 ± 0.07
${\mu_{RA}}^a$ (mas yr^{-1})	27.528 ± 0.007
${\mu_{Dec}}^a$ (mas yr^{-1})	19.524 ± 0.012
${R_\star}^b$ ($R_\odot$)	$0.949^{+0.008}_{-0.012}$
${M_\star}^b$ ($M_\odot$)	$0.956^{+0.050}_{-0.026}$
${\rho_*}^b$ (g cm^{-3})	1.58 ± 0.19
${L_\star}^b$ ($L_\odot$)	0.82 ± 0.02
Age^b (Gyr)	$4.4^{+1.5}_{-3.1}$
${T_{\rm eff}}^b$ (K)	5585 ± 60
$\log {g_\star}^b$	4.47 ± 0.05
[Fe/H]^b	−0.04 ± 0.05
[Ca/H]^b	−0.01 ± 0.05
[Mg/H]^b	+0.03 ± 0.05
[Na/H]^b	+0.04 ± 0.05
[Si/H]^b	+0.02 ± 0.05
$V \sin i^b$ (km s^{-1})	2.2 ± 0.7

Notes. $^{(a)}$ Gaia DR3. $^{(b)}$ This work (Sect. 3).

2.1. Photometry from TESS

The field of sector 9 was observed during the first TESS cycle between 2019 Feb 28 UT and 2019 Mar 25 UT, and of sector 36 – in the third cycle, between 2021 Mar 07 UT and 2021 Apr 01 UT. TOI-733 (TIC 106402532) was observed by camera 2, CCD 2 in the nominal 2-minute cadence, in both sectors.

The data were processed in the TESS Science Processing Operations Center (SPOC, Jenkins et al. 2016) at NASA Ames Research Center. The SPOC conducted a transit search of the sector 9 lightcurve on 2019 Apr 25 and of sector 36 lightcurve on 2021 Apr 14 with an adaptive, noise-compensating matched

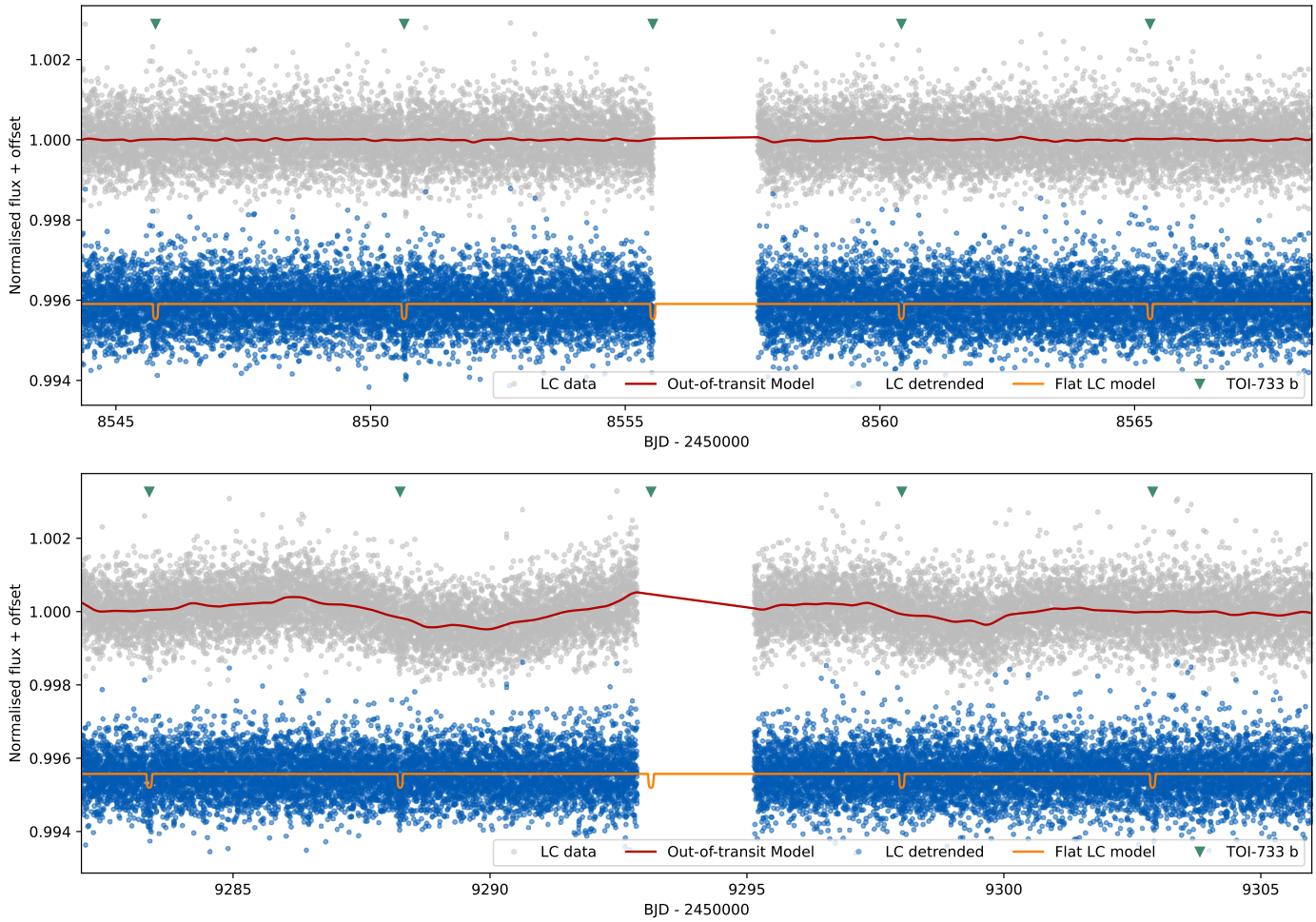

Fig. 1. 2-minute cadence sectors 9 (top) and 36 (bottom) TESS PDCSAP light curves (LC) plotted in grey, with the locations of the individual transits of TOI-733 b marked by green triangles. The Gaussian process-inferred model for the out-of-transit data is marked by the red curve. The vertically offset blue dots show the resulting detrended light curve, and orange fit with transits overplotted

.

filter (Jenkins 2002; Jenkins et al. 2010, 2020). The search produced a Threshold Crossing Event (TCE) with 4.887 d period for which an initial limb-darkened transit model was fitted (Li et al. 2019) and a suite of diagnostic tests were conducted to help make or break the planetary nature of the signal. The results of these tests can be found in the Data Validation Reports (DVR, Twicken et al. 2018) available for download via Mikulski Archive for Space Telescopes (MAST)[2] and the `EXOFOP-TESS` website[3]. The TESS Science Office (TSO) reviewed the vetting report and issued an alert for TOI 733.01 on 2019 Jun 6 (Guerrero et al. 2021). The reports for the two sectors show no concerning traits regarding any contaminating sources in the SPOC pipeline's aperture, generated for production of Simple Aperture Photometry (SAP, Twicken et al. 2010; Morris et al. 2020).

In the absence of such potential complications and as per common practice, we downloaded the Presearch Data Conditioning (PDCSAP) (Smith et al. 2012; Stumpe et al. 2012, 2014) lightcurves from MAST, proceeded to use them for the transit analysis and lightcurve modelling (4).

For the lightcurve detrending we turn to a Gaussian process (GP) type detrending using the code `citlalicue`[4], which is a wrapper of `george`[5] (Foreman-Mackey et al. 2014; Ambikasaran et al. 2016) and `pytransit`[6] (Parviainen 2015). This Python package fits a model to the out-of-transit data using likelihood maximisation to account for the stellar variability (for more details, see e.g., Barragán et al. 2021; Persson et al. 2022). The same procedure was applied to the data from both sectors. Figure 1 shows the sector 36 PDCSAP lightcurve, the GP model and resulting detrended lightcurve. For the joint modelling (Sect. 4), we only used the cutout transits, instead of the entire lightcurve to speed up the computation.

2.2. Ground-based Light Curve Follow-up

The TESS pixel scale is $\sim 21''$ pixel^{-1} and photometric apertures typically extend out to roughly 1 arcminute, which generally results in multiple stars blending in the TESS aperture. To attempt to determine the true source of the TESS detection, we conducted ground-based photometric follow-up observations of the field around TOI-733 as part of the TESS Follow-up Ob-

[2] `https://archive.stsci.edu/`
[3] `https://exofop.ipac.caltech.edu/tess/target.php?id=106402532`
[4] `https://github.com/oscaribv/citlalicue`
[5] `https://github.com/dfm/george`
[6] `https://github.com/hpparvi/PyTransit`

serving Program[7] Sub Group 1 (TFOP; Collins 2019). If the event detected in the TESS data is indeed on-target, the shallow SPOC reported depth of ∼ 400 ppm would not generally be detectable in ground-based observations. Instead, we slightly saturated TOI-733 to enable the extraction of nearby fainter star light curves to attempt to rule out or identify nearby eclipsing binaries (NEBs) as potential sources of the TESS detection.

We observed a predicted transit window of TOI-733.01 in Sloan i' band using the LCOGT (Brown et al. 2013) 1.0 m network node at Cerro Tololo Inter-American Observatory (CTIO) on 2019 August 18 UT. The 1 m telescopes are equipped with 4096×4096 SINISTRO cameras having an image scale of 0.″389 per pixel, resulting in a 26′ × 26′ field of view. The images were calibrated by the standard LCOGT `BANZAI` pipeline (McCully et al. 2018), and photometric data were extracted using `AstroImageJ` (Collins et al. 2017).

We observed a second predicted transit of TOI-733.01 from the Perth Exoplanet Survey Telescope (PEST) near Perth, Australia. The 0.3 m telescope was equipped with a 1530 × 1020 SBIG ST-8XME camera with an image scale of 1.″2 pixel^{-1} resulting in a 31′ × 21′ field of view. A custom pipeline based on `C-Munipack`[8] was used to calibrate the images and extract the differential photometry.

We scheduled full transit observations using the initial SPOC TESS sector 9 nominal ephemeris (P = 4.88651 d, T0 = 1545.7732 BTJD). A later SPOC sector 9 and 36 multi-year ephemeris (P = 4.88478 ± 0.00002 d, T0 = 1545.7755 ± 0.0015 BTJD) showed that our follow-up observations missed the revised predicted ingress, but covered the egress window with more than ±7σ timing uncertainty coverage. The multi-year SPOC centroid shift results limit the source to within ∼ 30″ of TOI-733 (3σ), so we focus our NEB search on the 9 known Gaia DR3 and TICv8 stars within 60″ of TOI-733 that are bright enough in TESS band to produce the TESS detection.

We calculate the root mean square (RMS) over the full duration of the raw light curve after normalising it to a mean value of 1.0. We do this for each of the 9 nearby star light curves (binned in 5 minute bins) and find that the LCOGT light curve RMS values are smaller by more than a factor of 5 compared to the expected NEB depth in each respective star, except for the 3″ neighbor TIC 865377947 and the 16″ neighbor TIC 106402536. The TIC 865377947 photometric aperture suffers from strong blending from the much brighter target star TOI-733, and TIC 106402536 is contaminated with a TOI-733 diffraction spike which contains strong photometric systematics from the saturated target star. Although NEB signals cannot be ruled out in TIC 865377947 and TIC 106402536, we find that NEB signals are ruled out in the remaining 7 nearby stars. In addition, the PEST light curve of TIC 106402536 excludes an NEB egress at a level of 3 × RMS. We then visually inspected each neighboring star's light curve to ensure no obvious deep eclipse-like signal. Through a process of elimination, we find that the TESS signal must be occurring in TOI-733 or the 3″ neighbor TIC 865377947, relative to known Gaia DR3 and TICv8 stars. Our follow-up light curves are available on the `EXOFOP-TESS` website.

2.3. Speckle imaging from Gemini-South/Zorro

If an exoplanet host star has a spatially close companion, that companion (bound or line of sight) can create a false-positive transit signal if it is, for example, an eclipsing binary (EB). "Third-light" flux from a close companion star can lead to an underestimated planetary radius if not accounted for in the transit model (Ciardi et al. 2015) and even cause non-detections of small planets residing within the same exoplanetary system (Lester et al. 2021). Discovery of close, bound companion stars provides crucial information toward our understanding of exoplanetary formation, dynamics and evolution (Howell et al. 2021). Thus, to search for close-in bound companions unresolved in TESS or other ground-based follow-up observations, we obtained high-resolution imaging speckle observations of TOI-733.

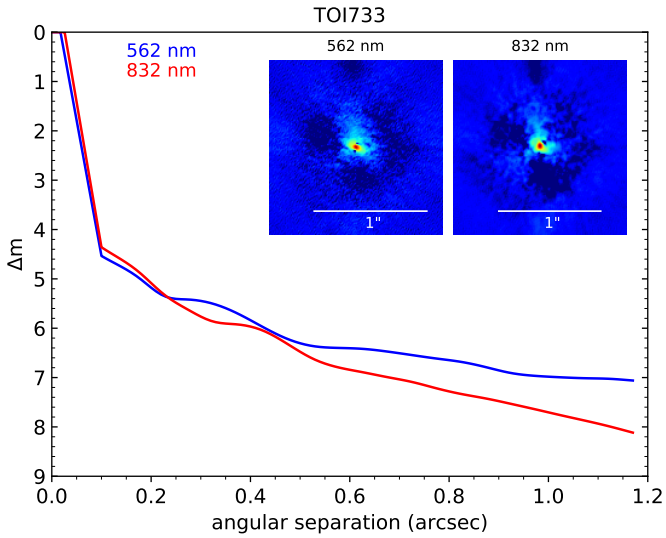

Fig. 2. 5-σ sensitivity curve resulting from the speckle imaging by Gemini South/Zorro. Reconstructed image shows no bright companions are detected within 1.2″.

TOI-733 was observed on 2020 March 15 UT using the Zorro speckle instrument on the Gemini South 8-m telescope (Scott et al. 2021). Zorro provides simultaneous speckle imaging in two bands (562nm and 832 nm) with output data products including a reconstructed image with robust contrast limits on companion detections. Three sets of 1000 X 0.06 sec exposures were collected and subjected to Fourier analysis in our standard reduction pipeline (see Howell et al. 2011). Figure 2 shows our final contrast curves and the two reconstructed speckle images. We find that TOI-733 is a single star with no companion brighter than 5-8 magnitudes (0.1″ to 1.0″) below that of the target star from the diffraction limit (20 mas) out to 1.2″. At the distance of TOI-733 (d=75 pc) these angular limits correspond to spatial limits of 1.5 to 90 au.

2.4. Spectroscopy and frequency analysis

We observed TOI-733 with the High Accuracy Radial velocity Planet Searcher (HARPS, Mayor et al. 2003) spectrograph mounted at the ESO-3.6 m telescope of La Silla Observatory in Chile. We obtained a total of 74 high-resolution (R ≈ 115 000, $\lambda \in$ 378– 691 nm) spectra between 17 February and 8 June 2022 UT, as part of our large observing program 106.21TJ.001 (PI: Gandolfi). The exposure time varied between 1200 and 1800 seconds, depending on weather conditions and observing schedule constraints, leading to a signal-to-noise (S/N) ratio per pixel at 550 nm between 45 and 109. We used the second fibre of the instrument to simultaneously observe a Fabry-Perot inter-

[7] `https://tess.mit.edu/followup`
[8] `http://c-munipack.sourceforge.net`

ferometer and trace possible nightly instrumental drifts (Wildi et al. 2010, 2011). The HARPS data were reduced using the dedicated Data Reduction Software (DRS, Lovis & Pepe 2007) available at the telescope. For each spectrum, the DRS also provides the full width at half maximum (FWHM) and the bisector inverse slope (BIS) of the cross-correlation function (CCF). We also extracted additional activity indicators and spectral diagnostics, namely the Hα, the S-index, the differential line width (dLW), and the chromatic index (crx) using the codes `serval` (Zechmeister et al. 2018) and TERRA (Anglada-Escudé & Butler 2012). A snippet of the data can be found in Table **??**.

As a first step into investigating the TOI-733 spectroscopic data, we perform a frequency analysis to search for significant signals as potential signatures of orbiting planets and/or stellar activity.

Figure 3 shows the Generalised Lomb Scargle (GLS, Zechmeister & Kürster 2009) periodograms of the HARPS RV data as extracted by the DRS pipeline, as well as common activity indicators from the DRS, `serval` and TERRA. We consider a signal to be significant if its false alarm probability (FAP, Kuerster et al. 1997) is lower than 0.1 %. We use the bootstrap method to estimate the FAP, denoted here by a blue horizontal line in all but the bottom panel.

The periodogram of the DRS RVs (upper panel) shows two significant (FAP < 0.1 %) peaks at 0.078 day^{-1} and 0.118 day^{-1} (semi-transparent purple), which correspond to periods of about 12.8 and 8.5 d, respectively. We note the presence of a third peak at the transit signal of TOI-733.01 (0.205 day^{-1}, teal vertical line). While this peak does not cross our FAP = 0.1 % threshold to consider it to be significant, we can use our prior knowledge of the frequency of the transit signal to estimate the probability that noise could produce a peak at the orbital frequency of the transit signal, and whose power exceeds the orbserved power of TOI-733.01. Following the method described in Hatzes (2019), we computed the GLS periodogram of 10^5 fake data sets obtained by randomly shuffling the RV measurements, while keeping the observation time-stamps fixed. We found that none of the 10^5 periodgram trials displays a peak at 0.205 day^{-1} with power greater than the observed one, implying a FAP < 0.001 %.

Moving down to the second panel showing a periodogram of the RV residuals after subtracting the signal of the planet candidate, we see that the latter two peaks remain undisturbed. Looking at the FWHM and dLW periodograms (panels d and e, respectively), we can clearly identify a peak at ~ 0.04 day^{-1} (25.6 days, solid purple line). Although not clearly identifiable in the activity indicators, subtracting a signal at this frequency from the FWHM causes the peak at 8.5 days to become apparent. Progressing further and subtracting the 8.5-day signal, makes the signal at 12.8 days become identifiable as well (Fig. B.1). All this shows that all three signals (25.6 days, 12.8 days and 8.5 days) are present in the FWHM, which in turn allows us to attribute the latter two (leftmost peaks in the top RV panel) to the first two harmonics of the 25.6-day signal. We thus consider the latter to be the true rotation period of the star and point out that such a $P_{\rm rot}$ is consistent with $R_\star$ and the $V \sin i$ estimated in Sect. 3.

It is also worth noting that the S-index panel also displays the significance of the so estimated $P_{\rm rot}$, but it is less prominent compared to the highest peak in this panel – 65.2 days. The bottom panel shows the periodogram of the window function, where we can see a peak at a frequency equal to the frequency spacing between 1/25.6 and 1/50 day^{-1}, i.e. 0.0237 day^{-1} (red arrow in bottom panel), pointing to the interpretation that the 65.2-day signal is an alias of the rotation frequency.

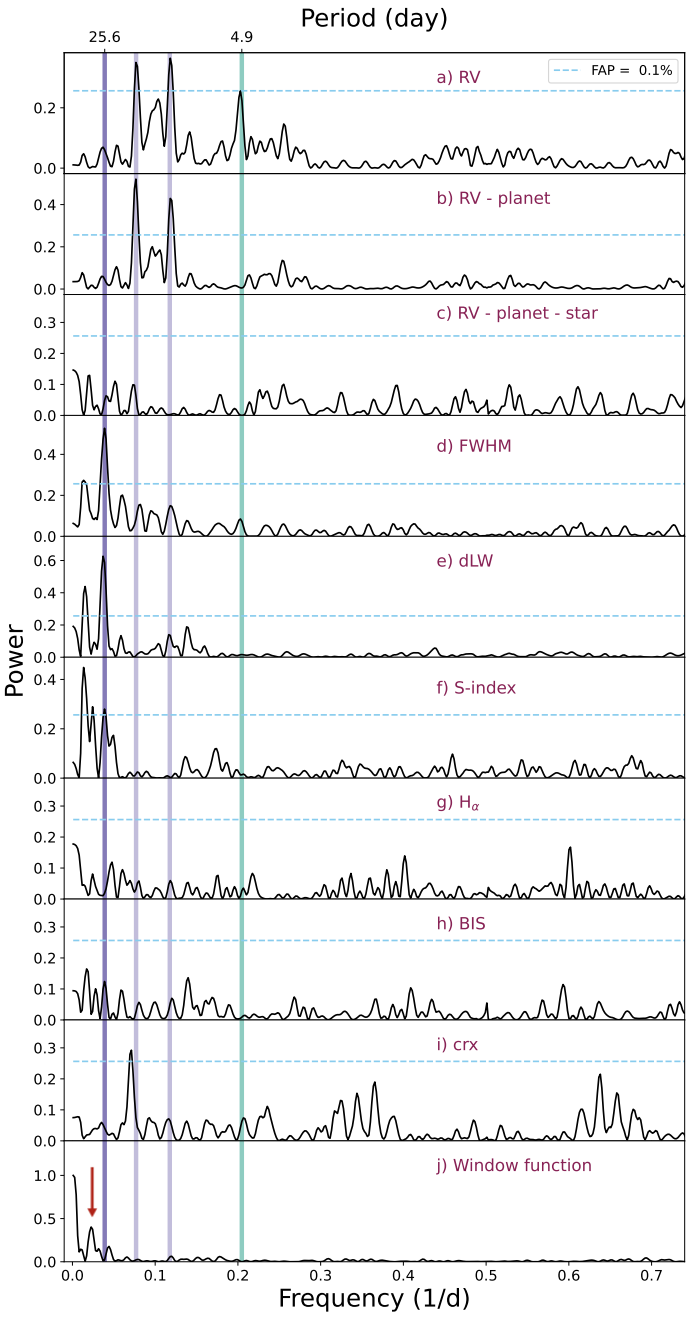

Fig. 3. Generalized Lomb-Scargle periodograms of the spectroscopic data for TOI-733. From top to bottom, the top three panels correspond to the DRS RVs; the RV residuals after fitting a sinusoid at the detected orbital period for TOI-733.01 marked as solid vertical teal line; and residuals after fitting final multi-GP model presented in Sect. 4. The following panels show periodograms of spectral activity indicators, ending with the window function at the bottom, as annotated in each panel. The solid purple lines represent the frequency of the GP signal, particularly visible in the FWHM and dLW, while its first two harmonics in semi-transparent purple are well pronounced in the RVs. A peak at the first harmonic is also seen in panel i). The horizontal blue line shows the 0.1 % FAP level.

Panel c) presents the periodogram of the RV residuals after the final model described in Sect. 4 is subtracted from the data – no more significant peaks are present in the data. This, together with a RV jitter term of ~1.1 m s^{-1} (Table 2), shows us that, based on the gathered observations, there is no evidence for an additional planet orbiting TOI-733.

3. Stellar modelling

For the spectroscopic modelling of TOI-733 we used two software: SpecMatch-Emp (Yee et al. 2017), and SME[9] (Spectroscopy Made Easy; Valenti & Piskunov 1996; Piskunov & Valenti 2017) version 5.2.2. The latter fits observations to synthetic spectra computed with atomic and molecular line data from VALD[10] (Ryabchikova et al. 2015) and stellar atmosphere grids (Atlas12, Kurucz 2013). SpecMatch-Emp is an emperical code that compares observations to a dense library of very well-characterised FGKM stars. This software finds an effective temperature $T_{\rm eff}$= 5554 ± 110 K, a surface gravity $\log g_\star$= 4.30 ± 0.12, and an iron abundance [Fe/H]= −0.09 ± 0.09. These values were used as a first input to the more elaborate SME modelling (further details on the SME modelling can be found in Persson et al. 2018). In short, we fitted one parameter at a time using spectral lines particularly sensitive to the fitted parameters. We fixed the micro-turbulent velocity, $V_{\rm mic}$ to 1.0 km s^{-1} (Bruntt et al. 2008), and the macro-turbulent velocity, $V_{\rm mac}$ to 2.8 km s^{-1} (Doyle et al. 2014). Our final SME model gives $T_{\rm eff}$= 5585 ± 60 K, [Fe/H]= −0.04 ± 0.05, [Ca/H]= −0.01 ± 0.05, [Si/H]= +0.02 ± 0.05, [Mg/H]= +0.03 ± 0.05, [Na/H]= +0.04 ± 0.05, $\log g_\star$= 4.47 ± 0.05, and a projected rotational velocity $V \sin i_\star$ = 2.2 ± 0.7 km s^{-1} in excellent agreement with Specmatch-emp. The SME modelling points to a G6 V star with typical mass and radius of 0.97 $M_\odot$ and 0.95 $R_\odot$, respectively.

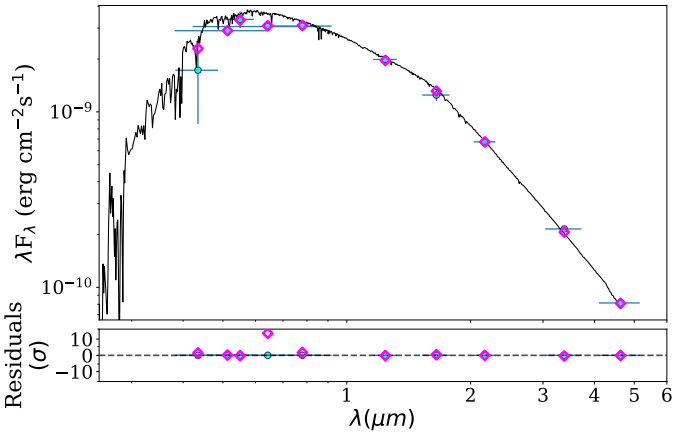

Fig. 4. The spectral energy distribution of TOI-733 and the best fitted model (Castelli & Kurucz 2004). Magenta diamonds outline the synthetic photometry, and the observed photometry is shown with blue points. We plot the 1 σ uncertainties of the magnitudes (vertical error bars), while the effective width of the passbands are marked with the horizontal bars. The residuals in the lower panel are normalised to the errors of the photometry.

For the modelling of the stellar radius, mass and age we used the python package ARIADNE[11] (Vines & Jenkins 2022). With this software, broadband photometry were fitted to the spectral energy distribution (SED). We fitted the following bandpasses: Johnson V and B (APASS), $GG_{\rm BP}G_{\rm RP}$ (DR3), JHK_S (*2MASS*), *WISE* W1-W2, and the Gaia DR3 parallax. We set an upper limit of A_V based on the dust maps of Schlegel et al. (1998). ARIADNE fits the photometric observations to four atmospheric model grids `Phoenix v2` (Husser et al. 2013), `BtSettl` (Allard et al. 2012), Castelli & Kurucz (2004), and Kurucz (1993), and computes the final radius with Bayesian Model Averaging. The final stellar radius is $R_\star = 0.949^{+0.008}_{-0.012}\ R_\star$. We also find a luminosity of $L_\star = 0.82 \pm 0.02\ L_\odot$, and an extinction that is consistent with zero ($A_{\rm V} = 0.01 \pm 0.02$). The stellar mass in ARIADNE is interpolated from the MIST (Choi et al. 2016) isochrones and is found to be $M_\star = 0.956^{+0.050}_{-0.026}\ M_\star$. Combining the radius from ARIADNE and $\log g_\star$ from SME, the gravitational mass is $0.97^{+0.11}_{-0.10}\ M_\odot$. The posteriors in the ARIADNE model for $T_{\rm eff}$, [Fe/H], and $\log g_\star$ are in very good agreement with the priors taken from SME.

We checked the ARIADNE results with `PARAM1.3`[12] (da Silva et al. 2006). This software uses Bayesian computation and the PARSEC isochrones with $T_{\rm eff}$, [Fe/H], the V magnitude, and the Gaia DR3 parallax as priors. The results are in excellent agreement within 1 σ with the results from ARIADNE.

The stellar age was derived with ARIADNE and `PARAM1.3` to $4.4^{+1.5}_{-3.1}$ Gyr and 6.2 ± 3.6 Gyr, respectively.

We used the stellar radius and mass from ARIADNE and $T_{\rm eff}$ from SME in our pyaneti modelling in Sect. 4 and the SME abundances for the planet interior modelling in Sect. 5.1.

4. Transit and RV modelling

For the joint modelling of TOI-733 we used the code `pyaneti`[13] (Barragán et al. 2019, 2022a) to obtain and refine system parameters. As mentioned in Sect. 2, we only use trimmed versions of the `citlalicue`-detrended light curves from the two TESS sectors. Each segment contains 24 hours of data, including and around each transit (total transit duration ∼2.6 hours). We account for stellar limb darkening using the Kipping (2013) q_1 and q_2 parametrisation, and model the transits using the Mandel & Agol (2002) approach. The orbit inclination is estimated via the impact parameter parametrisation (Winn 2010), which ultimately allows us to estimate the true planet mass.

Contrary to what the quiet look of the lightcurves (Fig. 1) may suggest, TOI-733 has a pronounced activity signature (Sects. 2.4, 3). We thus applied a multi-dimensional Gaussian process approach, the `pyaneti` implementation of which is as described in Rajpaul et al. (2015). The activity indicator of choice to pair with the DRS RVs and guide the GP is the FWHM as it clearly shows the imprint of the star (Sect. 2.4). We tested combinations with other available activity indicators extracted via the different pipelines, but for the purpose of this analysis, none yielded superior results to the pairing with the FWHM. Given the clear periodocity of the stellar-induced signal, we use the quasi-periodic (QP, Eq. 1) kernel and place an uninformative prior with a range containing the value corresponding to the peak of the FWHM (and dLW) GLS periodogram (∼25 days, see Fig. 3, fourth panel). Given that the first two harmonics of this signal are clearly detected in the RV data, we consider this to be the true stellar rotation period, $P_{\rm rot}$. We add that, while the S-index shows a significant peak suggesting a $P_{\rm rot}$ of ∼65.2 days, modelling it instead of the FWHM and adjusting the priors accordingly, still converges on the same $P_{\rm rot}$ as the one given by the FWHM, thus further affirming our conclusion.

The $P_{\rm GP}$ term in Eq. 1 is to be interpreted as said $P_{\rm rot}$, while λ_p describes (the inverse of) the harmonic complexity of the data, and λ_e represents the time evolution of the active features as they move along the stellar surface.

[9] `http://www.stsci.edu/~valenti/sme.html`
[10] `http://vald.astro.uu.se`
[11] `https://github.com/jvines/astroARIADNE`
[12] `http://stev.oapd.inaf.it/cgi-bin/param_1.3`
[13] `https://github.com/oscaribv/pyaneti`

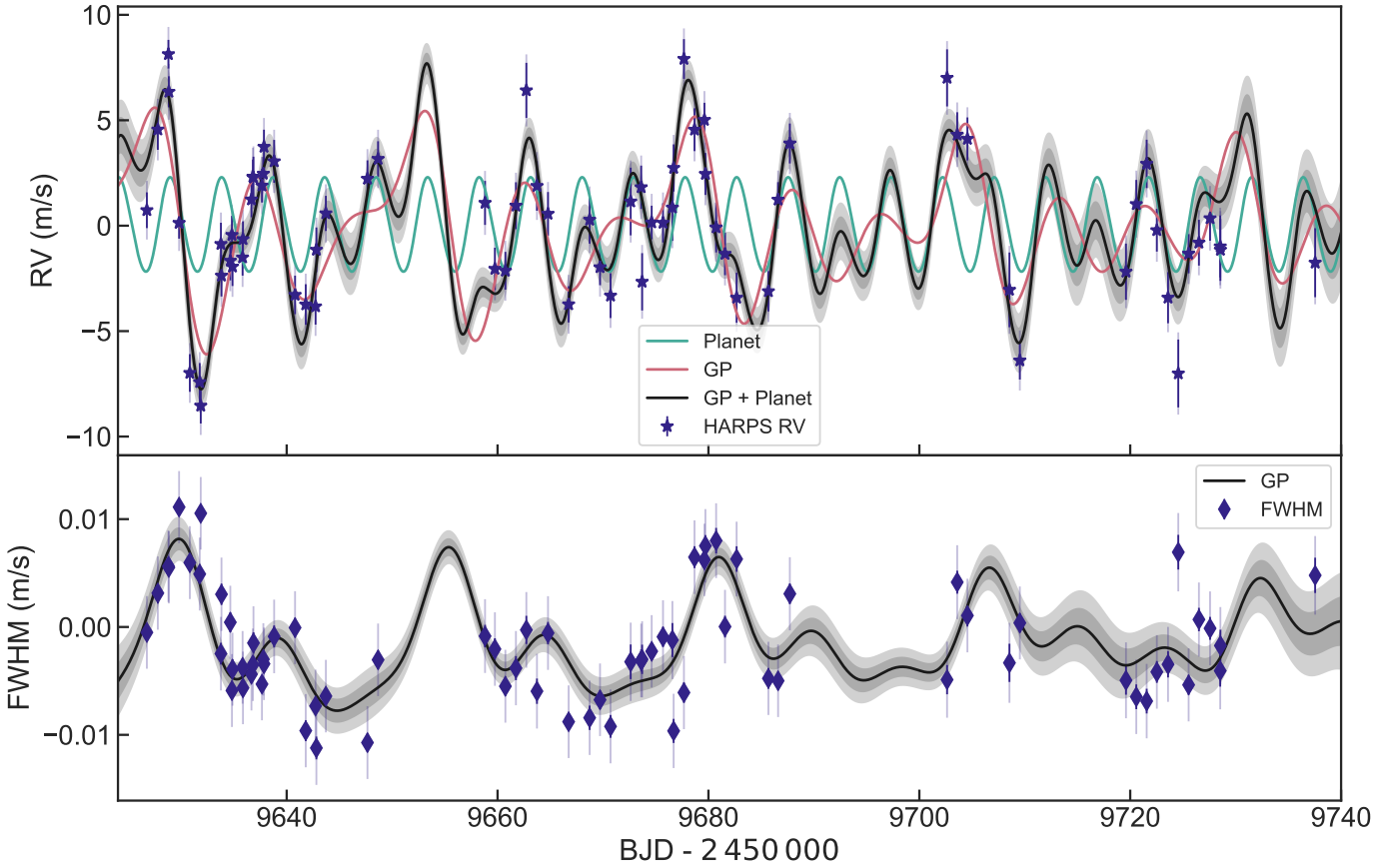

Fig. 5. RV (top panel) and FWHM (bottom panel) time-series. The purple markers in each panel represent the HARPS RV and FWHM measurements with inferred offsets extracted. The inferred multi-GP model is shown as a solid black curve, where the dark and light shaded areas show the 1- and 2- sigma credible intervals from said model, and can also explain the data but with a correspondingly lower probability. The solid red line in the top panel shows the star-only model, while the teal sine curve – the Keplerian for TOI-733 b. In both panels the nominal error bars are in solid purple, and the jitter error bars ($\sigma_{\rm HARPS}$) are semi-transparent purple.

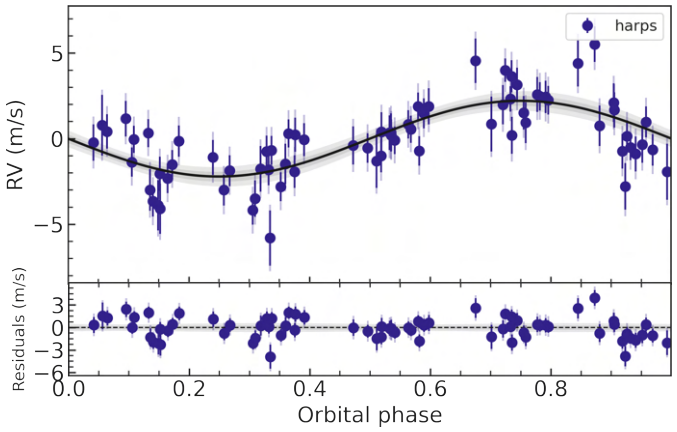

Fig. 6. HARPS RV data (purple points) and inferred model (solid black curve) phasefolded on the orbital period of TOI-733 b. 1- and 2 σ credible intervals in shaded grey regions are also shown. Nominal and jitter error bars are plotted in solid and semi-transparent purple, respectively.

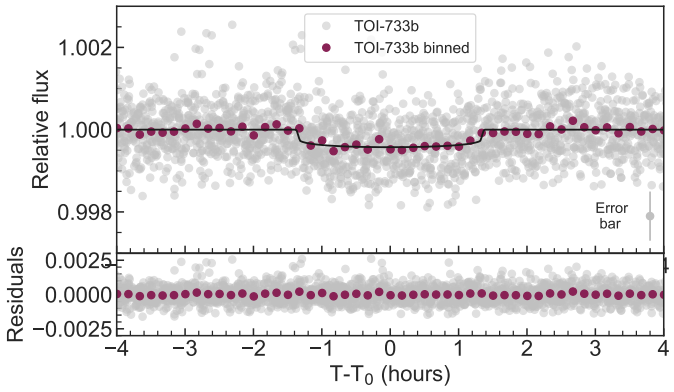

Fig. 7. TOI-733 b phasefolded and detrended transits from both TESS sectors, with residuals. The best-fitting transit model is marked by the black curve. 2-min nominal cadence data points binned to 10 min are shown in grey and green, respectively, with typical error bar in the bottom right.

$$\gamma(t_i, t_j) = \exp\left[-\frac{\sin^2[\pi(t_i - t_j)/P_{\rm GP}]}{2\lambda_{\rm p}^2} - \frac{(t_i - t_j)^2}{2\lambda_{\rm e}^2}\right], \quad (1)$$

Similarly to e.g., Georgieva et al. (2021) and Barragán et al. (2022b), the two-dimensional GP we used to characterise the TOI-733 system is formulated as in Eq. 2 below:

$$\begin{aligned} \Delta RV &= V_c G(t) + V_r \dot{G}(t), \\ \Delta FWHM &= F_c G(t), \end{aligned} \quad (2)$$

Table 2. The `pyaneti` model of TOI-733 described in Sect. 4.

Parameter	Priors[a]	Final value
Fitted parameters		
Transit epoch T_0 (BJD - 2 450 000)	$\mathcal{U}$[8545.73, 8545.79]	$8545.7767^{+0.0031}_{-0.0023}$ days
Orbital period $P_{\rm orb}$	$\mathcal{U}$[4.8845, 4.8860]	$4.884765^{+1.9e-5}_{-2.4e-5}$ days
$\sqrt{e}\sin\omega_\star$	$\mathcal{U}[-1, 1]$	-0.08 ± 0.19
$\sqrt{e}\cos\omega_\star$	$\mathcal{U}[-1, 1]$	$0.01^{+0.15}_{-0.16}$
Impact parameter b	$\mathcal{U}[0, 1]$	$0.29^{+0.20}_{-0.19}$
Scaled semi-major axis $a/R_\star$	$\mathcal{N}[14, 1]$	$14.0^{+0.80}_{-0.88}$
Scaled planet radius $R_{\rm p}/R_\star$	$\mathcal{U}[0, 0.05]$	$0.01925^{+0.00079}_{-0.00085}$
Doppler semi-amplitude variation K ...	$\mathcal{U}[0, 50]$	2.23 ± 0.26 m s^{-1}
Limb-darkening coefficient q_1	$\mathcal{U}[0, 1]$	$0.31^{+0.39}_{-0.22}$
Limb-darkening coefficient q_2	$\mathcal{U}[0, 1]$	$0.31^{+0.35}_{-0.22}$
GP hyperparameters		
GP Period $P_{\rm GP}$	$\mathcal{U}[24.5, 26.5]$	$25.48^{+0.15}_{-0.14}$ days
$\lambda_{\rm p}$	$\mathcal{U}[0.1, 3]$	$0.57^{+0.29}_{-0.15}$
$\lambda_{\rm e}$	$\mathcal{U}[1, 200]$	$162.4^{+27.3}_{-41.2}$ days
$V_{\rm c}$	$\mathcal{U}[0, 100]$	$0.00081^{+0.00178}_{-0.00056}$ m s^{-1}
$V_{\rm r}$	$\mathcal{U}[0, 500]$	$0.0187^{+0.0278}_{-0.0083}$ m s^{-1} d^{-1}
$F_{\rm c}$	$\mathcal{U}[0, 150]$	$0.0116^{+0.0160}_{-0.0051}$ m s^{-1}
Derived Parameters		
Planet mass $M_{\rm p}$	...	$5.72^{+0.70}_{-0.68}$ $M_\oplus$
Planet radius $R_{\rm p}$	...	$1.992^{+0.085}_{-0.090}$ $R_\oplus$
Inclination i	...	$88.85^{+0.77}_{-0.82}$ deg
Eccentricity e	...	$0.046^{+0.056}_{-0.033}$
Angle of periastron $\omega_\star$	...	$-53.2^{+158.9}_{-68.1}$ deg
Semi-major axis a	...	$0.0618^{+0.0036}_{-0.0039}$ AU
Insolation F	...	$207.1^{+29.9}_{-23.5}$ F$_\oplus$
Planet density $\rho_{\rm p}$	...	$3.98^{+0.77}_{-0.66}$ g cm^{-3}
Planet surface gravity $\log(g_{\rm b})$	...	1752^{+340}_{-321} cm s^{-2}
Equilibrium temperature $T_{\rm eq}{}^b$	...	$1055.8^{+36.2}_{-31.3}$ K
Jeans escape parameter Λ^c	...	$20.61^{+2.78}_{-2.68}$
Transmission spectroscopy metric TSM[d]	...	$46.29^{+9.26}_{-7.47}$
Total transit duration T_{14}	...	$2.61^{+0.15}_{-0.10}$ hours
Full transit duration T_{23}	...	$2.50^{+0.15}_{-0.11}$ hours
Ingress and egress transit duration T_{12} ..	...	$0.0542^{+0.0112}_{-0.0047}$ hours
Additional Parameters		
Offset RV HARPS	$\mathcal{U}$[-24.3256 , -23.3089]	$-23.81711^{+0.00083}_{-0.00061}$ km s^{-1}
Offset FWHM	$\mathcal{U}$[6.4434 , 7.4657]	$6.9541^{+0.0105}_{-0.0083}$ km s^{-1}
RV jitter HARPS	$\mathcal{J}[0, 1000]$	$1.08^{+0.23}_{-0.21}$ m s^{-1}
FWHM jitter	$\mathcal{J}[0, 1000]$	$3.24^{+0.40}_{-0.34}$ m s^{-1}
TESS light curve jitter σ_{TESS} ($\times 10^{-6}$) ..	$\mathcal{J}[0, 1000]$	$597.8^{+5.4}_{-5.3}$

Notes. [a] $\mathcal{U}$[a,b] refers to uniform priors in the range a – b, and $\mathcal{J}$[a,b] to modified Jeffrey's priors (Eq. 16 in Gregory 2005). [b] Dayside equilibrium temperature, assuming no heat redistribution and zero albedo. [c] $\Lambda = GM_{\rm p}m_{\rm H}/(k_{\rm B}T_{\rm eq}R_{\rm p})$ (Fossati et al. 2017). [d] Kempton et al. (2018).

G(t) is assumed to describe both timeseries and is a latent variable modelled by the QP covariance function in Eq. 1. V_c, V_r and F_c are coefficients, which relate G(t) to the observables. G(t) and $\dot{\rm G}$(t) respectively represent the GP function and its first derivative. The dependency of the position of the spots on

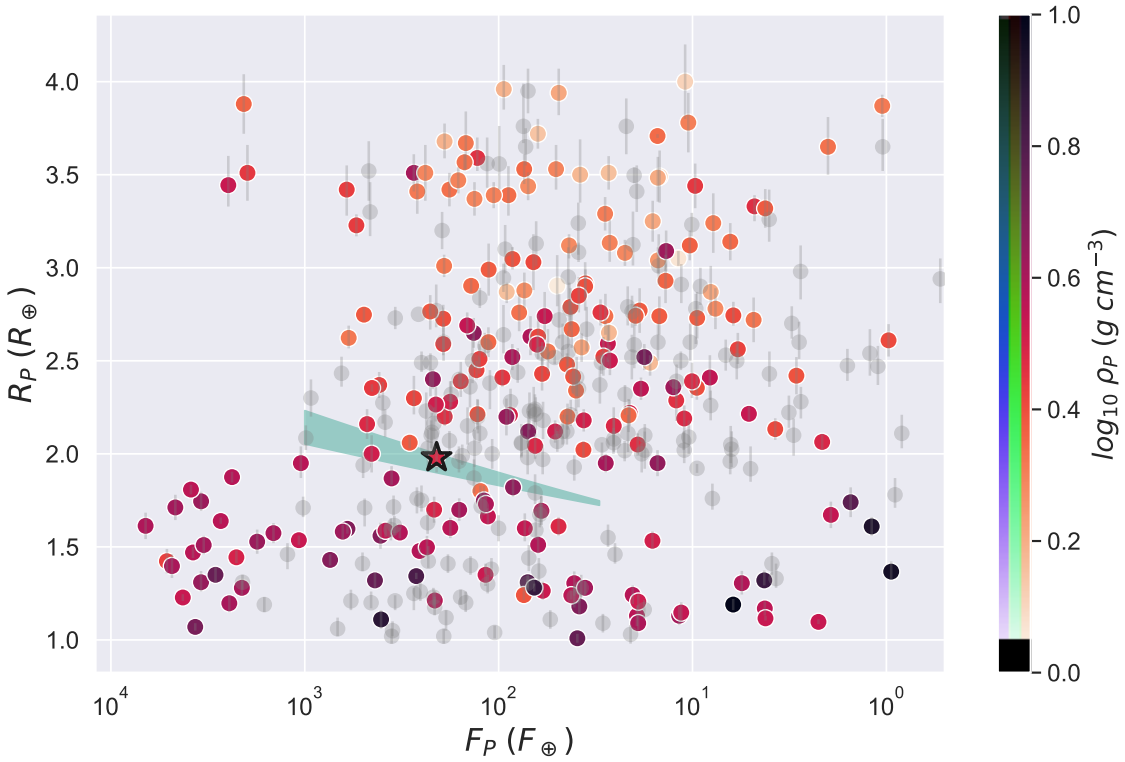

Fig. 8. Radius vs incident flux (in units of flux received on Earth) for small planets ($1 - 4\ R_\oplus$) orbiting stars $0.7 - 1.4\ M_\odot$ and radii estimates with precision better than 5 %. All data were taken from the NASA Exoplanet Archive. Points in colour correspond to planets with density (and thus mass) estimates, where lighter and darker colours correspond to lower and higher densities, respectively. Grey points are planets whose masses have not been measured, and thus their densities are unknown. A fit to the radius valley following the relation in Petigura et al. (2022) is plotted in semi-transparent teal. TOI-733 b, marked with a black star symbol, is found lying well within the sparsely-populated region of the radius gap.

the stellar hemisphere is what is modelled by the dG/dt part. In the case of the RVs the latter is particularly relevant (as evidenced by the value of V_r, see Table 2) since RVs depend not only on the fraction of the stellar disc covered by active regions, but also on how the size and shape of said surface features change in time.

Using the polar form parametrisation for e and $\omega_\star$ and adding a jitter term for both the photometric and spectroscopic data, we proceeded with the aforementioned model configuration to sample the parameter space with 500 Markov chains. Convergence was checked at every 5000 steps, and when reached – the last set of 5000 was used, along with a thin factor of 10, to create posterior distributions for the sampled parameters, each built with 250 000 independent points. All parameters, the priors used and derived values are listed in Table 2. Our resulting final multi-GP model is shown in Fig. 5, where the top panel shows the RV, and the bottom one – the FWHM timeseries. The phase-folded RV and transit plots of TOI-733 b are in Figs. 6 and 7, respectively. For clarity, the latter shows only 8 hours centered around the transit.

We thus find TOI-733 b to be in a circular 4.885-day orbit around a G6 V star, which in turn has a stellar rotation period estimated as $P_{\rm rot}$ = 25.48 days. The activity of the star is once again evidenced by the value of λ_p ($0.57^{+0.29}_{-0.15}$), indicating a high harmonic complexity, which in turn is a sign of rapid changes within a single rotation period. The lifetime of the active regions can also be used to infer high activity but unfortunately our model is not able to constrain λ_e well.

5. Discussion

Based on the two sectors of TESS data, we obtain a planet radius of $R_{\rm p} = 1.992^{+0.085}_{-0.090}\ R_\oplus$ (4.4 % precision), while the HARPS RVs yield a semi-amplitude of $K = 2.23 \pm 0.26$ m s^{-1}. These in turn give a planet mass of $M_{\rm p} = 5.72^{+0.70}_{-0.68}\ M_\oplus$ (12 % precision), and bulk density of $\rho_{\rm p} = 3.98^{+0.77}_{-0.66}$ g cm^{-3}. With an orbital period of 4.88 days around a G6 V star, TOI-733 b is in a highly irradiated orbit ($F_{\rm p} = 207.1^{+29.9}_{-23.5}\ F_\oplus$), and, as seen in Fig. 8, is found lying in the middle of the small planet radius valley, here calculated following the work of Petigura et al. (2022). All planets plotted have radii with maximum 5 % uncertainty in radius. The data were downloaded from the NASA Exoplanet archive, where for planets with several entries the most recent results showing the highest precision were chosen. In cases of similar precision, the latest publications were favoured. If stellar irradiation was not among the listed parameters, we calculated it using the following relation:

$$F_{\rm p} = \left(\frac{R_\star}{R_\odot}\right)^2 \left(\frac{T_{eff}}{T_\odot}\right)^4 \left(\frac{\rm AU}{a}\right)^2 F_\oplus \quad (3)$$

where $F_{\rm p}$ is the incoming stellar flux, $T_{\rm eff}$ is stellar effective temperature, and a – the semi-major axis. Colour-coded dots are planets with known bulk densities, while the densities of the planets in grey cannot be calculated since their masses have not yet been measured. As evident from this figure, the densities of super-Earths are higher when compared to the mini-Neptune population, as the latter feature a significant volatile content.

The planet to the immediate left of TOI-733 b in Fig. 8 and thus the closest well-characterised planet to it in this parameter

space, is π Men c (Gandolfi et al. 2018; Huang et al. 2018; Hatzes et al. 2022). García Muñoz et al. (2020) report the non-detection of photodissociated hydrogen, suggesting that π Men c could instead be H_2O or dominated by other heavy molecules rather than H/He. The latter hypothesis was later affirmed by further observations with the detection of, most likely escaping, Ca II ions (García Muñoz et al. 2021). Despite its relatively mature age (~ 4 Gyr, Damasso et al. 2020), atmospheric escape was expected for π Men c as its radius (2.06 ± 0.03 $R_\oplus$) is large relative to its mass (4.52 ± 0.81 $M_\oplus$)[14]. While still of relatively low density ($3.98^{+0.77}_{-0.66}$ g cm^{-3} vs 2.1 ± 0.4 g cm^{-3} for π Men c), it is less likely that TOI-733 b is undergoing intense atmospheric loss.

Water worlds have been put forward as a possible explanation for planets with similar parameters (e.g., Zeng et al. 2019, 2021). Recently, Luque & Pallé (2022) showed that the small planet population around M dwarfs is inconsistent with a radius gap as observed around higher mass stars. They suggest that photoevaporation is not needed to explain the observed trends and that water worlds, forming beyond the snow line and migrating inward are the planets that straddle the area between rocky planets and those with non-negligible envelopes. The census of well-characterised planets around Sun-like stars, however, prevented this conclusion from being extended to higher mass stars.

To try and understand TOI-733 b better and elucidate its composition, and whether it is more likely that its atmosphere has or is in a process of being lost, or if instead it formed more or less as we currently find it, we performed interior and atmospheric modelling, as described in the following sections.

5.1. Interior structure

To illustrate the position of TOI-733 b in mass-radius space, we show in Fig. 9 the iso-composition curves for refractory interiors (Brugger et al. 2016; Brugger et al. 2017), planets with supercritical water (SW) envelopes (Acuña et al. 2021; Aguichine et al. 2021), and planets with H/He envelopes (Lopez & Fortney 2014). We choose to use the data grid of Lopez & Fortney (2014) to plot different percentages of H/He models, over the more widely used model of Zeng et al. (2019), since the latter indicate the temperature in the Zeng et al. (2019) is that at the P = 100 bar level, whereas the temperature in the Lopez & Fortney (2014) model reflects the planet's irradiation or equilibrium temperature. This concept is further elaborated in e.g., Rogers et al. (2023).

Looking at Fig. 9, we can see that the density of TOI-733 b is lower than that of a pure mantle rock planet, suggesting that it contains a volatile layer. A 5.7 $M_\oplus$ planet with a H/He-dominated envelope of ~0.2 % has a radius of $\simeq$ 2 $R_\oplus$ (Lopez & Fortney 2014). Therefore, with a radius of R = 2.0 $R_\oplus$, TOI-733 b's most likely inventory of volatiles does not include a significant H/He component and is instead that of a secondary atmosphere (H_2O, CO_2, CH_4, etc., Madhusudhan et al. 2021; Krissansen-Totton & Fortney 2022), which is the envelope composition we assume in our interior structure model.

We perform a Markov chain Monte Carlo (MCMC) Bayesian analysis (Acuña in prep.a; Director et al. 2017) of the interior structure and composition of TOI-733 b. Our 1D interior structure model considers three layers: a Fe-rich core, a silicate mantle (Brugger et al. 2016; Brugger et al. 2017), and a water-dominated envelope in supercritical and steam phases, given the high irradiation TOI-733 b receives from its host star (Mousis et al. 2020; Acuña et al. 2021). To include self-consistently the effect of this high irradiation on the total radius, we couple our interior model to an atmospheric model that computes the emitted total radiation and reflection of the atmosphere to determine radiative-convective equilibrium (Acuña et al. 2021; Acuña in prep.a). Our interior-atmosphere models calculate the radius from the center of the planet, up to a transit radius of 20 mbar (Grimm et al. 2018; Mousis et al. 2020).

In our analysis, we consider two scenarios. Scenario 1 is the most conservative one, since it only takes into account the planetary mass and radius as input for the MCMC method, whereas in scenario 2, we adopt as input for the MCMC the stellar Fe/Si mole ratio in addition to the mass and radius of the planet. We obtain a Fe/Si = 0.67 ± 0.11, following the approach described in Brugger et al. (2017); Sotin et al. (2007) to convert the stellar abundances in Table 1 to a mole ratio. We adopt solar composition reference values from Gray (2005). The MCMC provides the posterior distribution functions (PDF) of the compositional parameters, which are the core mass fraction (CMF), and water mass fraction (WMF). In addition, the atmospheric parameters are also obtained by the MCMC, and consist of the temperature at the interior-atmosphere coupling interface (300 bar), the Bond albedo, and the atmospheric thickness from 300 bar up to the transit radius.

Table 3. 1σ confidence intervals of the interior and atmosphere MCMC output parameters in the two different compositional scenarios (see text).

Parameter	Scenario 1	Scenario 2
Core mass fraction, CMF	0.27±0.14	0.20±0.03
Water mass fraction, WMF	0.11±0.06	0.07±0.05
Fe-to-Si mole ratio, Fe/Si	1.11±0.74	0.67±0.11
Temperature at 300 bar, T_{300} [K]	3458±38	3448±30
Thickness at 300 bar, z_{300} [km]	616^{+92}_{-185}	447^{+111}_{-21}
Albedo, a_p	0.24±0.01	
Core+Mantle radius, [R_p units]	0.77±0.06	$0.86^{+0.07}_{-0.02}$

Table 3 shows the mean and 1σ confidence intervals of the MCMC output parameters. In scenario 1, which is the most general and conservative scenario since we do not make any assumptions on the planetary Fe/Si mole ratio, the CMF distribution is centered at a similar value to the mean of the CMF distribution of the rocky super-Earth population (Plotnykov & Valencia 2020). In addition, in scenario 1 the CMF is compatible within uncertainties with the Earth CMF value ($CMF_\oplus$ = 0.32). The CMF in scenario 2 is significantly lower than that of Earth, which is a consequence of a lower Fe/Si mole ratio of the stellar host compared to the Sun ($Fe/Si_\odot$ = 0.96), although the planetary CMF is still well within the range of CMFs observed in super-Earths ($\simeq$ 0.10 to 0.50). The WMF of TOI-733 b ranges from 5 to 17% in scenario 1, and from 2 to 12% in scenario 2, suggesting that TOI-733 b's water content is in-between relative to what is expected in super-Earths (WMF < 5%) and sub-Neptunes (WMF > 20%) (Acuña in prep.b; Luque & Pallé 2022).

5.2. Atmospheric escape

The low surface gravity of TOI-733 b combined with its high equilibrium temperature results in a moderately low value of the Jeans escape parameter Λ = 20.6. Neptune-like planets for which $\Lambda \lesssim 20$ are expected to have quickly escaping atmospheres (Owen & Wu 2016; Cubillos et al. 2017). Their size

[14] The radius and mass values are as taken by García Muñoz et al. (2020). More accurate parameters have since been presented in Hatzes et al. (2022)

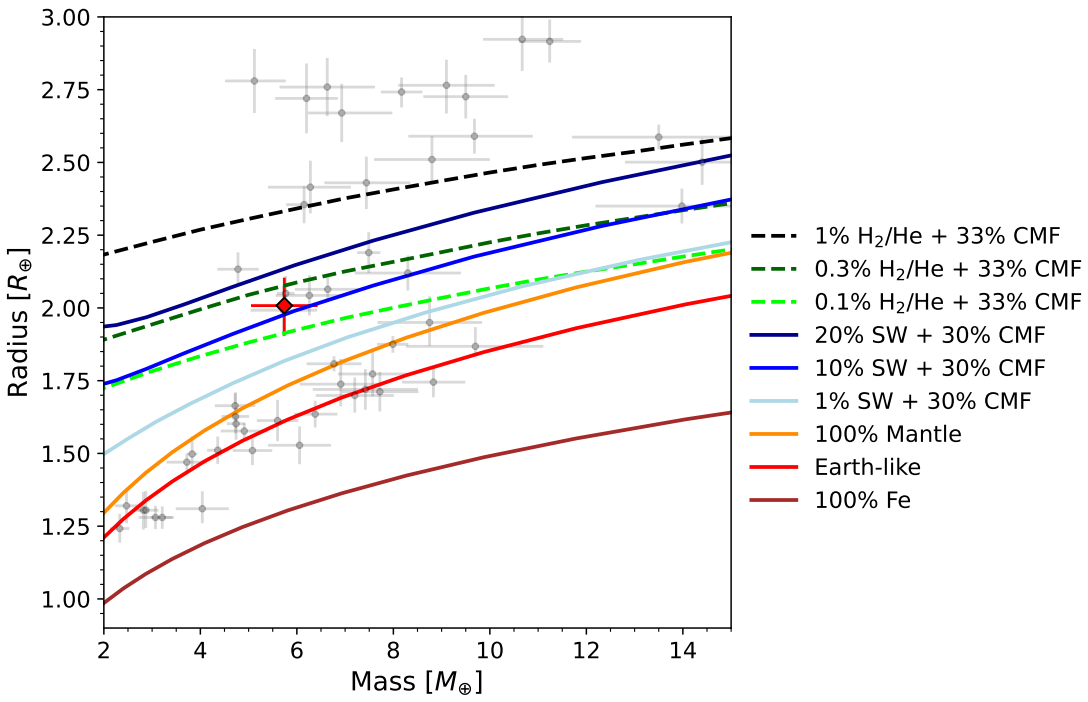

Fig. 9. Mass-radius relationships for supercritical water (SW) planets (Acuña et al. 2021; Aguichine et al. 2021), planets with Earth-like cores and H/He envelopes (Lopez & Fortney 2014), and rocky planets with different iron contents (bottom three curves, Brugger et al. 2017). The atmospheres in volatile-rich planets are in radiative equilibrium for irradiation temperatures of 1200 K and 1000 K for water and H/He envelopes, respectively. Assuming an age of 4.4 Gyr, the position of TOI-733 b is as highlighted in red. Grey points correspond to planets less massive than 15 $M_\oplus$ with mass and radius data available from the NASA Exoplanet Archive. All planets have a limit on the radius uncertainty of 5 %, and on the mass of 15 %. The mantle composition is as per the Brugger et al. (2016) model with both CMF and WMF equal to zero, and is made up of silicate rock. Earth has a CMF of 0.32 and a WMF of 0.0005.

would decrease to smaller radii, so that Λ would increase to reach higher values, reducing atmospheric escape rates (Fossati et al. 2017).

To quantify this effect, we follow the approach from Aguichine et al. (2021) to estimate the total mass of H/He that TOI-733 b may have had in the past. The photoevaporation mass-loss rate from the atmosphere in the energy-limited regime is (Erkaev et al. 2007; Owen & Wu 2013):

$$\dot{M} = \epsilon \frac{\pi F_{\rm XUV} R_{\rm p}^3}{G M_{\rm p}}, \tag{4}$$

where $F_{\rm XUV}$ is the XUV flux received by the planet, G the gravitational constant, and ϵ is an efficiency parameter. We approximate the XUV luminosity by the analytical fit obtained by Sanz-Forcada et al. (2011), and we estimate $\epsilon \simeq 0.07$ from Owen & Jackson (2012). Since the XUV luminosity is a decreasing function of time, the mass-loss rate also decreases with time. This yields a mass-loss of 9.3×10^{-1} $M_\oplus$/Gyr during the saturation regime, and a present-day mass-loss rate of 2.1×10^{-3} $M_\oplus$/Gyr at the estimated age of 4.4 Gyr. Following the approach of Aguichine et al. (2021), we estimate the total mass of H/He lost by photoevaporation by integrating the mass-loss rate, assuming that $M_{\rm p}$, $R_{\rm p}$ and $T_{\rm eq}$ remained roughly constant, and that only the XUV flux decreased during the planet's evolution. In this case, we find that TOI-733 b could have lost ~ 0.12 $M_\oplus$ of H/He, i.e. $\sim$ 2% of its initial mass. This estimate is consistent with the computation made by Rogers et al. (2023), who predict that at $T_{\rm eq} = 800$ K planets with core masses $\lesssim 6$ $M_\oplus$ are entirely stripped of their envelopes, assuming the latter are made of pure H_2. This is expected to remain valid at higher equilibrium temperatures.

Despite the efficient hydrogen escape at early ages, recent studies show that a secondary atmosphere may be formed by outgassing volatile gases from the magma after the photoevaporation phase (Kite & Barnett 2020; Tian & Heng 2023). The present-day mass-loss rate by photoevaporation may be insufficient to remove the outgassed hydrogen due to the low XUV flux from the host star. Nevertheless, other mechanisms of thermal escape can be responsible for the preferential loss of hydrogen. The Jeans parameter of TOI-733 b is lower than that of Earth ($\Lambda_\oplus = 27.4$), which results in a hydrogen Jeans escape rate $\sim 10^3$ times greater for TOI-733 b than for Earth (see Catling & Kasting 2017, for the Jeans escape rate formula). It is therefore very likely that any outgassed hydrogen was removed by thermally-driven escape, leaving behind a secondary atmosphere made of heavier volatiles as on Earth.

This supports the hypothesis that TOI-733 b may have formed with an envelope that is a mixture of various volatile compounds, but only heavier species remained after the escape of H/He. In other words, the planet may have formed with H/He and water, but H/He was lost, and what is presently left behind is a mixture of the initial water reservoir together with any outgassed gases.

Furthermore, it is possible that TOI-733 b formed with more than 2% of H/He by mass. As seen in Figure 9, H/He envelopes are very inflated at such high temperatures, meaning that using the present-day radius underestimates the mass-loss rate.

A further possibility is that TOI-733 b directly formed as an ocean planet and did not experience atmospheric loss, since water has a much lower escape efficiency (Ito & Ikoma 2021).

In other words, the planet formed with an initial high WMF, and was able to retain it because water is more resistant to XUV photoevaporation than H/He.

In both cases, the loss of the entire H/He content from the atmosphere of TOI-733 b supports the presence of a secondary atmosphere that is possibly water-dominated. However, atmospheres of other heavy volatiles (Hu et al. 2015; Bolmont et al. 2017; Ito & Ikoma 2021) cannot be excluded.

5.3. Prospects for atmospheric characterisation

Based on our interior structure analysis, we can say that TOI-733 b most probably features a volatile envelope. The composition of this envelope is likely to be that of a secondary atmosphere, although the presence of a few tens of percent of H or He cannot be completely ruled out. Therefore, TOI-733 b is an interesting target for atmospheric characterisation observations to confirm that its atmosphere is dominated by H_2O, CO_2, CH_4 or other compounds present in a secondary atmosphere instead of H/He. These observations would enable us to break the degeneracy between envelope mass and composition typically found in sub-Neptunes. Unfortunately, the estimated TSM (transmission spectroscopy metric) and ESM (emission spectroscopy metric) of TOI-733 b are 46.29 and 4.4, respectively, which both place it below the threshold of the optimal targets for transmission and emission spectroscopy with the James Webb Space Telescope (JWST) (Kempton et al. 2018). However, an extended atmosphere signature could be significantly larger than the TSM would imply since the latter is based on the assumption of a bound atmosphere. It is thus worth mentioning, that it could be possible to search from ground for an Hα or He I signature, of any extended, escaping H/He atmosphere, or possibly even H from the photodissociated ocean world (e.g., Jensen et al. 2012; Cauley et al. 2017). For any attempts to observe this planet in the hope of learning more about its bound atmosphere, however, will have to be postponed until the next generation of telescopes.

6. Conclusions

In this paper we presented the discovery and characterisation of TOI-733 b. Our stellar and joint RV and transit modelling show that this planet is orbiting a G6 V star and is located well within the small planet radius valley when considering solar-type stars. We performed interior and atmospheric modelling to try and narrow down the possible structure and composition of this planet. We found that if TOI-733 b ever had a H/He atmosphere, it was mostly, if not completely, lost, leaving behind a secondary atmosphere of heavier elements. Our analysis also points to the possibility that the planet may have also formed as a water world and did not experience atmospheric mass loss.

Answering the question of whether TOI-733 b has a secondary atmosphere or is an ocean planet boils down to differentiating between a Neptune-like planet that lost its ∼10 % of H/He (as estimated by our atmospheric mass loss models) to leave behind a steam atmosphere of heavier volatiles, and one that formed and remained relatively the same throughout its evolution. While being beyond the scope of this paper, finding an answer to this question will have broad implications on our understanding of exoplanets.

The similarity between TOI-733 b and π Men c does not end at the radius – incident flux connection. Apart from receiving a similar amount of stellar irradiation, the two planets orbit stars of similar type and age. Models suggest that H_2O plays a significant role in the interior and possibly the envelope of both planets. Recent transmission spectroscopy observations point to an increasing probability of this actually being the case. Given the observability limitations of TOI-733 b, a more in depth comparison study between the two planets and their hosts could help determine to what extent, if at all, the conclusions derived for π Men c can be extended to TOI-733 b. If these two, and other planets with similar characteristics, become confirmed to indeed be water-dominated, this could point to there being a population of planets that belongs in the radius gap, and are not just "passing through". This, of course, does not diminish the importance of, or the need for, mechanisms which explain atmospheric loss, but it may mean that they, and the planets considered to be or to have been subjected to them at some point in their history, need to be rethought. Whatever the case of TOI-733 b, however, since both the core-powered mass loss (formation) and the XUV photoevaporation (evolution) mechanisms are able to physically explain the presence of the radius valley separating super-Earths from mini-Neptunes, well-characterised planets in this parameter space are essential to facilitate understanding of which of these mechanisms is dominant.

By all accounts TOI-733 b looks to be an interesting planet and holds the potential of being a small but key piece to solving big puzzles in exoplanet science. With ever increasing in-depth theoretical analyses and the promise of high-precision follow-up by present and upcoming facilities, we seem to be well on the way to finding answers to major questions relating to planet formation and evolution.

Acknowledgements. This paper includes data collected by the TESS mission. Funding for the TESS mission is provided by the NASA Explorer Program. We acknowledge the use of public TOI Release data from pipelines at the TESS Science Office and at the TESS Science Processing Operations Center. Resources supporting this work were provided by the NASA High-End Computing (HEC) Program through the NASA Advanced Supercomputing (NAS) Division at Ames Research Center for the production of the SPOC data products. This research has made use of the Exoplanet Follow-up Observation Program website, which is operated by the California Institute of Technology, under contract with the National Aeronautics and Space Administration under the Exoplanet Exploration Program. This work has made use of data from the European Space Agency (ESA) mission *Gaia* (`https://www.cosmos.esa.int/gaia`), processed by the *Gaia* Data Processing and Analysis Consortium (DPAC, `https://www.cosmos.esa.int/web/gaia/dpac/consortium`). Funding for the DPAC has been provided by national institutions, in particular the institutions participating in the *Gaia* Multilateral Agreement. This work was supported by the KESPRINT collaboration, an international consortium devoted to the characterization and research of exoplanets discovered with space-based missions (`http://www.kesprint.science`). Data availability: The data underlying this article are available in machine-readable format at the CDS, as well as ExoFOP-TESS[15]. I.Y.G., C.M.P., J.K, and M.F. gratefully acknowledge the support of the Swedish National Space Agency (DNR 174/18, 65/19, 2020-00104, 177/19). K.W.F.L. was supported by Deutsche Forschungsgemeinschaft grants RA714/14-1 within the DFG Schwerpunkt SPP 1992, Exploring the Diversity of Extrasolar Planets. This material is based upon work supported by NASA'S Interdisciplinary Consortia for Astrobiology Research (NNH19ZDA001N-ICAR) under award number 19-ICAR19_2-0041. K.A.C. acknowledges support from the TESS mission via subaward s3449 from MIT. This work makes use of observations from the LCOGT network. Part of the LCOGT telescope time was granted by NOIRLab through the Mid-Scale Innovations Program (MSIP). MSIP is funded by NSF. Some of the observations in this paper made use of the High-Resolution Imaging instrument Zorro and were obtained under Gemini LLP Proposal Number: GN/S-2021A-LP-105. Zorro was funded by the NASA Exoplanet Exploration Program and built at the NASA Ames Research Center by Steve B. Howell, Nic Scott, Elliott P. Horch, and Emmett Quigley. Zorro was mounted on the Gemini South telescope of the international Gemini Observatory, a program of NSF's OIR Lab, which is managed by the Association of Universities for Research in Astronomy (AURA) under a cooperative agreement with the National Science Foundation. on behalf of the Gemini partnership: the National Science Foundation (United States), National Research Council (Canada), Agencia Nacional de Investigación y Desarrollo (Chile), Ministerio de Ciencia, Tecnología e Innovación (Argentina), Ministério da Ciência, Tecnologia, Inovações e Comunicações (Brazil), and Korea Astronomy and Space Science Institute (Republic of

[15] `https://exofop.ipac.caltech.edu/tess`

Korea).
R.L. acknowledges funding from University of La Laguna through the Margarita Salas Fellowship from the Spanish Ministry of Universities ref. UNI/551/2021-May 26, and under the EU Next Generation funds. HD acknowledges support from the Spanish Research Agency of the Ministry of Science and Innovation (AEI-MICINN) under the grant with reference PID2019-107061GB-C66, DOI: 10.13039/501100011033. This paper includes data collected by the TESS mission. Funding for the TESS mission is provided by the NASA Explorer Program. We acknowledge the use of public TOI Release data from pipelines at the TESS Science Office and at the TESS Science Processing Operations Center. Resources supporting this work were provided by the NASA High-End Computing (HEC) Program through the NASA Advanced Supercomputing (NAS) Division at Ames Research Center for the production of the SPOC data products. This research has made use of the Exoplanet Follow-up Observation Program (ExoFOP; DOI: 10.26134/ExoFOP5) website, which is operated by the California Institute of Technology, under contract with the National Aeronautics and Space Administration under the Exoplanet Exploration Program.
This work has made use of data from the European Space Agency (ESA) mission *Gaia* (`https://www.cosmos.esa.int/gaia`), processed by the *Gaia* Data Processing and Analysis Consortium (DPAC, `https://www.cosmos.esa.int/web/gaia/dpac/consortium`). Funding for the DPAC has been provided by national institutions, in particular the institutions participating in the *Gaia* Multilateral Agreement.
This research has made use of the NASA Exoplanet Archive, which is operated by the California Institute of Technology, under contract with the National Aeronautics and Space Administration under the Exoplanet Exploration Program.

References

Acuña, L., Deleuil, Magali, Mousis, Olivier, et al. 2021, A&A, 647, A53
Acuña, L. in prep.a
Acuña, L. in prep.b
Aguichine, A., Mousis, O., Deleuil, M., & Marcq, E. 2021, ApJ, 914, 84
Allard, F., Homeier, D., & Freytag, B. 2012, Philosophical Transactions of the Royal Society of London Series A, 370, 2765
Ambikasaran, S., Foreman-Mackey, D., Greengard, L., Hogg, D. W., & O'Neil, M. 2016, IEEE Transactions on Pattern Analysis and Machine Intelligence, 38, 252
Anglada-Escudé, G. & Butler, R. P. 2012, ApJS, 200, 15
Baglin, A., Auvergne, M., Boisnard, L., et al. 2006, in 36th COSPAR Scientific Assembly, Vol. 36, 3749
Barragán, O., Aigrain, S., Gillen, E., & Gutiérrez-Canales, F. 2021, Research Notes of the American Astronomical Society, 5, 51
Barragán, O., Aigrain, S., Rajpaul, V. M., & Zicher, N. 2022a, MNRAS, 509, 866
Barragán, O., Armstrong, D. J., Gandolfi, D., et al. 2022b, MNRAS, 514, 1606
Barragán, O., Gandolfi, D., & Antoniciello, G. 2019, MNRAS, 482, 1017
Bolmont, E., Selsis, F., Owen, J. E., et al. 2017, MNRAS, 464, 3728
Borucki, W. J., Koch, D., Basri, G., et al. 2010, Science, 327, 977
Brown, T. M., Baliber, N., Bianco, F. B., et al. 2013, Publications of the Astronomical Society of the Pacific, 125, 1031
Brugger, B., Mousis, O., Deleuil, M., & Deschamps, F. 2017, The Astrophysical Journal, 850, 93
Brugger, B., Mousis, O., Deleuil, M., & Lunine, J. I. 2016, The Astrophysical Journal, 831, L16
Bruntt, H., De Cat, P., & Aerts, C. 2008, A&A, 478, 487
Castelli, F. & Kurucz, R. L. 2004, astro-ph/0405087 [`astro-ph/0405087`]
Catling, D. C. & Kasting, J. F. 2017, Atmospheric Evolution on Inhabited and Lifeless Worlds
Cauley, P. W., Redfield, S., & Jensen, A. G. 2017, AJ, 153, 217
Cherubim, C., Cloutier, R., Charbonneau, D., et al. 2023, The Astronomical Journal, 165, 167
Choi, J., Dotter, A., Conroy, C., et al. 2016, ApJ, 823, 102
Ciardi, D. R., Beichman, C. A., Horch, E. P., & Howell, S. B. 2015, ApJ, 805, 16
Collins, K. 2019, in American Astronomical Society Meeting Abstracts, Vol. 233, American Astronomical Society Meeting Abstracts #233, 140.05
Collins, K. A., Kielkopf, J. F., Stassun, K. G., & Hessman, F. V. 2017, AJ, 153, 77
Cubillos, P., Erkaev, N. V., Juvan, I., et al. 2017, MNRAS, 466, 1868
da Silva, L., Girardi, L., Pasquini, L., et al. 2006, A&A, 458, 609
Damasso, M., Sozzetti, A., Lovis, C., et al. 2020, A&A, 642, A31
Diamond-Lowe, H., Kreidberg, L., Harman, C. E., et al. 2022, AJ, 164, 172
Director, H. M., Gattiker, J., Lawrence, E., & Wiel, S. V. 2017, Journal of Statistical Computation and Simulation, 87, 3521
Doyle, A. P., Davies, G. R., Smalley, B., Chaplin, W. J., & Elsworth, Y. 2014, MNRAS, 444, 3592
Erkaev, N. V., Kulikov, Y. N., Lammer, H., et al. 2007, A&A, 472, 329
Foreman-Mackey, D., Hoyer, S., Bernhard, J., & Angus, R. 2014, george: George (v0.2.0)
Fossati, L., Erkaev, N. V., Lammer, H., et al. 2017, A&A, 598, A90
Fulton, B. J., Petigura, E. A., Howard, A. W., et al. 2017, AJ, 154, 109
Gandolfi, D., Barragán, O., Livingston, J. H., et al. 2018, A&A, 619, L10
García Muñoz, A., Fossati, L., Youngblood, A., et al. 2021, ApJ, 907, L36
García Muñoz, A., Youngblood, A., Fossati, L., et al. 2020, ApJ, 888, L21
Georgieva, I. Y., Persson, C. M., Barragán, O., et al. 2021, MNRAS, 505, 4684
Ginzburg, S., Schlichting, H. E., & Sari, R. 2018, MNRAS, 476, 759
Gray, D. F. 2005, The Observation and Analysis of Stellar Photospheres
Gregory, P. C. 2005, ApJ, 631, 1198
Grimm, S. L., Demory, B.-O., Gillon, M., et al. 2018, A&A, 613, A68
Guerrero, N. M., Seager, S., Huang, C. X., et al. 2021, ApJS, 254, 39
Gupta, A. & Schlichting, H. E. 2019, MNRAS, 487, 24
Hatzes, A. P. 2019, The Doppler Method for the Detection of Exoplanets
Hatzes, A. P., Gandolfi, D., Korth, J., et al. 2022, AJ, 163, 223
Howell, S. B., Everett, M. E., Sherry, W., Horch, E., & Ciardi, D. R. 2011, AJ, 142, 19
Howell, S. B., Matson, R. A., Ciardi, D. R., et al. 2021, AJ, 161, 164
Howell, S. B., Sobeck, C., Haas, M., et al. 2014, PASP, 126, 398
Hu, R., Seager, S., & Yung, Y. L. 2015, ApJ, 807, 8
Huang, C. X., Burt, J., Vanderburg, A., et al. 2018, ApJ, 868, L39
Husser, T. O., Wende-von Berg, S., Dreizler, S., et al. 2013, A&A, 553, A6
Ito, Y. & Ikoma, M. 2021, MNRAS, 502, 750
Jenkins, J. M. 2002, ApJ, 575, 493
Jenkins, J. M., Chandrasekaran, H., McCauliff, S. D., et al. 2010, in Society of Photo-Optical Instrumentation Engineers (SPIE) Conference Series, Vol. 7740, Software and Cyberinfrastructure for Astronomy, ed. N. M. Radziwill & A. Bridger, 77400D
Jenkins, J. M., Tenenbaum, P., Seader, S., et al. 2020, Kepler Data Processing Handbook: Transiting Planet Search, Kepler Science Document KSCI-19081-003, id. 9. Edited by Jon M. Jenkins.
Jenkins, J. M., Twicken, J. D., McCauliff, S., et al. 2016, in Society of Photo-Optical Instrumentation Engineers (SPIE) Conference Series, Vol. 9913, Proc. SPIE, 99133E
Jensen, A. G., Redfield, S., Endl, M., et al. 2012, ApJ, 751, 86
Kempton, E. M. R., Bean, J. L., Louie, D. R., et al. 2018, PASP, 130, 114401
Kipping, D. M. 2013, MNRAS, 435, 2152
Kite, E. S. & Barnett, M. N. 2020, Proceedings of the National Academy of Science, 117, 18264
Krissansen-Totton, J. & Fortney, J. J. 2022, The Astrophysical Journal, 933, 115
Kubyshkina, D. & Fossati, L. 2022, A&A, 668, A178
Kuerster, M., Schmitt, J. H. M. M., Cutispoto, G., & Dennerl, K. 1997, A&A, 320, 831
Kurucz, R. L. 1993, VizieR Online Data Catalog, VI/39
Kurucz, R. L. 2013, ATLAS12: Opacity sampling model atmosphere program, Astrophysics Source Code Library
Lester, K. V., Matson, R. A., Howell, S. B., et al. 2021, AJ, 162, 75
Li, J., Tenenbaum, P., Twicken, J. D., et al. 2019, PASP, 131, 024506
Lopez, E. D. & Fortney, J. J. 2013, ApJ, 776, 2
Lopez, E. D. & Fortney, J. J. 2014, ApJ, 792, 1
Lovis, C. & Pepe, F. 2007, A&A, 468, 1115
Luque, R. & Pallé, E. 2022, Science, 377, 1211
Madhusudhan, N., Piette, A. A. A., & Constantinou, S. 2021, ApJ, 918, 1
Malsky, I., Rogers, L., Kempton, E. M. R., & Marounina, N. 2022, Nature Astronomy
Mandel, K. & Agol, E. 2002, ApJ, 580, L171
Mayor, M., Pepe, F., Queloz, D., et al. 2003, The Messenger, 114, 20
McCully, C., Volgenau, N. H., Harbeck, D.-R., et al. 2018, in Society of Photo-Optical Instrumentation Engineers (SPIE) Conference Series, Vol. 10707, Proc. SPIE, 107070K
Morris, R. L., Twicken, J. D., Smith, J. C., et al. 2020, Kepler Data Processing Handbook: Photometric Analysis, Kepler Science Document KSCI-19081-003, id. 6. Edited by Jon M. Jenkins.
Mousis, O., Deleuil, M., Aguichine, A., et al. 2020, The Astrophysical Journal, 896, L22
Owen, J. E. & Jackson, A. P. 2012, MNRAS, 425, 2931
Owen, J. E. & Wu, Y. 2013, ApJ, 775, 105
Owen, J. E. & Wu, Y. 2016, ApJ, 817, 107
Parviainen, H. 2015, MNRAS, 450, 3233
Persson, C. M., Fridlund, M., Barragán, O., et al. 2018, A&A, 618, A33
Persson, C. M., Georgieva, I. Y., Gandolfi, D., et al. 2022, A&A, 666, A184
Petigura, E. A., Rogers, J. G., Isaacson, H., et al. 2022, AJ, 163, 179
Piaulet, C., Benneke, B., Almenara, J. M., et al. 2023, Nature Astronomy, 7, 206
Piskunov, N. & Valenti, J. A. 2017, A&A, 597, A16
Plotnykov, M. & Valencia, D. 2020, MNRAS, 499, 932
Rajpaul, V., Aigrain, S., Osborne, M. A., Reece, S., & Roberts, S. 2015, MNRAS, 452, 2269
Ricker, G. R., Winn, J. N., Vanderspek, R., et al. 2015, Journal of Astronomical Telescopes, Instruments, and Systems, 1, 014003

Rogers, J. G., Gupta, A., Owen, J. E., & Schlichting, H. E. 2021, MNRAS, 508, 5886
Rogers, J. G., Schlichting, H. E., & Owen, J. E. 2023, arXiv e-prints, arXiv:2301.04321
Ryabchikova, T., Piskunov, N., Kurucz, R. L., et al. 2015, Phys. Scr, 90, 054005
Sanz-Forcada, J., Micela, G., Ribas, I., et al. 2011, A&A, 532, A6
Schlegel, D. J., Finkbeiner, D. P., & Davis, M. 1998, ApJ, 500, 525
Scott, N. J., Howell, S. B., Gnilka, C. L., et al. 2021, Frontiers in Astronomy and Space Sciences, 8, 138
Smith, J. C., Stumpe, M. C., Van Cleve, J. E., et al. 2012, PASP, 124, 1000
Sotin, C., Grasset, O., & Mocquet, A. 2007, Icarus, 191, 337
Stumpe, M. C., Smith, J. C., Catanzarite, J. H., et al. 2014, PASP, 126, 100
Stumpe, M. C., Smith, J. C., Van Cleve, J. E., et al. 2012, PASP, 124, 985
Tian, M. & Heng, K. 2023, arXiv e-prints, arXiv:2301.10217
Twicken, J. D., Catanzarite, J. H., Clarke, B. D., et al. 2018, PASP, 130, 064502
Twicken, J. D., Clarke, B. D., Bryson, S. T., et al. 2010, in Society of Photo-Optical Instrumentation Engineers (SPIE) Conference Series, Vol. 7740, Software and Cyberinfrastructure for Astronomy, ed. N. M. Radziwill & A. Bridger, 774023
Valencia, D., Sasselov, D. D., & O'Connell, R. J. 2007, ApJ, 665, 1413
Valenti, J. A. & Piskunov, N. 1996, A&AS, 118, 595
Van Eylen, V., Agentoft, C., Lundkvist, M. S., et al. 2018, MNRAS, 479, 4786
Vines, J. I. & Jenkins, J. S. 2022, MNRAS, 513, 2719
Wildi, F., Pepe, F., Chazelas, B., Lo Curto, G., & Lovis, C. 2010, in Society of Photo-Optical Instrumentation Engineers (SPIE) Conference Series, Vol. 7735, Ground-based and Airborne Instrumentation for Astronomy III, ed. I. S. McLean, S. K. Ramsay, & H. Takami, 77354X
Wildi, F., Pepe, F., Chazelas, B., Lo Curto, G., & Lovis, C. 2011, in Society of Photo-Optical Instrumentation Engineers (SPIE) Conference Series, Vol. 8151, Techniques and Instrumentation for Detection of Exoplanets V, ed. S. Shaklan, 81511F
Winn, J. N. 2010, Exoplanet Transits and Occultations, ed. S. Seager (University of Arizona Press), 55–77
Yee, S. W., Petigura, E. A., & von Braun, K. 2017, ApJ, 836, 77
Zechmeister, M. & Kürster, M. 2009, A&A, 496, 577
Zechmeister, M., Reiners, A., Amado, P. J., et al. 2018, A&A, 609, A12
Zeng, L., Jacobsen, S. B., Hyung, E., et al. 2021, ApJ, 923, 247
Zeng, L., Jacobsen, S. B., Sasselov, D. D., et al. 2019, Proceedings of the National Academy of Science, 116, 9723
Zeng, L., Sasselov, D. D., & Jacobsen, S. B. 2016, ApJ, 819, 127

[1] Department of Space, Earth and Environment, Chalmers University of Technology, Onsala Space Observatory, SE-439 92 Onsala, Sweden. e-mail: iskra.georgieva@chalmers.se
[2] Dipartimento di Fisica, Universita degli Studi di Torino, via Pietro Giuria 1, I-10125, Torino, Italy
[3] Thüringer Landessternwarte Tautenburg, Sternwarte 5, 07778 Tautenburg, Germany
[4] Aix Marseille Université, Institut Origines, CNRS, CNES, LAM, Marseille, France
[5] Max-Planck-Institut für Astronomie, Königstuhl 17, D-69117 Heidelberg, Germany
[6] Department of Astronomy & Astrophysics, University of California, Santa Cruz, CA 95064, USA
[7] Institute of Planetary Research, German Aerospace Center (DLR), Rutherfordstrasse 2, D-12489 Berlin, Germany
[8] Center for Astrophysics | Harvard & Smithsonian, 60 Garden Street, Cambridge, MA 02138, USA
[9] NASA Ames Research Center, Moffett Field, CA 94035, USA
[10] Division of Geological and Planetary Sciences, 1200 E California Blvd, Pasadena, CA, 91125, USA
[11] Department of Astronomy, California Institute of Technology, Pasadena, CA 91125, USA
[12] NASA Sagan Fellow
[13] Leiden Observatory, University of Leiden, PO Box 9513, 2300 RA, Leiden, The Netherlands
[14] Lund Observatory, Division of Astrophysics, Department of Physics, Lund University, Box 43, SE-221 00 Lund, Sweden
[15] Department of Space, Earth and Environment, Chalmers University of Technology, Chalmersplatsen 4, 412 96 Gothenburg, Sweden
[16] Sub-department of Astrophysics, Department of Physics, University of Oxford, Oxford, OX1 3RH, UK
[17] McDonald Observatory and Center for Planetary Systems Habitability, The University of Texas, Austin Texas USA
[18] Instituto de Astrofísica de Canarias, C. Via Lactea S/N, E-38205 La Laguna, Tenerife, Spain
[19] Universidad de La Laguna, Dept. de Astrofísica, E-38206 La Laguna, Tenerife, Spain
[20] Astrobiology Center, 2-21-1 Osawa, Mitaka, Tokyo 181-8588, Japan
[21] Department of Astronomical Science, The Graduate University for Advanced Studies (SOKENDAI), 2-21-1 Osawa, Mitaka, Tokyo, Japan
[22] National Astronomical Observatory of Japan, 2-21-1 Osawa, Mitaka, Tokyo 181-8588, Japan
[23] Department of Astronomy & Astrophysics, University of Chicago, Chicago, IL 60637, USA
[24] Mullard Space Science Laboratory, University College London, Holmbury St Mary, Dorking, Surrey RH5 6NT, UK
[25] Astronomy Department and Van Vleck Observatory, Wesleyan University, Middletown, CT 06459, USA
[26] SETI Institute, Mountain View, CA 94043, USA.
[27] Department of Astrophysical Sciences, Princeton University, Princeton, NJ 08544, USA
[28] George Mason University, 4400 University Drive, Fairfax, VA, 22030 USA.
[29] Space Telescope Science Institute, 3700 San Martin Drive, Baltimore, MD, 21218, USA
[30] NASA Exoplanet Science Institute, Caltech/IPAC, Mail Code 100-22, 1200 E. California Blvd., Pasadena, CA 91125, USA
[31] MIT Kavli Institute for Astrophysics and Space Research & MIT Physics Department
[32] Royal Astronomical Society, Burlington House, Piccadilly, London W1J 0BQ, UK
[33] Department of Earth, Atmospheric, and Planetary Sciences, Massachusetts Institute of Technology, Cambridge, MA 02139, USA
[34] Department of Physics and Kavli Institute for Astrophysics and Space Research, Massachusetts Institute of Technology, Cambridge, MA 02139, USA
[35] Department of Aeronautics and Astronautics, Massachusetts Institute of Technology, Cambridge, MA 02139, USA
[36] Perth Exoplanet Survey Telescope, Perth, Western Australia
[37] Department of Astronomy, The University of Wisconsin–Madison, Madison, WI 53706, USA
[38] Department of Astronomy, The University of Texas at Austin, Austin, TX 78712, USA

Appendix A: HARPS data

Appendix B: Frequency analysis of the FWHM residuals

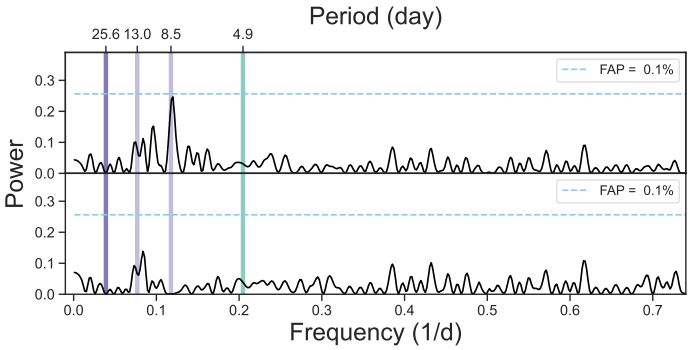

Fig. B.1. GLS periodogram of the FWHM residuals after subtracting the 25.6-day signal (Fig.3, panel d)

is shown in the top panel. The 8.5-day signal seen in the RV panels of Fig.3 becomes significant. The bottom panel shows the FWHM after subtracting both the 25.6-, and the 8.5-day signals. Here, the 12.8-day signal remains, but is not significant.

PAPER C

On the RV detection of low-mass transiting planets with multi-dimensional Gaussian processes

Iskra Y. Georgieva, Oscar Barragán, Carina M. Persson

To be submitted

Astronomy & Astrophysics manuscript no. output
May 22, 2023

On the RV detection of low-mass transiting planets with multidimensional Gaussian processes

Iskra Y. Georgieva[1]⋆ Oscar Barragán[2], Carina M. Persson[1]

[1] Department of Space, Earth and Environment, Chalmers University of Technology, Onsala Space Observatory, SE-439 92 Onsala, Sweden
[2] Sub-department of Astrophysics, Department of Physics, University of Oxford, Oxford, OX1 3RH, UK

Received Date Month YYYY; accepted Date Month YYYY

ABSTRACT

Context. The Keplerian signatures of low-mass planets in radial velocity data are often challenging, and sometimes impossible, to uncover. The three main culprits to this problem are instrument precision, stellar behaviour, and data sampling.
Aims. In this paper we aim to demonstrate the make-or-break effect of data availability, and the resulting often-detrimental effects on low-mass planet detection. We focus particularly on the cases of stars, whose activity behaviour can be described as stochastic.
Methods. We employ multi-dimensional Gaussian process regression on synthetic radial velocity data – one of the more advanced methods for modelling of such timeseries – particularly suited for stars exhibiting a complex activity pattern. With this approach, we test the detectability of single planets orbiting such stars by exploring different sampling scenarios, as well as the ability to recover certain GP hyperparameters, and their effects on one another.
Results. We find that the GP hyperparameter λ_p – the inverse of the harmonic complexity – has the highest impact on the detectability of the injected planets and the ability of the model to explain the data. We also note a correlation between the lowest value of λ_p and a tendency toward overfitting. This is particularly exacerbated in the cases when the GP period is the shortest. On the other hand, the most active stellar configuration tested here precludes even the highest semi-amplitude planets to be detected with 40 points.
Conclusions. In this paper we demonstrate the detrimental effect that stellar activity has on detecting small planets, particularly in the cases of insufficient data. Our simulations show that behaviour observed to be characteristic of young stars (fast rotators, stochastically behaving magnetic activity) pose a significant challenge to planet detection of any kind.

Key words. dfsfs-sssd

1. Introduction

The vast majority of the ~5300 extrasolar planets confirmed to date have been discovered using indirect observational methods. Accounting for about 19% of the discovered exoplanets, the radial velocity (RV) method is one such example. While second to the transit method in terms of exoplanet yield, the potential of the RV method was demonstrated much earlier.

Prior to the famous discovery of 51 Peg b (Mayor & Queloz 1995), several other claims of planets orbiting their stars were made (Campbell et al. 1988; Latham et al. 1989; Hatzes & Cochran 1993) and later confirmed (Hatzes et al. 2003; Cochran et al. 1991; Hatzes et al. 2006), all of which using the RV method. Given the nature of RV and the sensitivity of the instruments at the time (m s^{-1} vs the current state-of-the-art cm s^{-1}), these detections, as well as the RV-confirmed planets of the following decade or so, were understandably all of massive planets. Sparse, ad-hoc and opportunistic observational campaigns were sufficient for these types of planets. By the early 2000s, however, the tendency toward lower mass detections was becoming apparent (e.g. Vogt et al. 2000; Rivera et al. 2005), and with it – the need for high-precision, high-cadence data was pressing.

In the era of hunting for smaller and less massive planets, this need naturally impedes their detection in RV timeseries – a fact further exacerbated by exoplanet-oriented RV surveys' greatest nemesis: stellar activity (Queloz et al. 2001; Dumusque et al. 2017). Magnetically driven stellar surface formations (star spots, faculae, plages) form as a result of different processes and operate on different timescales, causing stellar activity to exhibit a high degree of variability. In some cases the activity is more than capable of concealing the presence of lower mass planets around active stars (e.g. Barragán et al. 2019, 2022b; Fridlund et al. 2023), sometimes meaning that the star-induced signal can exceed the planetary one multiple times.

Since accounting for the stellar activity part of the signal has been plaguing exoplanet astronomers for decades, a number of techniques have been developed in an effort to alleviate this situation. These range from filtering out the activity-induced signal via sinusoid fitting (Hatzes et al. 2010; Hatzes 2013) to, most recently, identifying and removing signatures of stellar activity from the timeseries data during the RV extraction process (e.g. Collier Cameron et al. 2021; de Beurs et al. 2022; Simola et al. 2019, 2022). While often sufficient, the former may bare the risk of oversimplifying the stellar behaviour and introducing spurious signals in the data, thus creating scenarios in which erroneous detections can be made (see e.g., Rajpaul et al. 2016).

However, the unpredictability of the formation and evolution of stellar surface features has given rise to another possibility to account for nuisance signals of stellar origin. In recent years, modelling the spectroscopic data using Gaussian process (GP) regression has gained traction. Laid out by Roberts et al. (2012)

⋆ iskra.georgieva@chalmers.se

and demonstrated in the context of RVs and stellar activity by Haywood et al. (2014), the growing popularity of GPs is unsurprising given their ability to describe signals of stochastic nature. This ability makes them highly flexible, which is their main attraction. In the absence of sufficient information to guide the GP, however, this ability should be considered with caution as existing planets could be absorbed by the GP.

The idea behind GP regression is that data can be assumed to be random samples of a finite multivariate normal distribution with a given covariance matrix and a mean vector. Both the covariance matrix and the mean vector come from functions defined on the continuous space evaluated at the times of our observations. In RV analyses, the mean vector is created via a mean function (typically a Keplerian one), while the covariance matrix is generated by a parametric entity called a kernel that depends on some parameters (called hyperparameters) and the correlation between the points. By constraining the values of the mean and kernel function parameters we can then predict the underlying function that can explain our data containing planet and stellar signals (see e.g. Aigrain & Foreman-Mackey 2022, for more details). Then, our ability to recover said signals depends on how our finite data can constrain the parameters that describe continuous functions. This implies that the signals that we want to recover via GP regression are sensitive to the cadence of our data being, or not, tailored to the timescales that we want to characterise.

It is this approach that we employ in this work, but we curb the aforementioned flexibility by using a multidimensional GP (multi-GP) approach, as described by Rajpaul et al. (2015) and as implemented in the code `pyaneti` (Barragán et al. 2019; Barragán et al. 2022a). This technique uses the information provided by activity indicators to help constrain the stellar signal, and has now been used multiple times to successfully extract planetary Doppler signals from otherwise overly temperamental stars (e.g. Carleo et al. 2020; Georgieva et al. 2021, 2023; Barragán et al. 2022b).

We explore the detectability of small planetary signals in spectroscopic timeseries when the signal ephemerides are known, as well as the recovery of the GP hyperparameters for different value ranges, and we speculate on the interpretation of our findings.

2. Qualitative analysis of the Quasi-Periodic kernel

Stars often generate quasi-periodic signals in time-series data, including RVs, due to their inherent rotation. Therefore, a quasi-periodic (QP) kernel is usually chosen when performing GP regression on stellar data. Following the formulation of Roberts et al. (2012), the QP kernel is defined as

$$K(t_i, t_j) = A^2 \exp\left[-\frac{\sin^2[\pi(t_i - t_j)/P_{\rm GP}]}{2\lambda_{\rm p}^2} - \frac{(t_i - t_j)^2}{2\lambda_{\rm e}^2}\right], \quad (1)$$

where A is an amplitude term, $P_{\rm GP}$ is the covariance period, $\lambda_{\rm p}$ is the inverse of the harmonic complexity of the rotation, and $\lambda_{\rm e}$ is the long-term evolution timescale. In time-series of active stars, $P_{\rm GP}$ is to be interpreted as the star's rotation period; $\lambda_{\rm e}$ as the timescale most closely related to the time it takes for active regions to evolve and decay; and $\lambda_{\rm p}$ as a parametrisation of the complexity pattern of active regions on the stellar surface. We note that there are different flavours of QP kernels, but they all constrain the same time-scales, just with different parametrisations (see e.g., Nicholson & Aigrain 2022).

It is thus intuitive, that in GP regressions applied to stellar signals the recovered parameters are the ones from the QP kernel. We therefore perform an analysis of the dependence of the QP correlation matrix on the QP hyper-parameters to understand possible correlations between parameters, as well as to explore the time-scales that the parameters constrain. Figure 1 shows three-dimensional plots of the covariance matrix of the QP kernel as a function of $(t_i - t_j)/P_{\rm GP}$ and $\lambda_{\rm p}$ assuming a QP amplitude of 1. We show different plots given by different values of $\lambda_{\rm e}/P_{\rm GP}$ to show how $\lambda_{\rm e}$ affects the periodic part of the QP kernel. Note that we removed the dependence on the period by normalising all temporal quantities by $P_{\rm GP}$. This allows us to perform an analysis based on $\lambda_{\rm p}$ and $\lambda_{\rm e}$ only.

The first thing we can infer from Figure 1 is that if $\lambda_{\rm e}/P_{\rm GP}$ is smaller than 1 (top left panel), then the covariance dependence on the periodicity is weak. Therefore, modelling results and interpretations should be approached cautiously with GP regression using a QP kernel in the case in which $\lambda_{\rm e}/P_{\rm GP} < 1$. We note that this behaviour has been discussed previously by Rajpaul et al. (2015).

A characteristic behaviour in all panes of Figure 1 is that the covariance changes drastically for small values of $\lambda_{\rm p}$. The covariance is relatively strong for points that are separated by integers of $P_{\rm GP}$, and it can drop drastically otherwise. This implies that for low values of $\lambda_{\rm p}$, the points within a period are not well correlated amongst themselves. This suggests that in order to characterise the covariance matrix of a QP kernel with small $\lambda_{\rm p}$ it is necessary to cover the whole phase of the signal intensively over several periods.

On the other extreme of $\lambda_{\rm p}$ values, we can see that there is a plateau towards the maximum value of the covariance. In this case the correlation of points within a cycle depends more on the value of $\lambda_{\rm e}$ than on the value of $\lambda_{\rm p}$ or $P_{\rm GP}$. This suggests that there may be an ambiguity for large values of $\lambda_{\rm p}$ because they would all produce similar values of covariance. This also implies that signals which can be described with a QP with large values of $\lambda_{\rm e}$ may be easier to characterise (where the periodic signal behaves more as a sinusoidal).

The last qualitative analysis that we do based on Figure 1 is shown in the bottom two panels. They both show the same covariance with the exact same QP hyperparameters, but the time range in which we analyse the covariance is different. The bottom left panel shows how if the time range in which we analyse the covariance of the QP kernel is significantly shorter than $\lambda_{\rm e}/P_{\rm GP}$ we cannot see the effects of $\lambda_{\rm e}$ on our covariance, and in this case the covariance behaves more as a periodic kernel than a QP kernel. In contrast, in the bottom right panel we can see how the effects of $\lambda_{\rm e}$ are present and therefore the QP nature of the correlation manifests. This suggests that the determination of $\lambda_{\rm e}$ from data would not be possible if the observations range is shorter than the intrinsic $\lambda_{\rm e}$ value.

This qualitative analysis of the QP kernel will help to interpret the results from our simulations by allowing us to isolate the characteristics of the correlations that are intrinsic to the QP kernel. In real life, we have a more complicated problem, in which we do not know the values of the parameters creating the underlying covariance function. An additional problem lies in the degradation of the sampling because our data can be interpreted as a convolution of the covariance function with the times of sampling.

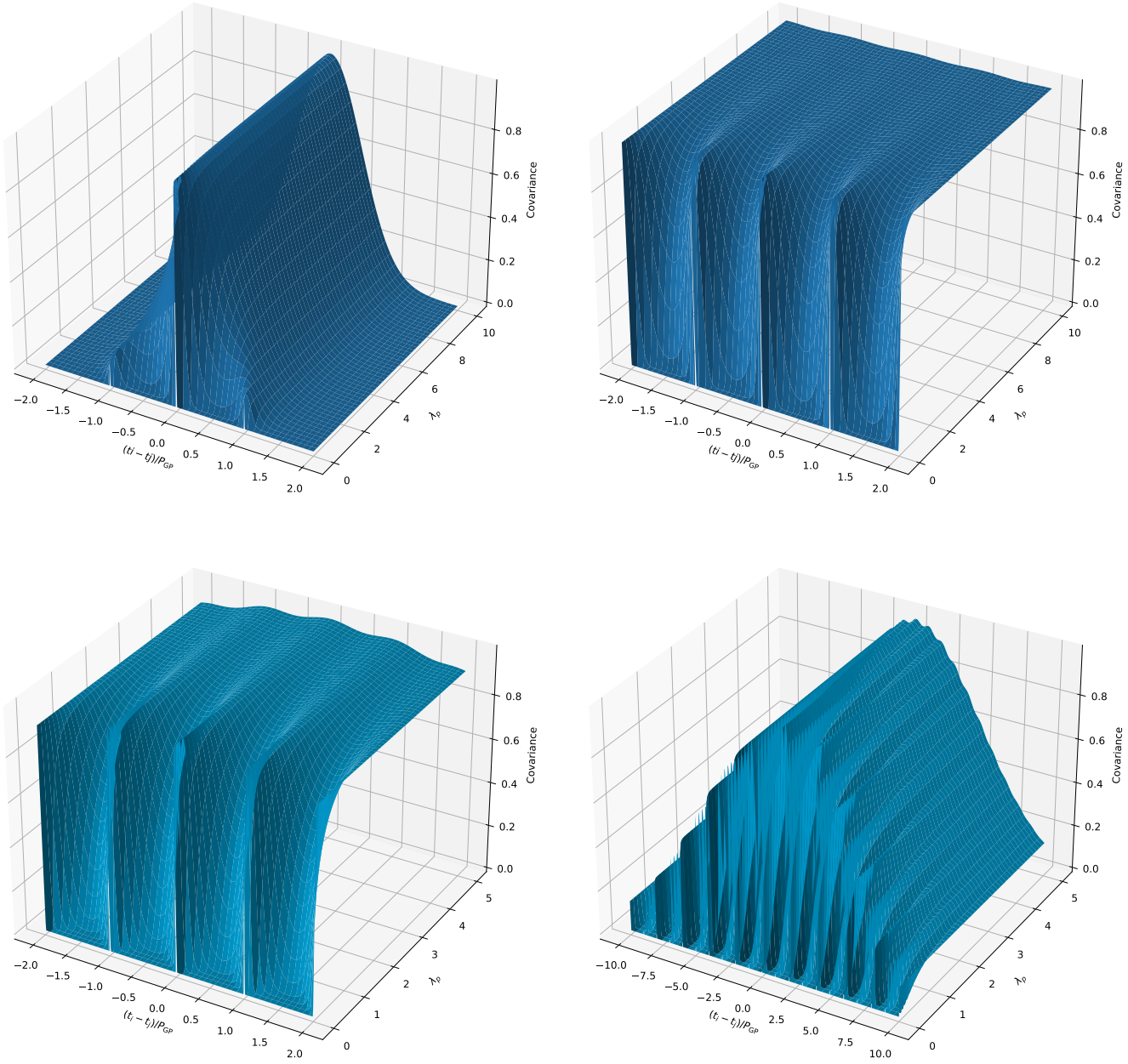

Fig. 1. Covariance of the Quasi-periodic kernel as function of $(t_i - t_j)/P_{GP}$ and λ_p for λ_e/P_{GP} values of 0.5 (top left), 50 (top right), and 5 (two bottom panels). Note that the two bottom panels show the covariance for the same set of parameters, but with a different range on the x-axis ($[t_i - t_j]/P_{GP}$).

3. Simulations

A common approach in the exoplanet community to characterising transiting exoplanets is to first find the transiting planets using ground or space-based surveys. This allows to obtain an orbit ephemeris and to have a prior on the phase and scales of the planet orbits. The next step is to perform RV follow-up during an observational season that is constrained by telescope facilities and target observability. These seasons typically last for a few months. This approach has yielded hundreds of well-characterised exoplanets that populate the mass-radius diagram.

In this work we will assume that we have one transiting planet with well-constrained orbital ephemeris, and that we want to detect said planet in a RV time-series of an active star observed during one follow-up season contained within 120 days. As previously mentioned, the common approach when modelling stellar signals with GPs assumes that our data can be described by a multi-variate Gaussian distribution. Under this assumption, we proceed to create synthetic spectroscopic-like time-series using random samples of a GP using `citlalatonac` (Barragán et al. 2022a).

We pick three different values for the hyperparameters of the QP kernel, i.e. λ_p, λ_e and P_{GP} and generate data of all possible combinations between those (27 in total). For each of these we inject one planet assuming a circular orbit, testing three different semi-amplitudes – 3 m s^{-1}, 10 m s^{-1} and 30 m s^{-1}, and placing each at 4 different orbital periods. This results in 12 different

Table 1. Values of injected planetary signals and hyperparameters.

P_{orb} (days)	K (m s^{-1})	P_{GP} (days)	λ_p	λ_e (days)
1.5	3	2.5	0.3	20
8.7	10	11.3	1.0	60
15.1	30	27.6	5.0	180
29.2	...	...	...	...

planet combinations, the detectability of each of which is tested against each of the 27 simulated stars, yielding 324 planet-star scenarios. Finally, all of these scenarios were built with 40, 60 and 80 data points, totalling 972 synthetic timeseries data sets, adding white noise of 3 m s^{-1} in all cases. The data points are distributed uniformly and randomly within a time span of 120 days. While relatively simplistic and not particularly representative of a realistic observing strategy, we did this with the intention of identifying to a first order the effects of insufficient data on our ability to constrain the different signals present in the data. All parameters used for the above-described data sets are listed in Table 1.

4. Modelling approach

We model the above-described synthetic RV and activity indicator time series data sets using the code `pyaneti` (Barragán et al. 2019; Barragán et al. 2022a). `pyaneti` uses a Bayesian approach and relies on a Markov chain Monte Carlo (MCMC) algorithm to explore the parameter space and estimate posterior distributions. To characterise the stellar and planetary signals we apply the `pyaneti` implementation of the multi-dimensional Gaussian process approach with a QP covariance function (Sect. 2) as per the framework laid out by Rajpaul et al. (2015). The general idea is expressed as follows:

$$\begin{aligned} \mathcal{A}_1 &= A_1 G(t) + B_1 \dot{G}(t), \\ &\vdots \\ \mathcal{A}_N &= A_N G(t) + B_N \dot{G}(t). \end{aligned} \tag{2}$$

In the above equation (Eq. 2), $\mathcal{A}_1$ through $\mathcal{A}_N$ are the N timeseries that are modelled in parallel. $G(t)$ is a GP drawn function to be interpreted as the fraction of the stellar surface covered by active regions, and $\dot{G}(t)$ is the first derivative of said function and is thus also a GP. The derivative is necessary, particularly in the case of the RVs, since the latter are affected by both the location of the active regions, and their evolution in time. On the other hand, photometric-like activity indicators (e.g. full width at half maximum, differential line width, log R'_{HK}, among others), such as the type used in the current application, are described only by $G(t)$. Finally, $A_1 \ldots A_N$ and $B_1 \ldots B_N$ are coefficients relating the different timeseries to the GP functions.

Since we are only using one activity indicator timeseries to model alongside the RVs, Eq. 2 becomes a 2D GP and simplifies to:

$$\begin{aligned} \Delta RV &= A_1 G(t) + B_1 \dot{G}(t), \\ \Delta AI &= A_2 G(t), \end{aligned} \tag{3}$$

where AI refers to activity indicator. The above relies on the fundamental assumption that the underlying function $G(t)$ and its derivatives (if any), describe the signal intended to be modelled in all contemporaneous timeseries. This is, of course, ensured in the case of synthetic data, but it is worth keeping in mind that finding a suitable activity indicator is not always straightforward.

Table 2. The `pyaneti` modelling priors.

Parameter	Priors[a]	Units
Fitted parameters		
Epoch T_0	$\mathcal{N}[1, 0.005]$	days
Orbital period P_{orb}	$\mathcal{N}[x, 0.005]$	days
e	$\mathcal{F}[0]$	...
$\omega_\star$	$\mathcal{F}[\pi/2]$	...
Doppler semi-amplitude K	$\mathcal{U}[0, 50]$	m s^{-1}
GP hyperparameters		
GP Period P_{GP}	$\mathcal{U}[0.7 * x, 1.3 * x]$	days
λ_p	$\mathcal{U}[0.1, 10]$	...
λ_e	$\mathcal{U}[1, 400]$	days
A_1	$\mathcal{U}[0, 500]$	m s^{-1}
A_2	$\mathcal{U}[0, 500]$	m s^{-1} d^{-1}
B_1	$\mathcal{U}[0, 500]$	m s^{-1}
Other Parameters		
RV jitter	$\mathcal{J}[0, 1000]$	m s^{-1}
Activity indicator jitter ...	$\mathcal{J}[0, 1000]$	m s^{-1}

Notes. [(a)] $\mathcal{U}$[a,b] refers to uniform priors in the range $a - b$, $\mathcal{N}$[a,b] to Gaussian priors with mean a and standard deviation b, and $\mathcal{J}$[a,b] to modified Jeffrey's priors (Eq. 16 in Gregory 2005). The letter x refers to each injected value of the corresponding parameter.

The modelling of each data set was automated and done consecutively. Since we are assuming that the ephemerides of the planetary signals are known (e.g. in the case of transiting planets), we placed Gaussian priors on the period, P_{orb}, and the time of mid-transit, T_0. We set the mean of T_0 to 1 and the means of the orbital periods corresponding to the injected P_{orb} values (Table 1), and set the standard deviation to 0.005 days for all cases for these two parameters. Since we assume circular orbits in all cases, the eccentricity and angle of periastron were fixed. Modified Jeffreys priors (Gregory 2005) were set for the jitter terms. For all other parameters we used uniform priors with set ranges irrespective of the injected value, with the exception of the GP period, P_{GP}, where we set the range to be 30% on either side of the injected P_{GP} value. All priors are listed in Table 2.

5. Results

In the following sections we show and discuss the results of the different runs. We first review our ability to recover the stellar signals for all the different stellar and sampling configurations, followed by an analysis on how this affects our ability to recover the injected planetary signals.

5.1. Stellar signal characterisations

The first question we want to answer is if we are able to recover the stellar signals independently of the injected planet signal. This will help us to understand if a planetary signal in the RVs can affect the GP model, in turn affecting the recovered GP hyperparameters.

5.1.1. The high harmonic complexity problem

From looking at Fig. 1 we can say that high harmonic complexity should be easy to recover. Our models do indeed show this, and we see that our models are able to recover this parameter in practically all $\lambda_p = 0.3$ cases. In contrast, however, the value of this parameter is seen to be the biggest obstacle to the overall ability of a model to explain a given dataset. This becomes evident from Figs. 3, 5 and 7, where we find the highest jitter term values to be largely concentrated in the regions of $\lambda_p = 0.3$. This is alleviated as we move toward the right side of the jitter heatmaps, implying that a large λ_e value can reduce the impact of the high harmonic complexity. This is not unexpected as both high harmonic complexity and short evolution timescales lead to a GP function with many complex and sharply changing features. Thus, when one or both of these parameters are characterised by a higher value, a GP curve is less complex, making it easier for a model to follow the data more closely. Comparing the individual panels of each of the jitter heatmaps, we also see the unambiguous result that denser sampling can significantly help toward making the small λ_p problem easier to handle.

Finally, we note that the tendency of a model to overfit is, in most cases, related to high harmonic complexity (lowest λ_p). The situation is often further exacerbated when coupled with a small P_{GP} value. This is likely due to the fact that the model becomes overly complex and captures noise rather than the underlying periodic pattern.

5.1.2. The low harmonic complexity problem

A key result is that low harmonic complexity ($\lambda_p = 5$) cannot be recovered. This can be seen in all panels of Fig. 1, where it becomes clear that a λ_p value of $\gtrsim 1.5$ is unrecognisable. This has implications on the prior ranges that are adequate when fitting for this hyperparameter. Our results consistently show that using a prior with a maximum limit of $\gtrsim 5$ is pointless since it does not lead to the parameter being constrained any better. Cases when a posterior distribution is pushing toward higher values should thus rather be interpreted as the signal having low harmonic complexity.

5.2. Planetary signal characterisations

The next step is to analyse in which cases we can recover the injected planetary signal, and if this depends on the stellar behaviour, as well as on the planetary mass and orbital parameters.

As previously mentioned, our analysis shows that the cases where λ_e is lower than P_{GP} seems to preclude the GP period from being correctly derived. But perhaps somewhat unexpectedly, this scenario does not have any effect on the detectability of the planetary signals or the ability of the model to explain the data overall, as seen in Figs. 2 - 7. This means that, while such hyperparameter values may be difficult to make sense of physically and may not necessarily translate clearly into interpretable information about the star's behaviour, the planet(s) potentially orbiting such a star may still be recovered with a high degree of reliability.

Only 4 of the highest K planets are completely undetected. These correspond to the scenario of the lowest number of datapoints (40) and the most active stellar configuration (smallest values for the three hyperparameters) at each of the orbital periods. This means that this stellar configuration can impede the detection of even the most pronounced semi-amplitudes. Such stellar behaviour is characteristic of young stars, and/or fast rotators. Real life examples of such systems are e.g. Au Mic (Zicher et al. 2022) and K2-233 (Barragán et al. 2023).

Figures 2, 4 and 6 show that our smallest planet signals (K = 3 m s^{-1}) at the longest P_{orb} (29.2 days) are detected only in two cases when λ_p is 0.3, and all of those cases feature high values of λ_e and P_{GP}. Beyond detectability, however, a general trend is clearly visible in all of the detection significance plots. The colour intensity steadily increases toward higher values of λ_p. This leads back to the point made in Sect. 5.1.1 regarding the relation of λ_p and the value of the jitter term as an indicator for a model's accuracy. The harmonic complexity thus proves itself to be the most impactful of the hyperparameters. It is both as a hindrance to small planet detection, particularly in wider orbits, but also to the general ability of the model to explain the data.

When modelling data we can never be sure of the extent to which our derived parameters are actually accurate. It is prevalent that we use the median value of a planet's radius and mass, whether accompanied by a 1σ error bars or not, from joint RV and transit modelling with the aim of further characterisation of individual planets and planetary systems. We usually ignore the possibility that our derived parameters do not, in fact, lie within this confidence interval, and sometimes not even inside the posterior distribution. We trust the accuracy of our modelling results and make quantitative (often probabilistic), and sometimes qualitative conclusions about atmospheric and interior compositions of the planets we discover, comparing with formation and migration models to try and understand the history of a system.

In this context, an important observation can be made from our heat maps in Figs. 2, 4 and 6. For all K value cases we see that the longest P_{orb} signals are often $> 1\sigma$ (sometimes $> 2\sigma$) distance away from the injected value, as indicated by the numbers in the boxes. This is a trend seen in both the $\geq 3\sigma$ detected (hatched) and undetected planetary signals.

We finally point out that well-constrained hyperparameters are no guarantee for a significant detection of a planetary signal, or of the accuracy of the detection, if one is achieved. A testament to this is the fact that our models find it easy to infer the low λ_p values correctly, but that is not an indicator of whether a planetary signal is detected or how far the derived median value deviates from the true value.

5.3. Other findings

As mentioned in Sect. 2, models that suggest a lower λ_e than P_{GP} should be treated carefully. Without practical examples, however, it is difficult to know how such a scenario would impact the rest of the model parameters. We find that our results help to elucidate our theoretical analysis: in the cases when $\lambda_e = 20$ days, $\lambda_p = 5.0$ and $P_{GP} = 27.6$ days, our model is not able to constrain P_{GP}. This is somewhat intuitive since the higher periodicity of λ_e makes the P_{GP} irrelevant. As the top left panel of Fig. 1 illustrates, the quasi-periodic behaviour is only hinted in the part of the plot with the lowest values of λ_p. For higher values, the covariance becomes insensitive to this parameter. We note that this behaviour is seen amongst all three datapoint scenarios.

The combination of the hyperparameter values, i.e. the activity of the star, affects not only whether or not their injected values and those of the planetary signals are recovered, but also the extent to which the recovered value is (in)correct. Broadly speaking, heatmaps showing the jitter term for each model (Figs. 3, 5 and 7) point to the fact that the scenarios where the model has the greatest difficulty in explaining the data are the ones with the highest overall complexity (lowest values of the GP hyperparameters). In line with this, we discover that no planets around the

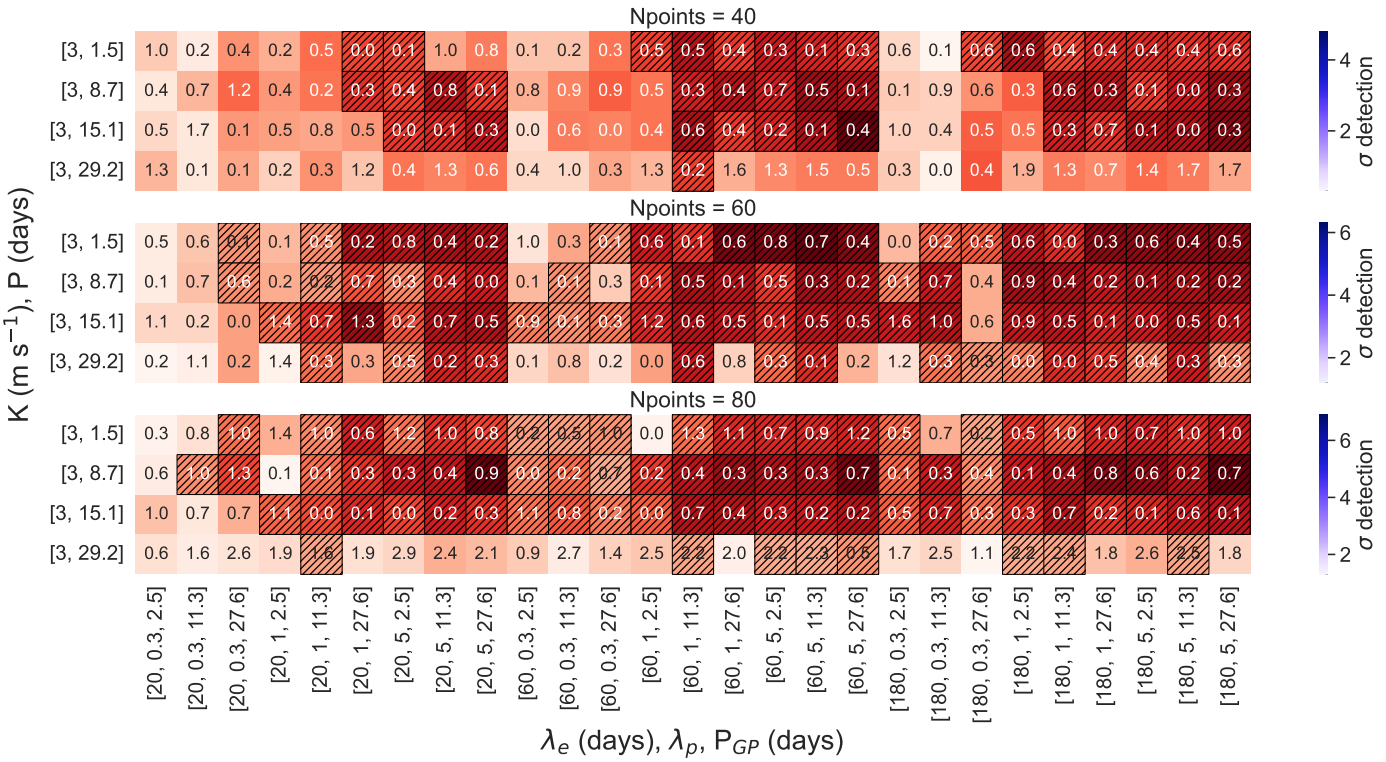

Fig. 2. Heatmap of the detection significance of the planetary signals with injected semi-amplitude value of K = 3 m s^{-1}. Darker red implies higher significance.The vertical axis labels show the injected K value and orbital period, while the horizontal axis shows the different hyperparameter combinations tested. The hatched boxes denote the planets that are detected at > 3σ. The numbers in the boxes correspond to the number of σ away the detected K value is from the injected one.

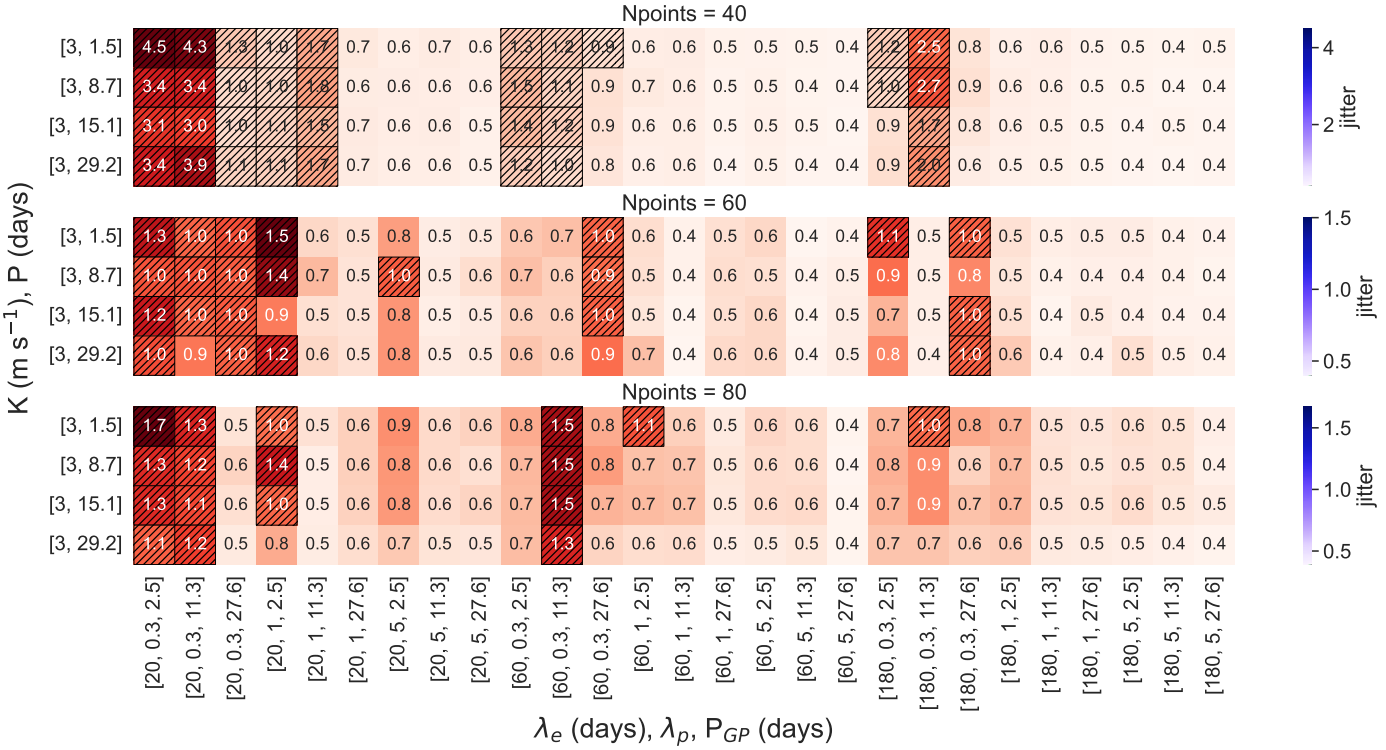

Fig. 3. Heatmap of the jitter term for each model with injected semi-amplitude value of K = 3 m s^{-1}, with darker red meaning higher jitter term. The vertical axis labels show the injected K value and orbital period, while the horizontal axis shows the different hyperparameter combinations tested. The hatched boxes correspond to jitter terms > 1.

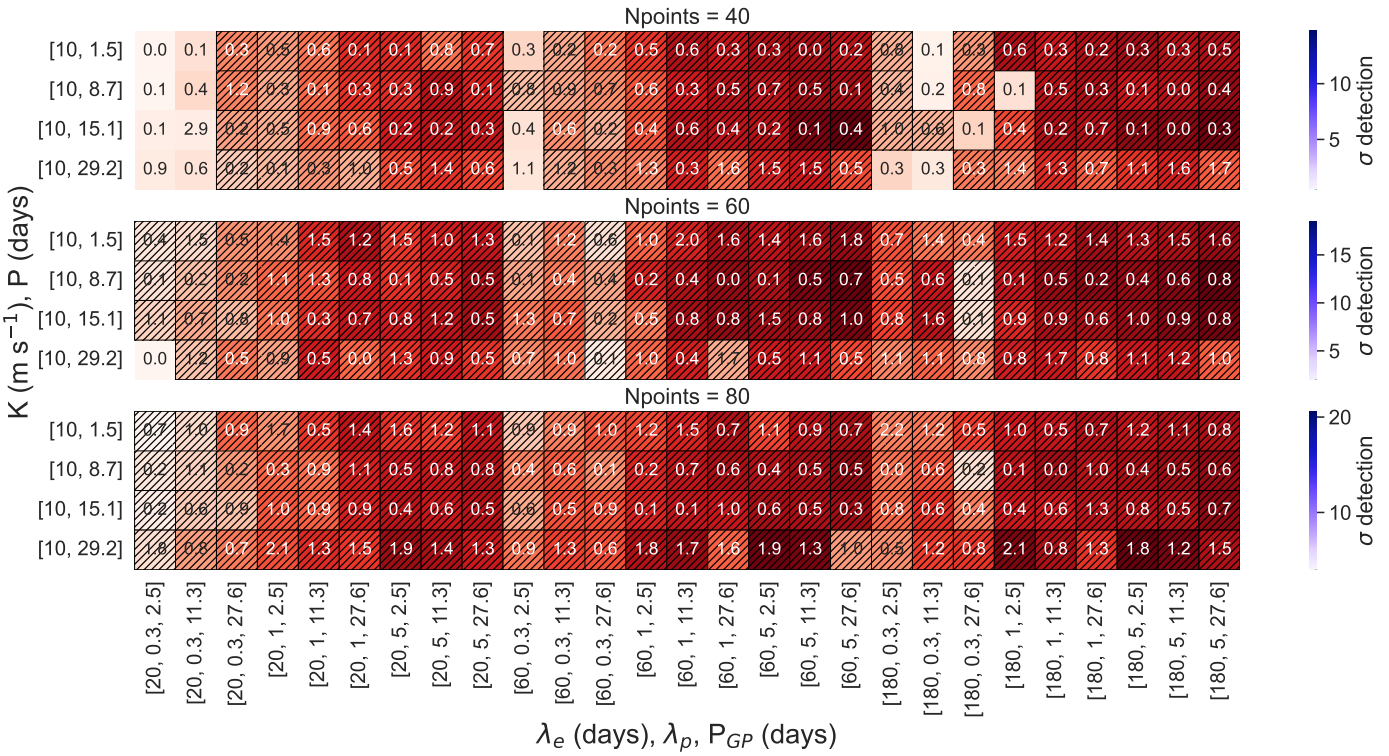

Fig. 4. Same as Fig. 2 above but with injected semi-amplitude of K = 10 m s^{-1}.

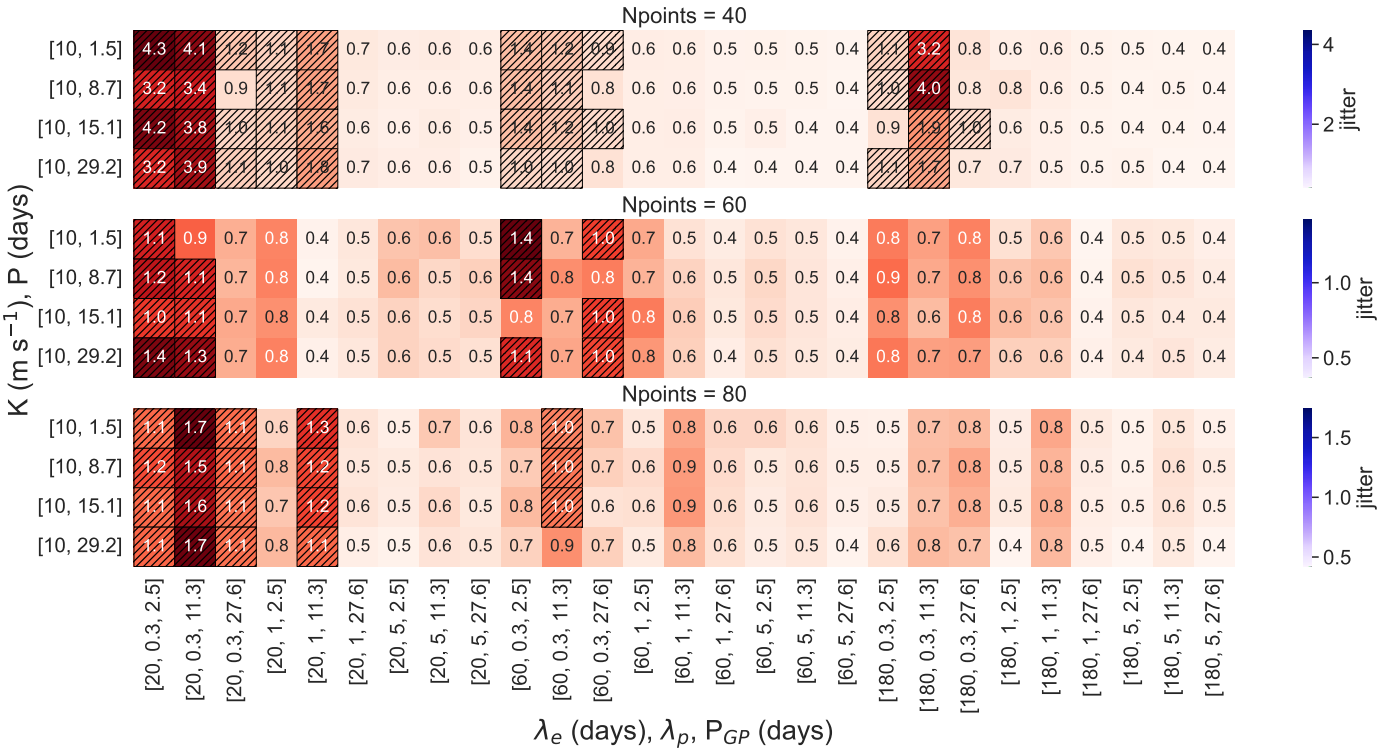

Fig. 5. Same as Fig. 3 but with injected semi-amplitude of K = 10 m s^{-1}.

most active stellar configuration (smallest values for the three hyperparameters) are detected with 40 points. This affirms the challenge that detecting any kind of planet orbiting a star with a particularly complex activity pattern is practically impossible without relatively frequent sampling (frequency dependent on the planet to be detected).

6. Conclusions

Not long after the first extrasolar planet discoveries were made, the problem with stellar activity in RV timeseries data became apparent. We now know that stars with a complex, not strictly periodic activity pattern need to be modelled with extra care.

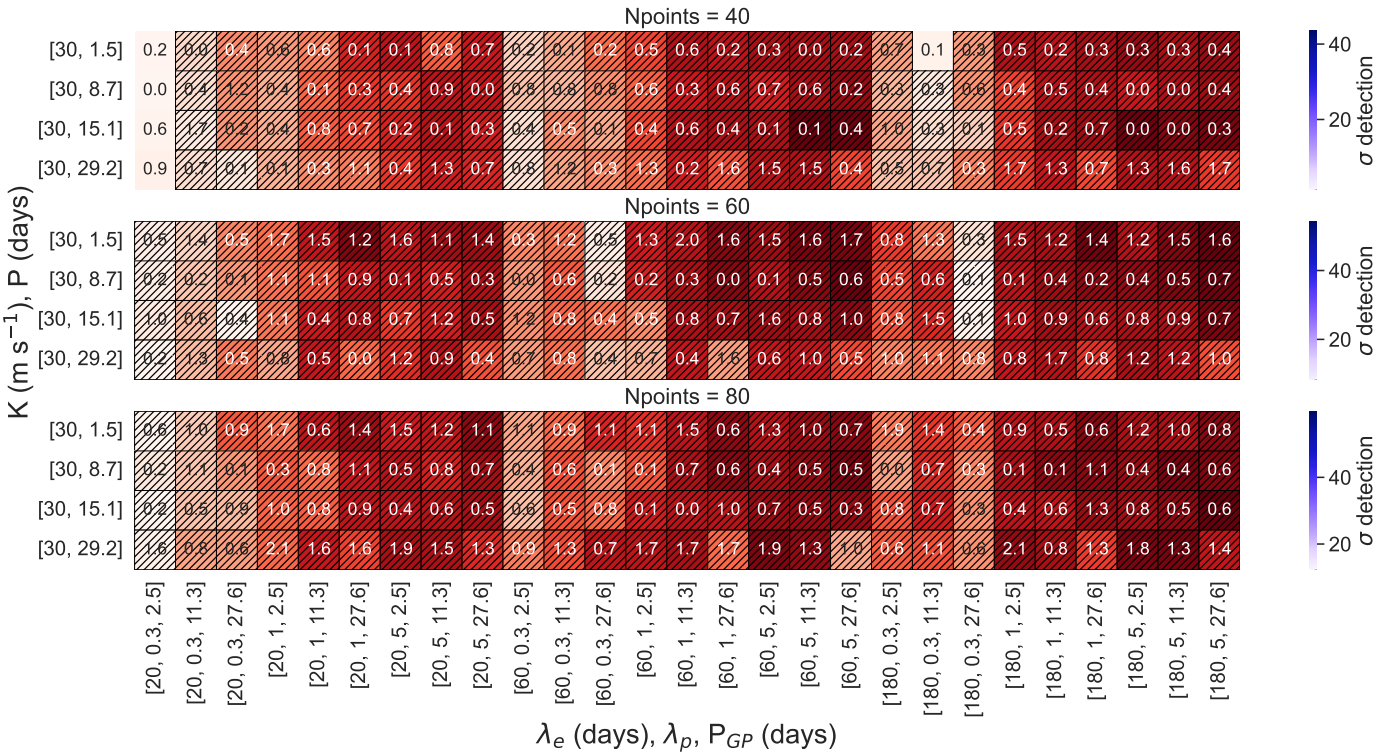

Fig. 6. Same as Fig. 2 but with injected semi-amplitude of K = 30 m s^{-1}.

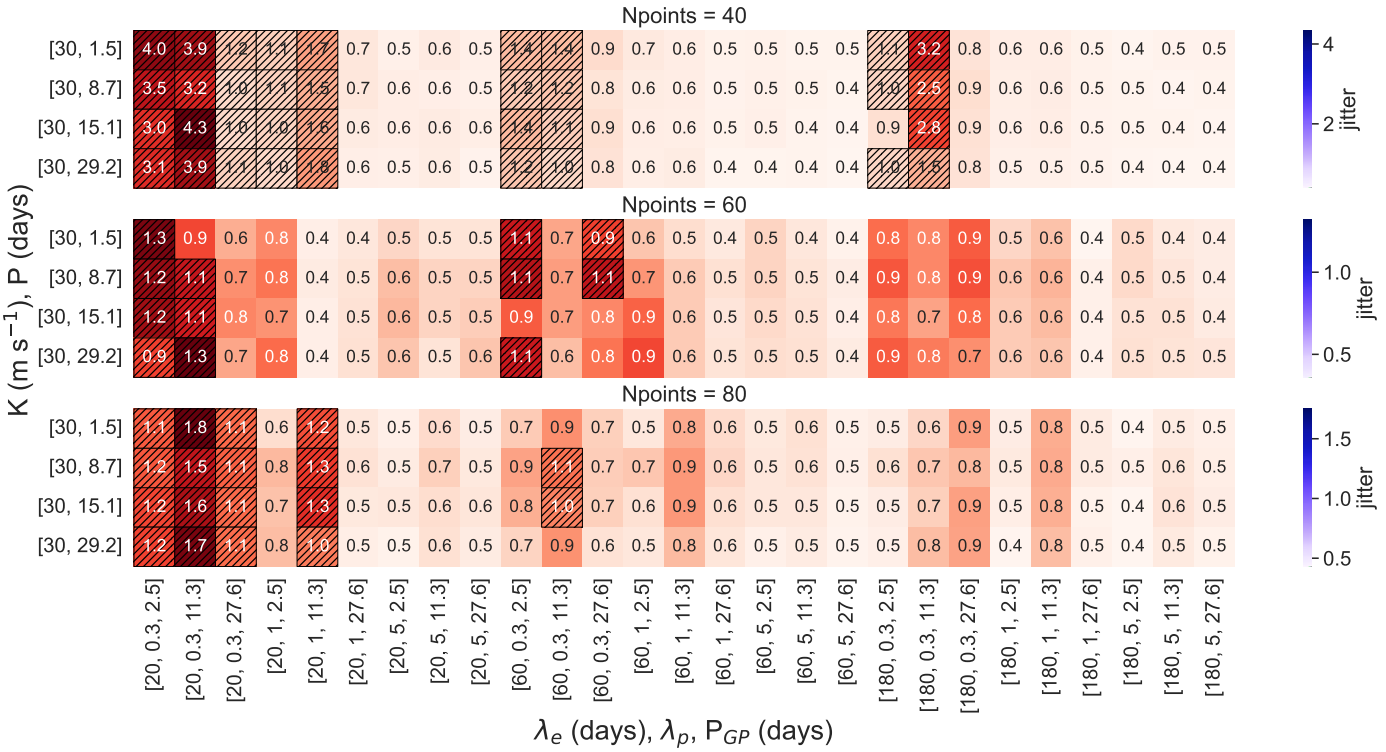

Fig. 7. Same as Fig. 3 but with injected semi-amplitude of K = 30 m s^{-1}.

Developing means to solving this problem has become ever more pressing in the era of extreme precision radial velocities as the search for smaller and less massive planets, including other Earths, intensifies. Unfortunately, our detection methods and the instruments we use do not offer the precision needed to easily extract a tiny planetary RV signature dwarfed by the signal of an active star. This problem is inadvertently made worse by random sampling of such planet hosting stars, causing low-mass planets to be difficult or impossible to detect.

In this paper, we showed a variety of scenarios. We tested the detectability of three different semi-amplitudes (3 m s^{-1}, 10 m s^{-1}and 30 m s^{-1}) in combination with four different or-

bital periods around stars characterised by a variety of active behaviours as conditioned by GP hyperparameters. We test all planet and star parameter combinations with 40, 60 and 80 datapoints. We did this by simulating spectroscopic-like time-series using random samples of a GP. We modelled said timeseries using a multi-dimensional GP approach – modelling RVs alongside contemporaneous activity indicators – with a quasi-periodic covariance function. We find tendencies of non-detections as well as a general inability of the model to explain the data in the most active stellar configurations cases. Many of these cases correspond to what we would see in the RVs of a young planet-hosting star. Gleaning insight into the RV behaviour of such stars is crucial in solving degenerate problems in exoplanet science, such as defining the domains of the atmospheric mass loss mechanisms of photoevaporation and core-powered mass loss.

We find that, while the QP kernel is generally well-suited to finding the right stellar rotation period (i.e. $P_{\rm GP}$), this is not the case when the active regions' evolution timescale, $\lambda_{\rm e}$, is shorter than $P_{\rm GP}$. This, however, does not appear to have any impact on finding the planets in these cases. Our results point to the conclusion that, out of the three hyperparameters discussed here, high harmonic complexity is the biggest setback to model explaining the data well. We relate $\lambda_{\rm p}$ also to the probability of a model to overfit, with low values of $\lambda_{\rm p}$ increasing this probability. Constraining this, or any of he hyperparameters, well, however, is no guarantee of planet detection or of accuracy of the derived semi-amplitude.

We show all of the above for the simplest case of one orbiting planet and leave more advanced and detailed investigations with multi-planet scenarios to future work.

Acknowledgements.
I.Y.G. and C.M.P. gratefully acknowledge the support of the Swedish National Space Agency (DNR 174/18 and 65/19).

References

Aigrain, S. & Foreman-Mackey, D. 2022, arXiv e-prints, arXiv:2209.08940
Barragán, O., Aigrain, S., Kubyshkina, D., et al. 2019, MNRAS, 490, 698
Barragán, O., Aigrain, S., Rajpaul, V. M., & Zicher, N. 2022a, MNRAS, 509, 866
Barragán, O., Armstrong, D. J., Gandolfi, D., et al. 2022b, MNRAS, 514, 1606
Barragán, O., Gandolfi, D., & Antoniciello, G. 2019, MNRAS, 482, 1017
Barragán, O., Gillen, E., Aigrain, S., et al. 2023, MNRAS, 522, 3458
Campbell, B., Walker, G. A. H., & Yang, S. 1988, ApJ, 331, 902
Carleo, I., Gandolfi, D., Barragán, O., et al. 2020, AJ, 160, 114
Cochran, W. D., Hatzes, A. P., & Hancock, T. J. 1991, ApJ, 380, L35
Collier Cameron, A., Ford, E. B., Shahaf, S., et al. 2021, MNRAS, 505, 1699
de Beurs, Z. L., Vanderburg, A., Shallue, C. J., et al. 2022, AJ, 164, 49
Dumusque, X., Borsa, F., Damasso, M., et al. 2017, A&A, 598, A133
Fridlund, M., Georgieva, I., Bonfanti, A., et al. 2023, manuscript submitted for publication
Georgieva, I. Y., Persson, C. M., Barragán, O., et al. 2021, MNRAS, 505, 4684
Georgieva, I. Y., Persson, C. M., Goffo, E., et al. 2023, arXiv e-prints, arXiv:2304.06655
Gregory, P. C. 2005, ApJ, 631, 1198
Hatzes, A. P. 2013, ApJ, 770, 133
Hatzes, A. P. & Cochran, W. D. 1993, ApJ, 413, 339
Hatzes, A. P., Cochran, W. D., Endl, M., et al. 2006, A&A, 457, 335
Hatzes, A. P., Cochran, W. D., Endl, M., et al. 2003, ApJ, 599, 1383
Hatzes, A. P., Dvorak, R., Wuchterl, G., et al. 2010, A&A, 520, A93
Haywood, R. D., Collier Cameron, A., Queloz, D., et al. 2014, MNRAS, 443, 2517
Latham, D. W., Mazeh, T., Stefanik, R. P., Mayor, M., & Burki, G. 1989, Nature, 339, 38
Mayor, M. & Queloz, D. 1995, Nature, 378, 355
Nicholson, B. A. & Aigrain, S. 2022, MNRAS, 515, 5251
Queloz, D., Henry, G. W., Sivan, J. P., et al. 2001, A&A, 379, 279
Rajpaul, V., Aigrain, S., Osborne, M. A., Reece, S., & Roberts, S. 2015, MNRAS, 452, 2269
Rajpaul, V., Aigrain, S., & Roberts, S. 2016, MNRAS, 456, L6
Rivera, E. J., Lissauer, J. J., Butler, R. P., et al. 2005, ApJ, 634, 625
Roberts, S., Osborne, M., Ebden, M., et al. 2012, Philosophical Transactions of the Royal Society of London Series A, 371, 20110550
Simola, U., Bonfanti, A., Dumusque, X., et al. 2022, A&A, 664, A127
Simola, U., Dumusque, X., & Cisewski-Kehe, J. 2019, A&A, 622, A131
Vogt, S. S., Marcy, G. W., Butler, R. P., & Apps, K. 2000, ApJ, 536, 902
Zicher, N., Barragán, O., Klein, B., et al. 2022, MNRAS, 512, 3060

PAPER D

TOI-2196 b: A rare planet in the hot Neptune desert transiting a G-type star

Carina M. Persson, **Iskra Y. Georgieva**, D Gandolfi, L. Acuña, A. Aguichine, A. Muresan, E. Guenther, J. Livingston, K. A. Collins, F. Dai, M. Fridlund, E. Goffo, J. S. Jenkins, P. Kabáth, J. Korth, A. M. Levine, L. M. Serrano, J. Vines, O. Barragán, I. Carleo, K. D. Colon, W. D. Cochran, J. L. Christiansen, H. J. Deeg, M. Deleuil, D. Dragomir, M. Esposito, T. Gan, S. Grziwa, A. P. Hatzes, K. Hesse, K. Horne, J M. Jenkins, J. F. Kielkopf, P. Klagyivik, K. W. F. Lam, D. W. Latham, R. Luque, J. Orell-Miquel, A. Mortier, O. Mousis, N. Narita, H. L. M. Osborne, E. Palle1, R. Papini, G. R. Ricker, H. Schmerling, S. Seager, K. G. Stassun, V. Van Eylen, R. Vanderspek, G. Wang, J. N. Winn, B. Wohler, R. Zambelli, and C. Ziegler

Published in Astronomy & Astrophysics
vol. 666, no. 10, id.A184, 15 pp.
October 2022
©DOI: 10.1051/0004-6361/202244118

A&A 666, A184 (2022)
https://doi.org/10.1051/0004-6361/202244118

Astronomy & Astrophysics

TOI-2196 b: Rare planet in the hot Neptune desert transiting a G-type star

Carina M. Persson[1], Iskra Y. Georgieva[1], Davide Gandolfi[2], Lorena Acuña[3], Artem Aguichine[3], Alexandra Muresan[4], Eike Guenther[5], John Livingston[6,7,8], Karen A. Collins[9], Fei Dai[10], Malcolm Fridlund[1,11], Elisa Goffo[2,5], James S. Jenkins[12,13], Petr Kabáth[14], Judith Korth[4], Alan M. Levine[15], Luisa M. Serrano[2], José Vines[13], Oscar Barragán[16], Ilaria Carleo[17], Knicole D. Colon[18], William D. Cochran[19], Jessie L. Christiansen[20], Hans J. Deeg[17,21], Magali Deleuil[3], Diana Dragomir[22], Massimiliamo Esposito[5], Tianjun Gan[23], Sascha Grziwa[24], Artie P. Hatzes[5], Katharine Hesse[15], Keith Horne[25], Jon M. Jenkins[26], John F. Kielkopf[27], P. Klagyivik[28], Kristine W. F. Lam[29], David W. Latham[9], Rafa Luque[30], Jaume Orell-Miquel[17,21], Annelies Mortier[31,32], Olivier Mousis[3], Noria Narita[6,17,33], Hannah L. M. Osborne[34], Enric Palle[17], Riccardo Papini[35], George R. Ricker[15], Hendrik Schmerling[24], Sara Seager[15,36,37], Keivan G. Stassun[38], Vincent Van Eylen[34], Roland Vanderspek[15], Gavin Wang[39], Joshua N. Winn[40], Bill Wohler[26,41], Roberto Zambelli[42], and Carl Ziegler[43]

(Affiliations can be found after the references)

Received 25 May 2022 / Accepted 11 July 2022

ABSTRACT

The hot Neptune desert is a region hosting a small number of short-period Neptunes in the radius–instellation diagram. Highly irradiated planets are usually either small ($R \lesssim 2\ R_\oplus$) and rocky or they are gas giants with radii of $\gtrsim 1\ R_J$. Here, we report on the intermediate-sized planet TOI-2196 b (TIC 372172128.01) on a 1.2 day orbit around a G-type star ($V = 12.0$, [Fe/H] = 0.14 dex) discovered by the Transiting Exoplanet Survey Satellite in sector 27. We collected 41 radial velocity measurements with the HARPS spectrograph to confirm the planetary nature of the transit signal and to determine the mass. The radius of TOI-2196 b is $3.51 \pm 0.15\ R_\oplus$, which, combined with the mass of $26.0 \pm 1.3\ M_\oplus$, results in a bulk density of $3.31^{+0.51}_{-0.43}$ g cm^{-3}. Hence, the radius implies that this planet is a sub-Neptune, although the density is twice than that of Neptune. A significant trend in the HARPS radial velocity measurements points to the presence of a distant companion with a lower limit on the period and mass of 220 days and 0.65 M_J, respectively, assuming zero eccentricity. The short period of planet b implies a high equilibrium temperature of 1860 ± 20 K, for zero albedo and isotropic emission. This places the planet in the hot Neptune desert, joining a group of very few planets in this parameter space discovered in recent years. These planets suggest that the hot Neptune desert may be divided in two parts for planets with equilibrium temperatures of $\gtrsim$1800 K: a hot sub-Neptune desert devoid of planets with radii of $\approx$1.8–3 $R_\oplus$ and a sub-Jovian desert for radii of $\approx$5–12 $R_\oplus$. More planets in this parameter space are needed to further investigate this finding. Planetary interior structure models of TOI-2196 b are consistent with a H/He atmosphere mass fraction between 0.4% and 3%, with a mean value of 0.7% on top of a rocky interior. We estimated the amount of mass this planet might have lost at a young age and we find that while the mass loss could have been significant, the planet had not changed in terms of character: it was born as a small volatile-rich planet and it remains one at present.

Key words. planets and satellites: composition – planetary systems – planets and satellites: detection – planets and satellites: individual: TOI-2196 – techniques: photometric – techniques: radial velocities

1. Introduction

With the large number of *Kepler* (Borucki et al. 2010) planets, evidence of a bimodal population has emerged, made up of small planets with a gap in the size distribution between ~1.5 and 2 $R_\oplus$, often referred to as the radius gap (Fulton et al. 2017; Van Eylen et al. 2018, 2021; Petigura et al. 2022). This feature was predicted before the observational discovery by several groups as a result of envelope mass loss due to photoevaporation (Lopez & Fortney 2013; Owen & Wu 2013; Jin et al. 2014; Chen & Rogers 2016). Other studies have shown that core-powered envelope mass loss could also carve out a gap in the radius distribution of small planets (Ginzburg et al. 2018; Gupta & Schlichting 2019).

The two populations on either side of the radius gap are: super-Earths, commonly defined as having radii of $1.2 \lesssim R/R_\oplus \lesssim 1.7$ and believed to be mainly rocky, and volatile-rich sub-Neptunes with radii of $1.7 \lesssim R/R_\oplus \lesssim 4$. According to available models, a part of the super-Earth population could, in fact, be remnant cores of sub-Neptunes stripped of their atmospheres. Consequently, mass loss plays an important role in the first few hundred million years of exoplanet evolution (Adams & Laughlin 2006; Kubyshkina et al. 2018).

Despite the abundance of small planets, there is a dearth of hot sub-Neptunes and Neptunes in the radius–instellation (or equilibrium temperature) diagram, namely, the so-called hot Neptune desert or sub-Jovian desert (Szabó & Kiss 2011; Benítez-Llambay et al. 2011; Sanchis-Ojeda et al. 2014; Mazeh et al. 2016), or (otherwise) the hot super-Earth desert as referred to by Lundkvist et al. (2016) for smaller planets with radii between 2.2 and 3.8 $R_\oplus$. The observed period distribution already drops for $P_{orb} < 3$ days despite a strong selection bias due to easy detection which indicates that short period planets are rare. Most planets facing high instellation are either small and rocky with

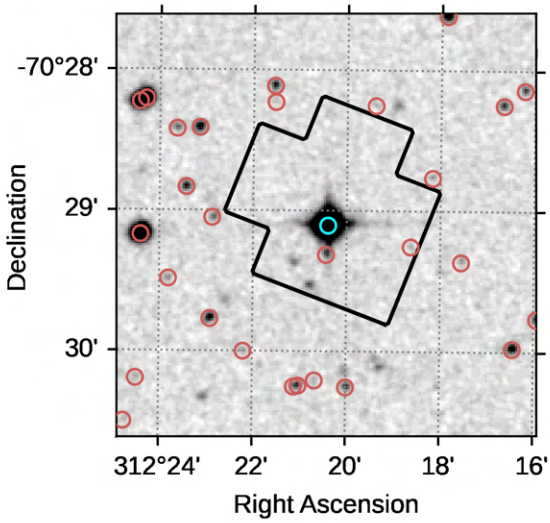

Fig. 1. $3' \times 3'$ DSS2 image (red filter) centered on TOI-2196 (cyan circle). The SPOC photometric aperture of sector 27 is outlined in black while *Gaia* DR2 sources within $2'$ from the target are marked by the red circles.

masses below 10 $M_\oplus$ and radii $\lesssim$2 $R_\oplus$, or massive gas giants with radii $\gtrsim$1 R_J.

Up until a few years ago, the hot Neptune desert was almost completely empty in terms of observed planets. New discoveries have begun to uncover a population of planets in the desert, although their small number does not allow for the exact circumstances of their existence to be defined. High precision radius and mass measurements of these planets are crucial to constrain theoretical models of their formation and evolution. The lack of planets in this parameter space suggests difficulties of retaining an extended atmosphere in strong irradiation environments (Lopez & Fortney 2014), possibly indicating different formation and evolution mechanisms, or high-eccentricity migration (Mazeh et al. 2013; Owen & Lai 2018).

Within the hot Neptune desert, there are currently only three known planets with equilibrium temperatures above 1800 K[1], corresponding to a 1.3 day orbit for sun-like stars, with a precision of 10% and 30% or better in measured radii and masses: K2-100 b (Barragán et al. 2019a), TOI-849 b (Armstrong et al. 2020), and LTT 9779 b (Jenkins et al. 2020b). Two additional planets with radii measured to a precision of 10% or better but without measured masses are also known: K2-278 b (Livingston et al. 2018) and Kepler-644 b (Berger et al. 2018).

This paper presents the discovery and characterisation of the intermediate-sized planet TOI-2196 b (TIC 372172128.01) in the hot Neptune desert discovered by The Transiting Exoplanet Survey Satellite (TESS; Ricker et al. 2015) in 2020. Following the discovery, our international KESPRINT[2] collaboration performed follow-up radial velocity observations of this planet candidate to confirm the planetary nature and determine its mass. The star's equatorial coordinates together with other basic parameters are listed in Table 1.

We present the observations in Sect. 2 and the data analysis in Sect. 3. In Sect. 4, we discuss the hot Neptune desert, the planet interior, and atmospheric mass loss. We end the paper with our conclusions in Sect. 5.

[1] Assuming a Bond albedo of zero and a heat redistribution factor of unity (isotropic emission).

[2] KESPRINT is an international consortium devoted to the characterisation and research of exoplanets discovered with space-based missions, http://kesprint.science

Table 1. Basic parameters for TOI-2196.

Parameter	Value
Main identifiers	
TIC	372172128
2MASS	J20492158-7029058
WISE	J204921.59-702906.1
TYC	9325-00163-1
UCAC4	098-095039
Gaia	6375983988633147392
Equatorial coordinates	
RA ($J2000.0$)	$20^\mathrm{h}49^\mathrm{m}21\overset{\mathrm{s}}{.}57$
Dec ($J2000.0$)	$-70°29'05\overset{''}{.}95$
Magnitudes	
TESS	11.3643 ± 0.0060
Johnson B	12.6740 ± 0.0160
Johnson V	11.9530 ± 0.0120
$G^{(a)}$	11.8175 ± 0.0002
G_RP $^{(a)}$	11.3030 ± 0.0007
G_BP $^{(a)}$	12.1712 ± 0.0014
g	12.2770 ± 0.0200
r	11.7500 ± 0.0150
i	11.6300 ± 0.0060
J	10.743 ± 0.024
H	10.452 ± 0.026
K	10.346 ± 0.023
WISE $W1$	10.326 ± 0.022
WISE $W2$	10.344 ± 0.019
Parallax $^{(a)}$ (mas)	3.7882 ± 0.0132
Systemic velocity $^{(a)}$ (km s^{-1})	35.51 ± 0.56
μ_RA $^{(a)}$ (mas yr^{-1})	16.326 ± 0.011
μ_Dec $^{(a)}$ (mas yr^{-1})	−20.168 ± 0.013
T_eff $^{(b)}$ (K)	5634 ± 31
$M_\star$ $^{(b)}$ ($M_\odot$)	1.032 ± 0.038
$R_\star$ $^{(b)}$ ($R_\odot$)	1.043 ± 0.017
ρ_* $^{(b)}$ (g cm^{-3})	1.25 ± 0.09
$L_\star$ $^{(b)}$ ($L_\odot$)	0.99 ± 0.04
$\log g_\star$ $^{(b)}$	4.42 ± 0.04
[Fe/H] $^{(b)}$	0.14 ± 0.05
[Ca/H] $^{(b)}$	0.15 ± 0.06
[Mg/H] $^{(b)}$	0.18 ± 0.09
[Na/H] $^{(b)}$	0.20 ± 0.08
[Si/H] $^{(b)}$	0.15 ± 0.08
$V \sin i_\star$ $^{(b)}$ (km s^{-1})	2.0 ± 0.4
Age $^{(b)}$ (Gyr)	4.5 ± 2.0

Notes. $^{(a)}$*Gaia* eDR3. $^{(b)}$This work (Sect. 3.2).

2. Observations

2.1. TESS photometry

Figure 1 shows a $3' \times 3'$ image from the Digitized Sky Survey 2 (DSS2) centered on TIC 372172128 (TOI-2196), marked with a cyan circle. TOI-2196 was observed by TESS[3] in sector 13,

[3] https://tess.mit.edu

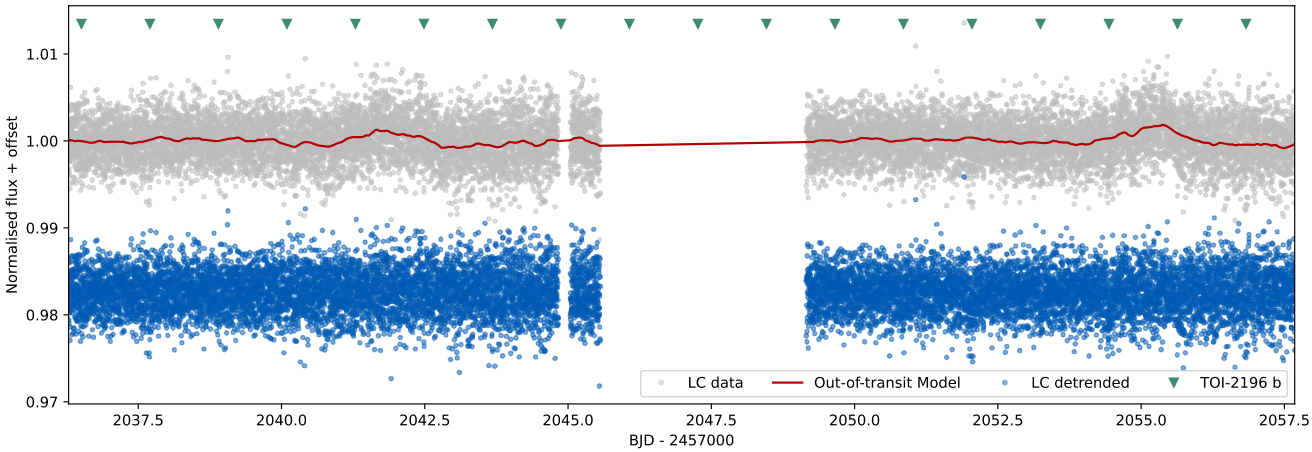

Fig. 2. TESS light curve for sector 27 (short cadence) is plotted in grey with the Gaussian Process model of the out-of-transit data overplotted in red. The detrended and normalised light curve is shown in blue, and, for the purposes of visualisation, a vertical offset has been applied. The triangles mark the locations of the individual transits of TOI-2196 b.

during the primary mission, and in sector 27 in the first set of observations of the TESS extended mission. The outline of the Science Processing Operations Center (SPOC) photometric aperture of sector 27 is overplotted in black in Fig. 1, while the red circles mark the positions of *Gaia* DR2 sources within 2′ from the target. The photometric dilution from other sources is negligible and adjusted for by the pipeline.

TOI-2196 was observed in sector 13 with camera 2 in full-frame images at a cadence of 30 min from 19 June to 17 July 2019. The observations of sector 27 spanned the interval 5 July through 30 July 2020, with a gap in the middle of approximately one day, when the data were being downloaded. This produced 23.35 days of science data at 2-min cadence, including 14 transits of TIC 372172128 monitored with camera 2, CCD 1.

Due to the combination of the short period of the planet (1.2 days) and the long cadence in sector 13, the planet candidate TOI-2196.01 was not discovered orbiting its G-type host star until it was observed in sector 27 at a 2-min cadence and processed by SPOC at NASA Ames Research Center (Jenkins et al. 2016). A search of the sector 27 data with an adaptive, wavelet-based matched filter (Jenkins 2002; Jenkins et al. 2010, 2020a) identified the transit signature of TOI-2196 b just above the detection threshold at 7.2 σ. The data validation reports (DVR; Twicken et al. 2018; Li et al. 2019) process fit a limb-darkened transit model with a signal-to-noise ratio (S/N) of 9.2, a period of 1.1954 days, a duration of 1.6 h, and a transit depth of 1127 ppm, corresponding to a preliminary planet radius of $\sim$3.5 $R_\oplus$. We independently detected the transit signal using the DST (Cabrera et al. 2012) pipeline and found a planet candidate with an orbital period of 1.19387 ± 0.00043 days and a transit depth of 1359 ± 147 ppm.

We downloaded the light curves processed by the SPOC pipeline from the Mikulski Archive for Space Telescopes (MAST[4]) and used the Pre-search Data Conditioning Simple Aperture Photometry (PDCSAP) data. This was generated by the pipeline by identifying and correcting the SAP flux for instrumental signatures using cotrending basis vectors drawn from the light curves of an ensemble of quiet and highly temporally correlated stars long-term trends, thus resulting in a cleaner data set with fewer systematics (Stumpe et al. 2014; Jenkins et al. 2020a).

In order to remove any remaining low-frequency signals in preparation for the modelling described in Sect. 3.3, we further detrended the light curve by applying a Gaussian Process (GP). This was achieved using the package `citlalicue`[5] (e.g. Georgieva et al. 2021; Barragán et al. 2022a), a `PYTHON` wrapper of `george` (Foreman-Mackey et al. 2014) and `pytransit` (Parviainen 2015). We masked out the transits of the planet and applied a squared exponential covariance function as well as a 5 σ clipping algorithm to remove outliers. Figure 2 displays both the PDCSAP data in sector 27 with the GP model overplotted, and the detrended normalised light curve. The latter is subsequently used in the joint transit and RV analysis in Sect. 3.3.

2.2. Follow-up photometry from ground: LCOGT 1 m

The TESS pixel scale is $\sim$21″ pixel^{-1} and photometric apertures typically extend out to roughly 1 arcmin. This generally results in multiple stars blending in the TESS aperture. An eclipsing binary in one of the nearby blended stars could mimic a transit-like event in the large TESS aperture. We therefore acquired ground-based transit follow-up photometry of TOI-2196 b as part of the TESS Follow-up Observing Program Sub Group 1 (TFOP SG1; Collins 2019)[6] to attempt to (1) rule out or identify nearby eclipsing binaries (NEBs) as potential sources of the detection in the TESS data; (2) check for the transit-like event on-target using smaller photometric apertures than TESS to confirm that the event is occurring on-target or, otherwise, in a star so close to TOI-2196 that it was not detectable by *Gaia* eDR3; (3) refine the TESS ephemeris; and (4) place constraints on transit depth across optical filter bands.

We observed the transits of TOI-2196 from the Las Cumbres Observatory Global Telescope (LCOGT; Brown et al. 2013) 1.0 m network on UTC 28 September 2020, 23 May 2021, and 6 June 2021 in Sloan i' band and on UTC 20 June 2021 in Sloan g' band. We used the `TESS Transit Finder` to schedule our transit observations. The 1.0 m telescopes are equipped with 4096 × 4096 SINISTRO cameras having an image scale of 0.″389 per pixel, resulting in a 26′ × 26′ field of view. The images were calibrated by the standard LCOGT `BANZAI` pipeline

[4] https://mast.stsci.edu/portal/Mashup/Clients/Mast/Portal.html

[5] https://github.com/oscaribv/citlalicue

[6] https://tess.mit.edu/followup

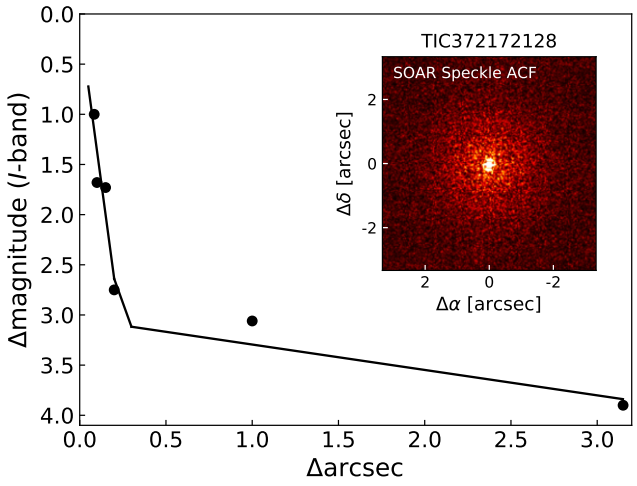

Fig. 3. Contrast curve computed from observations in Cousins I-band on the 4.1 m Southern Astrophysical Research telescope. No bright companions are detected within 3″ of TOI-2196.

(McCully et al. 2018). Photometric data were extracted using `AstroImageJ` (Collins et al. 2017) and circular photometric apertures with radii in the range 4.″7 to 7.″0. The TOI-2196 apertures exclude virtually all flux from the nearest *Gaia* eDR3 and TESS Input Catalog neighbor (TIC 1988186200) 12.″5 South. We find no evidence for an NEB within 2.′5 of TOI-2196, and detect the transit event within the TOI-2196 photometric apertures.

2.3. Follow-up speckle imaging from ground

High-angular resolution imaging is needed to search for nearby sources that can contaminate the TESS photometry. This can result in an underestimated planetary radius or may be the source of astrophysical false positives such as background eclipsing binaries. We searched for stellar companions to TOI-2196 with speckle imaging on the 4.1 m Southern Astrophysical Research (SOAR) telescope (Tokovinin 2018) on 31 October 2020, observing in Cousins I-band, a visible bandpass similar to that of TESS. This observation was sensitive to a 3 magnitude fainter star at an angular distance of 1″ from the target. More details of the observation are available in Ziegler et al. (2020). The 5 σ detection sensitivity and speckle auto-correlation functions from the observations are shown in Fig. 3. No nearby stars were detected within 3″ of TOI-2196 in the SOAR observations.

2.4. Radial velocity follow-up with HARPS

We performed high-resolution ($R \approx 115\,000$) spectroscopic observations of TOI-2196 using the High Accuracy Radial velocity Planet Searcher (HARPS; Mayor et al. 2003) spectrograph mounted at the ESO 3.6 m telescope (La Silla observatory, Chile). We obtained a total of 41 spectra between 24 July 2021 and 12 November 2021 UT as part of our HARPS large program (ID: 106.21TJ.001, PI: Gandolfi). All RVs and activity indicators are listed in Table A.1 along with $\mathrm{BJD_{TBD}}$, exposure time, and S/N. We reduced the data with the dedicated HARPS data reduction software (DRS) available at the observatory (Lovis & Pepe 2007) and extracted the radial velocity (RV) measurements using the code HARPS-TERRA (Anglada-Escudé & Butler 2012), which employs a template-matching algorithm to derive precise relative velocities. We also extracted a variety of stellar activity and line profile variation indicators: the Hα and S-index were extracted using TERRA; the FWHM and the bisector inverse slope (BIS) were derived by cross-correlating the HARPS spectra with a G2 numerical mask (Baranne et al. 1996; Pepe et al. 2002); and the differential line width (dLW) was extracted using the code SERVAL (Zechmeister et al. 2018).

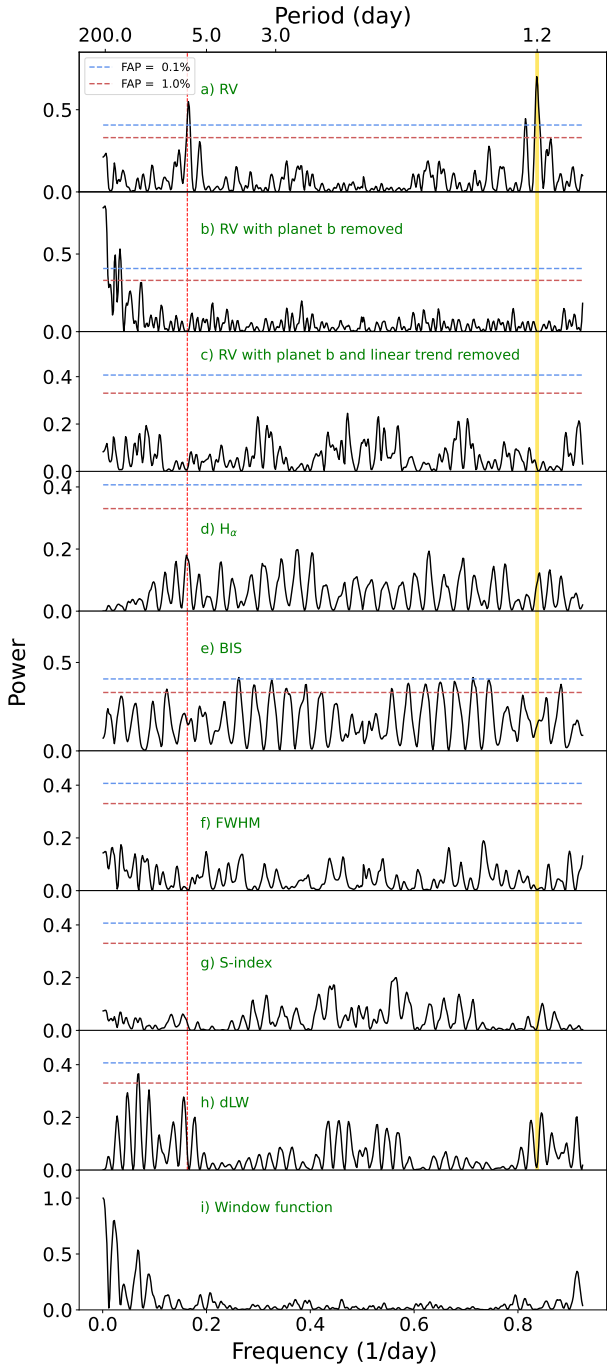

Fig. 4. Generalised Lomb–Scargle periodogram of the HARPS RVs and stellar activity indicators. The horizontal lines mark the bootstrap false alarm probabilities at 0.1 and 1.0% as indicated in the legend. The orbital frequency of TOI-2196 b ($\nu_b = 0.837$ day^{-1}) is marked with a vertical thick yellow line, while the corresponding period is reported in the upper x-axis ($P_{orb} \approx 1.2$ day). The 1 day alias of planet b is marked with a vertical dashed red line ($1 - 0.837 = 0.163$ day^{-1}). *a)* RV measurements. *b)* RV residuals with the best-fitting Keplerian orbit of planet b subtracted. *c)* RV residuals following the subtraction of both the linear trend and the Doppler signal induced by planet b. *d–h)* Activity indicators and line profile variations. *i)* The window function.

Table 2. Spectroscopic parameters for TOI-2196 modelled with SME and SpecMatch-Emp, posteriors from the ARIADNE, and the effective stellar temperature from *Gaia* DR2.

Method	$T_{\rm eff}$ (K)	log(g) (dex)	[Fe/H] (cgs)	[Ca/H] (km s^{-1})	[Mg/H]	[Na/H]	[Si/H]	$V \sin i_\star$
SME [a]	5552 ± 85	4.42 ± 0.05	0.14 ± 0.05	0.15 ± 0.06	0.18 ± 0.09	0.20 ± 0.08	0.15 ± 0.08	2.0 ± 0.4
SpecMatch-Emp	5623 ± 110	4.22 ± 0.12	0.18 ± 0.09	...	...	...	...	...
ARIADNE [b]	5634 ± 31	4.42 ± 0.04	0.13 ± 0.05	...	...	...	...	...
Gaia DR2	5462^{+176}_{-66}	...	...	...	...	...	...	...

Notes. [a]Adopted as priors for the stellar mass and radius modelling in Sect. 3.2. [b]Posteriors from Bayesian Model Averaging with ARIADNE.

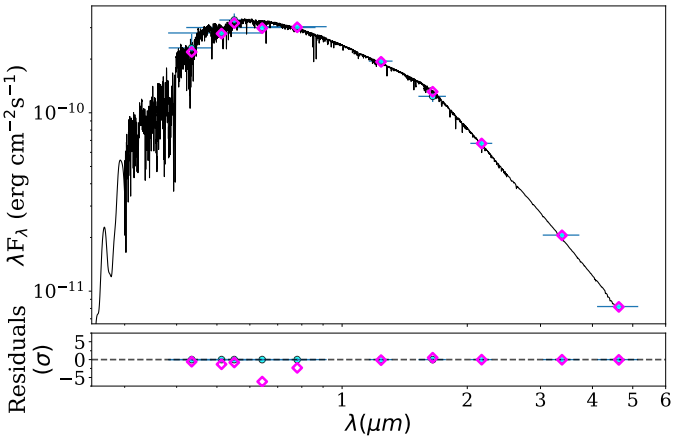

Fig. 5. Spectral energy distribution (SED) of TOI-2196 and the model with highest probability from Husser et al. (2013, Phoenix v2). We plot the synthetic photometry with magenta diamonds and the observed photometry with blue points. The 1 σ uncertainties are shown with vertical error bars, while the horizontal bars display the effective width of the passbands. In the *lower panel* we show the residuals normalised to the errors of the photometry.

3. Data analysis

3.1. Frequency analysis of HARPS data

In order to search for the Doppler reflex motion induced by the transiting planet and unveil the presence of additional RV signals, we performed a frequency analysis of the HARPS RV measurements and activity indicators. To this aim, we computed the generalised Lomb-Scargle (GLS; Zechmeister & Kürster 2009) periodograms of the HARPS time series (shown in Fig. 4) and estimated the false alarm probabilities (FAPs) using the bootstrap technique described in Kuerster et al. (1997). We considered a peak to be significant if its FAP is less than 0.1%.

The GLS periodogram of the HARPS RVs displays a significant peak at $\nu_{\rm b}$ = 0.837 day^{-1} which is the transit frequency of TOI-2196 b (Fig. 4, upper panel, thick vertical yellow line). This peak is not significantly detected in any of the activity indicators confirming the planetary nature of the transit signal found in the TESS light curve. We note the presence of a second significant peak at 0.163 day^{-1} (vertical dashed red line), which is an alias of the orbital frequency of the transiting planet due to the 1 day sampling of our observations.

The second panel of Fig. 4 displays the periodogram of the HARPS RV residuals following the subtraction of the best-fitting Doppler orbit of TOI-2196 b (Sect. 3.3). We found a significant excess of power at frequencies lower than the frequency resolution of our observations (≈1/110 day = 0.009 day^{-1}, where 110 days is the baseline of our observations). This power has no counterpart in any of the activity indicators, suggesting that it is likely caused by an outer orbiting companion. As described in Sect. 3.3, we accounted for this long-period Doppler signal by adding a linear trend to the RV model. When both the Doppler signal of the transiting planet and the linear trend are subtracted from the HARPS RVs, no additional significant signals are found in the RV residuals (Fig. 4, third panel).

3.2. Stellar properties

In order to derive the fundamental parameters of the host star, we analysed our co-added high-resolution HARPS spectra with two methods, the SpecMatch-Emp code (Yee et al. 2017) and SME[7] (Spectroscopy Made Easy; Valenti & Piskunov 1996; Piskunov & Valenti 2017). In particular, SpecMatch-Emp is an empirical code that compares observations of optical spectra to a dense library of well-characterised FGKM stars, while SME fits observed spectra to computed synthetic spectra for a chosen set of parameters based on atomic and molecular line data from VALD[8] (Ryabchikova et al. 2015) and a stellar atmosphere grid. We chose Atlas12 (Kurucz 2013) and derived the stellar effective temperature, $T_{\rm eff}$, the surface gravity, log $g_\star$, abundances, and the projected rotational velocity, $V \sin i_\star$. Each parameter is modelled, one at a time, from specific spectral lines: the broad line wings of H_α are particularly sensitive to $T_{\rm eff}$, and the line wings of the Ca I triplet 6102, 6122, and 6162 Å are sensitive to the surface gravity. Abundances and the projected stellar rotational velocity, $V \sin i_\star$, were modelled from narrow and unblended lines between 6000 and 6600 Å. We held the micro- (Bruntt et al. 2008) and macro-turbulent (Doyle et al. 2014) velocities fixed to 1.0 km s^{-1}, and 2.8 km s^{-1}, respectively. Further details on the modelling can be found in Fridlund et al. (2017) and Persson et al. (2018). Results from both models listed in Table 2 are in good agreement within the uncertainties and with the effective temperature from *Gaia*[9] DR2.

We used the spectral parameters from SME as priors to model the stellar radius and mass with the python code ARIADNE[10] (Vines & Jenkins 2022). We fit the broadband photometry bandpasses $GG_{\rm BP}G_{\rm RP}$ from *Gaia* eDR3 and WISE W1–W2, along with $JHK_{\rm S}$ magnitudes from *2MASS*, the Johnson B and V magnitudes from APASS, and the *Gaia* eDR3 parallax, to the Phoenix v2 (Husser et al. 2013), BtSettl (Allard et al. 2012), Castelli & Kurucz (2004), and Kurucz (1993) atmospheric

[7] http://www.stsci.edu/~valenti/sme.html
[8] http://vald.astro.uu.se
[9] https://gea.esac.esa.int/archive/
[10] https://github.com/jvines/astroARIADNE

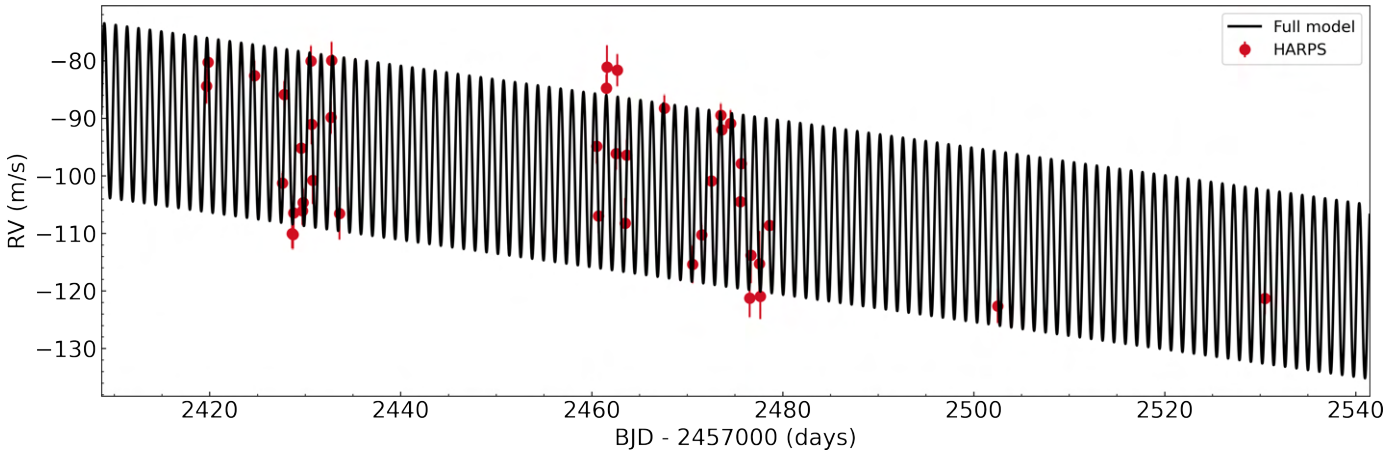

Fig. 6. Radial velocity times series of TOI-2196 and the best-fitting RV model. The linear trend suggesting the presence of an outer companion is clearly identifiable.

model grids. The dust maps of Schlegel et al. (1998) were used to obtain an upper limit on A_V. The relative probabilities of the models were used to compute a weighted average of each parameter and the final stellar radius is computed with Bayesian model averaging. Figure 5 shows the SED model and the fitted bands. The `Phoenix v2` model, which has the highest probability, was used to calculate the synthetic photometry. We also obtained a luminosity of $0.99 \pm 0.04\ L_\odot$, an extinction that is consistent with zero ($A_V = 0.03 \pm 0.02$), as well as the stellar mass based on MIST (Choi et al. 2016) isochrones. The model was checked with `BASTA`[11] (the BAyesian STellar Algorithm; Aguirre Børsen-Koch et al. 2022) using the stellar atmosphere grid from Hidalgo et al. (2018) and the same photometry passbands and priors as above, as well as `PARAM1.3`[12] (da Silva et al. 2006). The latter model uses Bayesian computation of stellar parameters based on PARSEC isochrones using V magnitude, $T_{\rm eff}$, [Fe/H], and the *Gaia* eDR3 parallax as priors.

The results, listed in Table 3, are in excellent agreement within the 1 σ uncertainties. We adopted the stellar parameters derived with `ARIADNE` in our joint modelling of the radial velocities and light curves in Sect. 3.3.

The stellar age was estimated with the observed NUV excess utilising empirical activity–age relations. We transformed the NUV and $B - V$ photometry to $\log R'_{\rm HK} = -4.92 \pm 0.08$ via the empirical relations of Findeisen et al. (2011), which implies an age of $\tau_\star = 5.2 \pm 1.3$ Gyr, according to the empirical relations of Mamajek & Hillenbrand (2008). This is in agreement with 4.5 ± 2.0 Gyr and 7.1 ± 3.4 Gyr derived from the MIST and PARSEC isochrones, respectively, in the above modelling. We note that there is no emission in the Ca I H and K lines, suggesting that the star is not chromospherically active.

3.3. Joint transit and radial velocity modelling

For the modelling of the TOI-2196 system, we turned to the open-source code `pyaneti`[13] (Barragán et al. 2019b, 2022a) to sample the parameter space using Markov chain Monte Carlo (MCMC) sampling combined with a Bayesian approach. Following Barragán et al. (2022b), we used `pyaneti`'s capability to perform multi-band fits and included the flattened TESS light curve (Sect. 2.1), the LCOGT light curves (Sect. 2.2), and the RVs listed in Table A.1 in our joint model.

Table 3. Comparison of models of the stellar mass and radius.

Method	$M_\star$ ($M_\odot$)	$R_\star$ ($R_\odot$)	$\rho_\star$ (g cm^{-3})
`ARIADNE`[(a)]	1.032 ± 0.038	1.043 ± 0.017	1.25 ± 0.09
Gravitational mass	1.0 ± 0.1	...	...
`BASTA`	0.973 ± 0.053	1.045 ± 0.025	1.20 ± 0.11
`PARAM 1.3`	0.982 ± 0.037	1.049 ± 0.034	1.23 ± 0.14
Gaia DR2	...	$1.103^{+0.027}_{-0.068}$	...

Notes. [(a)]Adopted for the modelling in Sect. 3.3.

The parametrisation of the limb darkening coefficients q_1 and q_2 was handled as per Kipping (2013), while the limb darkening model followed the quadratic approach by Mandel & Agol (2002). We placed a loose informative prior on the scaled semi-major axis, as well as on q_1 and q_2, based on the tables by Claret (2017) for the TESS band, and Claret et al. (2013) for the ground-based photometry. For the remaining parameters, we used uniform priors. We tested a model in putting a beta prior on the eccentricity of the planet and find an eccentricity consistent with zero. Given the short period of the planet, we thus assumed a circular orbit and sampled the parameter space using 250 independent chains thinned with a factor of ten and created posterior distributions with the last 5000 iterations. This translates to 125 000 points for each sampled parameter per distribution.

We first carried out a sampling for the independent scaled planet radii ($R_p/R_\star$) for the TESS and each of the LCOGT bands. We obtain values of $R_{\rm SAAO} = 3.37^{+0.36}_{-0.57}\ R_\oplus$, $R_{\rm CTIO} = 3.42^{+0.58}_{-0.36}\ R_\oplus$, $R_{\rm SSO} = 3.34 \pm 0.37\ R_\oplus$, and $R_{\rm TESS} = 3.61 \pm 0.26\ R_\oplus$ individually, thus demonstrating independent detections from each facility and full consistency (within 1 σ) between the different estimates. We thereby assumed the same transit depth for each band for our final model.

The RV times series with the best-fitting RV model is shown in Fig. 6, which clearly displays a linear trend in the RVs pointing toward the presence of an outer companion (see Sect. 3.4). The model containing the linear trend is significantly favoured over the one with no trend (ΔBIC = 54). The RVs folded to the orbital period of the planet are shown in Fig. 7 with the RV model and

[11] https://github.com/timkahlke/BASTA
[12] http://stev.oapd.inaf.it/cgi-bin/param_1.3
[13] https://github.com/oscaribv/pyaneti

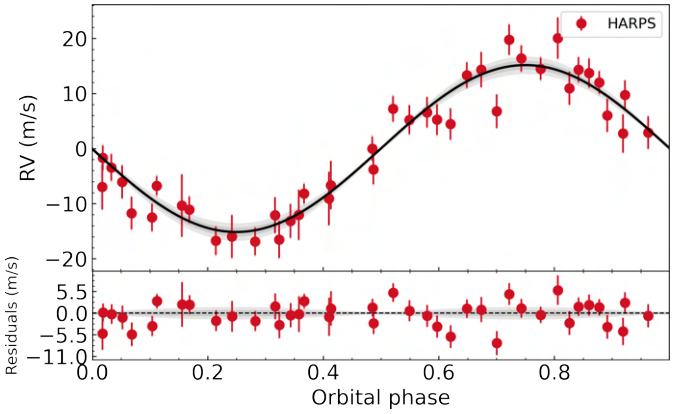

Fig. 7. HARPS radial velocity data phase-folded on the orbital period of TOI-2196 b after subtraction of the stellar systemic velocity and the linear trend. The solid black line is the RV model with 1 σ and 2 σ credible intervals in shaded grey areas.

1 σ and 2 σ credible intervals in shaded grey areas. The four light curves of TOI-2196 b are shown in Fig. 8, together with the best-fit transit model with a single radius plotted in solid black in each panel.

All results and priors are listed in Table 4 along with the adopted stellar parameters derived in Sect. 3.2 used in the modelling. All adopted stellar parameters are also listed in Table 1.

3.4. Evidence of an outer companion

The assumption of a long-period companion is supported by the periodogram (panel 2 in Fig. 4) and the linear trend in the RV data (Table 4 and Fig. 6). We computed the minimum mass of this outer companion, here denoted with c, using the measured linear trend of -0.238 ± 0.019 m s^{-1} day^{-1} from our RV analysis in Sect. 3.3 and Eq. (2) of Bowler (2016):

$$\frac{M_c}{a_c^2} > 0.0145 \left| \frac{\dot{\gamma}}{\mathrm{m\ s^{-1}\ yr^{-1}}} \right| = 1.3\ M_J\ \mathrm{au}^{-2}, \quad (1)$$

where $\dot{\gamma}$ is the slope of the linear trend (acceleration), and a_c is the minimum semi-major axis compatible with the RV data. Following Smith et al. (2017), we assumed zero eccentricity and a minimum orbital period of twice the baseline of our RV measurements ($P_{\mathrm{orb,c}} > 222$ days), resulting in a minimum semi-major axis of 0.717 $\pm$ 0.009 au and a corresponding minimum mass of 0.65 $\pm$ 0.05 M_J.

We note that the *Gaia* renormalised unit weight error (RUWE) value[14] is 0.99 for TOI-2196, corresponding to a low astrometric signal. This implies that a low-mass stellar companion scenario is unlikely. However, future long-term RV monitoring of the star is needed to firmly determine the nature of the signal.

4. Discussion

4.1. The hot Neptune desert

TOI-2196 b is one of very few planets found in the hot Neptune desert (shown in Fig. 9). In this figure, we plot in grey the radius of all known planets with radius measurements from transit surveys with a precision of 10% or better as a function of equilibrium temperature. About a third of the planets in Fig. 9 also have masses from RV measurements with a precision of 30% or better and are colour-coded with mass. The data were downloaded from the NASA Exoplanet archive[15] and

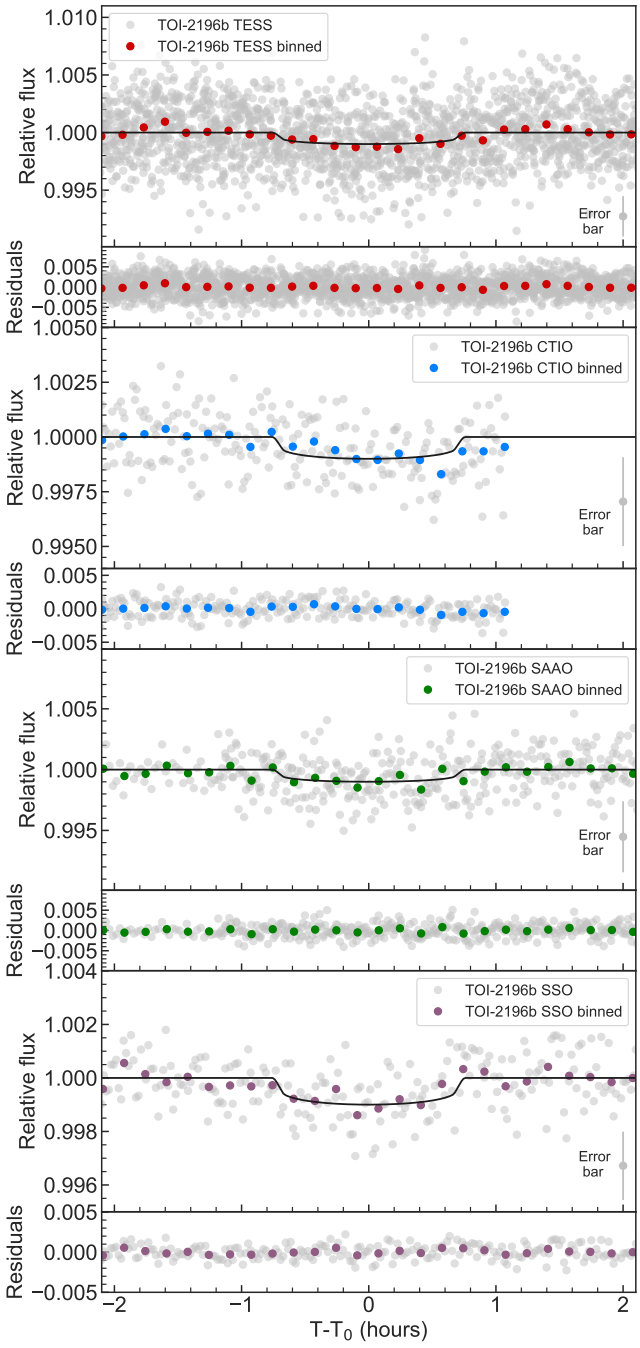

Fig. 8. Flattened and phase-folded TESS light curve with the best-fitting transit model in black in the *top panel*, and follow-up photometry from ground performed with the LCOGT CTIO, SAAO, and SSO telescopes in the *second to fourth panels* as marked in the legends. The CTIO and SSO panels show the single transits those facilities observed, while the SAAO panel shows the two stacked transits detected with that telescope. The nominal short cadence data are plotted in grey in all panels and binned to 10 min in colour.

[14] https://gea.esac.esa.int/archive/documentation/GDR2/Gaia_archive/chap_datamodel/sec_dm_main_tables/ssec_dm_ruwe.html

[15] https://exoplanetarchive.ipac.caltech.edu

Table 4. Description of the `pyaneti` model of TOI-2196 b from Sect. 3.3 and the adopted stellar parameters used in the model from Sect. 3.2.

Parameter	Units	Priors [a]	Final value
Stellar parameters			
$M_\star$	Stellar mass ($M_\odot$)	$\mathcal{F}[1.032]$	1.032 ± 0.038
$R_\star$	Stellar radius ($R_\odot$)	$\mathcal{F}[1.043]$	1.043 ± 0.017
$T_{\rm eff}$	Effective temperature (K)	$\mathcal{F}[5634]$	5634 ± 31
Fitted parameters			
T_0	Transit epoch ($\mathrm{BJD_{TDB}}$ - 2 457 000)	$\mathcal{U}[2036.4888, 2036.5288]$	$2036.5126^{+0.0019}_{-0.0016}$
$P_{\rm orb}$	Orbital period (days)	$\mathcal{U}[1.1943, 1.1963]$	$1.1947268^{+7.9e-06}_{-9.3e-06}$
e	Eccentricity	$\mathcal{F}[0]$	0
ω	Argument of periastron (degrees)	$\mathcal{F}[90]$	90
b	Impact parameter	$\mathcal{U}[0, 1]$	$0.712^{+0.034}_{-0.036}$
$a/R_\star$	Scaled semi-major axis	$\mathcal{N}[4.6, 0.1]$	4.61 ± 0.10
$R_{\rm p}/R_\star$	Scaled planet radius	$\mathcal{U}[0.01, 0.10]$	$0.0308^{+0.0013}_{-0.0012}$
K	Doppler semi-amplitude variation (m s^{-1})	$\mathcal{U}[0, 50]$	$15.16^{+0.67}_{-0.69}$
q_1	Limb-darkening coefficient, TESS	$\mathcal{N}[0.26, 0.10]$	0.27 ± 0.10
q_2	Limb-darkening coefficient, TESS	$\mathcal{N}[0.47, 0.10]$	0.47 ± 0.10
q_1	Limb-darkening coefficient, LCOGT CTIO	$\mathcal{N}[0.52, 0.10]$	0.51 ± 0.10
q_2	Limb-darkening coefficient, LCOGT CTIO	$\mathcal{N}[0.17, 0.10]$	0.18 ± 0.09
q_1	Limb-darkening coefficient, LCOGT SSO	$\mathcal{N}[0.52, 0.10]$	0.54 ± 0.10
q_2	Limb-darkening coefficient, LCOGT SSO	$\mathcal{N}[0.17, 0.10]$	0.18 ± 0.09
q_1	Limb-darkening coefficient, LCOGT SAAO	$\mathcal{N}[0.52, 0.10]$	0.53 ± 0.10
q_2	Limb-darkening coefficient, LCOGT SAAO	$\mathcal{N}[0.17, 0.10]$	0.17 ± 0.10
Derived parameters			
$M_{\rm b}$	Planet mass ($M_\oplus$)	...	26.0 ± 1.3
$R_{\rm b}$	Planet radius ($R_\oplus$)	...	3.51 ± 0.15
i [b]	Inclination (degrees)	...	$81.11^{+0.57}_{-0.55}$
a	Semi-major axis (au)	...	0.02234 ± 0.00060
F	Instellation ($F_\oplus$)	...	2000 ± 100
$\rho_{\rm b}$	Planet density (g cm^{-3})	...	$3.31^{+0.51}_{-0.43}$
$g_{\rm b}$	Planet surface gravity (cm s^{-2})	...	2100 ± 200
$T_{\rm eq}$ [c]	Equilibrium temperature (K)	...	1860 ± 20
Λ [d]	Jeans escape parameter	...	30 ± 2
TSM [e]	Transmission spectroscopy metric	...	$25.8^{+3.6}_{-3.3}$
T_{14}	Total transit duration (h)	...	$1.504^{+0.054}_{-0.059}$
T_{23}	Full transit duration (h)	...	$1.325^{+0.065}_{-0.072}$
T_{12}	Ingress and egress transit duration (h)	...	$0.0892^{+0.0087}_{-0.0076}$
Additional parameters			
$\dot{\gamma}_1$	Linear trend HARPS (m s^{-1} days^{-1})	$\mathcal{U}[-100, 100]$	-0.238 ± 0.019
$\dot{\gamma}_1$	Systemic velocity HARPS (km s^{-1})	$\mathcal{U}[-1.0218, 1.0208]$	0.1008 ± 0.0079
σ_{F1}	RV jitter HARPS (m s^{-1})	$\mathcal{J}[10^{-3}, 10^{-1}]$	$1.2^{+0.77}_{-0.80}$
$\sigma_{\rm TESS}$	TESS light curve jitter	$\mathcal{J}[10^{-2}, 10^{-3}]$	$0.002433 \pm 1.7e-05$
$\sigma_{\rm CTIO}$	LCOGT CTIO light curve jitter	$\mathcal{J}[10^{-2}, 10^{-3}]$	$0.001376^{+5.1e-05}_{-4.8e-05}$
$\sigma_{\rm SSO}$	LCOGT SSO light curve jitter	$\mathcal{J}[10^{-2}, 10^{-3}]$	$0.000939^{+3.9e-05}_{-3.7e-05}$
$\sigma_{\rm SAAO}$	LCOGT SAAO light curve jitter	$\mathcal{J}[10^{-2}, 10^{-3}]$	$0.001706^{+5.4e-05}_{-5.0e-05}$

Notes. [a]$\mathcal{U}[a, b]$ refers to uniform priors in the range a– b, $\mathcal{F}[a]$ to a fixed value a, $\mathcal{N}[a, b]$ to Gaussian priors with mean a and standard deviation b, and $\mathcal{J}[a, b]$ to modified Jeffrey's priors (Eq. (16) in Gregory 2005). [b]Orbit inclination relative to the plane of the sky. [c]Dayside equilibrium temperature, assuming no heat redistribution and zero albedo (Eq. (2)). [d]Jeans escape parameter defined as $\Lambda = GM_{\rm p}m_{\rm H}/(k_{\rm B}T_{\rm eq}R_{\rm p})$ in Fossati et al. (2017). [e]Kempton et al. (2018).

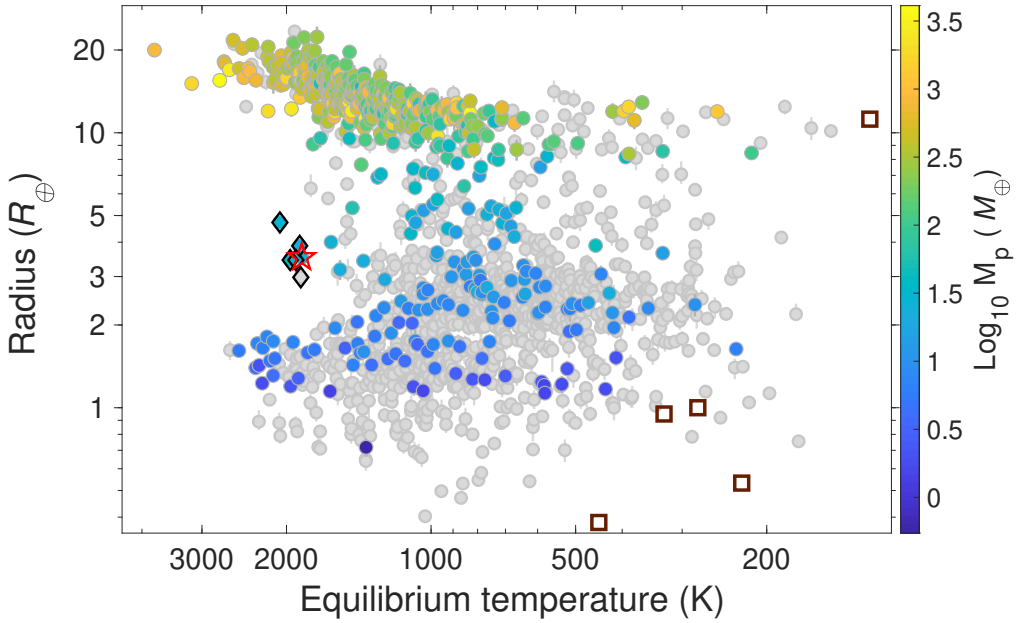

Fig. 9. Radius vs. equilibrium temperature diagram: known planets with a precision of 10% or better in radius are plotted in grey. About a third of these planets have also RV mass measurements with a precision of 30% or better and are colour-coded with planet mass. We set upper limits to planet masses at 13 M_J. TOI-2196 b is marked with a red star symbol, the five additional planets in the hot Neptune desert with black diamonds, and solar system planets with brown squares. The five additional planets located in the desert are: K2-100 b (Barragán et al. 2019a), TOI-849 b (Armstrong et al. 2020), LTT 9779 b (Jenkins et al. 2020b), K2-278 b (Livingston et al. 2018), and Kepler-644 b (Berger et al. 2018) of which the latter two have only radius measurements.

Table 5. Known sub-Neptune and Neptune planets in the hot Neptune desert (T_{eq} > 1800 K) with a precision in radius of 10% or better. In addition to TOI-2196 b, three of the planets have RV measurements with a precision of 30% or better.

Planet	Radius ($R_\oplus$)	Mass ($M_\oplus$)	Bulk density (g cm^{-3})	P_{orb} (days)	T_{eq} (K)	T_{eff} (K)	[Fe/H]	Λ [a]	Age (Gyr)	Ref.
TOI-2196 b	3.51 ± 0.15	26.0 ± 1.3	$3.31^{+0.51}_{-0.43}$	1.20	1860	5634	0.14 ± 0.05	29.6	4.5 ± 2.0	(b)
K2-278 b	2.98 ± 0.23	...	...	3.33	1867	6747	0.00 ± 0.17	...	...	(c)
K2-100 b	3.88 ± 0.16	21.8 ± 6.2	2.05 ± 0.64	1.67	1878	5945	0.22 ± 0.09	22.8	$0.75^{+0.004}_{-0.007}$	(d)
TOI-849 b	$3.44^{+0.16}_{-0.12}$	39.1 ± 2.6	5.26 ± 0.71	0.77	1966	5374	0.19 ± 0.03	43.9	$6.7^{+2.8}_{-2.4}$	(e)
Kepler-644 b	$3.44^{+0.18}_{-0.35}$	...	...	3.17	1912	6540	0.08 ± 0.15	...	$1.6^{+0.52}_{-0.32}$	(f)
LTT 9779 b	4.72 ± 0.23	29.3 ± 0.8	1.53 ± 0.23	0.79	2064	5443	0.27 ± 0.03	22.9	$1.9^{+1.7}_{-1.2}$	(g)

References. [a]Fossati et al. (2017). [b]This work. [c]Livingston et al. (2018). [d]Barragán et al. (2019a). [e]Armstrong et al. (2020). [f]Berger et al. (2018). [g]Jenkins et al. (2020b).

we chose the latest results with the highest precision for planets with several entries or, if they share a similar precision, we chose the most recent results. Since the information about equilibrium temperature is not always given by the references, we computed T_{eq} in the same way for all planets with (e.g. Charbonneau et al. 2005):

$$T_{eq} = \sqrt{\frac{R_\star}{2\,a}}\, T_{eff}\, [f\,(1 - A_B)]^{1/4}, \quad (2)$$

where a is the planet's semi-major axis (computed with Kepler III), A_B is the Bond albedo, and f is the heat redistribution factor. The latter two parameters are here assumed to be zero and unity, respectively. We prefer to use T_{eq} over orbital period since the latter does not take into account differences of stellar types which may give misleading results. With fixed Bond albedo and heat redistribution, an ultra-short period planet with P_{orb} < 1 day around an M-dwarf has a lower equilibrium temperature than a planet with an orbital period of several days orbiting a sun-like star.

The dearth of short-period Neptunes is clearly seen in Fig. 9. In this plot, the desert starts around 1600 K for medium-sized planets, which corresponds to orbital periods of 1.9 days around sun-like stars. For equilibrium temperatures higher than 1800 K, most planets have $R_p \lesssim 1.8\ R_\oplus$ or $R_p \gtrsim 1\ R_J$. In addition to TOI-2196 b, we identified five more planets confirmed in the desert, which are listed in Table 5: K2-100 b (Barragán et al. 2019a), TOI-849 b (Armstrong et al. 2020), LTT 9779 b (Jenkins et al. 2020b), K2-278 b (Livingston et al. 2018), and Kepler-644 b (Berger et al. 2018) of which the latter two have no mass measurements. This diagram suggests that this small group of planets delimits two regimes: a hot sub-Neptune desert for planets with radii between 1.8 and 3 $R_\oplus$, and a sub-Jovian desert for radii 5–12 $R_\oplus$. More planets in this parameter space are needed

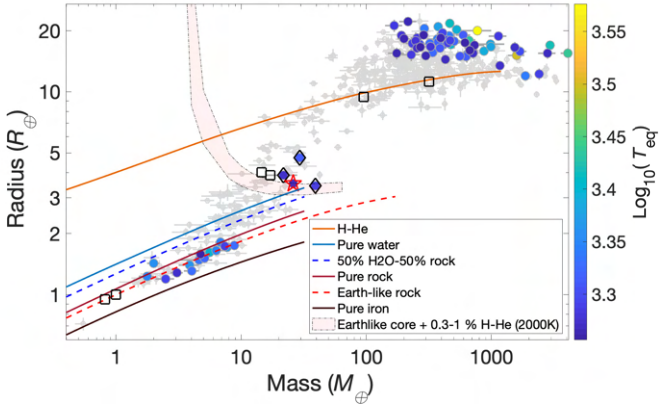

Fig. 10. Diagram of all known planets with masses from radial velocity measurements up to 13 M_J and radii from transit photometry with 30% and 10% uncertainties or lower in mass and radius, respectively. Planets with $T_{eq} \geq 1800$ K are colour-coded with T_{eq}, and the rest are plotted in light grey. In total, there are four planets (including TOI-2196 b) with radii between 3 and 5 $R_\oplus$ in this diagram that are identified as hot Neptune desert planets (cf. Fig. 9). TOI-2196 b is marked with a red star symbol and the three additional planets with black diamonds. Solar system planets are marked with brown squares. Interior models from Zeng et al. (2019) are plotted as listed in the legend. The 100% water line is for a planet with condensed water phases.

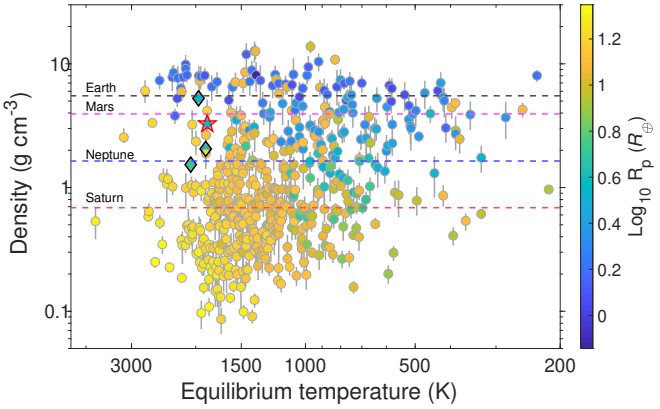

Fig. 11. Bulk density-equilibrium temperature diagram of the same planets as in Fig. 10 colour-coded here with planet radius. The densities of Earth, Mars, Neptune, and Saturn are marked with dashed-coloured lines.

to establish whether this is a selection effect or some kind of stability island in the desert.

In Fig. 10, we show the position of TOI-2196 b in a mass–radius diagram. We plot the same planets with both radii and RV masses as plotted in Fig. 9. Here, all planets are plotted in grey except for planets with $T_{eq} \geq 1800$ K which are colour-coded with equilibrium temperature. TOI-2196 b has a radius smaller than Neptune but an approximately 50% higher mass and, hence, twice Neptune's density. As already noted in Fig. 9, it joins the small group of the three planets found between small, rocky planets and gaseous giants. We also plot interior structure models from Zeng et al. (2019)[16] with and without the addition of atmospheres as listed in the legend. According to these models, the composition of TOI-2196 b is consistent with an Earth-like core with an 0.3–1% H-He atmosphere at an equilibrium temperature of 2000 K, and also lies slightly above a pure (condensed) water planet model. We investigated the atmospheric loss and interior composition with a model that considers water or H/He phases for highly-irradiated planets such as TOI-2196 b in Sects. 4.2 and 4.3, respectively.

To allow for a comparison to both previous plots, we plotted planet bulk densities versus equilibrium temperatures in Fig. 11, colour-coded according to planetary radius. The hot Neptune desert is also visible in this plot, albeit less prominent since planets with $\gtrsim 1$ M_J have increasingly higher densities, thereby filling in the lower parts of the $\rho - T_{eq}$ desert. Most planets in this plot with high T_{eq} have either high densities or large radii if the densities are low.

To investigate any potential correlations with stellar metallicity, we plotted the radius versus the iron abundance relative to hydrogen in Fig. 12. In panel a) we plot all planets and in panel b) we plot planets with $T_{eq} \geq 1800$ K. We note that all hot Neptune desert planets have greater than solar iron abundances, although the sample is too small to draw any firm conclusions.

[16] https://lweb.cfa.harvard.edu/~lzeng/planetmodels.html

4.2. Atmospheric loss

Planets in close proximity to their host stars are exposed to high levels of X-ray and extreme UV radiation (XUV) that can erode planetary atmospheres. If the escape is energy limited, the atmospheric mass loss rate of TOI-2196 b can be written as (Erkaev et al. 2007; Owen & Wu 2013):

$$\dot{M} = \epsilon \frac{\pi F_{XUV} R_p^3}{G M_p}, \quad (3)$$

where F_{XUV} is the XUV flux received by the planet, G the gravitational constant, and ϵ is an efficiency parameter. Planets with low densities in close orbits are most susceptible to mass loss, with ϵ that can also depend on the mass and radius of the planet (Owen & Jackson 2012). Since the mass of the atmosphere of average sub-Neptunes is typically 1−10% of the planetary mass (Lopez & Fortney 2014), atmospheric loss is possible and can transform the planet into a rocky super-Earth (Lopez & Fortney 2013; Owen & Wu 2013).

The XUV irradiation produced by solar-type stars is the most prominent at the earliest stage of their evolution (saturation regime). After this stage, the XUV luminosity decreases with time. For a 1 $M_\odot$ star, we estimate that the saturation regime lasts 30 Myr and emits 1.1×10^{31} erg s^{-1} of XUV (Sanz-Forcada et al. 2011), resulting in a mass loss rate of 6.9 $M_\oplus$ Gyr^{-1} for TOI-2196 b. While the XUV irradiation decreases with time after the saturation regime, it continues to contribute to atmospheric losses over ∼1 Gyr. To quantify this effect, we followed the approach of Aguichine et al. (2021) and integrated the average XUV radiation produced by a 1 $M_\odot$ star (Sanz-Forcada et al. 2011), assuming that the planet properties remained roughly constant during its evolution. With an efficiency of 5% (see Fig. 13 of Owen & Jackson 2012), we found that TOI-2196 b has lost ∼0.8 $M_\oplus$ of H/He. This implies that TOI-2196 b could have formed with a volatile mass fraction of 4–6%, and lost 50% to 90% of its atmosphere, a result that is consistent with the findings of Estrela et al. (2020).

Rapidly rotating stars can have longer saturation regimes, lasting up to 300 Myr (Tu et al. 2015; Poppenhaeger et al. 2021). When setting the duration of the saturation regime to 300 Myr, that is, ten times longer than in the computation above, the planet receives almost ten times more XUV energy, thus increasing the

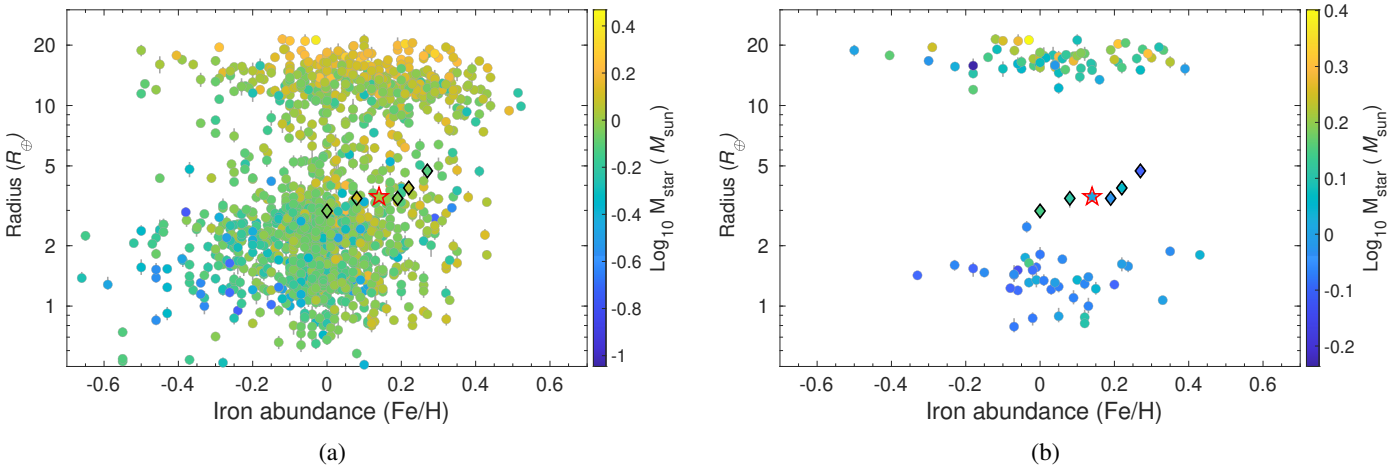

Fig. 12. Planet radius vs. iron abundance diagram of the same planets as in Fig. 9. In *a*) colour-coded with stellar mass and *b*) showing only planets with $T_{eq} \geq 1800$ K, which corresponds to $P_{orb} \lesssim 1.3$ d for a sun-like star assuming zero Bond albedo and a heat redistribution factor of unity, or $P_{orb} \lesssim 0.43$ day for a K5 V star.

total lost mass by a factor of 10 (see Eq. (3)). In this extreme case, we estimate a mass loss corresponding to ~8 $M_\oplus$ of H/He envelope, placing the initial volatile mass fraction of TOI-2196 b at 35%. An envelope that massive contradicts the observed 1–10% range for sub-Neptunes, suggesting moderate or low activity levels for TOI-2196. However, these computations assume a constant planet mass and radius over time. The mass loss estimates should consider the coupling of the mass loss and interior structure. The apparent correlation between the planet age and the Jeans escape parameter Λ in Table 5 is supported by the study of Rossati et al. (2017). They found that planets with $\Lambda \geq 15$–35 experience important mass loss until their mass or radius (or both) adapts to increase Λ. We conclude that TOI-2196 b experienced atmospheric mass loss, which may still be taking place with a present-day mass loss rate of 0.01 $M_\oplus$ Gyr^{-1}. Its atmosphere has, however, not yet been removed entirely, placing it in the sub-Neptune category of exoplanets. The decrease in the mass-loss rate that prevented TOI-2196 b from losing its atmosphere could possibly be due to a change in the atmospheric composition. Atomic hydrogen, which can be produced by photo-dissociation of H_2 or H_2O, tends to escape at high rates mostly because of its low mass, but also because of its long radiative cooling time. A longer radiative cooling time implies that the gas will lose its heat through mechanical work, that is, through evaporative flow, rather than through radiation (Owen & Jackson 2012). A selective loss of H could result in atmospheres that are dominated by He, O_2, H_2O, or other heavy species with much lower escape rates (see Hu et al. 2015; Bolmont et al. 2017; Aguichine et al. 2021; Ito & Ikoma 2021, respectively). Since this planet inhabits a sparsely populated part of the radius versus equilibrium temperature diagram, it is a good candidate to study exceptions to the evaporation valley and evaporating planets in general.

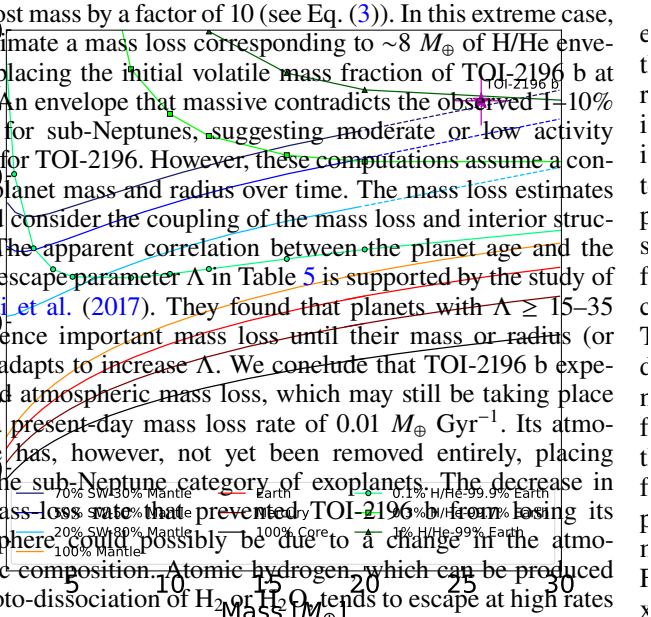

Fig. 13. Position of TOI-2196 b in the mass-radius diagram. We also show mass-radius relationships for dry planets with different core mass fractions (Brugger et al. 2016, 2017), water planets with varying supercritical water (SW) contents (Mousis et al. 2020; Acuna et al. 2021) and Earth and volatile mass fraction would be around 6 $R_\oplus$, according to the mass-radius relation of 5 % H/He from Zeng et al. (2019), which changes the density from 3.3 g cm^{-3} to 0.7 g cm^{-3}. This shifts the position of TOI-2196 b in the density diagram in Fig. 11 downwards to the Saturn density with the difference of having a much lower mass than the gas giants in this parameter space. If we place the planet with the past radius and mass in the mass-radius diagram, it would be slightly above the small group of planets that includes LTT 9779 b, K2-100 b, and TOI-849 b, but still located in the hot Neptune desert and would still be classified as a planet in the Neptune regime, not a gaseous giant.

4.3. Internal structure

If the composition of TOI-2196 b would partly include volatiles such as H/He or water, these elements would be in high-pressure and high-temperature phases due to the thickness of the volatile envelope. In Fig. 13, we compare TOI-2196 b with mass-radius relations of planets with several different amounts of water in a supercritical state calculated with the CMPE presented in Mousis et al. (2020) and Acuna et al. (2021), and with those of rocky planets with gaseous H/He atmospheres (Zeng et al. 2019). TOI-2196 b lies slightly above the 70% supercritical water (SW) composition under the assumption of a 100% mantle bulk. If we were to assume a core mass fraction (CMF) in agreement with its host stellar abundances (Table 6), the water content would increase since we would have to fit a similar total density with a more dense core. A water mass fraction (WMF) of ~70% is

5. Conclusions

We present the detection and the analysis of the hot and volatile rich planet TOI-2196 b. It is smaller than Neptune but 50 % more massive resulting in a high bulk density for this type of planet.

Fig. 13: Position of TOI-2196 b in the mass-radius diagram. We also show mass-radius relationships for dry planets with different core mass fractions (Brugger et al. 2016; Brugger et al. 2017), water planets with varying supercritical water (SW) contents (Mousis et al. 2020; Acuna et al. 2021) and Earth-like cores with different H/He mass fractions (Zeng et al. 2019). We assume equilibrium temperatures of 1200 K and 2000 K for water planets and rocky planets with H/He atmospheres, respectively. Dashed lines indicate an extrapolation of the SW relations beyond their valid mass ranges. The lines for Earth, Mercury, and 100 % core are lines of constant composition of respective type of planet.

and Mg/Si = 1.192±0.337. The MCMC analysis yields posterior distribution functions (PDF) of the core mass fraction and the H/He mass fraction.

The CMF and the H/He mass fraction, $M_{H/He}$, represent our free parameters in the MCMC analysis. The CMF in scenario 1 is sampled as a uniform distribution between 0 and 1 which are the minimum and maximum values of the compositional param-

Table 6. MCMC parameters of the interior structure analysis and their 1 σ confidence intervals for scenario 1 (planet mass and radius as input) and scenario 2 (Fe/Si mole ratio in addition to mass and radius as input).

Parameter	Scenario 1	Scenario 2
CMF [(a)]	$\mathcal{U}(0,1)$	$0.244^{+0.057}_{-0.049}$
CRF [(b)]	$0.45^{+0.05}_{-0.14}$	$0.31^{+0.03}_{-0.02}$
$x_{H/He}$ [(c)]	$0.0077^{+0.0094}_{-0.0032}$	$0.0066^{+0.0031}_{-0.0020}$
M ($M_\oplus$)	26.031±1.389	$25.998^{+1.410}_{-1.360}$
R ($R_\oplus$)	3.517±0.170	$3.470^{+0.202}_{-0.127}$
Fe/Si	$6.261^{+11.538}_{-6.261}$	0.747±0.175
z_{atm} [(d)] (km)	8143^{+1662}_{-1289}	7185^{+1298}_{-840}

Notes. [(a)]Core mass fraction. [(b)]Core radius fraction simultaneously computed with the CMF. [(c)]Hydrogen and helium mass fraction. [(d)]Planet atmosphere thickness.

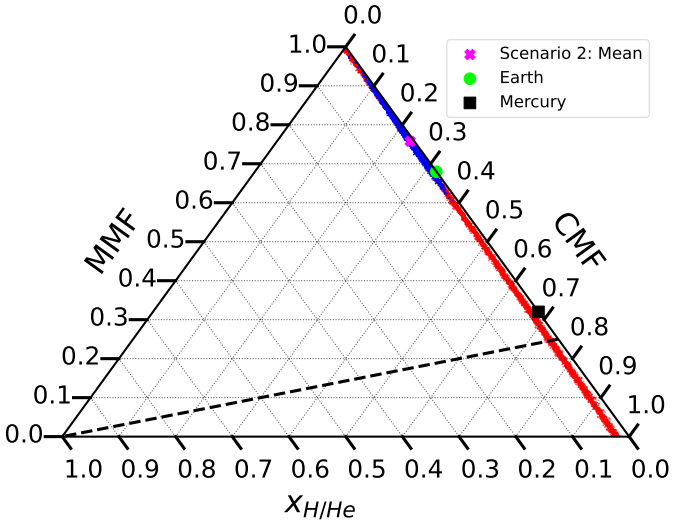

Fig. 14. Ternary diagram of the MCMC models for TOI-2196 b in scenario 1 (red), with the planet mass and the radius as input to the model, and in scenario 2 (blue), where also the stellar abundances are included. The mantle mass fraction (MMF) is defined as MMF = 1 – CMF – $x_{H/He}$ where the latter parameter is the H/He mass fraction and CMF is the core mass fraction. The green circle and black square indicate the position of Earth and Mercury in the ternary diagram, respectively. The maximum CMF constrained by planet formation is limited by the black dashed line (see Sect. 4.3).

similar to the maximum water content found in Solar System bodies (McKay et al. 2019). Thus, the atmosphere of TOI-2196 b is likely to be dominated by H/He which are less dense than water; otherwise, the water content of TOI-2196 b would be unrealistically high.

We therefore performed a MCMC Bayesian analysis (Acuña et al. 2021; Director et al. 2017) of the internal composition of TOI-2196 b assuming a H/He atmosphere. Following Brugger et al. (2016, 2017), we included two layers: an Fe-rich core and a silicate-rich mantle. To the calculated radius of the interior, we added the thickness of the H/He atmosphere, z_{atm}, to estimate the total planetary radius. We obtained the atmospheric thickness by subtracting the radius of a bare Earth-like core from the mass-radius relationships of an Earth-like core with a H/He atmosphere, presented by Zeng et al. (2019). The atmospheric thickness is then a function of the surface gravity, $g_0 = GM/R^2$, where G is the gravitational constant, and the H/He mass fraction, $z_{atm} = z_{atm}(g_0, x_{H/He})$. We set the surface conditions for the interior model as 2000 K and 1 bar, since Zeng et al. (2019) considered an isothermal temperature profile for their atmosphere. Changing our surface pressure to other values would have a trivial effect on our interior bulk radius, since this parameter does not have an influence on the total radius of solid mantle–core planets (Otegi et al. 2020).

We considered two scenarios to obtain the interior structure of TOI-2196 b. Scenario 1 uses the planet mass and radius as input to the MCMC analysis, while scenario 2 also uses the stellar Fe/Si and Mg/Si mole ratios (Table 2) as input. To compute the Fe/Si and Mg/Si mole ratios with the stellar abundances, we follow the approach depicted in Brugger et al. (2017) and Sotin et al. (2007) and obtain Fe/Si = 0.775 ± 0.170 and Mg/Si = 1.192 ± 0.337. The MCMC analysis yields posterior distribution functions (PDF) of the core mass fraction and the H/He mass fraction.

The CMF and the H/He mass fraction, $x_{H/He}$, represent our free parameters in the MCMC analysis. The CMF in scenario 1 is sampled as a uniform distribution between 0 and 1 which are the minimum and maximum values of the compositional parameters. In scenario 2, the CMF is constrained by the inclusion of the Fe/Si mole ratio as an input to the MCMC framework. This results in a mean value of the CMF of $0.244^{+0.057}_{-0.049}$ (Table 6) which is slightly lower than the CMF of Earth (0.32). The Earth value is, however, approximately at the limit of its 1 σ confidence interval as seen in Fig. 14. These results from scenario 2 are expected since the Fe/Si mole ratio of TOI-2196 b is lower than the solar value (0.96). The resulting mean value of the H/He mass fraction, $x_{H/He}$, is approximately 0.7% in both scenarios. In the case of scenario 2, the uncertainties are lower than in scenario 1. This is due to the use of the Fe/Si mole ratio, which breaks the degeneracy between the CMF and the H/He mass fraction in scenario 2. Both scenarios agree that the minimum volatile mass fraction is $\simeq$ 0.4%. In addition, we can consider scenario 1 as the most conservative one to derive the maximum volatile mass fraction for TOI-2196 b. The maximum CMF estimated from the protosolar nebula composition (Lodders et al. 2009) is 0.75. We mark this limit as a black dashed line in the ternary diagram in Fig. 14. We estimated the maximum volatile mass fraction as the $x_{H/He}$ at which this line crosses the red points that correspond to the MCMC simulations in scenario 1, which is approximately 3%.

In Sect. 4.2, we show that the past volatile mass fraction of TOI-2196 b was approximately 4–6%, with an accompanying increase in mass of 0.8 $M_\oplus$. The radius for a planet of such mass and volatile mass fraction would be around 6 $R_\oplus$, according to the mass–radius relation of 5% H/He from Zeng et al. (2019), which changes the density from 3.3 g cm^{-3} to 0.7 g cm^{-3}. This shifts the position of TOI-2196 b in the density diagram in Fig. 11 downwards to the Saturn density with the difference of having a much lower mass than the gas giants in this parameter space. If we place the planet with the past radius and mass in the mass-radius diagram, it would be slightly above the small group of planets that includes LTT 9779 b, K2-100 b, and TOI-849 b, but still located in the hot Neptune desert and would still be classified as a planet in the Neptune regime, not a gaseous giant.

5. Conclusions

We present the detection and the analysis of the hot and volatile rich planet TOI-2196 b. It is smaller than Neptune but 50% more

massive resulting in a high bulk density for this type of planet. Another interesting result is the presence of a longer period body in this system detected in the radial velocity measurements as a linear trend with a minimum mass of ~0.65 M_J, assuming zero eccentricity. The outer body may be a warm or cold gas-giant planet, although a brown dwarf, or a very low-mass stellar companion, cannot be fully excluded at the present stage. A future long-term RV monitoring of the star is needed to determine the true nature of the signal. We estimate the mass loss of volatiles for planet b at a young age and find that while the mass loss could have been significant, the planet has not changed in terms of its character. It formed as a small volatile-rich planet and has remained one until today. The high equilibrium temperature of 1860 K, together with its radius and mass, places TOI-2196 b in the hot Neptune desert as a member of a very small population found so far. This small population suggests that the desert is divided in two parts: a hot sub-Neptune desert ($R_p \approx 1.8$–$3\ R_\oplus$) and a sub-Jovian desert ($R_p \approx 5$–$12\ R_\oplus$). However, more planets are needed for further studies for this special region.

Acknowledgements. This paper includes data collected by the TESS mission. Funding for the TESS mission is provided by the NASA Explorer Program. We acknowledge the use of public TESS data from pipelines at the TESS Science Office and at the TESS Science Processing Operations Center. Resources supporting this work were provided by the NASA High-End Computing (HEC) Program through the NASA Advanced Supercomputing (NAS) Division at Ames Research Center for the production of the SPOC data products. This work makes use of observations from the LCOGT network. Part of the LCOGT telescope time was granted by NOIRLab through the Mid-Scale Innovations Program (MSIP). This work uses observations made with ESO 3.6-m telescope at La Silla Observatory under programme ID 106.21TJ.001. We are grateful to the ESO staff members for their support during the observations, and to François Bouchy and Xavier Dumusque for coordinating the HARPS time sharing agreement. This work has made use of SME package, which benefits from the continuing development work by J. Valenti and N. Piskunov and we gratefully acknowledge their continued support. (Kupka et al. 2000; Ryabchikova et al. 2015). to page 5 C.M.P., M.F., I.G., and J.K. gratefully acknowledges the support of the Swedish National Space Agency (DNR 65/19, 174/18, 177/19, 2020-00104). L.M.S and D.G. gratefully acknowledge financial support from the CRT foundation under Grant No. 2018.2323 "Gaseous or rocky? Unveiling the nature of small worlds". P.K. acknowledges support from grant LTT-20015. E.G. acknowledges the support of the Thüringer Ministerium für Wirtschaft, Wissenschaft und Digitale Gesellschaft. J.S.J. greatfully acknowledges support by FONDECYT grant 1201371 and from the ANID BASAL projects ACE210002 and FB210003. H.J.D. acknowledges support from the Spanish Research Agency of the Ministry of Science and Innovation (AEI-MICINN) under grant PID2019-107061GB-C66, DOI: 10.13039/501100011033. D.D. acknowledges support from the TESS Guest Investigator Program grants 80NSSC21K0108 and 80NSSC22K0185. M.E. acknowledges the support of the DFG priority program SPP 1992 "Exploring the Diversity of Extrasolar Planets" (HA 3279/12-1). K.W.F.L. was supported by Deutsche Forschungsgemeinschaft grants RA714/14-1 within the DFG Schwerpunkt SPP 1992, Exploring the Diversity of Extrasolar Planets. N.N. acknowledges support from JSPS KAKENHI Grant Number JP18H05439, JST CREST Grant Number JPMJCR1761. M.S.I.P. is funded by NSF.

References

Acuña, L., Deleuil, Magali, Mousis, Olivier, et al. 2021, A&A, 647, A53
Adams, F. C., & Laughlin, G. 2006, ApJ, 649, 1004
Aguichine, A., Mousis, O., Deleuil, M., & Marcq, E. 2021, ApJ, 914, 84
Aguirre Børsen-Koch, V., Rørsted, J. L., Justesen, A. B., et al. 2022, MNRAS, 509, 4344
Allard, F., Homeier, D., & Freytag, B. 2012, Philos. Trans. Roy. Soc. Lond. A, 370, 2765
Anglada-Escudé, G., & Butler, R. P. 2012, ApJS, 200, 15
Armstrong, D. J., Lopez, T. A., Adibekyan, V., et al. 2020, Nature, 583, 39
Baranne, A., Queloz, D., Mayor, M., et al. 1996, A&AS, 119, 373
Barragán, O., Aigrain, S., Kubyshkina, D., et al. 2019a, MNRAS, 490, 698
Barragán, O., Gandolfi, D., & Antoniciello, G. 2019b, MNRAS, 482, 1017
Barragán, O., Aigrain, S., Rajpaul, V. M., & Zicher, N. 2022a, MNRAS, 509, 866
Barragán, O., Armstrong, D. J., Gandolfi, D., et al. 2022b, MNRAS, 514, 1606
Benítez-Llambay, P., Masset, F., & Beaugé, C. 2011, A&A, 528, A2
Berger, T. A., Huber, D., Gaidos, E., & van Saders, J. L. 2018, ApJ, 866, 99
Bolmont, E., Selsis, F., Owen, J. E., et al. 2017, MNRAS, 464, 3728
Borucki, W. J., Koch, D., Basri, G., et al. 2010, Science, 327, 977
Bowler, B. P. 2016, PASP, 128, 102001
Brown, T. M., Baliber, N., Bianco, F. B., et al. 2013, PASP, 125, 1031
Brugger, B., Mousis, O., Deleuil, M., & Lunine, J. I. 2016, ApJ, 831, L16
Brugger, B., Mousis, O., Deleuil, M., & Deschamps, F. 2017, ApJ, 850, 93
Bruntt, H., De Cat, P., & Aerts, C. 2008, A&A, 478, 487
Cabrera, J., Csizmadia, S., Erikson, A., Rauer, H., & Kirste, S. 2012, A&A, 548, A44
Castelli, F., & Kurucz, R. L. 2004, ArXiv e-prints [astro-ph/0405087]
Charbonneau, D., Allen, L. E., Megeath, S. T., et al. 2005, ApJ, 626, 523
Chen, H., & Rogers, L. A. 2016, ApJ, 831, 180
Choi, J., Dotter, A., Conroy, C., et al. 2016, ApJ, 823, 102
Claret, A. 2017, A&A, 600, A30
Claret, A., Hauschildt, P. H., & Witte, S. 2013, A&A, 552, A16
Collins, K. 2019, American Astronomical Society Meeting Abstracts, 233, 140.05
Collins, K. A., Kielkopf, J. F., Stassun, K. G., & Hessman, F. V. 2017, AJ, 153, 77
da Silva, L., Girardi, L., Pasquini, L., et al. 2006, A&A, 458, 609
Director, H. M., Gattiker, J., Lawrence, E., & Wiel, S. V. 2017, J. Stat. Comput. Simul., 87, 3521
Doyle, A. P., Davies, G. R., Smalley, B., Chaplin, W. J., & Elsworth, Y. 2014, MNRAS, 444, 3592
Erkaev, N. V., Kulikov, Y. N., Lammer, H., et al. 2007, A&A, 472, 329
Estrela, R., Swain, M. R., Gupta, A., Sotin, C., & Valio, A. 2020, ApJ, 898, 104
Findeisen, K., Hillenbrand, L., & Soderblom, D. 2011, AJ, 142, 23
Foreman-Mackey, D., Hoyer, S., Bernhard, J., & Angus, R. 2014, https://doi.org/10.5281/zenodo.11989
Fossati, L., Erkaev, N. V., Lammer, H., et al. 2017, A&A, 598, A90
Fridlund, M., Gaidos, E., Barragán, O., et al. 2017, A&A, 604, A16
Fulton, B. J., Petigura, E. A., Howard, A. W., et al. 2017, AJ, 154, 109
Georgieva, I. Y., Persson, C. M., Barragán, O., et al. 2021, MNRAS, 505, 4684
Ginzburg, S., Schlichting, H. E., & Sari, R. 2018, MNRAS, 476, 759
Gregory, P. C. 2005, ApJ, 631, 1198
Gupta, A., & Schlichting, H. E. 2019, MNRAS, 487, 24
Hidalgo, S. L., Pietrinferni, A., Cassisi, S., et al. 2018, ApJ, 856, 125
Hu, R., Seager, S., & Yung, Y. L. 2015, ApJ, 807, 8
Husser, T. O., Wende-von Berg, S., Dreizler, S., et al. 2013, A&A, 553, A6
Ito, Y., & Ikoma, M. 2021, MNRAS, 502, 750
Jenkins, J. M. 2002, ApJ, 575, 493
Jenkins, J. M., Chandrasekaran, H., McCauliff, S. D., et al. 2010, SPIE Conf. Ser., 7740, 77400D
Jenkins, J. M., Twicken, J. D., McCauliff, S., et al. 2016, SPIE Conf. Ser., 9913, 99133E
Jenkins, J. M., Tenenbaum, P., Seader, S., et al. 2020a, Kepler Data Processing Handbook: Transiting Planet Search, Kepler Science Document KSCI-19081-003
Jenkins, J. S., Díaz, M. R., Kurtovic, N. T., et al. 2020b, Nat. Astron., 4, 1148
Jin, S., Mordasini, C., Parmentier, V., et al. 2014, ApJ, 795, 65
Kempton, E. M. R., Bean, J. L., Louie, D. R., et al. 2018, PASP, 130, 114401
Kipping, D. M. 2013, MNRAS, 435, 2152
Kubyshkina, D., Lendl, M., Fossati, L., et al. 2018, A&A, 612, A25
Kuerster, M., Schmitt, J. H. M. M., Cutispoto, G., & Dennerl, K. 1997, A&A, 320, 831
Kupka, F. G., Ryabchikova, T. A., Piskunov, N. E., Stempels, H. C., & Weiss, W. W. 2000, Baltic Astron., 9, 590
Kurucz, R. L. 1993, VizieR Online Data Catalog: VI/39
Kurucz, R. L. 2013, ATLAS12: Opacity sampling model atmosphere program, Astrophysics Source Code Library [record ascl:1303.024]
Li, J., Tenenbaum, P., Twicken, J. D., et al. 2019, PASP, 131, 024506
Livingston, J. H., Crossfield, I. J. M., Petigura, E. A., et al. 2018, AJ, 156, 277
Lodders, K., Palme, H., & Gail, H. P. 2009, Landolt Börnstein, 4B, 712
Lopez, E. D., & Fortney, J. J. 2013, ApJ, 776, 2
Lopez, E. D., & Fortney, J. J. 2014, ApJ, 792, 1
Lovis, C., & Pepe, F. 2007, A&A, 468, 1115
Lundkvist, M. S., Kjeldsen, H., Albrecht, S., et al. 2016, Nat. Commun., 7, 11201
Mamajek, E. E., & Hillenbrand, L. A. 2008, ApJ, 687, 1264
Mandel, K., & Agol, E. 2002, ApJ, 580, L171
Mayor, M., Pepe, F., Queloz, D., et al. 2003, The Messenger, 114, 20
Mazeh, T., Nachmani, G., Holczer, T., et al. 2013, ApJS, 208, 16
Mazeh, T., Holczer, T., & Faigler, S. 2016, A&A, 589, A75

McCully, C., Volgenau, N. H., Harbeck, D.-R., et al. 2018, SPIE Conf. Ser., 10707, 107070K
McKay, A. J., DiSanti, M. A., Kelley, M. S. P., et al. 2019, AJ, 158, 128
Mousis, O., Deleuil, M., Aguichine, A., et al. 2020, ApJ, 896, L22
Otegi, J. F., Dorn, C., Helled, R., et al. 2020, A&A, 640, A135
Owen, J. E., & Jackson, A. P. 2012, MNRAS, 425, 2931
Owen, J. E., & Lai, D. 2018, MNRAS, 479, 5012
Owen, J. E., & Wu, Y. 2013, ApJ, 775, 105
Parviainen, H. 2015, MNRAS, 450, 3233
Pepe, F., Mayor, M., Galland, F., et al. 2002, A&A, 388, 632
Persson, C. M., Fridlund, M., Barragán, O., et al. 2018, A&A, 618, A33
Petigura, E. A., Rogers, J. G., Isaacson, H., et al. 2022, AJ, 163, 179
Piskunov, N., & Valenti, J. A. 2017, A&A, 597, A16
Poppenhaeger, K., Ketzer, L., & Mallonn, M. 2021, MNRAS, 500, 4560
Ricker, G. R., Winn, J. N., Vanderspek, R., et al. 2015, J. Astron. Telescopes Instrum. Syst., 1, 014003
Ryabchikova, T., Piskunov, N., Kurucz, R. L., et al. 2015, Phys. Scr, 90, 054005
Sanchis-Ojeda, R., Rappaport, S., Winn, J. N., et al. 2014, ApJ, 787, 47
Sanz-Forcada, J., Micela, G., Ribas, I., et al. 2011, A&A, 532, A6
Schlegel, D. J., Finkbeiner, D. P., & Davis, M. 1998, ApJ, 500, 525
Smith, A. M. S., Gandolfi, D., Barragán, O., et al. 2017, MNRAS, 464, 2708
Sotin, C., Grasset, O., & Mocquet, A. 2007, Icarus, 191, 337
Stumpe, M. C., Smith, J. C., Catanzarite, J. H., et al. 2014, PASP, 126, 100
Szabó, G. M., & Kiss, L. L. 2011, ApJ, 727, L44
Tokovinin, A. 2018, PASP, 130, 035002
Tu, L., Johnstone, C. P., Güdel, M., & Lammer, H. 2015, A&A, 577, A3
Twicken, J. D., Catanzarite, J. H., Clarke, B. D., et al. 2018, PASP, 130, 064502
Valenti, J. A., & Piskunov, N. 1996, A&AS, 118, 595
Van Eylen, V., Agentoft, C., Lundkvist, M. S., et al. 2018, MNRAS, 479, 4786
Van Eylen, V., Astudillo-Defru, N., Bonfils, X., et al. 2021, MNRAS, 507, 2154
Vines, J. I., & Jenkins, J. S. 2022, MNRAS, 513, 2719
Yee, S. W., Petigura, E. A., & von Braun, K. 2017, ApJ, 836, 77
Zechmeister, M., & Kürster, M. 2009, A&A, 496, 577
Zechmeister, M., Reiners, A., Amado, P. J., et al. 2018, A&A, 609, A12
Zeng, L., Jacobsen, S. B., Sasselov, D. D., et al. 2019, Proc. Natl. Acad. Sci., 116, 9723
Ziegler, C., Tokovinin, A., Briceño, C., et al. 2020, AJ, 159, 19

[1] Department of Space, Earth and Environment, Chalmers University of Technology, Onsala Space Observatory, 439 92 Onsala, Sweden
e-mail: carina.persson@chalmers.se
[2] Dipartimento di Fisica, Universita degli Studi di Torino, via Pietro Giuria 1, 10125 Torino, Italy
[3] Aix Marseille Université, Institut Origines, CNRS, CNES, LAM, Marseille, France
[4] Department of Space, Earth and Environment, Chalmers University of Technology, Chalmersplatsen 4, 412 96 Gothenburg, Sweden
[5] Thüringer Landessternwarte Tautenburg, Sternwarte 5, 07778 Tautenburg, Germany
[6] Astrobiology Center, 2-21-1 Osawa, Mitaka, Tokyo 181-8588, Japan
[7] National Astronomical Observatory of Japan, 2-21-1 Osawa, Mitaka, Tokyo 181-8588, Japan
[8] Department of Astronomy, The Graduate University for Advanced Studies (SOKENDAI), 2-21-1 Osawa, Mitaka, Tokyo, Japan
[9] Center for Astrophysics, Harvard & Smithsonian, 60 Garden Street, Cambridge, MA 02138, USA
[10] Division of Geological and Planetary Sciences, 1200 E California Blvd, Pasadena, CA 91125, USA
[11] Leiden Observatory, University of Leiden, PO Box 9513, 2300 RA Leiden, The Netherlands
[12] Núcleo de Astronomía, Facultad de Ingeniería y Ciencias, Universidad Diego Portales, Av. Ejército 441, Santiago, Chile
[13] Centro de Astrofísica y Tecnologías Afines (CATA), Casilla 36-D, Santiago, Chile
[14] Astronomical Institute of the Czech Academy of Sciences, Fričova 298, 25165 Ondřejov, Czech Republic
[15] Department of Physics and Kavli Institute for Astrophysics and Space Research, Massachusetts Institute of Technology, Cambridge, MA 02139, USA
[16] Sub-department of Astrophysics, Department of Physics, University of Oxford, Oxford OX1 3RH, UK
[17] Instituto de Astrofísica de Canarias, C. Via Lactea S/N, E-38205 La Laguna, Tenerife, Spain
[18] NASA Goddard Space Flight Center, Exoplanets and Stellar Astrophysics Laboratory (Code 667), Greenbelt, MD 20771, USA
[19] McDonald Observatory and Center for Planetary Systems Habitability, The University of Texas, Austin, TX USA
[20] Caltech/IPAC-NASA Exoplanet Science Institute, 770 S. Wilson Avenue, Pasadena, CA 91106, USA
[21] Universidad de La Laguna, Dept. de Astrofísica, 38206 La Laguna, Tenerife, Spain
[22] Department of Physics and Astronomy, University of New Mexico, 210 Yale Blvd NE, Albuquerque, NM 87106, USA
[23] Department of Astronomy and Tsinghua Centre for Astrophysics, Tsinghua University, Beijing 100084, PR China
[24] Rheinisches Institut für Umweltforschung an der Universität zu Köln, Aachener Strasse 209, 50931 Köln, Germany
[25] SUPA Physics and Astronomy, University of St. Andrews, Fife KY16 9SS Scotland, UK
[26] NASA Ames Research Center, Moffett Field, CA 94035, USA
[27] Department of Physics and Astronomy, University of Louisville, Louisville, KY 40292, USA
[28] Freie Universität Berlin, Institute of Geological Sciences, Malteserstr. 74-100, 12249 Berlin, Germany
[29] Institute of Planetary Research, German Aerospace Center (DLR), Rutherfordstrasse 2, 12489 Berlin, Germany
[30] Department of Astronomy & Astrophysics, University of Chicago, Chicago, IL 60637, USA
[31] Astrophysics Group, Cavendish Laboratory, University of Cambridge, J.J. Thomson Avenue, Cambridge CB3 0HE, UK
[32] Kavli Institute for Cosmology, University of Cambridge, Madingley Road, Cambridge CB3 0HA, UK
[33] Komaba Institute for Science, The University of Tokyo, 3-8-1 Komaba, Meguro, Tokyo 153-8902, Japan
[34] Mullard Space Science Laboratory, University College London, Holmbury St Mary, Dorking, Surrey RH5 6NT, UK
[35] Wild Boar Remote Observatory, San Casciano in val di Pesa, Firenze, 50026, Italy
[36] Department of Earth, Atmospheric, and Planetary Sciences, Massachusetts Institute of Technology, Cambridge, MA 02139, USA
[37] Department of Aeronautics and Astronautics, Massachusetts Institute of Technology, Cambridge, MA 02139, USA
[38] Department of Physics & Astronomy, Vanderbilt University, Nashville, TN 37235, USA
[39] Tsinghua International School, Beijing 100084, PR China
[40] Department of Astrophysical Sciences, Princeton University, Princeton, NJ 08544, USA
[41] SETI Institute, Mountain View, CA 94043, USA
[42] Societá Astronomica Lunae, Castelnuovo Magra, Italy
[43] Department of Physics, Engineering and Astronomy, Stephen F. Austin State University, 1936 North St, Nacogdoches, TX 75962, USA

Appendix A: HARPS data

Table A.1: Radial velocities and spectral activity indicators extracted from HARPS spectra.

BJD_{TBD} (days)	RV	σ_{RV}	BIS[a]	FHWM	σ_{FWHM}	dlW	σ_{dlW}	S-index	$\sigma_{S-index}$	H_α [a]	T_{exp}	SNR
-2457000	(m s^{-1})	(m s^{-1})	(m s^{-1})	(km s^{-1})	(km s^{-1})	(km s^{-1})	(km s^{-1})	—	—	—	(s)	@550 nm
2419.661798	0.016377394	0.002998808	-0.029284737	7.140376417	0.357018821	11.22278765	1.846614321	0.172559779	0.003497890	0.998197146	2100	28.4
2419.812144	0.020510551	0.002956139	-0.014619464	7.138481028	0.356924051	11.05843113	2.062412649	0.181116594	0.003877305	0.999901855	2100	29.1
2424.705788	0.018156264	0.002574676	-0.006295520	7.137545136	0.356877257	-1.018335758	1.512092568	0.160211164	0.002998846	0.995506908	2400	33.5
2427.626567	-0.000481393	0.001746737	-0.014103206	7.137688356	0.356884418	-8.910686514	1.508117865	0.162656713	0.002592005	1.005319679	2400	38.5
2427.810834	0.014869853	0.002302020	-0.014228541	7.151375312	0.357568766	-7.928578176	1.652097812	0.172320637	0.003198341	1.003490323	2400	37.9
2428.639266	-0.009267622	0.002545470	-0.011727208	7.143755477	0.357187774	2.109340183	1.791528912	0.161061807	0.003508646	0.989901071	2400	28.1
2428.720190	-0.009409333	0.002468478	-0.014294956	7.143700306	0.357185015	-5.089153308	1.945891805	0.164078903	0.003161212	0.985814569	2100	25.7
2428.793337	-0.005702919	0.003047684	-0.017037973	7.147611628	0.357380581	-0.909110563	1.543522493	0.171465389	0.004068059	0.988770164	2100	28.1
2429.600426	0.005566032	0.002201269	-0.022909545	7.142051926	0.357102596	-3.451494525	1.456484985	0.177564159	0.003168727	0.990316656	2400	32.4
2429.701720	-0.005281992	0.002460195	-0.018750634	7.154825057	0.357741253	-2.086622561	1.290738998	0.172611870	0.003022147	0.986268731	2400	31.1
2429.779264	-0.003881037	0.002363704	-0.003667828	7.149787004	0.357489350	-2.847121560	1.483978769	0.182034670	0.003499536	0.999352266	2400	31.7
2430.605449	0.020690196	0.002615154	-0.026428800	7.140959158	0.357047958	-0.876773808	1.898119925	0.170006651	0.003561435	0.988708161	2400	28.5
2430.675216	0.009714846	0.003448313	-0.029337161	7.142366435	0.357118322	3.997268509	2.841797354	0.156868483	0.004172708	1.009883115	2400	22.7
2430.793963	0	0.004101949	-0.014566066	7.154824695	0.357741235	17.76124298	2.793467679	0.152186686	0.005026666	0.990507323	2400	19.5
2432.708547	0.010934787	0.002813860	-0.017938111	7.142515648	0.357125782	3.522072813	2.007823948	0.173702481	0.004060536	0.996595505	2100	26.7
2432.771624	0.020807163	0.003165590	0.005396245	7.146888465	0.357344423	1.482052001	2.180986562	0.197696011	0.004567345	1.000737242	2400	25.7
2433.589404	-0.005759122	0.004543362	-0.012638667	7.141966902	0.357098345	13.73210968	3.238231507	0.156301540	0.004919294	1.005853124	2400	18.4
2460.511224	0.005895298	0.002957171	-0.023272945	7.138558338	0.356927917	0.173120003	2.294055305	0.160858365	0.003977862	0.990624216	2400	24.2
2460.703136	-0.006202675	0.002962588	-0.018801690	7.132139304	0.356606965	1.994551964	2.507608654	0.167471110	0.004007204	0.996410287	2400	26.6
2461.528107	0.015996184	0.002325161	-0.025352893	7.120917671	0.356045884	-4.356761078	1.674535666	0.167688344	0.003392494	0.993608739	2400	29.1
2461.603775	0.019667017	0.003719634	-0.019049084	7.139453642	0.356972682	6.047329254	2.393000701	0.234380548	0.005077442	0.985384534	2700	23.5
2462.548288	0.004650384	0.002753746	-0.013112217	7.148418697	0.357420935	-2.298627181	1.835342272	0.163604136	0.003269482	1.003634973	2400	28.8
2462.697690	0.019120366	0.002733685	-0.023693674	7.140938077	0.357046904	1.663468315	2.176539325	0.163773867	0.003736499	1.005965119	2400	28.4
2463.523956	-0.007480005	0.004354283	0.003485374	7.122732003	0.356136600	12.53839580	2.886964792	0.246356354	0.005634937	0.984976420	2400	21.3
2463.686332	0.004361950	0.002607838	-0.022706813	7.151924899	0.357596245	4.120020246	2.327407159	0.186998648	0.004292668	0.996282723	2400	25.9
2467.619853	0.012521115	0.002237602	-0.018435484	7.134447548	0.356722377	-4.351583321	1.134570545	0.170492054	0.003035039	0.998282998	2100	36.2
2470.576694	-0.014622498	0.003224917	-0.006783539	7.135561560	0.356778078	0.830073320	2.446677634	0.222651785	0.004940337	0.994695320	2400	24.7
2471.526954	-0.009509969	0.001711479	-0.016340895	7.135242022	0.356762101	-9.899564167	1.551739631	0.169208331	0.002841745	0.994933456	2400	38.4
2472.542615	-0.000106014	0.002917387	-0.016347214	7.121805322	0.356090266	5.079370467	2.249824118	0.170382224	0.003877015	0.994651399	2400	26.9
2473.515372	0.011278635	0.001998208	-0.014749743	7.145702914	0.357285146	-4.351123275	1.618986012	0.162113008	0.002889922	0.991353982	2400	35.4
2473.636500	0.008755525	0.002003567	-0.021534768	7.138369046	0.356918452	-9.531662223	1.359621503	0.187348591	0.003337473	0.994049878	2400	37.2
2474.557662	0.009871217	0.002272828	-0.020330444	7.141533353	0.357076668	-0.237590000	1.540770964	0.171545292	0.003304167	1.000336629	2400	32.2
2475.556563	-0.003711372	0.002152913	-0.015830215	7.147198245	0.357359912	0.211648000	1.715704638	0.174905076	0.003290315	1.011519561	2400	32.1
2475.670168	0.002865511	0.002723374	-0.010147531	7.136697027	0.356834851	8.052287871	2.305851198	0.175846935	0.004053048	0.992356017	2400	27.7
2476.559248	-0.020460820	0.003324717	-0.008768004	7.143915814	0.357195791	8.236826883	2.036921846	0.160440241	0.003685363	0.998942580	2400	26.4
2476.661638	-0.013027107	0.004830712	-0.014629884	7.111509280	0.355575464	45.07848938	3.356598711	0.183341839	0.005507660	0.999140509	2400	19.6
2477.552408	-0.014509429	0.005655293	-0.023830532	7.148861028	0.357443051	31.61015391	3.608882476	0.211182628	0.006363658	1.000245782	2400	16.9
2477.656210	-0.020161994	0.003897063	-0.038365216	7.144018458	0.357200923	16.59729732	2.786390384	0.201276239	0.005205999	0.988922086	2400	22.3
2478.601501	-0.007845141	0.002402883	-0.017684734	7.153895769	0.357694788	5.732488697	2.000829919	0.173492875	0.003579341	0.993562249	2400	30
2502.537972	-0.021841648	0.002927285	-0.014627725	7.121132243	0.356056612	1.435156202	1.865134741	0.194001634	0.004109944	0.998458563	2400	28.6
2530.516620	-0.020554079	0.002689375	-0.015004302	7.132953081	0.356647654	-2.396505538	1.873603833	0.183751932	0.003612815	0.993572861	2400	31.3

Notes. [(a)] We used 5% of the activity indicator as uncertainties.

PAPER E

Planets observed with CHEOPS – Two super Earths orbiting the red dwarf star TOI-776

M. Fridlund, **I.Y. Georgieva**, A. Bonfanti, Y. Alibert, C.M. Persson, D. Gandolfi, M. Beck, A. Deline, S. Hoyer, G. Olofsson, T.G. Wilson, O. Barragán, L. Fossati, A.J. Mustill, A. Brandeker, A. Hatzes, H.-G. Florén, U. Simola, M.J. Hooton, R. Luque, S.G. Sousa, J.A. Egger, A. Antoniadis Karnavas, S. Salmon, V. Adibekyan, R. Alonso, G. Anglada, T. Bárczy, D. Barrado Navascues, S.C.C. Barros, W. Baumjohann, T. Beck, W. Benz, X. Bonfils, C. Broeg, J. Cabrera, S. Charnoz, A. Collier Cameron, Sz. Csizmadia, M.B. Davies, H. Deeg, M. Deleuil, L. Delrez, O.D.S. Demangeon, B.-O. Demory, D. Ehrenreich, A. Erikson, M. Esposito, A. Fortier, M. Gillon, M. Güdel, K. Heng, K.G. Isaak, L.L. Kiss, J. Korth, J. Laskar, A. Lecavelier des Etangs, M. Lendl, J. Livingstone, C. Lovis, D. Magrin, P.F.L. Maxted, A.J. Muresan, V. Nascimbeni, R. Ottensamer, I. Pagano, E. Pallé, G. Peter, G. Piotto, D. Pollacco, D. Queloz, R. Ragazzoni, N. Rando, H. Rauer, S. Redfield, I. Ribas, N.C. Santos, G. Scandariato, D. Ségransan, L.M. Serrano, A.E. Simon, A.M.S. Smith, M. Steller, Gy.M. Szabó, N. Thomas, S. Udry, V. Van Eylen, V. Van Grootel, and N.A. Walton

Submitted to Astronomy & Astrophysics

Astronomy & Astrophysics manuscript no. output
March 6, 2023

Planets observed with CHEOPS

Two super Earths orbiting the red dwarf star TOI-776⋆

M. Fridlund[1,2], I. Y. Georgieva[1], A. Bonfanti[3], Y. Alibert[4], C. M. Persson[1], D. Gandolfi[5], M. B eck[6], A. Deline[6], S. Hoyer[7], G. Olofsson[8], T. G. Wilson[9], O. Barragán[10], L. Fossati[3], A. J. Mustill[11], A. Brandeker[8], A. Hatzes[12], H.-G. Florén[8], U. Simola[13], M. J. Hooton[14,4], R. Luque[15,16], S. G. Sousa[17], J. A. Egger[4], A. Antoniadis Karnavas[17], S. Salmon[6], V. Adibekyan[17], R. Alonso[18,19], G. Anglada[20,21], T. Bárczy[22], D. Barrado Navascues[23], S. C. C. Barros[17,24], W. Baumjohann[3], T. Beck[4], W. Benz[4,25], X. Bonfils[26], C. Broeg[4,25], J. Cabrera[27], S. Charnoz[28], A. Collier Cameron[9], Sz. Csizmadia[27], M. B. Davies[29], H. Deeg[18,19], M. Deleuil[7], L. Delrez[30,31], O. D. S. Demangeon[17,24], B.-O. Demory[25,4], D. Ehrenreich[6,32], A. Erikson[27], M. Esposito[12], A. Fortier[4,25], M. Gillon[30], M. Güdel[33], K. Heng[25,34], K. G. Isaak[35], L. L. Kiss[36,37], J. Korth[1,11], J. Laskar[38], A. Lecavelier des Etangs[39], M. Lendl[6], J. Livingstone[40,41,42,43], C. Lovis[6], D. Magrin[44], P. F. L. Maxted[45], A. J. Muresan[1], V. Nascimbeni[44], R. Ottensamer[33], I. Pagano[46], E. Pallé[18], G. Peter[47], G. Piotto[44,48], D. Pollacco[49], D. Queloz[50,14], R. Ragazzoni[44,48], N. Rando[51], H. Rauer[27,52,53], S. Redfield[54], I. Ribas[20,2], N. C. Santos[17,2], G. S candariato[46], D. S égransan[6], L. M. S errano[5], A. E. Simon[4], A. M. S. Smith[27], M. Steller[3], Gy. M. Szabó[55,56], N. Thomas[4], S. Udry[6], V. Van Eylen[57], V. Van Grootel[31], and N. A. Walton[58]

(Affiliations can be found after the references)

Received XXX; accepted XXX

ABSTRACT

Context. M-dwarf stars are the most common of potential exoplanet host stars in the Galaxy. It is therefore very important to understand planetary systems orbiting such stars and to determine the physical parameters of such planets with high precision. Also with the launch of the James Webb Space Telescope (JWST) the observation of atmospheric parameters of planets orbiting these stars is becoming imminent. It is therefore required to determine properties of potential targets.

Aims. The objective of our study is to use transit observations obtained by the *CHEOPS* space mission to improve the current precision of the planetary radii, as well as additional radial velocity data to improve the mass estimates of two known planets. With the above quantities, we derive the bulk densities of the planets discovered by *TESS* to be orbiting the red dwarf TOI-776, and use this information to put the planets in the context of other exoplanetary systems involving very low mass stars. These results can then be used to calibrate models of planetary formation, evolution, and to evaluate further observations with space missions.

Methods. Utilizing new transit data from the *CHEOPS* satellite and its photometric telescope, we obtained very high precision planetary transit measurements. Interpretation of these provides updated planetary radii, along with other system parameters. A concurrent ESO large observing program using the high precision spectrograph HARPS has doubled the available radial velocity data. Calculating the power spectrum of a number of stellar activity indices **we update the previously estimated stellar rotation period to a lower value.**

Results. The *CHEOPS* data provide precise transit depths of 930 and 1006 ppm translating into radii of $R_b = 1.798^{+0.078}_{-0.077}\,R_\oplus$ and $R_c = 2.047^{+0.081}_{-0.078}\,R_\oplus$, respectively. Our interpretation of the radial velocities and activity indicator time series data estimates a stellar rotation period for this early M-dwarf of ∼ 21.1 days.**A further multi-dimensional Gaussian process approach confirm this new estimate. By performing a Skew-Normal fit onto the Cross Correlation Functions we extracted the RV data and the activity indicators to estimate the planetary masses, obtaining** $M_b = 5.0^{+1.6}_{-1.6}\,M_\oplus$ **and** $M_c = 6.9^{+2.6}_{-2.5}\,M_\oplus$**.**

Conclusions. We improve the precision in planetary radius for TOI-776 b and c by a factor of more than two. Our data and modelling give us masses of both bodies more like super-Earths than mini-Neptunes, albeit with a low density. The stellar activity of TOI-776 is found to have increased by a factor larger than 2 since the last set of observations.

Key words. techniques: photometric – techniques: spectroscopic – planets and satellites: detection – planets and satellites:individual: TOI-776b, TOI776c – stars:individual: LP 961-53

1. Introduction

From the pioneering *CoRoT* space mission (Fridlund 2008) that discovered the first rocky super-Earth (Léger et al. 2009), through the *Kepler* space telescope (Borucki et al.

⋆ **This article uses data from *CHEOPS* programme CH_PR100031.**

2010), which truly showed the diversity of exoplanets, to the now active all-sky transit survey *TESS* (Ricker et al. 2015), and most recently the very precise *CHEOPS* (CHaracterising ExOPlanet Satellite, Benz et al. 2021), the advent of space-based transit photometry has been a game changer.

The more than 5000 planets detected to date seem to be just the tip of the iceberg. While the discovery of new systems is continuing at a fast pace, we are simultaneously faced with the formidable task of obtaining the first grains of comprehension of the incredible diversity of both the planets we discover and the host stars they orbit. *CHEOPS* is the first small space mission in the European Space Agency (ESA) Science Program. It was successfully launched by ESA on December 18, 2019, from Kourou, French Guiana, and is a partnership between ESA and Switzerland with important contributions from other ESA Member States. *CHEOPS* is the first mission dedicated to directly observing transits of already identified individual exoplanets. While achieving hitherto unprecedented precision in the transit light curves (LCs) and thus allowing significant improvement in planetary parameters, this space mission operates in a manner completely different from those of the previous exoplanetary missions. The previously mentioned spacecraft have all been survey missions, while *CHEOPS* has as its objective the detailed study of individual planets with the purpose of providing greater precision of the individual parameters (e.g. Lacedelli et al. 2022; Wilson et al. 2022). The mission observes predicted transits of single, specific targets, orbiting bright stars and using ultrahigh precision photometry. Another objective of *CHEOPS* is the search for transiting exoplanets in systems where radial velocity (RV) observations have already identified potential transits. In these observations, *CHEOPS* is also providing prime targets for new instruments carrying out spectroscopic characterisation of exoplanetary atmospheres (e.g. the James Webb Space Telescope JWST, Gardner et al. 2006).

In recent years, the low-mass M-dwarf stars have been gaining traction among the exoplanet community in the search for new worlds. This is understandable for a number of reasons. Given that the frequency of planets orbiting in the habitable zone around all dwarf stars is the same, transit and radial velocity surveys are much more likely to detect potentially habitable worlds given the proximity of the habitable zone to an M-dwarf host star. Because of their small radii and low masses, compared to Sun-like stars, relatively large transit depths and RV amplitudes are induced by planets transiting M-dwarfs. The probability of uncovering planetary habitability is further exploited by the fact that red dwarfs have been estimated to be by far the most numerous types of stars and comprise ∼75% (Scalo et al. 2007) of the stars in our galaxy.

While impressive, the above advantages should be taken with a pinch of salt since the faintness of M-dwarfs can also make them difficult to study in the context of exoplanets. Another important factor to consider in the case of RV surveys is the stellar activity-induced signal, which would be higher for the typically more magnetically active cool stars (e.g. Reiners et al. 2010; Andersen & Korhonen 2015). In some cases the activity displays stochastic behaviour and cannot be described by traditional methods, such as e.g. sinusoid-fitting. Such situations can further be exacerbated by gaps in the data caused by interruptions to the observing run. In cases where the reason characterisation is poor or completely lacking is insufficient and/or poor quality data, a follow-up campaign of already known targets can thus make a big difference. Such is the case with TOI-776 which is an early M-dwarf hosting two small transiting planets in the super-Earth – mini-Neptune transition regime (Luque et al. 2021, **hereafter L21**). The mass range of a few to ∼10 $M_\oplus$ that these planets populate is an interesting one since such planets are not only the most numerous, but they are also not represented in our Solar system, despite its apparent diversity of members. The discovery as first reported by L21 relied primarily on TESS photometry providing three transits of the inner planet and two transits of the outer one, with additional help by four ground-based transits for both planets, three of which were partial. This led to a precision of the radii of about 7%. The mass determinations of the two planets orbiting this relatively active M-dwarf are based on 29 RV measurements leading to **a precision** of approximately 30%.

Given the estimated location of these planets with regards to the radius valley for M-dwarfs (Van Eylen et al. 2021), the potential they have for gaining further insight into planet formation and evolution mechanisms is substantial. Moreover, TOI-776b and TOI-776c are particularly suitable for atmospheric characterisation studies, as highlighted by L21. Adding the fact that these two objects are already selected for observations in cycle 1 (program ID 2512, PI: Batalha) of JWST (Gialluca et al. 2021), updated planetary and orbital parameters will certainly also be very useful.

With the above justification in hand, TOI-776 was given a high priority as a target for observations with the *CHEOPS* space mission and the KESPRINT program utilizing the HARPS high-precision spectrograph. Our studies using *CHEOPS* are intended to determine facts about planets and planetary systems that could be helpful in narrowing down the correct formation models, and beginning to understand the causes for the large diversity that exists among types of planets, as well as the different distribution of individual planets within their systems. Furthermore, so far it appears that the properties of systems depend to a large degree on the properties of the host star, but the role of the type of host star in these issues in general needs to be investigated in greater detail (Perryman 2018; Deeg & Belmonte 2018; Fridlund et al. 2020).

In order to make a precise characterization of the sizes of the planets, our observations of TOI-776 with *CHEOPS* are aimed at improving the precision in planetary radii by at least a factor of two with respect to L21. We also wanted to expand on the RV work of L21 with the aim of improving the precision in the mass determinations and, thus, in the mean densities. The latter goal proved elusive given **both** the apparently changed stellar behaviour between the two radial velocity campaigns **and the questionable approach based on sinusoid-fitting adopted by L21 in their RV analysis. To determine the planetary masses we instead used a novel approach, which is based on applying a Skew-Normal (SN) fit onto the cross correlation functions (CCFs) retrieved from the HARPS spectra (Simola et al. 2019). This allowed us to extract the RV measurements and stellar activity indicators, without introducing any *ad hoc* hypotheses to model the stellar activity during the detrending phase**.

In this paper we present the new observations **(Sec. 2)** and derive the stellar parameters as well as determine the activity in **Sec. 3. Our analysis is described in Sec. 4 with the multi-GP method in 4.1 while our reference SN-fit method for extracting the RV data is described in Sec. 4.2**

In Sec. 5 we derive the planetary parameters, and in sections 6 and 7 we discuss the increased stellar activity and its impact on the achievable determination of planetary parameters, and draw conclusions about how these results serve as

a model for observations to be carried out in space missions like ESA's PLATO (Rauer et al. 2014) later this decade. We have also modelled the interior structures of the two individual planets and put the results for the physics of these planets into the context of the host star.

2. Observations and data

We collected photometric and spectroscopic observations with the aim of performing a joint fit of the data (Sec. 5.1) and retrieving specifically radii and masses of TOI-776 b and TOI-776 c.

2.1. TESS photometry

The NASA *TESS* space mission (Ricker et al. 2015) has been launched with the objective of discovering transiting exoplanets. Its wide field is intended to make possible the identification and immediate characterization of exoplanets orbiting brighter stars then its predecessors. TOI-776 was first observed by *TESS* **(2-minute cadence mode)** in March-April 2019 in Sector 10 on camera 2, CCD 4, **when two exoplanets now identified as b and c** were initially flagged by the *TESS* Science Processing Operations Center (SPOC, Jenkins et al. 2016). The target was further observed by *TESS* in its 2-minute cadence mode in Sector 37 between 2 and 28 April 2021, once again on camera 2, CCD 4.

For the transit analysis, we used the TOI-776 *TESS* light curves as extracted by the SPOC pipelines (Twicken et al. 2010; Morris et al. 2017), with instrumental systematics and dilution corrected for via the presearch data conditioning simple aperture photometry (PDCSAP) algorithm (Smith et al. 2012; Stumpe et al. 2012). **We performed a 5-median-absolute-deviation (MAD) clipping to reject flux outliers. From each observation run containing ~1 month of data, we extracted those temporal windows centred around each transit of TOI-776 b and c, keeping also ~4 hours of out-of-transit data both before and after the transit event for detrending purposes. We ended up with 4 LCs from Sector 10 (where one contains two transits events as they are very close in time) and 5 LCs from Sector 37. Besides the time and the flux with its errors, each of the 9 TESS LCs contains also the PDCSAP data product vectors to test whether any further detrending is needed.**

2.2. CHEOPS photometry

The *CHEOPS* payload consists of a back-illuminated CCD photometer operating between 0.33 μm and 1.1 μm wavelength range, which is installed on a 32 cm Ritchey-Chretien telescope. The *CHEOPS* spacecraft is in a Low Earth Orbit (LEO) **and takes approximately 98.77 minutes to complete an orbital period around the Earth. As a consequence of such a LEO,** part of each revolution is unusable for data taking. This is due mainly to high levels of scattered light, occultations of the **observed target** by the Earth as well as to regular passages through the South Atlantic Anomaly (SAA)**, which is** a region mainly above Brazil and the accompanying Atlantic Ocean, where high levels of radiation cause a very large number of particle impacts on the CCD. **This means that gaps in the data occur, which needs to be filled out by suitable observations until an evenly covered transit LC can be obtained. The raw LCs are shown in Fig. B.1.** For more details about *CHEOPS* we refer to Benz et al. (2021).

We used *CHEOPS* to observe TOI-776 between 14 March and 4 May 2021, during 5 visits. These observations yielded a total of 52.8 h of LC data. We detected the transits of TOI-776b in 2 visits and of TOI-776c in 3 visits (see Table 1 **and Fig. B.1**). **The observations were carried out and then reduced using the *CHEOPS* data reduction pipeline (DRP, v.13 Hoyer et al. 2020). In brief, after downlinking the data as CCD windows of ~200″ diameter, the DRP subtracts the bias and corrects for non-linearity and dark current, while taking flat field variation into account. The DRP corrects also for the sky-background, cosmic ray impacts, and also smearing trails of stars close to the line of sight. The DRP performs automatic aperture photometry on the processed *CHEOPS* images using different circular masks centred around the target. In our case we carry out photometry using the DEFAULT aperture (i.e., 25″). A stable photometry is achieved by letting the mask follow the movements of TOI-776 as the spacecraft jitters and rolls around the optical axis.**

The DRP also creates a set of vectors allowing the user to maximize performance during the following stages of reduction. These vectors consist (among others) of the orbital roll angle (`roll`), the x- and y-position on the CCD of the centre of the point spread function (PSF), the estimated background light (`bg`, e.g. due to zodiacal light), the level and position of the smear factor (`smear`) and the degree of contamination by background stars (`conta`). This data can be found in the *CHEOPS* archive at Data & Analysis Center for Exoplanets (DACE)[1]

2.3. Ground based photometry

In order to treat the available data in an optimal way, we also considered the ground based light curve photometry obtained by L21 from the MEarth-South, and three nodes of the LCO, namely LCO-CTIO, LCO-SSO, and LCO-SAAO. We refer to L21 for details. The lightcurve data from these observations were integrated together with the old and new *TESS* observations as well as the *CHEOPS* observations and thus contribute to the determination of the rotation period of the host star.

2.4. Spectroscopic Observations

The two planetary candidates identified by *TESS* (Sect. 2.1) were confirmed through spectroscopic follow-up observations by the KESPRINT consortium[2] **(see L21), using also the ground-based transit photometry quoted above (Sect. 2.3). With the aim of constraining the amplitudes of the Doppler signals induced by the two planets, and hence the precision in their mass determinations, we collected 35 additional RV data. We observed TOI-776 with the HARPS spectrograph (R = 115 000) mounted at the ESO 3.6m telescope (La Silla observatory, Chile), as part of the large program 106.21TJ.001 (P.I. D. Gandolfi). We used the second fiber of the spectrograph to monitor the sky background and set the exposure time to 1800-2520 s depending on the sky conditions and scheduling constraints, leading to a median signal-to-noise ratio of ~42 per pixel at 550 nm. We reduced the data using the dedicated data reduction software (DRS, Pepe et al. 2002a; Lovis & Pepe 2007) and extracted the cross-correlation functions (CCFs) from each Echelle spectum using a numerical M2 mask (Baranne et al. 1996).**

[1] `http://https://dace.unige.ch/`
[2] `http://www.kesprint.science`.

Table 1: ***CHEOPS*** **observing times and file keys.**

Planet	Start rBJD[(a)]	Duration(h)	File key
TOI-776 b	9288.735155	9.24	PR100031_TG037301_V0200
TOI-776 b	9354.599040	8.77	PR100031_TG039901_V0200
TOI-776 c	9292.899499	12.49	PR100031_TG037401_V0200
TOI-776 c	9324.329361	10.42	PR100031_TG039801_V0200
TOI-776 c	9339.994886	11.86	PR100031_TG039802_V0200

Notes. [(a)] rBJDs are shifted by −2 450 000.

Table 2: TOI-776's main identifies, coordinates, magnitudes, parallax, proper motion, and systemic radia velocity.

Parameter	Value
Main Identifiers	
Name	LP961-53
TOI	776
TIC	306996324
2MASS	J11541839-3733097
WISEA	J115418.61-373311.4
UCAC4	263-063112
GAIA[a]	3460438662009633408
Coordinates	
α (J2000.0)	$11^{\rm h}\,54^{\rm m}\,18\overset{\rm s}{.}39$
δ (J2000.0)	$-37^\circ\,16'\,20\overset{''}{.}62$
Magnitudes	
Johnson B	13.041 ± 0.051
Johnson V	11.536 ± 0.041
G_{BP}[(a)]	11.7645 ± 0.0013
G[(a)]	10.7429 ± 0.0005
G_{RP}[(a)]	9.7412 ± 0.0013
J[(b)]	8.483 ± 0.018
H[(b)]	7.877 ± 0.040
Ks[(b)]	7.615 ± 0.020
$W1$[(c)]	7.474 ± 0.032
$W2$[(c)]	7.472 ± 0.021
Parallax[(a)] (mas)	36.829 ± 0.018
μ_{RA}[(a)] (mas yr^{-1})	250.996 ± 0.018
μ_{Dec}[(a)] (mas yr^{-1})	−144.946 ± 0.013
Systemic radial velocity[(a)] (km s^{-1})	49.342 ± 0.223

Notes. [(a)] Gaia eDR3. [(b)] 2MASS. [(c)] WISE RSR.

With 35 new HARPS spectra, the resulting data-set contains 64 HARPS spectra in total**, which is** more than twice the number of Doppler measurements presented L21. **The RV observations now cover the time between BJD = 2458884.756669 and BJD = 2459430.476566, but with a significant gap between BJD = 2451931 and BJD = 2452358 due to the COVID-19 pandemic (see Fig. 2 and Fig. 5).**

Table 3: Adopted stellar parameters for TOI-776 (Sect. 3). We note that the parameters are in very good agreement with those published by L21.

Parameter	Unit	Value
$T_{\rm eff}$[(a)]	K	3725 ± 60
$\log g$[(b)]	cgs	4.81 ± 0.12
[Fe/H][(a)]	dex	−0.21 ± 0.08
[Mg/H][(a)]	dex	−0.23 ± 0.10
[Ca/H][(a)]	dex	−0.44 ± 0.17
$v \sin i_\star$[(a)]	km s^{-1}	2.2 ± 1.0
$R_\star$[(c)]	$R_\odot$	0.547 ± 0.017
$M_\star$[(d)]	$M_\odot$	$0.542^{+0.040}_{-0.039}$
Age[(d)]	Gyr	$6.1^{+7.0}_{-5.5}$
$P_{\rm rot}$[(e)]	**days**	$21.129^{+0.062}_{-0.058}$

Notes. [(a)] SME. [(b)] ARIADNE. [(c)] IRFM. [(d)] PARSEC & CLES. [(e)] **Activity indicators.**

3. Stellar parameters

3.1. Spectroscopic and isochronal parameters

The physical parameters of red dwarf stars are notoriously difficult to determine. In order to facilitate the determination of the stellar parameters, we use several different methods based on stellar photometric data (see Table 2), as well as analysis of the observed high resolution spectrum and synthetic spectra calculated from relevant stellar models. We achieve a high signal-to-noise spectrum **(350 per pixel at 550 nm)**, by co-adding the individual 64 HARPS spectra obtained with the purpose to determine the RV curves of the planets (see Sect. 3.2 and 4.2). This summed spectrum is then normalized and can be used as input for our stellar analysis.

Following L21 we first fitted the co-added spectrum and analysed it using the `Specmatch-emp`, spectral analysis package (Yee et al. 2017). Briefly, this code[3], after re-formatting our co-added spectrum to a compatible format (Hirano et al. 2018), compares it with a library of over 400 spectra of stars, of all types, with well determined physical parameters. A minimizing and interpolation calculation provide estimates of $T_{\rm eff}$, $\log g$, [Fe/H], as well as $M_\star$, $R_\star$ and age. For further details we refer the reader to e.g. Fridlund et al. (2020) and references therein.

Using the $T_{\rm eff}$, $\log g$, [Fe/H] from `Specmatch-emp` as input, we then applied the IDL package Spectroscopy Made Easy (SME) which **synthesises a model of individual absorption**

[3] `https://github.com/samuelyeewl/specmatch-emp`.

lines in the observed spectrum based on several well determined stellar atmospheric models (Valenti & Piskunov 1996; Piskunov & Valenti 2017) and using atomic and molecular parameters from the VALD database (Piskunov et al. 1995). We applied the MARCS 2012 model grid (Gustafsson et al. 2008) for the synthesis. Following again schemes outlined in e.g. Fridlund et al. (2020) and references therein, and while keeping the turbulent velocities $V_{\rm mac}$ and $V_{\rm mic}$ fixed at the empirical values found in the literature (Gray 2008), we find $v \sin i_\star$ to be 2.2 ± 1.0 km s^{-1}. Using SME to fit several hundred TiO lines with $T_{\rm eff}$ as the only free parameter, we then find $T_{\rm eff}$ to be 3725 ± 50 K in very good agreement with the result of Specmatch ($T_{\rm eff}$ 3702 ± 70 K).

As a further strategy to derive $T_{\rm eff}$ and [Fe/H], we have also used ODUSSEAS (Observing Dwarfs Using Stellar Spectroscopic Energy-Absorption Shapes), a code[4] (Antoniadis-Karnavas et al. 2020) which is based on the measurement of the pseudo equivalent widths from more than 4000 stellar absorption lines and on the use of the machine learning Python package `scikit-learn` for predicting the $T_{\rm eff}$ and [Fe/H]. This tool is able to derive parameters accurately and with high precision, having statistical precision errors of 30 K for $T_{\rm eff}$ and 0.04 dex for [Fe/H]. The results are consistent for spectra with resolutions of between 48 000 and 115 000 and a signal-to-noise ratio above 20. This code uses a library of HARPS spectra of M stars, utilizing reference parameters for these stars which come from inteferometric calibrations. In the library spectra "pseudo" equivalent widths are measured for hundreds of lines, and then the code is trained using the reference parameters. We provide a new spectrum, adjust the resolution to that of the HARPS spectrograph matching the library and then running the machine learning trained model on the pseudo equivalent widths of the spectra in study. These give us the two parameters ($T_{\rm eff}$ and metallicity).

The stellar radius $R_\star$ was determined by fitting catalogue photometry to the spectral energy distribution (SED) of TOI-776, using two different codes, namely astroARIADNE[5] (Vines & Jenkins 2022) and a modified infrared flux method (IRFM; Blackwell & Shallis 1977). Since the output from both ODUSSEAS and SME is heavily model dependent, as priors to support the fitting routines we adopted the spectroscopic parameters inferred through `Specmatch-emp`.

We started with the Python code astroARIADNE. This software uses Bayesian model averaging of four stellar atmospheric model grids from `Phoenix v2`, (Husser et al. 2013), `Bt-Settl`, `Bt-Cond`, and `Bt-NextGen` (Allard et al. 2012; Hauschildt et al. 1999), for stars with $T_{\rm eff} < 4000$ K convolved with various filter response functions. We used magnitudes from Gaia eDR3 ($G, G_{\rm BP}, G_{\rm RP}$), *WISE* (W1-W2), J, H, K_S from *2MASS*, and Johnson B and V from APASS (see Table 2). The parallax was also taken from Gaia eDR3 applying the parallax offset of Lindegren et al. (2021). The software interpolates model grids of $T_{\rm eff}$, $\log g$ and [Fe/H] assuming distance, extinction (A_V), and stellar radius as free parameters. The maximum line-of-sight value from the dust maps of Schlegel et al. (1998) were used as an upper limit of A_V. **This results in $R_\star = 0.552 \pm 0.008\, R_\odot$.**

Then we also applied the IRFM method that uses a Markov chain Monte Carlo (MCMC) approach to determine the stellar angular diameter and effective temperature, as recently detailed in Schanche et al. (2020). To produce synthetic photometry used in the calculation of the apparent bolometric flux, we constructed spectral energy distributions (SEDs) using **again** the stellar parameters derived from our spectral analysis as priors, and that were subsequently attenuated to account for reddening. We find essentially the same (within 1σ) results as with astroARIADNE**, that is $R_\star = 0.547 \pm 0.017\, R_\odot$, which we assume as our reference value because of the larger more realistic uncertainty.**

We thus get a set of values of $T_{\rm eff}$ ranging from 3702±70K (`Specmatch-emp`), 3725±50K (SME and astroARIADNE) and 3752±101K (ODUSSEAS), of $\log g$ ranging from 4.76±0.12 dex (`Specmatch-emp`) to 4.81±0.1 dex (astroARIADNE). We chose to use the values from astroARIADNE and SME since they are in almost total agreement. The abundances of different metals are mostly derived with SME and we chose to use those values**, where in particular** [Fe/H] $= -0.21 \pm 0.08$ **dex**. We note that the values of [Fe/H] are in agreement with those from both `Specmatch-emp` (-0.2 ± 0.09), astroARIADNE (-0.22 ± 0.08) and ODUSSEAS (-0.15±0.08). Finally the $v \sin i_\star$ 2.2 ± 1.0 km s^{-1} is exclusively derived with SME on a large number of metal lines.

Adopting ($T_{\rm eff}$, [Fe/H], $R_\star$) as a reference input set, we derived a robust estimate of the stellar mass $M_\star$ by using two different stellar evolutionary codes, namely PARSEC[6] v1.2S (Marigo et al. 2017) and CLES[7] (Scuflaire et al. 2008). In particular, we fitted the input set into pre-computed PARSEC grids of isochrones and tracks through the isochrone placement algorithm developed by Bonfanti et al. (2015, 2016). We also inputted the $v \sin i$ value to improve the convergence of the interpolating routine as discussed in Bonfanti et al. (2016), and we obtained a first estimate of the stellar mass. Furthermore, starting from our reference input set, we employed the CLES code to generate the best-fit evolutionary track according to the Levenberg-Marquadt minimisation scheme (Salmon et al. 2021) and we inferred a second estimate for the stellar mass. Finally, we checked the consistency of the two outcomes through a χ^2-based criterion and we merged them together obtaining $M_\star = 0.542^{+0.040}_{-0.039}\, M_\odot$. Following a similar procedure we also arrive at the stellar age = $6.1^{+7.0}_{-5.5}$ Gyr (see Bonfanti et al. 2021a, for further details). All the **adopted stellar** parameters can be found in Table 3.

3.2. Stellar activity and rotation period

Red dwarf stars are generally found to be considerably more active than solar-like stars and TOI-776 is no exception. As mentioned in Sect. 2.4, there was a large gap in our RV sequence and it was found that TOI-776 is significantly more active during the second observing period. We used the DRS (pipeline output of the HARPS reduction package) data to extract three profile activity diagnostics of the cross-correlation function (CCF), namely, the contrast, the full width at half maximum (FWHM), and the bisector inverse slope (BIS). All three indexes demonstrate significant increased activity during the observing period.

We then follow the approach used in e.g. Fridlund et al. (2020), and apply two separate methods to further study the activity as discerned from the RV measurements, namely, the `TERRA` software package (Anglada-Escudé & Butler 2012), and the `SERVAL`[8] code (Zechmeister et al. 2018). While being similar in principle, the `SERVAL` code provides a different

[4] `https://github.com/AlexandrosAntoniadis/ODUSSEAS`.
[5] `https://github.com/jvines/astroARIADNE`.
[6] *PA*dova and T*R*ieste *S*tellar *E*volutionary *C*ode: `http://stev.oapd.inaf.it/cgi-bin/cmd`.
[7] Code Liègeois d'Évolution Stellaire.
[8] `https://github.com/mzechmeister/serval`.

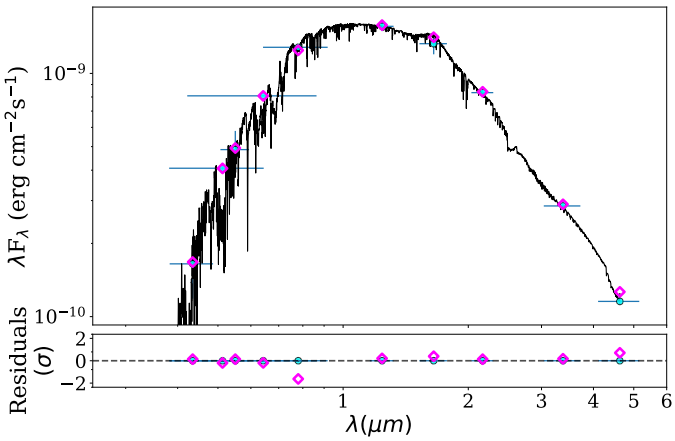

Fig. 1: The spectral energy distribution (SED) of TOI-776 using the BtSettl model (Allard et al. 2012) using the astroARIEDNE software (Vines & Jenkins 2022). The synthetic photometry is plotted with magenta diamonds and the blue points the observed photometry. The vertical error bars are the 1 σ uncertainties of the photometry, and the horizontal bars mark the effective width of the passbands. The residuals, normalised to the errors of the photometry, are shown in the lower panel.

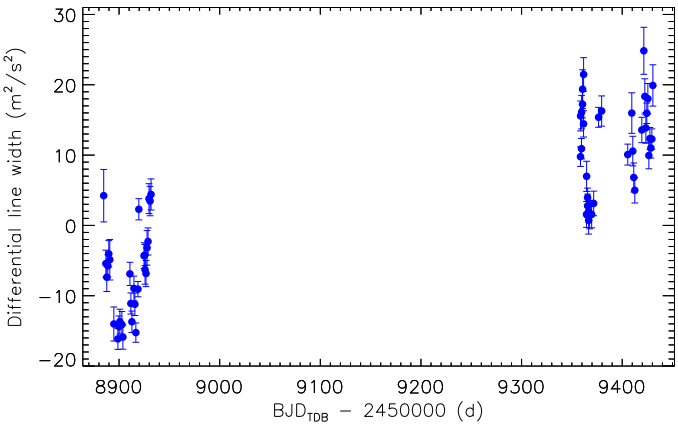

Fig. 2: The activity increase seen in the DLW index of SERVAL for the 2 sets of RV data.

set of activity related outputs. These routines measure relative RVs by first template-matching, and then extracting the chromatic index (CRX), the differential line width (DLW), the Hα and Na D1 and D2 indices. Both codes use algorithms that first create a template from the total assemblage of original and archived RV spectra and then compare each individual spectra with the template.

As noted by e.g. L21 these methods can achieve more precise radial velocities compared with the DRS package hitherto used with HARPS and similar spectrographs observations. This is true especially for M dwarfs and other types of stars where the atomic and molecular spectral line lists are incomplete, as well as the spectrum being more complicated by line blending and continuum suppression. The RVs have a median internal uncertainty of 1.5 m s^{-1}(resp. 1.5 m s^{-1}) and a root mean square of 5.2 m s^{-1}(resp. 3.5 m s^{-1}) around the mean value for the SERVAL (resp. TERRA) extractions.

We report the results of these reductions of the HARPS measurements in the APPENDIX. In particular, the two different values of extracted RVs (SERVAL and TERRA) with their associated uncertainties, the Hα index, the Na I line indices, together with the CRX and DLW computed by the SERVAL code, are all reported in Table A.1. We also report the Mount Wilson S-index as computed by TERRA. Using these parameters (see Fig. 2 and Table A.1) we see an increasing trend in the DLW, a trend that is also seen in the S-index. A decreasing trend is also visible in the equivalent width of the Hα line. This is due to the fact, that with a higher level of activity, the emission component in the Hα become stronger, thus increasing the filling factor of the line, and, consequently, decreasing the equivalent width of the absorption line. Finally we also see the same time evolution of the CRX index as calculated by SERVAL. All of these tracers thus indicate a significantly higher level of stellar activity.

There are two aspects of this *changing* activity that need to be addressed. First can we use the complete RV data set ín order to also determine the stellar rotation period (P$_{\rm rot}$), and secondly, can we use the complete RV data set for the mass determination of both planets without introducing (as compared to using only the RV data of L21) more noise (and thus larger errors).

First we computed the generalized Lomb-Scargle (GLS) periodogram (Zechmeister & Kürster 2009) of the RV measurements, the Hα, the DLW, the CRX and the NaD1 indexes from SERVAL (see Fig. 3. After subtracting the known signals identified as the two planets "b" and "c" (with the periods obtained from the transits), from the RV and from the different activity indexes, we find a signal with a period of 21-22 days (peak at $21.129^{+0.062}_{-0.058}$ days or 0.0473 d^{-1} shown by yellow marker in Fig. 3). We analyse the data for each parameter in three ways: Epoch 1 which refers to the data first presented in L21; Epoch 2 where **we use only the new RV spectra taken after BJD = 2452358; and** finally we analysed these data together as a set. We find that the DLW give discrepant results until we remove the offset seen in Fig. 2. After this removal we get very close values **of the peak locations** from all indexes, indicating that we have managed to delete a significant amount of the difference in the level of activity.

It is therefore tempting to identify the 21.1d day signal with the rotation period of the star. This assumption is strengthened by our modelling efforts described in Sec. 4.1. A summary of the results can be seen in Fig. 3 where we also report the false alarm probability (FAP). We discuss further the second aspect, the impact of activity, on the RV analysis, below in Sec. 4.2.

4. Methods

4.1. Preliminary multi-GP analysis

We began our investigation of the system by modelling the data using the code pyaneti (Barragán et al. 2019; Barragán et al. 2022). As discussed in Sect. 3.2, the activity of TOI-776 has changed significantly since the first RV observations published by L21. As a result, we find modelling all RVs as a single dataset and using a wide uniform prior around the ∼34-day value (as reported by Luque et al. 2021) on the third sinusoid accounting for the activity, leads to deteriorated estimates of the previously presented planet parameters (∼ 2-sigma detection of planet c) and a multi-modal posterior for the period of the third sinusoid. While unfortunate, this is not so surprising given that the two sets of observations are sep-

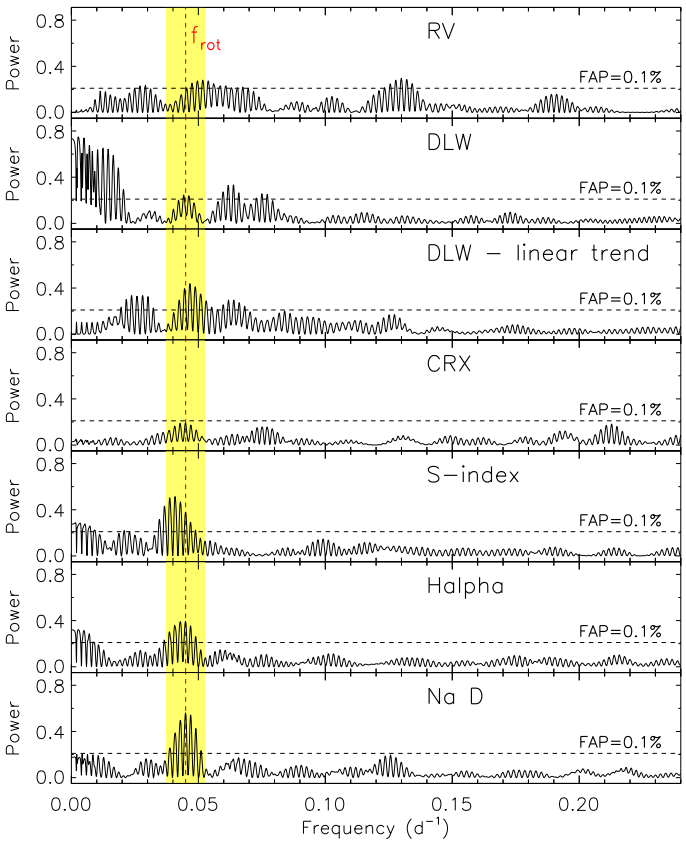

Fig. 3: **Generalized Lomb-Scargle periodogram of the HARPS RVs and different activity indexes derived with SERVAL. The dashed horizontal lines mark the FAP level at 0.1%. The vertical band marks the rotation period of TOI-776, $P_{\rm rot} = 21.129^{+0.062}_{-0.058}$ days (0.0473 d^{-1}) and its 3σ uncertainty.**

arated by over a year so the processes describing the star's behaviour have evidently changed in this time due to the dynamic configuration of the activity regions across the stellar surface (see e.g., Barragán et al. 2021).

As can be seen in our periodogram analysis (Sect. 3.2), adding the new RV data suggests a stellar rotation period of ~21 days. Initially, we approached this result skeptically as we considered it probable that it is affected by both nuisance signals dominating the second half of the data, and the two time gaps in data acquisition. For this reason, to try and understand the new RV dataset better, we used a `pyaneti`-implemented multi-dimensional Gaussian process (multi-GP) regression following Rajpaul et al. (2015), to analyse all data, as well as the first and second observing seasons separately. Modelling the dLW calculated by `SERVAL` alongside the TERRA RVs, using a wide uniform prior around ~30 days for the activity signal in a set-up similar to e.g., Georgieva et al. (2021) for all three cases, led to a non-detection of one or both planets. We thus finally turned to the ~21-day signal and used it to model the stellar rotation period in the multi-GP setup described above. This gave > 3-sigma results for both planets.

An important reason for the above-described outcomes is related to one key assumption of the multi-GP approach — that the same underlying GP can describe both the RVs and the activity indicator(s) timeseries, as well as the different observing seasons. A careful look at the behaviour of the timeseries and GP hyperparameters in the different analyses attempted, shows that this is not the case for these data – another indication that the multi-GP approach in the implementation used here is not best suited to modelling this system. Perhaps a future implementation which allows the GP hyperparameters to be set up in a more flexible way so as to describe stellar behaviour that has changed between observing seasons could lead to more fortunate results in cases such as this.

We note that, ironically, using the once popular but now ill-advised approach of simple-sinusoid fitting with a Gaussian prior on the ~21-day signal yielded the best results of all attempted thus far: we find semi-amplitudes of $K_b = 1.66 \pm 0.48$ m s^{-1}, $K_c = 2.06 \pm 0.55$ m s^{-1}, as well as a third amplitude identified as the stellar rotating $K_{rot} = 2.79 \pm 0.53$ m s^{-1}. While this latter approach does lead to a detection of all three signals (both planets and the stellar rotation) with the best precision, our novel approach – the SN-fit extraction of RV data, Sect. 4.2 – and its consequent results (Sect. 5.1) gives realistic error bars avoiding any bias or overfitting issues as discussed in Sect. 6.

4.2. SN-fit-based Radial Velocity extraction

We reduced all the HARPS data by using its dedicated Data Reduction Software (`DRS`); Lovis & Pepe 2007). The `DRS` first cross-correlates the extracted Echelle spectra with a numerical mask (selected to be the closest to the stellar spectral type, M2 in our case; see Baranne et al. 1996; Pepe et al. 2002b) to get one Cross Correlation Function (CCF) per observation.

Unlike the standard approach of fitting a Normal (N) function onto each CCF, following Simola et al. (2019) we performed the CCF-fitting using a Skew-Normal (SN) function (Azzalini 1985). In addition to a location and a scale parameter (the counterparts of the Gaussian mean and standard deviation, respectively), we recall that the SN has a further degree of freedom (hereafter denoted with γ), which quantifies its skewness. In this way we can directly account for the intrinsic asymmetry of the CCF within the fit, without implementing a separate procedure to estimate it (e.g. the Bisector Span computation, Queloz et al. 2001). After performing the SN-fit, our routine outputs the median of the best-fit function (i.e. the radial velocity measure $\overline{RV}$), its Full Width at Half Maximum (FWHM$_{\rm SN}$), its contrast (A), and its skewness (γ); these data are listed in Tab. A.2. We refer the reader to Simola et al. (2019) for a broad discussion about the specific output choices and the advantages of a SN-fit over an N-fit.

As the width and asymmetry of the CCF and their temporal evolution are typical tracers of the stellar activity (see e.g. Hatzes 1996; Queloz et al. 2001, 2009; Figueira et al. 2013; Simola et al. 2019; Bonfanti et al. 2023), the set of hyperparameters (FWHM$_{\rm SN}$, A, γ) together with the time t constitute the basis vector against which to detrend the $\overline{RV}$ measurements to remove the activity component $RV_\star$. The RV detrending has been performed within the LC+RV joint fit (see below, Sec. 5.1) using a polynomial baseline of the following form

$$RV_\star = \beta_0 + \sum_{k=1}^{k_t} \beta_{k,t} t^k + \sum_{k=1}^{k_F} \beta_{k,F} \mathrm{FWHM_{SN}}^k + \sum_{k=1}^{k_A} \beta_{k,A} A^k + \sum_{k=1}^{k_\gamma} \beta_{k,\gamma} \gamma^k, \quad (1)$$

where the β parameters are the polynomial coefficients, while $(k_t, k_F, k_A, k_\gamma)$ defines the polynomial order of the regression versus time t, $\mathrm{FWHM_{SN}}$, A, and γ, respectively.

Aware that the stellar activity of an M dwarf may dramatically impact the quality of our RV data, we explored the possibility of an RV detrending based on a piecewise interpolation rather than on an overall detrending over the entire time series. In other words, we investigated whether splitting the time series into segments and applying Eq. (1) on each single segment was supported by statistical evidence. To this end, we employed the breakpoint (*bp*) method, which is thoroughly presented in Simola et al. (2022). In short, given a time series ($RV(t)$ in our case) and a set of parameters of interest ($\mathrm{FWHM_{SN}}$, A, γ), the *bp* algorithm evaluates the changes in the correlations of the SN hyperparameters against $\overline{RV}$ over the time series. If those changes are statistically significant, then the *bp* method gives the optimal number of breaks and their location along the time series. As a consequence, the time series can be split into segments which are piecewise stationary. This means that ($\mathrm{FWHM_{SN}}$, A, γ) are supposed to show different trends between segments rather than within the segments. Therefore, if statistically justified, a piecewise detrending applied to each segment is expected to be more effective in removing the contribution from stellar activity as shown by Simola et al. (2022). We actually applied the *bp* method to our $\overline{RV}$ timeseries, but the Bayesian Information Criterion (BIC, Schwarz 1978) did not favour any splitting, hence we applied a unique polynomial detrending baseline in the form of Eq. (1) to the entire time series.

5. Results

5.1. LC and RV joint analysis

For the joint *TESS* +*CHEOPS* transit and SN-fit-based RV modelling we use the MCMCI code (Bonfanti & Gillon 2020). To save computational time, we switched off the simultaneous interaction with the stellar isochrones and tracks as the star was already well characterised using different approaches as detailed in Sec. 3.

We imposed Normal Gaussian priors on the stellar $T_{\rm eff}$ [Fe/H], $M_\star$, and $R_\star$, which has a double goal. First, the mean stellar density $\rho_\star$ inferred from $M_\star$ and $R_\star$ constrains the transit parameters via Kepler's third law. Second, stellar parameters are needed to get the limb darkening (LD) parameters for both the *TESS* (TE) and *CHEOPS* (CH) bandpasses following interpolation in the tables derived from ATLAS9 models by the code of Espinoza & Jordán (2015). Assuming a quadratic LD law (e.g. Claret 2000, and references therein), we estimated $u_{1,\mathrm{CH}} = 0.2472 \pm 0.0405$, $u_{2,\mathrm{CH}} = 0.4196 \pm 0.0303$, $u_{1,\mathrm{TE}} = 0.1774 \pm 0.0326$, and $u_{2,\mathrm{TE}} = 0.4208 \pm 0.0229$, which define the Normal priors of the LD coefficients.

The other jump parameters, namely the transit depth $\mathrm{d}F \equiv \left(\frac{R_p}{R_\star}\right)^2$, the impact parameter b, the orbital period P, the transit timing T_0, and the RV semi-amplitude K, were subject to wide uniform priors (bounded by physical bounds only). Instead, modelling the eccentricity e with a wide uninformative prior would yield to highly eccentric orbits for both TOI-776 b and c, which would play against the system stability as reported by L21. Nonetheless, the orbits of planets in multi-transiting systems are not necessarily circular even if they are expected to have low eccentricity values (Van Eylen & Albrecht 2015; Xie et al. 2016; Hadden & Lithwick 2017). Therefore, we imposed uniform priors on both $\sqrt{e}\cos\omega$ and $\sqrt{e}\sin\omega$, but bounded so to imply $e \lesssim 0.2$. This e-upper-limit has been set according to the analysis by L21, who followed similar considerations and found a 3σ upper limit on the eccentricities of both the two exoplanets equal to 0.18.

Both the LC- and RV-detrending are done simultaneously within the MCMC scheme and are based on polynomials, as shown e.g. in Eq. 1 for the RV side. To choose the best polynomial baseline (that is the set of polynomial orders to be attributed to the vectors of additional parameters complementing the LC and RV time series) we performed several MCMCI runs varying each time the polynomial order of the hyperparameters to establish the set of detrending orders favoured by the BIC. The adopted baseline is summarised in Tab. B.1.

Once the setup has been completed we launched a first preliminary MCMCI run to properly rescale the photometric errors as detailed in ?. After that, we performed a final MCMCI run comprising 3 chains of 200 000 steps each (burn-in phase equal to 20%). All the jump parameters converge nicely according to the Gelman-Rubin test (Gelman & Rubin 1992), and the posterior outcomes are listed in Tab. 4.

5.2. Interior and Atmospheric Modeling

We performed an analysis of the internal structure of the two planets in the TOI-776 system, using the radii, masses and stellar parameters derived above. The method we used is based on a global Bayesian model in which we fit the observed properties of the planets (planet-star radius ratio, the RV semi-amplitude, and the orbital period) and star (mass, radius, age, effective temperature, and the photospheric abundances [Si/Fe] and [Mg/Fe]. (Note that we assume that [Mg/Fe] = [Si/Fe] since we could not determine the Si abundance). The Bayesian analysis relies on a forward model that computes the expected planetary radius and bulk internal structure as a function of the hidden parameters (see Leleu et al. (2021) for details). The hidden parameters are, for each planet, the masses of solids (everything except the H or He gas), the mass fractions of the core, mantle and water, the mass of the gas envelope, the Si/Fe and Mg/Fe mole ratios in the planetary mantle, the S/Fe mole ratio in the core, and the equilibrium temperature. We also assume, in the forward model, that planets are fully differentiated, and made of a core (Fe and S), a mantle (Si, Mg, Fe, and O), a pure water layer, and a H and He layer. The equations of state (EoS) used for these calculations are taken from Hakim et al. (2018) and Fei et al. (2016) for the core materials, from Sotin et al. (2007) for the mantle materials, and Haldemann et al. (2020) for water. The temperature profile in the planets is adiabatic, with no temperature jump at the transition between each layer.

We use the semi-analytical model of Lopez & Fortney (2014) to compute the thickness of the gas envelope as a function of the gas mass fraction, the equilibrium temperature, the mass and radius of the solid planet, and the age (assumed to be equal to the stellar age). We stress the fact that the radius of the high-Z part of the planet (core, mantle and water layer) is computed independently of the thickness of the gas layer: neither the compression effect of the gas envelope onto the core, nor the effect of the temperature at the base of the gas envelope are included in the model.

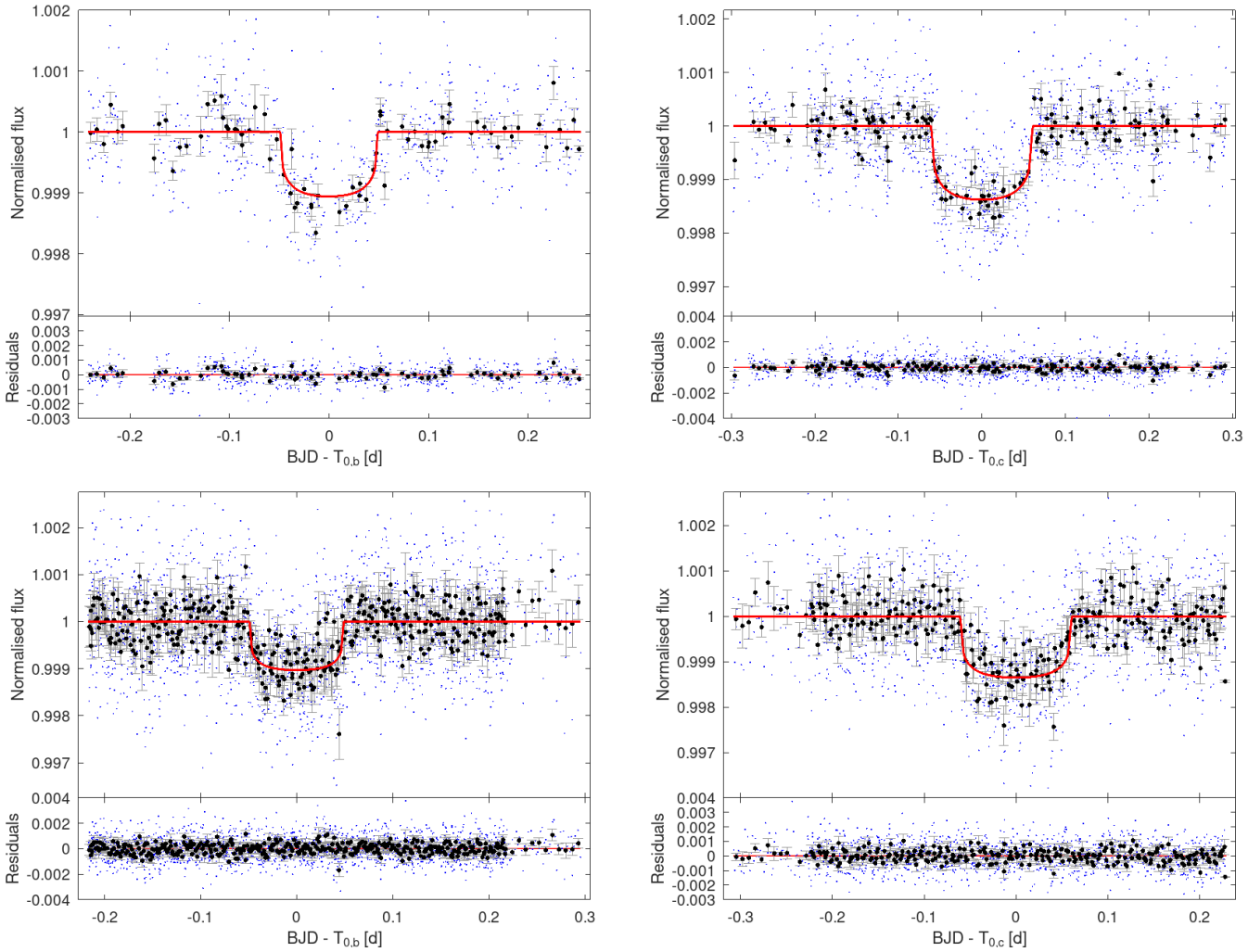

Fig. 4: **Phase-folded LCs showing the transits of TOI-776b (first column) and TOI-776c (second column).** ***Top panels*** **Detrended *CHEOPS* LCs; the best-fit transit models are shown as red lines together with their corresponding residuals.** ***Bottom panels.*** **Same as *Top*, but for the *TESS* LCs. Data are shown in the nominal cadence modes (blue dots) and also binned to 10 min (black markers) with their associated error bars.**

We assume the following priors of the hidden parameters: the mass fractions of the planetary cores, mantles, and water layers follow uniform positive priors, the mass fractions of water being limited to a maximum value of 0.5. The gas mass follows a uniform in log prior, and the bulk Si/Fe and Mg/Fe mole ratios in the planet are assumed to be equal to the values determined for the atmosphere of the star. We note, however, that Adibekyan et al. (2021) showed recently that, despite a clear correlation between the abundances of planets and host stars, the relation is not always strictly one-to-one.

The posterior distribution of the main planetary hidden parameters are presented in Fig. 6. Both planets have a very small fraction of gas, the mass of gas in the innermost planet being larger than in the outermost one. This trend is consistent with the trend in density of both planets, planet b having a density nearly two times smaller than planet c. Such a variation between the densities of the two planets is intriguing, and at odds with what is generally observed in planetary systems (where the density generally decreases for planets located further out from the central star, although there exist notable exceptions like in the TOI-178 system (Leleu et al. (2021)). The fraction of water, on the other hand, is essentially unconstrained.

We constrain the evolution of the stellar rotation period and the initial atmospheric mass fraction $f_{\rm atm}^{\rm start}$ of the detected planets employing the system parameters derived in this work and the PASTA planetary atmospheric evolution code (Bonfanti et al. 2021b), which is an updated version of the original code presented by Kubyshkina et al. (2019b,a). PASTA uses the evolution of the stellar rotation period as a proxy for the evolution of the stellar high-energy emission (X-ray plus extreme ultraviolet; XUV), which affects atmospheric escape. Furthermore, within the framework of PASTA, $f_{\rm atm}^{\rm start}$ is the planetary atmospheric mass at the dispersal of the protoplanetary disk. PASTA models the evolution of the atmosphere of all planets in a system simultaneously, combining a model predicting planetary atmospheric mass-loss rates based on hydrodynamic simulations (Kubyshkina et al. 2018), a model of the evolution of the stellar XUV flux (Bonfanti et al. 2021b), a model relating planetary parameters and atmospheric mass (Johnstone et al. 2015b), and stellar evolutionary tracks (Choi et al. 2016). We remark that the considered mass-loss rates overcome commonly used analytical estimates as they account for both XUV-driven and core-powered mass loss (Kubyshkina et al. 2018; Krenn et al. 2021). PASTA's main assumptions are that the planets were not subject

Table 4: **Summary of the system parameters outputted by joint LC and RV MCMC fit. Parameters and errors are defined as the median and 68.3% credible interval of the posterior distributions.**

Parameter	TOI-776 b	TOI-776 c
P [d]	$8.246620^{+0.000024}_{-0.000031}$	$15.665323^{+0.000075}_{-0.000070}$
T_0 [$\mathrm{BJD_{TDB}}$]	$9288.8713^{+0.0010}_{-0.0011}$	$9324.53478^{+0.00080}_{-0.00077}$
dF [ppm]	909 ± 55	1177^{+55}_{-53}
b	$0.26^{+0.16}_{-0.17}$	$0.35^{+0.16}_{-0.21}$
K [$\mathrm{m\,s^{-1}}$]	2.40 ± 0.75	$2.65^{+0.99}_{-0.97}$
W [h]	$2.382^{+0.050}_{-0.048}$	2.932 ± 0.038
a [AU]	$0.0653^{+0.0014}_{-0.0016}$	$0.1001^{+0.0022}_{-0.0024}$
i_p [°]	$89.41^{+0.39}_{-0.36}$	$89.49^{+0.30}_{-0.20}$
e	$0.052^{+0.037}_{-0.035}$	$0.089^{+0.048}_{-0.054}$
ω [°]	45^{+94}_{-110}	7^{+58}_{-52}
$T_{\mathrm{eq}}{}^{(a)}$ [K]	520 ± 12	420 ± 10
R_p [$R_\oplus$]	$1.798^{+0.078}_{-0.077}$	$2.047^{+0.081}_{-0.078}$
M_p [$M_\oplus$]	5.0 ± 1.6	$6.9^{+2.6}_{-2.5}$
ρ_p [$\mathrm{g\,cm^{-3}}$]	$4.8^{+1.8}_{-1.6}$	$4.4^{+1.8}_{-1.6}$
$u_{1,\mathrm{TESS}}$	$0.177^{+0.034}_{-0.033}$	
$u_{2,\mathrm{TESS}}$	0.421 ± 0.025	
$u_{1,\mathrm{CHEOPS}}$	$0.254^{+0.041}_{-0.042}$	
$u_{2,\mathrm{CHEOPS}}$	$0.421^{+0.032}_{-0.033}$	
RV jitter [$\mathrm{m\,s^{-1}}$]	$3.51^{+0.12}_{-0.11}$	

Notes. All the jump parameters were subject to uniform unbounded priors except for the LD coefficients (subject to Normal priors, see text) and the pair $(\sqrt{e}\cos\omega,\ \sqrt{e}\sin\omega)$**, whose uniformly-sampled steps obey the condition** $e \lesssim 0.2$**.**
$^{(a)}$ **Assuming zero albedo .**

to substantial migration following the dispersal of the protoplanetary disk and that all planets hosted, or still host, a hydrogen-dominated atmosphere. This is justified here as the orbits are not small enough for significant tidal decay.

PASTA uses the currently observed system parameters, and their uncertainties, as priors to constrain the free parameters, which are $f_{\mathrm{atm}}^{\mathrm{start}}$ and the parameters of the power law controlling the evolution of the stellar rotation period (Bonfanti et al. 2021b). The code is based on a Bayesian framework employing the MCMC tool presented by Cubillos et al. (2017). All details of the code are given by Bonfanti et al. (2021b) and the only difference is we opted here for fitting the planetary atmospheric mass fractions instead of the planetary radii, which enables higher accuracy by avoiding the continuous conversion of the atmospheric mass fraction into planetary radius, given the other system parameters (see also e.g. Delrez et al. (2021)).

Figure 9 shows the results of the PASTA run on the TOI-776 system. As a proxy for the evolution of the stellar rotation period, Figure 9 presents the posterior distribution of the stellar rotation period at an age of 150 Myr, further comparing it to the distribution of stellar rotation periods observed in stars which are members of young clusters of comparable age and with masses that deviate from the mass of TOI-776 by less than 0.1 solar masses from Johnstone et al. (2015a). The derived posterior distribution for the stellar rotation period suggests that TOI-776 was a slow rotator, slower than the average of open cluster stars of comparable mass and age. For both planets, PASTA returns flat posteriors for $f_{\mathrm{atm}}^{\mathrm{start}}$ indicating that both planets have most likely lost the vast majority of their primary, hydrogen-dominated atmospheres at some point in the past, in agreement with the results of the interior structure modeling.

6. Discussion

Combining *TESS* LCs with the ultra-high precision photometric observations from *CHEOPS* and the stellar host characterisation, we reached a precision on the planet radii of 4.3% and 3.9% for planet b and c, respectively. This marks an improvement of almost a factor of 2 with respect to the outcomes of L21. We note that we have thus approached the specific precision that is planned for planetary radii measurements with ESA's PLATO mission later this decade. Note also that this is done here with great effort in this *one* case. PLATO will reach the same precision in tens of thousands of cases, *simultaneously*. **We also note that the planetary radii approach the precision with which the stellar radii is known (3.0% – a very good value). This imply that the current data are very close to what is presently possible.**

On the dynamical side, we detected the RV semi-amplitudes of planets b and c at the 3.2σ and 2.7σ levels, respectively, which are slightly lower than what was obtained by L21. However, we find a few weaknesses in the approach followed by L21. First of all, besides the two Keplerian models of TOI-776 b and c, L21 further introduced a sinusoid based on the stellar rotation period for catching the activity-related signal of the host within the RV time series. This approach is discouraged in the literature as it is hard to physically justify that activity-induced RV signals are strictly sinusoidal (e.g. Lanza et al. 2001; Brinkworth et al. 2005). In general, those signals may also be quasi-periodic or aperiodic and subtracting sinusoids from the RV timeseries may introduce spurious harmonics, which would bias the following results (e.g. Pont et al. 2011; Tuomi et al. 2014; Rajpaul et al. 2015). Secondly, as detailed in Sec. 3.2, the analysis of all the activity indices leads us to infer a stellar rotation period $P_{\mathrm{rot}} = 21.129^{+0.062}_{-0.058}$ days. The significant difference with respect to the rotation period derived by L21 ($P_{\mathrm{rot,L21}} = 34.4^{+1.4}_{-2.0}$ d) suggests that subtracting a sinusoid with period $P_{\mathrm{rot,L21}}$ from the RV time series makes the previously described scenario even worse.

Finally, if the introduction of free parameters (e.g. the ones needed to directly model the stellar activity) has not a strong physical justification, the further bias may be an increased precision in the estimated planetary parameters, which is a result of an overfitting issue. Instead, our novel SN-extraction of RV data provides the basis functions for detrending the RV data without introducing ad-hoc hypotheses. The theoretical model we employed is the simplest being composed of the two Keplerian signals of TOI-776 b and c. Therefore, the data we provide to the literature are likely not affected by any bias and their error bars appear genuine.

In Fig. 8 we plot a density-radius diagram of all planets with available masses from RV observations and radii from transits with a precision in mass and radius of 45 % and 15 % or better, respectively, downloaded from the NASA Exoplanet Archive[9].

[9] https://exoplanetarchive.ipac.caltech.edu

In total there are 814 planets in 708 systems where most are giant planets up to 30 $M_{\rm Jup}$. There are only 61 planets in 43 systems orbiting M dwarfs, here defined as having $T_{\rm eff} = 2380 - 3850$ K, within the required uncertainty limits. The planets orbiting M dwarfs are color-coded with instellation in Fig. 8, and the remaining planets are plotted in grey. For the following M dwarf systems we used the latest publications with refined values as compared to the archive: TOI-270 (Van Eylen 2020), GJ 1132 (Bonfils et al. 2018) and GJ 436 (Turner et al. 2016).

In Fig. 9 we plot a density-radius diagram of planets with radii $< 3\ R_\oplus$ with the required uncertainties, demonstrating the location of the two TOI-776 planets. Their position relative to the density gap is obvious.

It is clear that many more planets orbiting all types of host stars are required with a high precision to properly assess planetary demographics, formation and evolution. This makes the scientific case for space missions like *CHEOPS* and PLATO extremely compelling. In the case of the $\lesssim 4$ % precision in radii of TOI-776 b and c, there are in total 36 planets with such precision (in 23 systems) orbiting M dwarfs, regardless of masses and uncertainties in mass, and 17 planet with radii $< 2\ R_\oplus$ (including the seven Trappist-1 planets).

We find somewhat different values of the stellar and planetary masses and radii compared with Luque et al. (2021). The difference is significant only as what concerns the planetary radii.

In Fig. 10 we show a mass-radius diagram with interior models with and without an atmosphere (Zeng et al. 2019). We find that the simple models with a $0.1 - 0.3$ % H-He atmosphere on top of an Earthlike core at an equilibrium temperature of 500 K agrees well with our observations. The Zeng models with a core composed of 50 % rock and 50 % water and the same amount of an H-He atmosphere requires a radius of about 2.5 $R_\oplus$ and hence such a composition is unlikely. This is also supported by the interior modelling in Sect. 5.2, where the flat posteriors for $f_{\rm atm}^{\rm start}$ indicate that both planets are likely to have lost their primary atmospheres, something which is also indicated by the results of the interior structure modeling.

7. Conclusions

1. **We investigated TOI-776 with new CHEOPS photometry, together with the available *TESS* data, and achieve improvement in the precision of the radii of the two planets, with a factor of two better than previously, reaching a precision of 4%. However, due to the increased activity of the host star only marginal or no improvement in precision of the other planetary parameters is reached.**
2. **This level is reached with 2 and 3 *CHEOPS* visits respectively for planets b and c, using a 32-cm telescope on a very active 11.5 magnitude star. This clearly demonstrates that PLATO with its significantly larger collecting area, its long times on target and consequently many observed transits is likely to supersedes its required precision – especially for a large number of red dwarfs.**
3. **The refined radii, together with the masses, allow us to classify the planets as super-Earths, rather than sub-Neptunes or at least as something in between**.
4. **We have characterised the increase in activity of TOI-776 since the data of L21 was obtained. Using our results we determine the rotation period of TOI-776 and find it to be significantly ($\approx 2/3$) shorter than the previous value quoted by L21.**
5. **We have demonstrated a possible method to treat RV and LC data from exoplanets transiting stars that are very active and/or changing the level of activity during the period of observation, in order to retrieve the best planetary parameters.**
6. TOI-776 is a very good case of how stellar-induced signals can change in a relatively short amount of time creating very large effects that may severely impact the disentangling of stellar signals in time-domain analyses. The somewhat surprising fact that the second observation campaign actually made the overall data quality *worse* due to the increased level of activity, has an impact for space missions like *JWST* and PLATO. Both these missions will observe large numbers of cooler stars and these will probably risk showing similar (temporal) behavior as TOI-776 implying a significant change in activity level on timescales of around one year similar to hotter stars such as the Sun. We therefore propose that a photometric monitoring program is instituted for target stars such as TOI-776 or cooler. This would allow a planning such that the best possible masses of the host star can be obtained. Even though PLATO will likely benefit from being designed to observe the micro variation of the host stars, a large and predictive observation program of photometry and spectroscopy would be required for at least the cooler part of the target list.
7. **Given that the planets orbiting TOI-776 appear to be very interesting and potentially important targets for further analyses, we consider the present investigation, with its significantly improved precision in the planetary radii to be contributing necessary data. Also taking into account the changed behaviour of the host star over a relatively short time span, demonstrate that our results will be important when considering future investigations.**

Acknowledgements. CHEOPS is an ESA mission in partnership with Switzerland with important contributions to the payload and the ground segment from Austria, Belgium, France, Germany, Hungary, Italy, Portugal, Spain, Sweden, and the United Kingdom. The CHEOPS Consortium would like to gratefully acknowledge the support received by all the agencies, offices, universities, and industries involved. Their flexibility and willingness to explore new approaches were essential to the success of this mission. Funding for the TESS mission is provided by NASA's Science Mission Directorate. We acknowledge the use of public TESS data from pipelines at the TESS Science Office and at the TESS Science Processing Operations Center. This work is done under the framework of the KESPRINT collaboration (http://www.kesprint.science). KESPRINT is an international consortium devoted to the characterization and research of exoplanets discovered with space-based missions. It is based in part on observations made with ESO Telescopes at the La Silla Observatory (Chile) under programme 106.21TJ.001 (P.I. D. Gandolfi). This research has made use of the NASA Exoplanet Archive, which is operated by the California Institute of Technology, under contract with the National Aeronautics and Space Administration under the Exoplanet Exploration Program. M.F., I.Y.G., J. K. and C.M.P. and A.Br. gratefully acknowledge the support of the Swedish National Space Agency (SNSA; DNR 177/19, 174/18,2020-00104 65/19). A.J.M gratefully acknowledge the support of the SNSA funding (Career grant 120/19C). T.G.W., A.C.C., and K.H. acknowledge support from STFC consolidated grant numbers ST/R000824/1 and ST/V000861/1, and UKSA grant ST/R003203/1. Y.A. and M.J.H. acknowledge the support of the Swiss National Fund under grant 200020.172746. D.G. and L.M.S. gratefully acknowledge financial support from the CRT foundation under Grant 2018.2323 "Gaseous or rocky? Unveiling the nature of small worlds". D.G., M.F., X.B., S.C., and J.L. acknowledge their roles as ESA-appointed CHEOPS science team members. A. De. and D.E. acknowledge support from the European Research Council (ERC) under the European Union's Horizon 2020 research and innovation programme (project Four Aces; grant agreement No 724427). A.De., A. Le., acknowledge support from the Swiss National Centre for Competence in Research "PlanetS" and the Swiss National Science Foundation (SNSF). R.L. acknowledges funding from University of La Laguna through the Margarita Salas Fellowship from the Spanish Ministry of Universities ref. UNI/551/2021-May 26, and under the EU Next Generation funds. S.H. gratefully acknowledges CNES funding through the grant 837319. The MOC activities have been supported by the

ESA contract No. 4000124370. S.C.C.B. and V.A. acknowledge support from FCT through FCT contracts nr. IF/01312/2014/CP1215/CT0004 and IF/00650/2015/CP1273/CT0001, respectively This work was supported by FCT - Fundação para a Ciência e a Tecnologia through national funds and by FEDER through COMPETE2020 - Programa Operacional Competitividade e Internacionalização by these grants: UID/FIS/04434/2019; UIDB/04434/2020; UIDP/04434/2020; PTDC/FIS-AST/32113/2017, POCI-01- 0145-FEDER-032113; PTDC/FIS-AST/28953/2017, POCI-01- 0145-FEDER-028953; PTDC/FIS-AST/28987/2017, POCI-01- 0145-FEDER-028987. S.G.S. acknowledge support from FCT through FCT contract nr. CEECIND/00826/2018 and POPH/FSE (EC). We acknowledge support from the Spanish Ministry of Science and Innovation and the European Regional Development Fund through grants ESP2016-80435-C2-1-R, ESP2016-80435-C2-2- R, PGC2018-098153-B-C33, PGC2018-098153-B-C31, ESP2017- 87676-C5-1-R, MDM-2017-0737 Unidad de Excelencia Maria de Maeztu-Centro de Astrobiología (INTA-CSIC), as well as the sup- port of the Generalitat de Catalunya/CERCA programme. This project was supported by the CNES. L.D. is an F.R.S.-FNRS Postdoctoral Researcher. The Belgian participation to CHEOPS has been supported by the Belgian Federal Science Policy Office (BELSPO) in the framework of the PRODEX Program, and by the University of Liège through an ARC grant for Concerted Research Actions financed by the Wallonia-Brussels Federation. K.G.I. is the ESA CHEOPS Project Scientist and is responsible for the ESA CHEOPS Guest Observers Programme. She does not participate in, or contribute to, the definition of the Guaranteed Time Programme of the CHEOPS mission through which observations described in this paper have been taken, nor to any aspect of target selection for the programme. G.L. acknowledges support by CARIPARO Founda- tion, according to the agreement CARIPARO-Università degli Studi di Padova (Pratica n. 2018/0098). This work was granted access to the HPC resources of MesoPSL financed by the Region Ile de France and the project Equip@Meso (reference ANR-10-EQPX- 29-01) of the programme Investissements d'Avenir supervised by the Agence Nationale pour la Recherche. M.L. acknowledges support from the Swiss National Science Foundation under grant number PCEFP2.194576. P.F.L.M. acknowledges support from STFC grant number ST/M001040/1. L.D.N. thanks the Swiss National Science Foundation for support under Early Postdoc. Mobility grant P2GEP2.200044. This work was also partially supported by a grant from the Simons Foundation (PI Queloz, grant number 327127). I.R. acknowledges support from the Spanish Ministry of Science and Innovation and the European Regional Development Fund through grant PGC2018-098153-B- C33, as well as the support of the Generalitat de Catalunya/CERCA programme. This project has been supported by the Hungarian National Research, Development and Innovation Office (NKFIH) grant K-125015, the MTA-ELTE Lendület Milky Way Research Group and the City of Szombathely under Agreement No. 67.177-21/2016. This research received funding from the European Research Council (ERC) under the European Union's Horizon 2020 research and innovation programme (grant agreement n 803193/BEBOP), and from the Science and Technology Facilities Council (STFC.; grant ST/S00193X/1 V.V.G. is an F.R.S-FNRS Research Associate. We thank the Mathworks community and, in particular, Peter (2023, `https://www.mathworks.com/matlabcentral/fileexchange/42905-break-x-axis`).

References

Adibekyan, V., Dorn, C., Sousa, S. G., et al. 2021, Science, 374, 330
Allard, F., Homeier, D., & Freytag, B. 2012, Philosophical Transactions of the Royal Society of London Series A, 370, 2765
Andersen, J. M. & Korhonen, H. 2015, MNRAS, 448, 3053
Anglada-Escudé, G. & Butler, R. P. 2012, ApJS, 200, 15
Antoniadis-Karnavas, A., Sousa, S. G., Delgado-Mena, E., et al. 2020, A&A, 636, A9
Azzalini, A. 1985, Scandinavian Journal of Statistics, 12, 171
Baraffe, I., Chabrier, G., & Barman, T. 2008, A&A, 482, 315
Baraffe, I., Chabrier, G., Barman, T. S., Allard, F., & Hauschildt, P. H. 2003, A&A, 402, 701
Baranne, A., Queloz, D., Mayor, M., et al. 1996, A&AS, 119, 373
Barragán, O., Aigrain, S., Gillen, E., & Gutiérrez-Canales, F. 2021, Research Notes of the American Astronomical Society, 5, 51
Barragán, O., Aigrain, S., Rajpaul, V. M., & Zicher, N. 2022, MNRAS, 509, 866
Barragán, O., Gandolfi, D., & Antoniciello, G. 2019, MNRAS, 482, 1017
Benz, W., Broeg, C., Fortier, A., et al. 2021, Experimental Astronomy, 51, 109
Blackwell, D. E. & Shallis, M. J. 1977, MNRAS, 180, 177
Bonfanti, A., Delrez, L., Hooton, M. J., et al. 2021a, arXiv e-prints, arXiv:2101.00663
Bonfanti, A., Fossati, L., Kubyshkina, D., & Cubillos, P. E. 2021b, A&A, 656, A157
Bonfanti, A., Gandolfi, D., Egger, J. A., et al. 2023, arXiv e-prints, arXiv:2302.10664
Bonfanti, A. & Gillon, M. 2020, A&A, 635, A6
Bonfanti, A., Ortolani, S., & Nascimbeni, V. 2016, A&A, 585, A5
Bonfanti, A., Ortolani, S., Piotto, G., & Nascimbeni, V. 2015, A&A, 575, A18
Bonfils, X., Almenara, J. M., Cloutier, R., et al. 2018, A&A, 618, A142
Borucki, W. J., Koch, D., Basri, G., et al. 2010, Science, 327, 977
Brinkworth, C. S., Marsh, T. R., Morales-Rueda, L., et al. 2005, MNRAS, 357, 333
Choi, J., Dotter, A., Conroy, C., et al. 2016, ApJ, 823, 102
Claret, A. 2000, A&A, 363, 1081
Cubillos, P., Harrington, J., Loredo, T. J., et al. 2017, AJ, 153, 3
Deeg, H. J. & Belmonte, J. A. 2018, Handbook of Exoplanets
Delrez, L., Ehrenreich, D., Alibert, Y., et al. 2021, Nature Astronomy, 5, 775
Espinoza, N. & Jordán, A. 2015, MNRAS, 450, 1879
Fei, Y., Murphy, C., Shibazaki, Y., Shahar, A., & Huang, H. 2016, Geophys. Res. Lett., 43, 6837
Figueira, P., Santos, N. C., Pepe, F., Lovis, C., & Nardetto, N. 2013, A&A, 557, A93
Fridlund, M. 2008, Space Sci. Rev., 135, 355
Fridlund, M., Livingston, J., Gandolfi, D., et al. 2020, MNRAS, 498, 4503
Gardner, J. P., Mather, J. C., Clampin, M., et al. 2006, Space Sci. Rev., 123, 485
Gelman, A. & Rubin, D. B. 1992, Statistical Science, 7, 457
Georgieva, I. Y., Persson, C. M., Barragán, O., et al. 2021, MNRAS, 505, 4684
Gialluca, M. T., Robinson, T. D., Rugheimer, S., & Wunderlich, F. 2021, PASP, 133, 054401
Gray, D. F. 2008, The Observation and Analysis of Stellar Photospheres
Gustafsson, B., Edvardsson, B., Eriksson, K., et al. 2008, A&A, 486, 951
Hadden, S. & Lithwick, Y. 2017, AJ, 154, 5
Hakim, K., Rivoldini, A., Van Hoolst, T., et al. 2018, Icarus, 313, 61
Haldemann, J., Alibert, Y., Mordasini, C., & Benz, W. 2020, A&A, 643, A105
Hatzes, A. P. 1996, PASP, 108, 839
Hauschildt, P. H., Allard, F., Ferguson, J., Baron, E., & Alexander, D. R. 1999, ApJ, 525, 871
Hirano, T., Dai, F., Gandolfi, D., et al. 2018, AJ, 155, 127
Hoyer, S., Guterman, P., Demangeon, O., et al. 2020, A&A, 635, A24
Husser, T. O., Wende-von Berg, S., Dreizler, S., et al. 2013, A&A, 553, A6
Jenkins, J. M., Twicken, J. D., McCauliff, S., et al. 2016, in Society of Photo-Optical Instrumentation Engineers (SPIE) Conference Series, Vol. 9913, Proc. SPIE, 99133E
Johnstone, C. P., Güdel, M., Brott, I., & Lüftinger, T. 2015a, A&A, 577, A28
Johnstone, C. P., Güdel, M., Stökl, A., et al. 2015b, ApJ, 815, L12
Krenn, A. F., Fossati, L., Kubyshkina, D., & Lammer, H. 2021, A&A, 650, A94
Kubyshkina, D., Cubillos, P. E., Fossati, L., et al. 2019a, ApJ, 879, 26
Kubyshkina, D., Fossati, L., Erkaev, N. V., et al. 2018, A&A, 619, A151
Kubyshkina, D., Fossati, L., Mustill, A. J., et al. 2019b, A&A, 632, A65
Lacedelli, G., Wilson, T. G., Malavolta, L., et al. 2022, MNRAS, 511, 4551
Lanza, A. F., Rodonò, M., Mazzola, L., & Messina, S. 2001, A&A, 376, 1011
Léger, A., Rouan, D., Schneider, J., et al. 2009, A&A, 506, 287
Leleu, A., Alibert, Y., Hara, N. C., et al. 2021, A&A, 649, A26
Lindegren, L., Bastian, U., Biermann, M., et al. 2021, A&A, 649, A4
Lopez, E. D. & Fortney, J. J. 2014, ApJ, 792, 1
Lovis, C. & Pepe, F. 2007, A&A, 468, 1115
Luque, R., Serrano, L. M., Molaverdikhani, K., et al. 2021, A&A, 645, A41
Marigo, P., Girardi, L., Bressan, A., et al. 2017, ApJ, 835, 77
Morris, R. L., Twicken, J. D., Smith, J. C., et al. 2017, Kepler Data Processing Handbook: Photometric Analysis, Kepler Science Document KSCI-19081-002
Pepe, F., Mayor, M., Galland, F., et al. 2002a, A&A, 388, 632
Pepe, F., Mayor, M., Galland, F., et al. 2002b, A&A, 388, 632
Perryman, M. 2018, The Exoplanet Handbook
Piskunov, N. & Valenti, J. A. 2017, A&A, 597, A16
Piskunov, N. E., Kupka, F., Ryabchikova, T. A., Weiss, W. W., & Jeffery, C. S. 1995, A&AS, 112, 525
Pont, F., Aigrain, S., & Zucker, S. 2011, MNRAS, 411, 1953
Queloz, D., Bouchy, F., Moutou, C., et al. 2009, A&A, 506, 303
Queloz, D., Henry, G. W., Sivan, J. P., et al. 2001, A&A, 379, 279
Rajpaul, V., Aigrain, S., Osborne, M. A., Reece, S., & Roberts, S. 2015, MNRAS, 452, 2269
Rauer, H., Catala, C., Aerts, C., et al. 2014, Experimental Astronomy, 38, 249
Reiners, A., Bean, J. L., Huber, K. F., et al. 2010, ApJ, 710, 432
Ricker, G. R., Winn, J. N., Vanderspek, R., et al. 2015, Journal of Astronomical Telescopes, Instruments, and Systems, 1, 014003
Salmon, S. J. A. J., Van Grootel, V., Buldgen, G., Dupret, M. A., & Eggenberger, P. 2021, A&A, 646, A7
Scalo, J., Kaltenegger, L., Segura, A., et al. 2007, Astrobiology, 7, 85
Schanche, N., Hébrard, G., Collier Cameron, A., et al. 2020, MNRAS, 499, 428
Schlegel, D. J., Finkbeiner, D. P., & Davis, M. 1998, ApJ, 500, 525
Schwarz, G. 1978, Annals of Statistics, 6, 461
Scuflaire, R., Théado, S., Montalbán, J., et al. 2008, Ap&SS, 316, 83
Simola, U., Bonfanti, A., Dumusque, X., et al. 2022, A&A, 664, A127
Simola, U., Dumusque, X., & Cisewski-Kehe, J. 2019, A&A, 622, A131

Smith, J. C., Stumpe, M. C., Van Cleve, J. E., et al. 2012, PASP, 124, 1000
Sotin, C., Grasset, O., & Mocquet, A. 2007, Icarus, 191, 337
Stumpe, M. C., Smith, J. C., Van Cleve, J. E., et al. 2012, PASP, 124, 985
Tuomi, M., Anglada-Escude, G., Jenkins, J. S., & Jones, H. R. A. 2014, arXiv e-prints, arXiv:1405.2016
Turner, J. D., Pearson, K. A., Biddle, L. I., et al. 2016, MNRAS, 459, 789
Twicken, J. D., Clarke, B. D., Bryson, S. T., et al. 2010, in Society of Photo-Optical Instrumentation Engineers (SPIE) Conference Series, Vol. 7740, Software and Cyberinfrastructure for Astronomy, ed. N. M. Radziwill & A. Bridger, 774023
Valenti, J. A. & Piskunov, N. 1996, A&AS, 118, 595
Van Eylen, V. 2020, submitted to MNRAS
Van Eylen, V. & Albrecht, S. 2015, ApJ, 808, 126
Van Eylen, V., Astudillo-Defru, N., Bonfils, X., et al. 2021, MNRAS, 507, 2154
Vines, J. I. & Jenkins, J. S. 2022, MNRAS, 513, 2719
Wilson, T. G., Goffo, E., Alibert, Y., et al. 2022, MNRAS, 511, 1043
Xie, J.-W., Dong, S., Zhu, Z., et al. 2016, Proceedings of the National Academy of Science, 113, 11431
Yee, S. W., Petigura, E. A., & von Braun, K. 2017, ApJ, 836, 77
Zechmeister, M. & Kürster, M. 2009, A&A, 496, 577
Zechmeister, M., Reiners, A., Amado, P. J., et al. 2018, A&A, 609, A12
Zeng, L., Jacobsen, S. B., Sasselov, D. D., et al. 2019, Proceedings of the National Academy of Science, 116, 9723

[1] Department of Space, Earth and Environment, Chalmers University of Technology, Onsala Space Observatory, 439 92 Onsala, Sweden e-mail: malcolm.fridlund@chalmers.se [10]
[2] Leiden Observatory, University of Leiden, PO Box 9513, 2300 RA Leiden, The Netherlands e-mail: fridlund@strw.leidenuniv.nl
[3] Space Research Institute, Austrian Academy of Sciences, Schmiedlstrasse 6, A-8042 Graz, Austria
[4] Physikalisches Institut, University of Bern, Gesellschaftsstrasse 6, 3012 Bern, Switzerland
[5] Dipartimento di Fisica, Universita degli Studi di Torino, via Pietro Giuria 1, I-10125, Torino, Italy
[6] Observatoire Astronomique de l'Université de Genève, Chemin Pegasi 51, CH-1290 Versoix, Switzerland
[7] Aix Marseille Univ, CNRS, CNES, LAM, 38 rue Frédéric Joliot-Curie, 13388 Marseille, France
[8] Department of Astronomy, Stockholm University, AlbaNova University Center, 10691 Stockholm, Sweden
[9] Centre for Exoplanet Science, SUPA School of Physics and Astronomy, University of St Andrews, North Haugh, St Andrews KY16 9SS, UK
[10] Sub-department of Astrophysics, Department of Physics, University of Oxford, Oxford, OX1 3RH, UK
[11] Lund Observatory, Dept. of Astronomy and Theoretical Physics, Lund University, Box 43, 22100 Lund, Sweden
[12] Thüringer Landessternwarte Tautenburg, Sternwarte 5, D-07778 Tautenburg, Germany
[13] 4Pharma, Tykistökatu 4D, FI-20520, Turku, Finland
[14] Cavendish Laboratory, JJ Thomson Avenue, Cambridge CB3 0HE, UK
[15] Instituto de Astrofísica de Andalucía (IAA-CSIC), Glorieta de la Astronomía s/n, 18008 Granada, Spain
[16] Department of Astronomy & Astrophysics, University of Chicago, Chicago, IL 60637, USA
[17] Instituto de Astrofisica e Ciencias do Espaco, Universidade do Porto, CAUP, Rua das Estrelas, 4150-762 Porto, Portugal
[18] Instituto de Astrofisica de Canarias, 38200 La Laguna, Tenerife, Spain
[19] Departamento de Astrofisica, Universidad de La Laguna, 38206 La Laguna, Tenerife, Spain
[20] Institut de Ciencies de l'Espai (ICE, CSIC), Campus UAB, Can Magrans s/n, 08193 Bellaterra, Spain
[21] Institut d'Estudis Espacials de Catalunya (IEEC), 08034 Barcelona, Spain
[22] Admatis, 5. Kandó Kálmán Street, 3534 Miskolc, Hungary
[23] Depto. de Astrofisica, Centro de Astrobiologia (CSIC-INTA), ESAC campus, 28692 Villanueva de la Cañada (Madrid), Spain
[24] Departamento de Fisica e Astronomia, Faculdade de Ciencias, Universidade do Porto, Rua do Campo Alegre, 4169-007 Porto, Portugal
[25] Center for Space and Habitability, University of Bern, Gesellschaftsstrasse 6, 3012 Bern, Switzerland
[26] Université Grenoble Alpes, CNRS, IPAG, 38000 Grenoble, France
[27] Institute of Planetary Research, German Aerospace Center (DLR), Rutherfordstrasse 2, 12489 Berlin, Germany
[28] Université de Paris, Institut de physique du globe de Paris, CNRS, F-75005 Paris, France
[29] Centre for Mathematical Sciences, Lund University, Box 118, 221 00 Lund, Sweden
[30] Astrobiology Research Unit, Université de Liège, Allée du 6 Août 19C, B-4000 Liège, Belgium
[31] Space sciences, Technologies and Astrophysics Research (STAR) Institute, Université de Liège, Allée du 6 Août 19C, 4000 Liège, Belgium
[32] Centre Vie dans l'Univers, Faculté des sciences, Université de Genève, Quai Ernest-Ansermet 30, CH-1211 Genève 4, Switzerland
[33] Department of Astrophysics, University of Vienna, Tuerkenschanzstrasse 17, 1180 Vienna, Austria
[34] Department of Physics and Astronomy, University of Leicester, Leicester LE1 7RH, United Kingdom
[35] Science and Operations Department - Science Division (SCI-SC), Directorate of Science, European Space Agency (ESA), European Space Research and Technology Centre (ESTEC), Keplerlaan 1, 2201-AZ Noordwijk, The Netherlands
[36] Konkoly Observatory, Research Centre for Astronomy and Earth Sciences, 1121 Budapest, Konkoly Thege Miklós út 15-17, Hungary
[37] ELTE Eötvös Loránd University, Institute of Physics, Pázmány Péter sétány 1/A, 1117 Budapest, Hungary
[38] IMCCE, UMR8028 CNRS, Observatoire de Paris, PSL Univ., Sorbonne Univ., 77 av. Denfert-Rochereau, 75014 Paris, France
[39] Institut d'astrophysique de Paris, UMR7095 CNRS, Université Pierre & Marie Curie, 98bis blvd. Arago, 75014 Paris, France
[40] Astrobiology Center, 2-21-1 Osawa, Mitaka, Tokyo 181-8588, Japan
[41] National Astronomical Observatory of Japan, 2-21-1 Osawa, Mitaka, Tokyo, 181-8588, Japan
[42] Department of Astronomy, University of Tokyo, 7-3-1 Hongo, Bunkyo, Tokyo 113-0033, Japan
[43] Department of Astronomy, The Graduate University for Advanced Studies (SOKENDAI), 2-21-1 Osawa, Mitaka, Tokyo, Japan
[44] INAF, Osservatorio Astronomico di Padova, Vicolo dell'Osservatorio 5, 35122 Padova, Italy
[45] Astrophysics Group, Keele University, Staffordshire, ST5 5BG, United Kingdom
[46] INAF, Osservatorio Astrofisico di Catania, Via S. Sofia 78, 95123 Catania, Italy
[47] Institute of Optical Sensor Systems, German Aerospace Center (DLR), Rutherfordstrasse 2, 12489 Berlin, Germany
[48] Dipartimento di Fisica e Astronomia "Galileo Galilei", Universita degli Studi di Padova, Vicolo dell'Osservatorio 3, 35122 Padova, Italy
[49] Department of Physics, University of Warwick, Gibbet Hill Road, Coventry CV4 7AL, United Kingdom
[50] ETH Zurich, Department of Physics, Wolfgang-Pauli-Strasse 2, CH-8093 Zurich, Switzerland
[51] ESTEC, European Space Agency, 2201AZ, Noordwijk, NL
[52] Zentrum für Astronomie und Astrophysik, Technische Universität Berlin, Hardenbergstr. 36, D-10623 Berlin, Germany
[53] Institut für Geologische Wissenschaften, Freie Universität Berlin, 12249 Berlin, Germany
[54] Astronomy Department and Van Vleck Observatory, Wesleyan University, Middletown, CT, 06459, USA
[55] ELTE Eötvös Loránd University, Gothard Astrophysical Observatory, 9700 Szombathely, Szent Imre h. u. 112, Hungary
[56] MTA-ELTE Exoplanet Research Group, 9700 Szombathely, Szent Imre h. u. 112, Hungary
[57] Mullard Space Science Laboratory, University College London,Holmbury St. Mary, Dorking, Surrey, RH5 6NT, UK

[58] Institute of Astronomy, University of Cambridge, Madingley Road, Cambridge, CB3 0HA, United Kingdom

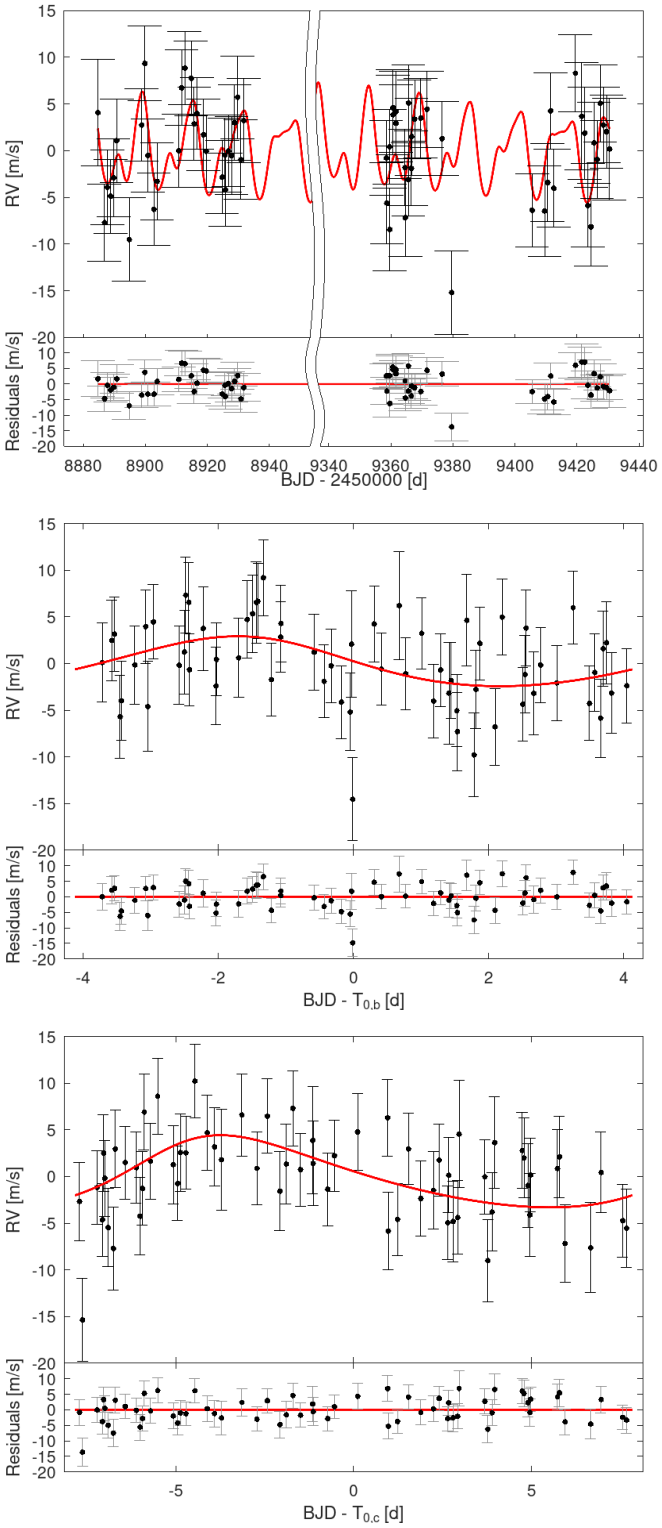

Fig. 5: **Detrended RV time series, where data are represented through black markers, while the red line is the best-fit model; the residuals are also shown. *Top panel*. Whole RV time series: the break on the temporal axis avoids the big gap in the data collection and improves the visualisation. *Middle and bottom panels*. Phase-folded RV data referring to TOI-776 b (*middle*) and TOI-776 c (*bottom*).**

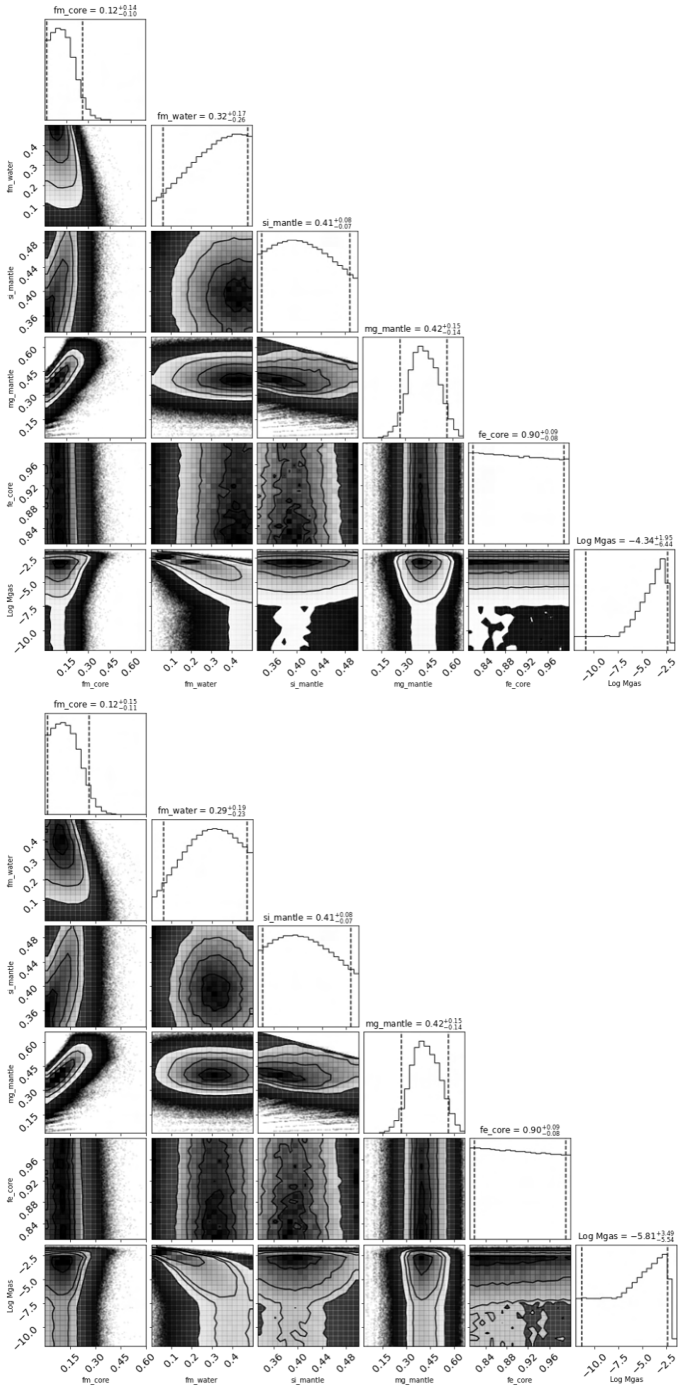

Fig. 6: Corner plot showing the results on the interior composition models of TOI-776 b (top) and TOI-776 c (bottom). The vertical dashed lines and the 'error bars' given at the top of each columns represent the 5 % and 95 % percentiles.

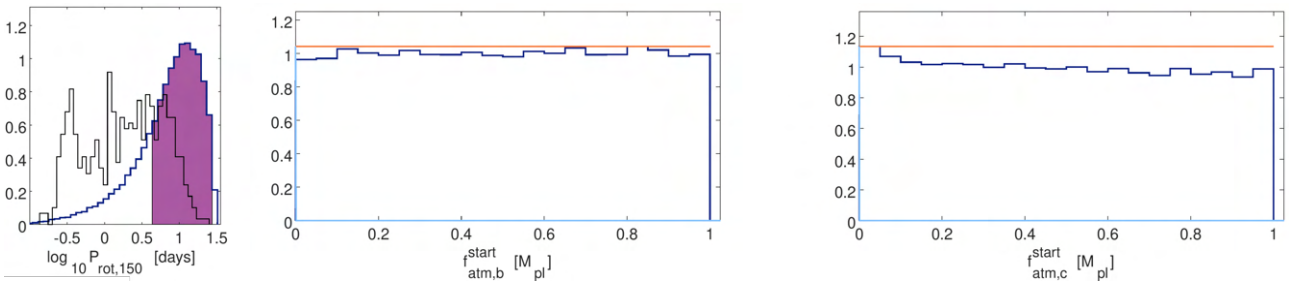

Fig. 7: *Leftmost panel.* Stellar rotation period at an age of 150 Myr (blue histogram) and 68%-highest probability density interval (purple region). The black histogram shows the rotation period of stars belonging to coeval open clusters and having masses which differ from the mass of TOI-776 less than 0.1 $M_{\odot}$ (Johnstone et al. 2015a). *Second and third panel.* Atmospheric mass fraction $f_{\rm atm}^{\rm start}$ distributions of planet b and c. The orange horizontal lines emphasize the uniform prior that has been imposed on $f_{\rm atm}^{\rm start}$. The light blue curves (barely visible and almost coincident with the vertical axis) represent the negligible present-day atmospheric content as inferred from our internal structure models.

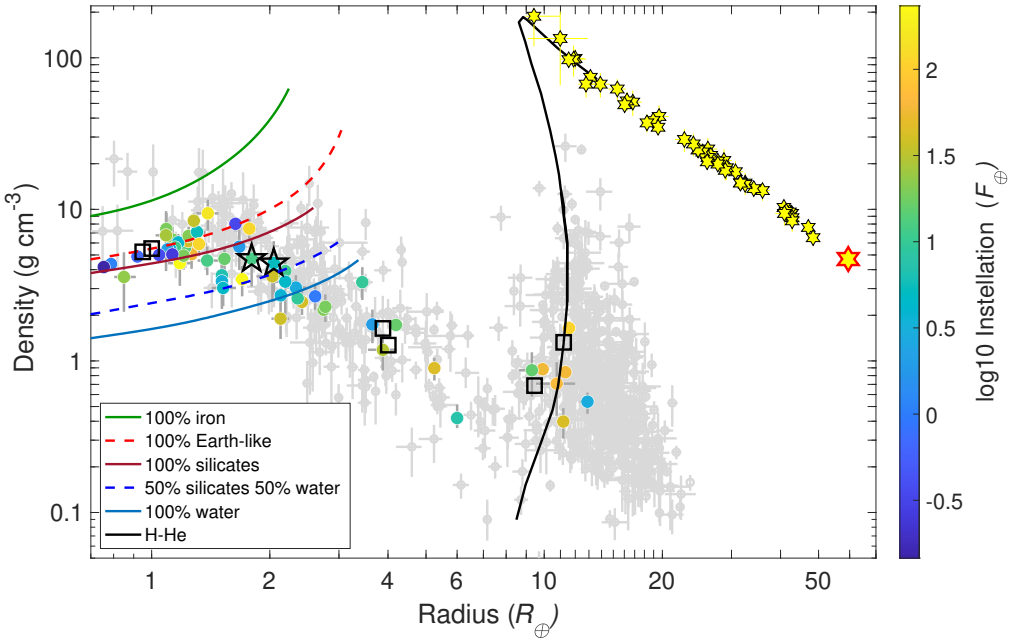

Fig. 8: Radius-density plot of all exoplanets where masses are known to a precision better than 45 %, and radii better than 15 %. In total there are 814 planets in 708 systems (including 11 planets with TTV masses without RVs). The two star symbols mark TOI-776 b (left) and TOI-776 c (right). There are 61 planets in 43 systems orbiting M-dwarfs ($T_{\rm eff}$ = 2380 – 3850 K) color-coded with instellation (all other planets are plotted in grey). Interior models from iron to water are plotted according to the legend (Zeng et al. 2019), and H-He is taken from Baraffe et al. (2003, 2008). Solar system planets are marked with black squares. Low-mass stars in eclipsing binaries are plotted as yellow hexagrams. The star with a red outline is the single-star TOI-776.

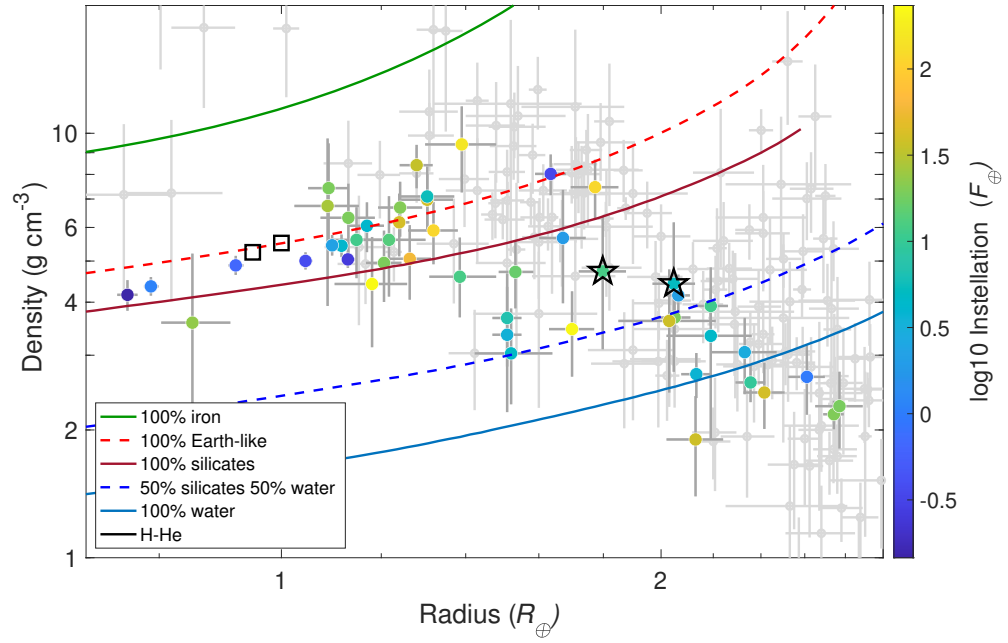

Fig. 9: Radius-density plot of planets with radii < 3 $R_\oplus$ with the required uncertainties (the 48 colour-coded planets in 30 systems orbit around M-dwarfs). Notation as in Fig. 8.

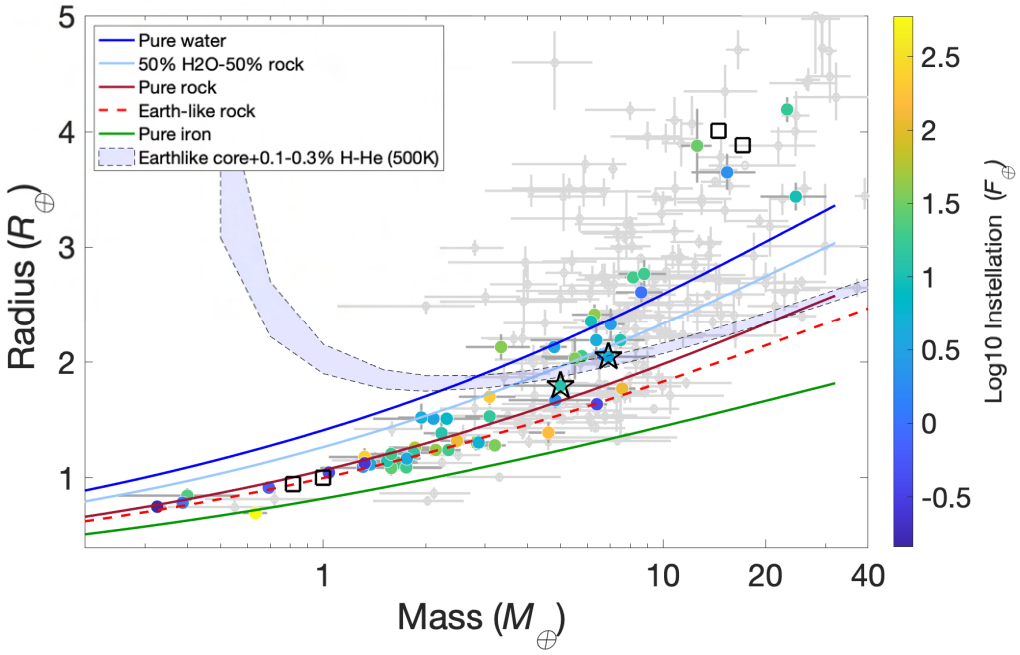

Fig. 10: Mass-radius plot of planets with masses and radii < 40 $M_\oplus$ and < 5 $R_\oplus$, respectively. In total there are 259 planets in 175 systems in the plotted mass and radius ranges with the required uncertainties, and 53 planets in 358 systems orbiting M dwarfs. Notation as in Fig. 8 with the addition of models with an Earth-like core and a 0.1 – 0.3 % H-He atmosphere for a temperature of 500 K (Zeng et al. 2019).

Table A.2: **Radial velocities $\overline{RV}$ as inferred from the SN fit onto the centred CCFs with their errors $\sigma_{\rm RV}$. They are followed by the SN hyperparameters (i.e. $\rm FWHM_{SN}$, A, and γ) and by the detrended RV values ($RV_{\rm det}$) with their errors which also account for the jitter ($\sigma_{\rm RV(det+jitter)}$).**

$\rm BJD_{TDB}$ [JD − 2 450 000]	$\overline{RV}$ [m s^{-1}]	$\sigma_{\rm RV}$ [m s^{-1}]	$\rm FWHM_{SN}$ [km s^{-1}]	A [%]	γ	$RV_{\rm det}$ [m s^{-1}]	$\sigma_{\rm RV(det+jitter)}$ [m s^{-1}]
8884.756669	7.543	4.614	3.371	5.049	-0.00015	4.074	5.726
8886.880432	-2.595	2.374	3.358	4.961	-0.00013	-7.706	4.139
8887.795265	-2.316	2.187	3.369	5.062	-0.00033	-3.921	4.034
8888.830869	-0.693	2.050	3.368	5.005	-0.00047	-4.882	3.962
8889.798112	0.144	2.460	3.373	5.071	-0.00001	-2.910	4.188
8890.808216	0.568	2.956	3.363	5.063	-0.00038	1.067	4.498
8894.816269	-9.969	2.914	3.368	5.090	-0.00029	-9.514	4.471
8898.852724	2.451	1.903	3.341	4.971	-0.00019	2.756	3.888
8899.863931	8.073	2.167	3.343	4.984	-0.00039	9.351	4.024
8900.843398	-1.325	1.954	3.335	4.949	-0.00021	-0.496	3.913
8902.807480	-5.418	1.856	3.352	5.002	-0.00014	-6.283	3.865
8903.815511	-3.064	2.403	3.342	4.954	-0.00035	-3.286	4.156
8910.814399	3.780	1.933	3.350	4.943	-0.00011	-0.021	3.902
8911.726536	9.431	2.218	3.366	5.036	-0.00006	6.731	4.051
8912.775450	9.752	1.954	3.350	4.990	-0.00009	8.849	3.913
8914.811394	7.123	2.109	3.350	5.021	-0.00001	7.755	3.992
8915.743794	-0.074	1.921	3.369	5.140	-0.00010	2.867	3.896
8916.696541	0.121	1.723	3.366	5.151	0.00002	3.982	3.803
8918.780649	-2.204	1.739	3.349	5.046	-0.00047	1.705	3.810
8919.643366	-2.397	1.900	3.359	5.082	-0.00013	-0.066	3.886
8924.805735	-4.448	1.941	3.344	4.993	-0.00030	-2.845	3.906
8925.688885	-4.112	2.056	3.362	5.129	0.00013	-0.476	3.965
8925.838889	-8.643	1.938	3.344	5.030	-0.00048	-4.197	3.905
8926.791276	-3.113	1.793	3.336	4.985	-0.00022	-0.036	3.835
8927.830748	-3.451	2.476	3.330	4.954	-0.00022	-0.530	4.198
8928.787346	0.074	2.187	3.341	4.978	-0.00067	2.985	4.034
8929.762114	6.186	2.851	3.364	5.064	-0.00001	5.721	4.430
8930.831188	0.122	2.581	3.337	4.930	0.00000	-0.957	4.261
8931.763892	3.304	2.974	3.358	5.043	0.00000	3.213	4.510
9358.539709	-0.681	2.164	3.372	4.979	-0.00009	-0.790	4.022
9358.663394	-3.550	2.705	3.353	4.853	-0.00020	-5.602	4.337
9359.555968	0.577	2.069	3.369	4.969	0.00004	0.421	3.971
9359.638302	-6.523	2.858	3.361	4.897	-0.00007	-8.443	4.434
9360.608278	6.086	2.283	3.358	4.899	0.00008	4.609	4.087
9360.654294	4.171	2.595	3.344	4.849	-0.00003	3.848	4.269
9361.598137	2.317	2.404	3.352	4.902	0.00001	2.928	4.156
9361.653909	5.161	2.725	3.355	4.872	-0.00031	4.172	4.349
9364.536796	-4.943	2.250	3.367	4.999	-0.00023	-1.815	4.069
9364.628515	-8.203	2.457	3.343	4.880	0.00022	-7.179	4.187
9365.597376	-4.623	2.001	3.355	4.920	-0.00020	-3.094	3.937
9365.645452	1.168	2.241	3.335	4.858	-0.00039	5.107	4.064
9366.582336	-5.182	2.081	3.354	4.939	-0.00031	-1.889	3.978
9366.661381	0.479	2.360	3.338	4.849	0.00009	1.502	4.131
9367.619941	-0.478	2.519	3.344	4.901	-0.00032	3.369	4.224
9369.639227	0.894	2.604	3.339	4.875	-0.00000	3.491	4.275
9371.644090	2.939	2.312	3.331	4.817	-0.00002	4.437	4.103
9376.509868	2.781	2.024	3.368	4.931	-0.00010	1.284	3.948
9379.572619	-13.542	2.892	3.370	4.950	0.00017	-15.205	4.456
9405.508895	-7.059	2.003	3.354	4.884	-0.00029	-6.383	3.938
9409.526917	-6.770	3.430	3.354	4.887	-0.00009	-6.472	4.822
9410.537241	-5.537	2.462	3.337	4.832	-0.00021	-3.419	4.190
9411.497686	2.176	2.302	3.349	4.898	0.00001	4.267	4.098
9412.523321	-6.191	2.416	3.339	4.859	0.00007	-4.025	4.163
9419.483839	9.004	2.309	3.353	4.877	0.00020	8.296	4.102
9421.492654	5.676	4.661	3.361	4.871	-0.00021	3.685	5.764

Appendix A: HARPS data

Table A.2: continued.

BJD_{TDB} [JD − 2 450 000]	$\overline{RV}$ [m s^{-1}]	σ_{RV} [m s^{-1}]	$FWHM_{SN}$ [km s^{-1}]	A [%]	γ	RV_{det} [m s^{-1}]	$\sigma_{RV(det+jitter)}$ [m s^{-1}]
9422.494950	1.462	3.563	3.355	4.888	-0.00014	1.875	4.918
9423.486148	-7.226	2.910	3.347	4.868	-0.00015	-5.878	4.468
9424.474337	-7.927	2.460	3.351	4.861	-0.00009	-8.151	4.188
9425.486818	2.102	2.710	3.349	4.863	0.00045	0.831	4.340
9426.484857	-1.518	2.442	3.345	4.849	-0.00003	-0.943	4.178
9427.491009	5.651	2.407	3.343	4.823	0.00001	5.070	4.157
9428.482128	2.439	2.242	3.339	4.816	-0.00002	2.737	4.064
9429.476269	1.512	1.898	3.341	4.818	-0.00024	2.033	3.885
9430.476566	-0.920	4.267	3.346	4.854	-0.00017	0.187	5.450

Appendix B: Supplementary material

Table A.1: Radial velocities and spectral activity indicators measured from TNG/HARPS-N spectra.

BJD_{TBD} (d)	RV TERRA	σ_{RV}	RV SERVAL	σ_{RV}	dlW	σ_{dlW}	CRX	σ_{CRX}	S-index	$\sigma_{S-index}$	H_α	NaD1	NaD2	T_{exp}	SNR
-2457000	(m s^{-1})	(m s^{-1})	(m s^{-1})	(m s^{-1})	(m^2 s^{-2})	(m^2 s^{-2})	(m $s^{-2}Np^{-1}$)	(m $s^{-2}Np^{-1}$)	—	—	—	—	—	(s)	@550 nm
1884.756669	0.12	3.34	-2.99	2.98	4.23	3.73	-13.32	24.38	1.5006	0.0252	0.3558	1.0507	0.7835	1500	22.1
1886.880432	-2.97	1.83	-7.36	1.58	-5.43	1.92	-6.13	12.91	1.5550	0.0178	0.3482	1.0569	0.8006	1500	42.5
1887.795265	-1.80	1.63	-4.92	1.89	-7.37	2.04	1.33	14.80	1.3797	0.0120	0.3610	1.0474	0.7918	1800	45.7
1888.830869	-3.46	1.60	-6.32	1.48	-5.75	1.59	-8.62	11.72	1.3912	0.0125	0.3595	1.0449	0.7957	1800	48.8
1889.798112	-2.12	1.49	-6.18	1.56	-4.04	1.88	10.82	12.08	1.4963	0.0133	0.3174	1.0418	0.7895	1800	40.4
1890.808216	1.23	2.13	0.06	2.16	-4.88	2.88	18.83	16.62	1.5079	0.0153	0.3385	1.0482	0.7968	1800	33.2
1894.816269	-5.02	1.85	-7.60	2.06	-14.02	2.42	24.84	15.68	1.4066	0.0158	0.3490	1.0580	0.7877	1800	33.2
1898.852724	1.21	1.41	-2.77	1.31	-16.14	1.49	-3.75	10.23	1.3558	0.0141	0.3643	1.0556	0.7972	1800	50.1
1899.863931	6.10	1.56	2.08	1.40	-14.38	1.50	6.80	11.00	1.3992	0.0161	0.3531	1.0612	0.7987	1800	43.5
1900.843398	3.07	1.56	-1.32	1.37	-13.68	1.77	-19.33	10.55	1.3358	0.0156	0.3668	1.0581	0.7990	1800	48.3
1902.807480	-2.95	1.38	-6.52	1.42	-14.11	1.87	7.03	10.97	1.3401	0.0132	0.3596	1.0638	0.7964	1800	51.1
1903.815511	-3.09	1.36	-8.01	1.66	-15.88	1.72	-13.54	12.98	1.3416	0.0177	0.3686	1.0610	0.7990	1800	39.5
1910.814399	3.73	1.28	-1.59	1.35	-6.89	1.65	-5.65	10.57	1.4455	0.0146	0.3418	1.0537	0.7988	1800	50.2
1911.726536	6.67	1.54	1.02	1.52	-11.10	1.50	0.02	11.72	1.3941	0.0133	0.3514	1.0504	0.8004	1800	43.5
1912.775450	6.15	1.40	2.65	1.47	-13.70	1.53	-8.65	11.37	1.5593	0.0147	0.3180	1.0554	0.7904	1800	48.8
1914.811394	6.98	1.46	2.99	1.46	-8.97	1.76	1.74	11.73	1.4598	0.0177	0.3439	1.0568	0.7966	1800	44.9
1915.743794	5.21	1.14	0.70	1.29	-11.21	1.60	2.32	10.17	1.4622	0.0130	0.3266	1.0569	0.7924	1800	49.2
1916.696541	3.10	1.23	-0.70	1.18	-15.24	1.38	8.99	9.16	1.3676	0.0110	0.3510	1.0605	0.8016	1800	54.6
1918.780649	-2.39	1.44	-7.33	1.27	-9.06	1.09	15.86	9.90	1.2979	0.0131	0.3611	1.0673	0.8040	1800	54.4
1919.643366	-0.05	1.29	-3.95	1.31	2.29	1.51	1.02	10.15	1.3378	0.0119	0.3586	1.0619	0.7939	2100	49.5
1924.805735	-2.97	1.30	-7.11	1.23	-4.32	1.84	-13.98	9.59	1.2457	0.0151	0.3633	1.0549	0.7982	1800	48.8
1925.688885	-1.51	1.34	-5.00	1.37	-4.21	1.50	-4.89	10.55	1.2865	0.0125	0.3781	1.0605	0.8049	1800	45.3
1925.838889	-3.86	1.53	-8.04	1.62	-6.28	2.07	-21.59	12.48	1.2667	0.0141	0.3720	1.0552	0.7897	1800	48.6
1926.791276	-1.56	1.27	-6.65	1.38	-6.84	1.87	-1.09	10.93	1.2315	0.0142	0.3673	1.0549	0.7976	1800	52.6
1927.830748	0.00	1.85	-5.12	1.58	-3.19	2.45	-7.33	12.50	1.2749	0.0181	0.3496	1.0470	0.7981	1800	37.9
1928.787346	-0.88	1.30	-4.31	1.44	-2.28	1.92	-7.53	11.30	1.3914	0.0170	0.3337	1.0481	0.7970	1800	43.0
1929.762114	1.78	1.65	-1.02	1.61	3.81	2.12	-14.41	12.47	1.3240	0.0179	0.3517	1.0453	0.8028	1800	33.1
1930.831188	3.84	1.66	-1.04	1.49	3.47	2.09	2.28	11.86	1.3862	0.0201	0.3584	1.0458	0.7821	1800	36.7
1931.763892	4.59	1.56	0.72	1.78	4.40	2.21	-10.73	14.00	1.4149	0.0200	0.3563	1.0397	0.7773	1800	31.7
2358.539709	0.99	1.44	-1.43	1.64	9.78	1.39	1.61	12.91	1.4300	0.0145	0.3326	1.0439	0.8036	1800	47.3
2358.663394	-1.10	1.72	-3.43	1.97	15.56	2.13	20.07	15.83	1.3071	0.0197	0.3402	1.0420	0.7910	1800	37.9
2359.555968	1.74	1.24	-2.86	1.35	10.92	1.45	4.29	10.74	1.3889	0.0144	0.3273	1.0446	0.7985	1800	49.5
2359.638302	-1.74	1.71	-4.74	1.62	16.11	2.38	1.00	13.07	1.3533	0.0196	0.3304	1.0442	0.7984	1800	36.1
2360.608278	6.21	1.48	3.89	1.70	17.22	1.94	15.97	13.51	1.3330	0.0164	0.3502	1.0468	0.7944	2100	44.9
2360.654294	3.77	1.71	1.90	1.90	19.37	2.76	20.77	15.26	1.2637	0.0180	0.3552	1.0340	0.8061	2100	39.4
2361.598137	2.94	1.57	-0.89	1.70	14.44	1.87	-6.89	13.65	1.3349	0.0171	0.3271	1.0440	0.7919	2100	42.3
2361.653909	5.09	1.97	0.94	1.83	21.47	2.39	-14.25	14.71	1.3048	0.0187	0.3429	1.0443	0.7907	2100	37.4
2364.536796	-3.22	1.51	-7.56	1.86	1.56	1.84	16.34	14.58	1.3817	0.0151	0.3429	1.0437	0.8020	2100	44.9
2364.628515	-5.68	1.97	-10.04	1.91	6.98	2.14	35.12	14.83	1.4417	0.0200	0.3222	1.0412	0.8075	2100	41.3
2365.597376	-1.22	1.59	-3.86	1.52	3.96	1.34	6.57	12.23	1.3736	0.0161	0.3511	1.0523	0.8128	2100	50.8
2365.645452	-2.15	1.61	-4.01	1.52	2.79	1.66	-15.21	12.26	1.3390	0.0185	0.3626	1.0483	0.8185	2100	45.1
2366.582336	-3.18	1.38	-6.64	1.48	1.99	1.50	1.66	11.83	1.3413	0.0155	0.3551	1.0473	0.8134	2100	48.5
2366.661381	-0.07	1.77	-3.45	1.40	0.71	1.94	-0.50	11.46	1.3213	0.0190	0.3696	1.0448	0.8196	2100	42.6
2367.619941	-1.46	1.85	-6.69	1.77	1.54	2.02	-29.80	13.69	1.3225	0.0185	0.3733	1.0441	0.8204	2100	39.8
2369.639227	0.45	1.91	-3.10	1.64	1.56	1.90	6.25	13.18	1.3115	0.0195	0.3728	1.0535	0.8167	2100	38.3
2371.644090	0.31	1.77	-2.61	1.79	3.13	1.75	11.35	14.61	1.3344	0.0202	0.3636	1.0447	0.8039	2100	43.7
2376.509868	3.72	1.42	0.59	1.27	15.37	1.41	-12.05	9.94	1.6157	0.0160	0.2897	1.0308	0.8008	2100	50.7
2379.572619	-6.30	2.14	-12.65	2.23	16.27	2.15	21.93	17.54	1.5596	0.0201	0.3098	1.0373	0.7940	2100	35.2
2405.508895	-3.75	1.19	-9.04	1.30	10.07	1.49	-5.29	10.35	1.6437	0.0174	0.2591	1.0431	0.7963	2400	50.3
2409.526917	-2.53	2.72	-7.68	2.89	15.98	2.88	6.64	23.51	1.3660	0.0238	0.3611	1.0402	0.8133	2400	29.9
2410.537241	-6.10	1.96	-8.39	1.57	10.57	2.10	5.12	12.83	1.4595	0.0209	0.3232	1.0432	0.7989	2400	41.3
2411.497686	-1.12	1.59	-4.43	1.50	6.81	2.06	17.51	11.90	1.3203	0.0172	0.3746	1.0408	0.7999	2520	44.0
2412.523321	-6.60	1.56	-11.18	1.72	4.99	1.81	-9.83	13.92	1.2131	0.0181	0.3804	1.0629	0.8107	2400	41.5
2419.483839	9.17	1.97	7.86	2.30	13.57	1.80	-7.42	18.44	1.3796	0.0170	0.3361	1.0416	0.8020	2520	43.3
2421.492654	-1.50	4.19	-3.89	3.33	24.83	3.35	2.00	27.27	1.6082	0.0325	0.3054	1.0416	0.7744	2520	22.1
2422.494950	3.55	2.15	-0.58	2.19	18.34	2.51	-4.35	17.84	1.4980	0.0255	0.3201	1.0449	0.7887	2520	28.7
2423.486148	-2.13	2.18	-3.51	2.05	13.87	2.18	-7.11	16.65	1.5585	0.0228	0.3101	1.0425	0.7936	2520	34.8
2424.474337	-2.46	1.87	-4.14	1.77	15.95	1.45	4.27	14.33	1.5826	0.0211	0.2810	1.0407	0.7934	2520	41.2
2425.486818	1.71	2.25	-3.15	1.90	18.03	2.16	8.18	15.36	1.7264	0.0234	0.3160	1.0390	0.7954	2520	37.5
2426.484857	1.02	1.96	-2.18	1.53	9.94	1.89	18.05	12.35	1.5531	0.0204	0.3061	1.0460	0.8051	2520	41.2
2427.491009	2.56	1.83	-1.55	1.72	12.35	1.58	6.74	13.90	1.5719	0.0212	0.3074	1.0476	0.7974	2520	41.8
2428.482128	1.87	1.73	-1.44	1.86	11.01	1.43	-8.62	15.10	1.5744	0.0204	0.2968	1.0463	0.8028	2400	44.5
2429.476269	2.60	1.40	0.12	1.32	12.28	1.45	-2.29	10.67	1.4531	0.0172	0.3402	1.0428	0.7970	2400	52.4
2430.476566	0.51	3.46	-4.14	2.82	19.91	2.94	-18.78	23.02	1.3513	0.0287	0.3275	1.0305	0.8136	2400	23.5

Table B.1: Polynomial detrending baseline models.

Time series	T_0 [BJD][(a)]	Planet	Detrending model
CHEOPS TG037301	9288.8716	b	$t^1 + \mathtt{roll}^4 + \mathtt{bg}^3$
CHEOPS TG037401	9293.2036	c	$t^2 + \mathtt{smear}^1 + \mathtt{roll}^4 + \mathtt{bg}^2$
CHEOPS TG039801	9324.5342	c	$t^1 + \mathtt{smear}^1 + \mathtt{roll}^4$
CHEOPS TG039802	9340.1995	c	$\mathtt{roll}^4 + \mathtt{bg}^2$
CHEOPS TG039901	9354.8447	b	$\mathtt{roll}^3 + \mathtt{bg}^2$
TESS1, Sector 10	8571.4143	b	t^4
TESS4, Sector 10	8587.9075 8588.2643	b c	t^1
HARPS RV		b,c	$t^1 + \mathrm{FWHM_{SN}}^1 + \gamma^1 + A^1$

Notes. [(a)] Shifted by −2 450 000.
All the other 7 TESS LCs only requires a normalisation scalar.

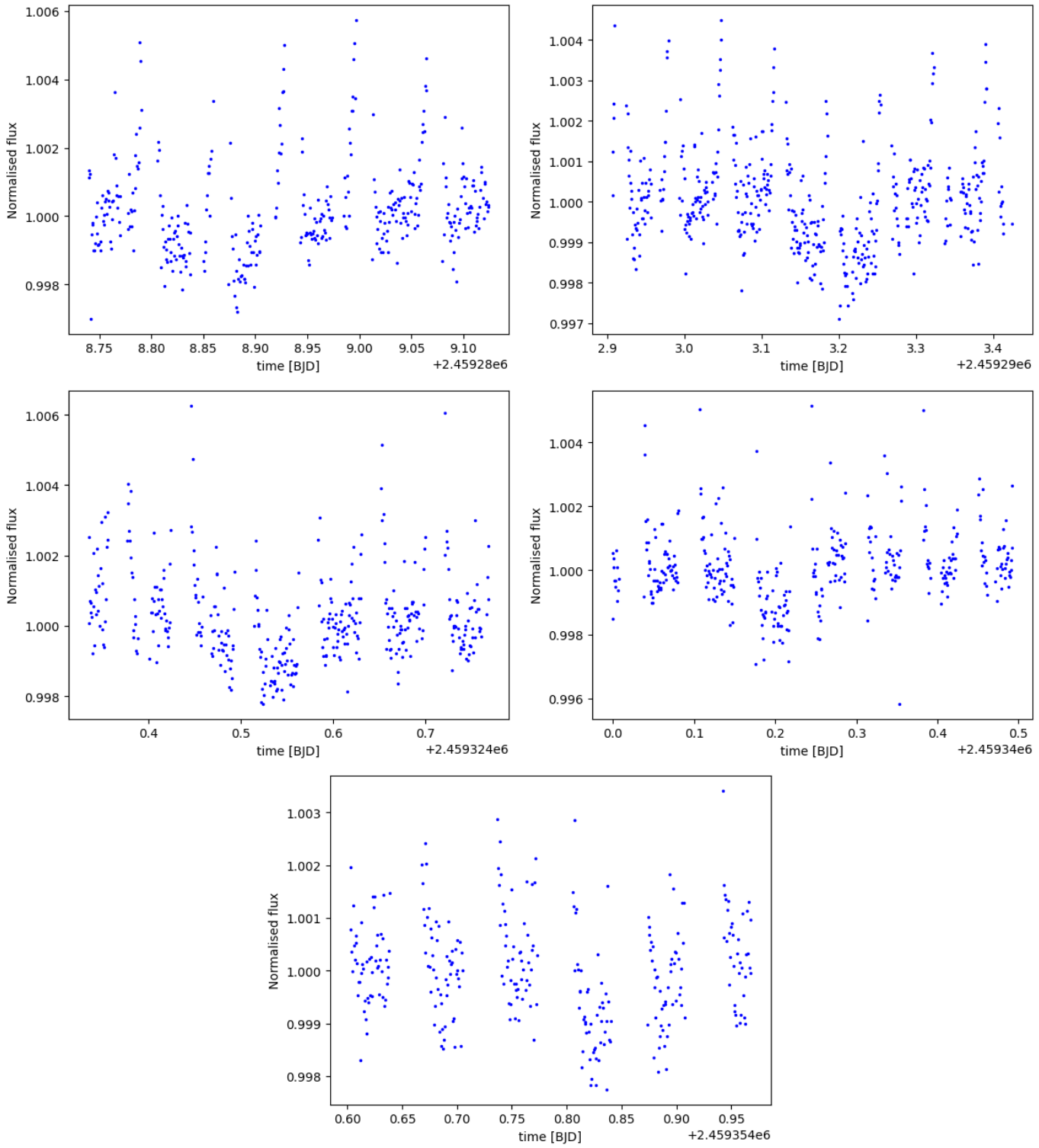

Fig. B.1: **Raw *CHEOPS* LCs shown in chronological order of observation from *top* to *bottom*.**

PAPER F

TOI-1416: A system with a super-Earth planet with a 1.07d period

H. J. Deeg, **I.Y. Georgieva**, G. Nowak, C.M. Persson, B.L. Cale, F. Murgas, E. Pallé, D. Godoy Rivera, F. Dai, D. R. Ciardi, J.M. Akana Murphy, P.G. Beck, C.J. Burke, I. Carleo, W.D. Cochran, K.A. Collins, Sz. Csizmadia, M. El Mufti, M. Fridlund, A. Fukui, D. Gandolfi, R.A. García, E. W. Guenther, P. Guerra, S. Grziwa, H. Isaacson, K. Isogai, P. Kábath, J. Korth, K.W.F. Lam, D.W. Latham, R. Luque, M.B. Lund, J.H. Livingston, S. Mathis, S. Mathur, N. Narita, J. Orell-Miquel, H.L.M. Osborne, H. Parviainen, P.P. Plavchan, S. Redfield, D.R. Rodriguez, R.P. Schwarz, S. Seager, A.M.S. Smith, V. Van Eylen, J. Van Zandt, J.N. Winn, and C. Ziegler

Accepted in Astronomy & Astrophysics

Astronomy & Astrophysics manuscript no. 1416wk61_2ndsubmit
May 9, 2023

TOI-1416: A system with a super-Earth planet with a 1.07d period

H. J. Deeg[1,2], I. Y. Georgieva[3], G. Nowak[1,2,4], C. M. Persson[3], B. L. Cale[8], F. Murgas[1,2], E. Pallé[1,2], D. Godoy Rivera[1,2], F. Dai[7], D. R. Ciardi[8], J. M. Akana Murphy[34], P. G. Beck[2,1,37], C. J. Burke[21], J. Cabrera[11], I. Carleo[1,2,20], W. D. Cochran[13], K. A. Collins[14], Sz. Csizmadia[11], M. El Mufti[6], M. Fridlund[15,3], A. Fukui[18,1], D. Gandolfi[5], R. A. García[28], E. W. Guenther[12], P. Guerra[30], S. Grziwa[17], H. Isaacson[35,36], K. Isogai[26,27], J. M. Jenkinsames, P. Kábath[16], J. Korth[3], K.W.F. Lam[11], D. W. Latham[14], R. Luque[24,1,2], M. B. Lund[8], J. H. Livingston[19,32,33], S. Mathis[28], S. Mathur[1,2], N. Narita[18,19,1], J. Orell-Miquel[1,2], H.L.M. Osborne[10], H. Parviainen[1,2], P. P. Plavchan[6], S. Redfield[20], D. R. Rodriguez[9], R. P. Schwarz[14], S. Seager[21,22,23], A.M.S. Smith[11], V. Van Eylen[10], J. Van Zandt[25], J. N Winn[29], and C. Ziegler[31]

(Affiliations after the references)

Received dd March 2023 / Accepted dd Month 2023

ABSTRACT

TOI 1416 (BD+42 2504, HIP 70705) is a V=10 late G or early K-type dwarf star. TESS detected transits in its Sectors 16, 23 and 50 with a depth of about 455 ppm and a period of 1.07 days. Radial velocities taken with the *HARPS-N*, CARMENES, Automated Planet Finder (APF) and iSHELL instruments verify the presence of the transiting planet TOI-1416 *b*, with a mass of 3.48 ± 0.47$M_\oplus$ and a radius of 1.62 ± 0.08$R_\oplus$, implying a slightly sub-Earth density of $4.50^{+0.99}_{-0.83}$ g cm^{-3}. The RV data also further indicate a tentative planet *c* with a period of 27.4 or 29.5 days, whose nature cannot be verified due to strong suspicions about contamination by a signal related to the Moon's synodic period of 29.53 days. The near-USP (Ultra Short Period) planet TOI-1416 *b* is a typical representative of a short-period and hot (T_{eq} ≈ 1570 K) super-Earth like planet. A planet model of an interior of molten magma containing a significant fraction of dissolved water provides a plausible explanation for its composition, and its atmosphere could be suitable for transmission spectroscopy with JWST. The position of TOI-1416 *b* within the radius-period distribution corroborates that USPs with periods of less than one day do not form any special group of planets. Rather, USPs belong to a continuous distribution of super-Earth like planets with periods ranging from the shortest known ones up to ≈ 30 days, whose period-radius distribution is delimitated against larger radii by the Neptune desert and by the period-radius valley that separates super-Earths from sub-Neptune planets. **In the abundance of small-short periodic planets against period, a plateau between periods of 0.6 to 1.4 days has however become notable that is compatible with the low-eccentricity formation channel.** For the Neptune desert, its lower limits required a revision due to the increasing population of USPs; for periods shorter then 2 days, we establish a radius of 1.6 $R_\oplus$ and a mass of 0.028 $M_{\rm jup}$ respectively 8.9 $M_\oplus$ as the desert's lower limits. **We also provide corresponding limits to the Neptune Desert against the planets' insulation and effective temperature**

Key words. planetary systems – planets and satellites: detection – techniques: photometric – techniques: radial velocities – techniques: spectroscopic – stars: individual (HIP 70705 TIC 158025009, TOI 1416) stars: late-type

1. Introduction

Small-sized exoplanets ($R \lesssim 2.5R_\oplus$) constitute currently the most numerous group among the known exoplanets. Their population properties were first studied by Sanchis-Ojeda et al. (2014), who identified several tens of planets (or planet candidates) with periods of less than 1 day in data from the Kepler mission (Borucki et al. 2010), and called them Ultra Short Period Planets (USP). Nearly all of these planets were smaller than 2 R_*Earth* and a preference for the presence of further planets with periods of up to 50 days was identified. The upper limit of 1 day for USPs - besides being a convenient number - was due to the lower period limit of the Kepler planet detection pipeline (Jenkins et al. 2010), which had missed out on these planets, but not due to any physical limit. However, the term 'USP' with that period limit has remained with the community, and currently there are 126 such planets known, albeit there are only 34 for which both masses and radii have been determined[1]. For overviews over this population and for theories for their development we refer to Winn et al. (2018) and Murgas et al. (2022) and references therein.

In this work, we describe the detection of a planet around the late G or early K star TOI-1416 (see Table 1), with a period of 1.067 days, just outside of the conventional definition of USPs, and place it in context with the population comprised of USP planets and of planets with slightly longer orbits. TOI-1416 *b* was found in lightcurves by the TESS mission (Ricker et al. 2015), and whose all-sky transit survey with relatively short coverages is well-suited of the detection of short-periodic planets. The TESS observations and their processing is described in Sect. 2. A ground-based follow-up campaign involving imaging and radial velocity observations is described in Sect. 3; where the analysis of the data by stellar modelling (Sect. 4) and planet system modelling (Sect. 5) led also to the detection of a potential second planet TOI-1416*c*, with a period of 27 - 29 days, for which strong doubts remain about the origin of its RV signal from Moon-reflected solar light (with details about this Appendix A). The implications of these findings, in particular with regard to the planet's composition and its placement relative to the short-period planet population are provided in Sect. 6, with conclusions in Sect. 7.

[1] Retrieved from the NASA Exoplanet Archive in February 2023.

Table 1: Parameters of TOI-1416 from catalogues

Parameter	Value	Reference
Identifiers		
TOI 1416		ExoFOP
TIC 158025009		TIC
BD+42 2504		
HIP 70705		
WISE J142741.68+415711.2		
2MASS J14274177+4157124		
TYC 3039-00749-1		
Gaia DR3 1491634483976350720		
Coordinates and kinematics		
ICRS coord (J2000)	14 27 41.766 +41 57 12.32	Gaia EDR3
Pr. motion [mas/yr]	$-92.254 \pm 0.010, -101.233 \pm 0.012$	Gaia EDR3
Parallax [mas]	18.1671 ± 0.0126	Gaia EDR3
d [pc]	55.044 ± 0.038	Gaia EDR3
Systemic velocity [km/s]	1.1712 ± 0.0010	This Work
Magnitudes and spectral type		
B [mag]	10.93 ± 0.05	Tycho-2
V [mag]	9.98 ± 0.03	Tycho-2
Gaia [mag]	9.6588 ± 0.0028	Gaia EDR3
TESS [mag]	9.0739 ± 0.006	TIC v.8.2
J [mag]	8.266 ± 0.024	2MASS
H [mag]	7.815 ± 0.017	2MASS
K [mag]	7.708 ± 0.024	2MASS
Extinction A_v[mag]	< 0.024	IRSA
Spectral type	G9V	This work

References. ExoFOP: TESS Exoplanet Follow-up Observing Program (ExoFOP) website (DOI: 10.26134/ExoFOP5) *Gaia* EDR3: Gaia Collaboration (2020); Tycho-2: Høg et al. (2000); 2MASS: Skrutskie et al. (2006); TIC: Tess Input Catalogue, Stassun et al. (2018, 2019); IRSA: Upper limit from total Galactic extinction in target direction. Value from IRSA Galactic Reddening and Extinction Calculator, based on Schlafly & Finkbeiner (2011).

2. Photometry by TESS

TESS observed TOI-1416 in its Sectors 16, 23, and 50, with more detailed information given in Table 2. Planet *b* was initially detected as a Tess Object of Interest (TOI) by the SPOC pipeline (Jenkins et al. 2016) in data from S16, as TOI 1416.01. A subsequent analysis of the combined S16, S23 **and S50 data by the same pipeline specified a transit-like signal with a period of P=1.06975[1] d and an amplitude of 391.5± 24.0 ppm** [2], indicating a candidate for a small planet of $\approx 1.6 R_\oplus$. **The difference imaging test (Twicken et al. 2018) also revealed that the origin of the transit is within** $2.47''$ **of the location of the target.**

For our own transit detection analysis, we used the algorithms DST (Détection Spécialisée de Transits, Cabrera et al. 2012) and TLS (Transit Least Square, Hippke & Heller 2019) to search for transit signals in the existing TESS data and found a signal with period of P=1.07d which were consistent with the detection reported by SPOC. We then masked the transits at 1.07 d and searched for further signals in the dataset but found no detection that indicates the presence of additional transiting planet candidate. This process was repeated later with a focus on signals with periods of ≈ 10 d and 27 to 30 d, corresponding to peaks in radial velocity periodograms reported in Sect. 5 of this work, but again to no avail.

For all further analysis of lightcurves, we used the presearch data conditioned simple aperture photometry (PDCSAP) fluxes (Stumpe et al. 2012; Smith et al. 2012; Stumpe et al. 2014; Smith et al. 2020b) available at MAST. Flux points in which some[3] quality flags are raised were removed. Also, the fluxes were normalized to an average flux of 1 in each sector independently. This lightcurve was used for the fit using Gaussian Processes with `pyaneti` described in Sect. 5.2.

The field around TOI-1416 is moderately crowded and the TIC indicates a contamination ratio[4] of $c_{TIC} = 0.193$. Very similar values for contamination are also indicated by the `CROWDSAP` keyword[4] in the headers of the SPOC lightcurves from S16 and S23, whereas the S50 lightcurves indicates only very minor contamination. PDCSAP fluxes are in principle corrected against contamination (Smith et al. 2020a). We evaluated however the impact that an error in c_{TIC} (or in the corresponding `CROWDSAP` values) might have onto the final system parameters reported in Tables 7 and 8. The impact of an error of c_{TIC} was however found to be negligible as long as c_{TIC} is correct within ≈ 25%. Lacking any indications about the uncertainty of c_{TIC} (or `CROWDSAP`), we did not propagate this uncertainty into the finally given parameter errors.

Individual transits of TOI-1416 *b* have a S/N of ≈ 3.6 and they are too shallow to be individually detectable in the lightcurve. For the preparation of the lightcurve to be used in transit fits with `UTM/UFIT` (described in Appendix C), we extracted short sections between orbital phases of ± 0.125 around the transit center of planet *b* (initially using the ephemeris provided by SPOC, and then improved ones from our own transit fits), and performed a linear fit across both off-transit sections around each transit. The fluxes were then divided by that fit, which leads to an off-transit flux that is normalised to 1. Only transits that were fully covered by TESS have been included in the final lightcurve; see Table 2 for the number of transits in each sector. The phase-folded lightcurve **containing 48 transits** is shown in Fig. 1. With the transit ephemeris that was finally adopted and which is given in Table 7, it shows a transit-shape that is much better defined – with steeper in- and egress – than one produced by a folding with the original period indicated by SPOC. The standard deviation (or *rms* noise) of the unbinned off-eclipse data is 765 ppm, and the noise of a smoothed and binned version of the phased lightcurve, with a temporal resolution similar to TESS' 2-minute cadence (green crosses in Fig. 1) is 86 ppm, while the depth of the transits is ≈ 455 ppm **and the S/N of the phased transit is ≈ 25**.

Table 2 indicates also transit epochs for each sector (corresponding to a transit near the middle of each sector's data), which had been derived using `UTM/UFIT` with a set-up that was identical to the the transit-fit on the combined (S16 to S50) light curve described in Appendix C. Against the adopted ephemeris from Table 7, a diagram of observed minus calculated (O-C) times (Fig. 2) shows no relevant deviation that might indicate the presence of transit timing variations.

[2] These values are from the Data Validation Report Summary of TOI 1416.01 for the combined S14, S23 and S50 data, available at MAST (`https://mast.stsci.edu`) as file `tess20191992019 29-s0014-s0050-0000000158025009-00611_dvm.pdf`.

[3] Cadences of expected low quality are identified by a bit-wise AND of the quality flag of a given data-point with the binary number 0101001010111111, as recommended in the TESS Archive Manual at `https://outerspace.stsci.edu/display/TESS/2.0+-+Data+Product+Overview`.

[4] The contamination ratio c_{TIC} is defined as the ratio of flux from nearby objects that falls in the aperture of the target star, divided by the target star flux in the aperture (Stassun et al. 2018). CROWDSAP is defined as the ratio of the flux from the target to the total flux in the aperture (Tenenbaum & Jenkins, 2018). A conversion is therefore given by `CROWDSAP` $= 1/(1 + c_{TIC})$.

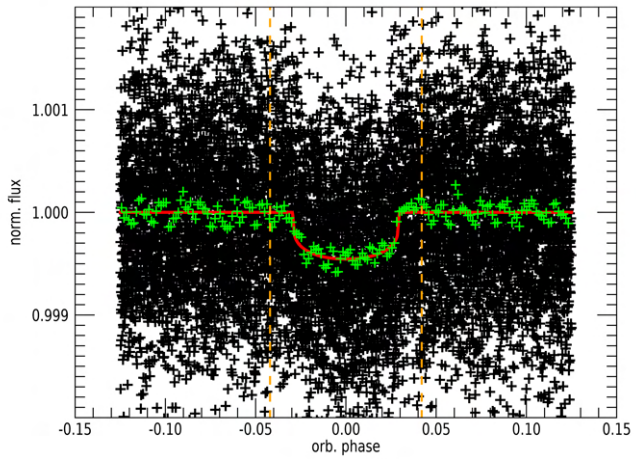

Fig. 1: Black crosses: TESS lightcurve around the transits of planet *b*, after phasing by the planet's period against the adopted ephemeris and the correction against gradients in the off-eclipse sections (indicated by the orange vertical dashed lines) as described in Sect. 2. Green crosses: The same curve, after a boxcar smoothing over 100 phased data points and posterior binning over 50 points. We note that the average time-increment between the binned points is 126 seconds, which is very similar to the 120 s temporal resolution of TESS lightcurves. The red curve is the transit model generated with `UTM/UFIT`, described in Appendix C.

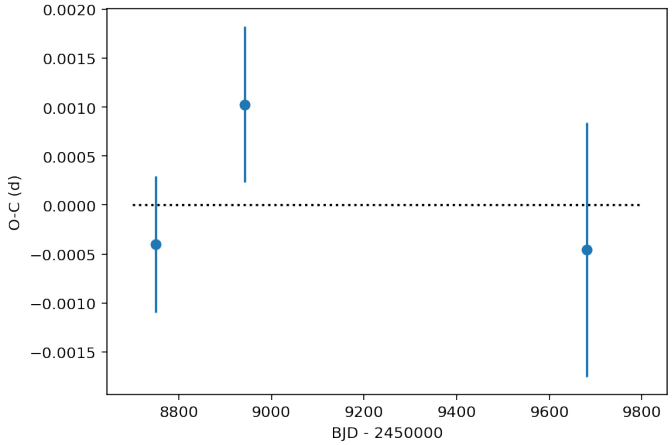

Fig. 2: O-C diagram of the transit epochs of TESS Sectors 16, 23 and 50, against the adopted ephemeris (dotted black line).

.
.

3. Ground-based follow-up

3.1. High-Resolution spectroscopy

High-resolution spectroscopic observations of TOI-1416 were obtained by several instruments, described in more detail in the following sections, with an overview on the observations given in Table 3. Fig. 3 shows a time-series of all the RVs that have been collected. Corresponding tables with the RVs from each instrument and – if available – spectral indices can be found at the CDS. Also provided at CDS is a joint table in which all acquired RVs are listed in temporal order.

Table 2: *TESS* observations of TOI-1416

Sector	Camera	CCD	Start date UT	End date UT	N_{tr}	Epoch $T_{0,b}$ BJD-2450000
16	4	4	2019-09-12	2019-10-06	20	8750.1592[7]
23	2	1	2020-03-21	2020-04-15	17	8942.7168[8]
50	2	2	2022-03-26	2022-04-22	11	9680.8473[13]

Notes. The start and end dates refer to the first and last points of the lightcurves after processing as described in Sect. 2. N_{tr} is the number of complete transits of planet *b*. $T_{0,b}$ is the transit epoch of planet *b* in the given TESS Sector

Table 3: RV observations of TOI-1416

Instrum.	spect. range μm	Start date UT	End date UT	t_{cov} d	N_{RV}	σ_{RV} m s^{-1}
CARMENES	0.52-0.96	2019-12-10	2020-03-09	90	34	1.96
HARPS-N	0.38-0.69	2020-01-14	2022-01-31	748	96	1.06
APF	0.37-0.90	2020-01-23	2020-07-05	164	52	5.67
HIRES	0.41-1.02	2020-01-04	2020-08-05	214	12	0.85
iSHELL	2.17-2.47	2020-02-17	2020-06-04	108	11	4.07

Notes. t_{cov} is the time-span covered, N_{RV} the number of RV values, and σ_{RV} is the mean of the formal uncertainties of individual RVs.

3.1.1. 3.5 m Calar Alto/CARMENES

We started the RV follow-up of TOI-1416 using the CARMENES instrument mounted on the 3.5 m telescope at Calar Alto Observatory, Almería, Spain, under the observing programs F19-3.5-014 and F20-3.5-011 (PI Nowak), setting the exposure times to 1800 seconds. The CARMENES spectrograph has two arms (Quirrenbach et al. 2014, 2018), the visible (VIS) arm covering the spectral range 0.52–0.96 μm and a near-infrared (NIR) arm covering the spectral range 0.96–1.71 μm. Due to the S/N that was obtained, only the VIS channel observations could be used to derive useful RV measurements. All observations were taken with exposure times of 1800 s, resulting in a SNR per pixel (at 4635,7 nm in the VIS spectra) in the range of 42 to 113. CARMENES performance, data reduction and wavelength calibration are described in Trifonov et al. (2018) and Kaminski et al. (2018). Relative radial velocity values, chromatic index (CRX), differential line width (dLW), and Hα index values were obtained using `serval`[5] (Zechmeister et al. 2018). For each spectrum, we also computed the cross-correlation function and its full width half maximum, contrast and bisector velocity span values, following Lafarga et al. (2020). The RV measurements were corrected for barycentric motion, secular acceleration and nightly zero-points.

3.1.2. TNG/HARPS-N

96 spectra in three observing seasons were collected with the *HARPS-N* spectrograph with R≈ 115 000 (Cosentino et al. 2012), mounted at the 3.58-m Telescopio Nazionale Galileo (TNG) of Roque de los Muchachos Observatory in La Palma, Spain. The exposure times were set to 636–2700 s, based on weather conditions and scheduling constraints, leading to a SNR per pixel (at 5500 Å) of 48–138. The spectra were extracted us-

[5] `https://github.com/mzechmeister/serval`

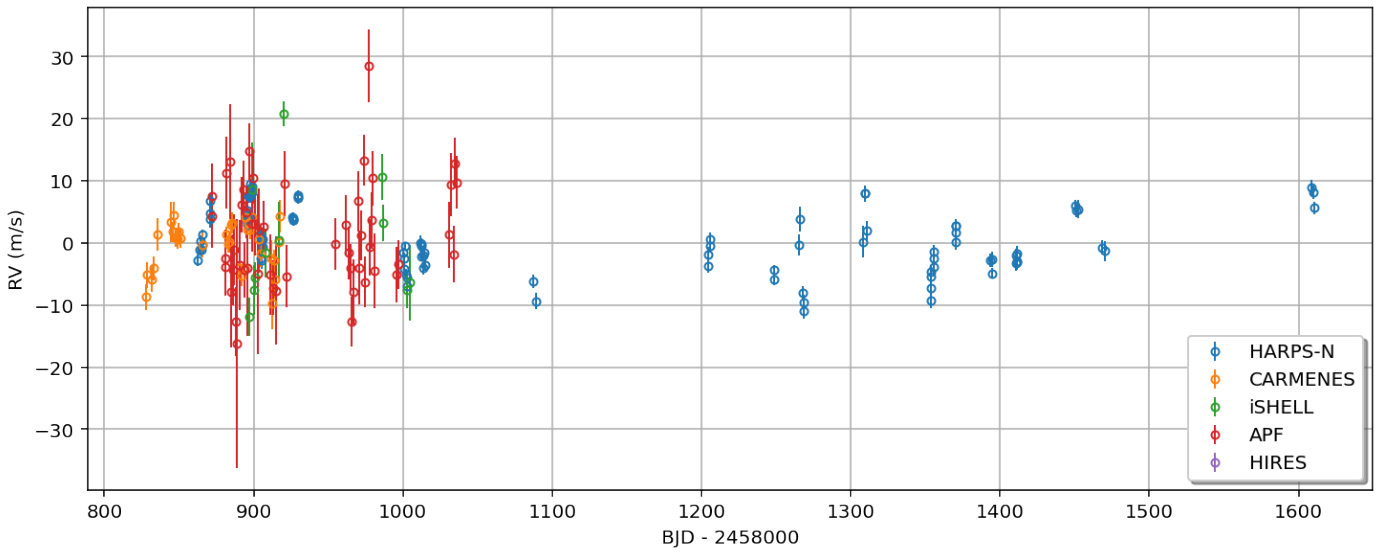

Fig. 3: Relative radial velocities of TOI-1416 from all contributing instruments. Each instrument's set of RVs was offset separately to an average of zero.

ing the *HARPS-N* DRS pipeline version 3.7 (Cosentino et al. 2014). Doppler measurements and spectral activity indicators (CCF_FWHM, CCF_CTR, BVS and the Mont-Wilson S-index) were measured using the DRS and the YABI tool[6], by cross-correlating the extracted spectra with a K5 mask (Baranne et al. 1996). Furthermore, we used `serval` to measure relative RVs, chromatic RV index, differential line width, and the Hα index, as defined in Zechmeister et al. (2018). While both DRS and `serval` derive very similar RVs, we adopted those from `serval` for further analysis, due to issues with the DRS in those exposures that were terminated prematurely; see also Fig. F.1 in Appendix F. The table of *HARPS-N* measurements available at CDS contains the 96 RVs from both pipelines, together with all activity indicators extracted by either pipeline, in the following columns (for most indicators, a column with the errors is also provided, not shown below):

```
bjd_tdb       - BJD_TDB
rvs_srv       - SERVAL barycentric corrected relative RV
                (against a zero average)
rvs_drs       - DRS  barycentric corrected absolute RV
ccf_bis_drs   - DRS Bisector Inverse Slope (BIS) measured
                from Cross-Correlation Functions (CCFs)
ccf_fwhm_drs  - DRS Full Width at Half Maximum of CCF
ccf_ctr_drs   - DRS CCF contrast
smw_drs       - DRS Mont-Wilson S-index
log_rhk_drs   - DRS log(R_{HK})
crx_srv       - SERVAL chromatic RV index (CRX)
dlw_srv       - SERVAL differential line width (dLW)
halpha_srv    - SERVAL H-alpha index
nad1_srv      - SERVAL sodium Na~D1 index
nad2_srv      - SERVAL sodium Na~D2 index
snr_550nm_drs - DRS SNR at spectral order 46 (~550 nm)
expt            - exposure time from FITS header
```

3.1.3. IRTF/iSHELL

A total of 11 observations of TOI-1416 was obtained in as many nights with the iSHELL instrument at NASA InfraRed Telescope Facility (IRTF, Rayner et al. 2022) atop Mauna Kea, Hawaii, USA, using its KGAS mode covering the wavelengths of 2.17-2.47 μm. The exposure times were always set at 300 seconds, and exposures were repeated anywhere from 4-16 times consecutively per night, in order to obtain a signal-to-noise ratio (SNR) per spectral pixel of $\approx$ 120, though the actual results varied from 85-186 due to variable seeing and atmospheric transparency conditions. A methane isotopologue (13CH4) gas cell is used in the instrument (Cale et al. 2019) to constrain the line-spread function and to provide a common reference for the optical path wavelength. Along with each observation, a set of five 15-second flat-field images was also collected, with the gas cell removed for data reduction purposes, in order to mitigate flexure-dependent and time-variable fringing present in the spectra. The 11 RVs included in the electronic tables at CDS are nightly averaged values from the individual exposures.

3.1.4. Keck/HIRES and Lick Observatory APF

The High Resolution Echelle Spectrometer (HIRES) on the 10m Keck Observatory (Vogt et al. 1994) was used to obtain 12 high-resolution spectra of TOI-1416, and the Automatic Planet Finder (APF) on the Lick Observatory (Vogt et al. 2014) was used to obtain 52 high-resolution spectra. Each exposure of TOI-1416 was about 500 s on HIRES and 1200 s on APF. We also obtained an iodine-free spectrum on HIRES as the template for the radial velocity extraction for both the HIRES and APF observations. The HIRES radial velocities collected using the telescope setup, the instrument setup, and the analysis pipeline described in Howard et al. (2010). The APF radial velocities were collected using a 1″ decker and analyzed with the standard California Planet Search pipeline (Fulton et al. 2015).

3.2. Ground-based imaging and time-series photometry

The TESS pixel scale is $\sim$ 21″ per pixel and its photometric apertures typically extend out to roughly 1′, generally causing multiple stars to blend in the TESS aperture. To attempt to determine the true source of our detection in the TESS data, we conducted ground-based imaging and photometric time-series observations of the field around TOI-1416 as part of the TESS

[6] Available at `http://ia2-harps.oats.inaf.it:8000`

Follow-up Observing Program[7] (TFOP) Sub Group 3 (High-resolution Imaging) and Sub Group 1 (Seeing limited Photometry; Collins 2019).

3.2.1. High-resolution imaging at Palomar Observatory

As part of our standard process for validating transiting exoplanets to assess the possible contamination of bound or unbound companions on the derived planetary radii (Ciardi et al. 2015), we observed TOI-1416 with infrared high-resolution adaptive optics (AO) imaging at Palomar Observatory. The Palomar Observatory observations were made with the PHARO instrument (Hayward et al. 2001) behind the natural guide star AO system P3K (Dekany et al. 2013) on 2020-01-08 UT in a standard 5-point quincunx dither pattern with steps of 5″. Each dither position was observed three times, offset in position from each other by 0.5″ for a total of 15 frames. The camera was in the narrow-angle mode with a full field of view of ≈ 25″ and a pixel scale of approximately 0.025″ per pixel. Observations were made in the narrow-band $Br-\gamma$ filter ($\lambda_o = 2.1686; \Delta\lambda = 0.0326\mu$m) with an integration time of 5.6 s per frame (118 seconds total).

The AO data were processed and analyzed with a custom set of tools written in IDL. The science frames were flat-fielded and sky-subtracted. The flat fields were generated from a median average of dark subtracted flats taken on-sky. The flats were normalized such that the median value of the flats is unity. The sky frames were generated from the median average of the 15 dithered science frames; each science image was then sky-subtracted and flat-fielded. The reduced science frames were combined into a single combined image using an intra-pixel interpolation that conserves flux, shifts the individual dithered frames by the appropriate fractional pixels, and median-coadds the frames (Fig. 4). The final resolution of the combined dither was determined from the FWHM of the point spread function, of 0.11″ (Fig. 5).

No sources, other than the primary target, were detected. The sensitivities of the final combined AO image were determined by injecting simulated sources azimuthally around the primary target every 45° at separations of integer multiples of the central source's FWHM (Furlan et al. 2017, Lund, M.B. et al., in prep.). The brightness of each injected source was scaled until standard aperture photometry detected it with 5σ significance. The resulting brightness of the injected sources relative to the target sets the contrast limits at that injection location. The final 5σ limit at each separation was determined from the average of all of the determined limits at that separation and the uncertainty on the limit was set by the *rms* dispersion of the azimuthal slices at a given radial distance. The sensitivity curve is shown in Fig. 5 along with an image zoomed around the target, showing no other companion stars. We also note that an interrogation of the GAIA EDR3 showed as the most nearby star one that is 23" W of the target and 11.4 mag fainter, whereas as the second closest one is 51" NE and 9.5 mag fainter; due to their faintness neither of these stars can be responsible for the transits on TOI-1416.

3.2.2. Time-series photometry with MUSCAT2

TOI-1416 was observed with the MUSCAT2 multi-colour imager (Narita et al. 2019) mounted at the 1.5m Telescopio Carlos Sánchez at Teide Observatory, Tenerife, Spain, on several dates: Between 2020-01-17 03:42 UT and 06:12 covering a full transit of planet *b*; 2021-05-03 22:19 and 2021-05-03 02:09 UT with a partial transit (ingress) and 2022-04-20 20:45 and 2022-04-20 00:07 UT for a full transit. The raw data were reduced by the MuSCAT2 pipeline (Parviainen et al. 2019) which performs standard image calibration, aperture photometry, and is capable of modelling the instrumental systematics present in the data while simultaneously fitting a transit model to the light curve. Due to the target's brightness, only short exposure times could be used. Given the noise present, no evidence for a transit could be found on the target. There are 77 sources listed in the GAIA DR3 in a radius of 2.5′ around the target, of which 7 have a brightness large enough that they could potentially be an eclips-

[7] https://tess.mit.edu/followup

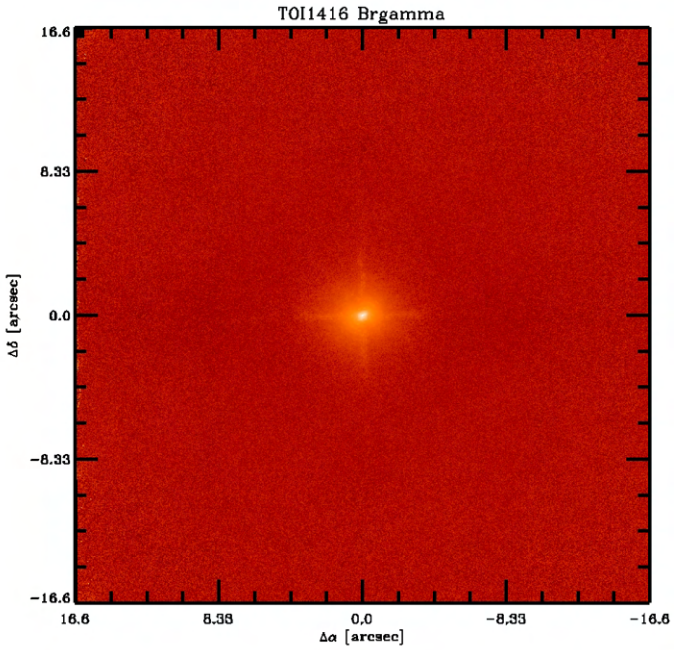

Fig. 4: Full field of view image of the final combined dither pattern for the Palomar AO imaging.

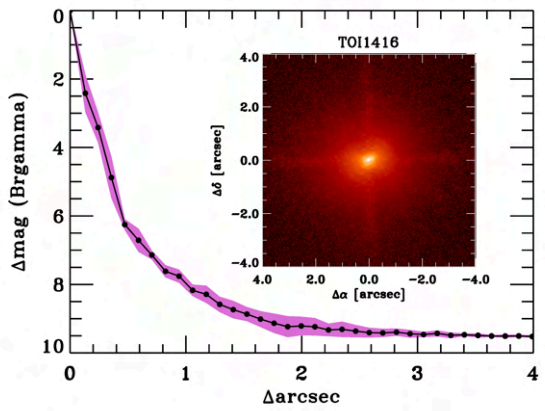

Fig. 5: Companion sensitivity for the Palomar AO imaging. The black points represent the 5σ limits and are separated in steps of 1 FWHM (≈ 0.1″); the purple zone represents the azimuthal dispersion (1σ) of the contrast determinations (see text). The inset image is of the primary target showing no additional companions within 3″ of the target.

ing binary that mimics the transit observed by TESS. Of these, however, only the star TIC 158025007, which is the brightest nearby contaminant and about 1.5′ south of the target, could be excluded with certainty as a source for a false alarm.

3.2.3. Time-series photometry with LCOGT

We observed full predicted transit windows of TOI-1416 *b* on 2020-05-21 UT and 2021-03-08 UT using the Las Cumbres Observatory Global Telescope (LCOGT; Brown et al. 2013) 1.0 m network node at McDonald Observatory. The 1 m telescopes are equipped with 4096 × 4096 pixel SINISTRO cameras having an image scale of 0.″389 per pixel, resulting in a 26′ × 26′ field of view. The images were calibrated by the standard LCOGT `BANZAI` pipeline (McCully et al. 2018) and differential photometric data were extracted using `AstroImageJ` (Collins et al. 2017).

We extracted light curves from the 2020-05-21 UT data for all 6 known Gaia DR3 and TICv8 neighboring stars within 2.′5 of TOI-1416 that are bright enough in the TESS band to produce detection by TESS. We thus checked all stars down to 8.4 magnitudes fainter than TOI-1416 (i.e. down to 17.5 mag in TESS band). We calculate the *rms* of each of the 6 nearby star light curves (binned in 5 minute bins) and find that the LCOGT light curve *rms* values are smaller by at least a factor of 5 compared to the expected NEB (Nearby Eclipsing Binary) depth in each respective star. We then visually inspected the neighboring star light curves to ensure no obvious deep eclipse-like signal. We therefore rule out NEBs as the cause of the TOI-1416 *b* detection in the TESS data.

For the second observation on 2021-03-08 UT, we defocused the telescope to improve photometric precision and attempt to detect the shallow TOI-1416 *b* event on target. As shown in Fig. 6, we find a likely transit detection centered at 2459281.827±0.005 $\mathrm{BJD_{TDB}}$ with a depth of 350±100 ppm. **The difference between Bayesian Information Criterion (BIC) of the transit model shown and one without any transit was Δ-BIC = - 43 in favor of the transit model.**

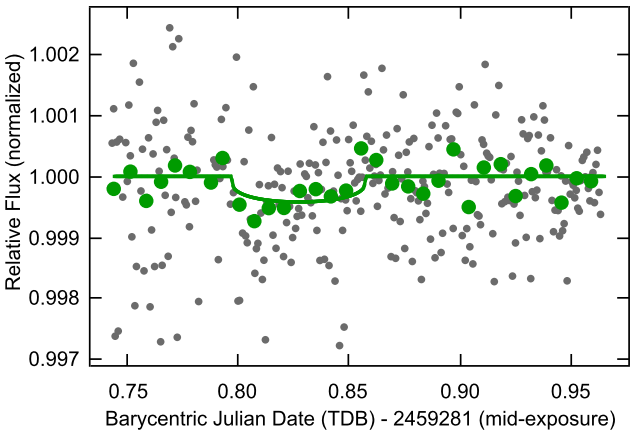

Fig. 6: Timeseries of a predicted transit of TOI-1416 *b* on 2021-03-08 UT, observed by the LCOGT. The grey dots are the unbinned differential photometry (no detrending applied) and the green dots show the data in 10 minute bins. The green line is a transit-model fit to the data using priors from the Data Validation Report mentioned in Sect. 2, except the epoch and the size of the planet, which were unconstrained parameters. The differ

4. Stellar modelling

4.1. Spectral analysis

We started our analysis of the host star by first deriving the stellar effective temperature, $T_{\rm eff}$, the stellar radius, $R_\star$, and the abundance of the key species iron relative to hydrogen, [Fe/H], with the empirical `SpecMatch-Emp` code (Yee et al. 2017). We modelled our co-added high resolution (R = 115000) *HARPS-N* spectra with a SNR of 346 at 6100 Å. This software characterises stars from their optical spectra and compares observations to a dense spectral library of well-characterised FGKM stars observed with Keck/HIRES.

In addition to `SpecMatch-Emp`, we analysed the co-added *HARPS-N* spectra with version 5.22 of the spectral analysis package `SME` (Spectroscopy Made Easy; Valenti & Piskunov 1996; Piskunov & Valenti 2017). This software is fitting observed spectra to calculated synthetic stellar spectra for a given set of parameters. We chose the Atlas12 (Kurucz 2013) atmosphere grids, and retrieved the atomic and molecular line data from VALD (Ryabchikova et al. 2015) to synthesise the spectra. We modelled $T_{\rm eff}$ from the line wings of the hydrogen λ6563 line, and the surface gravity, $\log g$, from the calcium triplet at 6102, 6122, and 6162 Å, and the 6439 Å line. We fitted the iron and calcium abundances, the projected stellar rotational velocity, $V \sin i_\star$, and the macroturbulent velocity, $V_{\rm mac}$ from unblended lines between 6000 and 6600 Å. The sodium abundance was fitted from spectral lines between 5600 and 6200 Å. We found similar abundances of iron, calcium and sodium, and determined $V \sin i_\star = 2.0 \pm 0.7$ km s^{-1} and $V_{\rm mac} = 1.5 \pm 1.0$ km s^{-1}. To check and further refine our model, we used the Na I doublet at 5888 and 5895 Å. The resulting model suggests that TOI-1416 is a an early K dwarf star.

Results from both models are listed in Table 4 and are in good agreement within the uncertainties. They also agree well with the corresponding values from the Gaia DR2 and from the TESS Input Catalogue (TIC, Stassun et al. 2018, 2019).

The metalicity and kinematics of TOI-1416point to a membership in the galactic thin disk; following the precepts of Reddy et al. (2006), we obtain a thin-disk membership probability of 0.975±0.012.

4.2. Stellar mass, radius and age

To obtain an independent estimate of the stellar radius, we analysed the spectral energy distribution (SED) of TOI-1416 with the python code `ARIADNE` (Vines & Jenkins 2022). This software fits broadband photometry to the `Phoenix v2` (Husser et al. 2013), `BtSettl` (Allard et al. 2012), Castelli & Kurucz (2004), and Kurucz (1993) atmospheric model grids for stars with $T_{\rm eff} > 4000$ K convolved with various filter response functions. For TOI-1416, we utilised data in the bandpasses $GG_{\rm BP}G_{\rm RP}$ from Gaia eDR3, *WISE* W1-W2, JHK_S magnitudes from *2MASS*, and the Johnson *B* and *V* magnitudes from APASS DR9 (AAVSO Photometric All-Sky Survey; Henden et al. 2016). By interpolating the $T_{\rm eff}$, $\log g_\star$, and [Fe/H] model grids, SED models were produced where distance, extinction (A_V), and stellar radius are treated as free parameters. The Gaia eDR3 parallax was used to obtain the distance, and priors for $T_{\rm eff}$, $\log g_\star$, and [Fe/H] were taken from `SME`. We used flat priors for $R_\star$ between 0.05 and 20 $R_\odot$, and for A_V between zero and the maximum line-of-sight value from the

dust maps of Schlegel et al. (1998). Each SED model was integrated to get the bolometric flux which together with $T_{\rm eff}$ and the *Gaia* eDR3 parallax gives the stellar radius for each fitted model. The weighted average of each parameter is computed based on the relative probabilities of the models, and the final value of the stellar radius is computed with Bayesian Model Averaging. The `Phoenix v2` model grid which has the highest probability was used to calculate the synthetic photometry. The model is shown in Fig. 7 along with the fitted bands.

In addition to the above modelling we used the python code `isochrones` (Morton 2015) to obtain a homogeneous model of TOI-1416. This code is fitting stellar parameters with an MCMC fitting tool and the MIST (Choi et al. 2016) stellar evolution tracks. We used the same bands and priors as in the `ARIADNE` model. We find $A_V = 0.05 \pm 0.04$ mag, and a bolometric luminosity of $0.34 \pm 0.03\ L_\odot$. The resulting stellar properties are in very good agreement with the values found by the above models.

As a comparison, we used the `Param 1.5` on-line tool (da Silva et al. 2006; Rodrigues et al. 2014, 2017) with the PARSEC isochrones (Bressan et al. 2012) and the same bands and priors as in the above models. And finally, we used the empirical calibration equations of Torres (2010) to compute stellar mass and radius from $T_{\rm eff}$, $\log g$, and [Fe/] from `SME`.

All results are in excellent agreement. The stellar masses, radii, and corresponding bulk densities, are listed in Table 5 together with the Gaia radius for comparison. The adopted values, which were also used in the joint modelling of the radial velocities and light curves in Sect. 5.2, were derived by the adding of simulated probability distributions that are associated to each of the values from the different methods (the values from the TIC were not used for this), using two-sided Gaussian distributions with 1 million elements. Hence, each of the methods has been taken with equal weight. In the resultant distribution, the percentiles at 15.9, 50, and 84.1 percent where then used to quote the median and the ± 1-sigma errors. The derived values for the temperature place TOI-1416 right at the border between spectral classes G and K, with a slight preference for spectral class G9V, due to the notable Ca H& K lines (Fig. 8), which are defining feature of the class G (Cannon & Pickering 1901, p. 158). The mean R'_{HK} index among the 96 *HARPS-N* spectra of $log(R'_{HK}) = -4.86 \pm 0.03$ indicates however only very moderate chromospheric activity. This activity implies also an age in the range of 4 – 7 Gyr, based on the activity-age relation by Mamajek & Hillenbrand (2008). Ages from the aforementioned isochrone analyses are not very well constrained but indicate a similar evolutionary phase, with MIST isochrones indicating an age of $10.6^{+0.5}_{-3.2}$ Gyr and `Param 1.5` one of $13.8^{+0.2}_{-3.9}$ Gyr, which in either case excludes that TOI-1416 is a very young system. With TOI-1416 being a likely thin-disk member and age estimates for the local thin disk being 6.8 – 7.0 Gyr (Kilic et al. 2017), the age of TOI-1416 is most likely close to that value.

In Appendix A we also present an analysis of the stellar rotation based on the TESS lightcurves, leading to $P_{\rm rot} = 17.6$ d, which is also compatible with a rotation period of $P_{\rm rot}/\sin i = 20^{11}_{-5}$ d from the star's $V \sin i$, and which leads to a gyrochronological age of 1 -2 Gyr. This apparently young age might however be a consequence from a delay in the star's age-related spin-down due to the presence of the close planet *b*, given that its orbital period is shorter than the stellar rotation period, with a transfer of angular momentum from the planet to the host star (Hut 1980).

The work by Ahuir et al. (2021) indicates that a planet with the mass and orbital period of TOI-1416 *b* might have a moderate effect on the star's rotation through magnetic interactions (Strugarek 2016), and hence invalidate its gyrochronological age. However, more detailed studies that include also mass-loss scenarios for the planet (e.g. Attia et al. 2021) would be needed for a better estimate of the planet's effects onto the stellar rotation throughout its evolution, which then might enable a correction of its gyrochronological age.

Table 4: Spectroscopic parameters for TOI-1416 derived with `SME` and `SpecMatch-Emp` and comparison values from Gaia and the TIC.

Method	$T_{\rm eff}$ (K)	[Fe/H] (dex)	$\log(g)$ (cgs)	$V \sin(i)$ (km s^{-1})
`SME`[a]	4884 ± 70	+0.08 ± 0.05	4.52 ± 0.05	2.0 ± 0.7
`SpecMatch-Emp`	4966 ± 110	+0.19 ± 0.09	...	...
Gaia DR2	4909^{+97}_{-58}	...	...	...
TIC	4946 ± 129	...	4.54 ± 0.09	...

[a] Adopted for the modelling of stellar mass and radius in Sect. 4.2.

Table 5: Stellar masses and radii with corresponding mean densities of TOI-1416 derived with different models with priors from `SME`.

Method	$M_\star$ ($M_\odot$)	$R_\star$ ($R_\odot$)	$\rho_\star$ (g cm^{-3})
`isochrones`	0.813 ± 0.013	0.786 ± 0.007	2.36 ± 0.09
`Param1.5`[a]	$0.778^{+0.020}_{-0.018}$	$0.785^{+0.009}_{-0.041}$	2.27 ± 0.22
SED[b]	$0.770^{+0.078}_{-0.065}$	0.798 ± 0.008	2.14 ± 0.21
`SpecMatch-Emp`	...	0.788 ± 0.079	...
Torres[c]	0.812 ± 0.055	0.807 ± 0.056	2.18 ± 0.48
Gaia DR2	...	$0.819^{+0.020}_{-0.031}$	...
TIC[d]	0.81 ± 0.10	0.80 ± 0.05	2.21 ± 0.60
Adopted value	$0.798^{+0.035}_{-0.044}$	$0.793^{+0.036}_{-0.028}$	$2.21^{+0.32}_{-0.21}$

[a] Param1.5 with PARSEC isochrones.
[b] ARIADNE SED fitting with Bayesian Model Averaging.
[c] Torres (2010) calibration equations.
[d] Not used for adopted values.

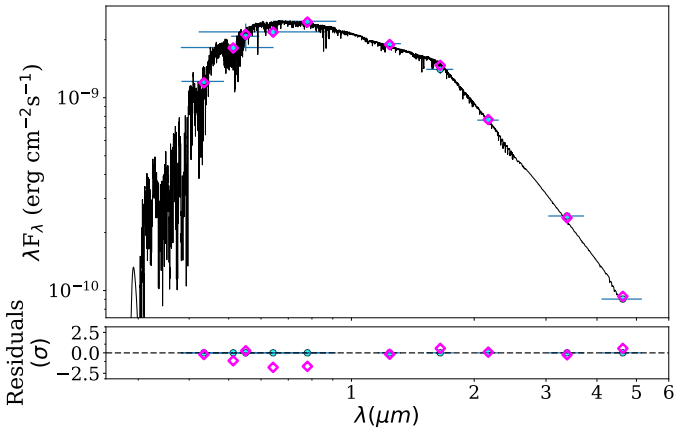

Fig. 7: The spectral energy distribution (SED) of TOI-1416. The best fitting model `Phoenix v2` is shown in black. The observed photometry is marked with cyan circles, and the synthetic photometry with magenta diamonds. The horizontal bars of the observations indicate the effective widths of the passbands, while the vertical bars mark the 1 σ uncertainties. The lower panel shows the residuals normalised to the errors of the photometry which implies that precise photometry shows the largest scatter.

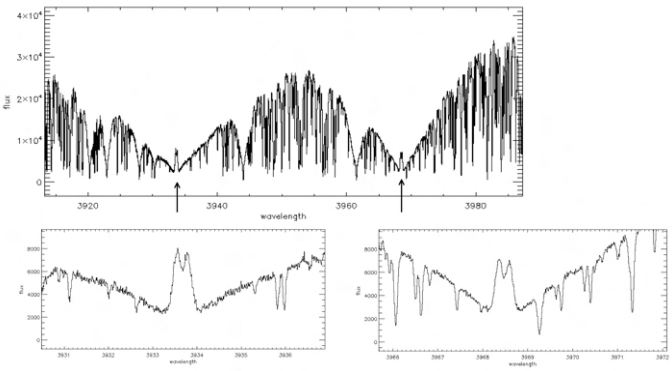

Fig. 8: Upper panel: Co-added *HARPS-N* spectrum of TOI-1416 analysed with SME (Valenti & Piskunov 1996; Piskunov & Valenti 2017), in the range of the Ca H & K lines (arrows). Lower panels: Zooms around the Ca K (3933.66 Å) and Ca H (3968.47 Å) lines.

5. Planet system modelling

In this section, we first provide an analysis of the periodicities and activity indicators in the RV data, with a detailed evaluation of a potential contamination of RV signals by lunar light given in Appendix B. This is followed by a joint RV/transit RV fit using Gaussian Processes, in which several models with and without a second planet were evaluated. A fit to the RVs using the Floating Chunk Offset (FCO) method (Hatzes et al. 2010; Hatzes 2014) provided a clear detection of the transiting plane b and is described in Appendix D. Also, a classical (non-Bayesian) fitting to the transit lightcurve was performed with the UTM/UFIT package (Deeg 2014). Fits with UTM/UFIT, which were also used in some other parts of this work, are described in Appendix C. The results from all methods are included in Table 7.

5.1. Periodicities in the RV data: planetary signals or stellar activity?

Beyond the anticipated detection of RV signals from the P=1.06 d transit-candidate found by TESS, the RV data may contain further signals that need a revision about their nature, be they one or more further planet(s) in the system, or from other sources. **The data acquired with *HARPS-N* provide the most precise measurements (with the exception of data from HIRES, from which however only 12 RV points were acquired) and is it is the dataset with the most consistent coverage by far (see also Table 3); our analysis will hence concentrate on these data. Tests including other datasets showed in all cases a degradation in the detection of the 1.06 d signal. The data from the other instruments are however used in the evaluation of a potential contamination of the RV signals by the Moon mentioned later, which is described in more detail in Appendix B.**

In Fig. 9 we show Generalized Bayesian Lomb-Scargle periodograms (BGLS) of the HN RVs and of the more common activity indicators from the list in Sect. 3.1.2. The BGLS (Mortier et al. 2015)[8] provides several improvements over the common LS periodograms: It weights the data-points by their errors, it is independent of the setting of the data's zero-point and lastly, it provides a quantifiable probability of the relevance of the periodogram peaks. Fig. 9 shows also the spectral window function (Roberts et al. 1987; Dawson & Fabrycky 2010), whose peaks indicate the likely presence of artefacts due to the temporal distribution of the observations. In the periodogram of the RVs, of prominence is a double peak with the highest probability at 29.4 d, with a slightly lower peak (albeit by a factor of log $p \approx 10$) at 27.4 d (see also Fig. B.1 in the Appendix). Among the activity indicators, only the chromatic RV index (CRX) has peak near $\approx$ 30d, while the window function is rather flat in this region. We note that the period of the higher one of the double-peak is very close to the lunar synodic period of 29.53 days. The Appendix to this paper provides a more detailed evaluation of this signal as a candidate for a second planet c.

A further signal is notable at $\approx$ 10 d which corresponds to local maxima of most activity indicators. Hence it is likely due to stellar activity[9], albeit at a shorter period than the stellar rotation period of $P_{\rm rot}/\sin i = 20^{11}_{-5}$ d determined from $V \sin i_\star$ and $R_\star$ or the 17.6 ± 2 d from the lightcurve analysis of Sect. A. The same goes for an RV peak at 138 d, with several activity indicators showing maxima at a slight larger period of $\approx$ 160d, and which we will not consider further. The periodicity of the transits of 1.07 d does not appear well in the BGLS periodogram, which instead shows a series of peaks around P $\approx$ 1d, with the highest and second highest ones at P = 1.035 d and P = 0.967d respectively. These are clearly aliases of the 29.4d signal due to a sample period of 1 day (Fig. 10), given by the aliasing equation $f_{\rm alias} = |f_{\rm real} + N f_{\rm sample}|$ with $N = \pm 1$, where the f are the frequencies of the alias signal, the real signal and the sample frequency, respectively.

In a further evaluation, we use the framework provided by the online-tool Agatha[10] (Feng et al. 2017). With this tool, in a first step a model comparison between different models describing the data is performed. In this process, agatha evaluates 'MA' (Moving Average) models of varying complexity to describe the RV's red noise. These MA models are simplified Gaussian processes that only account for the correlation between previous data points and the current point, for which models with zero (corresponding to purely white noise), one or more 'MA' components are evaluated. We then used agatha to evaluate models with 0 to 2 MA componentes and also with one or several (or without any) noise-proxies among the activity indicators. For the different MA models (with or without the presence of proxies) that were evaluated, agatha generated Bayes Factors which account for the varying complexity of the models. In the case of our *HARPS-N* data, a one-component MA model without any noise proxies was indicated as the best model. This model was then also used by agatha to generate a Bayes Factor Periodogram (BFP, as defined by Feng et al. 2017)), shown in Fig. 11. In this periodogram, the highest peak by a wide margin corresponds to the 1.07 d period of the transits. Beyond the peaks around P=1 d and the aforementioned one near 135 days, next highest peak (albeit by a small margin) is again the signal near 29.4 d, identified previously with the BGLS periodograms.

In a further evaluation, we generated correlations between the various activity indicators and the RVs, following the precepts of Díaz et al. (2018), which was based on prior work by Santos et al. (2014). Fig. 12 shows no strong correlation between

[8] The figures were generated with the latest version of the code for the BGLS and related plots, available from A. Mortier in https://anneliesmortier.wordpress.com/sbgls/

[9] Fits to the *HARPS-N* RVs using Gaussian Processes, as described in Sect. 5.2, were made for models including this 10 d signal as a Keplerian one arising from a further planet, but this led to fits that were significantly worse than those presented in Sect. 5.2

[10] https://phillippro.shinyapps.io/Agatha/

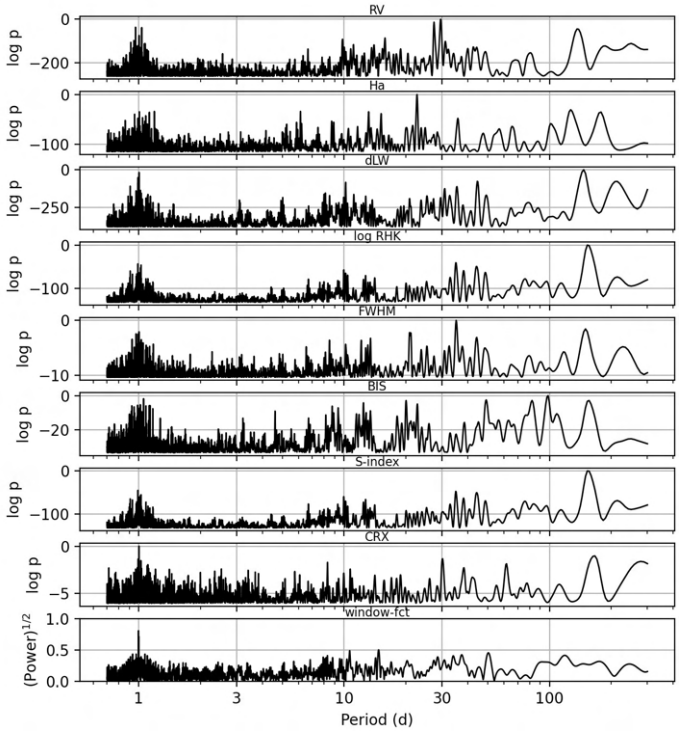

Fig. 9: BGLS periodograms of the *HARPS-N* observations, for the measured RVs and for several activity indicators. The vertical scale is given in units of the logarithm of the Bayesian probability of a signal with a given period, where the highest peak is normalised to log p = 0. The lowest panel shows the spectral window function of the sampled data. See also the Appendix, Figs. 10 and B.1 for zoomed-in views around the 1.07d and 29.4d periods of planet *b* and the candidate *c*, respectively.

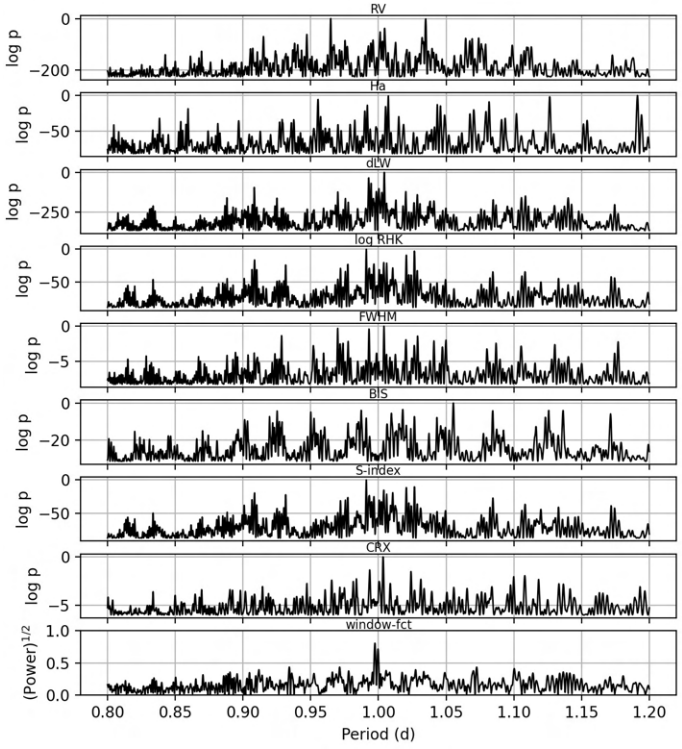

Fig. 10: Zoomed-in view of the BGLS periodogram of Fig. 9, around the 1.07 d period of the transiting planet *b*, where only a minor peak is discernible in the RVs (top panel). The highest RV peaks at P=1.035 d and P=0.967d are aliases of the 29.4d signal over the sample period of the solar or the sidereal day. Their periods of 1.0 resp. 0.9973 days show up as the principal double peak in the window function (lowest panel).

any of these indicators and the RVs, with a notable absence of any correlation between the RVs and the bisector inverse slope (BIS, in Fig. 12 labelled as `dsr_ccf_bis`). The only correlations of mention are the weak ones between the RVs and the differential line-width (dLW) and the Hα index, with correlation coefficients of 0.39± 0.08 and 0.36± 0.08, respectively.

Considering the significant differences between periodograms generated by different methods (for further examples of strongly differing results among different periodograms, see Feng et al. 2017, Figs. 1, 3 and 5), none of them should be taken to provide definite results. In any case, these periodograms suggest the presence of planet-like RV signals with periods of 1.07 and 29.4 days. A more detailed evaluation about the 29.4 d signal being caused by the Moon (see the Appendix) is not fully conclusive and a strong chance remains that it is a residual from contamination by Moon light; hence at most it may be treated as a tentative planet. Further modelling of the data concentrates therefore on the short-periodic transiting planet *b*.

5.2. Joint RV and lightcurve modelling

'Classical' Keplerian RV fits that assume white noise in the jitter of the RV values performed well in fits to the *HARPS-N* RVs from the first observing season, finding a distinct RV amplitude of ≈ 2 m s^{-1} at the period and epoch of the transits. However, with the addition of RVs from subsequent observing sessions, the quality of these fits degraded substantially, implying the presence of activity and other longer-term variations in the data.

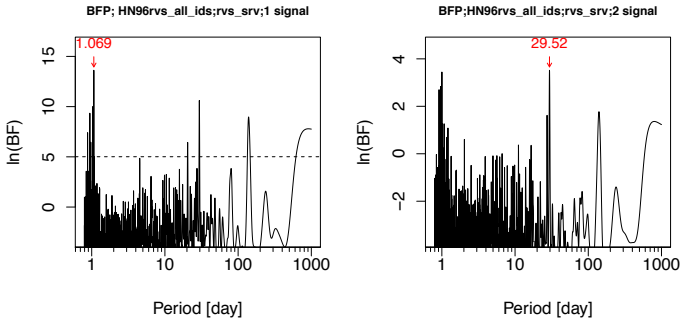

Fig. 11: Left panel: BFP periodogram of the *HARPS-N* radial velocities generated by `agatha` (Feng et al. 2017), using one MA component. The vertical axis provides the probability of peaks being real, in terms of the logarithm of their Bayes Factor (BF). The period of the highest peak is indicated, which corresponds to the period of the transits of TOI-1416 *b*. Right panel: Like the left panel, after the removal of the 1.069 d signal, showing now the signal at 29.5d as the highest one.

Hence, to allow for the presence of additional signals and especially those arising from stellar activity, we model the spectroscopic data from *HARPS-N* (and jointly also the transit lightcurve) with `pyaneti`, which uses the multi-dimensional Gaussian process (multi-GP) technique as described by Rajpaul et al. (2015). This approach models the RVs alongside activity indicators, taking advantage of the fact that these indicators should only be coupled to the RV components that arise from stellar variability. For the case of TOI-1416, we use the differ-

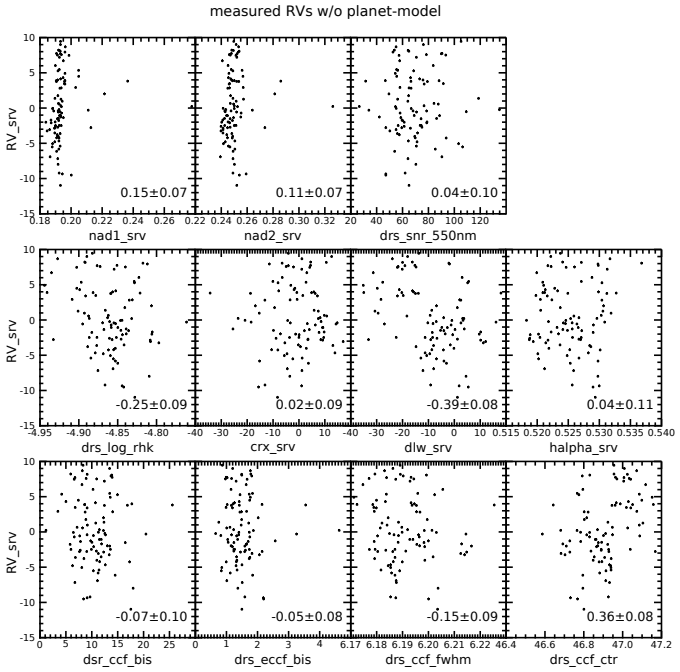

Fig. 12: Correlations in the *HARPS-N* data between the RVs (labelled as `RV_srv` and the activity indicators listed in Sect. 3.1.2. The Pearson correlation coefficient is indicated in each panel.

ential line width (dLW) – a line shape indicator, and construct a two-dimensional GP model as follows:

$$\begin{aligned} RV_{\rm ac} &= \quad A_{\rm RV}G(t) + B_{\rm RV}\dot{G}(t), \\ dLW &= \quad A_{\rm dLW}G(t), \end{aligned} \tag{1}$$

where $RV_{\rm ac}$ is the RV component arising from stellar activity; $A_{\rm RV}$, $B_{\rm RV}$, and $A_{\rm dLW}$ are free parameters relating the individual timeseries to the GP-generated function $G(t)$ and its derivative $\dot{G}(t)$. $G(t)$, in turn, can be viewed as a function that describes the projected area of the visible stellar disc as covered by active regions at a given time. The dLW indicator measures the width of the spectral lines and is mostly affected by the fraction of the visible stellar disc covered by active regions, and is thus represented by $G(t)$. The RVs, on the other hand, are affected by both the location of the active regions, and their temporal evolution. To account for this time dependence thus requires the addition of the first derivative term, $\dot{G}(t)$.

The multi-GP regression was performed on the *HARPS-N* RVs and dLW using a quasi-periodic (QP) covariance function,

$$\gamma(t_i, t_j) = \exp\left[-\frac{\sin^2[\pi(t_i - t_j)/P_{\rm GP}]}{2\lambda_{\rm p}^2} - \frac{(t_i - t_j)^2}{2\lambda_{\rm e}^2}\right], \tag{2}$$

and its derivatives, as described in (Barragán et al. 2022). $P_{\rm GP}$ is the period of the activity signal, λ_p the inverse of the harmonic complexity, i.e. the variability complexity inside each $P_{\rm GP}$, and λ_e is the long term evolution timescale, or the lifetime of the active regions.

For the simultaneous transit analysis, we used the TESS lightcurve after being prepared as described in Sect. 2. In `pyaneti`, the transits are modelled using the Mandel & Agol (2002) algorithm. The parameterisation of the transits is the same one as described in Appendix C for the `UTM/UFIT` fitter; most notably with a sampling of the limb darkening parameters using the q_1 and q_2 parametrisation by Kipping (2013) and the stellar density as a fundamental parameter to be fitted.

Besides the generation of models for both the RVs and the lightcurves, `pyaneti` employs a Markov Chain Monte Carlo (MCMC) sampling in a Bayesian framework to calculate posterior distributions of planetary system parameters. Using this setup, we sampled the parameter space with 500 independent Markov chains, out of which we built posterior distributions for each sampled parameter with a thinning factor of 20, using the last 10000 steps of the converged chains. Several planet-system models were then investigated; an overview of them is given in Table 6. In all of these models, parameters that are depending on the TESS light-curve turned up virtually identical and resulted in transit models that are visually indistinguishable from the one plotted in Fig. 1, and only the parameters depending on the RVs had different outcomes among the models.

For Model 1, only the transits from TESS and an RV signal with an ephemeris based on the transits were modelled, which yields a clearly detected RV semi-amplitude K_b of 2.28 ± 0.33 m s^{-1}(see Fig. 13), consistent within 1σ with an independent determination obtained by the FCO method (see Appendix D). In this model and the following ones, the orbit of planet b is consistent with a circular one ($e_b = 0.034^{+0.038}_{-0.022}$), which is unsurprising given its very short period. For further work in this paper we are therefore assuming a circular orbit of planet b.

For Model 2, we added a Keplerian signal (denoted as c) with a period of ≈ 29 days to our model, corresponding to the highest peak in the BGLS periodogram (Fig. 9 and the discussion in Sect. 5.1). Using an uniform prior on this signal's period of [28.0 d, 30.0 d], the signal c is well-detected, with a semi-amplitude of ≈ 5.2 m s^{-1}. Also, the amplitude of the 1.06 d signal increases slightly in Model 2, to K_b =2.5 ± 0.32 m s^{-1}, still well within the error bars of our previous estimates. Looking at the Bayesian Information Criterion (BIC), we further note that Model 2 has a significant advantage over Model 1, with its BIC being lower by 24, despite the increased complexity (see also Table 6). While these results are encouraging for the confirmation of the longer period signal c as a genuine planet, the derived period of $29.509^{+0.070}_{-0.065}$ days is fully consistent with the lunar synodic period of 29.5306 days (see Appendix B for further discussion).

We note that fitting for an eccentricity of signal c in Model 2 yielded a value of $e_c = 0.34^{+0.18}_{-0.21}$. However, **the revised Lucy-Sweeney test (Lucy 2013) indicates this as compatible with the absence of eccentricity, with the value to be replaced by an upper (95% confidence) limit of $e_c < 0.68$.** Given also the lack of apparent improvement of an eccentric versus a circular model, and the suboptimally sampled phase-coverage (with RVs falling into two groups, see Fig. F.2, bottom right), we remain skeptical of the authenticity of a significant eccentricity and zero eccentricity is assumed. Also, we point out that the GP period cannot be better constrained due to the fact that the lifetime of the active regions, λ_e, is comparable to the GP period.

In Model 3, we repeat Model 2 but now the period of signal c is fixed to the lunar synodic period. This leads to a BIC that is ≈ 11 lower against model 2, favouring this approach. Irrespective of the nature of the 29.5-day signal, the presence of this signal appears to be genuine, with a semi-amplitude similar to the one from Model 2. The fitting results for Model 3 have no relevant differences to those from Model 2; the corresponding RV and dLW timeseries plots, together with the inferred Keplerian RV models, are found in the Appendix in Figure F.2. The priors and

Table 6: Models evaluated with pyaneti

Model	ΔBIC	σ_{RV} m s^{-1}
Model 1 planet *b* only	0	0.92
Model 2 planet *b*, signal *c* of P≈29.5 d with free ephemeris	-23.8	1.11
Model 3 planet *b*, signal *c* fixed to P=29.5306 d	-34.5	1.11
Model 4 planet *b*, signal *c* of P≈27.4 d with free ephemeris	5.5	1.04

Notes. ΔBIC indicates the BIC relative to model 1. σ_{RV} is the *rms* of the RV residuals relative to the best-fit models.

fitting results of Model 3 are shown in Table 7, and are taken as the adopted values in this work.

Model 4 is similar to Model 2, but assumes a signal with a period of ≈ 27.5 days, resulting however in a significantly higher BIC than models 2 or 3. Given however the fact that the 27.4 d signal displayed the strongest peak in the periodogram of RV data from all contributing instruments (Fig. B.6) and the potential aliasing between this signal and the 29.5d one (see discussion in Appendix B), we do not want to discard that an eventual planet *c* might instead have this period.

Regarding the apparent contradiction in Table 6 between Model 3 having the best (lowest) BIC and Model 1 the smallest *rms* of the RV residuals, we note that the *rms* indicates only a goodness-of-fit of the model against the RV data, whereas the BIC derived by pyaneti includes (besides the quality of the transit-fit to the lightcurve, which should be identical in Model 1 – 4) also several more parameters related to the Gaussian processes, among them the assumed amount of RV jitter and the likelihood of the correlated noise; the *rms* and the BIC are therefore not directly comparable.

In the light of this, we choose a conservative approach and for the further discussion we assume only a tentative planet *c* with a period near 27.5 or 29.5 d and a mass of M sin *i* of 19 to 25 $M_{\oplus}$, whose confirmation as a second planet in TOI-1416 remains pending.

As mentioned in Sect. 5.1, there is a significant signal at ≈ 10 days evident in the RV data, which is well pronounced in the activity indicators but unlikely to be caused by stellar rotation. We tried modelling it as a Keplerian to investigate the possibility that it may be an additional planet. Our fits, however, were convincingly inferior compared to all of the scenarios discussed thus far in this section. To further exclude it as a potential stellar rotation period, we tested placing a $P_{\rm GP}$ prior using that rotation period of 9.6±1.4 d. We find that this leads to significant changes in the GP hyperparameters, to the point that their interpretation becomes unphysical, while the detection significance of the *b* and *c* signals is practically unchanged. This scenario is also disfavoured with a ΔBIC of ≈ 8 against the one it was derived from (Model 3). Lastly, we note that this 10-day signal would be approximately the first harmonic of our favoured ≈ 20-day rotation period. This is not surprising given that harmonics often dominate over the true signals. A likely explanation for this is the presence of two spotted regions on the stellar surface separated by ≈ 180 deg, each thus manifesting at half the rotation period.

5.3. Limits to secondary eclipses

Here, we first estimate the maximum secondary eclipse depth of planet *b* that can be expected, and then revise their presence in the data. The depth of a planet's eclipse behind its host-star is given by the brightness of the planet relative to the star, with the planet's brightness being the sum of its emitted thermal emission and the amount of stellar light that is reflected from the planet. Regarding thermal emission, Table 8 indicates an equilibrium temperature of 1517K for planet *b*, which was calculated for a zero Bond albedo and assuming a uniform heat redistribution over its entire sphere (corresponding to a heat recirculation efficiency of $f = 1/4$, e.g. Cowan & Agol (2011)). For the estimation of the maximum secondary eclipse depth from thermal emission, we assume however a realistic maximum temperature of 1900K, which is based on the assumption that with none of the absorbed radiation gets circulated to the planet's night-side (corresponding to a value of $f = 2/3$). Based on that temperature, and using again the adopted parameters from Table 8, we find that thermal emission from planet *b* may generate eclipses with a depth of only 1.2 ppm in the wavelengths of the TESS bandpass. For a maximum value of secondary eclipse depth from reflected light, a geometric albedo of 1 is assumed, which leads to an eclipse depth of 14 ppm.

Combining thermal and reflected light, we conclude that secondary eclipses of TOI-1416 *b* may not exceed a depth of 15 ppm. This value might barely be detectable in the lightcurve. For its detection, we assume that the secondary eclipse is well centred on an orbital phase of 0.5, and generated a phase-folded lightcurve similar to the one that was prepared for the transit-fits with UTM/UFIT in Sect. 2 and shown in Fig. 1, with off-eclipse fluxes that are normalised to 1, but now centred at phase 0.5. The fluxes within the expected phase-range of total eclipse (phases from 0.48 to 0.52) were then obtained, which resulted in a flux that is 30±25 ppm higher than the off-eclipse flux. Hence, a secondary eclipse was not detected, and we may estimate that secondary eclipses deeper than ≈ 20 ppm can be excluded with a high (2-sigma) confidence from the observed data.

6. Results and their interpretation

Final system parameters: As the two sets of analysis performed with pyaneti and UTM/UFIT showed, no relevant differences arose in those parameters that arose the TESS lightcurves, with pyaneti employing Gaussian Processes and UTM/UFIT a white-noise model on a lightcurve that had undergone a prior filtering against signals that were significantly longer than the transit-duration. The same goes for the RV fit to TOI-1416 *b*, where the FCO method – which is essentially a pass-through filter at the planet's period – and pyaneti obtained a very similar result. This outcome is similar to one on TOI-1235 b, where Bluhm et al. (2020) adopted a white-noise-only fit to the TESS lightcurves, after finding no relevant difference to results obtained from fits based on Gaussian processes. For the finally adopted values in Table 8, we quote however those from pyaneti, as only this procedure produced an integral analysis of the combined set of lightcurves and RVs that was also suitable to evaluate the various models involving a signal from a potential further planet *c*. This planet remains however tentative due to strong doubts that its signal might arise for contamination from the Moon. Furthermore, with the current data we are not able to ascertain if the tentative planet's period would be 29.5 or 27.4 days. Such a second planet with a large period ratio of ≈ 26 against the inner planet would however not be unex-

Table 7: Priors and inferred parameters[(a)] from transit and RV modelling with `pyaneti` (Model 3) and UTM/UFIT resp. FCO.

Parameter	Prior[(b)]	`pyaneti`	UFIT / FCO
TOI-1416 b			
Orbital period $P_{\rm orb}$ (days)	$\mathcal{U}[1.0690, 1.0705]$	1.0697568± 2.8e-06	1.0697564 ± 2.8e-06
Transit epoch T_0 ($\rm BJD_{TDB}$ - 2,450,000)	$\mathcal{U}[8739.455, 8739.466]$	8739.4621 ± 0.0008	8739.4620±0.0008
Eccentricity e	$\mathcal{F}[0]$	0	0
Scaled planetary radius $R_{\rm p}/R_\star$	$\mathcal{U}[0.01, 0.10]$	0.01873 ± 0.00054	0.01963 ± 0.00059
Impact parameter, b	$\mathcal{U}[0, 1]$	$0.39^{+0.10}_{-0.14}$	$0.35^{+0.11}_{-0.15}$
RV semi-amplitude K ($\rm m\,s^{-1}$)	$\mathcal{U}[0, 25]$	2.52 ± 0.32	2.14 ± 0.35
TOI-1416 *c*			
Orbital period $P_{\rm orb}$ (days)	$\mathcal{F}[29.5306]$	29.5306	–
Transit epoch T_0 ($\rm BJD_{TDB}$ - 2,450,000)	$\mathcal{U}[8868.00, 8885.00]$	8876.78 ± 0.69	–
Eccentricity e	$\mathcal{F}[0]$	0	–
RV semi-amplitude K ($\rm m\,s^{-1}$)	$\mathcal{U}[0, 25]$	$5.20^{+0.71}_{-0.65}$	–
GP Period $P_{\rm GP}$ (days)	$\mathcal{U}[15, 28]$	$20.6^{+1.9}_{-1.0}$	–
$\lambda_{\rm P}$	$\mathcal{U}[0.1, 5]$	0.62 ± 0.10	–
$\lambda_{\rm e}$ (days)	$\mathcal{U}[1, 200]$	24.0 ± 6.2	–
A_{RV} ($\rm m\,s^{-1}$)	$\mathcal{U}[0, 100]$	$0.96^{+0.68}_{-0.54}$	–
B_{RV} ($\rm m\,s^{-1}$)	$\mathcal{U}[0, 1000]$	$15.7^{+3.6}_{-2.7}$	–
A_{dLW} ($100\ \rm m^2\,s^{-2}$)	$\mathcal{U}[0, 1]$	$0.121^{+0.026}_{-0.019}$	–
Offset *HARPS-N*[(c)] ($\rm m\,s^{-1}$)	$\mathcal{U}[-511, 509]$	0.79 ± 0.52	−0.05 ± 0.87
Offset dLW ($\rm m^2\,s^{-2}$)	$\mathcal{U}[-0.5351, 0.5180]$	−0.063 ± 0.033	–
Jitter term $\sigma_{\rm HARPS-N}$ ($\rm m\,s^{-1}$)	$\mathcal{J}[1, 1000]$	0.30 ± 0.25	–
Jitter term $\sigma_{\rm dLW}$ ($100\ \rm m^2\,s^{-2}$)	$\mathcal{J}[1, 1000]$	26.9 ± 3.6	–
Limb darkening q_1	$\mathcal{G}[0.413, 0.091]$	0.429 ± 0.087	0.430 ± 0.089
Limb darkening q_2	$\mathcal{G}[0.354, 0.030]$	0.355 ± 0.030	0.355 ± 0.031
Jitter term σ_{TESS} ($\times 10^{-6}$)	$\mathcal{U}[0, 1\times10^3]$	788.2 ± 2.8	–
Stellar density $\rho_\star$ ($\rm g\,cm^{-3}$)	$\mathcal{G}[2.21, 0.27]$	2.31 ± 0.28	2.40 ± 0.27

Notes – [(a)] Inferred parameters and errors are defined as the median and 68.3% credible interval of the posterior distribution. [(b)] $\mathcal{U}[a, b]$ refers to uniform priors between a and b (only for `pyaneti`; for UFIT or the FCO method, no priors were set except on the impact parameter b); $\mathcal{G}[a, b]$ to a Gaussian prior centered on a with a 1σ width of b; $\mathcal{J}[a, b]$ to modified Jeffrey's priors calculated using eq. 16 in Gregory (2005); $\mathcal{F}[a]$ to parameters that are fixed to a. [(c)] Offset against the zero-averaged *HARPS-N* RVs from `serval` (column `rvs_srv` in electronic data).

Table 8: Adopted derived parameters

Parameter	TOI-1416 *b*	TOI-1416 *c*
Planet mass ($M_\oplus$)	3.48 ± 0.47	$21.6^{+3.1}_{-2.8}$ ($M \sin i$)
Planet radius ($R_\oplus$)	1.62 ± 0.08	–
Planet density ($\rm g\,cm^{-3}$)	$4.50^{+0.99}_{-0.83}$	–
Scaled semi-major axis $a/R_\star$	5.14±0.24	47.0±2.4
Semi-major axis a (AU)	0.0190±0.0003	0.1734±0.0030
Orbital inclination i (deg)	$85.7^{+1.7}_{-1.4}$	< 88.7
Transit duration $t_{\rm tot}$ (hours)	1.50 ± 0.035	–
Equilibrium temperature [(a)] $T_{\rm eq}$ (K)	1517 ± 39	510 ± 20
Insolation $S/S_\oplus$	883 ± 96	11.2 ± 1.3
Planet surface gravity ($\rm cm\,s^{-2}$)	1300 ± 220	–

Note – Adopted stellar parameters from Tables 4 and 5 were used for values that are dependent on them. [(a)] Assuming an albedo of 0 and uniform heat redistribution over the entire surface. See also Sect 5.3.

pected; the preference for USPs for companions with relatively large period-ratios has been known since the first description of USPs (Sanchis-Ojeda et al. 2014; Winn et al. 2018). From the absence of transits of *c*, a maximum orbital inclination of 88.7° can be determined. Dai et al. (2018) find that in USPs with a further transiting planet, the systems with the largest period-ratio also tend to have larger mutual inclinations of $\gtrsim 7°$. However, the TOI-1416 system is inconclusive in that respect: With TOI-1416 *b*'s inclination of 85.7°, even a fully coplanar planet *c* would not have caused any transits and no conclusions about the system's mutual inclination, or about limits to it, can be made. The RV fits for an eventual planet *c* were compatible with eccentricities up to 0.5, which upon the availability of more reliable RV results might lead to the establishment of a formation pathway for TOI-1416 *b*.

Composition of TOI-1416 b: For the transiting planet TOI-1416 *b*, its radius of $1.62 \pm 0.08\ R_\oplus$ and mass of $3.48 \pm 0.47\ M_\oplus$ indicate that it is a short-periodic Super-Earth like planet, with

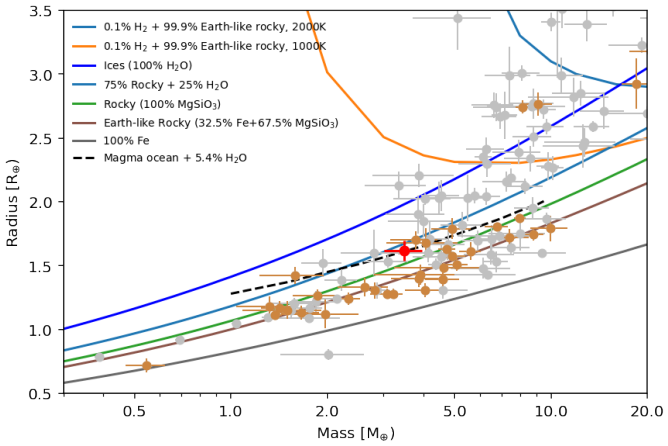

Fig. 14: Planet masses and radii, versus composition models: Grey markers: planets with well-determined masses (errors smaller than 30%, from adopted values in the NASA Exoplanet Archive). Planets with periods smaller than 2d are shown with brown markers. Composition models indicated by solid lines are from Zeng et al. (2016, 2019), whereas the dashed line is a model from Dorn & Lichtenberg (2021) for an Earth-like rocky composition (66% Mg-Si oxides and silicates and 33% iron), where the molten rock contains a water mass fraction of 5.4%. TOI-1416 *b* is indicated by the red dot.

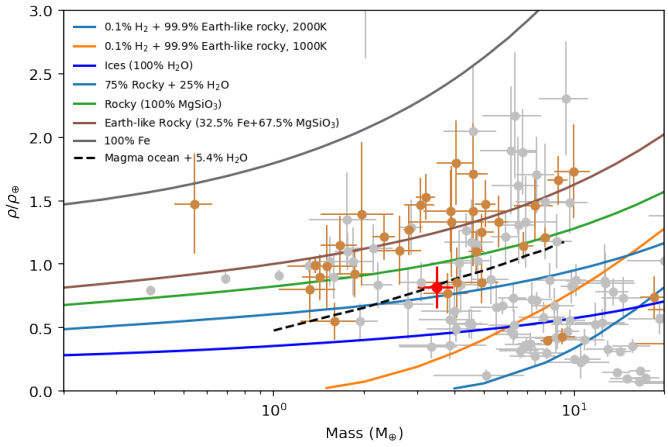

Fig. 15: Like Fig. 14, but in mass - density space.

a density of $4.50^{+0.99}_{-0.83}$ g cm^{-3}. Fig. 14 shows a mass-radius (MR) diagram with several composition models from Zeng et al. (2016, 2019), while Fig. 15 shows the same in mass-density space; We note that TOI-1416 *b* is above the line for a purely rocky (100% Mg Si O_3) composition, with a density relative to an Earth-like composition (scaled to the mass of TOI-1416 *b*) of $\rho\rho_{\oplus,S} \approx 0.67$. This separates TOI-1416 *b* from most other short-period planets; Dai et al. (2019) found for a sample of comparable Hot Earths (11 planets with insolations > 650 times that of the Earth and periods of $\lesssim$2 days) that most of these are consistent with an Earth Like composition of 30% Fe - 70% Mg Si O_3. We also use the HARDCORE tool (Suissa et al. 2018) which is exploiting boundary conditions to bracket a planet's minimum and maximum core radius fraction (CRF), assuming a fully differentiated planet and iron to be the core material. For TOI-1416 *b* we obtain a marginal (most likely) CRF of 0.35 ± 0.20. Similar to the planet's density, this is slightly less but within the limits of the Earth's CRF of 0.55, whereas the potential minimum and maximum values of the CRF are zero and 0.71, respectively. Following Zeng & Jacobsen (2017), we may also derive the core mass fraction (CMF) from the approximation CMF ≈ CRF^2, leading to a value of CMF = $0.12^{+0.18}_{-0.10}$. This value is again relatively small in comparison to the sample of Hot Earths by Dai et al., who determined for them a mean CMF of 26% with a standard deviation of 23%.

We also determine the planet's restricted Jeans escape parameter, given by $\Lambda = \frac{GM_p m_H}{k_B T_{eq} R_p}$, where T_{eq} is the planets' equilibrium temperature, m_H the mass of the hydrogen atom, G the gravitational constant, and k_B the Boltzmann constant (Fossati et al. 2017). The parameter Λ is a global one for a given planet, without dependence on altitude within the atmosphere, for which Fossati et al. find from empirical study a critical value of $\Lambda_T = 15 - 35$, below which a planet's atmosphere is unstable against evaporation, by lying in a boil-off regime that would shrink its radius within a few hundreds of My. For TOI-1416 *b*, $\Lambda = 10.7$; it is hence unlikely to have retained a hydrogen-dominated atmosphere that could contribute significantly to its mass or radius. For highly irradiated planets, the evaporation of hydrogen might however lead to an enrichment of other light elements, be it Helium, or Oxygen from the thermolysis of H_2O. For these elements, the hydrogen mass m_H in the equation above can be replaced with the element's atomic mass . For TOI-1416 *b*, we then obtain values of $\Lambda \approx 40$ and 160 for Helium and Oxygen , respectively, meaning that these elements are not affected by evaporation.

With TOI-1416 *b* having at most a small core and a density that is less than a composition exclusively of silicates would require, but orbiting also too close to the central star to enable the retention of a significant H - He atmosphere, the most likely outcome is the presence of a significant mass-fraction of H_2O or other volatiles. Under this assumption, several types of planet compositions have been brought forward: For one, the original and widely discussed models of rocky cores of various fractions of iron and silicates, with mantles of condensed water, (e.g. Seager et al. 2007; Mordasini et al. 2012; Zeng & Sasselov 2013; Zeng et al. 2016). For planets that are more irradiated than the runaway greenhouse irradiation limit of $\approx 1.1 S_\oplus$, Turbet et al. (2020) provide mass-radius models of silicate cores with a mantle of various fractions of H_2O the form of steam, which lead to larger planet sizes for a given mass-fraction of H_2O than in the condensed-water models. The work by Turbet et al. provides a procedure to generate MR relations of steam planets for insolations from $\approx$ 1 to 30 $S_\oplus$. An extension of this work to highly irradiated planets, like TOI-1416 *b* with 880 $S/S_\oplus$ is still pending, and the feasibility of a steam atmospheres at the insolation resp. temperature of TOI-1416 *b* would have to be evaluated.

With its equilibrium temperature of 1517±39 K, TOI-1416 *b* is likely to consist of molten rock (magma) at or closely below the surface. We also note that tidal heating might have contributed a significant further source of internal heating that is potentially capable of melting a USPs entire interior (Lanza 2021). In any case, magma has recently been shown (Dorn & Lichtenberg 2021) to be able to absorb significant quantities of H_2O, which may lead to radius-increments of up to 16% over the common interior compositions that do not take dissolved water into account. In Figs. 14 and Fig. 15 we include the MR relation from Dorn & Lichtenberg for their favoured 'wet-melt' interior (their 'model C'), which assumes the dissolution of water in an Earth-like magma, with various water mass-fractions. This model provides a close agreement with the mass and radius of TOI-1416

b, and hence provides the interpretation of the composition of TOI-1416 b that we favour in this work: A planet of partially solid and molten interior of Earth-like composition, with water being distributed between the mantle belt and a a surface steam layer, with a total water mass-fraction of 1-15% of water[11] in the melt. A more detailed modelling of TOI-1416 b's composition is beyond the scope of our present work and would have to take into account the potential range in values of the CMF, and hence in the fraction between iron and silicates. Potential outcomes could be a relatively small core, with the average density of TOI-1416 b dominated by silicates, or a larger core, that requires a then a larger contribution of H_2O to offset the high density of iron.

Suitability for atmospheric characterisation: The suitability of a target for its atmospheric characterisation by transmission spectroscopy during a transit has been parametrised by Kempton et al. (2018) with the transmission spectroscopy metric (TSM). The TSM of TOI-1416 b is 83, so it could be a suitable target for such observations with the JWST[12]. We also note that its emission spectroscopic metric (ESM) is 13.8, which is well above the threshold of 7.5 that Kempton et al. recommend for the top atmospheric characterisation targets for JWST follow-up, albeit for a sample of slightly smaller planets with $R_p < 1.5R_\oplus$. Neither the TSM nor the ESM consider the orbital period, with the TSM relating to the S/N from observing a single transit. Hence USP planets have the further advantage that more transits or orbital revolutions can be acquired in a given time-span. In conclusion, TOI-1416 b might be a very suitable target for JWST follow-up.

Position of TOI-1416 b and c relative to the radius valley: Planet b is located slightly below (Fig. 16, top panel) the mass-radius valley (also known as radius gap or Fulton gap) near radii of 2 $R_\oplus$(Fulton et al. 2017; Van Eylen et al. 2018; Petigura et al. 2022) that separates the population of Super Earth planets from the larger Sub-Neptune-like planets. At the short orbital period of TOI-1416 b however, the valley is only poorly defined and only a population of smaller planets remains; see also Fig. 17. On the other hand, for the tentative planet c, with its mass of $M \sin i \approx 22M_\oplus$, we estimate a radius of $5.5 \pm 2.5R_\oplus$ from the radius-mass relation by Chen & Kipping (2017). This indicates a Neptune-like planet which would lie well above the mass-radius valley and would convert TOI-1416 into a system with a USP planet below the radius valley and a second planet that is above it. Of course, we do not know the size of the tentative planet c, but a radius that would place it below the radius valley would have to be smaller than $\approx 1.7R_\oplus$. Such a small radius is unrealistic from both the observed radius-mass relation and from the required densities in excess of 20 g cm^{-3}; hence this outcome can be excluded with near-certainty.

The Neptune Desert and its borders: In the planet radius and planet mass versus period diagrams (Fig. 16), we note the well-known 'Neptune Desert' as defined by Mazeh et al. (2016), with the lower boundary for the planet radius given by $\log R_{lo}/R_\oplus = 0.68 \log P$, with the period P in days, and the lower boundary in the mass-period planet given by $\log M_{lo}/M_{\rm jup} = 0.98 * (\log P) - 1.85$. However, given the mass and period distributions in Fig. 16, which contain many recently discovered planets with periods $\lesssim 1$ day, we doubt the validity of the lower boundaries for periods shorter than ≈ 2 days, because most of the known USP's, including TOI-1416 b, would be within the

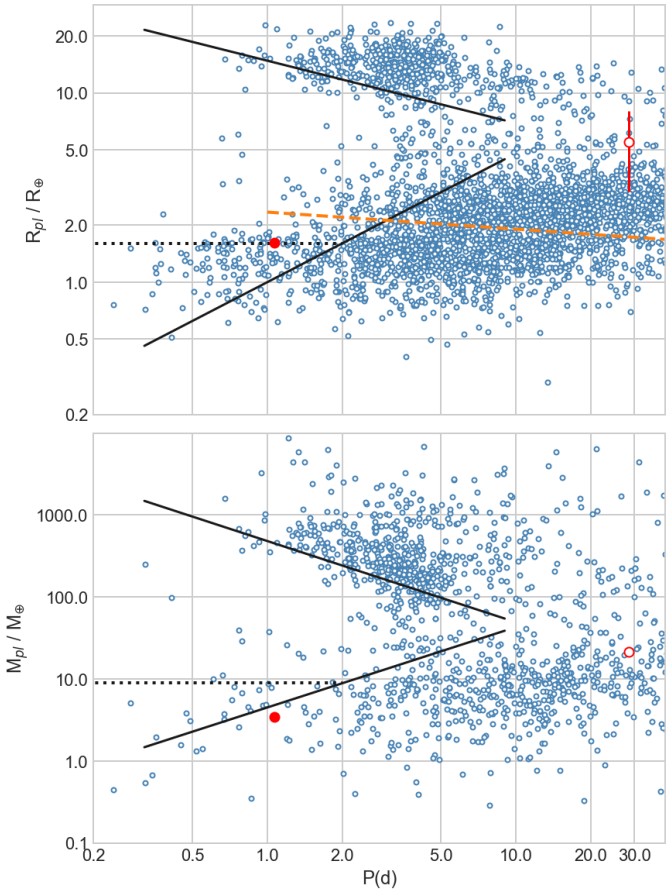

Fig. 16: Diagram of the radii (top panel) and. masses (bottom panel) versus period of the known planets, from the NASA Exoplanet Archive. The solid black lines show the delineation of the 'Neptune Desert' from Mazeh et al. (2016), whereas the horizontal dotted black lines show the lower limits to the Neptune Desert for periods ≤ 2 days that are proposed in this work. The dashed orange line in the upper panel indicates the period-radius valley from Van Eylen et al. (2018). TOI-1416 b is indicated by the filled red circle and the tentative planet c by the unfilled one.

'desert'. Indeed, only a few years ago the period regime below 1 to 2 days was only sparsely populated, with relatively small planets of $< 1.6R_\oplus$. This also gave rise to statistical evaluations claiming that P$\approx$ 1 days separates the shortest period planets regarding their size and numbers against the slightly longer-periodic planets (Pu & Lai 2019; Winn et al. 2018; Lee & Chiang 2017). One of the principal impacts of the TESS mission has however been the discovery of over 20 planets with $P \lesssim 1$ d, with nearly all of them happening since the year 2020 and also counting on mass measurements from ground-based follow-up. In the period regime of P $\leq$ 2 d, we hence propose to replace the desert's lower boundary with a constant corresponding to the desert's lower boundary at P = 2 days for both radius and mass, leading for P < 2 d to a boundary at a radius of 1.60 $R_\oplus$ ($\log R_{lo}/R_\oplus = 0.2$) and a mass of 0.028 $M_{\rm jup}$ ($\log M_{lo}/M_{\rm jup}$ = -1.55) resp. 8.9 $M_\oplus$ (dotted lines in Fig. 16). In support of these lower limits to the desert, Fig. 17 (top panel) shows the radius distribution of the short-period small planet population $\log R/R_\oplus < 0.8$ resp. $R/R_\oplus < 6.3$), where we note that the radius distribution has little dependence on the orbital period, with

[11] Water mass-fractions derived from interpolation within Fig. 4 of Dorn & Lichtenberg (2021), considering the mass and radius uncertainties of TOI-1416 b

[12] Kempton et al. (2018) give a suggested cutoff of 92 in their Table 1, but we note that TOI-1416 b's radius of $1.6R_\oplus$ is near the lower limit of their $1.5 < R_p < 2.75R_\oplus$ radius-bin.

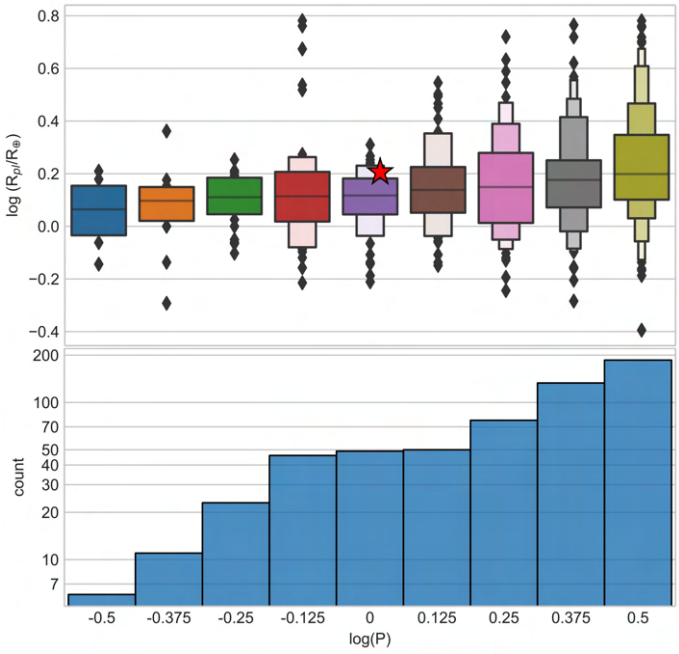

Fig. 17: Top panel: Distribution of planet-radii for small planets of $\log R/R_\oplus < 0.8$ (resp. $R/R_\oplus < 6.3$), versus the orbital period $\log P$(day), after categorising the planet population into bins with a width of $\log P = 0.125$ and for periods shorter than 3.6 d. The distributions are shown as 'Boxenplots' or 'Letter Value Plots' (Hofmann et al. 2011). TOI-1416 *b* is indicated by the red star. **Bottom panel: Counts of the small planets versus the same bins in orbital period.**

the planet's median size following the relation

$$R/R_\oplus = 1.4\ P^{0.11}\ ;\ \ 0.3 \lesssim P(\mathrm{day}) \lesssim 3\,.$$

In Appendix C we show in Fig. E.1 a plot similar to that of Fig. 16, but against the planets' insolation **and effective temperature**, where the upper boundary of the Neptune desert has become notably better defined, and propose corresponding limits of the Neptune desert against these parameters.

From these distributions, it appears that TOI-1416 *b* belongs to a continuous distribution of super-Earths with periods ranging from the shortest known ones up to ≈ 30 days, with neither the period-radius nor the period-mass distributions showing any signs for a discontinuity near the common limit of P = 1 days for USPs. The maximum radii of Super Earths are delimitated at the shortest periods by the Neptune desert (for which we propose a lower limit of $\approx 1.6\,R_\oplus$ for periods shorter than 2 days, albeit planets with radii up to $\approx 2\,R_\oplus$ would belong to the same population[13]), while for longer periods, Super-Earth radii are delimited by the period-radius valley that separates them against Sub-Neptune type planets.

Distribution of small planets against period and USP formation pathways: **Regarding the abundance of small planets against period (Fig. 17, bottom panel), we note the emergence of a plateau between** $\log P$ **of -0.125 and +0.125 (P ≈ 0.6 to 1.4 d). This plateau might correspond to a bump that was previously noted as an excess of 50 % more planets just below P = 1 than above it (Pu & Lai 2019, based on the work by Lee & Chiang 2017)[14], with abundance slopes that are steeper below 1 day than above 1 day. The newer planet discoveries imply however that this bump has smoothed out into the observed plateau, but the abundance slope remains somewhat steeper to the left than to the right of the plateau. Alternatively, there might be uniform slope in abundances against period, with an additional accumulation of planets at periods between 0.6 and 1 days.**

Pu & Lai (2019) proposed the formation of USPs within multi-planetary systems from low-eccentricity migration due to secular interactions among the planets. This pathway involves the initial birth of an innermost planet with a period of several days and a moderate eccentricity of 0.05 to 0.15. Through tidal interactions with further outer planets, the eccentricity of the innermost one is gradually damped to nearly zero, while its semi-major axis undergoes a quasi-equilibrium shrinkage. As a result of this process, the innermost planet transforms into a USP, while the outer planet stabilises at an orbital period that is larger by ≳ 15 times. Pu & Lai also provide synthetic planet distributions that have undergone this formation pathway, with a variety of initial parameters (varying the mass and eccentricity of the innermost planets and also the tidal quality factor Q of both stars and inner planets). It is of note that their simulation with the highest initial orbital eccentricity, of 0.15±0.025 (their Fig. 15), agrees very well with the observed abundances from Fig. 17, with the reproduction of the abundance plateau around $P \approx 1$ d and the steeper slope to the left than to the right of it. Notably, the initial eccentricity was identified by Pu & Lai 2019 as the parameter that most clearly affected the final results of their simulations. This leads to the suggestion that USP formation from inwards migration of inner planets with an initial eccentricity of ≈ 0.15 might be a common one. Several further formation pathways have been proposed in the literature, with a notable contrast being the high-eccentricity pathway by Petrovich et al. (2019) that requires an initial eccentricity of $e \gtrsim 0.8$. However, without simulated planet distributions against basic parameters such as period, radius and mass being available, the presence of these pathways needs to be evaluated from other diagnostics, such as ratios of orbital periods or mutual inclinations between inner and outer planets, or measurements of spin-orbit angles, which are beyond the scope of the present work.

7. Conclusions

We report the discovery of the Super-Earth planet TOI-1416 *b* orbiting with a period of 1.07 days around a middle-aged G9V star of likely membership in the galactic thin disk, with a tentative second planet *c* of Neptune-like mass and a period of 27.4 or 29.5 days. The highest peaks in RV periodograms and keplerian fits for *c* indicate a best-fit period that coincides very closely with the lunar synodic period. Consequently, the true nature of *c* had to remain tentative despite an intense campaign of RV observations, because contamination of the RV data by a signal arising from Moon-reflected solar light cannot be ruled out. If planet *c* is real, its radius of 3 - 8 $R_\oplus$ would position it above the period-radius valley, while planet *b* is below the valley, albeit in

[13] We note that the limits for the Neptune Desert given by Mazeh et al. (2016) do not attempt to delineate an area that is empty of planets, but rather they were placed to produce the best contrast between the lower-density 'desert' and its more densely populated surroundings.

[14] We note that the 1-d bump in Lee & Chiang (2017) might be a result from the integration of two different studies, one for period of less than one day, and one for periods larger than 1 day, with different stellar host types.

a zone in the period-radius plane where the valley is only poorly defined.

Several composition models are discussed for TOI-1416 *b*. Given the expected high temperature of both planet surface and interior, we consider a model describing a molten interior in which a significant fraction of water is dissolved in magma as the most promising one to explain the planet's density, which is significantly below the expected one from a pure silicate composition. An eventual atmosphere is unlikely to contribute significantly to the planet's mass but could be suitable to observation by transmission spectroscopy with the JWST, while the planet's surface might also be within the reach of emission spectroscopy.

The lower limit of the Neptune desert, initially identified by Mazeh et al. (2016), is revised for planets with periods of less than 2 days. For these, the original definition of the lower boundary is clearly inconsistent with recent discoveries of significant numbers of short-periodic planets. For periods of P < 2 days, a lower boundary to the desert at radii of 1.60 $R_\oplus$ and masses of 8.9 $M_\oplus$ is therefore proposed.. We also delimit the desert using the planets' insolation instead of the period as a basic parameter. In both radius vs. insolation and mass vs. insolation distributions, the upper limit of the desert is more pronounced and corresponding relations limiting the desert are given.

The borderline position of TOI-1416 *b* just outside the conventional definition of USPs, as planets with periods of less than 1 day motivated an evaluation of its position within the planet population, in period-radius and period-mass diagrams. From these, we deduce that planets with periods of less than one day do not constitute a special group of planets. Rather, USPs appear to be the extreme end of a continuous distribution of super-Earths, with periods extending from the shortest known ones up to around 30 days, with upper radii limited by the Neptune desert for periods shorter than ≈ 2 days, and by the period-radius valley for longer periods. Within the super-Earths, sub-groups with specific properties may however become increasingly better characterised, depending e.g. on the insolation, type or age of central star, and/or the presence of further planets. **One such hint is the plateau that has emerged in the small-planet abundance against period, in a range from 0.6 and 1.4 days, and which is compatible with the low-eccentricity formation pathway proposed by Pu & Lai (2019). The recent discoveries of numerous short-period planets, such as TOI-1416 *b*, should inspire comprehensive investigations to assess the suitability of the various proposed formation mechanisms in explaining the present distribution of these planets across the broadest spectrum of parameters feasible.**

Acknowledgements. This work was supported by the KESPRINT collaboration, an international consortium devoted to the characterization and research of exoplanets discovered with space-based missions (`http://www.kesprint.science`). This paper includes data collected by the *TESS* mission. Funding for the *TESS* mission is provided by the NASA Explorer Program. We acknowledge the use of public TOI Release data from pipelines at the *TESS* Science Office and at the *TESS* Science Processing Operations Center. Resources supporting this work were provided by the NASA High-End Computing (HEC) Program through the NASA Advanced Supercomputing (NAS) Division at Ames Research Center for the production of the SPOC data products. This research has made use of the Exoplanet Follow-up Observation Program (ExoFOP; DOI: 10.26134/ExoFOP5) website, which is operated by the California Institute of Technology, under contract with the National Aeronautics and Space Administration under the Exoplanet Exploration Program. This work has made use of data from the European Space Agency (ESA) mission *Gaia* (`https://www.cosmos.esa.int/gaia`), processed by the *Gaia* Data Processing and Analysis Consortium (DPAC, `https://www.cosmos.esa.int/web/gaia/dpac/consortium`). Funding for the DPAC has been provided by national institutions, in particular the institutions participating in the *Gaia* Multilateral Agreement. Based on observations made with the Italian Telescopio Nazionale Galileo (TNG) operated on the island of La Palma by the Fundación Galileo Galilei of the INAF (Instituto Nazionale di Astrofisica) at the Spanish Observatorio del Roque de los Muchachos of the Instituto de Astrofísica de Canarias under programmes CAT19A_162, CAT21A_119, CAT22A_111 and ITP19_1. CARMENES is an instrument for the Centro Astronómico Hispano-Alemán de Calar Alto (CAHA, Almería, Spain). CARMENES is funded by the German Max-Planck-Gesellschaft (MPG), the Spanish Consejo Superior de Investigaciones Científicas (CSIC), the European Union through FEDER/ERF FICTS-2011-02 funds, and the members of the CARMENES Consortium (Max-Planck-Institut für Astronomie, Instituto de Astrofísica de Andalucía, Landessternwarte Königstuhl, Institut de Ciències de l'Espai, Institut für Astrophysik Göttingen, Universidad Complutense de Madrid, Thüringer Landessternwarte Tautenburg, Instituto de Astrofísica de Canarias, Hamburger Sternwarte, Centro de Astrobiología and Centro Astronómico Hispano-Alemán), with additional contributions by the Spanish Ministry of Economy, the German Science Foundation through the Major Research Instrumentation Programme and DFG Research Unit FOR2544 "Blue Planets around Red Stars", the Klaus Tschira Stiftung, the states of Baden-Württemberg and Niedersachsen, and by the Junta de Andalucía. This article is partly based on observations made with the MuSCAT2 instrument, developed by ABC, at the Telescopio Carlos Sánchez operated on the island of Tenerife by the IAC in the Spanish Observatorio del Teide. This work makes use of observations from the LCOGT network. Part of the LCOGT telescope time was granted by NOIRLab through the Mid-Scale Innovations Program (MSIP). MSIP is funded by NSF. We thank the following iSHELL observers: Kevin I Collins, Michael Reefe, Farzaneh Zohrabi, Eric Gaidos, Angelle Tanner and Claire Geneser. We thank Annelies Mortier for the provision of the latest versions of her code for the BGLS and related plots. HJD and SM acknowledge support from the Spanish Research Agency of the Ministry of Science and Innovation (AEI-MICINN) under grant 'Contribution of the IAC to the PLATO Space Mission' with references ESP2017-87676-C5-4-R and PID2019-107061GB-C66, DOI: 10.13039/501100011033. S.M. and D.G.R acknowledge support form the same source with the grant no. PID2019-107187GB-I00. SM acknowledgtes from the same source support through the Severo Ochoa Centres of Excellence Programme 2020–2023 (CEX2019-000920-S). PGB acknowledges from the same source support with the *Ramón y Cajal* fellowship number RYC-2021-033137-I. G.N. thanks for the research funding from the Polish Ministry of Education and Science programme the "Excellence Initiative - Research University" conducted at the Centre of Excellence in Astrophysics and Astrochemistry of the Nicolaus Copernicus University in Toruń, Poland. This work is partly supported by JSPS KAKENHI Grant Number P17H04574, JP18H05439 and JP20K14521, and JST CREST Grant Number JPMJCR1761. J.M.A.M. is supported by the National Science Foundation Graduate Research Fellowship Program under Grant No. DGE-1842400. J.M.A.M. acknowledges the LSSTC Data Science Fellowship Program, which is funded by LSSTC, NSF Cybertraining Grant No. 1829740, the Brinson Foundation, and the Moore Foundation; his participation in the program has benefited this work. KAC and DWL acknowledge support from the TESS mission via sub-award s3449 from MIT. K.W.F.L. was supported by Deutsche Forschungsgemeinschaft grant RA714/14-1, within the DFG Schwerpunkt SPP 1992, 'Exploring the Diversity of Extrasolar Planets'.

References

Ahuir, J., Strugarek, A., Brun, A. S., & Mathis, S. 2021, A&A, 650, A126
Allard, F., Homeier, D., & Freytag, B. 2012, Philosophical Transactions of the Royal Society of London Series A, 370, 2765
Angus, R., Aigrain, S., Foreman-Mackey, D., & McQuillan, A. 2015, MNRAS, 450, 1787
Angus, R., Morton, T. D., Foreman-Mackey, D., et al. 2019, AJ, 158, 173
Attia, O., Bourrier, V., Eggenberger, P., et al. 2021, A&A, 647, A40
Baranne, A., Queloz, D., Mayor, M., et al. 1996, A&AS, 119, 373
Barnes, S. A. 2007, ApJ, 669, 1167
Barragán, O., Aigrain, S., Rajpaul, V. M., & Zicher, N. 2022, MNRAS, 509, 866
Barragán, O., Gandolfi, D., & Antoniciello, G. 2019, MNRAS, 482, 1017
Bluhm, P., Luque, R., Espinoza, N., et al. 2020, A&A, 639, A132
Borucki, W. J., Koch, D., Basri, G., et al. 2010, Science, 327, 977
Bressan, A., Marigo, P., Girardi, L., et al. 2012, MNRAS, 427, 127
Brown, T. M., Baliber, N., Bianco, F. B., et al. 2013, Publications of the Astronomical Society of the Pacific, 125, 1031
Cabrera, J., Csizmadia, S., Erikson, A., Rauer, H., & Kirste, S. 2012, A&A, 548, A44
Cale, B., Plavchan, P., LeBrun, D., et al. 2019, AJ, 158, 170
Cannon, A. J. & Pickering, E. C. 1901, Annals of Harvard College Observatory, 28, 129
Castelli, F. & Kurucz, R. L. 2004, astro-ph/0405087 [`astro-ph/0405087`]
Ceillier, T., Tayar, J., Mathur, S., et al. 2017, A&A, 605, A111
Ceillier, T., van Saders, J., García, R. A., et al. 2016, MNRAS, 456, 119
Chen, J. & Kipping, D. 2017, ApJ, 834, 17

Choi, J., Dotter, A., Conroy, C., et al. 2016, ApJ, 823, 102
Ciardi, D. R., Beichman, C. A., Horch, E. P., & Howell, S. B. 2015, ApJ, 805, 16
Claret, A. 2017, A&A, 600, A30
Collins, K. 2019, in American Astronomical Society Meeting Abstracts, Vol. 233, American Astronomical Society Meeting Abstracts #233, 140.05
Collins, K. A., Kielkopf, J. F., Stassun, K. G., & Hessman, F. V. 2017, AJ, 153, 77
Cosentino, R., Lovis, C., Pepe, F., et al. 2012, in Society of Photo-Optical Instrumentation Engineers (SPIE) Conference Series, Vol. 8446, Proc. SPIE, 84461V
Cosentino, R., Lovis, C., Pepe, F., et al. 2014, in Society of Photo-Optical Instrumentation Engineers (SPIE) Conference Series, Vol. 9147, Ground-based and Airborne Instrumentation for Astronomy V, 91478C
Cowan, N. B. & Agol, E. 2011, ApJ, 729, 54
da Silva, L., Girardi, L., Pasquini, L., et al. 2006, A&A, 458, 609
Dai, F., Masuda, K., & Winn, J. N. 2018, ApJ, 864, L38
Dai, F., Masuda, K., Winn, J. N., & Zeng, L. 2019, ApJ, 883, 79
Dawson, R. I. & Fabrycky, D. C. 2010, ApJ, 722, 937
Deeg, H. J. 2014, UTM: Universal Transit Modeller, Astrophysics Source Code Library, record ascl:1412.003
Dekany, R., Roberts, J., Burruss, R., et al. 2013, ApJ, 776, 130
Díaz, M. R., Jenkins, J. S., Tuomi, M., et al. 2018, AJ, 155, 126
Dorn, C. & Lichtenberg, T. 2021, ApJ, 922, L4
Eastman, J., Gaudi, B. S., & Agol, E. 2013, PASP, 125, 83
Eastman, J. D., Rodriguez, J. E., Agol, E., et al. 2019, arXiv e-prints, arXiv:1907.09480
Feng, F., Tuomi, M., & Jones, H. R. A. 2017, MNRAS, 470, 4794
Ford, E. B. 2006, ApJ, 642, 505
Fossati, L., Erkaev, N. V., Lammer, H., et al. 2017, A&A, 598, A90
Frémat, Y., Royer, F., Marchal, O., et al. 2022, arXiv e-prints, arXiv:2206.10986
Fulton, B. J., Petigura, E. A., Howard, A. W., et al. 2017, AJ, 154, 109
Fulton, B. J., Weiss, L. M., Sinukoff, E., et al. 2015, ApJ, 805, 175
Furlan, E., Ciardi, D. R., Everett, M. E., et al. 2017, AJ, 153, 71
Gaia Collaboration. 2020, VizieR Online Data Catalog, I/350
García, R. A., Ceillier, T., Salabert, D., et al. 2014a, A&A, 572, A34
García, R. A., Mathur, S., González Otero, J., Santos, A. R. G., & Breton, S. N. 2021, in Posters from the TESS Science Conference II (TSC2), 180
García, R. A., Mathur, S., Pires, S., et al. 2014b, A&A, 568, A10
Gray, D. F. 2018, ApJ, 857, 139
Gregory, P. C. 2005, ApJ, 631, 1198
Hatzes, A. P. 2014, A&A, 568, A84
Hatzes, A. P., Dvorak, R., Wuchterl, G., et al. 2010, A&A, 520, A93
Hayward, T. L., Brandl, B., Pirger, B., et al. 2001, PASP, 113, 105
Henden, A. A., Templeton, M., Terrell, D., et al. 2016, VizieR Online Data Catalog, II/336
Hippke, M. & Heller, R. 2019, A&A, 623, A39
Hofmann, H., Kafadar, K., & Wickham, H. 2011, Letter-value plots: Boxplots for large data, Tech. rep., had.co.nz
Høg, E., Fabricius, C., Makarov, V. V., et al. 2000, A&A, 355, L27
Howard, A. W., Johnson, J. A., Marcy, G. W., et al. 2010, ApJ, 721, 1467
Husser, T. O., Wende-von Berg, S., Dreizler, S., et al. 2013, A&A, 553, A6
Hut, P. 1980, A&A, 92, 167
Jenkins, J. M., Caldwell, D. A., Chandrasekaran, H., et al. 2010, ApJ, 713, L87
Jenkins, J. M., Twicken, J. D., McCauliff, S., et al. 2016, in Proc. SPIE, Vol. 9913, Software and Cyberinfrastructure for Astronomy IV, 99133E
Kaminski, A., Trifonov, T., Caballero, J. A., et al. 2018, A&A, 618, A115
Kempton, E. M. R., Bean, J. L., Louie, D. R., et al. 2018, PASP, 130, 114401
Kilic, M., Munn, J. A., Harris, H. C., et al. 2017, ApJ, 837, 162
Kipping, D. M. 2013, MNRAS, 435, 2152
Kurucz, R. L. 1993, VizieR Online Data Catalog, VI/39
Kurucz, R. L. 2013, ATLAS12: Opacity sampling model atmosphere program, Astrophysics Source Code Library
Lafarga, M., Ribas, I., Lovis, C., et al. 2020, A&A, 636, A36
Lanza, A. F. 2021, A&A, 653, A112
Lee, E. J. & Chiang, E. 2017, ApJ, 842, 40
Lucy, L. B. 2013, A&A, 551, A47
Mamajek, E. E. & Hillenbrand, L. A. 2008, ApJ, 687, 1264
Mandel, K. & Agol, E. 2002, ApJ, 580, L171
Mathur, S., García, R. A., Ballot, J., et al. 2014, A&A, 562, A124
Mathur, S., García, R. A., Régulo, C., et al. 2010, A&A, 511, A46
Mazeh, T., Holczer, T., & Faigler, S. 2016, A&A, 589, A75
McCully, C., Volgenau, N. H., Harbeck, D.-R., et al. 2018, in Society of Photo-Optical Instrumentation Engineers (SPIE) Conference Series, Vol. 10707, Proc. SPIE, 107070K
McQuillan, A., Aigrain, S., & Mazeh, T. 2013, MNRAS, 432, 1203
McQuillan, A., Mazeh, T., & Aigrain, S. 2014, ApJS, 211, 24
Mordasini, C., Alibert, Y., Georgy, C., et al. 2012, A&A, 547, A112
Mortier, A. & Collier Cameron, A. 2017, A&A, 601, A110
Mortier, A., Faria, J. P., Correia, C. M., Santerne, A., & Santos, N. C. 2015, A&A, 573, A101
Morton, T. D. 2015, isochrones: Stellar model grid package
Murgas, F., Nowak, G., Masseron, T., et al. 2022, A&A, 668, A158
Narita, N., Fukui, A., Kusakabe, N., et al. 2019, Journal of Astronomical Telescopes, Instruments, and Systems, 5, 015001
Parviainen, H., Tingley, B., Deeg, H. J., et al. 2019, A&A, 630, A89
Petigura, E. A., Rogers, J. G., Isaacson, H., et al. 2022, AJ, 163, 179
Petrovich, C., Deibert, E., & Wu, Y. 2019, AJ, 157, 180
Piskunov, N. & Valenti, J. A. 2017, A&A, 597, A16
Pu, B. & Lai, D. 2019, MNRAS, 488, 3568
Quirrenbach, A., Amado, P. J., Caballero, J. A., et al. 2014, in Society of Photo-Optical Instrumentation Engineers (SPIE) Conference Series, Vol. 9147, Ground-based and Airborne Instrumentation for Astronomy V, 91471F
Quirrenbach, A., Amado, P. J., Ribas, I., et al. 2018, in Society of Photo-Optical Instrumentation Engineers (SPIE) Conference Series, Vol. 10702, Ground-based and Airborne Instrumentation for Astronomy VII, 107020W
Rajpaul, V., Aigrain, S., Osborne, M. A., Reece, S., & Roberts, S. 2015, MNRAS, 452, 2269
Rayner, J., Tokunaga, A., Jaffe, D., et al. 2022, PASP, 134, 015002
Reddy, B. E., Lambert, D. L., & Allende Prieto, C. 2006, MNRAS, 367, 1329
Rhodes, B. 2019, Skyfield: High precision research-grade positions for planets and Earth satellites generator, Astrophysics Source Code Library, record ascl:1907.024
Ricker, G. R., Winn, J. N., Vanderspek, R., et al. 2015, Journal of Astronomical Telescopes, Instruments, and Systems, 1, 014003
Roberts, D. H., Lehar, J., & Dreher, J. W. 1987, AJ, 93, 968
Rodrigues, T. S., Bossini, D., Miglio, A., et al. 2017, MNRAS, 467, 1433
Rodrigues, T. S., Girardi, L., Miglio, A., et al. 2014, MNRAS, 445, 2758
Ryabchikova, T., Piskunov, N., Kurucz, R. L., et al. 2015, Phys. Scr, 90, 054005
Sanchis-Ojeda, R., Rappaport, S., Winn, J. N., et al. 2014, ApJ, 787, 47
Santos, A. R. G., Breton, S. N., Mathur, S., & García, R. A. 2021, ApJS, 255, 17
Santos, A. R. G., García, R. A., Mathur, S., et al. 2019, ApJS, 244, 21
Santos, N. C., Mortier, A., Faria, J. P., et al. 2014, A&A, 566, A35
Schlafly, E. F. & Finkbeiner, D. P. 2011, ApJ, 737, 103
Schlegel, D. J., Finkbeiner, D. P., & Davis, M. 1998, ApJ, 500, 525
Seager, S., Kuchner, M., Hier-Majumder, C. A., & Militzer, B. 2007, ApJ, 669, 1279
Skrutskie, M. F., Cutri, R. M., Stiening, R., et al. 2006, AJ, 131, 1163
Smith, J. C., Stumpe, M. C., Jenkins, J. M., et al. 2020a, Kepler Data Processing Handbook: Presearch Data Conditioning, Kepler Science Document KSCI-19081-003, id. 8. Edited by Jon M. Jenkins.
Smith, J. C., Stumpe, M. C., Jenkins, J. M., et al. 2020b, in Kepler Data Processing Handbook, ed. J. Jenkins (NASA, Kepler Science Document KSCI-19081-003), 131
Smith, J. C., Stumpe, M. C., Van Cleve, J. E., et al. 2012, PASP, 124, 1000
Spada, F. & Lanzafame, A. C. 2020, A&A, 636, A76
Stassun, K. G., Oelkers, R. J., Paegert, M., et al. 2019, AJ, 158, 138
Stassun, K. G., Oelkers, R. J., Pepper, J., et al. 2018, AJ, 156, 102
Strugarek, A. 2016, ApJ, 833, 140
Stumpe, M. C., Smith, J. C., Catanzarite, J. H., et al. 2014, PASP, 126, 100
Stumpe, M. C., Smith, J. C., Van Cleve, J. E., et al. 2012, PASP, 124, 985
Suissa, G., Chen, J., & Kipping, D. 2018, MNRAS, 476, 2613
Tenenbaum, P. & Jenkins,, J. M. 2018, TESS Science Data Products Description Document EXP-TESS-ARC-ICD-0014 Rev D (NASA Ames Research Center, Moffet Field, California)
Ter Braak, C. J. F. 2006, Statistics and Computing, 16, 239
Torrence, C. & Compo, G. P. 1998, Bulletin of the American Meteorological Society, 79, 61
Torres, G. 2010, AJ, 140, 1158
Trifonov, T., Kürster, M., Zechmeister, M., et al. 2018, A&A, 609, A117
Turbet, M., Bolmont, E., Ehrenreich, D., et al. 2020, A&A, 638, A41
Twicken, J. D., Catanzarite, J. H., Clarke, B. D., et al. 2018, PASP, 130, 064502
Valenti, J. A. & Piskunov, N. 1996, A&AS, 118, 595
Van Eylen, V., Agentoft, C., Lundkvist, M. S., et al. 2018, MNRAS, 479, 4786
Vines, J. I. & Jenkins, J. S. 2022, MNRAS, 513, 2719
Vogt, S. S., Allen, S. L., Bigelow, B. C., et al. 1994, in Society of Photo-Optical Instrumentation Engineers (SPIE) Conference Series, Vol. 2198, Instrumentation in Astronomy VIII, ed. D. L. Crawford & E. R. Craine, 362
Vogt, S. S., Radovan, M., Kibrick, R., et al. 2014, PASP, 126, 359
Winn, J. N., Sanchis-Ojeda, R., & Rappaport, S. 2018, New A Rev., 83, 37
Yee, S. W., Petigura, E. A., & von Braun, K. 2017, ApJ, 836, 77
Zechmeister, M., Reiners, A., Amado, P. J., et al. 2018, A&A, 609, A12
Zeng, L. & Jacobsen, S. B. 2017, ApJ, 837, 164
Zeng, L., Jacobsen, S. B., Sasselov, D. D., et al. 2019, Proceedings of the National Academy of Science, 116, 9723
Zeng, L. & Sasselov, D. 2013, PASP, 125, 227
Zeng, L., Sasselov, D. D., & Jacobsen, S. B. 2016, ApJ, 819, 127

[1] Instituto de Astrofísica de Canarias, 38205 La Laguna, Tenerife, Spain e-mail: hdeeg@iac.es
[2] Departamento de Astrofísica, Universidad de La Laguna, 38206 La Laguna, Tenerife, Spain
[3] Department of Space, Earth and Environment, Chalmers University of Technology, Onsala Space Observatory, 439 92 Onsala, Sweden
[4] Institute of Astronomy, Faculty of Physics, Astronomy and Informatics, Nicolaus Copernicus University, Grudziądzka 5, 87-100 Toruń, Poland
[5] Dipartimento di Fisica, Università degli Studi di Torino, Torino, Italy
[6] Department of Physics and Astronomy, George Mason University, 4400 University Drive, Fairfax, VA 22030, USA
[7] Division of Geological and Planetary Sciences, California Institute of Technology, 1200 E California Boulevard, Pasadena, CA 91125, USA
[8] NASA Exoplanet Science Institute, 770 South Wilson Ave., Pasadena, CA 91125, USA
[9] Space Telescope Science Institute, 3700 San Martin Drive, Baltimore, MD 21218, USA
[10] Mullard Space Science Laboratory, University College London, Holmbury St. Mary, Dorking, Surrey, RH5 6NT, UK
[11] Deutsches Zentrum für Luft- und Raumfahrt, Institut für Planetenforschung, 12489 Berlin, Rutherfordstrasse 2., Germany
[12] Thüringer Landessternwarte Tautenburg, Sternwarte 5, 07778 Tautenburg, Germany
[13] McDonald Observatory and Center for Planetary Systems Habitability, The University of Texas, Austin, TX 78730, USA
[14] Center for Astrophysics | Harvard & Smithsonian, 60 Garden Street, Cambridge, MA 02138, USA
[15] Leiden Observatory, Leiden University, 2333CA Leiden, The Netherlands
[16] Astronomical Institute, Czech Academy of Sciences, Fričova 298, 25165, Ondřejov, Czech Republic
[17] Rheinisches Institut für Umweltforschung an der Universität zu Köln, Aachener Strasse 209, 50931 Köln, Germany
[18] Komaba Institute for Science, The University of Tokyo, 3-8-1 Komaba, Meguro, Tokyo 153-8902, Japan
[19] Astrobiology Center, 2-21-1 Osawa, Mitaka, Tokyo 181-8588, Japan
[20] Astronomy Department and Van Vleck Observatory, Wesleyan University, Middletown, CT 06459, USA
[21] Department of Physics and Kavli Institute for Astrophysics and Space Research, Massachusetts Institute of Technology, Cambridge, MA 02139, USA
[22] Department of Earth, Atmospheric and Planetary Sciences, Massachusetts Institute of Technology, Cambridge, MA 02139, USA
[23] Department of Aeronautics and Astronautics, Massachusetts Institute of Technology, 77 Massachusetts Avenue, Cambridge, MA 02139, USA
[24] Department of Astronomy & Astrophysics, University of Chicago, Chicago, IL 60637, USA
[25] Department of Physics & Astronomy, University of California Los Angeles, Los Angeles, CA 90095, USA
[26] Okayama Observatory, Kyoto University, 3037-5 Honjo, Kamogata-cho, Asakuchi, Okayama 719-0232, Japan
[27] Department of Multi-Disciplinary Sciences, Graduate School of Arts and Sciences, The University of Tokyo, 3-8-1 Komaba, Meguro, Tokyo 153-8902, Japan
[28] Département d'Astrophysique, IRFU/DRF/CEA Saclay, L'Orme des Merisiers, bat. 709, 91191 Gif-sur-Yvette Cedex, France
[29] Department of Astrophysical Sciences, Princeton University, Princeton, NJ 08544, USA
[30] Observatori Astronòmic Albanyà, Camí de Bassegoda S/N, Albanyà 17733, Girona, Spain
[31] Department of Physics, Engineering and Astronomy, Stephen F. Austin State University, 1936 North St, Nacogdoches, TX 75962, USA
[32] National Astronomical Observatory of Japan, 2-21-1 Osawa, Mitaka, Tokyo 181-8588, Japan
[33] Department of Astronomical Science, School of Physical Sciences, The Graduate University for Advanced Studies (SOKENDAI), 2-21-1, Osawa, Mitaka, Tokyo, 181-8588, Japan
[34] Department of Astronomy and Astrophysics, University of California, Santa Cruz, CA 95064, USA
[35] University of California at Berkeley, 501 Campbell Hall, Berkeley, CA 94720, USA
[36] Centre for Astrophysics, University of Southern Queensland, Toowoomba, QLD, Australia
[37] Institut für Physik, Karl-Franzens Universität Graz, Universitätsplatz 5/II, NAWI Graz, 8010 Graz, Austria

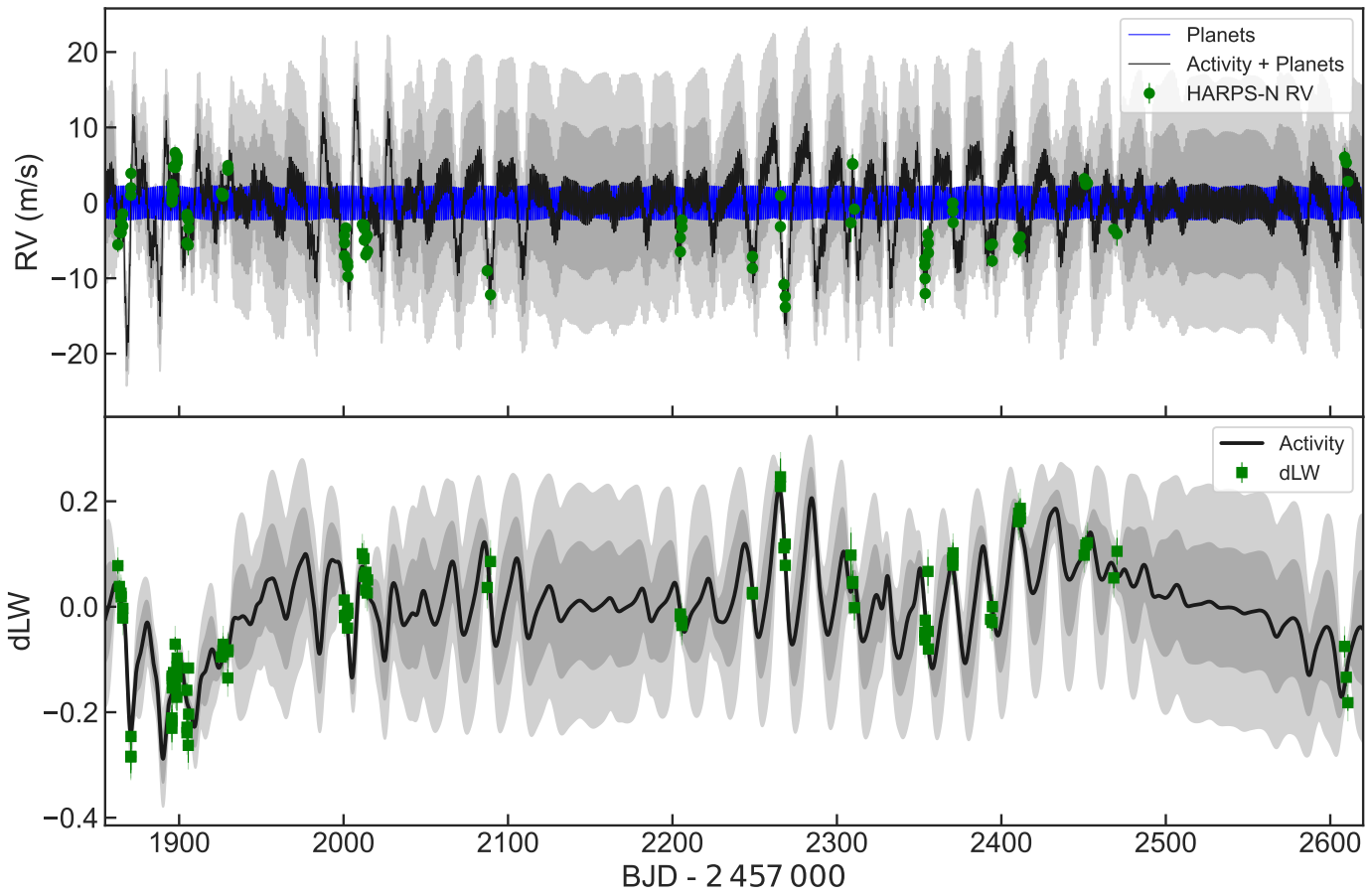

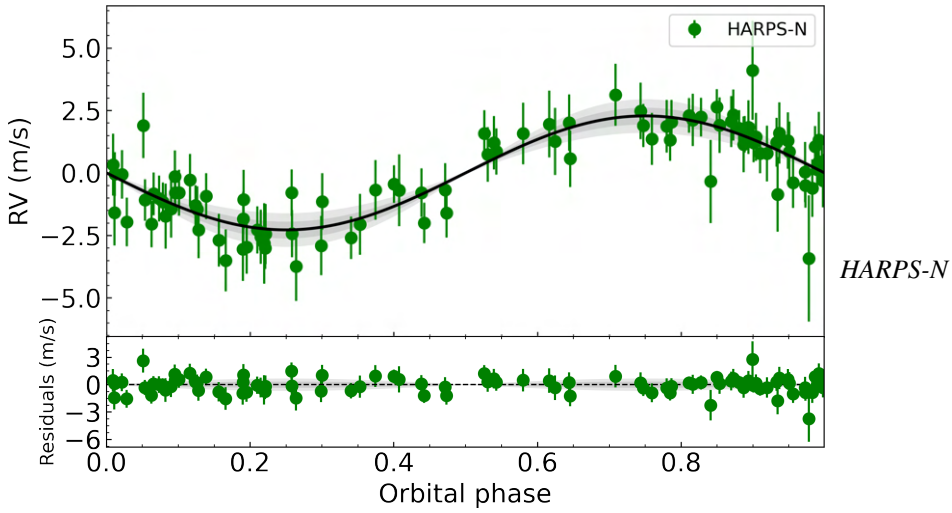

Fig. 13: Upper panel: *HARPS-N* RV and differential line width (dLW) time-series for `pyaneti` Model 1, assuming only the presence of a Keplerian signal with the 1.06d transit period. The green markers in each panel represent the RV and dLW measurements. The solid black curve shows the inferred multi-GP model, with dark and light shaded areas showing the one and two sigma credible intervals of the corresponding GP model. We note that the short period of the planet and the size of the plot make the RV sinusoids appear as a solid blue band. Lower panel: *HARPS-N* RV data folded on the 1.07 day orbital period of planet *b*, after subtraction of the systemic velocity and the GP noise model. The inferred RV model is shown as a solid black curve with 1- and 2-sigma credible intervals (shaded areas).

Appendix A: Stellar rotation period

We determine the rotation period from the lightcurve of TOI-1416 by following the procedure described in Santos et al. (2019) and Santos et al. (2021) ; see also Mathur et al. (2014) and García et al. (2014a). The analysis was based on TESS light curves that have undergone after the same processing as described in Sect. 2 for the analysis with `pyaneti`, from which we removed the exoplanet transits to avoid spurious signals (using the best-fit model obtained with `UTM/UFIT` as described in Appendix C). Due to the small number of data points that remained in sector 50 after removal of the bad quality data, only sectors 16 and 23 were used for the rotational analysis. Also, gaps in the light curve longer than 81 days (three consecutive TESS sectors) were removed, and inpainting techniques were used to fill in gaps shorter than 5 days (García et al. 2014b), leading to the light curve shown in the top-panel of Fig. A.1. From this curve, we derive three estimates of the rotation period: The first estimate is obtained from the global wavelet power spectrum (GWPS; Torrence & Compo 1998; Mathur et al. 2010), which examines the correlation between the data and the mother wavelet (taken to be a Morlet wavelet), and its projection onto the period axis. The second estimate is obtained via the autocorrelation function (ACF; McQuillan et al. 2013, 2014), which computes the correlation between the light curve and itself for a range of time shifts. The third estimate is obtained from the composite spectrum (Ceillier et al. 2016), which is calculated as the product between the GWPS and the normalized ACF and which helps to enhance the periods that are present in both methods.

Fig. A.1 shows the results from all three methods. From the ACF analysis, we can see three peaks with prominent absolute amplitudes. However, as shown in Ceillier et al. (2017), one of the criteria to select reliable rotation periods is based on the relative amplitudes of the peaks, called H_ACF, with significant periods having values of H_ACF > 0.3. Computing the H_ACF for these three peaks, the largest value is found for the period corresponding to 17.6 ± 2 days (with a value of H_ACF = 0.5). That is the period we adopt, which approximately corresponds to the third harmonic of the ≈ 5 day signal seen in both the ACF and the global wavelet power spectrum (GWPS). Moreover, García et al. (2021) applied the same method to over 2-million "Kepler-seen-as-TESS" light curves, for stars for which rotation periods had been measured by Santos et al. (2019, 2021). They divided the full Kepler light curves into 27-day chunks to mimic the TESS observations, and their results showed that periods of up to ≈ 20 days can be retrieved with one sector of data. For instance, for peaks with H_ACF > 0.3, they recovered periods in the 10 to 15 day window with a reliability of ≈ 70%.

We note that our adopted 17.6 ± 2 days ACF period is also compatible with the rotation period of $P_{\rm rot}/\sin i = 20^{11}_{-5}$ d determined from $V \sin i_\star$ and $R_\star$ of Tables 4 and 5. While the 17.6 day period does not show up in the GWPS, this is unsurprising as it would have been filtered out due to falling outside the cone of validity (hatched regions in Fig. A.1; see also García et al. 2021). Regarding a ≈ 10 day stellar rotation that would correspond to the second harmonic of the ≈ 5 day signal and for which activity indicators from the RV data indicate at notable peak in spectrograms (Sect. 5.1), it is argued at the end of Sect. 5.2 that this period is unlikely to be associated with stellar rotation.

From the adopted period of 17.6 d we furthermore derive ages from several rotation-age relations reported in the literature, resulting in ages of: 0.84 ± 0.18 Gyr (Barnes 2007); 1.26 ± 0.29 Gyr (Mamajek & Hillenbrand 2008); 1.58 ± 0.7 Gyr (Angus et al. 2015); 1.49 ± 0.23 Gyr (Angus et al. 2019) and 1.75 ± 0.25 Gyr (Spada & Lanzafame 2020). Ignoring the value from Barnes (2007) as the most discrepant one, gyrochronology indicates hence an age of 1 - 2 Gyr. We note however that the lightcurve analysis does not exclude a longer rotation period that is not perceived due to the limited coverage of the TESS lightcurves and which would also indicate older ages for TOI-1416.

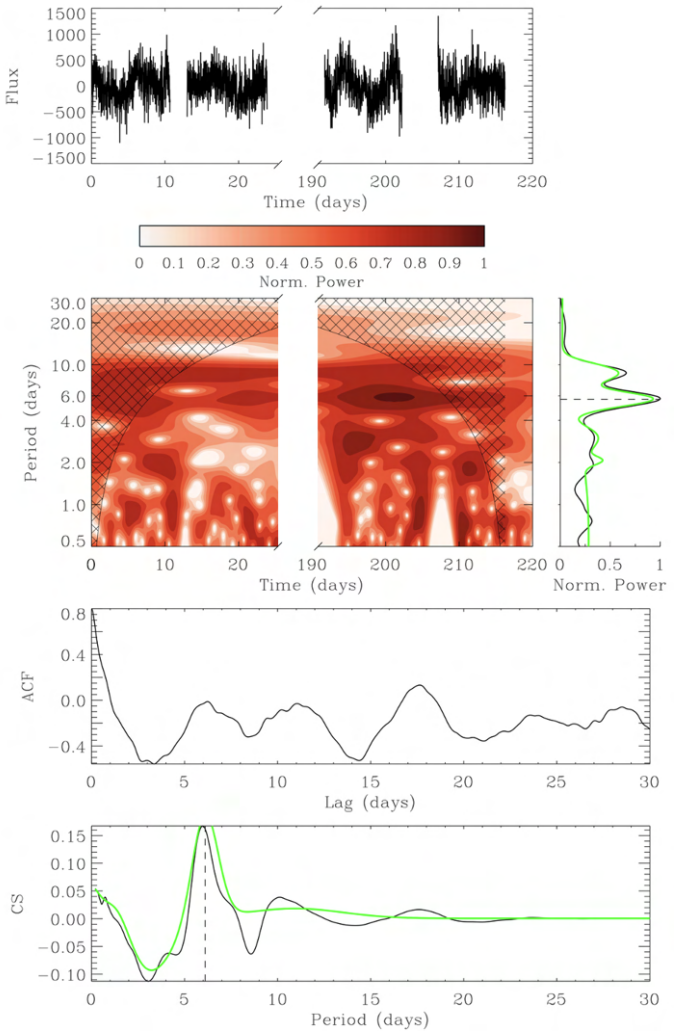

Fig. A.1: Analysis of TESS lightcurve for stellar rotation of TOI-1416. The top panel shows the lightcurve from Sector 16 and 23 that was used for the analysis. The following panels show the three methods used for the period determination (see text): wavelet power spectrum (GWPS) and its projection onto the period axis; the autocorrelation function (ACF); and the composite spectrum (CS). The hatched region in the panel for the wavelet power spectrum indicates the zone where the method is not valid.

Appendix B: The RV double peak at periods of 27.4 and 29.5 days: Planet candidate or influence from the Moon?

The spectral signatures presented in Sect. 5.1, from both the BGLS and the Bayes Factor periodogram from `agatha` indicate an RV signal in the *HARPS-N* data with a period of ≈ 29.4 d as the most promising one for an additional planet in TOI-1416. Fig. B.1 shows a zoom of the BGLS periodogram near that period, which also shows the somewhat lower neighbouring RV peak with P= 27.4 days. Potentially, one of these peaks (more

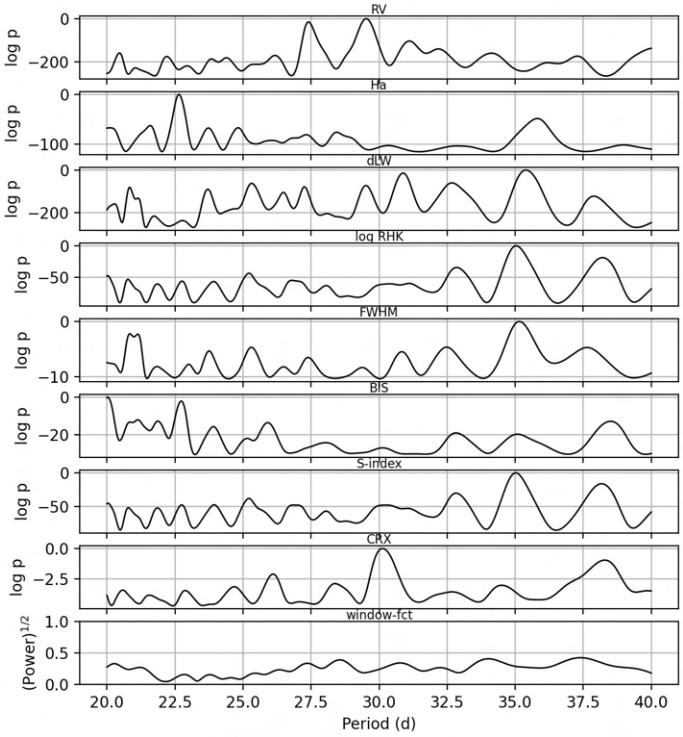

Fig. B.1: Zoomed-in view of the BGLS periodogram of Fig. 9, around the 29.4 d period of planet *c*.

likely the lower 27.4 d one) is an alias of the other one, related to each other by a seasonal sampling with a frequency of 1/365 d^{-1}.

Of principal concern regarding the interpretation of the 29.4 d peak is its close match with the length of the lunar synodic month of 29.53 d, which in the case of the 29.52 d signal found by `agatha` (see Fig. 11) is matched to the fourth digit. We also note a relative strong peak of the chromatic index (CRX) activity indicator near that period. Considering also TOI-1416's small systemic RV of $\approx$ 1.1 km s^{-1}, this leads to a strong suspicion that the observed RV peak might be due to a contamination by the Moon, or more precisely, be due to the influence of solar light that is reflected by the Moon. In Fig. B.5 we show a plot of the uncorrected *absolute* RVs of TOI-1416 against the RV of the Moon-reflected solar spectrum at the moment of observation. For differences between these two RVs of $\lessapprox$ 10 - 15 km/s, spectral lines in the reflected solar spectrum might overlap with similar lines in the target's spectrum[15] and hence might affect the measured RVs. We note that the 'above horizon' RVs in Fig. B.5 appear to be on a down-wards slope; this effect is however due to observing when TOI-1416 had a positive absolute RV preferentially during waning lunar phases (when the Moon moves towards the Earth and the Moon-reflected solar spectrum has a positive RV); whereas observations when TOI-1416 had a negative RV happened mainly at waxing lunar phases. This is a consequence of observing a target preferentially in the morning at the begin of an observing season (when a waning moon is seen), whereas towards the end of a season, a target is observed in the evening, when only a waxing Moon can be seen.

[15] Assuming a spectral line broadening of TOI-1416 of 7.0 ± 1.7 km/s (GAIA DR3, see also Frémat et al. 2022) and of the Sun of $\approx$ 5.6 km/s (Gray 2018, sum of rotational broadening and macro-turbulence).

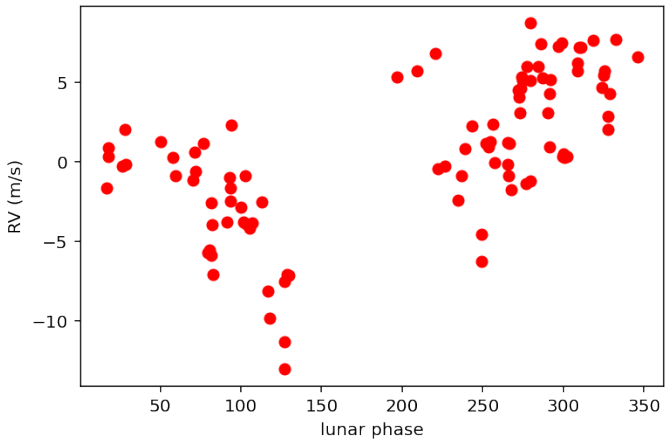

Fig. B.2: *HARPS-N* RV's folded against the lunar phase, where 0° or 360° corresponds to New Moon and 180° to Full Moon. The clumping of the RV data in two regions of lunar phases, with an avoidance of Full Moon and lesser coverage near New Moon, is a consequence of the scheduling of the *HARPS-N* observations, which were mostly executed in lunar grey time.

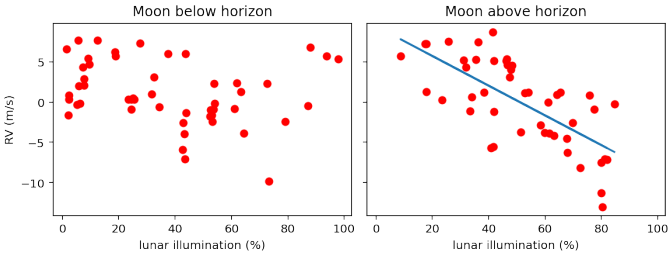

Fig. B.3: Similar to Fig. B.2, but the *HARPS-N* RVs are plotted against the lunar illumination at the time of observation, and the data are separated into panels containing only RVs that were taken when the Moon was below resp. above the horizon. The blue line in the right panel shows a linear fit to the RV versus illumination dependency, which has a correlation coefficient of -0.69.

Using the hypothesis of a contamination by the Moon, the barycentric-corrected *HARPS-N* RV values[16] were folded against the lunar synodic period, with their time-stamps converted to corresponding values of lunar phases. The result (Fig. B.2) shows a clear dependency between lunar phase and RV, with a symmetry against the full or the new Moon. However, this does not disprove that by coincidence, a planet in TOI-1416 might have a period that is very close to the lunar one. In a further step, we divided the RVs into those which are taken with the Moon being above horizon (46 RV points), and those were the Moon was below horizon[17] (50 points). Also, instead of the lunar phase, we plot the RVs against an approximation of the lunar illumination, given by the relation

$$\mathrm{illum}(\%) = (1 - \cos\phi) * 50, \qquad \text{(B.1)}$$

[16] The Keplerian signal corresponding to planet *b* was subtracted from these RVs. However, the presence or absence of the planet *b* signal does not alter the shown plots and the conclusions in any relevant way.

[17] The `skyfield` python package (Rhodes 2019) was used to calculate all values related to the Moon's position or velocity at the time of the observations

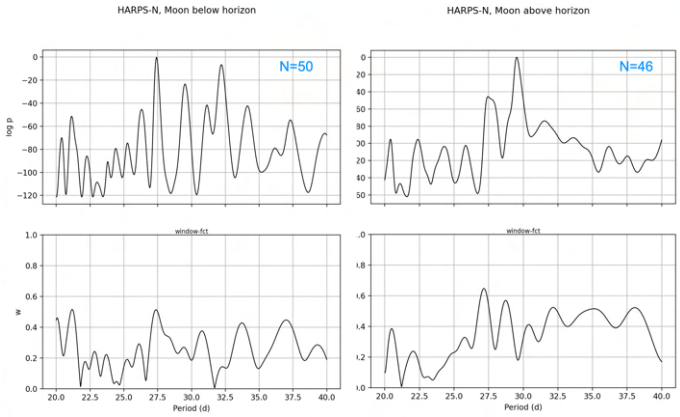

Fig. B.4: BGLS periodograms of the *HARPS-N* RVs and window functions, with the RV data being separated into those taken when the Moon was below resp. above the horizon. The blue numbers indicate the number of RV points.

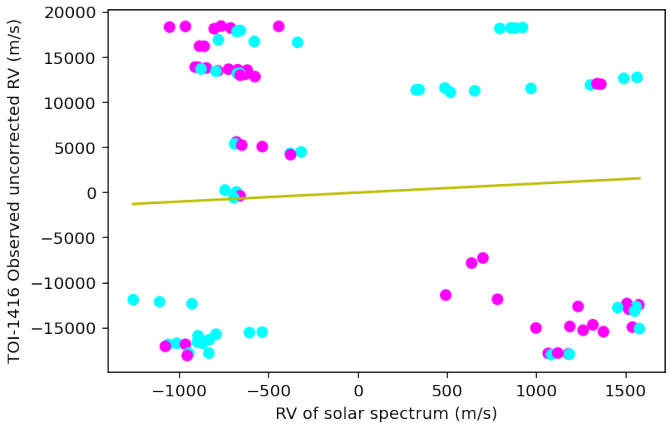

Fig. B.5: Absolute uncorrected RVs of TOI-1416 versus the RV of the Moon-reflected solar spectrum. The symbol colors indicate if the Moon was above (pink) or below the horizon (blue) at the moment of observation. The green line corresponds to identical RV values on both axes.

where ϕ is the lunar phase in radians, with $\phi = 0$ at New Moon. The result, shown in Fig B.3, shows no relevant correlation (with a correlation coefficient of -0.23) for the RVs against illumination (or phase) when the Moon was below the horizon[18]. However, a relevant correlation (with a coefficient of -0.69) is present when the Moon was above the horizon. Corresponding BGLS spectra for the RVs with/without Moon (Fig. B.4) show the 29.5 d peak very prominently in the 'above horizon' spectrum, whereas in the 'below horizon' spectrum, the 29.5 day peak is insignificant while the peak at 27.4 d has become more prominent and a second one at 32.2 d has appeared. The 32.2 d peak might be another alias of the 29.4 d peak against a yearly sampling frequency, but we also note the strongly disparate window-function between the 27.4 and the 32.2d peaks, which weakens any conclusions regarding the relations between these peaks. In any case, the prominence of the 29.5 d signal in the 'above horizon' spectrum and its disappearance in the 'below horizon' one, together with the correct phasing of this signal against the Moon's illumination is a strong indicator that the Moon is indeed responsible for this signal.

Dependencies of the RVs against the Moon altitude at the time of observations or against the angular separation of the Moon and TOI-1416 were evaluated as well, but these do not show any relevant correlation. Attempts were made to correct the above-horizon RVs against the illumination-dependency, using the linear fit shown in Fig. B.3 (and also higher-order fits, not shown) and to perform a modelling with `pyaneti` on the corrected RVs. The results were however unsatisfactory, showing only degraded fits for a Keplerian signal at either the 29.5 or at 275d period.

In order to identify potential RV shifts due to contamination by the Moon, we evaluated the effect of the Moon on the *HARPS-N* high resolution spectra's cross correlation function (CCF). Only in 65 of the 96 HARPS spectra, a second fiber (B) was placed on the sky, and only in a minority of these 65 fiber-B spectra, a signal from the Moon-reflected spectrum could be identified and the RVs be corrected against it. The difference from that correction was almost always below 1 m/s, which is small against the ≈ 5 m/s amplitude of the 29.5 d signal. Consequently, periodograms with or without this correction in the 65 *HARPS-N* RVs for which this could be done do not show relevant differences. We also investigated if there might a relation between the the RVs and the SNR in the spectra (e.g. due to sky-brightness from the Moon) but there is no correlation apparent (for the RVs taken with the most frequent exposure time of 1200 sec, a correlation coefficient of -0.05 was found). Hence, an *identifiable* effect of the Moon-reflected solar spectrum onto the measured RVs is hence very minor.

However, we consider that the 29.5 d peak in the *HARPS-N* spectrograms remains of questionable nature, and now turn our attention to the neighbouring peak at ≈ 27.4 days. Fig. B.6 shows BGLS spectrograms of all contributing instruments, and it is of note that data from the APF – which contributed with the the second largest set of RVs – have their strongest peak at 26.8 d. Also, the HIRES RVs show a peak in the same period-range, which is very broad due to the small sample of only 12 RVs. However, peaks in that range are absent in periodograms from CARMENES and iSHELL data. We note that these are also the instruments whose spectral coverage is the most red-wards (see Table 3), and a Moon-reflected reflected solar spectrum would generate a weaker signal in them. Lastly, in a combination of all available RVs, the peak at 27.4 d is the highest overall, and is significantly stronger than the one at 29.5 d.

[18] We also note that the three outliers near the lunar phase of 200° in Fig. B.2 agree now well with the other RVs; these were taken in twilight when a nearly full Moon was just below horizon

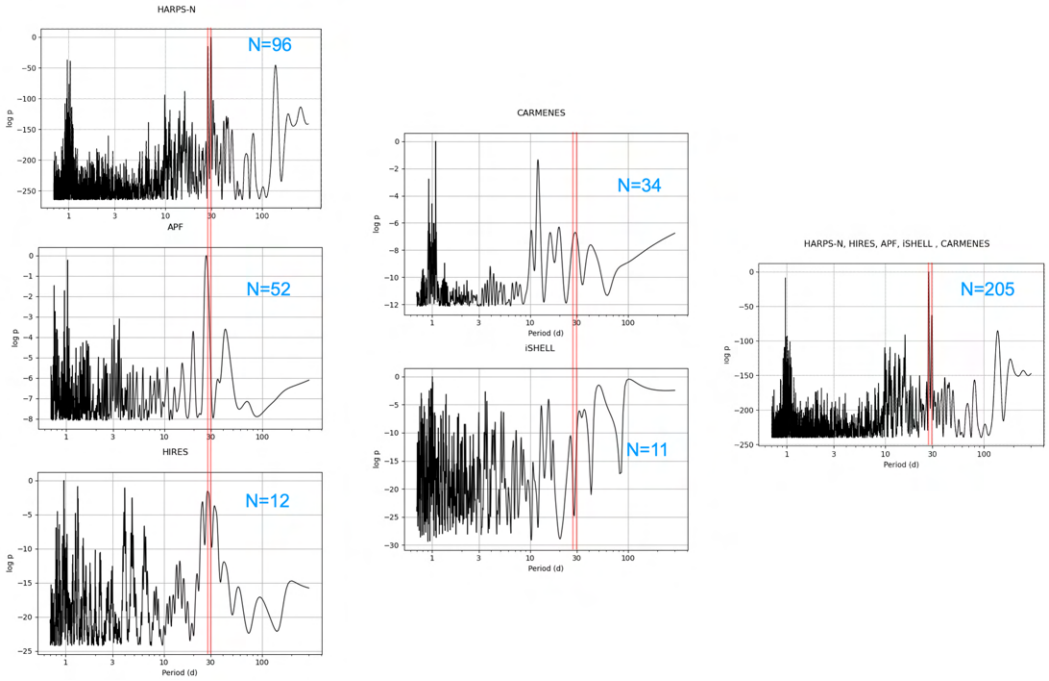

Fig. B.6: BGLS periodograms of the RVs of all contributing instruments. In the left column are those that show a peak near 27 or 29 days (vertical red lines); in the center are those that don't, and the right panel shows a periodogram with the RVs from all instruments. The blue numbers indicate the number of RVs used.

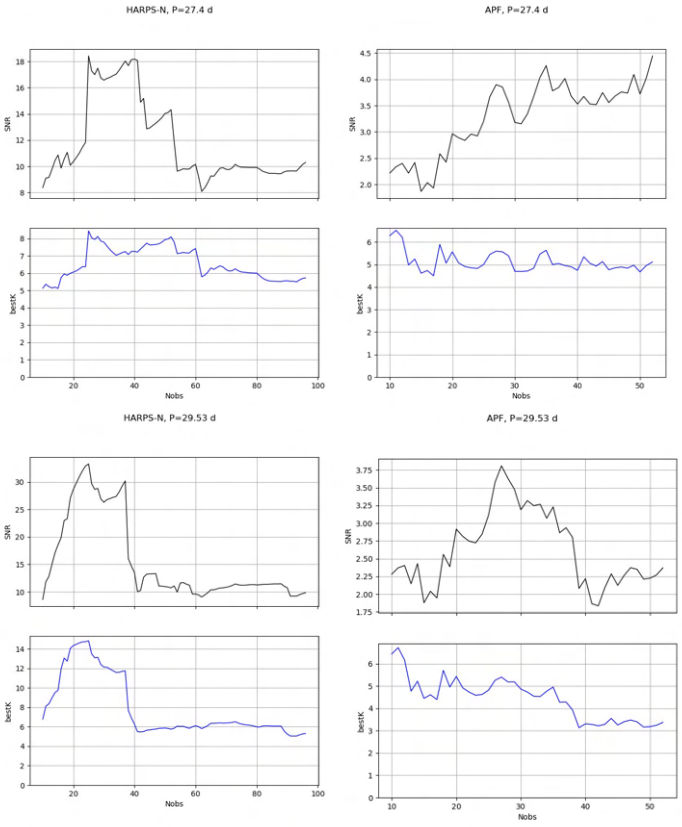

Fig. B.7: Development of the SNR (signal to noise ratio) and the best-fitting amplitude 'bestK' of RV signals of the 27.4d (top panels) and the 29.5 d period (bottom) , versus the number of RV points since the first measurement. The left panels are based on RVs data from *HARPS-N* and the right ones on data from the APF.

In Fig. B.7 we provide plots of the development of the SNR (signal to noise ratio) and the best-fitting amplitude K of RV signals at the 27.4 d and 29.53 d periods, versus the number of RV points (counting from the first measurement), following the precepts of Mortier & Collier Cameron (2017). These plots are shown for the two largest sets of RVs, those from *HARPS-N* and from the APF. In the plots for *HARPS-N*, the SNR degrades at either period near the 40th point, which is likely due to a lesser consistency of these signals across RV coverages spanning more than one observing season. On the other hand, in the plots for the APF (which cover only one observing season), the 27.4 d signal shows a steady increase in SNR and a rather constant amplitude K, whereas the 29.5 d signal shows a less consistent picture, more similar to the one from *HARPS-N*. As is stated in Sect. 5.2, fits of Keplerian orbits to the 27.4 d signal where however significantly worse than those to the 29.5 d one.

In summary, we cannot decide on a clear preference that either of these signals represent a true signal from TOI-1416, nor about their actual nature, and conclude that the RV signals with a 27.4 or 29.5 day period are at most tentative of a further planet at either of these periods.

Appendix C: Modelling of the lightcurve with `UTM/UFIT`

The normalised and gradient-corrected lightcurve around transits of planet *b*, whose preparation is described in Sect. 2, was used for transit fits using the Universal Transit Modeller / Fitter (`UTM/UFIT`, Deeg 2014)[19]. In brief, `UTM` is a lightcurve modeller for all kinds of eclipsing or transiting configurations between any number and kind of objects, such as stars, planets, moons and rings. `UFIT` was developed as a wrapper to UTM to perform fits, albeit it has been extended to accept several fur-

[19] Available at `https://github.com/hdeeg/utm_ufit/`

ther modelling modules (such as the one used for the FCO fit described in Appendix D). As the core modelling engine, UTM may use either pixelised object representations suitable for arbitrary configurations of multiple occulters, or an analytical 'fast mode' suitable for basic transit configurations, which employs the exofast_occultquad.pro routine from the EXOFAST library (Eastman et al. 2013, 2019); the latter one was used in this work. UFIT (Universal Fitter) permits the fitting of any of UTM's input parameters, either with the Amoeba algorithm or through the generation of MCMC chains using the Differential Evolution Markov Chain method of Ter Braak (2006). Its implementation is based on the EXOFAST_DEMC routine from the same library, but with an extension that permits the constraining of free parameters by several types of symmetric and asymmetric priors.

UTM permits the modelling of transit curves from any set of input parameters that is fully able to describe an orbiting system. For this work, we modelled the light-curves curves against the following set of parameters (these were also free parameters in the fits): Orbital period $P_{\rm orb}$, transit epoch T_0, scaled planetary radius $R_{\rm p}/R_\star$, the stellar density[20] $\rho_\star$ and the transit impact parameter b. Initial values for these fits were taken from the SPOC's data validation summary for TOI-1416. For the stellar limb-darkening (LD), a quadratic LD law was used, albeit for the fitting we used the q_1 and q_2 coefficients for an optimised sampling introduced by Kipping (2013). An absolute offset in flux values was a further free parameter in our fits, in order to account for potential errors in the normalisation of the flux described in Sect. 2. The orbital eccentricity was kept to zero.

Initial fits were performed with the Amoeba algorithm, leading to an intermediate transit-model that was used for the initial parameters for an MCMC sequence. First efforts without constraints on the input parameters showed significant correlation between the impact parameter, the stellar density, and the planet radius. Also, the limb-darkening parameters could only be poorly constrained from the fits. We therefore choose to impose Gaussian priors on the stellar density, taken from the adopted value in Table 5 and on the limb-darkening. For the later, we used the tabulation of LD coefficients for the TESS satellite bandpass by Claret (2017, Table 25 for the ATLAS model with plane-parallel geometry) and an interpolation to the adopted stellar parameters from Tables 4 and 5. The obtained values for a square LD law as defined in Eq. (2) of Claret (2017) were $u_1 = 0.4545 \pm 0.05$ and $u_2 = 0.1880 \pm 0.05$, which were converted into priors for the q_1 and q_2 coefficients, given in Table 7.

The final MCMC sequence consisted of 16 parallel chains that were iterated until a sufficient mixing of parameters was achieved, based on the Gelman-Rubin statistics following the precepts of Ford (2006) and Eastman et al. (2013). The resultant values (included in Table 7) were then derived from the posterior distributions of the parameters, based on 4280 steps, after a burn-in period of ≈ 1000 steps. These distributors were in all cases close to Gaussian shapes; see Fig. C.1 for this and several further diagnostic plots from the MCMC sequence. The best-fit transit model against the phase-folded input lightcurve is also included in Fig. 1.

[20] The stellar density was mainly chosen for compatibility with the set of input parameters used by pyaneti, described in Sect. 5.2. A preprocessor routine to UTM converts the stellar density into the usually used ratio of the semi-major axis versus the stellar radius, $a_{\rm p}/R_\star$, using e.g. Eq. (31) of Barragán et al. (2019).

Appendix D: Detection of the transiting planet in RV data by FCO analysis

The FCO (Floating Chunk Offset) method, developed by Hatzes et al. (2010) and Hatzes (2014), is best suited for the determination of RV amplitudes of short-periodic planets whose nightly RV variations are expected to be larger than the individual RV measures' uncertainties. In short, sets of nightly RV data – with at least two well separated data-points per night – are treated as independent chunks of data with unknown (free) RV offsets. Systematics (both instrumental and effects from other planets or stellar activity) on time-scales larger than a single night are therefore suppressed by the FCO method. RV offsets for each nightly set of RVs are then fitted against an RV model and the parameters of the best fit are obtained.

Only the RVs from *HARPS-N* were used in this analysis. The FCO method could not be applied to the data from the other telescopes, because all their RVs are single data-points in a given night (with the exception of two nights from APF, where RVs spaced about 20 min apart were obtained, which is too short a separation to be suitable for the FCO analysis). In the *HARPS-N* data, there are 28 nights in which two or more RVs were obtained, which enabled the use of 77 out of the 93 RVs from *HARPS-N*. For the fitting of the RVs, we used the same UFITfitter as described in Appendix C, but with a modelling module ufit_rvcurve for the generation of a Keplerian RV model from any number of RV data-sets, each with its own RV-offset γ_i. For the FCO method, each 'chunk' with a nightly set of two to six RVs is considered an independent set of data.

A fit using the FCO method for a candidate with an ephemeris known from transits and assuming a circular orbit is in principle very simple, as it contains as free parameters only the RV amplitude K and the nightly RV offsets γ_i, with $i = 1, ..., 28$ indexing the individual nights. However, when using UFIT with both the AMOEBA or the MCMC fitter, resultant RV amplitudes tended to be stuck close to the amplitude's initial value. This behaviour was caused by the large number of 28 nights, where each one corresponds to a free parameter γ_i. Due to this, either fitter found it difficult to vary the RV amplitude, since any improvement in the fit requires that most of the nightly RV offsets are changed *simultaneously* by the correct amounts. This is difficult to achieve for any fitting algorithm, and is an expected behaviour when free parameters are strongly correlated. We therefore kept the RV amplitude – and hence the entire RV model – fixed and fitted only for the RV offsets γ_i, which reduces the fitting task to a set of 28 simple linear fits. The input RV amplitude was then stepped through a series of suitable values and the χ^2 of each corresponding fit was logged, which led to the curve shown in Fig D.1. The minimum of this curve, and the range where χ^2 increases by 1, indicate an amplitude of $K_b = 2.14 \pm 0.35$ m s^{-1}. For the best-fit model with $K_b = 2.14$ m s^{-1}, the reduced χ^2 is 0.87 and the residuals of the RVs against the model have an *rms* of 0.82 m s^{-1}. Fig. D.2 shows the RVs of the nightly chunks against the best RV model, with a zoomed-out section across three nights of the RV time-series showing the excellent fit in that range. We note that a further FCO fit of the *HARPS-N*RVs with the open source code pyaneti[21] (Barragán et al. 2019, 2022, see also Sect. 5.2) gave a nearly identical result, of 2.12 ± 0.36 m s^{-1}.

[21] Available at https://github.com/oscaribv/pyaneti

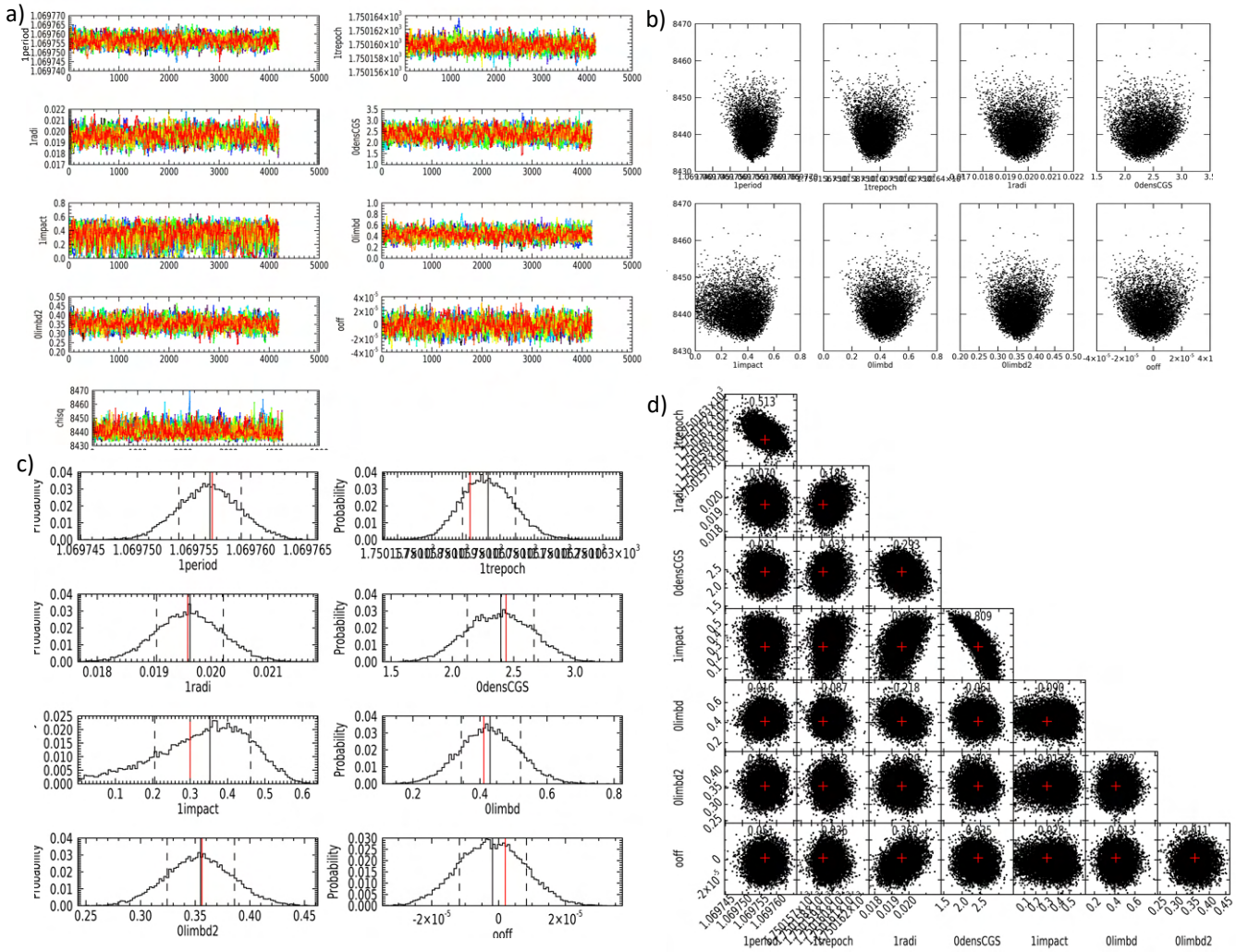

Fig. C.1: Graphical output from MCMC sequence performed by UFIT that led to the results reported in Table 7. In all panels, the parameters are indicated by the keywords used in UFIT: 1period: planet period, 1trepoch: epoch of transit, 1radi: relative planet radius, 0densCGS: stellar density in CGS units, 1impact: impact parameter, 0limbd and 0limbd2: Limdarkening coefficients q_1 and $q2$, ooff: off-transit flux-offset against zero. The sub-figures are: a) Values of the parameters against link-number of the MCMC sequence, excluding burn-in. Each MCMC chain is shown by a different color. The lowest panel shows the evaluation of the χ^2 values. b) Scatter plot of parameters versus the χ^2 value. c) Histograms of parameter distributions. The median value is shown by the vertical black line; the dashed lines delimit the 68.3% credible interval and the red line gives the value of the best fit. d) Cornerplot of the correlations among parameters. The red crosses give the values of the best fit.

Appendix E: The Neptune desert in radius or mass versus insolation or effective temperature

In Fig. E.1 we show plots similar to Fig. 16, but plotting the planets' radii and masses against the incident bolometric flux or insolation, instead of orbital period (Fig. 16). The insolation was calculated from first principles from values obtained from the NASA Exoplanet Archive. It is of note that the upper boundary of the Neptune desert is significantly sharper than in the plots against orbital period, whereas the lower boundary remains diffuse; in particular for the plot of planet masses. Given the sharper upper boundary, we propose an upper radius-limit of the Neptune desert against insolation as:

$$\log R_{hi}/R_\oplus = 0.248 \log S + 0.33\,, \qquad S \gtrsim 150, \tag{E.1}$$

where S is the insolation relative to the Earth's insolation. The corresponding lower limit is then

$$\log R_{lo}/R_\oplus = \begin{cases} -0.51 \log S + 1.74\,, & 150 \lesssim S \lesssim 1000 \\ 0.20\,, & S \gtrsim 1000, \end{cases} \tag{E.2}$$

where the same limit of $R_{lo} = 1.60 R_\oplus$ as given in Sect. 6 for very short orbital periods applies also to the strongest insolations. For the limit of the desert against mass, there are much fewer planets with mass measurements, and we only derive an upper limit of

$$\log M_{hi}/M_{Jup} = 0.74 \log S - 2.35\,, \qquad S \gtrsim 150, \tag{E.3}$$

whereas a lower limit cannot be discerned with reliability, given the small sample of known short-period low-mass planets, that is furthermore suffering a strong selection effect against detectability towards smaller masses. In Fig.E.1 we hence indicate only the same lower mass limit that is given in Sect. 6 for very short orbital periods, namely $M_{lo} = 8.9 M_\oplus$, resp. $\log M_{lo}/M_{\rm jup} = -1.55$.

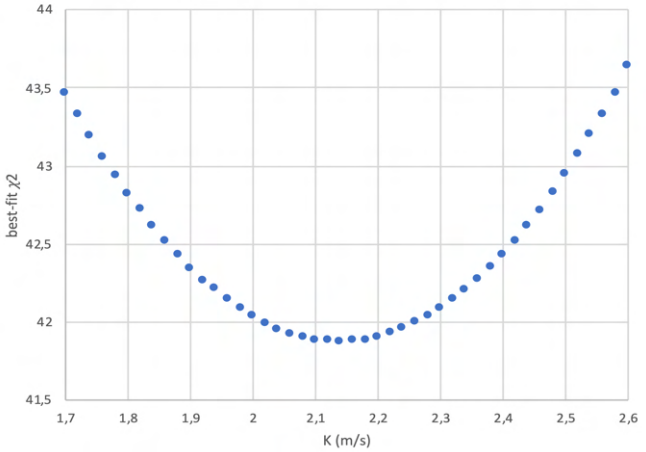

Fig. D.1: Best-fit χ^2 from FCO fits of *HARPS-N* data against RV models of TOI-1416b with fixed RV-amplitudes K.

In above limits for both radius and mass, we maintain the gradients of the limits against period by Mazeh et al. (2016), after multiplication of $\log P$ with a factor of -4/3, which arises from the dependency of S on the period.

For convenience, we also provide the same limits against the planets' effective temperature $T_{\rm eff}$, using the conversion $T_{\rm eff} = (S)^{1/4}\ 255$ K, with the 255 K corresponding to the effective temperature of the Earth. We then obtain for the limits of radius against $T_{\rm eff}$:

$$\log R_{hi}/R_\oplus = 0.99 \log T_{\rm eff} - 2.72\ , \qquad T_{\rm eff} \gtrsim 900K \tag{E.4}$$

$$\log R_{lo}/R_\oplus = \begin{cases} -2.04 \log T_{\rm eff} - 3.17\ , & 900K \lesssim T_{\rm eff} \lesssim 1450K \\ 0.20\ , & T_{\rm eff} \gtrsim 1450K \end{cases} \tag{E.5}$$

and for the upper mass limit of the desert:

$$\log M_{hi}/M_{Jup} = 3.0 \log T_{\rm eff} - 9.5\ , \qquad T_{\rm eff} \gtrsim 900K, \tag{E.6}$$

with the same lower limit as indicated previously against insolation. With $logM/M_\oplus = 2.50 \log M/M_{Jup}$, we may easily convert the desert mass limits to the units of Earth masses used in Fig E.1.

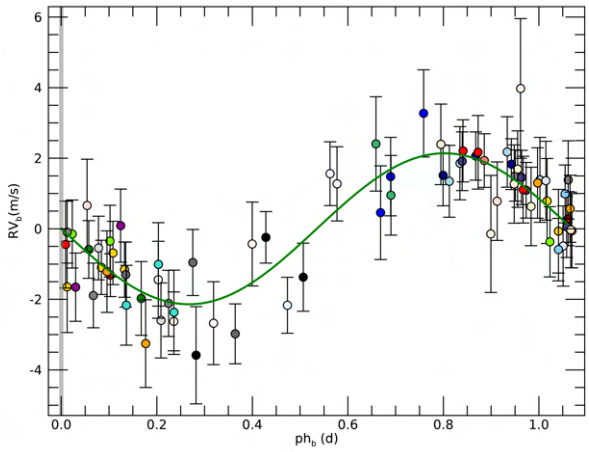

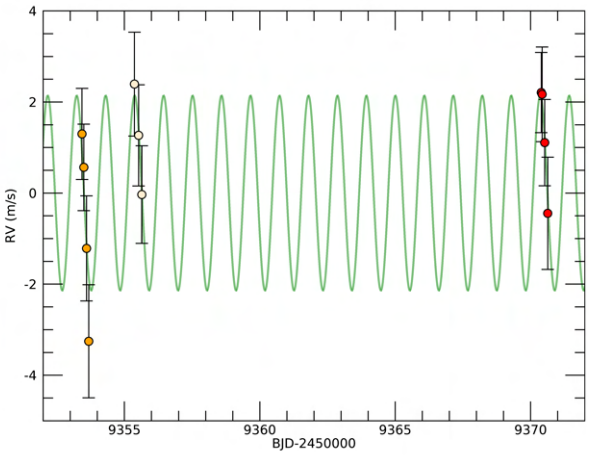

Fig. D.2: Upper panel: The phase-folded RV model (green line) of TOI-1416 b which corresponds to the best fit from the FCO method, obtained by vertically offsetting nightly chunks of RV data against the model. RV points from the same nights have identical colours. Lower panel: A small section of the RV model plotted against time, with RVs from three different nights.

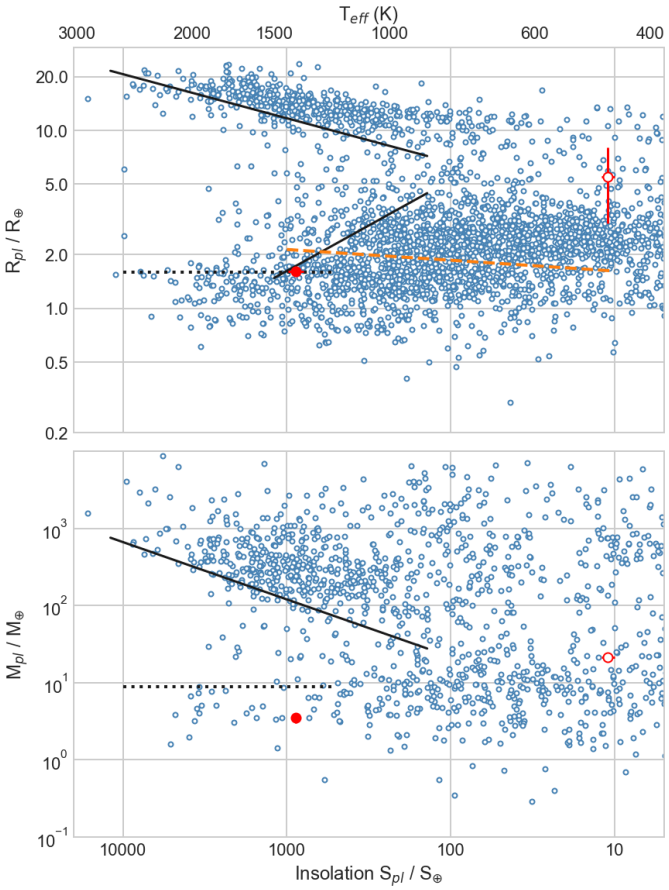

Fig. E.1: Similar to Fig. 16, but with planet radii (top panel) and masses (bottom panel) plotted against the planets' insolation (lower X-axis) **and their effective temperature (upper X-axis)**. The solid black lines show the delineation of the Neptune Desert against insolation resp. $T_{\rm eff}$, whereas the horizontal dotted black lines show the same lower limits to the Neptune Desert as those proposed for periods of $P \lesssim 2d$. The dashed orange line in the upper panel indicates the radius valley against insolation from Petigura et al. (2022). TOI-1416 *b* is indicated by the filled red circle and *c* by the unfilled one.

Appendix F: Further figures mentioned in main text

- Fig. F.1 gives a comparison of the RVs measured with *HARPS-N* using the DRS and the `serval` pipelines.
- Fig. F.2 shows the output of the `pyaneti` joint-fit for Model 3, with two planets *b* and *c*.

List of Objects

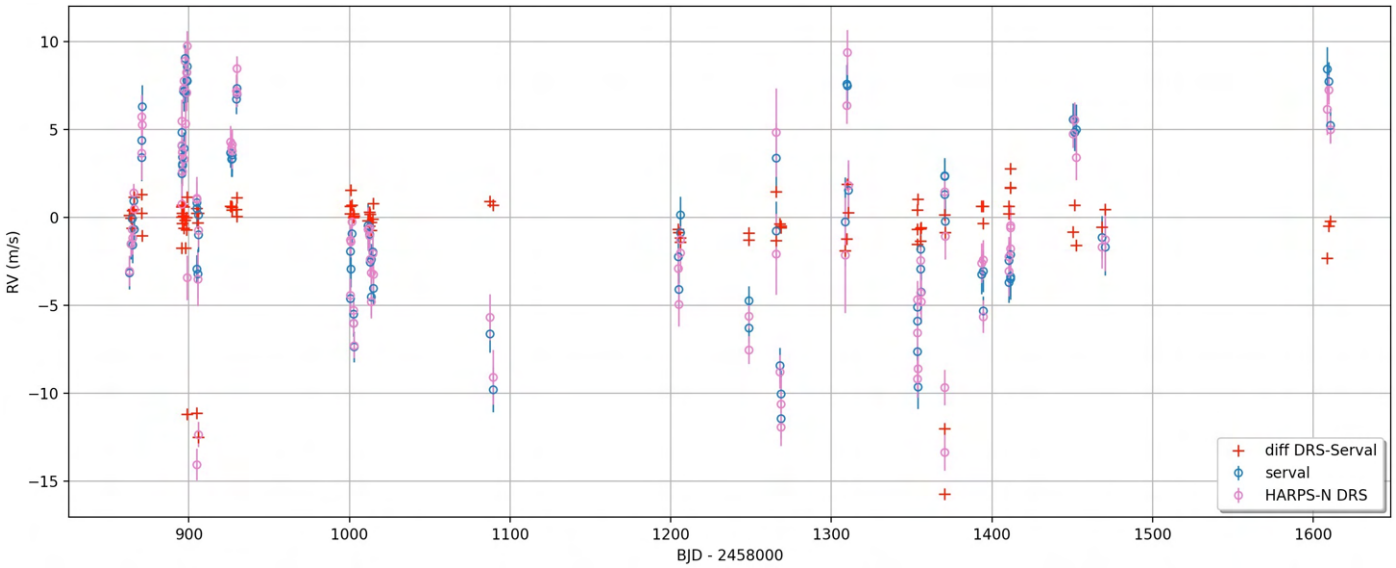

Fig. F.1: Comparison between *HARPS-N* RVs measured with the *HARPS-N* DRS from CCFs (open red circles) and with `serval` (open green circles). The red crosses show the difference between the two data-sets. The five points in which this difference is significantly negative correspond to exposures that were prematurely terminated, and which are not correctly processed by the DRS. Both data-sets have been averaged to zero without considering these five points. The difference between the two data-sets has a standard deviation of 0.92 m s^{-1} (excluding again these five points).

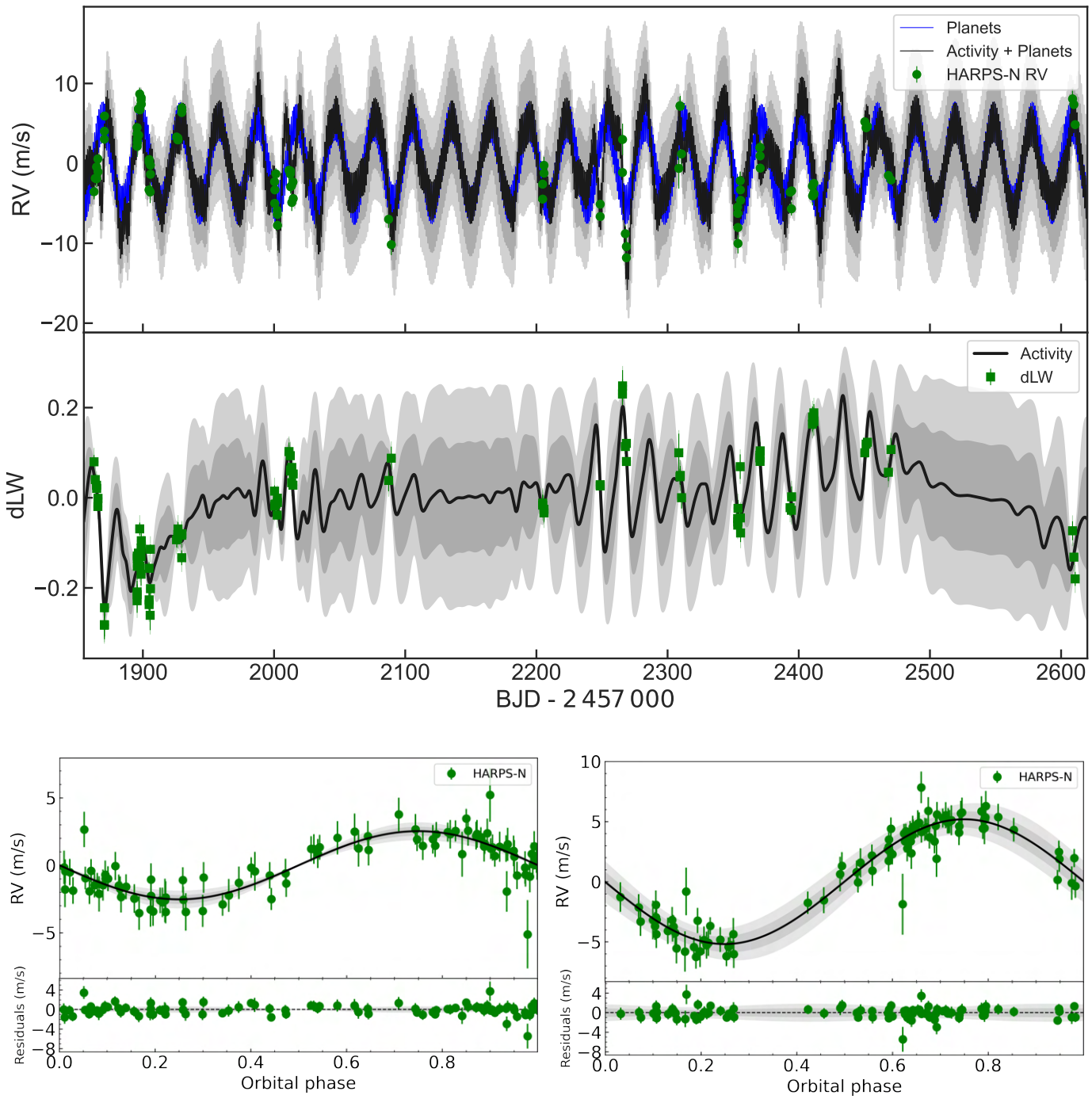

Fig. F.2: Like Fig. 13, but for Model 3 with the additional fit for a Keplerian signal with the lunar synodic period (29.53d). The lower left panel is again for the transiting planet *b*, while the lower right panel shows the RVs folded over the period of the additional signal. A similar plot for Model 2 does not show any relevant differences to the shown one.